The K/T boundary of Gams (Eastern Alps, Austria) and the nature of terminal Cretaceous mass extinction

Andrei F. Grachev
Editor

At the end of the Cretaceous (65 Ma ago) the Earth suffered the great biological crisis when estimated 60% of the former species, among them the dinosaurs, became extinct. More than 3000 papers were published for the last 30 years, concerning the discussion this question but the decision remains unresolved. Authors propose the new approach to this problem based on the detailed micropalaeontological, lithological, geochemical, nanomineralogical, isotopic and petromagnetic investigations of the unique sedimentary sequence at the Cretaceous-Paleogene boundary in the Gams area, Eastern Alps, Austria.

The conclusions drawn from the results of analysis principally differ from all preexisting data on the transitional layer between the Cretaceous and Paleogene and provide another look at the reasons for the mass extinction of living organisms at 65 Ma ago. These data eliminate the need for opposing volcanism to an impact event: both took place, but the changes in the biota were induced by volcanism, as also was the appearance of the Ir anomaly itself, whereas the fall of a cosmic body occurred approximately 500–800 years later.

Am Ende der Kreidezeit, vor 65 Millionen Jahren, erlebte die Erde eine bedeutende biologische Krise: Geschätzte 60% der Arten starben aus, unter ihnen die Dinosaurier. Obwohl über 3000 Publikationen zu diesem Thema in den letzten 30 Jahren erschienen sind, blieb die Ursache weiter im Dunkeln. In dem vorliegenden Band wird das Thema anhand mikropaläontologischer, lithologischer, geochemischer, nanomineralogischer, isotopischer und petromagnetischer Untersuchungen neu beleuchtet. Grundlage ist die einzigartige Abfolge des Grenzbereichs Kreide/Paläogen nahe des in den Ostalpen (Österreich) gelegenen Ortes Gams.

Die Schlußfolgerungen aus den Untersuchungen unterscheiden sich prinzipiell von früheren Interpretationen der Genzschicht an der Kreide/Paläogen-Grenze: Durch die neuen Ergebnisse wird die Diskussion Vulkanismus oder Impakt obsolet: Beide Vorgänge fanden statt, der große Einschnitt bei den Biota wurde so wie die Iridium-Anomalie jedoch durch den Vulkanismus verursacht und nicht durch einen kosmischen Körper. Dieser hat seine Spuren erst 500 800 Jahre später hinterlassen.

DOI: 10.2205/2009-GAMSbook

This book is published by The Geological Survey of Austria in cooperation with the Geophysical Center of the Russian Academy of Sciences. The camera-ready copy of this book is produced from electronic version composed using LaTeX2$_\varepsilon$ typesetting system under `gamsbook` template.

Preface

In mid-60s of the XX century I was privileged to get acquainted with Lev Gumiljev who, at that time, was overwhelmed by the influence of geographical environment on the development of the society. His ideas, stating that such periodic catastrophes as sharp changes of the climate, leading to drought and the disappearance of natural environment for planting and breeding, had caused mass, up to the millions, migration of people, wars and changes of state boundaries. These ideas were revolutionary: they neglected "the role of classes" and "class struggle". While talking to Lev Gumiljev, I was thinking that a time would come when I also get into studying a similar problem related to the influence of geographical environment on the biosphere in the geological Past.

My professional preferences, as a geologist, were related to tectonics and magmatism, as well as disclosing the evolution of these processes in the history of the Earth. In my lectures, which I had been delivering for 20 years in the Leningrad University, I, quite naturally, touched upon the problem of mass extinctions in Phanerozoic. The entire geological chronicle is devoted to them. Nevertheless, I was not focussing on this problem, being of the opinion that this was a purely palaeontological problem.

I became intrigued by the problem of catastrophic events in the history of the Earth much later, because of studying mantle plumes, especially one of its main manifestations – magmatic activity. Once, in a second-hand book-shop, I bought a book by Georges Cuvier "Cataclysms on the surface of the Earth" ("Discours sur les revolutions de la surface du globe"), translated into Russian by the Publishing House "Academy" in 1937. The idea about the role of catastrophic extinctions in the history of the Earth, as presented by G. Cuvier, strongly opposed the views of Ch. Lyell and his successors on slow-pace changes of the biosphere.

Knowing that "Something is rotten in the state of Denmark," I decided to find out how mantle plume volcanism influences the bioshpere. But, by this time, the ideas of G. Cuvier were unexpectedly supported by the study of L. Alvarez, Nobel prize-winner in physics. L. Alvarez and his colleagues identified anomalous concentrations of iridium, clearly exceeding known and maximal presences of these elements in the lithosphere, in the layers of the mountain rock at the K/T boundary (65 May ago) in the Gubbio (Italy) and Stevns-Klint sections (Denmark). They presumed that those anomalies were connected to the collision of a large-sized meteorite (or an asteroid) with the Earth which could have happened at that time: such bodies have the same amount of iridium as the layers at the K/T boundary. Such event could have caused the conditions of a "nuclear winter" as its consequence, within its first days leading to the extinction of the majority of terrestrial and ocean organisms, and the process of photosynthesis would have been ceased for many years.

The reaction of the global scientific community towards the article published by L. Alvarez et al. was unanimous: according to numerous follow-up publications, a high presence of iridium was found in practically all cross-sections at the K/T boundary. Doubts expressed by a number of scientists were not taken into account, though there were obvious grounds for them!

In 2000 I published an article in the magazine "Earth and Universe", where I presented the evidence of the connection between the volcanism of mantle plumes and mass extinctions within the last 540 Mar: those could not be explained every time by the fall of asteroids.

The desire to find by myself the solution to this problem led to the decision to study a cross-section with a clearly expressed iridium anomaly. Inside Russia, after the collapse of the Soviet Union, it was impossible to find a full cross-section at the K/T boundary, and a cross-section which was considered as closest to Moscow was located in Austria. In 2002, after having discussed the problem with O. Korchagin, paleontologist from the Geological Institute of the Russian Academy of Sciences, and was specializing in studying of foraminifera – leading one-cellar organisms, which permit to identify the age of marine sediments, we decided to combine our efforts in studying one of such cross-sections.

Two important circumstances contributed to the realization of this idea.

The first one was of family nature. My wife, Vera, was a diplomat and worked at that time in Vienna. She was very helpful in organizing "the base", as geologists say, and in creating a general atmosphere favorable for our work.

The second one was related to the Natural History Museum in Vienna, which provided us with a monolith cut out of a cross-section with an excellent and clearly expressed layer at the K/T boundary of Gams (officially Gams bei Hieflau) in Austria for the research. In the course of all those four years we have been enjoying the support and attention of our Austrian colleagues – Dr. Herbert Summesberger, Dr. Mathias Harzhauser, and Dr. Heinz Kollmann.

Having the monolith we could study the transitional layer like the surgeon in operating theatre, that it was impossible to do at the outcrop. The first results presented to the wide audience at the Museum of Natural history in Vienna on 6 February 2006, were unexpected: we found that extinction was induced by volcanism before an impact event.

In following years we studied another two outcrops in Gams to be sure that our results are correct. All these data are presented in this book.

We have to mention that we enjoyed constant attention to our research paid by the leaderships of the National Park and European Geopark Eisenwurzen in St. Gallen: Reinhard Mitterbaeck and Katharina Weiskopf and the Mayors of Gams: Hermann Lußmann and Erich Reiter.

We are grateful to S. Lyapunov, I. Kamensky, A. Kouchinsky, B. Krupskaya, N. Gorkova, I. Ipat'eva, A. Savichev, V. Zlobin, N. Scherbatcheva, A. Nekrasov, A. Gorbunov from Geological Institute, Russian Academy of Sciences, for their help in the preparations of samples and the chemical and isotopical study of the Gams section samples.

The electroinc version of this book was prepared at the Geophysical Center RAS by V. Nechitailenko (developing of template and associated software and designing CD and online versions) and T. Prisvetlaya (initial typesetting and technical proofreading). I greatly appreciate to Vitaly Nechitailenko for his comments and advices related to publishing of this book.

This study was financially supported by Program 5 "Interaction of a Mantle Plume with the Lithosphere" of the Division of Earth Sciences, Russian Academy of Sciences, and Grant RSH-1901.2003.5 from the President of the Russian Federation for support of research schools and Grant 030564303 of the Russian Basic Research Foundation.

Andrei F. Grachev, Editor

February 2009, Moscow–Vienna

Contents

The great tragedy of science – the slaying of a beautiful hypothesis by an ugly fact.
(T. H. Huxley, 1870)

Introduction

The discovery of anomalies of Ir and other platinum-group elements in clays at the boundary between the Cretaceous and Paleogene (the so-called Cretaceous-Tertiary, or K/T boundary) [*Alvarez et al.*, 1980, 1984; *Ganapathy et al.*, 1981; *Preisinger et al.*, 1986; *Smit, Hertogen*, 1980] gave rise to the paradigm that the mass extinction of the biota had been induced by an impact event and gave an impetus for studying this boundary throughout the world (see *A Rubey Colloquium*, 2002). This hypothesis was supported by the reasonable idea that high Ir concentrations, much higher than those know in terrestrial rocks, were related to the fall of a meteorite (or an asteroid) [*Alvarez et al.*, 1980].

The establishment of the impact paradigm of the mass extinction was facilitated by the discovery of the world's largest Chicxulub crater in Yucatan, Mexico [*Hildebrand et al.*, 1991; *Smith et al.*, 1992]. Moreover, some rock units at the K/T boundary were found out to bear shocked quartz and coesite [*Bohor et al.*, 1984; *Koeberl*, 1997; *Preisinger et al.*, 1986; *A Rubey Colloquium*, 2002, and several others].

Later papers by *Alvarez et al.* [1980] demonstrated that the Ir anomaly in the transitional layer at the K/T boundary was present in virtually all of the inspected rock sequences, both in continents and in deep-sea drilling holes in oceans [*Alvarez et al.*, 1992; *Hsu et al.*, 1982; *Kyte, Bostwick*, 1995; and several others].

The problem of the mass extinction at the Cretaceous-Paleogene boundary seemed to be resolved, although an almost unanimous consensus was distorted by some researchers who doubted the validity of the impact hypothesis and put forth arguments in support of magmatic (related to a mantle plume volcanism) reasons for the development of the transitional layer [*Officer, Drake*, 1985; *Officer et al.*, 1987; *Zoller et al.*, 1983]. In particular, several scientists pointed to data on the multiplicity of Ir anomalies and the possibility of explaining the unusual geochemistry of the transitional layer at the K/T boundary by the effect of volcanic activity [*Officer et al.*, 1987].

Research in early 1990s provided new, more detailed information on transitional layers at the K/T boundary. Along with new finds of shocked quartz in the transitional layers of different regions of the world, such high-pressure minerals as coesite and stishovite were found, as well as spinel with high (>5%) Ni concentration and diamond [*Leroux et al.*, 1995; *Preisinger et al.*, 2002; *Carlisle, Braman*, 1991; *Hough et al.*, 1997]. Although all of these materials considered together provided irrefutable evidence of an impact event, the mechanisms relating it to the mass extinction of the biota remained uncertain.

Meanwhile newly obtained data indicated that Ir anomalies could occur both below and above the K/T boundary [*Ellwood et al.*, 2003; *Graup, Spettel*, 1989; *Tandon*, 2002; *Zhao et al.*, 2002; and others]. Furthermore, Ir anomalies were found in rocks with no relation at all to the Cretaceous-Paleogene boundary [*Dolenec et*

al., 2000; *Keller, Stinnesbeck,* 2000; and others]. As Keller has recently shown [*Keller,* 2008], iridium anomalies are not unique and therefore not infallible K/T markers. Hence, the Ir anomaly itself, which was originally considered one of the milestone of the impact hypothesis for the mass extinction of living organisms at the K/T boundary [*Alvarez et al.,* 1980], could not be anymore (in light of newly obtained data) regarded as a geochemical indicator of such phenomena. It is also pertinent to recall that data on the Permian-Triassic boundary also did not confirm that the reasons for the extinction of that biota were of an impact [*Zhou, Kyte,* 1988].

The idea that the fundamental changes in the biota at the K/T boundary were related to volcanic processes became topical again [*Grachev,* 2000a, 2000b], particularly after the detailed studying of anomalies of Ir and other PGE in plume-related basalts in Greenland, at the British Islands, and Deccan [*Phillip et al.,* 2001; *Power et al.,* 2003; *Crocket, Poul,* 2004], which made it possible to explain the high Ir concentrations in sediments by the transportation of this element by aerosols during volcanic eruptions, as was earlier hypothesized in [*Zoller et al.,* 1983].

All of these discrepancies became so obvious that W. Alvarez, one of the main proponents of the impact hypothesis, admitted that "...although I have long been a proponent of impact at the K/T boundary, I hold no grief for all extinctions being caused by impact. If the evidence for a flood-extinction link is compelling, we should accept that conclusion" [*Alvarez,* 2002, p. 3]. He also wrote: "It would be useful to the community of researchers to have a compilation of evidence for impact and for volcanism at prominent extinction levels. This is probably something that should be prepared by a group of workers experienced in the field" [*Alvarez,* 2002, p. 4].

It is also worth mentioning two other approaches to the problem of relations between impact events and plume magmatism.

In one of them, an attempt was undertaken to relate the onset of plume magmatism to the decompression and melting of deep lithospheric layers under the effect of the development of craters of about 100 km diameter. Here the impact itself is considered to be a triggering mechanism for the origin of a plume [*Jones et al.,* 2003; and others]. Aside from the implausibility of this process from the physical standpoint [*Molodenskii,* 2005], there is direct and only one evidence of the impossibility of this process: the He isotopic signature of plume basalts. As is well known, these basalts have a $^3He/^4He$ ratio more than 20×10^{-6}, which could be caused by the uprise of the melts from depths of more than 670 km, i.e., from the lower mantle or, more probably, from the core-mantle boundary (D″ layer) [*Grachev,* 2000; and references therein].

In the latter instance, perhaps because no scientifically plausible resolution of the mass extinction could be found, it was proposed to regard mass extinction in the Phanerozoic as an accidental coincidence with coeval plume magmatism and impact events [*White, Saunders,* 2005].

Nevertheless, the problem remains unsettled as of yet. How can one explain the fact that the study of the transitional layers at the K/T boundary over the past 25 years, with the use of state-of-the-art analytical equipment and techniques, did not result in the solution of this problem?

In our opinion, the answer to this question stems from the methods employed in these studies: the layer was inspected as a unique item, and its characteristics obtained with different techniques were ascribed to the whole thickness of this rock unit. Given the thickness of the transitional layer at the K/T boundary varying from 1 cm [*Preisinger et al.,* 1986] to 20 cm [*Luciani,* 2002], sampling sites were commonly spaced 5–10 cm apart, or 1–2 cm apart near the boundary [*Gardin,* 2002; *Keller et al.,* 2002]. With regard for the known sedimentation rates of about 2 cm per 1000 years [*Stuben et al.,* 2002 and references therein], the transitional layers should have been produced over time spans from 500 to 10,000 years.

The time during which an impact event could affect the character of sedimentation can be estimated from the numerical simulations of the nuclear winter scenario, according to which the duration of this event at the Earth's surface should range from 10 to 30 days [*Turko et al.,* 1984]. Because of this, even if such events took place in the geologic past, and even if some records of them could be discerned in sediments, evidence of these events cannot be identified visually but require a detailed and scrupulous investigation.

Near the beginning of our investigations in the Gams section (Eastern Alps, Austria) we have provided another look at the reasons for the mass extinction at 65 Ma [*Grachev et al.,* 2005]. These first data rejected the need for opposing volcanism to an impact event: both took place, but the changes in the biota were induced by volcanism before an impact event. In following papers we adduced a new proof suggested the truth of such point of view [*Grachev et al.,* 2006a, 2007a, 2007b, 2008a, 2008b, 2008c; *Pechersky et al.,* 2006a, 2008]. This monograph sums up all results of our investigations of the K/T boundary in the Gams stratigraphic sequence.

Chapter 1. A Review of the Geology of the Late Cretaceous-Paleogene Basin of Gams (Eastern Alps, Austria)

1.1 Introduction

Gams, officially bearing the suffix "bei Hieflau" (near Hieflau) to distinguish it from other communities having the same name, is a village of approximately 600 inhabitants. It is located in the north of the Austrian province of Styria amid the Northern Calcareous Alps which are rising in its surroundings up to 2600 m. To ensure the protection of the area, Gams and other 5 communities have merged to the Nature Park Styrian Eisenwurzen. Because of its exceptional geological heritage and its public activities, the Nature Park has been accepted as a member of the European Geoparks Network in 2002 and consequently as a member of the Global Geoparks Network of UNESCO. A permanent exhibition and trails interpreting the local geology make Gams the centre of geological interpretation of the Park.

In general, the significance of the geological heritage becomes evident through scientific research. First geological explorations of the Park area date back to the first quarter of the 19th century. With the accumulation of knowledge, scientific methods and interpretations have changed almost constantly. Most impetus comes from findings which contradict previous theories. We believe that the observations presented in this volume will stimulate the discussion on the K/T boundary.

1.2 Outline of the Tectonic History

The Northern Calcareous Alps extend from west to east almost through the whole of Austria and adjacent parts of the German bundesland Bavaria. They form a thrust belt which is part of the Austroalpine unit and has originally been deposited on the Austroalpine microplate in the northwest of the Tethys Ocean [*Mandl,* 2000; *Wagreich,* 1993]. Deformation phases of folding and thrusting have removed the series of its crustal basement and have created a nappe complex of 20–50 km in width and approximately 500 km in length. In the north, it rests with overthrust contact on the Rhenodanubian Flysch which had been deposited in the northern segment of the Penninic Ocean trough. In the south it overlies, mostly with tectonic contact, the Variscan Greywacke Zone. A detailed description of the complex tectonic processes is given by *Wagreich, Decker* [2002].

Late Cretaceous uplift followed by significant subsidence has led to the formation of limited areas of increased subsidence during late Cretaceous-Paleogene times (Figure 1.1). After the community of Gosau in Upper Austria which is located on the largest of these sediment traps they are traditionally called Gosau Basins. Their sediments are summarized under the lithostratigraphic term Gosau Group (Gosau Beds or Gosauschichten of the earlier literature). Depending on the subsidence history, the sediment content of the individual basins and the time slice represented by them varies and boundaries between lithostratigraphic units are diachronous.

Resting unconformly on sediments which have undergone earlier tectonic deformations, the Gosau sedimentary cycle began in the Late Turonian and ended in the Lower Eocene. The Gosau Group is subdivided into the Lower and the Upper Gosau subgroups [*Faupl et al.,* 1987; *Piller et al.,* 2004]. The Lower Gosau Subgroup comprises a succession of continental to shallow marine sediments. They were deposited in small, partly fault-bounded extensional and/or pull-apart basins [*Sanders,* 1998; *Wagreich,* 1993; *Wagreich, Faupl,* 1994]. Facies and thickness of units changes horizontally within short distances.

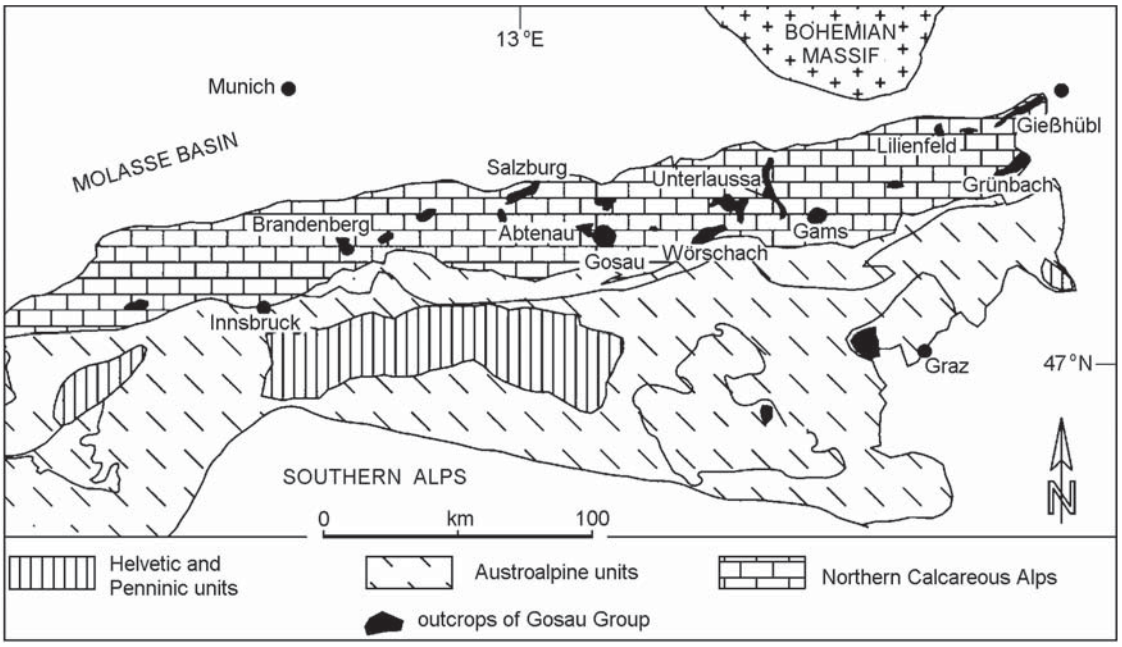

Figure 1.1. The distribution of Gosau Basins in the Eastern Alps [after *Wagreich, Krenmayer,* 1993].

The Upper Gosau subgroup (Santonian/Campanian – Lower Eocene) is characterized by pelagic sediments which indicate a general deepening [*Wagreich,* 1993, 1995]. This resulted in an overstepping of the formerly isolated basins. Subsidence during the deposition of the Upper Gosau subgroup is explained with tectonic erosion of the Austroalpine units as a consequence of subduction and/or underthrusting [*Wagreich, Decker,* 2002].

1.3 The Cretaceous-Paleogene Boundary in Alpine Deposits

First indications on Paleogene in the Gosau Group were given by *Kühn* [1930]. He deduced a Danian age (considered as terminal Cretaceous at that time) of the Zwieselalm Formation which forms the top of the sequence. Micropalaeontological studies in the Basin of Gosau by *Ganns, Knipscheer* [1954], *Küpper* [1956], and on Gams by *Wicher* [1956], gave a more comprehensive picture of Paleogene deposits. By applying planktonic foraminifera in a large scale, this was confirmed later by *Herm* [1962], and *Hillebrandt* [1962], for the Lattengebirge (Bavaria), *Kollmann* [1963, 1964], for the Gams area and by *Wille-Janoschek* [1996], for the western part of the Gosau area.

Stimulated by the world-wide discussion initiated by *Alvarez et al.* [1980], the nature of the K/T boundary was investigated in the Gosau Group in greater detail. There are three Gosau Basins where the K/T boundary transition layer has been traced. From the name-giving Basin of Gosau, which extends over the boundaries of the Austrian provinces Upper Austria and Salzburg, two sections have been described: the Elendgraben close to the village of Rußbach [*Preisinger et al.*, 1986] and the Rotwandgraben [*Peryt et al.*, 1993]. Herm and others, provided a micro- and nannostratigraphical frame for the K/T boundary layers of the Wasserfallgraben in the Lattengebirge (Bavarian Alps). A study by *Graup, Spettel,* [1989], revealed three iridium peaks in this section, of which one is located 16 cm below the K/T boundary.

The third Gosau basin is that of Gams which is the subject of this monograph. *Lahodynsky* [1988a, 1988b], has provided a detailed lithological section through the K/T boundary of the Knappengraben (Gams 1 in this monograph) which he had excavated together with H. Stradner in 1986. *Stradner, Rögl* [1988], reported about the microfauna and nannoflora of this section and emphasized the completeness of the stratigraphical record.

1.4 The Gosau Group of Gams

Because of its generally soft clastic rocks, the Gosau Basin of Gams (for the location see Figure 1.1) forms a morphological depression within carbonates of earlier Mesozoic age (Figure 1.2). The basin consists actually of two sedimentary areas of different subsidence history [*Kollmann,* 1963; *Kollmann, Summesberger,* 1982]. They are arranged in E-W direction and are sepa-

rated by a broad tectonic uplift zone of mainly Permian/Lower Triassic sediments. Following deposition, sediments have been compressed and overthrusted in the south by a higher tectonic unit of the Northern Calcareous Alps [*Kollmann,* 1964]. The tectonic contact was exposed in a tunnel for a power station at the very west of the western sedimentary area [*Spaun,* 1968].

The western sedimentary area (Figure 1.2) is broader than the eastern and partly covered by Pleistocene alluvial deposits of the river Enns. The thickness of its sediments is approximately 1150 m [*Kollmann,* 1963]. The sediments of the western Gams Basin belong almost exclusively to the Lower Gosau Subgoup [*Wagreich,* 2004]. Biostratigraphically, they represent a time interval between Late Turonian and Santonian [*Summesberger,* 1985; *Summesberger, Kennedy,* 1966]. From base to top, the following formations can be distinguished (see Figure 2.1):

Kreuzgraben Formation. The represent a series of coarse conglomerates first described from the Basin of Gosau by *Weigel* [1937].

Akogl Formation. This series of coal-bearing siltstones which is rich in megafossils was described from the Gams area by *Kollmann, Sachsenhofer* [1998].

Noth Formation. It consists of a series of serpentinitic sands and sandstones with coal seams and rudist bioherms and was established by *Siegl-Farkas, Wagreich* [1996] in the Gams Basin.

Grabenbach Formation. This series of shales and marlstones has been established in the Gosau area by *Weigel* [1937].

The sedimentation ends in the western Gams Basin with a unfavourably exposed, thin series of rudist-bearing sandy limestones on top of conglomerates of the Kreuzgraben Fm. They were deposited unconformly on a relief of the Grabenbach Formation (outcrop group Radstatthöhe – Übergangerhöhe) and are allocated to the Krimpenbach Formation by *Wagreich* [2004]. $^{87}Sr/^{86}Sr$ ratios in rudist valves indicate an age of 85.5 Ma which corresponds with the Lower Santonian (Th. Steuber, personal communication).

In the eastern sedimentary area (Figure 1.2), two distinct cycles have been recorded [*Summesberger et al.,* 1999; *Wagreich,* 2004]: The Krimpenbach Formation and the Upper Gosau Subgroup. The Krimpenbach Formation [*Wagreich,* 1994] is restricted to the Gams area and has a total thickness of 80 m. *Wicher* [1956], was first to mention this series which rests unconformly on earlier Mesozoic carbonates and clastic sediments of the Lower Gosau Subgroup (see next chapter). It displays a variety of lithologies including conglomerates, siliciclastic sandstones, calcarenites, grey siltstones and marlstones. Alluvial-fluvial conglomerates at the base indicate subaerial exposure and erosion following an uplift during the Lower to Middle Santonian. Further up the section, depositional depth increased. Ammonites, inoceramids, planktic foraminifera and nannofossils prove an early to late Campanian age [*Egger, Wagreich,* 2001; *Kollmann,* 1963, 1964; *Summesberger et al.,* 1999; *Wagreich,* 2004; *Wicher,* 1956]. Within the type section, the heavy mineral spectrum changes from epidote-dominated to chrom spinel dominated assemblages which indicates a change from more local to regional source areas [*Wagreich,* 2004].

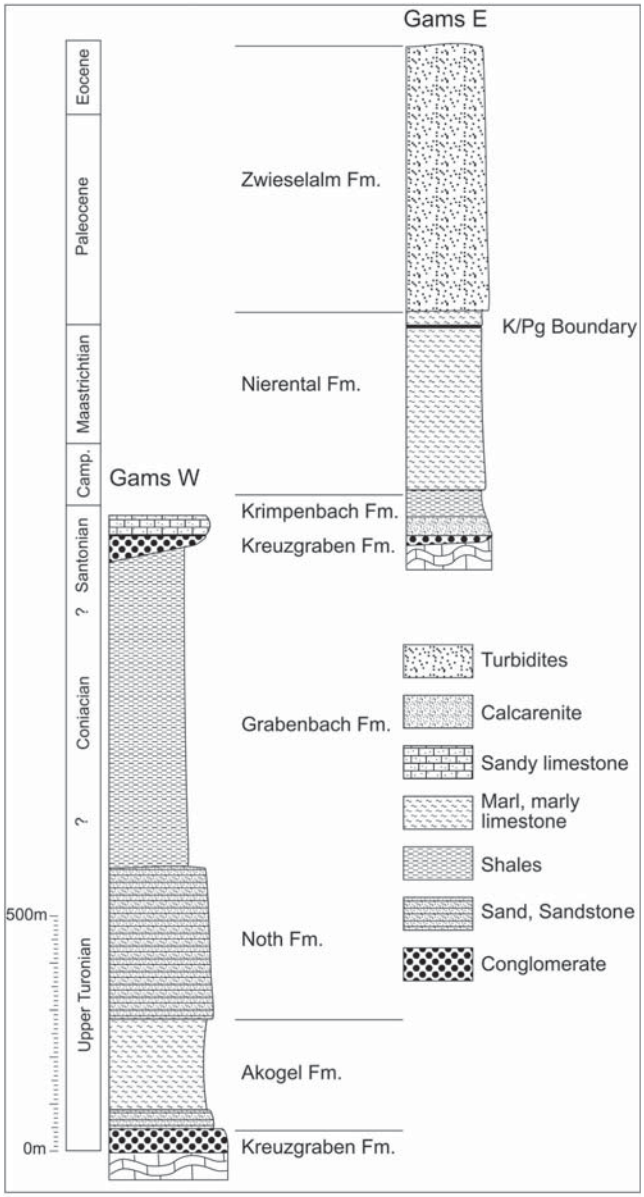

Figure 1.2. The stratigraphic range of the sedimentary areas of Gams.

The Upper Gosau Subgroup rests unconformly upon the Krimpenbach Formation. It embraces the Nierental Formation and the Zwieselalm Formation. These se-

Figure 1.3. The Gams 1 (Knappengraben) outcrop. The monolith was cut out from this outcrop.

ries are approximately 900 m thick and cover a time interval from the Late Campanian to the Ypresian (Early Eocene) which marks the end of Gosau sedimentation [*Egger et al.*, 2004; *Kollmann*, 1963, 1964].

The spreading of the Nierental Formation marks a pulse of tectonic subsidence during the late Campanian [*Wagreich*, 2004]. It consists of grey to reddish marlstones and marly limestones. Planktonic foraminifera [*Kollmann*, 1963, 1964] and nannofossils [*Wagreich, Krenmayr*, 1993] indicate a time interval of Late Campanian – Paleocene age. Late Maastrichtian sediments consist of light grey marly limestones. *Lahodynsky* [1988b] has pointed out the intensive bioturbation of the uppermost 4 to 5 cm below the K/T boundary clay. Chondrites, Zoophycos and Thalassinoides have been recorded from this part of the section. According to *Egger et al.* [2004] this part of the Maastrichtian shows pelagic sedimentation with a dominance of planktonic foraminifera. In the benthic assemblage, bathyal to abyssal forms are dominant. *Egger et al.* [2004] calculate a middle bathyal environment at a water depth between 600 and 1000 m.

The K/T boundary divides the Nierental formation into a Late Cretaceous and a Paleogene part. The K/T boundary clay was only developed in the eastern part of the eastern sedimentary area [*Lahodynsky*, 1988a]. The distinct change of lithology at this boundary is observable in the whole sedimentary area: In contrast to the highly bioturbated marly limestones of the top Cretaceous, the Paleogene Nierental Formation consists of grey to reddish marlstones and marly limestones with slump layers and siliciclastic turbidite beds. This change has already been shown by *Wicher* [1956] in a section in the Gamsbach river which currently is not exposed. It is also evident from the other Alpine sections described by *Herm et al.* [1981] in the Lattengebirge and on the two sections in the Gosau Basin [*Peryt et al.*, 1993; *Preisinger et al.*, 1986].

Biostratigraphically, *Grachev et al.* [2005], have recorded in Gams the planktonic foraminifera biozone P0 in the upper part of the boundary clay. The marlstone following above the K/T boundary clay has been assigned by *Egger et al.* [2004], to the planktonic foraminifera biozones P1 to the top of P4 [*Berggren, Norris*, 1997; *Olsson et al.*, 1999]. Within this interval, foraminifers indicate an increase of water depth to 1000–2000 m [*Egger et al.*, 2004].

Like in the Gosau area, where it has been first described by *Kühn* [1930] the Zwieselalm Formation (Breccien-Sandsteinkomplex of *Kollmann* [1963, 1964] constitutes the stratigraphically highest part of the Gams sequence. The contact to the Nierental Formation is diachronous and becomes younger towards east [*Wagreich, Krenmayr*, 1993]. The Zwieselalm Formation consists of turbidites. *Egger et al.* [2004] have distinguished 3 facies (Facies 2–4 of the Paleogene sequence of Gams) in this formation. The basal facies 2 (= basal "Breccien-Sandsteinkomplex" of Kollmann) consists of sandy turbidites with sandstone to pelite ratios of 1:1 and weak cementation due to a very low carbonate

Figure 1.4. Cretaceous-Paleogene boundary in the Gams 1 (Knappengraben) outcrop.

content. From the fossil assemblages a palaeodepth of the upper abyssal, slightly above the CCD is estimated. The palaeodepth of facies 3 following above, is dominated by carbonate turbidites. The sandstones are strongly cemented. Layers of coarse breccias with clasts consisting of phyllite, quartz, various limestones, algal limestone, shales and reworked sediments of the Gosau Group are abundant. Four layers consisting mainly of montmorillonite are interpreted as volcanic ashes. Planktonic foraminifera are absent. *Egger et al.* [2004] estimate a paleodepth of 2000–3000 m, slightly below the CCD. Facies 4 ("Tonmergelserie des Paleozän" of Kollmann, l.c.) consists of a thin-bedded succession of sandy turbidites and hemipelagic marls. Foraminifera are small and strongly sorted. The deep water species *Abyssamina poagi* indicates lower bathyal to abyssal palaeodepths and the appearance of calcareous foraminifera suggests a deposition slightly above the CCD.

1.5 Termination of the Gosau Cycle

The end of the Gosau cycle ends in Gams in the Lower Eocene (Ypresian) and corresponds with that of other Gosau sedimentary areas [*Kollmann*, 1963; *Piller et al.*, 2004; *Wagreich*, 2001]. Northward thrusting during Middle/Late Eocene has subaerially exposed the southern parts of the Northern Calcareous Alps and has terminated the marine sedimentation.

1.6 Locations of Sections Studied and Samples Preparation

In the upper course of the Gams river, the K/T boundary follows more or less the base of the valley. Because of wide-spread Pleistocene deposits, a thick soil cover and the vegetation, rocks are generally outcropping along streams and in roadcuts. They are therefore temporary in most cases.

A team led by A. Preisinger has determined the K/T boundary layer in the locality Knappengraben at Gams which was also a main source of data for this investigation. Besides the Knappengraben, this boundary is currently exposed in two other outcrops (Gams 2 and Gams 3).

Outcrop Gams 1 (coordinates: latitude 47°39.′783 N, longitude 14°52.′982 E). The outcrop is located 700 m south of the abandoned farmhouse Kronsteiner (see: Austrian map 1:50,000, sheet 101, Eisenerz), at the crossing between the forest road and the Knappengraben torrent (Figure 1.3 and Figure 1.4). It is protected by a fenced shelter and is only accessible by permission. The outcrop exposes a section of the Nierental Formation across the K/T boundary. Beds are dipping at 40° towards SSE (ss 170/40). The base is formed by pale grey, late Maastrichtian shaly limestones with a well-defined ichnofauna (Chondrites, Zoophycos, Thalassinoides). The boundary layer consists of dark grey plastic clay containing small mica particles. It is

Figure 1.5. General view of the Gams section monolith (photograph).

overlain by grey clays and thin, yellowish to brown fine-grained, sandstone layers. A detailed lithological section of this outcrop has been given by *Lahodynsky* [1988a, 1988b]. Nanno- and micropalaeontological work has been performed by *Stradner, Rögl* [1988], micropalaeontology by *Grachev et al.* [2005].

Figure 1.6. Photograph of transition layer J at the K/T boundary. Note the color and character of bottom and top of layer J.

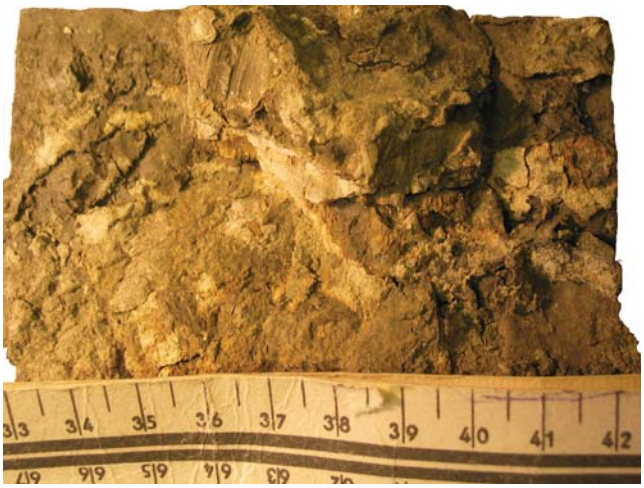

Figure 1.7. Slickensides on the surface of layer K.

The monolith. The major source of the present and previous investigations [*Grachev et al.*, 2005] is a block cut out from the outcrop Gams 1. It has been made available through the courtesy of the Department of Geology and Palaeontology of the Vienna Museum of Natural History. The block, shortly called "monolith", represents a section of 23 cm across the K/T boundary. It is 30 cm wide at the bottom and 22 cm at the top and has a thickness of 4 cm. As can be seen at the photographs (Figure 1.5 and Figure 1.6), which were taken before the complete drying of the monolith shows the colors of the units. Slickensides occur in a lens of grey, sandy clay resting on the eroded top of the transitional layer (Figure 1.7). It is overlain by yellow to brownish fine-grained sandstone and grey clays.

Dark spots of approximately 1 mm in diameter in the late Maastrichtian shaly limestone are sections through Chondrites. The burrows are filled with dark bound-

Figure 1.8. Traces of ichnofauna on the top of the Upper Maastrichtian sediments.

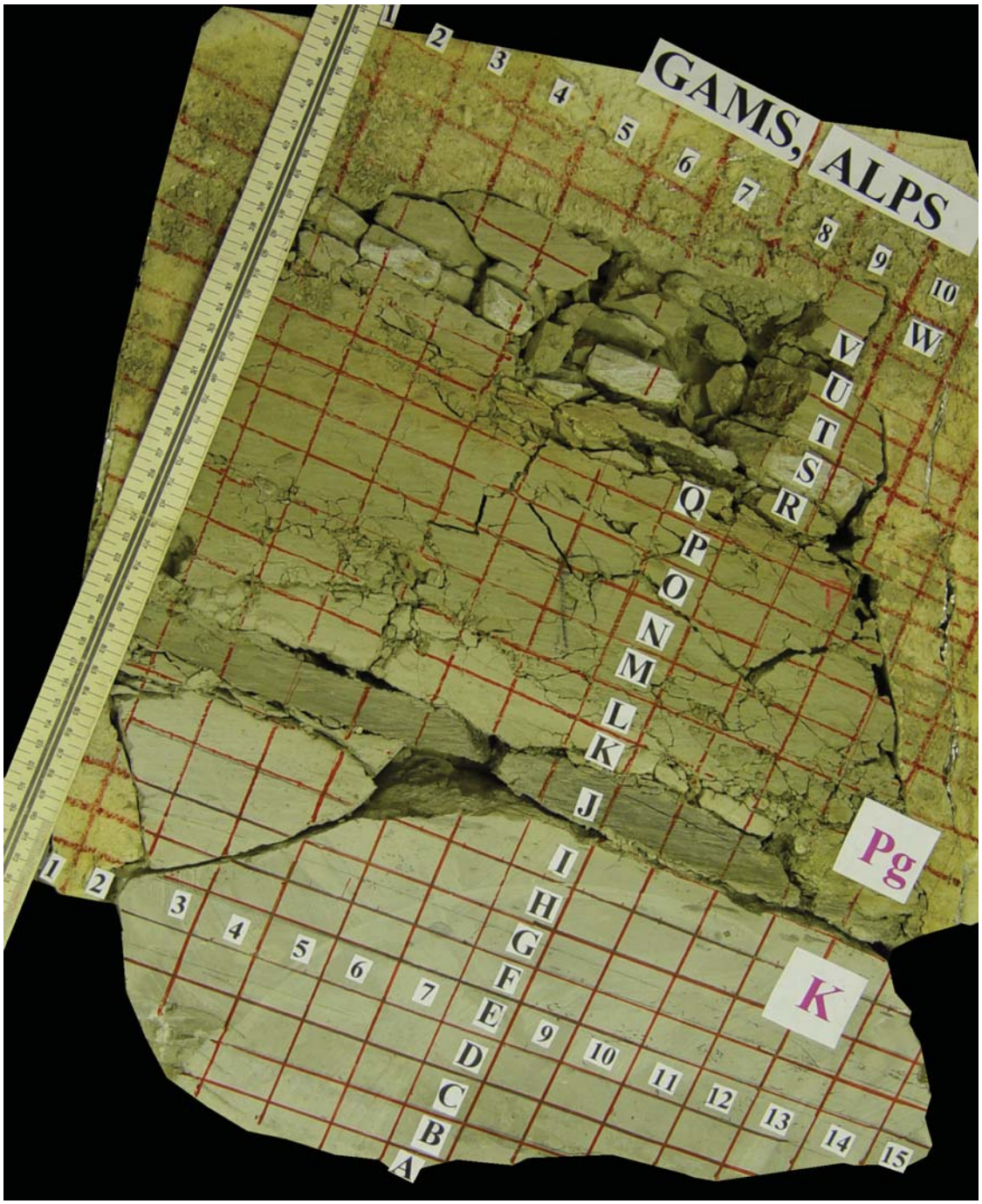

Figure 1.9. The Gams section monolith, prepared for sampling (photograph).

ary clay (Figure 1.8). Comparable traces are known from K/T boundary sections of Italy, France, Spain, Bulgaria and others and indicate an interruption in sedimentation [*Adatte et al.,* 2002; *Smit,* 2005, and others].

To obtain the general characteristics of the sequence, the monolith was divided into 2-cm units, which were labelled *A* through *W* (from the bottom to the top Figure 1.9). Each of the units was subdivided horizontally at intervals of 2 cm (1, 2, 3...).

The boundary Layer *J* at the K/T boundary is vertically heterogeneous and its texture varies by its clastic content and clay matrix distribution. It was subdivided into subunits of 2–3 mm thickness each (Figure 1.10)

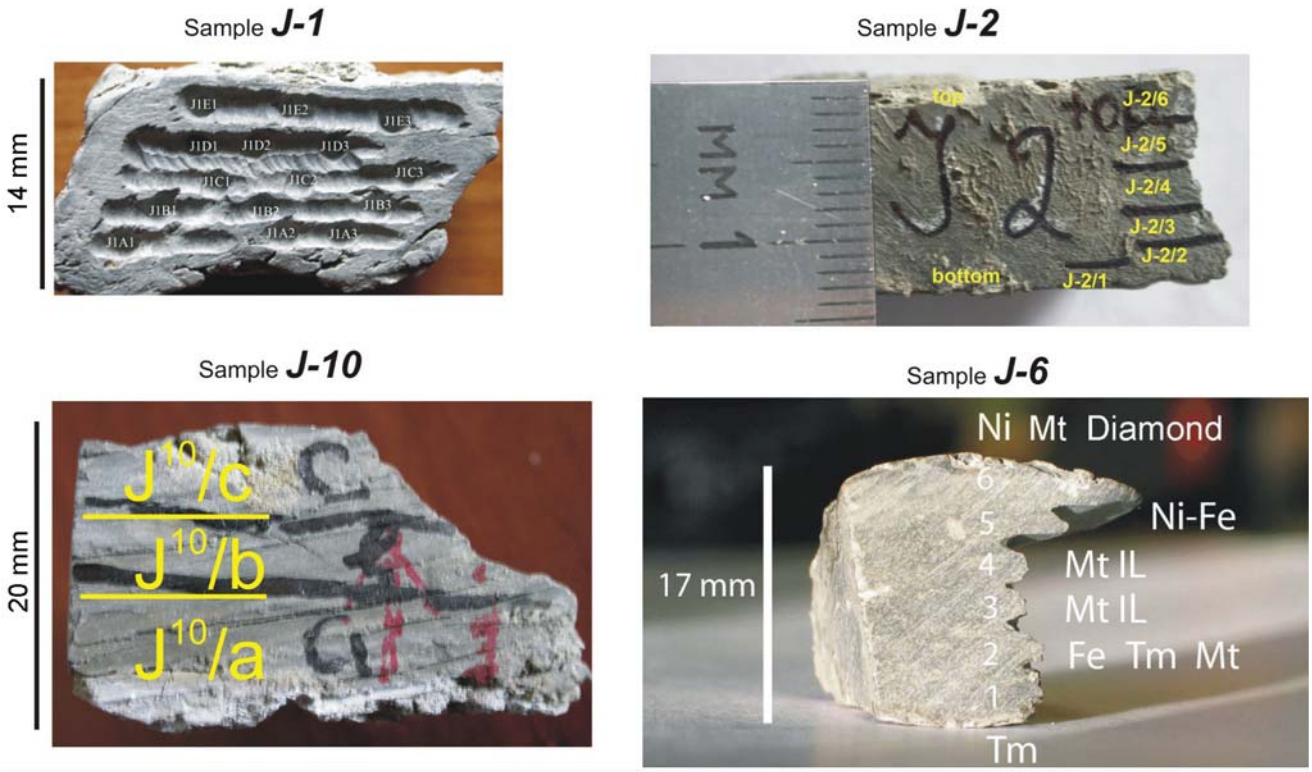

Figure 1.10. The subdivision of the transition layer *J* on the separate units for different kinds of analysis.

Figure 1.11. Cretaceous-Paleogene boundary in the Gams 2 outcrop.

Figure 1.12. Red-brown (rust) layer in a base of transitional layer.

for a detailed examination. In an oriented petrographic thin section of the transitional clay of the Gams 1 section (monolith) the following sub-units have been distinguished from the base to the top:

Subunit *J*-1. Dark brown clay with a wavy parallel texture, 5.5 mm thick.

Subunit *J*-2. Clay with regularly dispersed granular texture, bearing sandstone nodules and large benthic foraminifer tests, 4 mm thick.

Subunit *J*-3. Dark brown clay with a wavy parallel texture, 1.5 mm thick.

Subunit *J*-4. Clay with regularly dispersed granular texture and regularly dispersed admixed silt, 1.3 mm thick.

Subunit *J*-5. Microbreccia bearing poorly rounded quartz grains of different size and granular-clayey rock fragments, likely derived from the underlying *J*-*D* interval, 2.0 mm thick.

Subunit *J*-6. Dark brown clay with a wavy parallel diagonal texture, 3.2 mm thick.

Outcrop Gams 2 (coordinates: latitude 47°39.′47 N, longitude 14°52.′05 E). This hitherto undescribed outcrop E of the old Haid sawmill (see Austrian Map, 1:50,000, sheet 101, Eisenerz) is a river cut on the right (north) side of the Gamsbach river, just above the alluvial flat. Nierental Formation with the K/T boundary is exposed at a length of approximately 10 m. The rocks dip at 15–30° towards SW (Figure 1.11).

There are subangular fragments of cross-bedded, fine-grained sandstones of 1 cm in size just above the dark brown (rusty) layer of 1–2 mm (Figure 1.12), containing drop-like grains of Ni spinel [*Grachev et al.*, 2007a]. A neptunian dike extends into the Maastrichtian limestone from the top towards a depth of 1 m. Its infilling consists of clay with high mica content.

Figure 1.13. Neptunian dike cutting the Upper Maastrichtian limestones.

Figure 1.14. Cretaceous-Paleogene boundary in the Gams 3 outcrop.

Although it has been formed before the deposition of the transitional layer (Figure 1.13) the composition of clays in virtually the same.

Outcrop Gams 3 (coordinates: latitude 47°39.′79 N, longitude 14°52.′54 E). This hitherto undescribed small outcrop is located on the left bank of the Gamsbach river, 350 m W of the abandoned farm house Kronsteiner (see Austrian map 1:50,000, sheet 101, Eisenerz) (Figure 1.14). The sequence is the same as in the previous outcrops. The rocks dip at 45° towards S. The thickness of the K/T boundary clay 5 cm.

Chapter 2. Biostratigraphy

2.1 Introduction

The Cretaceous-Paleogene boundary in the Gams Basin has first been observed by *Wicher* [1956] in the Gamsbach river bed, close to the K/T boundary sites described in this volume. Without locating the boundary clay, he pointed out the faunal change between the shaly limestones with gigantic forms of *Abathomphalus mayaroensis, Contusotruncana contusa* and *Globotruncanita stuarti* and the shales containing abundant Globigerinidae following above. *Kollmann* [1963, 1964] has subdivided the Wicher's Maastrichtian II at Gams into 2 zone: The top zone (Maastrichtian IV after Kollmann), was characterized by rare *Abathomphalus mayaroensis* and extremely large-sized *Contusotruncana* sp.. In contrast to the underlying part of the section (Maastrichtian III of Kollmann), the percentage of agglutinated foraminifers is very high. The Cretaceous-Paleogene boundary was drawn at the first occurrence of *Parasubbotina pseudobulloides* and other globigerinids in the section. This agrees with observations in the other Gosau Basins [*Herm,* 1962; *Hillebrandt,* 1962; *Küpper,* 1956; *Wille-Janoschek,* 1996]. A detailed biostratigraphic subdivision of the boundary section of the Knappengraben (Gams 1 in this volume) was given by *Stradner, Rögl* [1988].

According to the decision of the International Union of Geological Sciences, the boundary between the Cretaceous and the Paleogene, which is also the lower boundary of the Danian stage of the Paleogene is determined by the Ir anomaly. It is more or less synchronous with the mass extinction of typical Cretaceous biota (foraminifera, nannoplankton, dinosaurs, etc.). The boundary stratotype was chosen in the El-Haria section near El Kef, Tunisia, at the base of the boundary clay [*Cowie et al.,* 1989]. Recently the GSSP (Global Stratigraphic Section and Point) was established at the base of dark layer of clay (1–2 mm) with Ni-spinel and high level concentration of Ir [*Molina et al.,* 2006]. In compliance with this, we have drawn the Cretaceous-Paleogene boundary in the Gams sequence (Northern Calcareous Alps, Austria) within the lower part of clay layer *J* [*Grachev et al.,* 2005].

2.2 Foraminiferal Assemblages

The studied interval of the section (units A–W) yields both planktonic and benthic foraminifera. Planktonic foraminifera are common in the lower calcareous marlstone part of the section (units A–I). The units contain numerous and diverse planktonic foraminifera though their tests are poorly preserved owing to properties of enclosing sediments and to imperfect techniques used for their extraction from these rocks. A poor preservation of many tests is manifested by the fact that certain elements of test morphology, for instance apertures, are covered with rock particles, which are unsusceptible to removal after washing. This fact makes a lot of planktonic foraminiferal shells badly illustrated on photos and hinders their study under electron microscope. In the upper, clayey part of the section (units J-W) planktonic foraminifera occur only in certain intervals. Most of tests in the assemblages are well preserved; intact tests are encountered together with that partially or completely squeezed and those possessing a smoothed-out exterior sculpture. However, specific assignments were defined for most of specimens permitting the exact age estimate of enclosing sediments.

Benthic foraminifera are diverse and numerous in both lower, calcareous marlstone, part of the section (units A–I) and upper, mainly clayey portion (units J–W). In the lower part they were identified in all studied units C, D, E, G, H, I. Species of *Gaudryina, Marssonella, Rzehakina, Gyroidinoides, Lenticulina, Arenobulimina, Trochammina, Eggrellina, Stensioeina*, and *Globorotalites* are the most common in the benthic assemblages. The benthic foraminifers are well preserved, commonly better than planktonic forms.

In the upper, clayey part of the section benthic foraminifers are more numerous than planktonic taxa, however, they are also found only in certain layers. In the

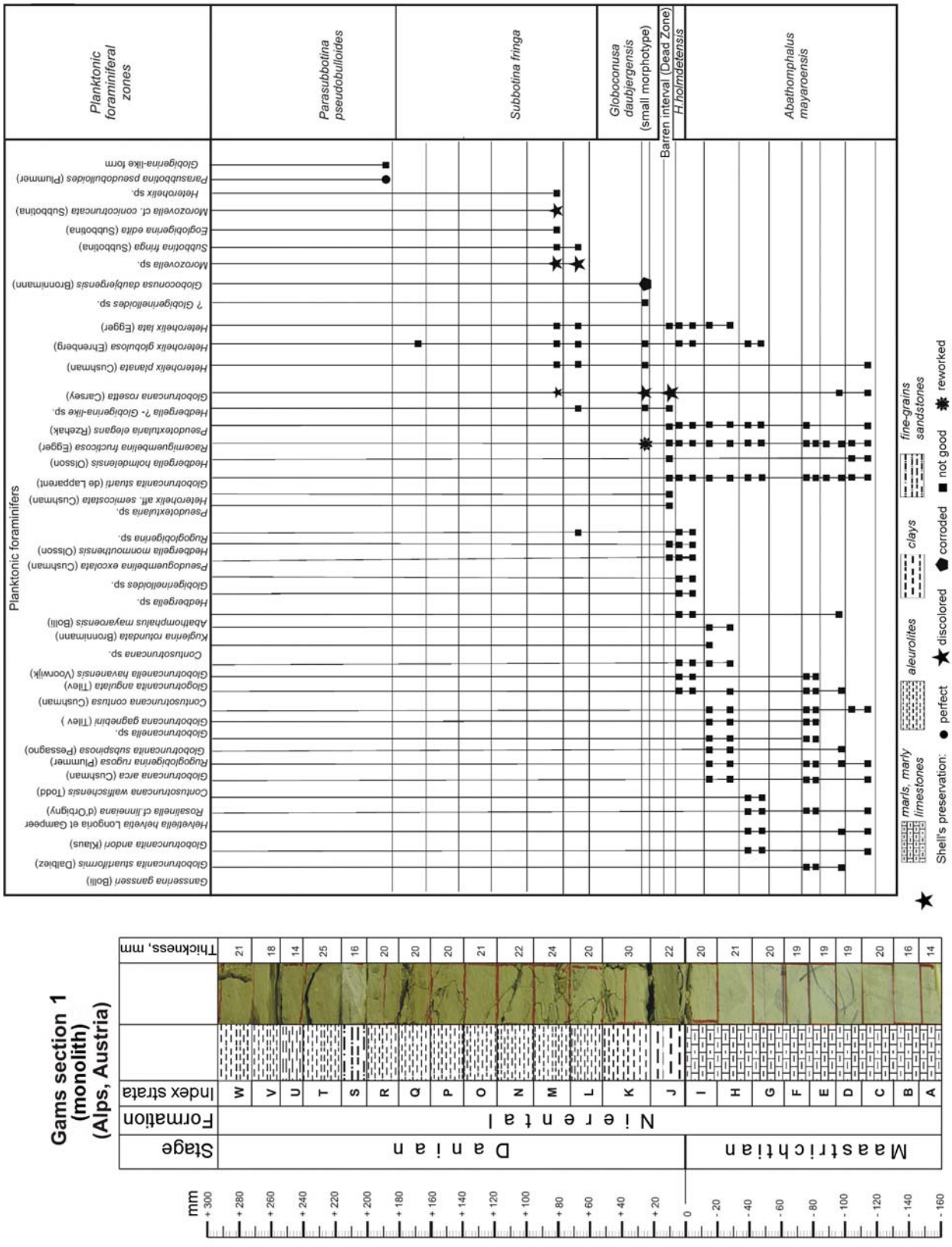

Figure 2.1. Distribution of the planktonic foraminifers in the Gams section.

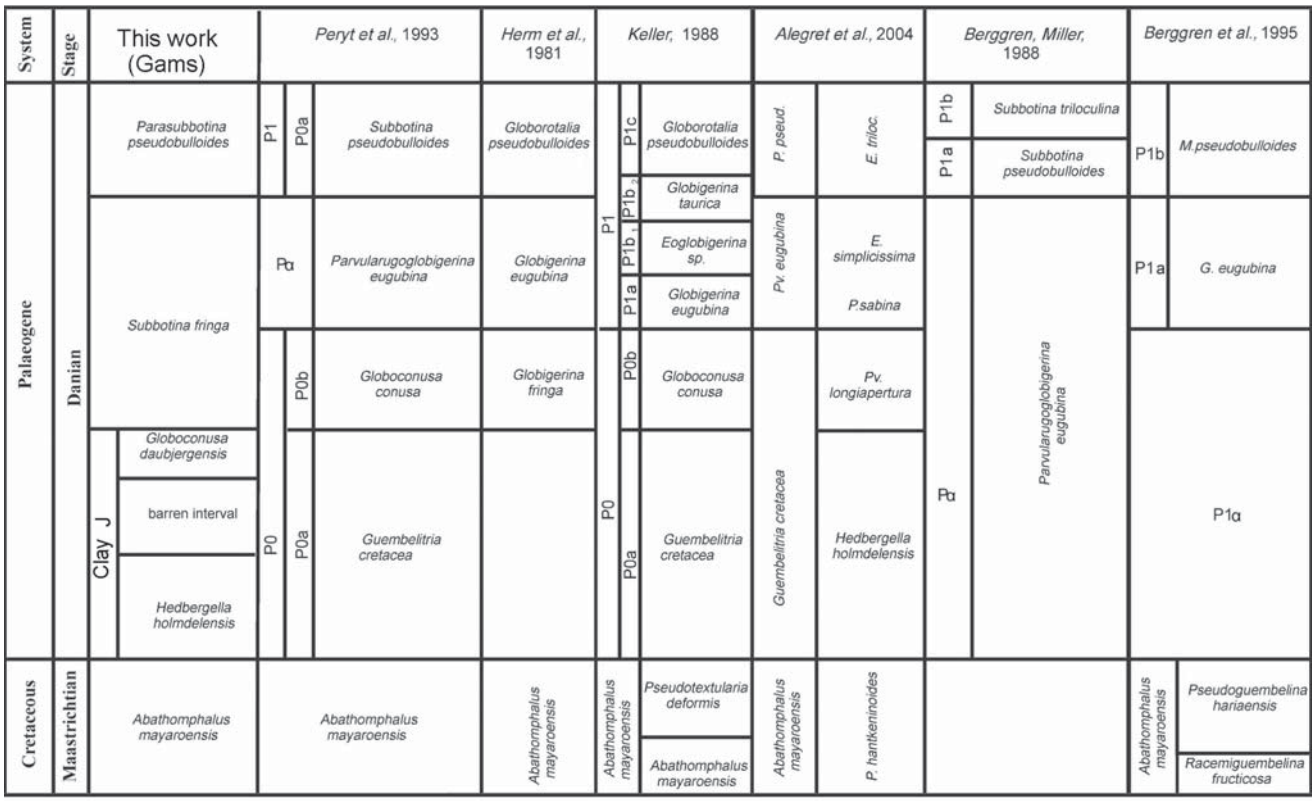

Figure 2.2. Correlation chart of the Cretaceous-Paleogene boundary divisions.

transitional layer *J* benthic foraminifers occur in the lower and upper portions and are missing in the middle one. Upward from the base they were encountered in units L, M, N, O, Q, R, T, and U.

Planktonic and benthic foraminifers were not encountered in the middle portion of layer *J* and are missing in layers *K* and *S*. Their absence in the latter units results from unfavorable for test preservation composition of enclosing sediments: such rocks are usually barren of foraminifers. However, the lack of foraminifers in middle part of layer *J* can hardly be explained by this reason.

In view of the decisive significance of planktonic foraminifers for study of stratigraphic position of the Cretaceous-Paleogene boundary and reconstruction of concurrent environmental changes, the priority is given just to that group.

2.3 Preservation of Foraminifera

In Gams, some planktonic foraminifera of the transitional layer (layer *J* and its analogues) and of overlying sediments are preserved differently from those found below. Thus, globotruncanids occuring in a layer of *J* and above are *discolored* and moderately *deformed*. Exactly the same *discoloration* and *deformation has been observed* on Paleogene keeled taxa such as *Morozovella* (?). Specimens of *Racemiguembelina fructicosa* in the upper portion of layer *J* are obviously redeposited. In the same layer of *J*, the typical Paleogene taxon *Globoconusa daubjergensis* is equally corroded and deformed.

The Cretaceous planktonic foraminifera genus *Hedbergella* and the *Heterohelicidae*, as well as Paleogene globigerinids of underlying sediments are well preserved. The best preservation may be found in *P. pseudobulloides*.

The distribution of planktonic foraminifer in the section and characteristics of their preservation are shown in Figure 2.1. The proposed zonal scheme of the transitional K/Pg boundary interval in Gams and adjacent territories is plotted against the standard biostratigraphic scheme in Figure 2.2.

2.4 Terminal Maastrichtian

The *Abathomphalus mayaroensis* Zone (upper part) (top defined by last occurrence (LO) of the index species) (= Upper part of *Abathomphalus mayaroensis* Zone in [*Grachev et al.*, 2005]). The sediments are rep-

resented by light grey clayey limestones and marls of units A-J.

The foraminifera assemblage is characteristic for the *Abathomphalus mayaroensis* or *Pseudoguembelina hariaensis* zones of the *Globotruncanidae* and *Heterohelicidae* standard zonation [*Hardenbol et al.,* 1998].

The occurrence of Cretaceous planktonic foraminifera groups, especially of *Abathomphalus maryaensis* and *Globotruncanita stuarti*, suggests a position at the top of the Zone *Abathomphalus maryaensis*. It corresponds well with other East Alpine sections in the Bavarian Alps [*Herm et al.,* 1981] and "Bed 9" in the Rotwandgraben of the Basin of Gosau, Austria [*Peryt et al.,* 1993]. Also in Tunisia [*Keller,* 1988] it was recorded close to the upper boundary of the *Abathomphalus maryaensis* Zone of the standard scale [*Hardenbol et al.,* 1998]. While *Gansserina gansseri* LO has been established in Gams slightly below the top of the marls underlying the transitional clay, it has been recorded in the El Kef section (Tunisia) at the top of Maastrichtian [*Peybernes et al.,* 1996]. We therefore infer the terminal Maastrichtian has been retained in the Gams section.

2.5 Lower Paleogene

The *Hedbergella holmdelensis* Zone (base defined by LO of *Abathomphalus maryaensis*; top by first occurrence (FO) of *Globoconusa daubjergensis* (= *Guembelitria cretacea* Interval Zone in [*Grachev et al.,* 2005]).

Previously we distinguished this interval of the section as the *Guembelitria cretacea* Interval Zone. However, it is generally known that *G. cretacea* occurred throughout the Upper Cretaceous and Lower Paleogene. The recognition of the lowermost zone of the Paleogene by the "flourishing" of this species seems not to be justified. In boundary clays of Mexico, Tunisia (El Kef, Ain-Settara) and Spain (Agost) *Hedbegrella homldelensis* has been suggested as zonal species along with *Guembelitria cretacea* [*Alegret et al.,* 2004]. The lower part of the transitional clay of Gams contains also an assemblage of small heterohelicids and hedbergellids including *H. holmdelensis* [*Grachev et al.,* 2005]. We can therefore distinguish the *holmdelensis* in Gams and correlate it with the boundary clay in Spain with more confidence. In this connection hereafter we prefer to distinguish the *holmdelensis* zone.

H. holmdelensis, has its first occurence in the Cretaceous species and its use for the designation of the lower Paleogene zone may appear unjustified. In addition, this species, as well as a lot of other typical Cretaceous planktonic foraminifera, might be redeposited.

Barren interval (dead zone). We referred to this interval the dark green to black clay of middle part of layer *J*. It is approximately 0.2 cm in thickness and lacks foraminifera. It is still premature to speculate about the geographical distribution of this interval because evidence is too scarce.

The recognition of the lack of foraminifera in the middle part of transitional clay *J* was difficult to interpret because no data from other sections related to this phenomenon existed. Only recently a comparable interval without planktonic and with very rare benthonic foraminifera was detected in the Forada section in Italy [*Fornaciari et al.,* 2007]. This interval is positioned in the lower part of the transitional clay. *Fornaciari et al.* [2007] have named it "dead zone". In accordance with layer *J* of Gams, it provides evidence for a regional (not local) decrease of diversity and quantity of biota (foraminifera) at this level. The "macrofossil dead zone" close to the K/T boundary in Mexico [*Keller et al.,* 2008] can perhaps be correlated.

The *Globoconusa daubjergensis* Zone (lower boundary defined by FO of index species) (= *Globoconusa daubjergensis* Zone in [*Grachev et al.,* 2005]).

In well-studied sections, *Globoconusa daubjergensis* occurs first in the following zones: P0 (0.80 m above GSSP) of the Elles II section in Tunisia [*Keller et al.,* 2002a] and slightly above; P1 in Guatemala [*Keller, Stinnesbeck,* 2002], Egypt [*Keller,* 2002], in Mexico [*Stinnesbeck et al.,* 2002] and Koshak section in Kazakhstan [*Pardo et al.,* 1999]; P1c (Bed 23b) in the Stevns Klint section, Denmark [*Schmitz et al.,* 1992].

Compared with the sections cited above, *Globoconusa daubjergensis* occurs first in Gams at a lower stratigraphical level, i.e. below the base of the *fringa* Zone [*Grachev et al.,* 2005]. Comparatively late, *Globoconusa daubjergensis* has been regarded as one of the earliest Paleogene species [*Patterson et al.,* 2004].

In Mexico, Spain (Agost) and Tunisia (El Kef) *Globoconusa* taxa were encountered at the base of the *Parvuloglobigerina longiapertura* Zone. In the Ain-Settara section (Tunisia), *Globoconusa* appeared first in the *H. holmdelensis* Zone within the proper transitional clay [*Alegret et al.,* 2004]. Similar to Ain-Settara, *Globoconusa*, namely *Globoconusa daubjergensi* appeared first in the Gams section in the upper part of the transitional clay, i.e. upper part of the *holmdelensis* Zone of the zonal scale [*Alegret et al.,* 2004]. In the southern hemisphere, *Globoconusa daubjergensis* characterizes the Lower Danian. It had its first appearance at the base of the *Eoglobigerina eobulloides* (= *Eoglobigerina fringa*) Zone. Because of its commonness it is considered as index fossil for the Lower Danian *Globoconusa daubjergensis* Zone [*Huber, Quillieri,* 2005]. Also in Gams [*Grachev et al.,* 2005] and Ain-Settara [*Alegret et al.,* 2004] *Globoconusa taxa* may be considered as the earliest Paleogene planktonic foraminifera.

The *Subbotina fringa* Zone (base defined by FO of index species) (= *Subbotina fringa* Zone in [*Grachev et al.*, 2005]).

Foraminifer assemblages in this part of the section, in unit L (Sample L-6), yield a typical Paleogene species *Subbotina fringa* (Subbotina) and Paleogene-like forms similar to it (?)Morozovella sp. cf. *M. conicotruncata* (Subbotina), *(?)Morozovella* sp., cannot be identified reliably due to small numbers and poor preservation. The typical Paleogene *(?)Hedbergella-Eoglobigerina trivialis* occurs as well. It is, however, accompanied by Upper Cretaceous taxa like *Heterohelix lata* (Egger), *Heterohelix planata* (Cushman), *Hetrohelix globulosa* (Ehrenberg), *Heterohelix* sp., single *Rugoglobigerina* sp., and by colorless *Globotruncana rosetta* (Carsey).

Stradner, Rögl [1988] reported the first occurrence of *S. fringa* in the Gams section 10 cm above the K/T boundary layer. Because to the planktonic foraminifer assemblage and the first occurrence *Subbotina fringa*, units "L" and "M" of Gams correspond to "Beds 17" and "18" in the Rotwandgraben section of Gosau and should be referred to the *Globoconusa conusa* Zone [*Peryt et al.*, 1993]. Units "L" and "M" can also totally or partially correspond to the *Subbotina fringa* Zone as it was distinguished in the Bavarian Alps [*Graup, Spettel,* 1989; *Herm et al.*, 1981] and in Tunisia [*Brinkhuis, Zachariasse,* 1998].

The *Parasubbotina pseudobulloides* Zone (base defined by FO of index species) (= *Parasubbotina pseudobulloides* Zone in [*Grachev et al.*, 2005]).

Planktonic foraminifers were found in Bed "R" (Sample R-6). It contains the typically Paleogene *Parasubbotina pseudobulloides* (Plummer) and few specimens of "Paleogene taxa" named *Globigerina*-like forms, which cannot be reliably identified due to their poor preservation. It can be inferred that Bed "R" belongs to the *Parasubbotina pseudobulloides* Zone and correlate to Bed "22" of the Rotwandgraben section [*Peryt et al.*, 1993], i.e. the base of Bed "R" corresponds to the base of the same zone [*Herm et al.*, 1981].

2.6 Association of Planktonic Foraminifera

The diversity of planktonic foraminiferal species is relatively high in the lower part of the section (Units A–I, the *Abathomphalus maryaensis* Zone) where it ranges from 6–7 to 14–15 species in the assemblage (Figure 2.3). The smallest number has been recorded in a layer of G. The diversity is highest in the lower portion of layer *J*, while planktonic foraminifers are missing in the middle part of layer *J*; although the species diversity is somewhat lower in the upper part of the transitional layer than in units A–I and in the lower part of layer *J*, it still reaches 6–7 species.

The total number of planktonic foraminifera specimens in units A–I is high; the maximum was recorded in units D and I, the minimum again in unit G. In the basal part of layer *J* planktonic foraminifera are as abundant as in the underlying units. In its upper portion the amount of planktonic foraminifera is reduced to about one half compared with the Maastrichtian (units A–I) and Lower Paleocene units (lower part of layer *J*). It slightly exceeds the abundance of the associations recorded above. It is remarkable that in the Maastrichtian assemblage (units A–I) and lower part of layer *J* the members of two families, *Globotruncanidae* and *Heterohelicidae*, dominate. Other families (*Rugoglobigerinidae* and *Hedbergellidae*) are represented by few species with a low number of specimens. It is notable that *Globotruncanidae* are characterized by numerous species but comparatively small amount of specimens in the assemblage, whereas *Heterohelicidae* are represented by two, rarely five species, of which *Racemiguembelina fructicosa* and *Pseudotextularia elegans* are extremely abundant (Figure 2.3).

It is noteworthy that associations of the lower part of the layer *J* are strongly dominated by *Heterohelicidae* taxa (five species, 53% of the number of speciments). In this part of the layer *J* the percentage of *Hedbergelidae* increases.

In the upper part of the layer *J*, where on the number of associations reduced compared with earlier ones, *Hetehohelicidae* with *Heterohelix lata* and *Heterohelix globulosa* are dominant.

In the uppermost parts of the section planktonic foraminifera occur only sporadically. Nevetheless, the association of the layers *L–M* contains 8–9 species. The units O and R contain scarcely planktonic foraminifera: only 1–2 species are represented by isolated specimens. *Heterohelicidae (Heterohelix globulosa, Heterohelix lata, Heterohelix planata, Heterohelix* sp.) are most abundant.

According to *Abramovich et al.* [2003], *Helvetiella helvetia, Contusotruncana walfischensis, Rugoglobigerina rugosa, Kuglerina rotundata, Pseudoguembelina excolata, Pseudotextularia elegans, Globotruncana rosetta, Heterohelix globulosa*, lived in the surface and subsurface layer of water column, while *Globotruncana gagnebini, Gansserina gansseri, Globotruncana arca, Globotruncanita subspinosa, Globotruncanita stuarti, Racemiguembelina fructicosa* lived close to the thermocline. *Globotruncanita stuartiformis, Globotruncanella havanensis, Abathomphalus mayaroensis* preferred the subthermocline deep water [*Grachev et al.*, 2005].

It is evident that the number of planctonic foraminifera is usually higher in the surface layers than in the thermocline. Only in the thermocline layer *D* the number is significantly higher (74% vs. 3%). The monolith

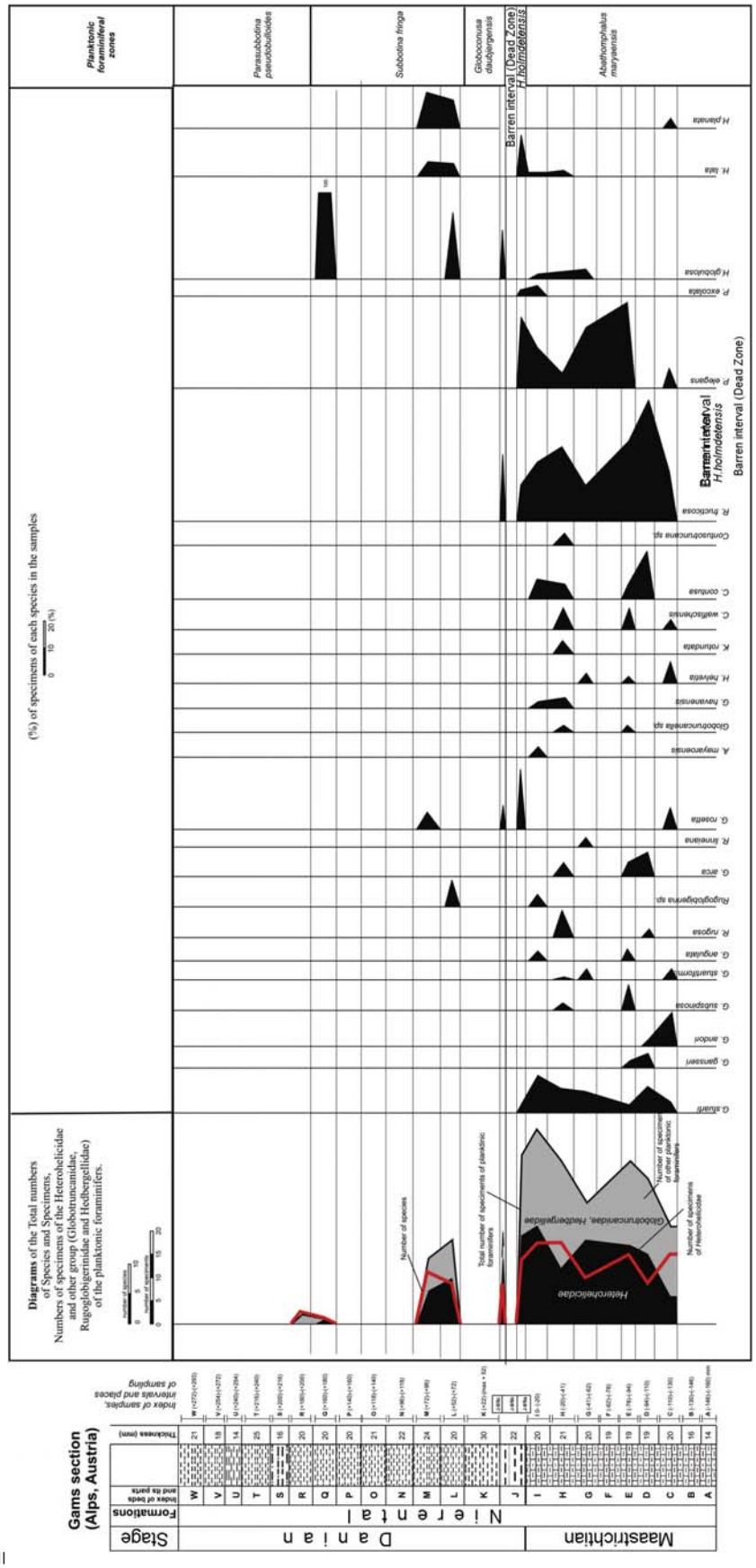

Figure 2.3. Diagram of quantities of specimens and relative percent abundances of planktonic foraminiferal species in the Gams section.

(Gams 1) demonstrates therefore that the planktonic foraminifera associations have changed twice dramatically before the deposition of layer *J*: The sharp decline of surface water dwellers is observed in the layer *D*, and the decline of the total number of taxa in the layer *G*.

During the deposition of the lower portion of the transitional layer, a foraminifera association of surface water dwellers developed. It is likely that at this time favorable habitat conditions persisted close to the surface of the water column while a worsening of conditions in the thermocline resulted in the disappearance of its inhabitants. The disappearance of thermocline taxa confirms the end of the "thermocline crisis" [*Premoli Silva, Sliter,* 1999] at the beginning of the Paleocene (Figure 2.4).

Like in other parts of the world, planktonic foraminifera are dominated by *Heterohelicidae* in the Gams section. The species it Chiloguembelina waiparaensis prevailed in Kazakhstan [*Pardo et al.*, 1999], several species of the genus Heterohelix in Tunisia [*Arenillas et al.,* 2000; *Karoui-Yaakoub et al.,* 2002; *Keller et al.,* 2002a], *Pseudoguembelina costulata* in the north-east of Mexico [*Keller et al.,* 2002b] and *Heterohelix globulosa* in Egypt [*Keller,* 2002].

In Gams, as well as in other parts of the world, the lower part of the transitional layer contains associations of planktonic foraminifera which are dominated by *Hedbergellidae* and small *Heterohelicidae* [*Grachev et al.,* 2005; *Karoui-Yaakoub et al.,* 2002; *Keller, Stinnesbeck,* 2002; *Keller et al.,* 2002a; *Pardo et al.,* 1999; *Peybernes et al.,* 1996; *Smit, Romein,* 1985; *Stinnesbeck et al.,* 2002; *Stuben et al.,* 2005]. *Globotruncanidae* occurring in this part of the section have been reworked from the underlying rocks. In the boundary layer and slightly above we encountered not only bleached and corroded *Globotruncanidae* but also typical Paleogene forms. Small *Hedbergellidae, Heterohelicidae*, as well as Paleogene *Globigerinidae* are preserved without alteration of the calcitic test. Corrosion and the brittleness of planktonic foraminifera may be associated with a decrease of the pH of water to 7.5 [*Le Carde et al.,* 2003], or to changes in the lisokline [*Dittert, Henrich,* 2000]. Thus, the question of "reworking" or "processing" in situ of the *discolored, brittle* or *corroded* planktonic foraminifera above the transitional layer remains open.

The most typical foraminifera species of Gams are shown in Figures 2.5 – 2.14.

Figure 2.5. Planktonic foraminifers Globotruncanidae (Globotruncanellinae), Hedbergellidae and Globigerinelloididae. For all images: a – view from spiral side, b – view from umbilical side, c – view from lateral side. Scale bar=100 μm. 1a–c, 2a–c. *Globotruncanella havanensis* (Voorwijk). 1a–c – sample F7/1; 2a–c – sample A7. 3a–c, 6a–b, 7a-c. *Globotruncanella citae* (Bolli). 3a–c – sample F7/1; 6a–b – sample A7; 7a–c – sample A7; 4a–c, 5a–c. *Globotruncanella petaloidea* (Gandolfi). 4a–c – sample H7/1; 5a–c – sample A7; 8a–c. *Hedbergella holmdelensis* (Olsson). 8a–c – sample A7 9a–c , 10a–c. *Globigerinelloides blowi* (Bolli). 9a–c – sample I7/1; 10a–c – sample A7;

Figure 2.6. Planktonic foraminifers Rugoglobigerinidae (Helvetiellinae and Rugoglobigerininae). For all images: a – view from spiral side, b – view from umbilical side, c – view from lateral side. Scale bar=100 μm. 1a–c, 2a–c. *Rugoglobigerina rugosa* (Plummer). 1a–c – sample D7/2; 2a–c – sample C7/2. 3 a–c. *Kuglerina rotundata* (Bronnimann). Sample C7/2. 4 a–c, 5 a–c. *Kuglerina* sp. 1. 4 a–c – sample F7/2, 5a–c – sample F7/1 6a–c. *Kuglerina* sp. 2. 6a–c – sample D7/2; 7a–c. *Trinitella scotti* (Bronnimann). Sample I7/2.

Figure 2.7. Planktonic foraminifers Globotruncanidae (Abathomphalinae). For all images: a – view from spiral side, b – view from umbilical side, c – view from lateral side. Scale bar=100 μm. 1a–c, 2a–c, 3a–c. *Abathomphalus mayaroensis* (Bolli). 1a-c – sample F7/1, 2a-c – sample C7/1, 3a-c – sample H7/2.

Figure 2.8. Planktonic foraminifers Globotruncanidae. For all images: a – view from spiral side, b – view from umbilical side, c – view from lateral side. Scale bar=100 μm. 1a–c. *Contusotruncana contusa* (Cushman). Sample C7/1.

Figure 2.9. Planktonic foraminifers Globotruncanidae (Globotruncaninae). For images for 2-5: a – view from spiral side, b- view from umbilical side, c- view from lateral side. Scale bar=100 μm. 1a-c. *Contusotruncana walfishensis* (Todd). Sinistral morphotype: 1a – view from umbilical side, 1b – view from spiral side, 1c – view from lateral side – sample I7/2. 2a–c. *Globotruncana ventricosa* (White). Sample B7/2. 3a–c. *Globotruncana lapparenti* (Brotzen). Sample F7/1. 4a–c. *Globotruncana arca* (Cushman). Sample C7/2. 5a–c. *Contusotruncana fornicata* (Plummer). Sample A7.

Figure 2.10. Planktonic foraminifers Globotruncanidae (Globotruncaninae) and Rugoglobigerinidae (Plummeritinae). For images 1-3, 5-6: a – view from spiral side, b – view from umbilical side, c – view from lateral side. Scale bar=100 μm. 1a–c. *Globotruncana linneiana* (dOrbigny). Sample A7. 2a–c. *Globotruncana arca* (Cushman). Sample I7/2 3a–c, 4a–c, 5a–c. *Globotruncana rosetta* (Carsey). 3a–c – sample I7/2, 4 a–c (sinistral morphotype): 4a – view from umbilical side, 4b – view from spiral side, 4 – view from lateral side – sample I7/2, 5a–c - sample I7/1. 6a–c. (?) *Plummerita hantkeninoides* (Bronnimann). Sample C7/1.

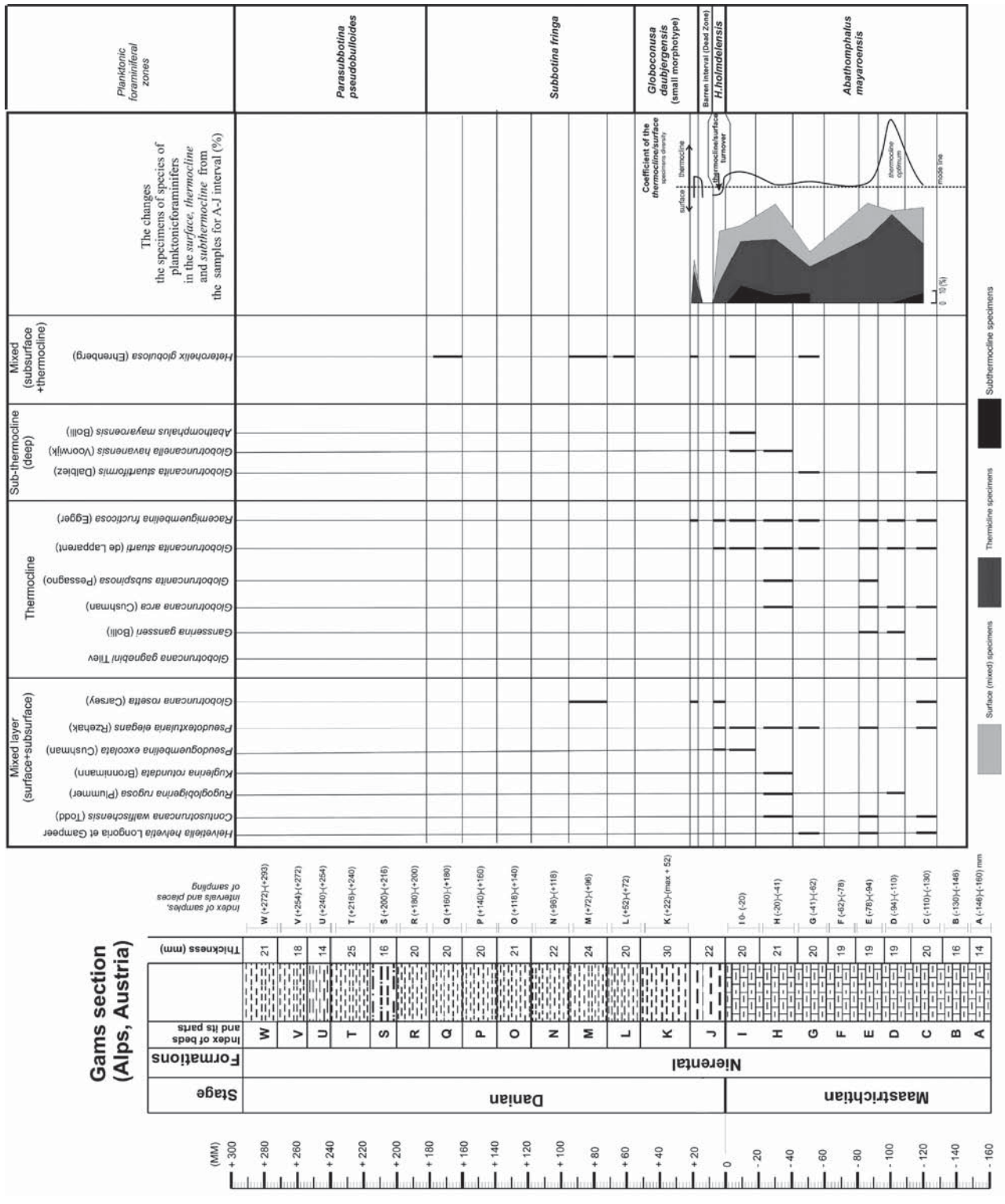

Figure 2.4. Distribution of surface, thermocline and subthermocline planktonic foraminifers in the Gams section.

Figure 2.11. Planktonic foraminifers Globotruncanidae. For all images: a – view from spiral side, b – view from umbilical side, c – view from lateral side. Scale bar=100 μm. 1a-c. *Globotruncanita elevata finita* (Korchagin). Sample D7/2. 2a-c, 3a-c. *Globotruncanita elevata elevata* (Brotzen). 2a-c sample B7/2, 3a-c sample D7/2.

Figure 2.12. Planktonic foraminifers Globotruncanidae. For all images: a – view from spiral side, b – view from umbilical side, c – view from lateral side. Scale bar=100 μm. 1a-c, 3a-c. *Globotruncanita stuarti* (de Lapparent). 1a-c sample B7/2, 3a–c – sample D7/2 2a–c. *Globotruncanita conica* (White). Sample B7/2. 4a–c. *Globotruncanita stuartiformis* (Dalbiez). Sample H7/2.

Figure 2.13. Planktonic foraminifers Heterohelicidae. For all images: a – view from lateral side, b – view from spiral side, c – view from aperture. Scale bar=100 μm. 1a–c, 2a–c, 9a–c. *Pseudatextularia elegans* (Rzehak). 1 a–c – sample G7/1, 2a–c – sample E7/1, 9 a–c – sample B7/2; 3a–c. *Heterohelix globulosa* (Ehrenberg). Sample G7/2. 4a–c., 8a-c. *Heterohelix striata* (Ehrenberg). 4 a–c – sample H7/1, 8a–c – sample G7/2. 5a–c, 6a–c. *Pseudoguembelina costulata* (Cushman). 5a–c – sample A7, 6a–c – sample I7/1. 7a–c. *Pseudoguembelina* aff. *palpebra* (Bronnimann & Brown). Sample G7/2. 10a–c. *Racemiguembelina fructicosa* (Egger). Sample E7/1.

Figure 2.14. Planktonic foraminifers Heterohelicidae. For all images: a – view from lateral side, b – view from spiral side, c – view from aperture. Scale bar=100 μm. 1a,c, 2, 3. *Racemiguembelina fructicosa* (Egger). 1 a, c sample A7, 2 – sample J-8/9a, 3 – sample J-8/9c; 4a–c, 5–8. *Pseudatextularia elegans* (Rzehak). 4a–c sample G7/1, 5 – sample J-8/9a, 6 – sample J-8/9a, 7 – sample J-8/9a, 8 – sample J-8/9c; 9, 10. *Pseudoguembelina excolata* (Cushman), lateral side, 9 – sample J-8/9a, 10 – sample I-6; 11, 12, 13. *Heterohelix lata* (Egger), view from lateral side: 11 – sample J-8/9a; 12 – sample J-8/9c, 13 – sample J-8/9a; 14. *Heterohelix* aff. *semicostata* (Cushman), lateral side, sample J-8/9a; 15, 16, 17. *Heterohelix planata* (Cushman), lateral side, 15 – sample M-4, 16 – sample M-4, 17 – sample M-4; 18. *Heterohelix globulosa* (Ehrenberg), lateral side, sample M-4;

Figure 2.15. Planktonic foraminifers Hedbergellidae, Globotruncanidae and Globigerinidae. Scale bar=100 μm. 1. *Parasubbotina pseudobulloides* (Plummer), spiral side, sample R-6; 2, 3. *Globoconusa daubjergensis* (Bronnimann) (small morphotype), spiral side: 2 sample J-8/9c, 3 sample J-8/9c; 4, 5 – *Subbotina fringa* (Subbotina), spiral side: 4 – sample M-4, 5 – sample M-4; 6, 7 – *Eoglobigerina edita* (Subbotina), 6 – spiral side, sample M-4, 7 – umbilical side, sample M-4; 8 – *Globigerina*-like form (close to Globigerina compressa Plummer var. compressa Plummer sensu (Subbotina), pl.II, Figure 4), umbilical side, sample R-6; 9, 10 – (?) *Morozovella* sp., spiral side, 9 – sample M-4, 10 – sample M-4; 11 – *Hedbergella holmdelensis* (Olsson), umbilical side, sample J-8/9a; 12, 13, 14 – *Hedbergella monmouthensis* (Olsson), umbilical side, 12 sample I-6, 13 – sample J-8/9a, 14 – sample J-8/9a; 15, 16, 17, 18, 19 – *Globotruncana rosetta* (Carsey), spiral side: 15 (sinistral morphotype) sample J-8/9, 16 – sample J-8/9c, 17 – sample M-4, 18 (sinistral morphotype) – sample J-8/9a, 19 – sample J-8/9a.

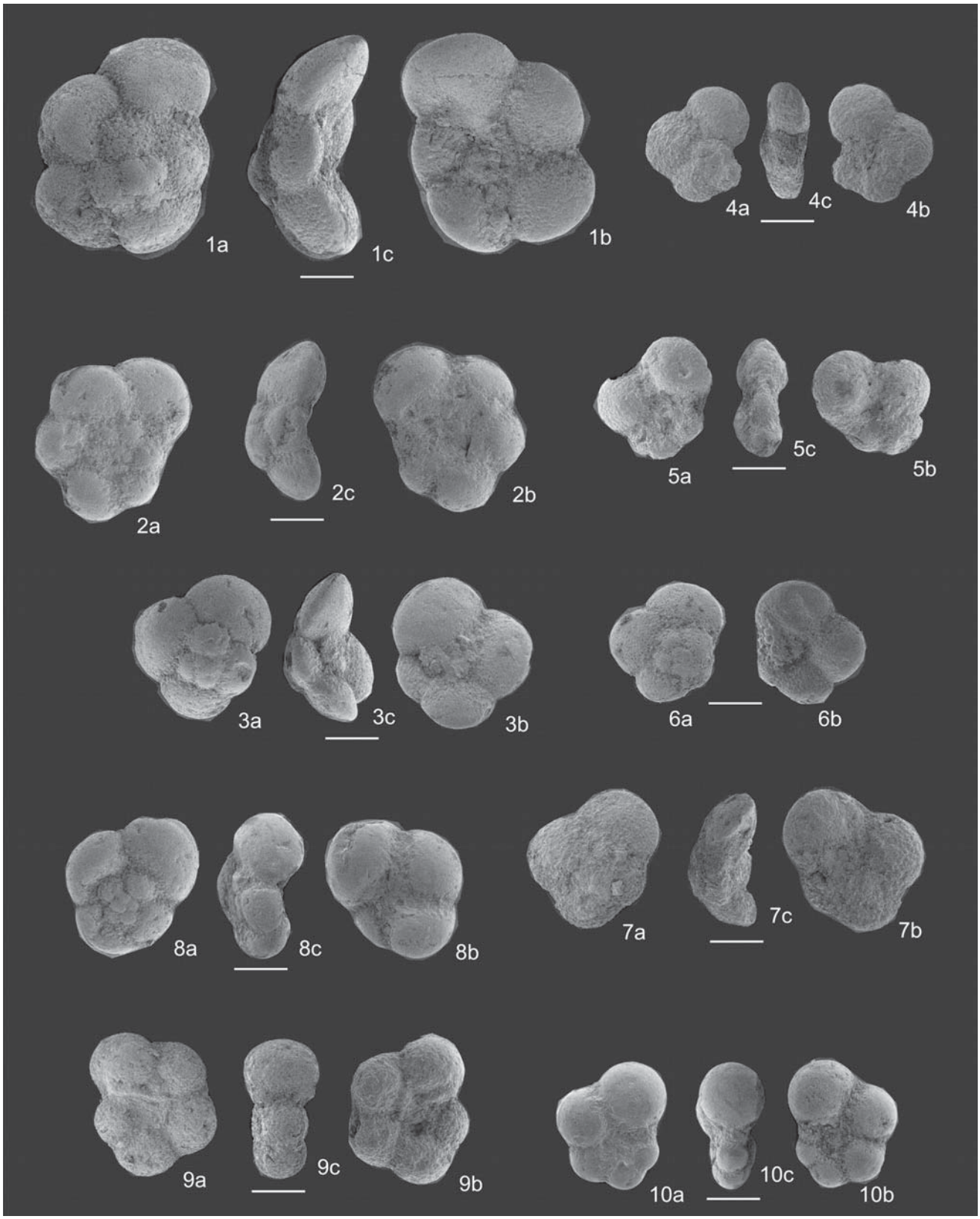

Figure 2.5. See explanation in the text.

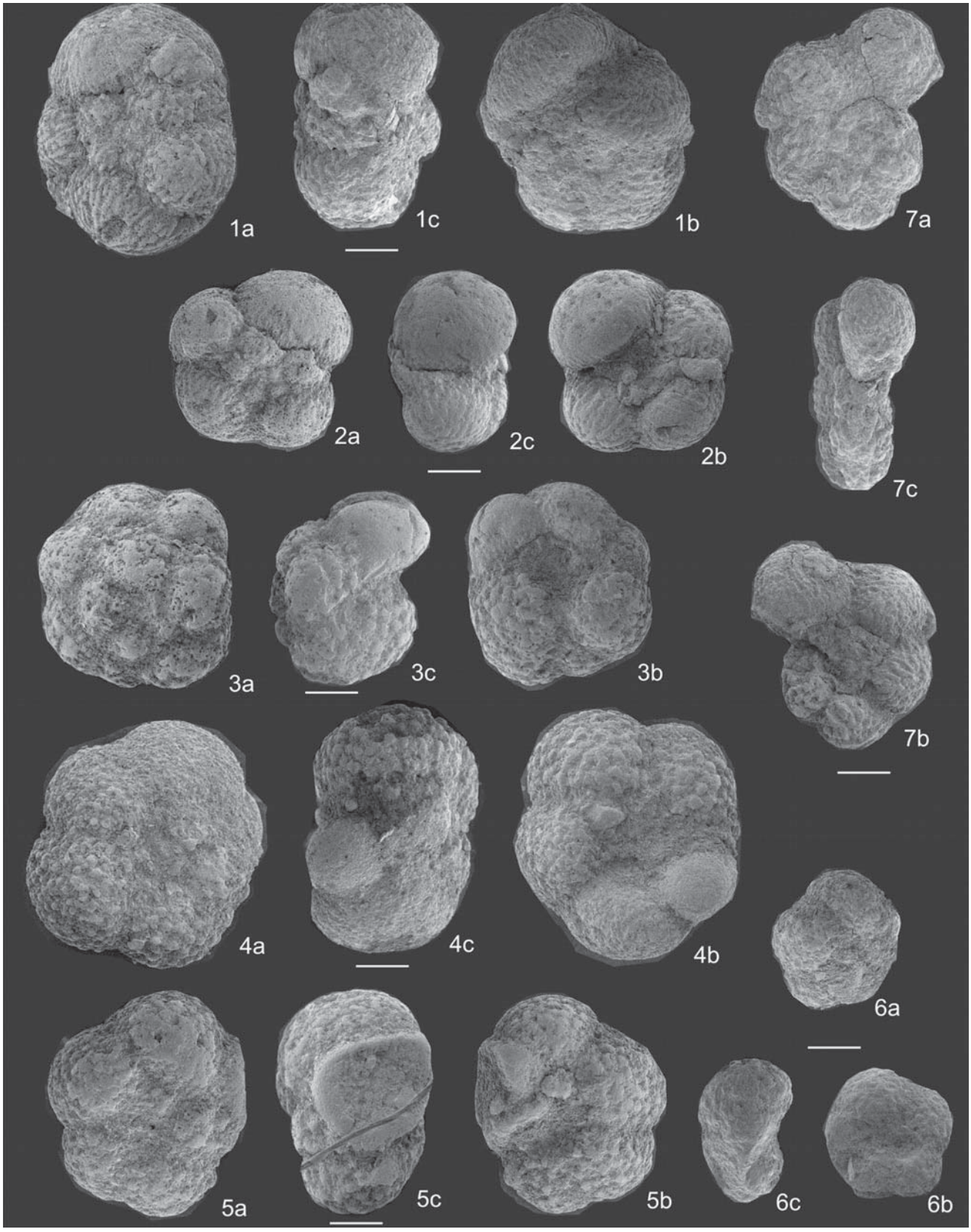

Figure 2.6. See explanation in the text.

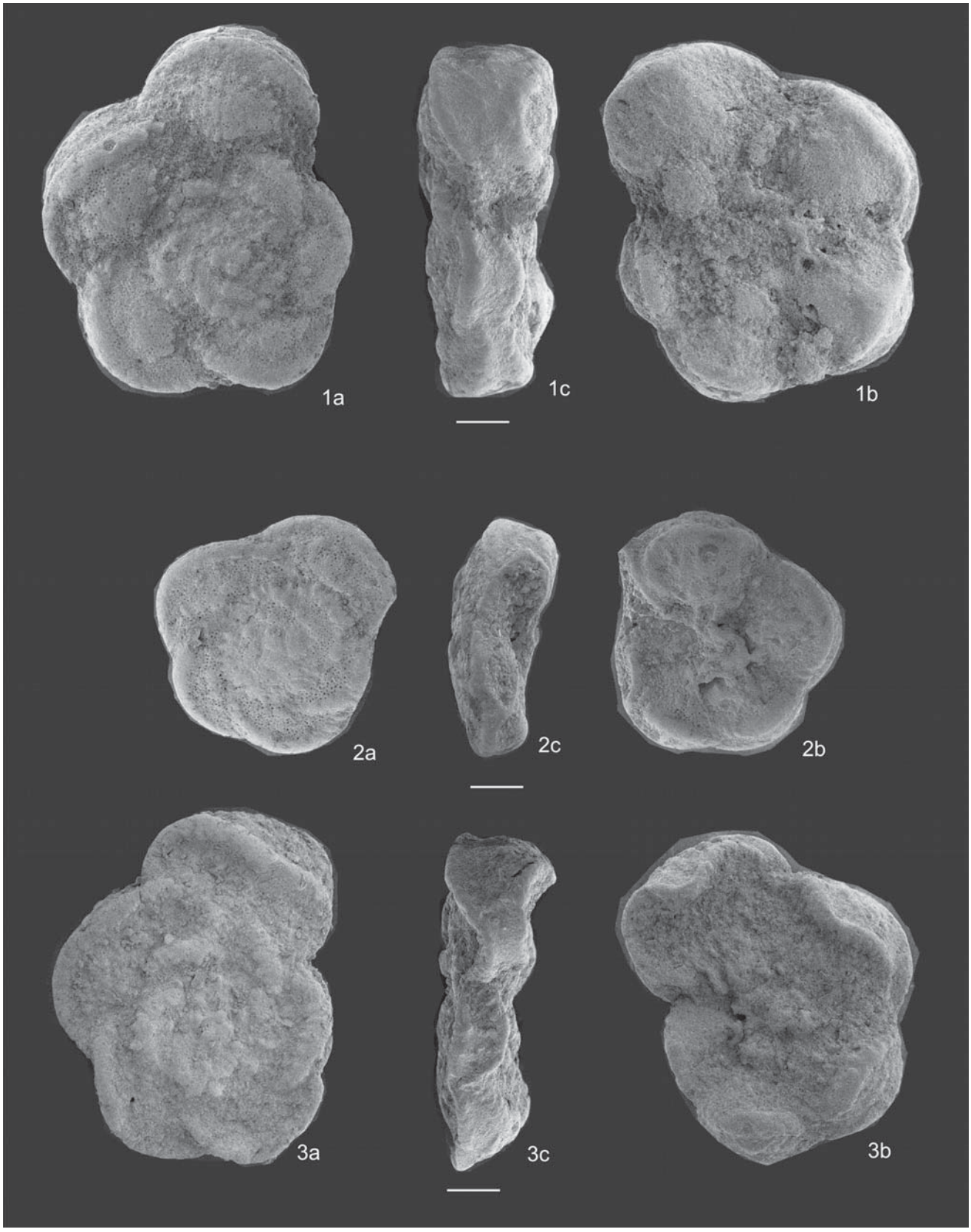

Figure 2.7. See explanation in the text.

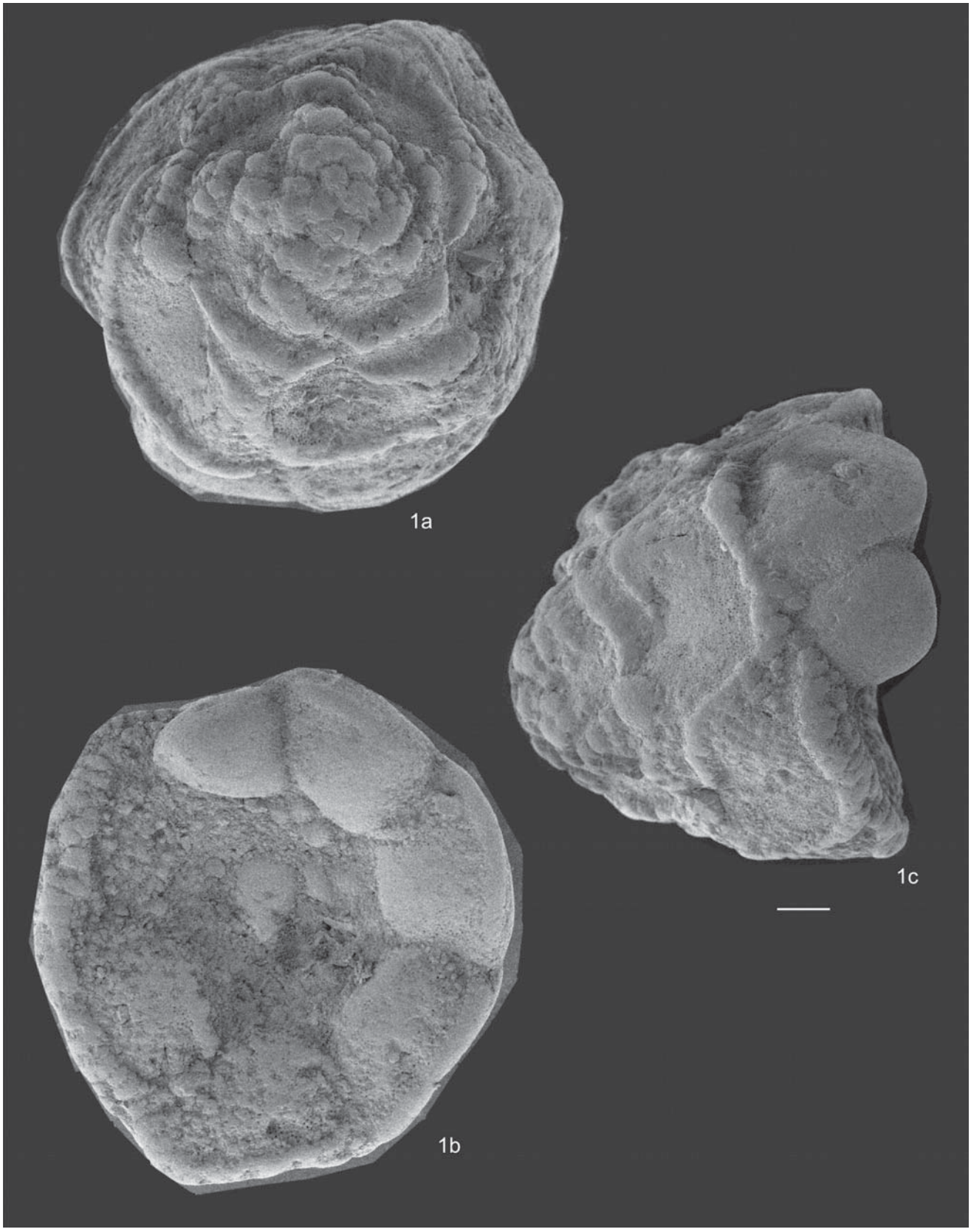

Figure 2.8. See explanation in the text.

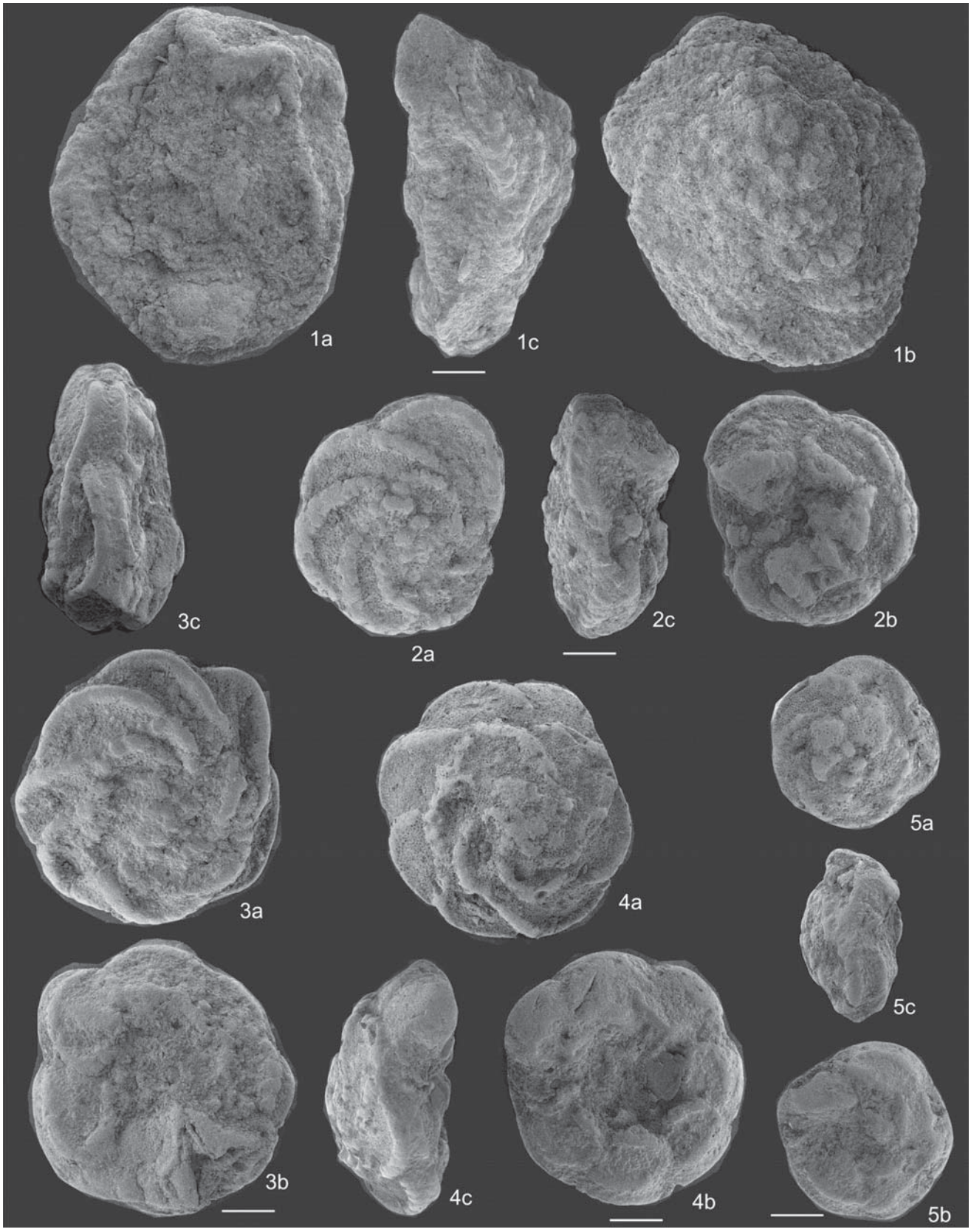

Figure 2.9. See explanation in the text.

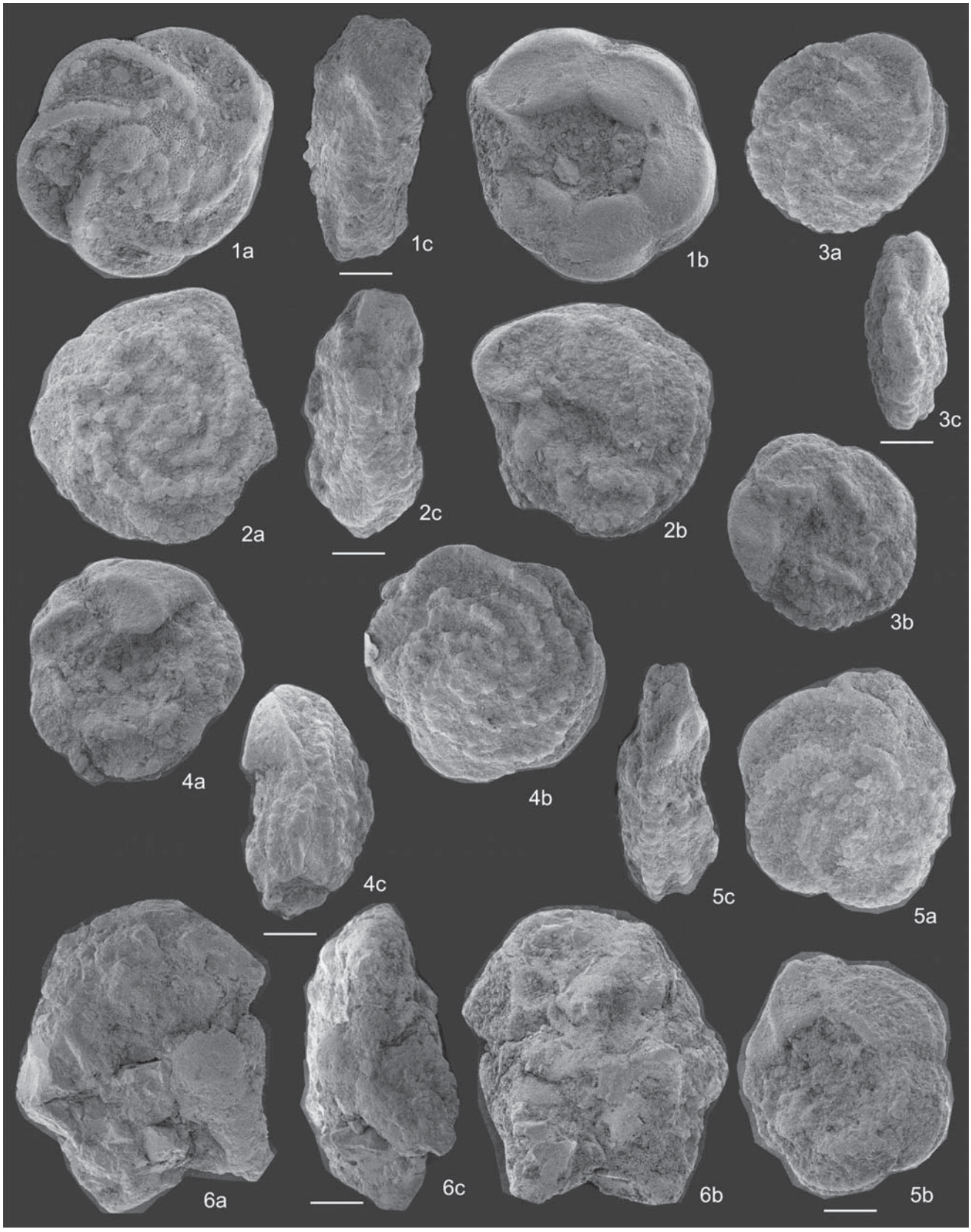

Figure 2.10. See explanation in the text.

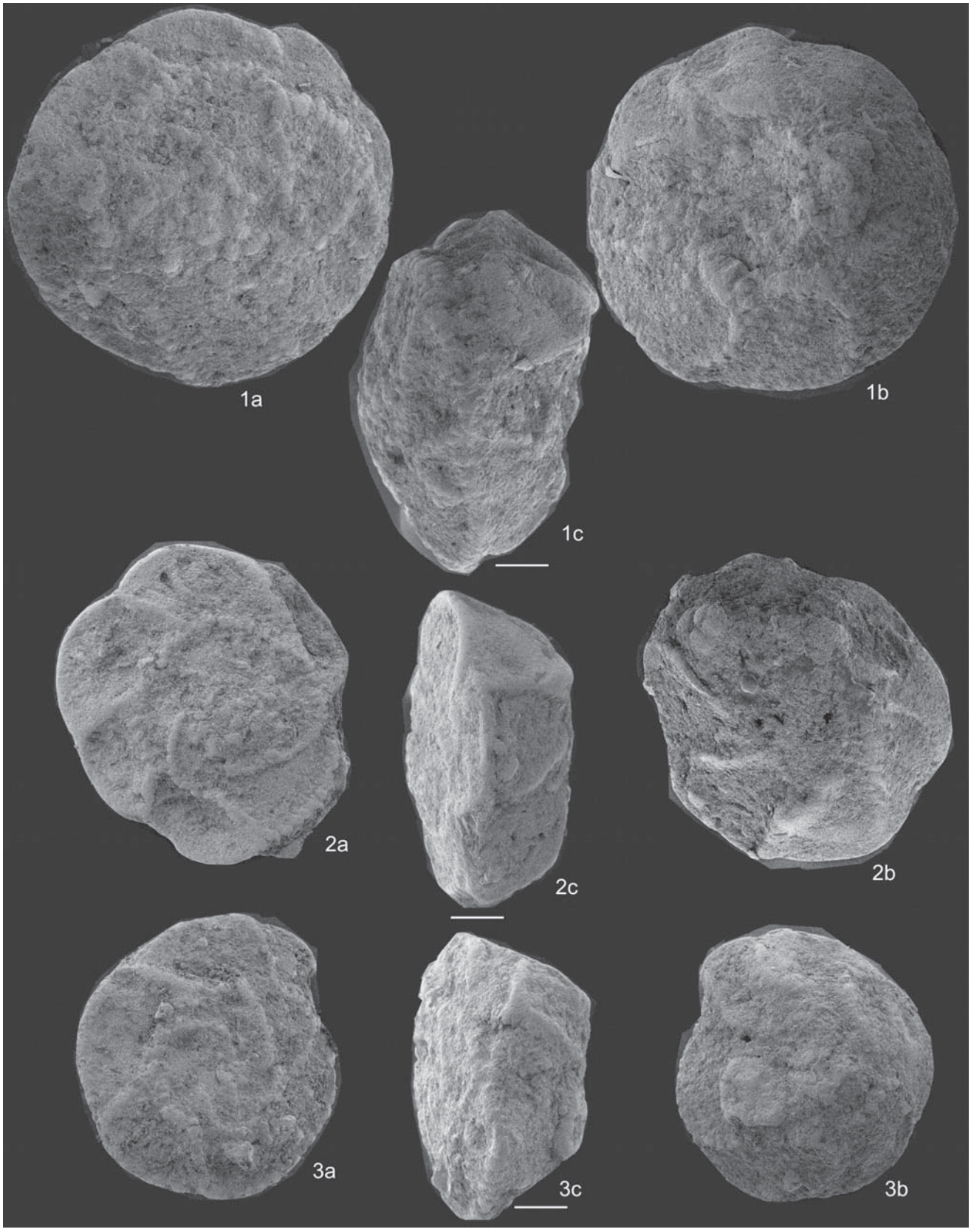

Figure 2.11. See explanation in the text.

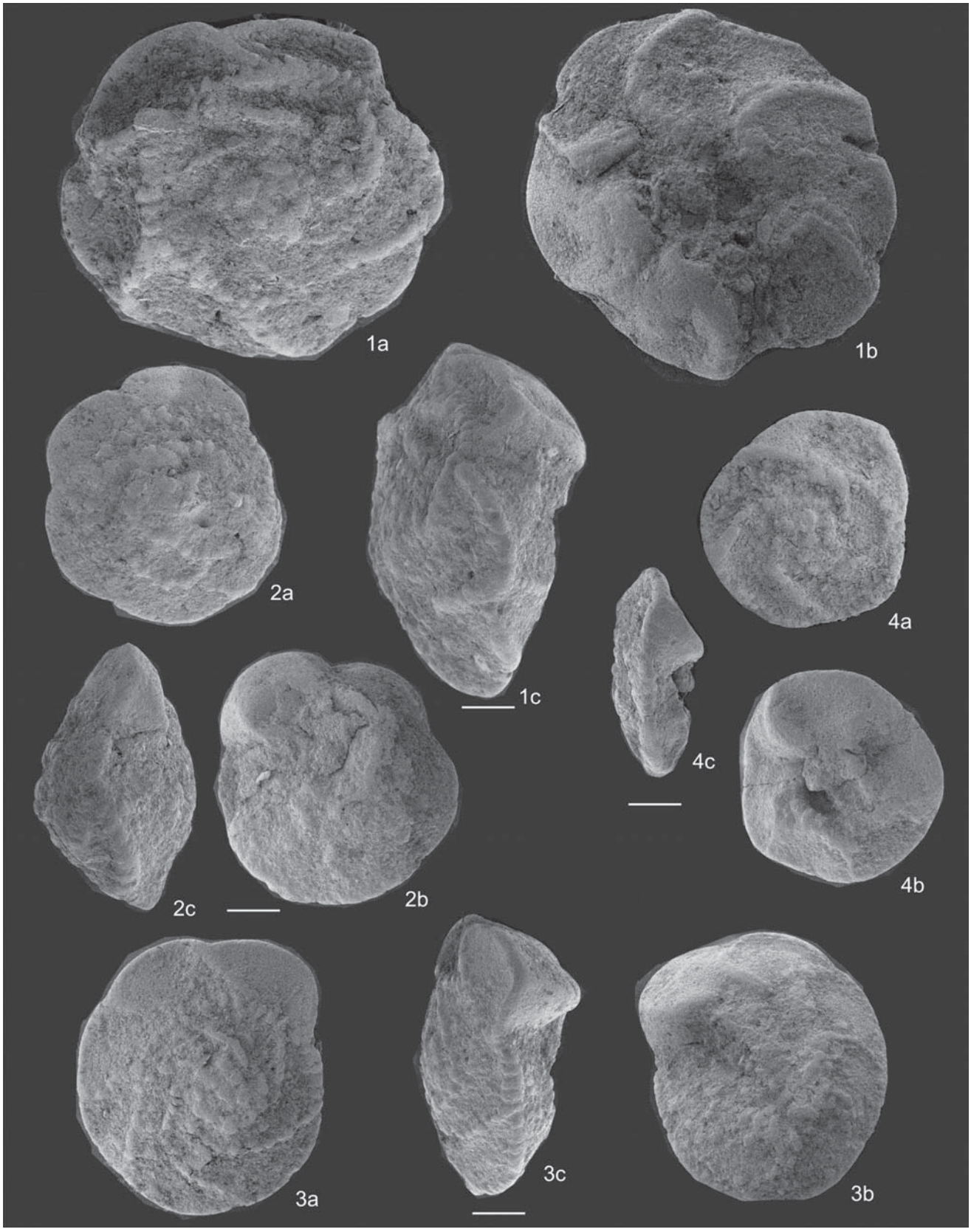

Figure 2.12. See explanation in the text.

Figure 2.13. See explanation in the text.

Figure 2.14. See explanation in the text.

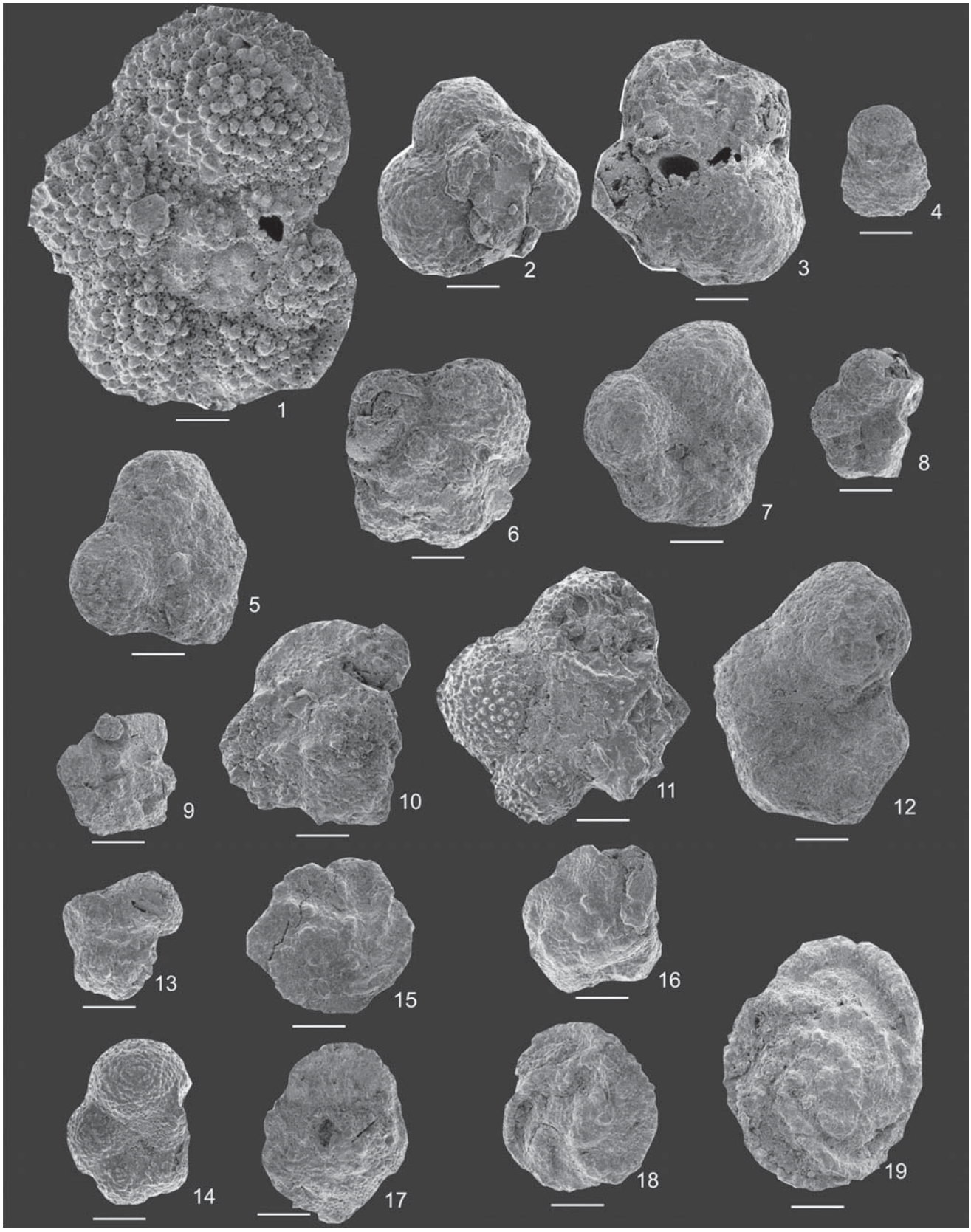

Figure 2.15. See explanation in the text.

Chapter 3. Geochemistry of Rocks in the Gams Stratigraphic Sequence

3.1 Introduction

Lahodynsky, [1988a, 1988b] was the first, who described the stratigraphic sequence in the Gams area (Knappengraben) and the transitional layer at the K/T boundary. This sequence consists of alternating calcareous marlstone and marly limestone, and the transitional clay layer is overlain by a clay dominated unit with variable proportions of Ca carbonate and occasional sandstone-siltstone intercalations. The transitional clay layer at the K/T boundary is enriched in smectite and has elevated concentrations of Ir (up to 10 ppb), Cr, Co, Ni, MgO, Al_2O_3, and TiO_2 [*Lahodynsky*, 1988a, 1988b]. The aforementioned paper presents no data concerning any factual materials on the major- and trace-element chemistry concentrations or information on the analytical techniques.

In 2005 we presented the first results of the detailed and complex examination of K/T transitional layer in the Gams area based on the study of monolith cut out from the Gams 1 (Knappengraben) section [*Grachev et al.*, 2005]. In 2006 and 2007 we repeated sampling from Gams 1 section and new Gams 2 section (see Chapter 1 for details). New chemical and isotopic analyses have been used in this chapter.

3.2 Methods of Material Preparation and Studying

To obtain the general characteristics of the sequence, the monolith was divided into 2-cm units, which were labeled A through W from the bottom to the top (Figure 1.9), and each of the units was then marked from (1, 2, 3, and so on) at intervals of 2 cm. Transitional layer J at the K/T boundary was subdivided into several subunits, 2–3 mm thick each (Figure 1.10).

Major components in bulk samples (SiO_2, TiO_2, Al_2O_3, total FeO, MgO, MnO, CaO, Na_2O, K_2O, P_2O_5, and total S) were defined by wet chemical and X-Ray fluorescence analysis (XRF) in 2005 and repeatedly in 2006.

Analysis for trace and rare earth elements. The sample selected for the analysis was decomposed in acids in a MULTIWAVE microwave furnace. 50- to 100-mg batches of the material were decomposed in a Teflon capsule in a mixture of hydrofluoric and nitric acids at the temperature of 240°C and under the pressure of no more than 72 bar for 50 min.

Fluorides of metals were decomposed by dissolving dry residues in 5–7 ml of 6.2 N HCl at 90°C for 1 h. After this the sample was spiked with an internal standard (In) and mixed with 3 ml of 3 N HNO_3. The chlorides were completely transformed into nitrates for 15–20 min at the temperature of about 200°C. The final concentration of HNO_3 was 0.5 N, and the dilution coefficient of the sample was close to 1000. This method ensured the complete decomposition of most minerals contained in the sedimentary rocks, including zircon and monazite (some spinels, such as chromite, were decomposed not fully). All of the acids utilized in this procedure were twice distilled in a quartz (or Teflon for HF) apparatus from initial analytical-grade reactants.

Mass spectrometry was conducted on an Elan 6100 DRC analytical system (Elan 6100 DRC, Software Kit, May 2000, Perkin Elmer SCIEX Instrument) in a standard mode, under the following operation conditions: nebulizer argon flow of 0.91–0.93 l min^{-1}, auxiliary argon flow of 1.17 l min^{-1}, plasma-forming argon flow of 15 l min^{-1}, the plasma generator operating at 1270–1300 W, and a voltage of 1000 V at the detector in the counting mode. The sensitivity of the analytical system was calibrated throughout the whole mass scale against standard solutions that included all elements to be analyzed in the samples. The accuracy of the analyses was monitored and the sensitivity drift was taken

=

Table 3.1. Whole-rock chemistry (wt %) of the Gams section samples

Layer	Distance, cm	SiO_2	TiO_2	Al_2O_3	Fe_2O_3	FeO	MnO	MgO	CaO	Na_2O	K_2O	P_2O_5	Al_2O_3/TiO_2	SiO_2/Al_2O_3
*A*7	–18	21.46	0.33	5.38	2.38	0.40	0.14	1.53	35.06	0.46	1.05	0.07	6.3	3.99
*B*7	–16	19.05	0.30	5.15	1.79	0.54	0.15	1.40	37.06	0.39	0.95	0.07	17.2	3.70
*C*4	–14	26.94	0.39	8.23	2.33	0.51	0.11	1.07	29.86	0.48	1.25	0.06	21.1	3.27
*D*4	–12	22.78	0.31	6.89	2.29	0.55	0.13	1.00	34.17	0.36	1.08	0.06	22.2	3.30
*E*4	–10	17.97	0.24	5.31	2.12	0.53	0.16	0.80	36.45	0.28	0.89	0.07	22.2	3.38
*F*4	–8	17.24	0.22	5.08	2.10	0.52	0.16	0.79	37.47	0.24	0.86	0.07	23.1	3.39
*G*3	–6	19.81	0.26	6.14	2.19	0.53	0.13	0.89	35.2	0.24	0.97	0.07	21.2	3.23
*H*6	–4	20.93	0.28	5.52	2.59	0.46	0.13	1.97	34.62	0.22	0.95	0.08	19.7	3.79
*I*3	–2	22.27	0.29	6.83	2.43	0.48	0.11	0.97	33.06	0.26	1.08	0.06	23.6	3.26
J2/2	**0**	**57.87**	**0.97**	**19.19**	**7.97**	**0.61**	**0.03**	**2.88**	**5.30**	**0.56**	**3.98**	**0.07**	**19.8**	**3.01**
J2/3	**0.4**	**62.33**	**0.92**	**19.26**	**7.25**	**0.75**	**0.02**	**2.73**	**2.20**	**0.37**	**3.54**	**0.05**	**20.9**	**3.23**
J2/4	**0.8**	**61.85**	**0.89**	**19.54**	**7.23**	**1.00**	**0.02**	**2.56**	**2.61**	**0.40**	**3.34**	**0.06**	**22.0**	**3.19**
J2/5	**1.2**	**61.85**	**0.91**	**19.37**	**7.37**	**0.85**	**0.02**	**2.76**	**2.50**	**0.42**	**3.46**	**0.06**	**21.3**	**3.19**
J2/6	**1.6**	**61.77**	**0.91**	**18.85**	**7.43**	**0.91**	**0.02**	**2.37**	**2.54**	**0.40**	**3.43**	**0.06**	**20.7**	**3.27**
*K*2	2	50.90	0.65	5.71	3.33	0.14	0.06	1.06	18.27	0.99	1.02	0.04	8.8	8.91
*L*6	4	51.24	0.80	13.37	5.83	0.35	0.04	2.10	8.40	0.86	2.26	0.07	16.7	3.83
*M*4	6	50.50	0.79	13.88	5.47	0.43	0.04	2.34	8.62	0.90	2.30	0.07	17.6	3.64
*N*6	8	54.14	0.89	15.54	5.62	0.54	0.04	2.27	12.43	0.92	2.89	0.08	17.5	3.48
*O*4/5	10	48.86	0.77	14.62	5.50	0.43	0.04	2.38	8.74	0.67	2.43	0.08	19.0	3.34
*P*7	12	54.57	0.82	13.90	6.54	0.40	0.05	2.67	12.77	0.43	2.63	0.05	17.0	3.92
*Q*3	14	56.80	0.84	15.18	6.93	0.29	0.04	1.83	6.93	0.69	2.84	0.05	18.1	3.74
*R*2	16	54.11	0.81	15.12	7.59	0.35	0.04	2.37	12.43	0.60	2.63	0.05	18.7	3.58
*S*7	18	70.14	0.67	7.98	2.40	0.40	0.09	1.23	11.35	1.55	1.55	0.07	11.9	8.79
*T*4/5	20	68.30	0.69	8.24	2.35	0.43	0.06	0.84	12.12	0.93	1.60	0.04	11.9	8.29
*U*8	22	55.96	0.88	15.98	7.31	0.30	0.05	2.83	11.52	0.52	2.70	0.06	18.2	3.50

Note: Transitional layer *J* is shown by bold.

into account by alternating the analyses of unknown samples and the monitor, which was standard basalt sample BCR-2 (United States Geological Survey). The detection limits (DL) were from 1–5 ppb for elements with heavy and medium masses (such as U, Th, and REE) to 20–50 ppb for light elements (such as Be and Sc). The analyses were conducted accurate to 3–10% for elemental concentrations >20–50 DL.

In a small number of samples, REE were determined by ICP-MS on a PLASMA QUARD PQ2+TURBO (VG Instruments) quadrupole mass spectrometer, following the procedure described in [*Dubinin,* 1993].

Analysis of clays. The mineralogical analysis of the pelitic fraction <4 μm was conducted on an D/MAX-2200 (Rigaku, Japan) X-ray diffractometer with Cu monochromatic radiation. The operating conditions were: 40 mA, 40 kV, 0.5°scattering slit, 0.5°and 3 mm receiving slits, 0.02°step, and 2 s collection time at a spot. The phase analysis of clay minerals was accomplished on oriented samples in air-dry and saturated with ethyleneglycol states. Minerals were identified by series of integer reflections OOl. The raw specters were processed with the Jade-6.0 (MDI, United States) computer program. The quantitative proportions of clay minerals were derived from the basal reflections in the saturated state, following the method described in [*Biskaye,* 1965]. The sum of clay minerals was normalized to 100%.

Carbon and oxygen isotopic analysis. Samples were cut, grounded, and cleaned; and their sections were examined under an optical microscope. The rocks were powdered with a Dremel MiniMite microdrill tool. The amount of the powder prepared for a single analysis was 300 μg or more, depending on expected content of carbonates. Each sample was analyzed at several spots. The spots of duplicate analyses were spaced –1 cm apart. Carbon isotopes in calcite from the samples were analyzed on Finnigan MAT 253 mass spectrometer with a Gasbench II at the Department of Earth and Space Sciences, University of California, Los Angeles. The carbon isotopic composition is defined as a deviation (in %) of the $^{13}C/^{12}C$ and $^{18}O/^{16}O$ ratios of a given sample from those of a standard, expressed in the conventional ^{13}C and ^{18}O notations relative to VPDB and SMOW. The secondary standards were NBS-19 and IAEA-CO-1. The accuracy of the analyses was higher than $\pm$0.1 % for carbon and $\pm$0.2 % for oxygen.

Helium isotopic analysis. The isotopic composition and He concentration were measured with an MI-1201 mass spectrometer no. 22-78, possessing a He sensitivity of 5×10^{-5} A Torr^{-1} for ^{3}He; the measurements were made at the Laboratory of Geochemistry and Geochronology of Isotopes, Geological Institute (Apatity), using the melting technique described in [*Kamensky et al.,* 1990]. The concentrations were measured by the peak height method with an uncertainty of 5% ($\pm1\sigma$), the errors of the isotopic ratios were $\pm$20% at $^3He/^4He = n\times10^{-8}$ and $\pm$2% at $^3He/^4He = n\times10^{-6}$. The blank experiments were conducted after the reloading of the holder, under the same conditions as those for the analysis of the samples.

Both the isotopic composition and concentration of He were measured on a MI-1201 no. 22-78 mass spectrometer at the Laboratory of Isotopic Analysis of the Geological Institute, Kola Research Center, Russian Academy of Science, in Apatity the sensitivity of 5×10^{-5} A Torr^{-1} for ^{3}He. The concentrations were deduced from the height of the peaks accurate to 5% ($\pm1\sigma$), the errors of the isotopic ratios were $\pm$20% at $^3He/^4He = n\times10^{-8}$ and $\pm$2% at $^3He/^4He = n\times10^{-6}$. The blank experiments were conducted after the reloading of the holder, under the same conditions as those for the analysis of the samples. The analyses were conducted on a MI-1201 no. 22-78 mass spectrometer using the method of melting, as described in [*Kamensky et al.,* 1990].

3.3 Whole Rock Chemistry

Table 3.1 presents data on the bulk-rock composition of the samples taken over the whole vertical section of the Gams stratigraphic sequence. It can be seen that the contents of such components as SiO_2, Al_2O_3, CaO, and K_2O definitely divide the section into three parts. The lower part (units *C–I*) has low concentrations of SiO_2, Al_2O_3, and K_2O and high contents of CaO. In the middle part (layer *J*), the composition of which was define at spots spaced 3 mm apart, the concentrations of SiO_2, Al_2O_3, and K_2O dramatically increase, and the concentrations of CaO and MnO notably decrease. The transition to the upper part of the sequence occurs through intermediate layer *K*, the contents of which Al_2O_3, FeO, CaO, Na_2O, and K_2O differ from those in both the underlaying and overlaying rocks. The top of the sequence (units *L–U*, except layers *S* and *T*) shows insignificant compositional variations.

As it is fairly difficult to quantitatively define the mineralogical composition of clay-rich sedimentary rocks, we recalculated the bulk chemical compositions of these rocks into normative minerals by the computer program [*Rosen et al.,* 2004]. This allowed us to conclude that, starting with layer *J*, the concentrations of normative quartz and clay minerals notably increase, whereas the content of calcite decreases (Table 3.2). The contents of quartz and plagioclase display a strong correlation (r = 0.8) but are not correlated with

Table 3.2. Normative mineral composition (%) of the Gams section samples

Sample	Distance from K/T boundary. cm	Ab	An	Or	Q	Mm	Ill	Chl	Kn	Cc	Ank	Rch	Ap	Rt	Ore	Total
C4	−14	0.65	0.07	–	10.59	15.04	13.91	1.87	–	53.72	3.41	0.19	0.15	0.41	0.56	99.82
D4	−12	0.51	0.06	–	9.46	10.96	11.85	2.63	–	61.13	2.72	0.22	0.15	0.32	0.47	99.79
E4	−10	1.05	0.11	–	8.64	6.18	10.11	3.15	–	67.94	2.11	0.28	0.18	0.26	0.44	99.73
F4	−8	0.77	0.08	–	8.39	5.76	9.70	3.21	–	69.43	1.98	0.27	0.18	0.23	0.41	99.73
G3	−6	–	–	–	8.75	8.98	10.92	2.78	0.61	64.78	2.52	0.22	0.17	0.27	0.44	99.78
H6	−4	1.95	0.21	0.42	17.72	9.17	9.86	9.17	–	63.85	–	0.22	0.20	0.29	0.49	100.06
I3	−2	–	–	–	10.09	9.73	12.16	3.04	0.84	60.67	2.82	0.19	0.15	0.31	0.49	99.81
J2/2	0	2.80	0.30	–	25.40	6.91	39.95	12.70	–	6.72	4.10	0.05	0.16	0.91	1.07	99.95
J2/3	0.4	–	–	–	29.63	12.57	36.18	10.67	3.61	1.33	4.99	0.03	0.11	0.88	0.99	99.97
J2/4	0.8	–	–	–	28.59	13.52	33.98	9.84	5.67	1.63	5.75	0.03	0.14	0.85	0.99	99.97
J2/5	1.2	–	–	–	28.37	14.21	35.23	10.55	3.58	1.60	5.43	0.03	0.14	0.87	1.01	99.98
J2/6	1.6	–	–	–	29.56	13.64	35.19	9.01	3.63	1.00	6.93	0.03	0.14	0.87	1.01	99.97
K2	2	8.62	0.92	4.21	39.38	–	3.61	8.84	–	32.77	0.79	0.05	0.10	1.02	0.77	99.91
K4	2	6.78	0.72	–	31.13	4.45	15.64	6.61	–	31.47	2.34	0.10	0.12	0.54	0.76	99.60
K5	2	5.25	0.56	–	33.35	–	16.28	4.25	–	32.09	5.82	0.01	0.02	0.58	0.60	99.90
L6	4	5.50	0.58	–	29.09	9.24	25.56	11.02	–	13.37	4.55	0.07	0.18	0.85	1.03	99.94
L6/1	4	1.09	0.12	–	28.69	15.03	26.20	5.19	–	14.12	8.61	0.05	0.09	0.81	0.90	99.86
M4	6	5.32	0.56	–	26.64	11.42	25.96	11.08	–	14.05	3.89	0.07	0.18	0.83	1.01	99.93
M7	6	7.37	0.78	–	28.68	0.77	29.54	12.46	–	17.07	2.24	0.05	0.20	0.84	1.04	99.95
N6	8	5.65	0.60	–	37.85	6.44	28.52	10.28	–	18.33	3.78	0.06	0.18	0.82	1.00	99.95
O2	10	–	–	–	25.70	14.39	26.66	9.73	1.37	15.31	5.93	0.04	0.20	0.76	0.87	99.96
O4/5	10	1.75	0.19	–	23.13	17.84	27.47	9.42	–	13.73	5.40	0.07	0.20	0.81	1.01	99.94
P7	12	2.19	0.23	–	29.99	5.00	26.16	13.11	–	19.82	2.56	0.06	0.11	0.76	0.87	99.93
P5/6	12	4.12	0.44	–	27.99	3.41	25.96	15.11	–	17.92	4.01	0.07	0.20	0.76	0.96	99.92
Q3	14	2.90	0.31	–	36.36	12.08	30.03	7.42	–	8.29	8.02	0.06	0.12	0.83	0.95	99.94
R2	16	1.90	0.20	–	25.68	11.58	25.08	10.54	–	17.39	5.99	0.06	0.11	0.74	0.85	99.93
S7	18	12.13	1.29	1.19	48.91	–	13.17	–	–	17.82	4.60	0.13	0.15	0.62	0.77	99.88
T4/5	22	7.39	0.79	0.66	50.09	–	14.89	–	–	19.22	1.60	0.09	0.09	0.65	0.74	99.92
U8	24	0.24	0.03	–	24.91	15.71	26.12	10.75	–	16.06	5.19	0.07	0.13	0.80	0.93	99.64

Note: Ab – Albite, An – Anortite, Or – Orthoclase, Q – Quartz, Mm – Montmorillonite, Ill – Illite, Chl – Chlorite, Kn – Kaolinite, Cc – Calcite, Ank – Ankerite, Rch – Rhodochrosite, Ap – Apatite, Rt – Rutile, Ore – Ore mineral.

the amounts of other minerals, a fact highlighting the terrigenous nature of these minerals.

An important characteristic of the Gams sequence is a drastic increase in the amount of terrigenous material in the upper part of the sequence: the percentages of normative quartz and feldspathoids (which weakly vary in the bottom part of the sequence and amount to approximately 10%) increase to 40–70% above layer *J* (Table 3.2). As follows from (Figure 3.1) and (Table 3.2), layer *K* differs from both the overlying and underlying rocks, and layer *J* has the minimum concentration of normative calcite but is rich in terrigenous components, a feature that makes it similar to the upper portion of the succession. The anomalous character of layer K can be easily explained: it has the shape of a lens, which was produced by a submarine landslide as a result of an earthquake during the Gams Basin formation (see Chapter 1).

It is pertinent to list the principal trends in the variations in the contents of major components in the vertical section of the Gams sequence.

Although correlation analysis reveals a linear character of correlations between major components in the lower and upper parts of the sequence and in its transitional layer *J* (Table 3.3, Table 3.4, and Table 3.5), it does clearly illustrate the similarities and differences. This can be done using the technique of principal components of factor analysis (Table 3.6).

Figure 3.2 presents a diagram of factors 1 and 2 on the basis of the matrix of factor loadings (Table 3.6), the sum of which makes a very significant contribution to the total dispersion (>80%), and shows the composition data points of the discrete layers of the sequence. Figure 3.2 clearly demonstrates that the layers of all of the three parts of the sequence compose three discrete fields, with the definitely separated compositions of units K, T, and S. This separation is related, first of all, to factor 1 (Al, K, Fe^{+3}, Mg, Ti, Si/Mn, and Ca),

in which Mn and Ca are opposed to the other principal components. It is pertinent to mention that layer J is characterized by elevated concentrations of K_2O, Al_2O_3, Fe_2O_3, and TiO_2 at a very low content of CaO. The variations in the concentrations of some major elements in the vertical section are displayed in Figure 3.3.

It is worth noting the Al_2O_3/TiO_2 ratio, which varies generally insignificantly in the Gams sequence below and above transitional layer J and remains within the limits of 17–23. The exceptions are layers K, S, and T, in which the Al_2O_3/TiO_2 ratio decreases to 9–13. In this context, it is pertinent to recall the well-known conclusion that "...the constancy of the Al_2O_3/TiO_2 ratio in sedimentary rocks is an indication of the terrigenous genesis of these rocks" [*Strakhov,* 1962, p. 190].

N. Strakhov also emphasized that variations in the concentrations of Al_2O_3 and TiO_2 during the post-Proterozoic evolution of the Earth were correlated. This fact led Strakhov to conclude that "...this correlation is established already when eluvium is formed and is later preserved when clays are redeposited mechanically in finite basins, for example, in seas" [*Strakhov,* 1962, p. 103]. An analogous viewpoint was expressed by *Lisitsyn* [1978]: "...The association of clay minerals in marine sediments is predetermined already in the drainage basins, i.e., the clay minerals of the World Ocean are not authigenic by terrigenous. Their systematic distributions correspond to the systematic distributions of terrigenous particles of corresponding size" [*Lisitsyn,* 1978, p. 156]. This conclusion was also confirmed (with some limitations) by the latest studies of clay minerals [*Thiry,* 2000].

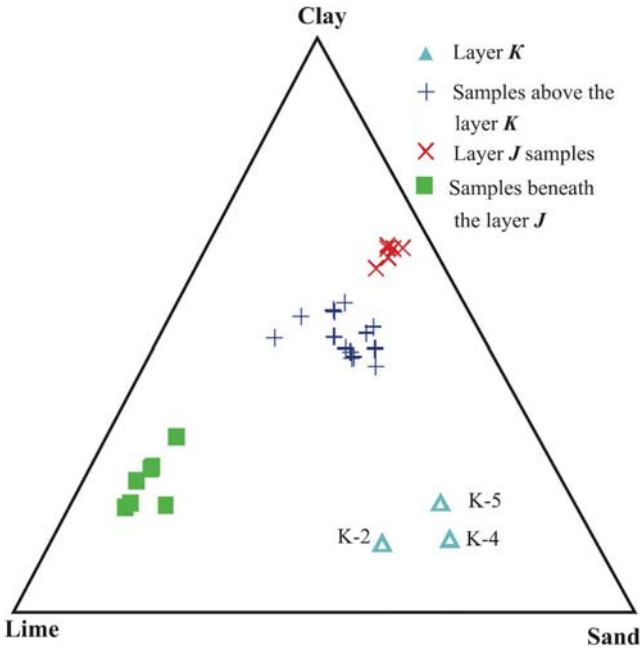

Figure 3.1. Diagram of Lime-Clay-Sand components for the Gams sections samples.

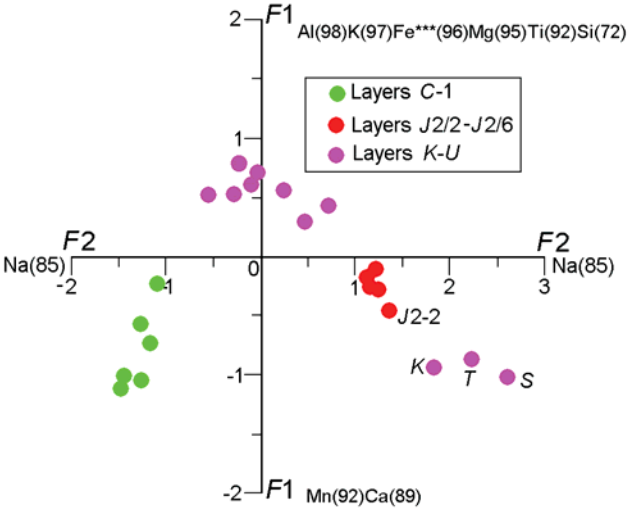

Figure 3.2. Factor diagram for the Gams sections samples.

3.4 Trace and Rare Earth Elements

Table 3.7 demonstrate the distribution of the concentrations of trace elements and REE in the vertical section of the sequence. The first results were published earlier [*Grachev et al.,* 2005] and we analysed again the additional number of samples in 2006. The variations of the most informative elements (lithophile Cr, V, Rb, Cs, Ba, Sr, Nb, and Zr; chalcophile Cu, Zn, and Ga; and siderophile Co, Ni, and Mo) are the most dramatic and mutually correlated in the vicinity of the transitional layer J.

In terms of the character of these variations, the lower part of the sequence (below layer J) notably differs from the upper part, which includes a number of units with anomalously high concentration of siderophile, chalcophile (Zn, Cu and Ni), and some other elements (layers K, S) (Figure 3.4). These variations in the upper part of the sequence were caused by the different conditions in the source area of the sediments, which is also reflected in the amounts of normative quartz (Table 3.2).

The results of correlation analysis for the upper and lower parts of the sequence and for the transitional layer (Table 3.3, Table 3.4, and Table 3.5) reveal differences between the elemental correlations. The most illustrative example is offered by the behavior of Cu: layer J displays negative relations of Cu with Ni, Co, Sc, V, and many other elements ($r > -0.7$), whereas

Table 3.3. Correlation matrix of the major and trace elements for the lower part of the Gams section (units C-I)

	SiO_2	TiO_2	Al_2O_3	FE_2O_3	MnO	MgO	CaO	Na_2O	K_2O	P_2O_5	Cr	Ni	Co	Sc	V	Cu	Pb
SiO_2	1.00	.99	.96	.50	–.86	.22	–.98	.82	.98	–.59	.68	.13	.06	.12	.46	.83	.10
TiO_2	.99	1.00	.95	.44	–.80	.21	–.97	.87	.97	–.56	.76	.03	–.05	.02	.35	.88	.01
Al_2O_3	.96	.95	1.00	.28	–.84	–.06	–.95	.85	.99	–.76	.74	.02	–.04	.02	.37	.80	–.06
Fe_2O_3	.50	.44	.28	1.00	–.66	.86	–.50	–.02	.38	.16	–.20	.80	.75	.74	.79	.19	.84
MnO	–.86	–.80	–.84	–.66	1.00	–.29	.89	–.45	–.86	.49	–.28	–.49	–.49	–.49	–.74	–.56	–.43
MgO	.22	.21	–.06	.86	–.29	1.00	–.20	–.17	.05	.58	–.28	.56	.51	.46	.42	.07	.66
CaO	–.98	–.97	–.95	–.50	.89	–.20	1.00	–.78	–.97	.56	–.66	–.19	–.11	–.20	–.50	–.85	–.16
Na_2O	.82	.87	.85	–.02	–.45	–.17	–.78	1.00	.84	–.68	.97	–.40	–.49	–.37	–.05	.87	–.42
K_2O	.98	.97	.99	.38	–.86	.05	–.97	.84	1.00	–.71	.72	.07	.02	.09	.43	.82	.02
P_2O_5	–.59	–.56	–.76	.16	.49	.58	.56	–.68	–.71	1.00	–.59	.14	.14	.05	–.24	–.44	.25
Cr	.68	.76	.74	–.20	–.28	–.28	–.66	.97	.72	–.59	1.00	–.56	–.66	–.53	–.24	.86	–.57
Ni	.13	.03	.01	.80	–.49	.56	–.19	–.40	.07	.14	–.56	1.00	.97	.99	.91	–.17	.99
Co	.06	–.05	–.04	.75	–.49	.51	–.11	–.49	.02	.14	–.66	.97	1.00	.95	.87	–.29	.95
Sc	.12	.02	.02	.74	–.49	.46	–.20	–.37	.09	.05	–.53	.99	.95	1.00	.92	–.16	.97
V	.46	.35	.37	.79	–.74	.42	–.50	–.05	.43	–.24	–.24	.91	.87	.92	1.00	.14	.86
Cu	.83	.88	.80	.19	–.56	.07	–.85	.87	.82	–.44	.86	–.17	–.29	–.16	.14	1.00	–.17
Pb	.10	.01	–.06	.84	–.43	.66	–.16	–.42	.02	.25	–.57	.99	.95	.97	.86	–.17	1.00
Zn	.96	.94	.90	.52	–.78	.22	–.91	–.81	.94	–.64	.65	.17	.09	.18	.50	.75	.14
Bi	.09	.01	–.10	.86	–.40	.73	–.14	–.43	–.01	.33	–.58	.97	.93	.94	.82	–.17	.99
W	.10	.01	–.06	.83	–.44	.64	–.16	–.42	.03	.23	–.57	.99	.95	.97	.87	–.17	.99
Mo	.08	.01	–.12	.87	–.38	.76	–.13	–.44	–.02	.37	–.58	.95	.91	.91	.80	–.17	.99
Rb	.33	.24	.19	.88	–.63	.59	–.39	–.20	.27	.01	–.38	.98	.93	.97	.95	.01	.96
Cs	.11	.01	–.03	.80	–.46	.58	–.18	–.40	.05	.17	–.56	.99	.96	.99	.89	–.17	.99
Ba	.63	.54	.55	.75	–.78	.35	–.65	.22	.61	.44	.02	.77	.70	.79	.95	.32	.72
Sr	.08	–.02	–.08	.83	–.42	.66	–.13	–.45	.02	.27	–.60	.99	.96	.96	.86	–.20	.99
Tl	.10	.01	–.05	.83	–.44	.63	–.16	–.41	.03	.22	–.57	.99	.95	.98	.87	–.17	.99
Ga	.11	.01	–.04	.82	–.45	.60	–.17	–.41	.04	.19	–.56	.99	.95	.98	.89	–.17	.99
Ta	.10	.01	–.07	.85	–.42	.67	–.15	–.42	.01	.27	–.57	.99	.94	.96	.86	–.17	.99
Nb	.11	.02	–.03	.80	–.46	.57	–.18	–.40	.05	.16	–.56	.99	.96	.99	.90	–.16	.99
Hf	–.03	–.03	–.30	.74	–.06	.97	–.04	–.37	–.20	.75	–.43	.53	.48	.42	.29	—.11	.64
Zr	.83	.78	.71	.80	–.86	.46	–.85	.46	.78	–.38	.28	.63	.52	.63	.83	.60	.61
Y	–.22	–.32	–.35	.64	–.18	.54	.17	–.69	–.28	.39	–.81	.92	.93	.90	.73	–.45	.93
Th	.11	.02	–.03	.80	–.46	.57	–.18	–.40	.05	.16	–.56	.99	.96	.99	.90	–.17	.99
U	.09	.01	–.08	.85	–.41	.70	–.15	–.43	.01	.30	–.58	.98	.93	.95	.84	–.17	.99
SiO_2	.96	.09	.10	.08	.33	.11	.63	.08	.10	.11	.10	.11	–.03	.83	–.22	.11	.09
TiO_2	.94	.01	.01	.01	.24	.01	.54	–.02	.01	.01	.01	.02	–.03	.78	–.32	.02	.01
Al_2O_3	.94	–.10	–.06	–.12	.19	–.03	.55	–.08	–.05	–.04	–.07	–.03	–.30	.71	–.35	–.03	–.08
Fe_2O_3	.90	.86	.83	.87	.88	.80	.75	.83	.83	.82	.85	.80	.74	.80	.64	.80	.85
MnO	.52	–.40	–.44	–.38	–.63	–.46	–.78	–.42	–.44	–.45	–.42	–.46	–.06	–.86	–.18	–.46	–.41
MgO	–.78	.73	.64	.76	.59	.58	.35	.66	.63	.60	.67	–.57	.97	.46	.54	.57	.70
CaO	–.91	–.14	–.16	–.13	–.39	–.18	–.65	–.13	–.16	–.17	–.15	–.18	.04	–.85	.17	–.18	–.15
Na_2O	.81	–.43	–.42	–.44	–.20	–.40	.22	–.45	–.41	–.41	–.42	–.40	–.37	.46	–.69	–.40	–.43
K_2O	.94	–.01	.03	–.02	.27	.05	.61	.01	.03	.04	.01	.05	–.20	.78	–.28	.05	.01
P_2O_5	–.64	.33	.23	.37	.01	.17	–.44	.27	.22	.19	.27	.16	.75	–.38	.39	.16	.30
Cr	.65	–.58	–.57	–.58	–.38	–.56	.02	–.60	–.57	–.56	–.57	–.56	–.43	.28	–.81	–.56	–.58
Ni	.17	.97	.99	.85	.98	.99	.77	.99	.99	.99	.99	.99	.53	.63	.92	.99	.98
Co	.09	.93	.95	.91	.93	.96	.70	.96	.94	.95	.94	.96	.48	.52	.93	.96	.93
Sc	.18	.94	.97	.91	.97	.99	.79	.96	.96	.98	.96	.99	.42	.63	.90	.99	.95
V	.50	.82	.87	.80	.95	.89	.95	.89	.86	.89	.86	.90	.29	.83	.73	.90	.84
Cu	.75	–.17	–.17	–.17	.01	–.17	.32	–.20	–.17	–.17	–.17	–.16	–.11	.60	.93	.99	.99
Pb	.14	.99	.99	.99	.96	.99	.72	.99	.99	.99	.99	.99	.64	.61	.93	.99	.99
Zn	1.00	.13	.15	.12	.37	.16	.71	.12	.15	.15	.14	.16	–.02	.84	–.17	.16	.13
Bi	.13	1.00	.99	.99	.94	.98	.68	.99	.99	.98	.99	.98	.71	.59	.92	.98	.99
W	.15	.99	1.00	.98	.97	.99	.73	.99	.99	.99	.99	.99	.62	.61	.93	.99	.99
Mo	.12	.99	.98	1.00	.93	.96	.66	.99	.98	.97	.99	.96	.75	.58	.92	.96	.99
Rb	.37	.94	.97	.93	1.00	.97	.86	.96	.97	.97	.96	.97	.50	.77	.82	.97	.95

Table 3.3. Continued

	Zn	Bi	W	Mo	Rb	Cs	Ba	Sr	Tl	Ga	Ta	Nb	Hf	Zr	Y	Th	U
Cs	.16	.98	.99	.96	.97	1.00	.76	.99	.99	.99	.99	.99	.55	.62	.93	.99	.99
Ba	.71	.68	.73	.66	.86	.76	1.00	.71	.74	.75	.72	.76	.18	.91	.53	.76	.70
Sr	.12	.99	.99	.99	.96	.99	.71	1.00	.99	.99	.99	.99	.64	.59	.94	.99	.99
Tl	.15	.99	.99	.98	.97	.99	.74	.99	1.00	.99	.99	.99	.61	.62	.93	.99	.99
Ga	.15	.98	.99	.97	.97	.99	.75	.99	.99	1.00	.99	.99	.58	.62	.93	.99	.99
Ta	.14	.99	.99	.99	.96	.99	.72	.99	.99	.99	1.00	.00	.65	.61	.93	.99	.99
Nb	.16	.98	.99	.96	.97	.99	.76	.99	.99	.99	.99	1.00	.55	.62	.93	.99	.99
Hf	-.02	.71	.62	.75	.50	.55	.18	.64	.61	.58	.65	.55	1.00	.27	.59	.55	.68
Zr	.84	.59	.61	.58	.77	.62	.91	.59	.62	.62	.61	.62	.27	1.00	.31	.62	.60
Y	-.17	.92	.93	.92	.82	.93	.53	.94	.93	.93	.93	.93	.59	.31	1.00	.93	.93
Th	.16	.98	.99	.96	.97	.99	.76	.99	.99	.99	.99	.99	.55	.62	.84	1.00	.99
U	.13	.99	.99	.99	.95	.99	.70	.99	.99	.99	.99	.99	.68	.60	.93	.99	1.00

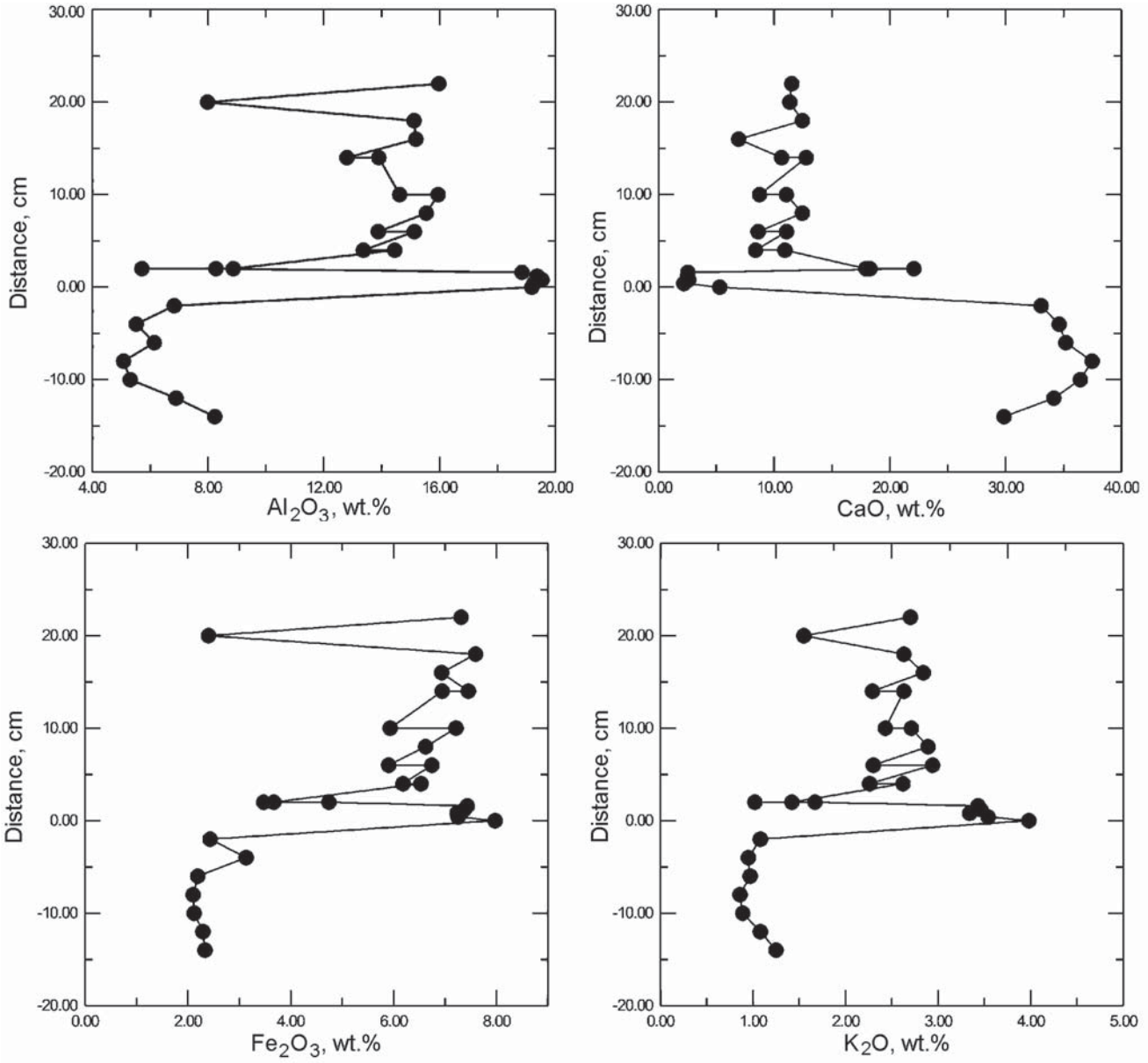

Figure 3.3. Variations of Al_2O_3, CaO, Fe_2O_3 and K_2O above and below the K/T boundary at the Gams section.

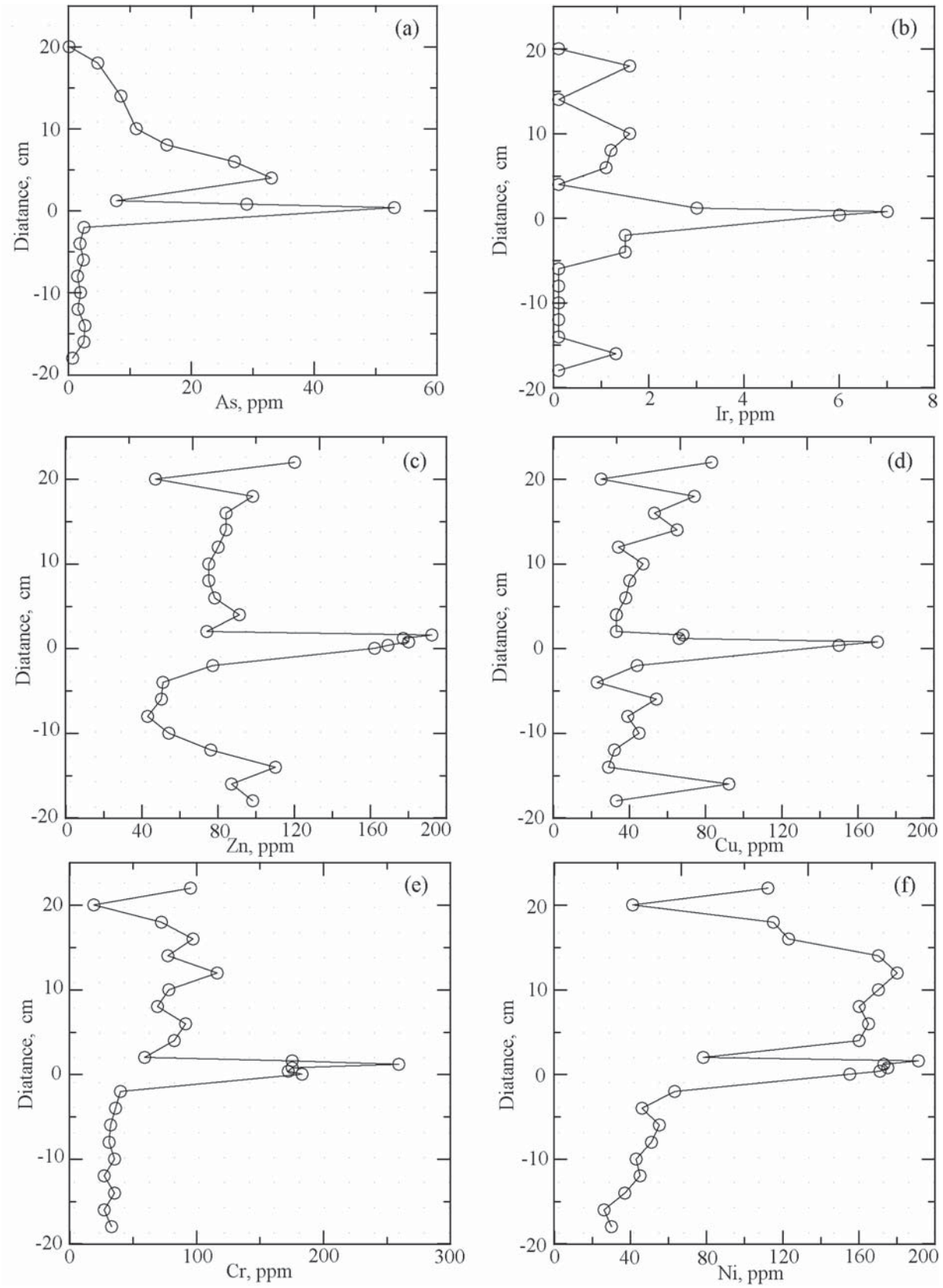

Figure 3.4. Variations of trace elements concentrations above and below the K/T boundary at the Gams section.

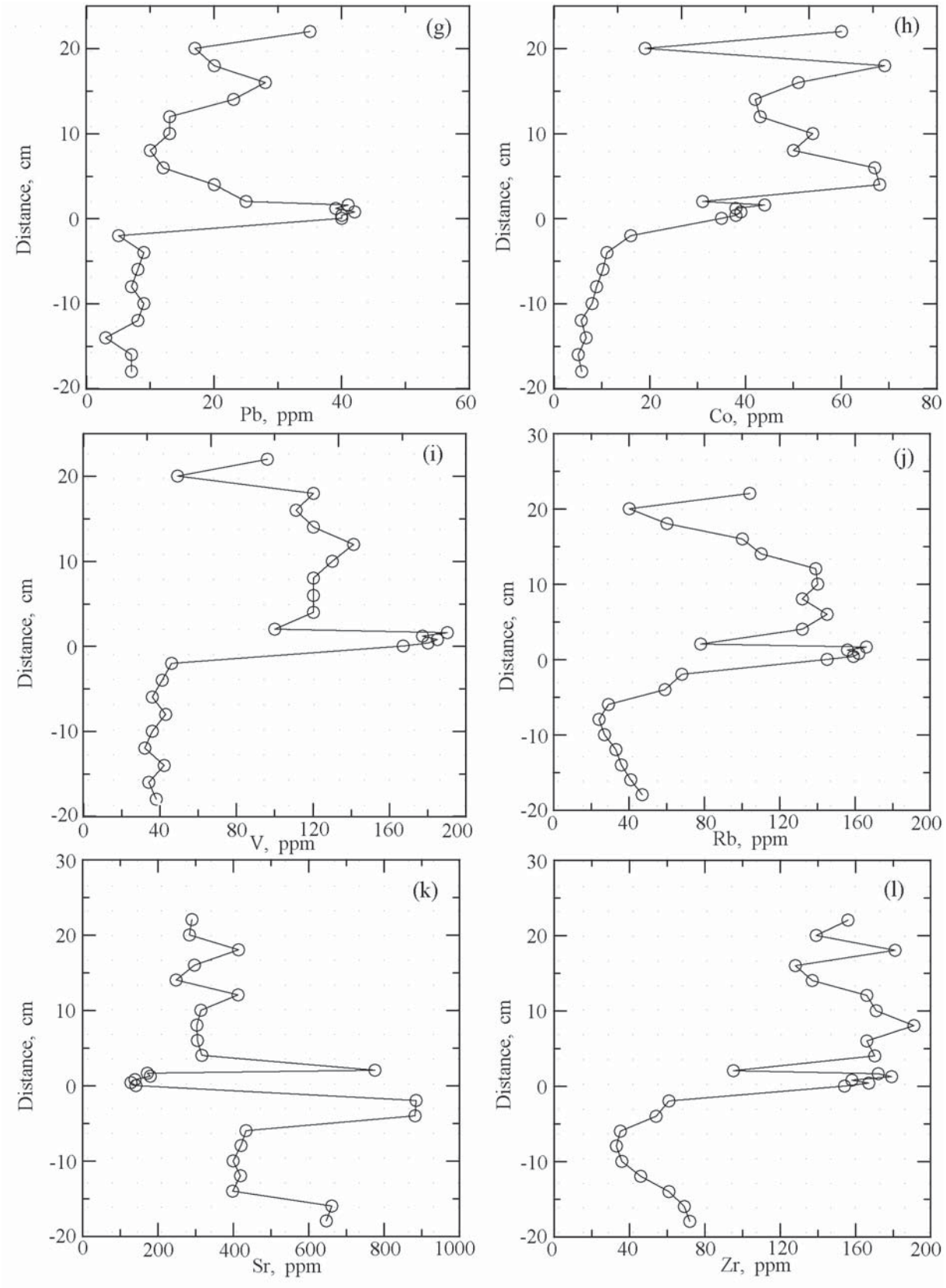

Figure 3.4. Continued.

Table 3.4. Correlation matrix of the major and trace elements for the transition layer of the Gams section (layers $J2 - J6$)

	SiO_2	TiO_2	Al_2O_3	Fe_2O_3	MnO	MgO	CaO	Na_2O	K_2O	P_2O_5	Cr	Ni	Co	Sc	V	Cu	Pb
SiO_2	1.00	–.90	.13	–.97	–.99	–.56	1.00	–.99	–.93	–.86	.11	.74	.60	.40	.79	–.67	.43
TiO_2	–.90	1.00	–.29	.93	.93	.67	.89	.87	.99	.59	–.10	–.74	–.61	–.46	–.83	.74	–.64
Al_2O_3	.13	–.29	1.00	–.32	–.11	.43	–.10	–.08	–.19	–.10	.27	–.42	–.57	–.67	–.24	.12	–.06
Fe_2O_3	–.97	.93	–.32	1.00	.96	.50	.96	.97	.93	.84	–.04	–.63	–.48	–.27	–.74	.57	–.49
MnO	–.99	.93	–.11	.96	1.00	.62	.99	.97	.96	.79	–.15	–.79	–.65	–.47	–.82	.75	–.47
MgO	–.56	.67	.43	.50	.62	1.00	.56	.59	.71	.27	.34	–.94	–.96	–.92	–.95	.63	–.85
CaO	1.00	.89	–.10	.96	.99	.56	1.00	.99	.92	.86	–.13	–.75	–.61	–.42	–.78	.68	–.41
Na_2O	–.99	.87	–.08	.97	.97	.59	.99	1.00	.90	.90	.03	–.74	–.61	–.41	–.81	.58	–.49
K_2O	–.93	.99	–.19	.93	.96	.71	.92	.90	1.00	.62	–.11	–.80	–.68	–.52	–.87	.78	–.63
P_2O_5	–.86	.59	–.10	.84	.79	.27	.86	.90	.62	1.00	.10	–.44	–.32	–.09	–.53	.24	–.21
Cr	.11	–.10	.27	–.04	–.15	.34	–.13	.03	–.11	.10	1.00	–.07	–.20	–.15	–.26	–.51	–.60
Ni	.74	–.74	–.42	–.63	–.79	–.94	–.75	–.74	–.80	–.44	–.07	1.00	.98	.91	.95	–.80	.65
Co	.60	–.61	–.57	–.48	–.65	–.96	–.61	–.61	–.68	–.32	–.20	.98	1.00	.97	.92	–.71	.68
Sc	.40	–.46	–.67	–.27	–.47	–.92	–.42	–.41	–.52	–.09	–.15	.91	.97	1.00	.81	–.69	.60
V	.79	–.83	–.24	–.74	–.82	–.95	–.78	–.81	–.87	–.53	–.26	.95	.92	.81	1.00	–.67	.82
Cu	–.67	.74	.12	.57	.75	.63	.68	.58	.78	.24	–.51	–.80	–.71	–.69	–.67	1.00	–.28
Pb	.43	–.64	–.06	–.49	–.47	–.85	–.41	–.49	–.63	–.21	–.60	.65	.68	.60	.82	–.28	1.00
Zn	.61	–.72	–.37	–.52	–.69	–.94	–.62	–.59	–.77	–.22	–.00	.96	.95	.94	.91	–.85	.68
Bi	.67	–.54	.40	–.77	–.59	–.17	–.65	–.74	–.52	–.85	–.40	.19	.09	–.15	.42	.09	.41
W	.28	–.47	.49	–.29	–.35	.03	–.28	–.14	–.44	.11	.85	.14	–.01	.01	.05	–.68	–.14
Mo	–.74	.68	.42	.60	.79	.77	.76	.71	.75	.45	–.23	–.94	–.89	–.84	–.81	.90	–.36
Rb	.85	–.88	–.15	–.82	–.88	–.90	–.85	–.87	–.91	–.61	–.21	.93	.88	.74	.99	–.68	.79
Cs	.70	–.73	–.37	–.65	–.73	–.97	–.70	–.75	–.77	–.49	–.39	.94	.94	.85	.98	–.58	.83
Ba	.67	–.70	–.42	–.54	–.73	–.87	–.68	–.63	–.76	–.30	.14	.97	.94	.92	.86	–.91	.52
Sr	.17	–.22	–.35	–.01	–.25	–.31	–.19	–.05	–.28	.22	.69	.49	.46	.58	.23	–.81	–.14
Tl	.72	–.63	–.49	–.57	–.77	–.76	–.74	–.69	–.71	–.46	.20	.93	.89	.85	.80	–.87	.34
Ga	.76	–.75	–.41	–.67	–.80	–.95	–.77	–.78	–.81	–.51	–.18	.99	.97	.89	.98	–.73	.70
Ta	.93	–.71	.03	–.90	–.89	–.43	–.94	–.96	–.75	–.98	–.07	.61	.49	.27	.67	–.41	.32
Nb	.89	–.82	–.27	–.81	–.91	–.85	–.90	–.91	–.87	–.70	–.11	.95	.89	.75	.95	–.72	.62
Hf	.44	–.25	–.39	–.25	–.47	–.22	–.47	–.36	–.34	–.27	.67	.52	.45	.46	.26	–.75	–.31
Zr	.64	–.45	–.23	–.47	–.66	–.27	–.66	–.55	–.53	–.45	.66	.59	.48	.44	.39	–.81	–.19
Y	.81	–.95	.56	–.87	–.84	–.42	–.79	–.75	–.91	–.49	.29	.51	.35	.20	.61	–.68	.46
Th	.95	–.87	.20	–.90	–.96	–.43	–.95	–.89	–.89	–.74	.41	.67	.50	.34	.65	–.79	.22
U	.98	–.89	–.04	–.91	–.99	–.69	–.98	–.96	–.94	–.77	.13	.86	.74	.58	.86	–.78	.47

these correlations are absent both below and above this layer. It is important to mention that this layer appeared to bear particles of native silver, copper, gold (see details in Chapter 4).

Since layer J is of particular interest, it was subdivided into a number of units in order to determine how concentrations of Ir and other elements vary from the bottom to the top of this layer.

Arsenic anomaly. The high As concentration in the lower part of the transitional layer in the Gams section together with an enrichment of Zn, Co, Cu, Pb (Figure 3.4) was recorded at the Cretaceous-Paleogene boundary in nearly all similar sections of the world. This fact cannot be explained in terms of the impact paradigm, because the As concentration does not exceed 2 ppm in meteorites [*Hamaguchi et al.*, 1969] and is three to four orders of magnitude higher at the base of the transitional layer! [*Brooks et al.*, 1984; *Ebihara, Miura*, 1996; *Grachev et al.*, 2005, and others].

Iridium anomaly. After the first discovery of Ir anomaly at the K/T boundary in Gubbio (Italy) and Stevns Klint (Denmark) [*Alvarez et al.*, 1980] a lot of localities was rapidly established both in continents and in deep-sea drilling holes in oceans [*Alvarez et al.*, 1992; *Hsu et al.*, 1982; *Kyte, Bostwick*, 1995, and several others]. The high Ir concentrations at the K/T boundary,

Table 3.4. Continued

	Zn	Bi	W	Mo	Rb	Cs	Ba	Sr	Tl	Ga	Ta	Nb	Hf	Zr	Y	Th	U
SiO_2	.61	.67	.28	–.74	.85	.70	.67	.17	.72	.76	.93	.89	.44	.64	.81	.95	.98
TiO_2	–.72	–.54	–.47	.68	–.88	–.73	–.70	–.22	–.63	–.75	–.71	–.82	–.25	–.45	–.95	–.87	–.89
Al_2O_3	–.37	.40	.49	.42	–.15	–.37	–.42	–.35	–.49	–.41	.03	–.27	–.39	–.23	.56	.20	–.04
Fe_2O_3	–.52	–.77	–.29	.60	–.82	–.65	–.54	–.01	–.57	–.67	–.90	–.81	–.25	–.47	–.87	–.90	–.91
MnO	–.69	–.59	–.35	.79	–.88	–.73	–.73	–.25	–.77	–.80	–.89	–.91	–.47	–.66	–.84	–.96	–.99
MgO	–.94	–.17	.03	.77	–.90	–.97	–.87	–.31	–.76	–.95	–.43	–.85	–.22	–.27	–.42	–.43	–.69
CaO	–.62	–.65	–.28	.76	–.85	–.70	–.68	–.19	–.74	–.77	–.94	–.90	–.47	–.66	–.79	–.95	–.98
Na_2O	–.59	–.74	–.14	.71	–.87	–.75	–.63	–.05	–.69	–.78	–.96	–.91	–.36	–.55	–.75	–.89	–.96
K_2O	–.77	–.52	–.44	.75	–.91	–.77	–.76	–.28	–.71	–.81	–.75	–.87	–.34	–.53	–.91	–.89	–.94
P_2O_5	–.22	–.85	.11	.45	–.61	–.49	–.30	.22	–.46	–.51	–.98	–.70	–.27	–.45	–.49	–.74	–.77
Cr	–.00	–.40	.85	–.23	–.21	–.39	.14	.69	.20	–.18	–.07	–.11	.67	.66	.29	.41	.13
Ni	.96	.19	.14	–.94	.93	.94	.97	.49	.93	.99	.61	.95	.52	.59	.51	.67	.86
Co	.95	.09	–.01	–.89	.88	.94	.94	.46	.89	.97	.49	.89	.45	.48	.35	.50	.74
Sc	.94	–.15	.01	–.84	.74	.85	.92	.58	.85	.89	.27	.75	.46	.44	.20	.34	.58
V	.91	.42	.05	–.81	.99	.98	.86	.23	.80	.98	.67	.95	.26	.39	.61	.65	.86
Cu	–.85	.09	–.68	.90	–.68	–.58	–.91	–.81	–.87	–.73	–.41	–.72	–.75	–.81	–.68	–.79	–.78
Pb	.68	.41	–.14	–.36	.79	.83	.52	–.14	.34	.70	.32	.62	–.31	–.19	.46	.22	.47
Zn	1.00	.01	.27	–.89	.87	.88	.97	.59	.87	.93	.41	.85	.46	.51	.53	.58	.76
Bi	.01	1.00	–.24	–.06	.50	.39	–.01	–.62	.06	.29	.79	.47	–.27	–.05	.50	.47	.52
W	.27	–.24	1.00	–.31	.10	–.11	.32	.65	.24	.04	–.02	.07	.45	.51	.66	.54	.30
Mo	–.89	–.06	–.31	1.00	–.81	–.78	–.97	–.68	1.00	–.90	–.61	–.89	–.77	–.82	–.49	–.77	–.87
Rb	.87	.50	.10	–.81	1.00	.96	.84	.20	.79	.96	.74	.97	.27	.42	.69	.73	.91
Cs	.88	.39	–.11	–.78	.96	1.00	.83	.18	.78	.97	.63	.93	.22	.31	.47	.54	.79
Ba	.97	–.01	.32	–.97	.84	.83	1.00	.68	.96	.93	.48	.87	.65	.69	.51	.67	.81
Sr	.59	–.62	.65	–.68	.20	.18	.68	1.00	.66	.37	–.07	.28	.83	.75	.20	.39	.33
Tl	.87	.06	.24	1.00	.79	.78	.96	.66	1.00	.90	.61	.89	.78	.82	.43	.74	.85
Ga	.93	.29	.04	–.90	.96	.97	.93	.37	.90	1.00	.66	.97	.44	.52	.51	.66	.87
Ta	.41	.79	–.02	–.61	.74	.63	.48	–.07	.61	.66	1.00	.82	.36	.54	.59	.82	.88
Nb	.85	.47	.07	–.89	.97	.93	.87	.28	.89	.97	.82	1.00	.47	.59	.61	.79	.95
Hf	.46	–.27	.45	–.77	.27	.22	.65	.83	.78	.44	.36	.47	1.00	.97	.19	.61	.55
Zr	.51	–.05	.51	–.82	.42	.31	.69	.75	.82	.52	.54	.59	.97	1.00	.40	.79	.71
Y	.53	.50	.66	–.49	.69	.47	.51	.20	.43	.51	.59	.61	.19	.40	1.00	.84	.76
Th	.58	.47	.54	–.77	.73	.54	.67	.39	.74	.66	.82	.79	.61	.79	.84	1.00	.94
U	.76	.52	.30	–.87	.91	.79	.81	.33	.85	.87	.88	.95	.55	.71	.76	.94	1.00

Note: Correlation matrix of the major and trace elements for the transition layer of the Gams section (layers $J2 - J6$).

much higher than those know in terrestrial rocks, were explained by the fall of a meteorite (or an asteroid) 65 Ma ago [*Alvarez et al.,* 1980].

However later multiple Ir anomalies were found in some localities [*Crockett et al.,* 2004; *Ganapathy et al.,* 1981; *Rocchia et al.,* 1990]. The best example is the K/T boundary section in Lattengebirge (Bavarian Alps), where three iridium anomalies were determined below, above and at the K/T boundary [*Graup, Spettel,* 1989].

Taking into account the importance of iridium study we repeated the sampling and analysis of Ir in the Gams section both as a whole and at the transitional layer. In comparison with the first results [*Grachev et al.,* 2005] we found four Ir anomalies: the large well expressed anomaly at the boundary, two other anomalies above and one anomaly below (Figure 3.4).

Important is the similar trend of Ir, Cr, Zn, Pb and Ni in the Gams section from the bottom to the top (Figure 3.4). These results are in contradiction with the K/T boundary stratotype at El Kef (Tunisia) where Ir anomaly coincides with a rust-coloured goethite clay

Table 3.5. Correlation matrix of the major elements for the upper part of the Gams section (units K/T)

	SiO_2	TiO_2	Al_2O_3	Fe_2O_3	MnO	MgO	CaO	Na_2O	K_2O	P_2O_5	Cr	Ni	Co	Sc	V	Cu	Pb
SiO_2	1.00	–.30	–.55	–.75	.65	–.59	–.01	.66	–.49	–.18	–.90	–.50	.60	–.26	–.74	.07	–.48
TiO_2	–.30	1.00	.92	.72	–.79	.77	–.51	–.37	.94	.39	.39	.81	.06	.07	.71	.12	–.27
Al_2O_3	–.55	.92	1.00	.88	–.90	.89	–.52	–.57	.97	.42	.57	.79	–.11	.24	.81	.13	.00
Fe_2O_3	–.75	.72	.88	1.00	–.88	.82	–.24	–.79	.88	.20	.69	.66	–.36	.33	.74	.16	.38
MnO	.65	–.79	–.90	–.88	1.00	–.81	.46	.75	–.85	–.29	–.61	–.78	.39	–.47	–.76	.07	–.26
MgO	–.59	.77	.89	.82	–.81	1.00	–.47	–.54	.83	.54	.67	.82	–.05	.40	.85	.09	.00
CaO	–.00	.51	–.52	–.24	.46	–.47	1.00	–.09	–.43	–.71	–.11	–.35	–.18	–.14	–.36	–.14	.25
Na_2O	.66	–.37	–.57	–.79	.75	–.54	–.09	1.00	–.58	.25	–.49	–.39	.66	–.50	–.44	.22	–.63
K_2O	–.49	.94	.97	.88	–.85	.83	–.43	–.58	1.00	.33	.49	.76	–.13	.09	.74	.21	–.04
P_2O_5	–.18	.39	.42	.20	–.29	.54	–.71	.25	.33	1.00	.30	.51	.20	.00	.54	.46	–.40
Cr	–.90	.39	.57	.69	–.61	.67	–.11	–.49	.49	.30	1.00	.65	–.28	.17	.87	–.15	.22
Ni	–.50	.81	.79	.66	–.78	.82	–.35	–.39	.76	.51	.65	1.00	–.00	.16	.90	.05	–.26
Co	.60	.06	–.11	–.36	.39	–.05	–.18	.66	–.13	.20	–.28	–.00	1.00	–.27	–.11	.20	–.65
Sc	–.26	.07	.24	.33	–.47	.40	–.14	–.50	.09	.00	.17	.16	–.27	1.00	.09	–.32	.59
V	–.74	.71	.81	.74	–.76	.85	–.36	–.44	.74	.54	.87	.90	–.11	.09	1.00	.02	–.12
Cu	.07	.12	.13	.16	.07	.09	–.14	.22	.21	.46	–.15	.05	.20	–.32	.02	1.00	–.13
Pb	–.48	–.27	.01	.38	–.26	.01	.25	–.63	–.04	–.40	.22	–.26	–.65	.59	–.12	–.13	1.00
Zn	–.87	.50	.72	.86	–.69	.73	–.21	–.62	.66	.23	.89	.51	–.32	.25	.78	–.04	.39
Bi	–.66	.05	.31	.42	–.48	.56	–.21	–.50	.18	.34	.71	.45	–.35	.44	.62	–.25	.28
W	–.34	–.32	–.29	–.07	.15	–.26	.57	–.12	–.32	–.53	.43	–.12	–.17	–.06	.05	–.62	.27
Mo	–.52	–.38	–.22	–.05	.09	–.16	.48	–.20	–.30	–.35	.51	–.12	–.40	–.01	.16	–.59	.32
Rb	–.69	.77	.84	.77	–.81	.89	–.38	–.52	.78	.41	.83	.90	–.09	.20	.95	–.13	–.08
Cs	–.66	.05	.30	.41	–.48	.55	–.18	–.50	.17	.28	.73	.46	–.32	.44	.63	–.33	.27
Ba	.17	–.39	–.34	–.44	.39	–.07	–.19	.48	–.42	.55	–.01	–.05	.29	–.19	.04	.17	–.40
Sr	–.10	–.60	–.56	–.31	.54	–.47	.89	.01	–.50	–.65	.06	–.42	–.14	–.28	–.27	–.30	.18
Tl	–.68	.01	.26	.39	–.44	.52	–.13	–.51	.14	.28	.72	.39	–.41	.40	.60	–.30	.30
Ga	–.67	.21	.51	.66	–.68	.58	–.30	–.75	.39	.03	.58	.24	–.49	.67	.44	–.34	.66
Ta	–.57	–.08	.10	.29	–.27	.30	.27	–.54	.03	–.21	.67	.30	–.29	.28	.46	–.57	.30
Nb	–.44	.21	.41	.53	–.64	.42	–.29	–.71	.31	–.18	.36	.14	–.45	.74	.23	–.51	.65
Hf	–.60	.09	.27	.37	–.44	.51	–.08	–.49	.15	.12	.75	.47	–.22	.41	.62	–.52	.21
Zr	.24	.51	.31	.01	–.14	.41	–.51	.37	.29	.66	.09	.61	.66	–.16	.43	.20	–.78
Y	–.48	.18	.37	.55	–.61	.33	–.12	–.79	.31	–.34	.31	.09	–.58	.65	.16	–.47	.73
Th	–.64	.08	.30	.39	–.48	.55	–.15	–.50	.17	.23	.75	.48	–.28	.43	.64	–.41	.24
U	–.69	–.08	.16	.32	–.35	.39	.06	–.49	.04	.05	.75	.35	–.36	.35	.55	–.47	.33
SiO_2	–.87	–.66	–.34	–.52	–.69	–.66	.17	–.10	–.68	–.67	–.57	–.44	–.60	.24	–.48	–.64	–.69
TiO_2	.50	.05	–.32	–.38	.77	.05	–.39	–.60	.01	.21	–.08	.21	.09	.51	.18	.08	–.08
Al_2O_3	.72	.31	–.29	–.22	.84	.30	–.34	–.56	.26	.51	.10	.41	.27	.31	.37	.30	.16
Fe_2O_3	.86	.42	–.07	–.05	.77	.41	–.44	–.31	.39	.66	.29	.53	.37	.00	.55	.39	.32
MnO	–.69	–.48	.15	.09	–.81	–.48	.39	.54	–.44	–.68	–.27	–.64	–.44	–.14	–.61	–.48	–.35
MgO	.73	.56	–.26	–.16	.89	.55	–.07	–.47	.52	.58	.30	.42	.51	.41	.33	.55	.39
CaO	–.21	–.21	.57	.48	–.38	–.18	–.19	.89	–.13	–.30	.27	–.29	–.08	–.51	–.12	–.15	.06
Na_2O	–.62	–.50	–.12	–.20	–.52	–.50	.48	.01	–.51	–.75	–.54	–.71	–.49	.37	–.79	–.50	–.49
K_2O	.66	.18	–.32	–.30	.78	.17	–.42	–.50	.14	.39	.03	.31	.15	.29	.31	.17	.04
P_2O_5	.23	.34	–.53	–.35	.41	.28	.55	–.65	.28	.03	–.21	–.18	.12	.66	–.34	.23	.05
Cr	.89	.71	.43	.51	.83	.73	–.01	.06	.72	.58	.67	.36	.75	.09	.31	.75	.75
Ni	.51	.45	–.12	–.12	.90	.46	–.05	–.42	.39	.24	.30	.14	.47	.61	.09	.48	.35
Co	–.32	–.35	–.17	–.40	–.09	–.32	.29	–.14	–.41	–.49	–.29	–.45	–.22	.66	–.58	–.28	–.36
Sc	.25	.44	–.06	–.01	.20	.44	–.19	–.28	.40	.67	.28	.74	.41	–.16	.65	.43	.35
V	.78	.62	.05	.16	.95	.63	.04	–.27	.60	.44	.46	.23	.62	.43	.16	.64	.55
Cu	–.04	–.25	–.62	–.59	–.13	–.33	.17	–.30	–.30	–.34	–.57	–.51	–.52	.20	–.47	–.41	–.47
Pb	.39	.28	.27	.32	–.08	.27	–.40	.18	.30	.66	.30	.65	.21	–.78	.73	.24	.33
Zn	1.00	.55	.26	.33	.77	.56	–.24	–.07	.56	.71	.48	.52	.55	–.07	.48	.56	.54
Bi	.55	1.00	.16	.40	.59	.99	.41	–.04	.99	.71	.78	.50	.91	.06	.41	.97	.92
W	.26	.16	1.00	.85	.07	.24	–.17	.74	.23	.11	.64	.14	.44	–.35	.18	.32	.51
Mo	.33	.40	.85	1.00	.10	.44	.04	.72	.49	.27	.69	.17	.52	–.48	.21	.48	.67

Table 3.5. Continued

	Zn	Bi	W	Mo	Rb	Cs	Ba	Sr	Tl	Ga	Ta	Nb	Hf	Zr	Y	Th	U
Rb	.77	.59	.07	.10	1.00	.62	–.12	–.30	.55	.53	.49	.40	.66	.42	.34	.64	.55
Cs	.56	.99	.24	.44	.62	.01	.37	.01	.99	.72	.83	.52	.95	.07	.43	.99	.95
Ba	–.24	.41	–.17	.04	–.12	.37	1.00	.01	.40	–.20	.13	–.41	.25	.41	–.54	.33	.27
Sr	–.07	–.04	.74	.72	–.30	.01	.00	1.00	.06	–.19	.46	–.24	.12	–.51	–.11	.04	.28
Tl	.56	.99	.23	.49	.55	.99	.40	.06	1.00	.70	.82	.48	.91	–.01	.41	.97	.94
Ga	.71	.71	.11	.27	.53	.72	–.20	–.19	.70	1.00	.56	.92	.67	–.31	.87	.71	.66
Ta	.48	.78	.64	.69	.49	.83	.13	.46	.82	.56	1.00	.45	.92	–.13	.44	.87	.94
Nb	.52	.50	.14	.17	.40	.52	–.41	–.24	.48	.92	.45	1.00	.54	–.34	.96	.54	.49
Hf	.55	.91	.44	.52	.66	.95	.25	.12	.91	.67	.92	.54	1.00	.11	.46	.98	.96
Zr	–.07	.06	–.35	–.48	.42	.07	.41	–.51	–.01	–.31	–.13	–.34	.11	1.00	.50	.09	–.09
Y	.48	.41	.18	.21	.34	.43	–.54	–.11	.41	.87	.44	.96	.46	–.50	1.00	.45	.44
Th	.56	.97	.32	.48	.64	.99	.33	.04	.97	.71	.87	.54	.98	.09	.45	1.00	.96
U	.54	.92	.51	.67	.55	.95	.27	.28	.94	.66	.94	.49	.96	–.09	.44	.96	1.00

layer, which is 1 mm to 3 mm thick [*Robin et al.,* 1991]. In our opinion the Ir enrichment in clays at the K/T boundary layer is not necessarily of cosmic origin, but may originated from mantle plume volcanism [*Koeberl,* 1989].

In any case these data could not be explained without a detailed study of mineral composition in every unit of the transitional layer. Such kind of investigations is simply absent in the most part of publications concerning the nature of the K/T boundary and we return to the discussion of this question later, taking into account the results of mineral investigations in the Gams section.

Rare earth elements. In contrast to trace elements, variations in the concentrations of REE in the Gams sequence are insignificant (Table 3.8). In a few samples, REE were analyzed in their whole-rock material and clay fractions. The REE concentration in sample *L*6 is systematically higher in the clay fraction than in the whole-rock sample.

The chondrite-normalized REE patterns of the Gams sequence generally confirm the known characteristic of clayey shales, namely, their uniform REE patterns [*Taylor, McLennan,* 1985]. The most conspicuous features of the REE patterns of the rocks are their pronounced enrichment in LREE and weak Eu anomalies. Com-

Table 3.6. Principal component analysis of the major elements for the Gams section

	Layers $A-I$		Layers J		Layers $K-U$	
	1 Factor	2 Factor	1 Factor	2 Factor	1 Factor	2 Factor
SiO_2	**0.98**	–0.02	**0.87**	–0.20	–0.13	–0.55
TiO_2	**0.93**	–0.33	**0.74**	0.50	**0.90**	–0.13
Al_2O_3	**0.85**	0.19	**0.90**	0.02	**0.98**	0.01
Fe_2O_3	0.39	**0.54**	**0.94**	0.25	**0.94**	–0.18
FeO	–0.14	**–0.94**	**–0.94**	–0.02	–0.14	**0.92**
MnO	**–0.87**	0.10	**–0.77**	0.18	**–0.86**	–0.09
MgO	0.18	–0.29	**0.80**	0.28	**0.90**	0.01
CaO	**–0.97**	–0.12	–0.26	0.47	**–0.68**	–0.46
Na_2O	**0.68**	–0.43	**–0.70**	**0.62**	**–0.67**	0.27
K_2O	**0.83**	–0.24	**0.78**	**0.52**	**0.96**	–0.03
P_2	**–0.59**	**–0.58**	**–0.77**	**0.53**	0.21	**0.80**
Factor loadings,%	54.2	18.2	62.5	14.7	55.8	19.6

Note: Bold for factor loadings >0.5.

=

Table 3.7. Trace elements concentrations (ppm) for the Gams section samples

Distance from K/T boundary, cm	Layer	Cr	Ni	Co	Sc	V	Cu	Pb	Zn	Bi	W	As	Mo	Rb	Cs	Ba	Sr	Tl	Ga	Ta	Nb	Hf	Zr	Y	Th	U	Ir, ng/g	Au, ng/g
–18	A	33	30	5.7	6	38	33	7	98	nd	nd	0.6	nd	47	nd	514	645	nd	nd	nd	7	nd	72	16	4.1	1.4	<1	4
16	B	31	27	5.2	5.5	34	68	7	87	nd	nd	2.5	nd	41	nd	463	660	nd	nd	nd	12	nd	69	15	3.8	1.6	1.4	3
–14	C	137	22	3	6.4	46	112	6	105	nd	nd	2.6	nd	36	nd	165	397	nd	nd	nd	10	nd	61	17	4.5	1.7	<1	5
–12	D	86	23	7	5.4	44	24	8	64	nd	nd	1.5	nd	33	nd	153	418	nd	nd	nd	8	nd	46	19	3.6	1.8	1.9	11
–10	E	76	21	3	6.4	36	13	10	53	nd	nd	1.8	nd	27	nd	99	398	nd	nd	nd	10	nd	36	19	4.2	1.3	<1	14
–8	F	65	21	5	5.9	40	21	7	44	nd	nd	2.7	nd	24	nd	113	420	nd	nd	nd	11	nd	33	21	3.9	1.7	<1	11
–6	G	60	24	9	6.3	40	17	8	50	nd	nd	2.4	nd	29	nd	100	433	nd	nd	nd	6	nd	35	20	4.0	1.4	<1	8
–4	H	44	64	18	7	51	25	7	51	0.3	16	3.1	0.57	59	2.6	162	881	0.36	9	1.03	6.1	1.46	54	25	4.5	1.13	1.5	6
–2	I	54	76	22	11	61	26	7	77	0.24	17	2.5	0.44	68	3.2	218	884	0.39	11	1.01	7.6	1.72	61	26	5.6	1.04	1.7	7
0	**J2**	**183**	**155**	**35**	**7**	**167**	**97**	**40**	**162**	**0.92**	**10**	**57**	**0.87**	**145**	**7.2**	**330**	**141**	**0.84**	**21**	**1.36**	**15.3**	**4.53**	**154**	**17**	**12.2**	**1.74**	**6.8**	**11**
0.4	**J3**	**172**	**171**	**38**	**8**	**180**	**88**	**40**	**169**	**1.16**	**8**	**49**	**0.66**	**159**	**7.9**	**372**	**127**	**1.01**	**2**	**1.51**	**17.1**	**4.76**	**167**	**19**	**14.0**	**1.89**	**7.8**	**6**
0.8	**J4**	**175**	**175**	**39**	**11**	**185**	**78**	**42**	**180**	**1.10**	**15**	**46**	**0.68**	**162**	**8.1**	**396**	**138**	**0.97**	**23**	**1.49**	**17.0**	**4.46**	**158**	**21**	**13.9**	**1.88**	**9.1**	**6**
1.2	**J5**	**259**	**173**	**38**	**10**	**177**	**66**	**39**	**177**	**0.97**	**20**	**12**	**0.55**	**156**	**7.6**	**411**	**179**	**1.08**	**23**	**1.45**	**16.7**	**3.00**	**179**	**20**	**14.4**	**1.89**	**9.0**	**10**
1.6	**J6**	**175**	**191**	**44**	**18**	**190**	**68**	**41**	**192**	**0.98**	**10**	**7.8**	**0.43**	**166**	**8.6**	**463**	**171**	**1.09**	**25**	**1.46**	**17.8**	**5.01**	**172**	**19**	**13.8**	**1.91**	**6.0**	**12**
2	K	115	78	31	5	100	33	25	74	0.15	158	4.3	1.55	78	2.8	415	775	0.48	13	1.92	10.0	2.45	95	20	5.5	1.59	<1	8
4	L	146	165	53	15	151	29	16	90	0.35	110	26	0.84	132	5.4	457	315	0.79	21	1.42	16.8	4.36	170	20	10.5	1.57	<1	26
6	M	130	186	55	17	150	37	13	78	0.41	47	27	0.53	145	6.5	449	303	0.77	22	1.32	17.5	4.29	166	24	11.4	1.79	1.1	14
8	N	115	229	54	13	161	63	10	73	nd	nd	17	nd	132	nd	437	302	0.48	nd	nd	12	nd	191	5	9.5	2.1	1.2	8
10	O	120	202	65	17	154	40	15	79	0.40	33	11	0.33	140	6.5	449	313	0.83	22	1.90	17.2	4.37	171	23	11.9	1.68	1.6	16
12	P	116	180	43	16	141	34	13	80	0.43	35	5.9	0.25	139	6.4	449	412	0.96	22	1.93	17.3	4.70	166	25	11.6	1.67	<1	18
14	Q	94	119	43	14	120	51	15	80	nd	nd	8.5	nd	110	nd	387	247	nd	19	nd	16	nd	137	25	10.0	2.8	<1	11
16	R	97	123	51	26	111	53	28	84	nd	nd	nd	nd	100	nd	360	296	nd	22	nd	18	nd	128	25	nd	nd	nd	nd
18	S	64	73	93	13	85	58	20	98	nd	nd	4.7	nd	60	nd	553	413	nd	nd	nd	nd	nd	181	1	8.7	2.4	1.6	21
20	T	43	87	39	18	62	36	17	47	nd	nd	0.2	nd	49	nd	441	282	nd	9	nd	13	nd	139	20	3.2	1.7	<1	12
22	U	95	112	60	17	96	83	35	120	nd	nd	nd	nd	104	nd	400	289	nd	20	nd	18	nd	156	30	nd	nd	nd	nd

Note: Transitional layer *J* is shown by bold; nd – not determined.

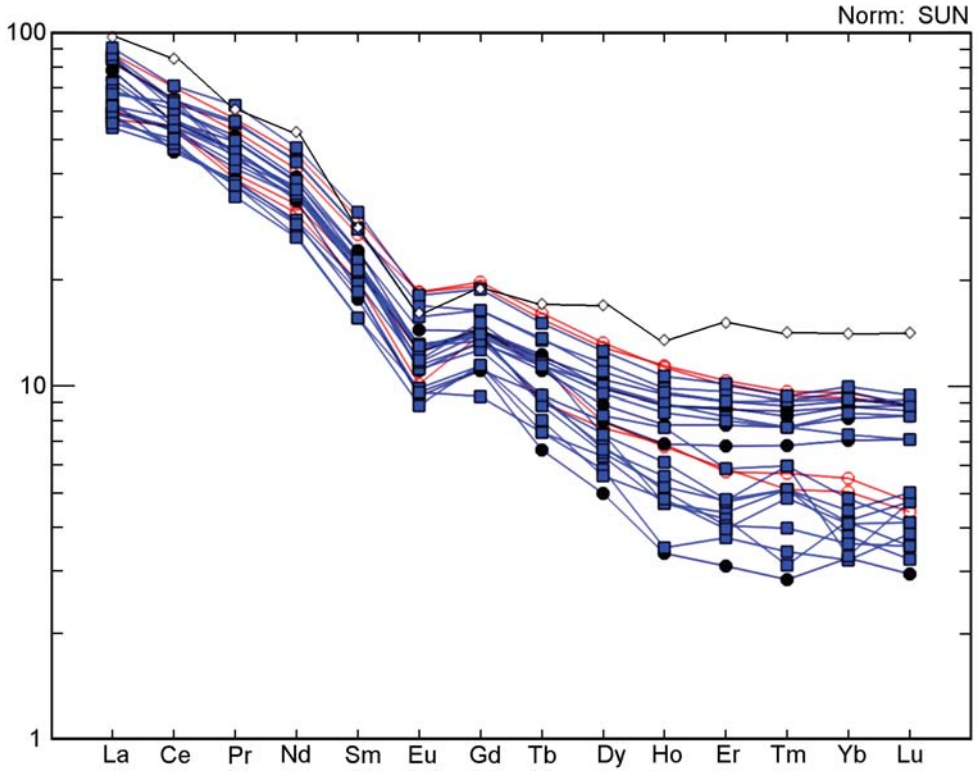

Figure 3.5. Chondrite-normalized REE pattern for the Gams sections samples. Box filled – samples of the upper portion of section, red open circle – samples of the lower portion of section, black filled circle – layer *J*, open black circle – NASC.

pared with the REE patterns of North American Clayey Shales (NASC) (Figure 3.5), our rocks are poorer in HREE. Figure 3.6, Figure 3.7, and Figure 3.8 demonstrate the NASC-normalized REE patterns of the upper and lower parts of the rock sequence and its transitional layer *J*. All of these patterns are similar and show weakly pronounced negative anomalies at Ce, Nd, and Dy.

This flat configuration of the NASC-normalized REE patterns is typical of the rocks of Mesozoic and Ceno-

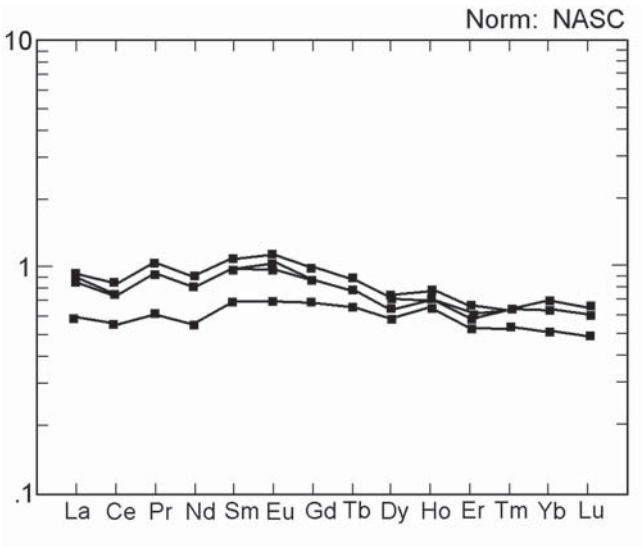

Figure 3.6. NASC-normalized REE patterns for the upper portion of the Gams sections.

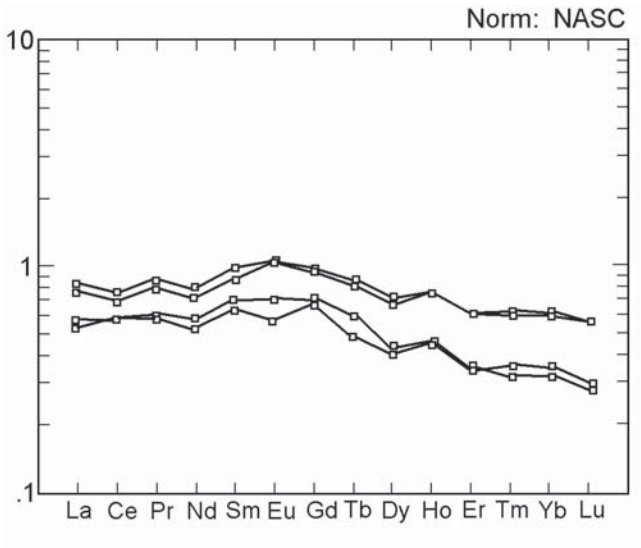

Figure 3.7. NASC-normalized REE patterns for the lower portion of the Gams sections.

Table 3.8. Rare earth element contents (ppm) of the Gams section samples

Sample	La	Ce	Pr	Nd	Sm	Eu	Gd	Tb	Dy	Ho	Er	Tm	Yb	Lu	$(La/Sm)_N$	$(La/Yb)_N$	Analytical method
H4	27.27	56.10	6.86	25.86	5.44	1.42	5.29	0.77	4.41	0.88	2.33	0.34	2.11	0.30	2.93	8.23	ICP-MS
I4	28.67	60.63	7.41	28.50	6.08	1.42	5.44	0.80	4.55	0.87	2.28	0.33	2.04	0.30	2.76	8.96	ICP-MS
J2/2	21.17	39.78	4.97	18.39	3.57	0.74	3.07	0.47	2.74	0.53	1.53	0.24	1.55	0.24	3.47	8.70	ICP-MS
J2/3	25.75	48.20	6.05	22.18	4.47	0.85	3.69	0.55	3.05	0.60	1.75	0.27	1.79	0.28	3.37	9.18	ICP-MS
J2/4	25.79	48.05	6.03	22.54	4.57	0.96	3.93	0.59	3.37	0.68	1.96	0.29	1.93	0.29	3.30	8.52	ICP-MS
J2/5	28.12	52.38	6.63	24.58	4.91	0.99	3.98	0.61	3.39	0.68	1.94	0.30	1.93	0.30	3.35	9.29	ICP-MS
J2/6	24.31	48.61	6.40	23.77	4.86	1.11	3.95	0.60	3.58	0.73	2.04	0.31	2.00	0.31	2.92	7.75	ICP-MS
J6	24.38	45.70	5.75	20.73	4.26	0.93	3.54	0.56	3.20	0.64	1.85	0.28	1.81	0.28	3.35	8.59	ICP-MS
K5	19.21	40.67	4.91	18.56	3.99	0.88	3.64	0.57	3.44	0.69	1.85	0.27	1.61	0.24	2.82	7.61	ICP-MS
K4	27.61	56.35	6.83	25.20	5.20	1.17	4.55	0.69	3.90	0.75	2.08	0.30	1.83	0.28	3.10	9.62	ICP-MS
L6	23.73	46.85	6.04	22.03	4.54	1.01	3.82	0.57	3.27	0.65	1.80	0.27	1.85	0.28	3.06	8.18	ICP-MS
L6*	26.67	51.13	6.60	24.43	5.08	1.12	4.49	0.67	3.83	0.76	2.14	0.31	2.01	0.31	3.08	8.46	ICP-MS
M7	27.70	54.54	7.21	27.38	5.66	1.30	4.52	0.67	3.97	0.76	2.17	0.32	2.12	0.32	2.86	8.33	ICP-MS
O4/5	27.70	55.34	7.33	27.26	5.63	1.24	4.56	0.68	3.78	0.73	1.97	0.30	2.00	0.30	2.88	8.83	ICP-MS
O2	28.43	55.76	7.30	27.10	5.65	1.21	4.52	0.68	3.77	0.74	2.04	0.32	2.02	0.30	2.95	8.98	ICP-MS
P7	29.77	61.18	8.10	29.76	6.30	1.39	5.19	0.75	4.31	0.82	2.28	0.33	2.19	0.32	2.76	8.67	ICP-MS
P5/6	28.33	56.81	7.37	27.38	5.78	1.37	4.68	0.71	4.03	0.76	2.09	0.32	2.04	0.30	2.87	8.83	ICP-MS
Q3	20.40	49.28	6.04	22.09	4.26	1.00	3.70	0.47	2.28	0.43	1.06	0.18	0.91	0.17	2.80	14.3	NAAA
R2	22.55	52.37	6.44	24.01	4.60	0.90	3.88	0.58	2.51	0.47	1.08	0.18	0.98	0.17	2.87	14.68	NAAA
S7	18.22	43.27	4.46	16.60	3.16	0.68	3.16	0.40	1.92	0.37	0.89	0.17	0.90	0.14	3.37	12.91	NAAA
T4/5	22.05	54.69	5.68	22.65	4.32	0.91	4.17	0.57	2.84	0.59	1.32	0.21	1.06	0.14	2.98	13.28	NAAA

Note: * – Element analyses for clay fraction.

zoic continental margins (including those in the modern Atlantic) [*Murray,* 1994] and testify to a significant contribution of terrigenous material to the character of REE fractionation. In this context, the similarities in the REE patterns of rocks from the examined portion of the Gams sequence suggest that the conditions in the source area (which was not far from the marine basin) did not vary.

3.5 Isotopic Composition of Helium, Carbon, and Oxygen

Significance of helium study. The discovery of primordial (planetary) ^{3}He in the Earth [*Mamyrin et al.*, 1969] stimulated research on helium isotopy in rocks of various compositions and origins. One of the first important objects of study was deep oceanic sediments, including red clay samples from the collection of the H.M.S. Challenger voyage (1872–1876) in the Pacific Ocean; traces of cosmic matter in sedimentary rocks were discovered for the first time in these samples. Samples of Fe-Ni nodules and magnetic spherules up to 100 μm in diameter, subsequently called cosmic spherules [*Murray, Renard,* 1891], were gathered by dredging at a depth of 4300 m in the Southern Pacific Ocean. The inner part of the spherules consists of metallic iron (90%) and nickel (10%), whereas their surface is covered by a fine crust of iron oxide (J. Jedwab, http://www,ub.ac.be/sci.erices/cosinicdust.pdf).

Even before the discovery of solar helium in the Earth's crust, high ratios ^{3}He/^{4}He exceeding the atmospheric value (1.39×10^{-6}) by a factor of 100 were established for the first time in recent Pacific deep red clays [*Merrihue,* 1964]. Later more detailed studies of He iso-

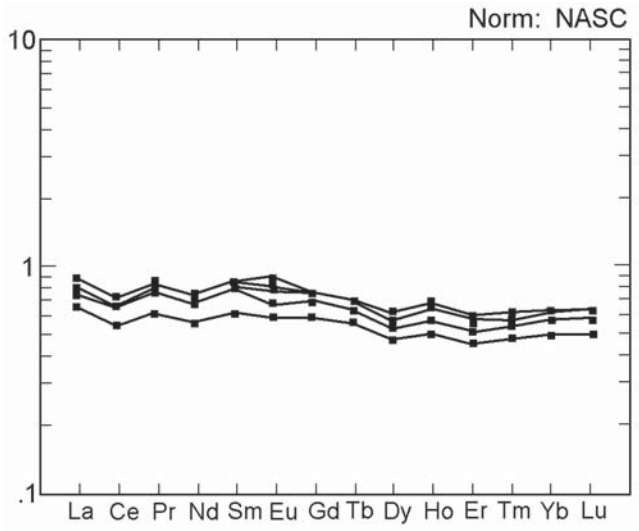

Figure 3.8. NASC-normalized REE patterns for layer *J* of the Gams sections.

topy in sediments of various compositions of the Pacific and Atlantic oceans showed that the $^3He/^4He$ ratio varied within wide limits, from 10^{-5} to 10^{-9} [*Krylov et al.*, 1973].

Deep oceanic red clays of the Central Pacific Ocean, distinguished by very low sedimentation rates, contain small Fe-Ni spherules that are close in composition to iron meteorites and, therefore, have high ratios $^3He/^4He$ (up to 2.5×10^{-5}), which indicates a nearly complete absence of a terrigenous component. On the other hand, the ratio $^3He/^4He$ varies from 8.7×10^{-9} to 2×10^{-7} in lutites and sandy silts of the Atlantic Ocean with a significant terrigenous component [*Krylov et al.*, 1973]. Later studies have provided new evidence for the role of the cosmogenic component, forming due to the cosmic dust accumulated in slowly depositing sediments and raising the ratio $^3He/^4He$ [*Marcantonio et al.*, 1998; *Nier et al.*, 1990; *Ozima et al.*, 1984;].

Very interesting results on He isotopy were obtained from suspended material of glacial water of Mount Elbrus [*Sobotovich,* 1976]. It was found that the cosmogenic He admixture in glacial water suspensions is significant and their values of $^3He/^4He$ vary from 4.5×10^{-6} to 5.5×10^{-5}, nearly coinciding with values obtained from deep oceanic red clays. On the other hand, the $^3He/^4He$ value obtained from a suspension of Baksan River water (under a glacier) amounts to 5.1×10^{-8}, which is two to three orders smaller and close to usual values of rocks of the continental crust [*Sobotovich,* 1976].

A new stage of research on He isotopy in sedimentary rocks was related to the discovery of anomalous concentrations of iridium and other elements of the platinum group in clays at the K/T boundary [*Alvarez et al.*, 1980, and many others].

Naturally, the study of He isotopy in the K/T layer is of great significance for the possibility of detecting solar helium traces. Helium isotopy in K/T sedimentary rocks was studied for the first time in four samples from the Stevns Klint section (Denmark) [*Eugster et al.*, 1985]. However, the ratio $^3He/^4He$ could be determined only for one bulk sample), in which the ratio of 14×10^{-6} was obtained at the atmospheric value of the ratio $^{40}Ar/^{36}Ar$.

A significant contribution to the study of variations in isotopes He and Ir was made by *Farley* [1995], who examined a Northern Pacific section of pelagic clays drilled to a depth of 24 m. This continuous section encompasses a time interval of about 70 Ma, which allowed Farley to come to the following conclusions:

(1) The ^4He concentration exhibits a weak tendency toward a decrease from the upper part of the section to its lower part, reaching a minimum at about 66 Ma, while a maximum concentration of ^3He was fixed at 37 Ma.

(2) The highest concentration of ^3He (125×10^{12} cm^3/g) was obtained for samples taken at a depth of 11.4 m (37 Ma), where an anomalous concentration of cosmic spherules was fixed, whereas no ^3He anomalies were discovered at the K/T boundary. Solar helium is supplied by cosmic dust particles less than 50 μm in size, because larger particles are degassed due to heating when they enter the atmosphere. Farley emphasized (and this is important) that, as compared with Ir, ^3He is a more sensitive indicator of cosmic dust present in a rock and noted the absence of correlation between ^3He and Ir concentrations.

Studies of He isotopy in Fe-Mn nodules [*Anufriev,* 1999; *Anufriev, Boltenkov,* 1996] showed that ^3He concentration varies in them from 0.41×10^{-12} to 7.86×10^{-12} cm^3/g, which is more than an order of magnitude smaller compared to Farley's data [*Farley,* 1995]. This is accounted for by a higher concentration of the terrigenous component in the nodules. Representative results were obtained from the Gubbio section (Italy), in which Ir anomaly was detected for the first time. The section was sampled from the lowest Maastrichtian to the Middle Eocene at a sampling interval of 1 to 2 m (0.5 m around the K/T boundary) [*Mukhopadhyay et al.,* 2001]. The ratio $^3He/^4He$ varies along the section from 0.3×10^{-6} to 5.2×10^{-6} and averages 1.7×10^{-6}, which is 100 times smaller than its values in Pacific pelagic sediments [*Farley,* 1995].

According to the interpretation of these data presented in [*Mukhopadhyay et al.,* 2001], the concentrations of the two He isotopes vary independently: the source of ^3He is interplanetary cosmic dust, while ^4He is of terrigenous origin, being controlled by a source area. The cosmic dust accretion rate was virtually constant immediately at the K/T boundary in the interval 65.5–64.8 Ma, and this served as a basis for the conclusion that the variations in the ratio $^3He/^4He$ were controlled by the sedimentation rate, with ^3He concentration in the terrigenous component being constant [*Mukhopadhyay et al.,* 2001]. We should note that the authors postulate a priori the presence of cosmic dust without presenting any arguments for this hypothesis.

Helium isotopy. Table 3.9 presents the measured concentrations and isotope ratios in each of the six units of the transitional boundary layer at the Gams section, as well as sample-average values obtained from bulk sample. It is evident that the ratio $^3He/^4He$ decreases from bottom to top of the boundary layer; the difference between the values in the lowermost (units *J*1–2) and uppermost (units *J*5–6) parts is significant (a tenfold change), considerably exceeds the measurement uncertainty (5%), and is 10 to 100 times higher than values typical for rocks of the continental crust [*Mamyrin, Tolstikhin,* 1981].

Table 3.9. Concentrations of He, U and Th and He isotope ratios in the K/T transitional clay layer (the Gams section, Eastern Alps)

Sample	Weight, g	^{4}He, $sm^3/g(10^{-6})$	^{3}He, $sm^3/g(10^{-14})$	^{3}He/^{4}He, 10^{-8}	^{40}Ar, $sm^3/g(10^{-6})$	^{40}Ar/^{36}Ar	U, ppm	Th, ppm
J^*_{2wr}	0.7946	2.9	15.4	5.3	14.3	1420	–	–
J_{2-6}	0.6044	0.25	0.64	10.3	–	–	1.89	13.8
J_{2-5}	0.8225	1.30	15.6	12.0	–	–	1.88	14.4
J_{2-4}	1.2436	0.81	12.2	15.0	–	–	1.89	13.9
J_{2-3}	0.5843	0.14	3.5	25.0	–	–	1.88	14.0
J_{2-2}	1.5381	1.1	72.6	66	11.7	1355	1.89	12.2
J_{2-1}	0.7880	0.70	83.3	119	13.5	871	1.85	13.0

Note: * Bulk values in the layer J.

This raises the problem of interpretation of variations in He isotope ratio occurring in a very short time interval, within a few thousand years even if we agree upon conservative estimates of the sedimentation rate [*Grachev et al.,* 2005].

As it was shown previously, the ratio ^{3}He/^{4}He in marine sedimentary rocks depends significantly on such factors as the sedimentation rate and the fraction of the terrigenous component [*Krylov et al.,* 1973; *Mukhopadhyay et al.,* 2001; *Nier et al.,* 1990; *Ozima et al.,* 1984; *Patterson et al.,* 1999]. However, the question whether the influx of ^{3}He supplied by cosmic dust is constant or varies with time remains open. Some authors believe that the influx rate of cosmic dust with a planetary value of the ratio ^{3}He/^{4}He (10^{-4}) varies little in the course of time [*Karner et al.,* 2003; *Winckler, Fisher,* 2006], but directly opposite data are also known [*Farley,* 1995; *Patterson et al.,* 1999; *Schmitz et al.,* 1996].

It is noteworthy that all existing estimates were obtained for different time intervals ranging from hundreds of thousands to tens of millions of years and rate values are known to strongly depend on the averaging interval.

Cosmic dust in the Gams section is represented by fine particles of various shapes; the most widespread among them are magnetic spherules 0.7 to 100 μm, in size containing 98% pure iron [*Grachev et al.,* 2006a, 2008b].

The source of radiogenic ^{4}He depends on U and Th concentrations that do not vary in the layer J (from units J_{2-1} to J_{2-6}): all of their variations remain within measurement uncertainties [*Grachev et al.,* 2007b]. The supply of radiogenic helium is often related to zircon [*Patterson et al.,* 1999], but, in the Gams section, zircon is present in approximately equal amounts in all parts of the transitional layer.

The ratio ^{3}He/^{4}He in the Earth's crust depends on the Li concentration [*Mamyrin, Tolstikhin,* 1981; *Tolstikhin et al.,* 1996]. However, no data point to the presence of Li minerals in the layer J. By analogy with the Gubbio section, where the Li concentration is less than 7 ppm, the change in the ratio ^{3}He/^{4}He due to the alpha-ray radiation of lithium should be no more than 0.0014 of the value characteristic of the atmosphere (1.39×10^{-6}) [*Mukhopadhyay et al.,* 2001]; i.e., this effect is negligibly small.

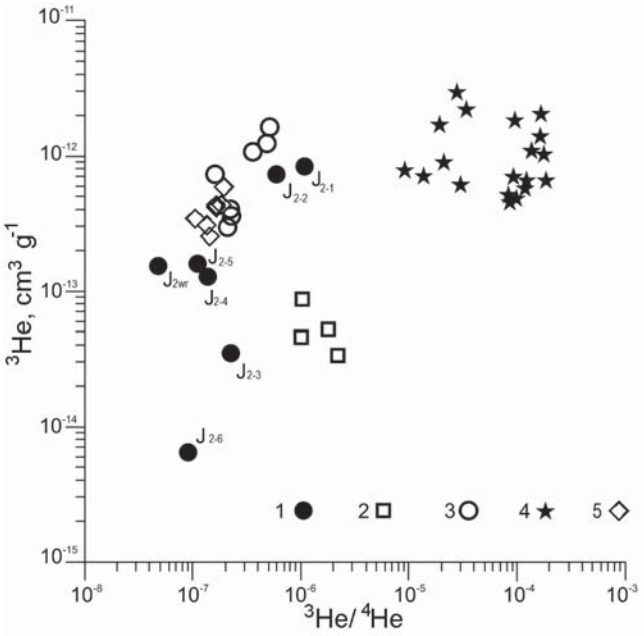

Figure 3.9. Diagram of ^{3}He versus ^{3}He/^{4}He from clays of the K/T transition layer of the Gams section (Eastern Alps) and sedimentary rocks of other areas: (1) Gams section (this work); (2) K/T transition bed in the Gubbio section (Italy) [*Mukhopadhyay et al.,* 2001]; (3) recent sediments of the Atlantic Ocean [*Marcantonio et al.,* 1998]; (4) deep-water sediments of the central Pacific Ocean [*Marcantonio et al.,* 1995]; (5) sediments of the continental margin in the area of the Amazon River delta [*Marcantonio et al.,* 1998].

Thus, the only remaining variant of the interpretation of the $^3He/^4He$ variations in the transitional layer is related to the changes in the composition of the terrigenous component (i.e., in the sedimentation conditions) during the deposition of the layer *J*.

Our results virtually coincide with data from the Gubbio section (Figure 3.9), where the Ir anomaly was discovered for the first time [*Mukhopadhyay et al.*, 2001]. However, the smallest values of the ratio $^3He/^4He$ are obtained for the upper part of the Gams section, where some features indicating an impact? (or meteorite ablation) event (pure Ni spherules, diamonds, and awaruite) were established [*Grachev et al.*, 2005, 2008b]. Figure 3.9 also shows that deep-sea red clays distinguished by very low sedimentation rates have very high ratios $^3He/^4He$ close to meteorite values [*Merrihue*, 1964; *Ozima et al.*, 1984].

The ratio $^3He/^4He$ in the Gams section decreases from the bottom to the top of the transitional layer, and the difference between the lowermost (J_{2-1}) and uppermost (J_{2-6}) units is significant and considerably (by more than ten times) exceeds the measurement uncertainty (5%). Although a terrigenous component played a significant role in the formation of the Gams transitional layer, the ratio $^3He/^4He$ in the lower part of the layer is 10 to 100 times greater than the values typical of the continental crust. It is shown that no correlation exists between the ^3He and Ir concentrations, which was observed for the first time in Pacific pelagic clays for the 70-Ma interval [*Farley*, 1995].

Thus, the ^3He enrichment of the lower part of the Gams section is associated not with cosmic matter but with a change in the source area conditions, most likely, due to volcanic activity whose influence, independent of He isotope studies, has been established from anomalous concentrations of As, Pb, Cu, and Zn and from the presence of particles of silver, gold, copper, and titanomagnetite (the latter is similar in composition to titanomagnetites of basalts) (see Chapter 4 for details).

Carbon and oxygen isotopy. The distribution of $\delta^{13}C$ in the vertical section is generally controlled by

Table 3.10. Carbon and oxygen isotope composition of the Gams section samples

Sample	$\delta^{13}C$, ‰PDB	$\delta^{18}O$, ‰PDB	$\delta^{18}O$, ‰SMOW
H2	1.72	−1.98	28.86
H2-2	1.79	−2.03	28.80
I2	1.34	−2.86	27.93
I2-2	1.69	−2.50	28.31
J1A3	−3.52	−22.90	7.11
J1B2	0.41	−4.64	26.09
J1C2	−0.89	−19.49	10.66
J1E1	−1.41	−22.67	7.36
J1E3	0.82	−4.81	25.91
K2	0.69	−3.95	26.80
K2-2	0.32	−4.21	26.53
L5	−1.16	−4.57	26.17
L5-2	−0.31	−4.22	26.53
M5	−1.11	−4.82	25.90
M5-2	−1.97	−5.04	25.67
N3	−1.49	−4.90	25.82
N3-2	−1.17	−4.88	25.84
O3	−1.74	−5.11	25.60
T2	0.86	−3.90	26.85
T2-2	0.77	−3.87	26.89

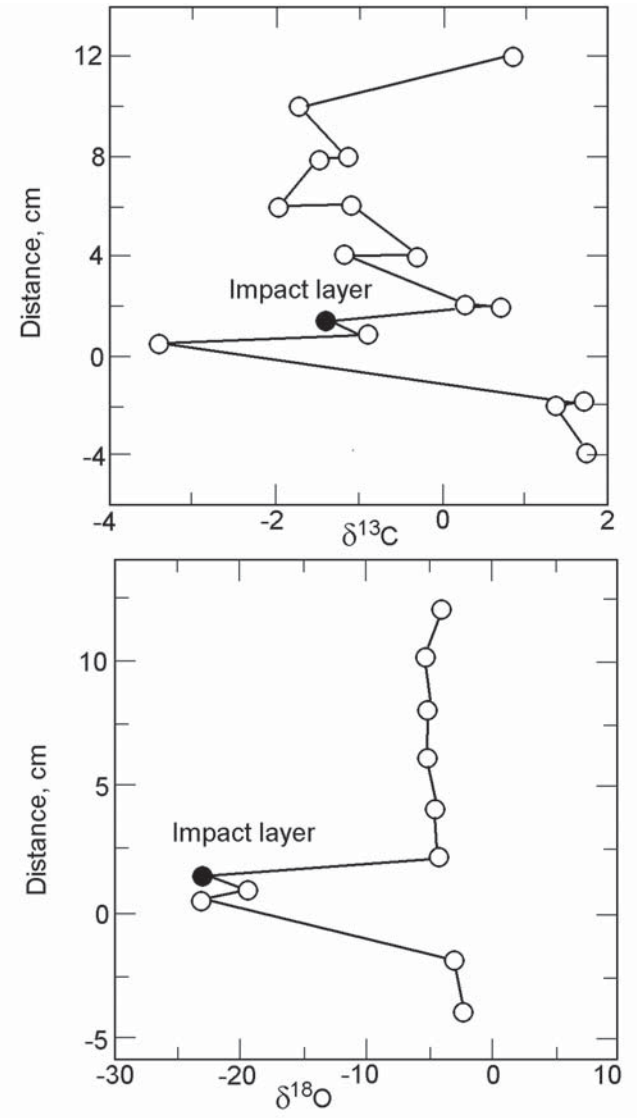

Figure 3.10. Variations of $\delta^{13}C$ and $\delta^{18}O$ values at the Gams section samples.

the distribution of the CaO concentrations, and transitional layer *J* is characterized, as could be expected, by a pronounced minimum in the content of this component and in $\delta^{13}C$ (Table 3.10; Figure 3.10). The variations in $\delta^{18}O$ in the vertical section reflect the general variations in $\delta^{13}C$ and show a clearly pronounced shift toward negative values at the K/T boundary, from 5% to 23% PDB $\delta^{18}O$ (Figure 3.10).

These anomalies in the variations in the carbon and oxygen isotopic composition in the Gams sequence are quite similar to those documented previously elsewhere [*Brinkhuis et al.,* 1998; *Magaritz,* 1989; *Stuben et al.,* 2002, and others] and resemble most closely the sequences at El Kef in Tunisia and Agost in SW Spain [*Keller et al.,* 1996; *Rodrigues-Tovar et al.,* 2004].

The global decrease in $\delta^{13}C$ at the K/T boundary is generally interpreted as resulting from a sudden reduction in oceanic primary productivity [*Stuben et al.,* 2002]. However there are other approaches to the explanation of carbon isotopes anomalies in Phanerozoic. First of them is the destabilization of methane hydrate in deep-sea sediments as a result of the sea regeressions [*Erwin,* 2005; *Tripati, Elderfield,* 2005; *Zachos et al.,* 2006], another one connects the drop in $\delta^{13}C$ with input volcanic CO_2 from plume volcanism (for example, Siberian traps, [*Berner,* 2002]). *Berner* [2002] modelled the release of CO_2 from volcanism occurring over a period of 200 kyr, and concluded that flood basalt volcanism would probably lead to an approximate doubling of atmospheric CO_2 (which would lead to a global temperature increase).

Taking into account that similar shift in $\delta^{13}C$ is well known characteristic for many sections at the critical boundaries in Phanerozoic, we will return to this question later after the discussion of the role of mantle plumes volcanism in lithosphere, hydrosphere and atmosphere evolution.

Chapter 4. Minerals of the Transitional Layer in Gams Sections

4.1 Introduction

Until recently mineralogy of the transitional layer at the K/T boundary has not been virtually studied in detail. Significant geochemical anomalies that have been observed and described in numerous publications after the appearance of the first paper of *Alvarez et al.* [1980] remained unexplained. As we pointed out [*Grachev et al.*, 2005], the transitional layer was inspected as a single whole, and its characteristics obtained with different analytical techniques were ascribed to the whole thickness of this rock unit.

In this chapter materials of new detailed researches of minerals in K/T boundary layer from two sections in Gams are presented. As it has been shown in Chapter 3, there is a significant vertical geochemical zonation in the transitonal layer from the bottom to the top. Taking unto account these results, we divided the transitional layer into three parts (lower, middle and upper) in order to get representative probes weight for the different kinds of analysis.

Independent investigations of the same samples were carried out at the labs of Geological Institute of the Russian Academy of Sciences, Geophysical observatory of Institute of Physics of the Earth of the Russian Academy of Sciences, Institute of Geology of Ore Deposits, Petrography, Mineralogy and Geochemistry of the Russian Academy of Sciences and Institute of Experimental Mineralogy of the Russian Academy of Sciences.

4.2 Sampling Procedure, Sample Preparation Techniques, and Study Methods

Samples of 10–15 g in mass were crushed in a porcelain mortar and sieved through a 0.25-mm screen. Heavy fraction minerals were separated from the carbonate-clay mass in heavy liquids (bromoform, density 2.89 g/cm^3). The heavy and light fractions were washed in alcohol and purified of the magnetic fraction (magnetite) with the use of a simple magnet. The heavy-fraction minerals were separated on a magnetic separator into a non-electromagnetic, weakly electromagnetic, and electromagnetic fractions, which were glued under binoculars to glass slides with a depression.

Other minerals were hand-picked under a binocular magnifier, using a needle and were glued to glass platelets with pits. The glue applied was Sherlok, which can be dissolved in alcohol. Quartz was obtained from the light fraction ($<$2.89 g/cm^3) by electromagnetic separation. In order to analyze the composition and microstructures of ferromagnetic minerals in the rocks, the samples were examined on a Camebax microprobe equipped with three wave-dispersive spectrometers and then on a Tescan Vega I and Tescan Vega II microprobes equipped with energy- and wave-dispersive spectrometers. Samples were usually mounted onto a pellet of 26 mm in diameter using Wood's metal, carefully polished and finished with diamond pastes, and then sputter-coated with carbon. The analysisi was conducted at an accelerating voltage of 20 kV and a beam current of 10 nA. The elements determined using their characteristic X-ray radiation ranged from Na to U. The effective diameter of the beam was thereby close to 1–2 μm and was systematically tested at small grains. We carried out quantitative analysis of ore minerals for TiO_2, FeO, MgO, MnO, Cr_2O_3, and Al_2O_3; preliminary analysis was carried out for all elements.

Nickel and iron particles detected with the Camebax microprobe were additionally examined by A. N. Nekrasov with the Tescan Vega microprobe at the Institute of Experimental Mineralogy, Russian Academy of Sciences. The Tescan Vega microprobe equipped

=

Table 4.1. List of minerals and metals identified at the K/T transitional layer (Gams section, Eastern Alps, Austria)

Minerals	Layer *J*		
	lower part	middle part	upper part
Class I. Native elements and metallic alloys			
Awaruite			
Brass			
Copper			
Diamond			
Gamsite			
Gold			
Iron			
Moissanite			
Nickel			
Osmiridium			
Platinum			
Rhenium			
Silver			
Class II. Sulfides			
Acanthite			
Arsenopyrite			
Bravoite			
Galena			
molybdenite			
Pentlandite			
Pyrite			
Pyrrotine			
Sphalerite			
Violarite			
Class III. Oxides			
Anatase			
Brookite			
Chromite			
Corundum			
Goethite			
Hematite			
Ilmenite			
Magnetite			
Rutile			
Spinel			
Titanomagnetite			
Class IV. Haloides			
Fluorite			
Class V. Carbonates			
Calcite			
Dolomite			
Magnesite			
Witherite			
Class VI. Sulphates			
Barite			
Class VII. Phosphates			
Apatite			
Monazite			
Xenotime			
Class VIII. Silicates			
Albite			
Amphibole			
Glauconite			
Cordierite			
Chlorite			
Diopside			
Epidote			
Garnet			
Quartz			
Kyanite			
Muscovite			
Olivine			
Orthoclase			
Plagioclase			
Sphene			
Tourmaline			
Zircon			

with an energy-dispersion spectrometer measured the carbon content, which allowed us to confirm independently the presence of diamond grains detected by their intense blue luminescence under the Camebax.

Selected magnetic mineral grains were prepared in compliance with a specially designed technique that ensured the ultrafine polishing of the material with the removal of its layer no thicker than 5 μm during the whole polishing process. The removed 5- to 10-μm-thick layer made it possible to expose pores in iron spherules 10–20 μm. Polishing sometimes exposed hollow metallic cosmic spherules with walls 0.5–2 μm thick. To achieve this, grains separated with the use of a powerful hand-held Nb-B-Fe magnet were placed on a flat (polished) surface and covered with epoxy resin. The plastic was selected in such a way to ensure the minimum adhesion of epoxy resin to it. This allowed us to easily remove the sample with the examined particles after the solidification of the epoxy resin. Prior to its use, the epoxy resin was degassed in vacuum to minimize the amount of bubbles in it. The sample was polished by ASM 2/1, 1/0, and 0.5/0 diamond pastes and suspension of ultrafinely dispersed diamonds on Montasupal polishing machines (on broadcloth and felt).

The minerals separated in heavy liquids were mounted on a double-layer conducting carbon adhesive tape. Each specimen comprised a few hundred mineral grains ranging from fractions of a micrometer to hundreds of micrometers in size. The grains were first examined on a Camebax microprobe equipped with an optical microscope and three wave dispersive spectrometers to rapidly locate luminescent grains (of, for example, diamond and moissanite). It was, however, hard to conduct qualitative analysis of each grain because of the very long required instrument time. Because of this, as soon as a new Tescan Vega II microprobe became available for us, we re-examined all the specimens on it. All of the identified grains were analyzed for all possible elements, from Be to Pu. The high sensitivity of the new detector made it possible to significantly decrease the electron-beam current: the analyses were carried out mostly at a current of 200 pA and 20 kV accelerating voltage. In complicated situations, the energy- and wave-dispersive spectrometers were utilized simultaneously to improve the reliability of the measurements. In the course of the re-examination of the specimens, we identified new minerals, which were often submicrometer-sized and had not been detected on the Camebax microprobe.

Magnetic minerals were separated from the crushed samples by a powerful hand-held Nd-Fe-B magnet. In order to separate magnetic particles from the fine clay fraction, we applied ultrasonic pulverization in water. The operating regimes of the generator were selected in such a manner that small (no larger than a few fractions of a micrometer) magnetic particles were reliably recovered but not destroyed in the course of ultrasonic cleaning. The mineral composition of rare phases of the ultraheavy fraction was scrutinized with a JEOL JXA-8100 microprobe.

4.3 Mineral Paragenesis in the Gams Transitional Layer

Before any details are discussed we first provide an overview on the distribution of minerals in the Gams transistional layer established as a result of the monolith and Gams 1 and Gams 2 sections study. Table 4.1 shows the variations of minerals identified in different portions of the transitional layer (lower, middle and upper) and reveals the well expressed vertical zonation or mineral "stratification".

We have determined the following classes of minerals:

1 – Native elements and metallic alloys,
2 – Sulfides,
3 – Oxides,
4 – Haloides,
5 – Carbonates,
6 – Sulphates,
7 – Phosphates,
8 – Silicates.

Below we give a summary of these mineral classes. Clay minerals are described in separate paragraph.

4.3.1 Native elements and metallic alloys

Diamonds. There are two populations of diamonds in the transitional layer of Gams. The first one was found under the study of monolith in a very thin part of unit J6 whose thickness does not exceed 200 μm [*Grachev et al.,* 2005]. Diamond crystals ranging by size from a submicrons to tens of microns form the aggregates with spherules of pure nickel (Figure 4.1a–c). The hexagonal polymorph of diamond (lonsdaleite) was observed (Figure 4.1d) and provides for the impact origin of this kind of diamonds.

The second population of diamonds has been discovered later under the study samples from Gams 1 outcrop. In this case we had a lot of material to prepare and study of nonmagnetic heavy fraction. As a result we found several tens of detrital diamond crystals in all parts of the transitional layer. The diamond crystals have the different habits (Figure 4.2, Figure 4.3), including slightly abraded grains (Figure 4.2).

Up to now there are only three localities where diamonds at the K/T boundary were reported: Canada,

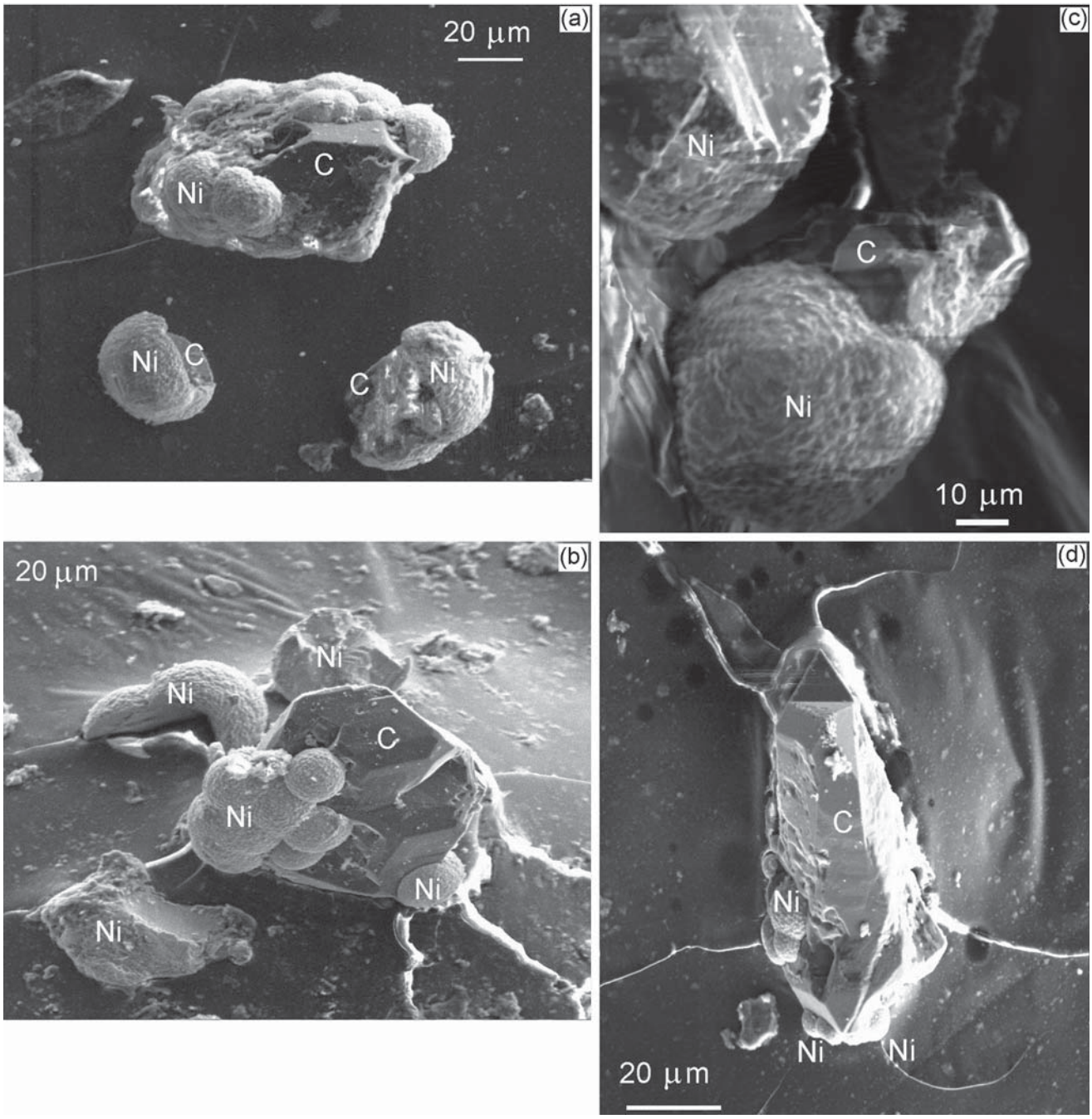

Figure 4.1. SEM images of diamonds with Ni spherules (see explanation in text).

Mexico and USA [*Carlisle, Braman*, 1991; *Hough et al.*, 1997]. In all these places the size of diamond grains is no greater than 6 μm and morphology of crystals is poor defined. This is why we underline the importance of findings the diamonds crystals of different sizes, habits and paragenesis with Ni spherules in Gams sections.

Moissanite (SiC). It is the first finding of moissanite (silicon carbide) at the K/T boundary layer. Presence of SiC was confirmed by optical microscope study and microprobe analysis. This mineral shows well-developed crystal faces either hexagonal or trigonal and occurs also as angular fragments only in the upper portion of Gams 1 section (Figure 4.4).

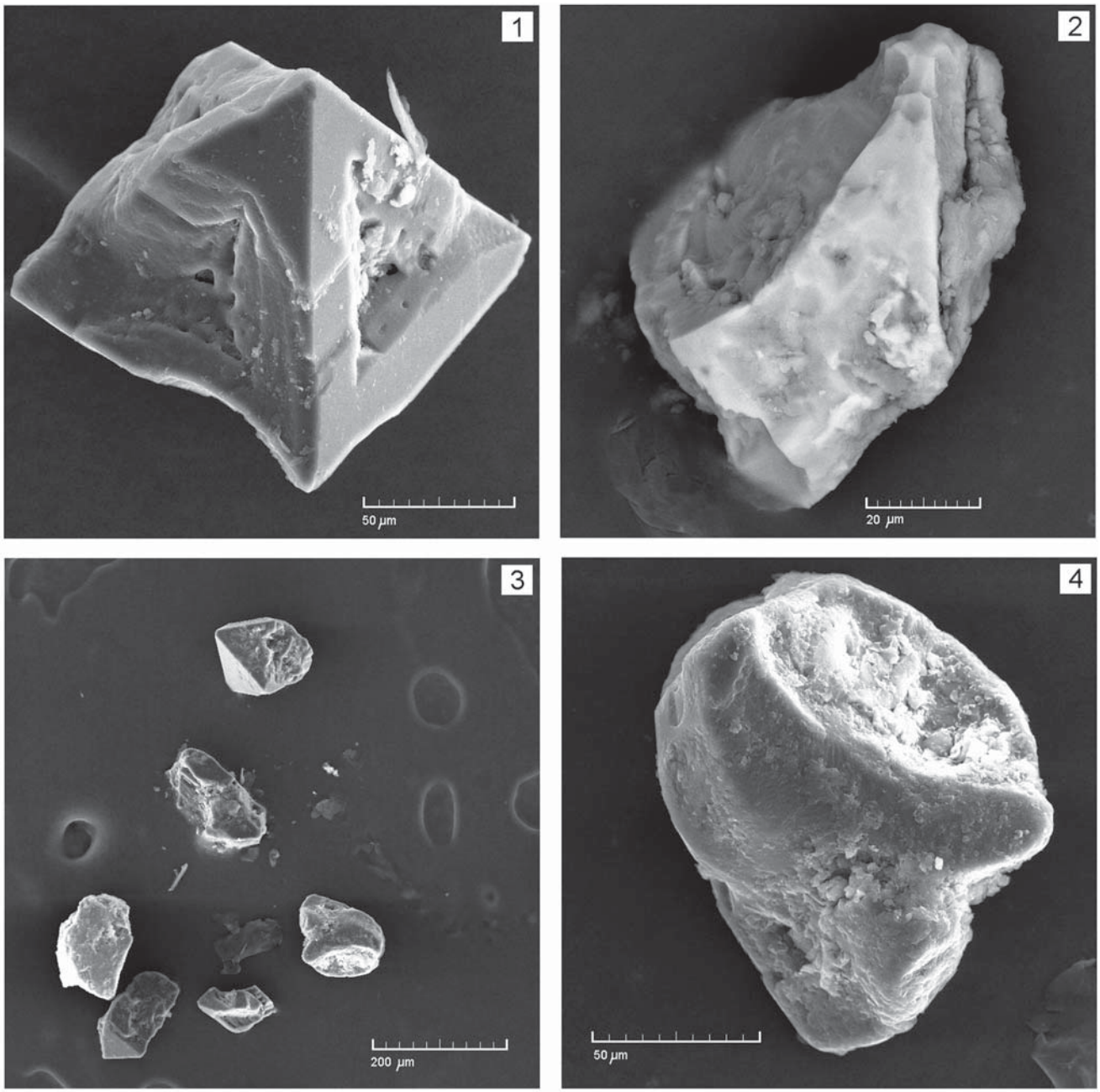

Figure 4.2. 1 – octahedral diamond crystal with trigons, 2 – angular fragment of diamond grain, 3 – different kinds of detrital diamond grains, 4 – slightly rounded diamond grain.

The natural occurrence of SiC with diamond association was first reported by F. H. Moissan in 1920 from the Diablo Canyon iron meteorite in Arizona. Later moissanite has been discovered in kimberlite pipes of Yakutia, China and S.Africa [*Bobrievich et al.*, 1957], volcanic breccia [*Bauer et al.*, 1963; *Di Pierro et al.*, 2003], recent hydrothermal system of Iturup island (Kuril-Kamchatka island arc) [*Rychagov et al.*, 1997], crater Riis together with diamond [*Hough et al.*, 1995] and also in interplanetary dust [*Stadermann et al.*, 2006].

Such variety of moissanite occurrences led some researchers to a conclusion, that "there is no one mechanism of moissanite formation that is either testable or totally consistent with all observations, and what

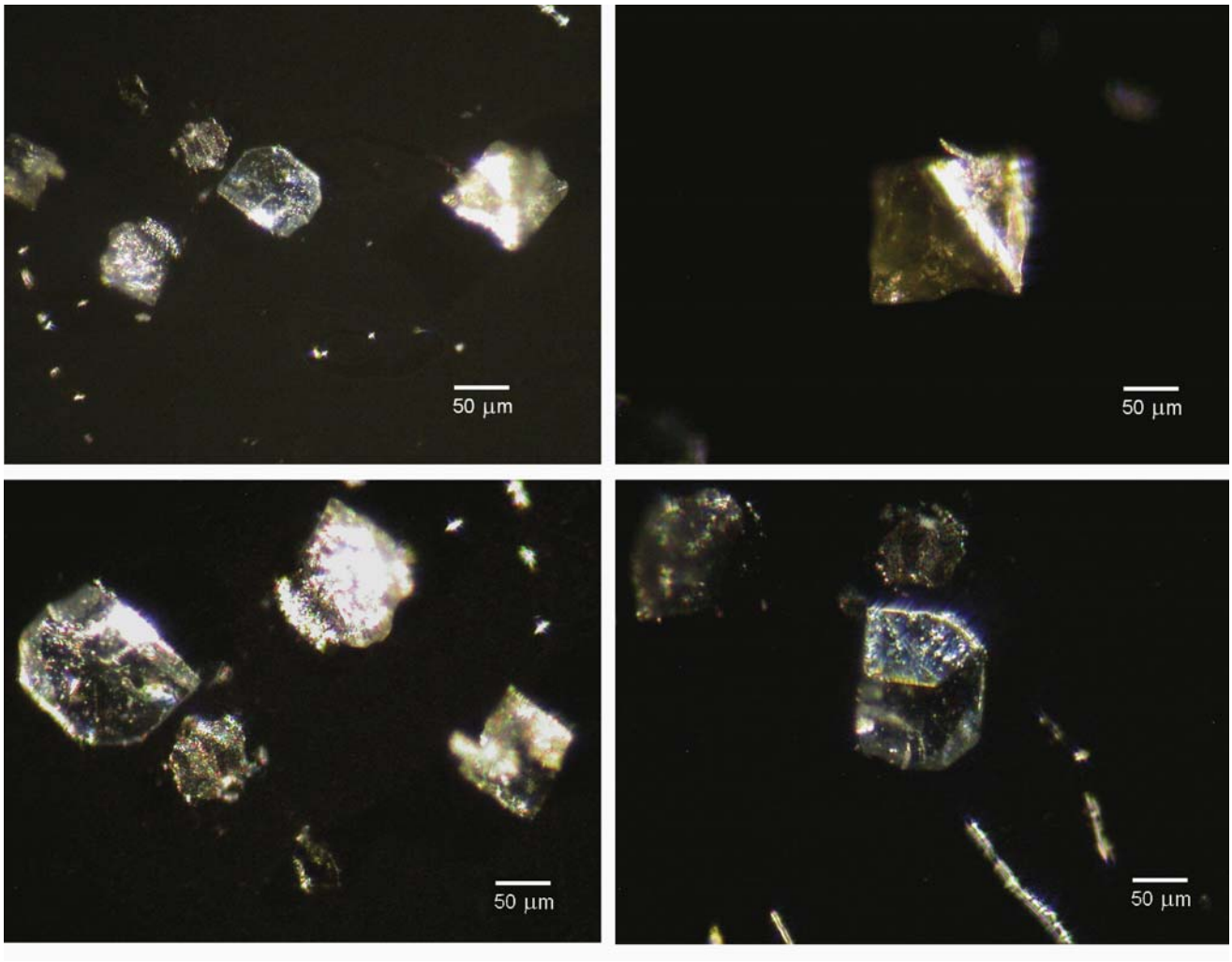

Figure 4.3. Optical photographs of diamonds.

moissanite tells us about processes and conditions of the deep Earth remain unknown" [*Mathez et al.*, 1995, p. 790).

Rhenium. The first finding of native rhenium in the transitional layer in the Gams 2 section has a great importance for understanding of the K/T boundary nature [*Grachev et al.*, 2008a]. The presence of native rhenium in nature is limited by the following information available at present. Native rhenium particles of different morphologies were found in samples of lunar ground: irregularly shaped dense particles from the Mare Fecunditatis and spheroidal particles from the Mare Crisium. Their size is less than 10 μm. Their origin was supposed to be related to exhalation [*Bogatikov et al.*, 2004; *Mokhov et al.*, 2007]. Native rhenium of extraterrestrial objects was found in nickel-iron and silicates of the Allende meteorite [*Goresey et al.*, 1977].

The first finding of a new rhenium mineral ReS_2 preliminarily named as rheniite [*Znamenskii et al.*, 2005] in sublimates of Kudryavyi Volcano (Iturup Island, Kuril Arc) played a crucial role for understanding the constraints on rhenium occurrence in nature. Based on microprobe data, this mineral has the following composition (wt. %): Re 74.46, S 25.95, Mo 0.22, and As 0.19. It should be noted that Kudryavyi Volcano is a Hawaiian-type volcano. According to the available estimates, 2000 t of Re have been released into the atmosphere over the last 100 yr. The Re content in the gaseous condensate of Kudryavyi Volcano is approximately 1 ng/g [Rhenium Sulfide—RheniiteReS_2 (http://www.cnt.ru/users/yakushev/mineral)].

We used a special technique of sample preparation designed of primary material with respect to density

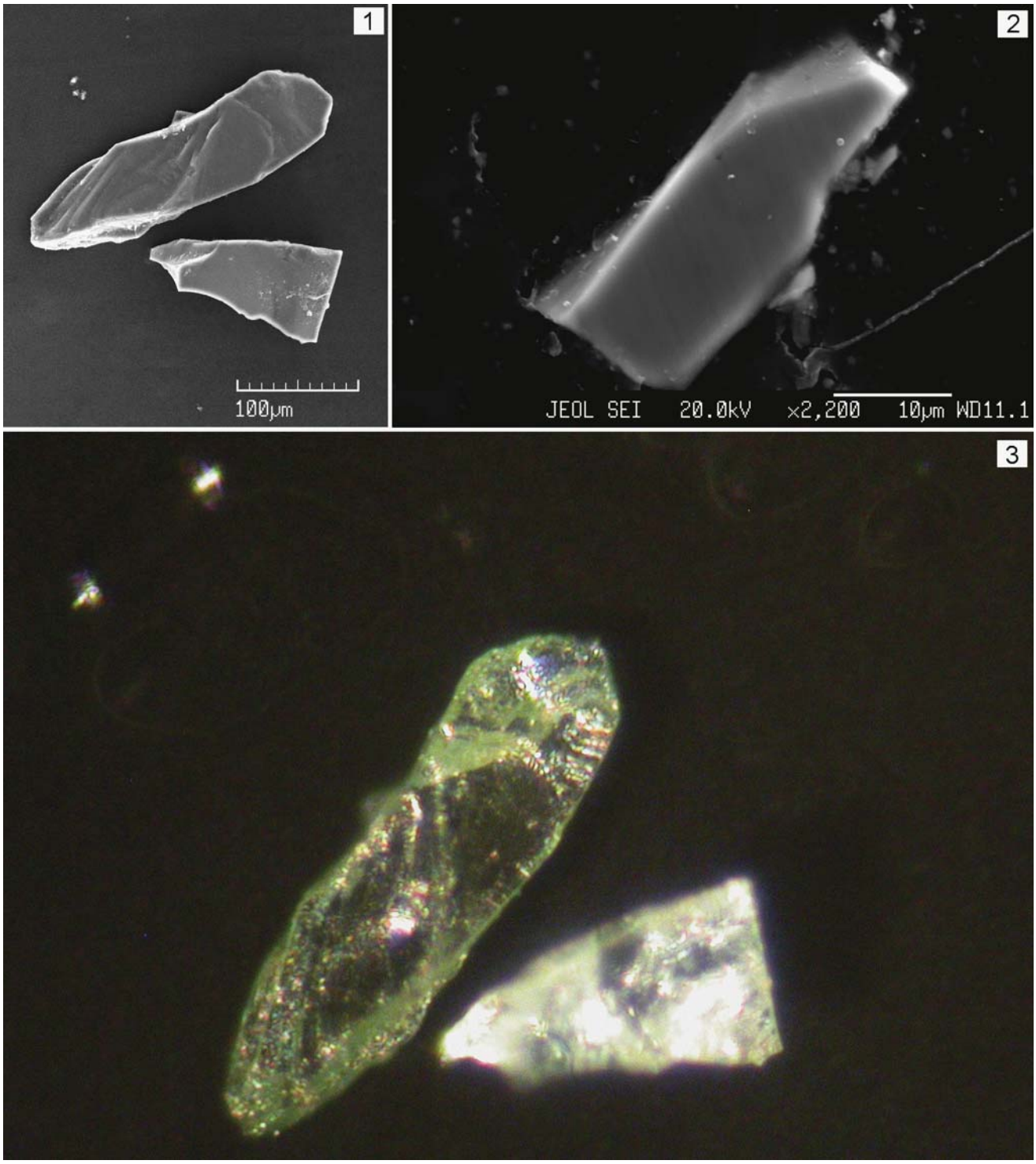

Figure 4.4. SEM images of moissanite (1, 2) and optical photograph of moissanite grains (3).

and grain size which provided fractions required. JEOL JXA-8100 electron microprobe analyzer (IGEM RAS) was used for detailed examination of grain composition [*Grachev et al.*, 2008a].

Figure 4.5 presents a photomircograph of a natural rhenium particle. Its composition is quite similar to that of pure rhenium with traces of Fe (0.07%) [*Grachev et al.*, 2008c]. The grain of rhenium has a prominent

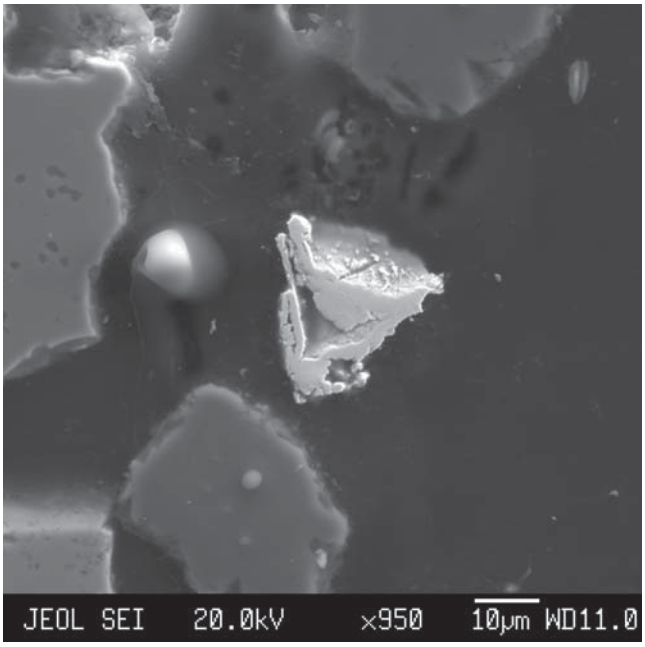

Figure 4.5. SEM image of native rhenium.

triangular shape with a ragged boundary and a crack (likely of thermal origin) at the top (Figure 4.5). The observer-facing edge shows a distinct porous texture probably related to degassing in the course of cooling. The particle morphology (absence of traces of reworking) rules out a terrigenous origin of rhenium.

We cannot rule out an impact origin of the native rhenium, because it is well known that rhenium is present in meteorites [*Goresey et al.,* 1977]. Moreover, the transitional layer at the Cretaceous-Paleogene boundary is characterized by high Re concentrations (up to 0.8 ng/g) relative to the overlying and underlying layers (0.1–0.2 ng/g) [*Lee et al.,* 2003]. However, it should be noted that estimates of the Re content in the continental crust are very contradictory (from 0.3–0.4 to 1.2 ng/g) [*Norman et al.,* 2004]. For the primitive mantle and OIB-type source, the Re content is estimated at 0.6 and 0.8 ng/g, respectively [*Norman et al.,* 2004], which matches Re concentrations in the transitional layer at the Cretaceous-Paleogene boundary in many regions of the world [*Lee et al.,* 2003].

It is more probable that the native rhenium was formed from volcanic ash. Evidence in favor of the role of volcanic ash is provided by the high As concentration in the lower part of the transitional layer (see Chapter 3). This feature is recorded at the Cretaceous-Paleogene boundary in nearly all similar sections of the world and cannot be explained in terms of the impact paradigm, because the As concentration does not exceed 2 ppm in meteorites [*Hamaguchi et al.,* 1969] and is three to four orders of magnitude higher at the base of the transitional layer! [*Brooks et al.,* 1984; *Ebihara, Miura,* 1996; *Grachev et al.,* 2005, and others].

The first investigations of degassing in volcanoes of the Hawaiian mantle plume revealed significant concentrations of As, Cu, Zn, Cd, Hg, Se, In, Au, and Ir. The As content in gases is as much as 1600 g/m^3 [*Zoller et al.,* 1983]. Even samplings at a distance of 50 km from the eruption site at an altitude of 3400 m, which exceeds the limit of aerial influence, revealed Se and In concentrations 400 times higher than the normal values. The enrichment factor (relative to the BGVO-1 standard) is 10–50 for S, Cu, Zn, and As and more than 50 for Ir, Se, Hg, Cd, and In. It is very important that anomalously high contents of Ir (up to 0.057 g/m^3) during volcanic eruptions are accompanied by high contents of F and Cl [*Gerlach, Graeber,* 1985]. The behavior of Re during the degassing of Hawaiian volcanoes is similar to that of other chalcophile elements (As, Se, and others) [*Norman et al.,* 2004]. Study of the composition of gases from several conduits of Kilauea Volcano revealed very high degrees of enrichment in Re, As, Se, and Au (10^5–10^7) relative to the degassed lava. For example, the amount of Re emitted into the atmosphere during the degassing of 3.5×10^5 m^3 of magma is as much as 200–400 kg/day [*Norman et al.,* 2004].

According to the hypothesis of the influence of volcanic aerosol on the transitional layer formation at the K/T boundary owing to plume magmatism 65 Ma ago, such aerosol should exist for a prolonged time (at least for tens of thousands of years). From this point of view, the high contents of As, Se, Re, and other chalcophile elements in the transitional layer are rather natural.

Platinum. Native platinum has been discovered under the study of residue fraction of clay. We dissolved of 200-g clay with HF and HCL using proce-

Table 4.2. Electron microprobe analyses (wt. %) of native platinum grains

Pt	Pd	Ir	Rh	Cu	Ni	Fe	Total
99.22	0.02	0.00	0.00	0.00	0.03	0.00	99.27
99.12	0.00	0.00	0.00	0.00	0.00	0.02	99.14
99.13	0.00	0.00	0.00	0.00	0.03	0.00	99.16
100.02	0.00	0.00	0.00	0.00	0.00	0.03	100.05
99.18	0.05	0.00	0.00	0.00	0.03	0.03	99.29
98.98	0.03	0.00	0.00	0.00	0.00	0.04	99.05
97.57	0.05	0.00	0.00	0.00	0.03	0.00	97.65
	0.01	*0.09*	*0.03*	*0.03*	*0.03*	*0.02*	

Note: Detection limit is shown by italics.

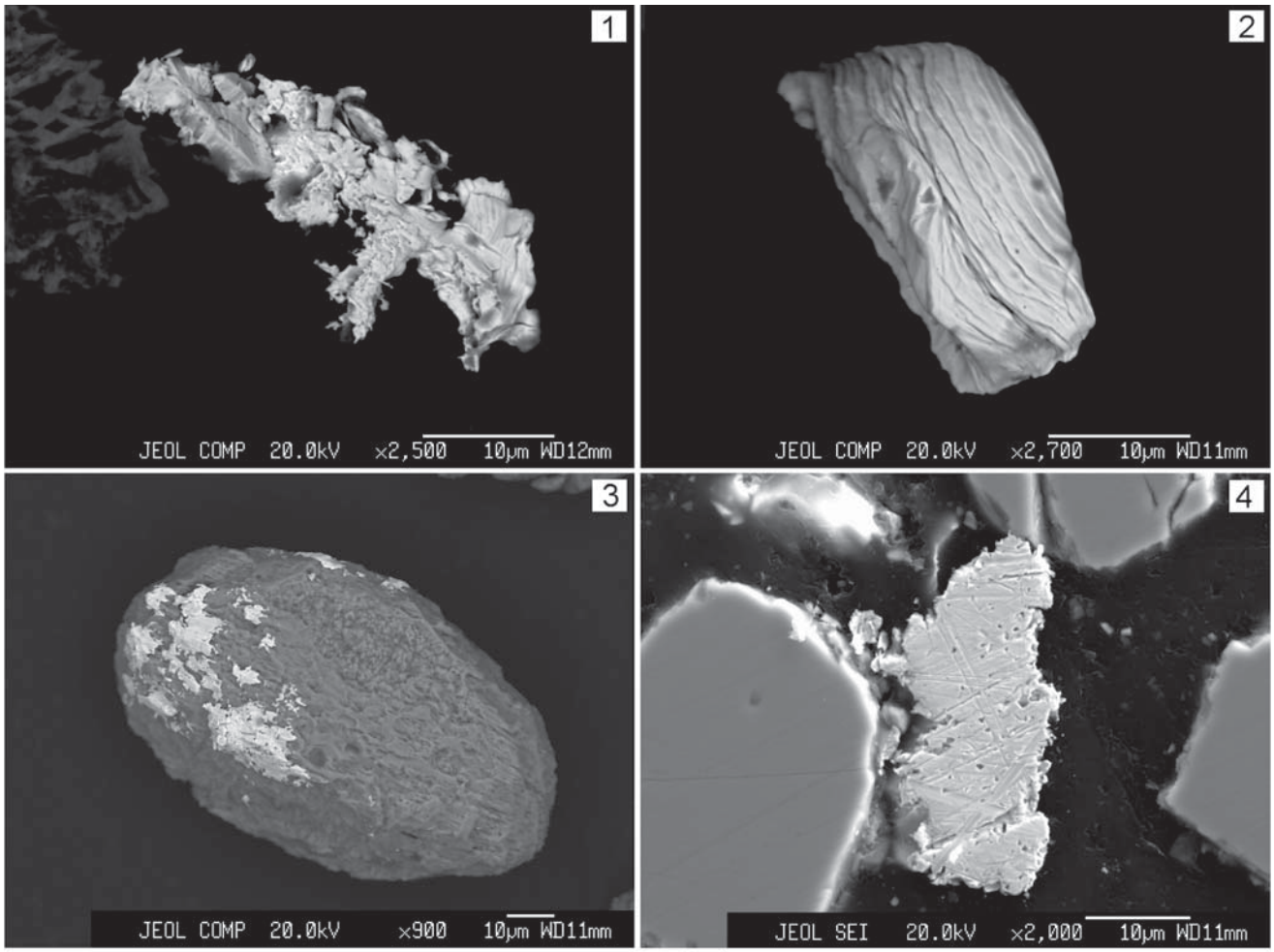

Figure 4.6. 1 – BSE image of dendritic platinum grain; 2 – BSE image of platinum grain with transverse-hummocky surface texture; 3 – BSE image of rounded zircon grain covered by thin film of native platinum, 4 – SEM image of platinum in polished box.

dure described by *Carlisle, Braman* [1991]. We found ten grains of platinum by total volume of $8\times10^4\mu m^3$ in a residue of 16 mg by weight. The simple recalculation gives the content of Pt in clays about 10 ppb.

Microprobe analyses of seven Pt grains (Table 4.2) shows the existence of pure platinum without alloyed with other metals. Such result is unexpected because pure platinum is unknown in nature and this finding may be explained as follows.

We paid attention to the specific morphology of Pt grains. As it follows from Figure 4.6 the grains have the irregular shape outlines with well-developed branching, tree-like and transverse-hummocky structures (Figure 4.6). Besides extremely surprising is the occurrence of the thin film of Pt covered the rounded zircon grain (Figure 4.6). It means that film of Pt has been formed in situ due authigenic flux from sea water during the transitional layer deposition. We propose that initially platinum was dispersed in sea water as a result of volcanic aerosol settling.

Silver. Two varieties of silver were recognized in the lower part of transitional layer of Gams 2 section.

The first one is present as native silver, which composition corresponds to 98.7% of Ag (microprobe analysis). Native silver occurs as twin crystal (Figure 4.7a) and its outline resembles the silver crystals formed in primary hydrothermal veins. The second occurrence is represented by nugget plates of $Ag_{47}Pd_{53}$ alloy (Figure 4.7b).

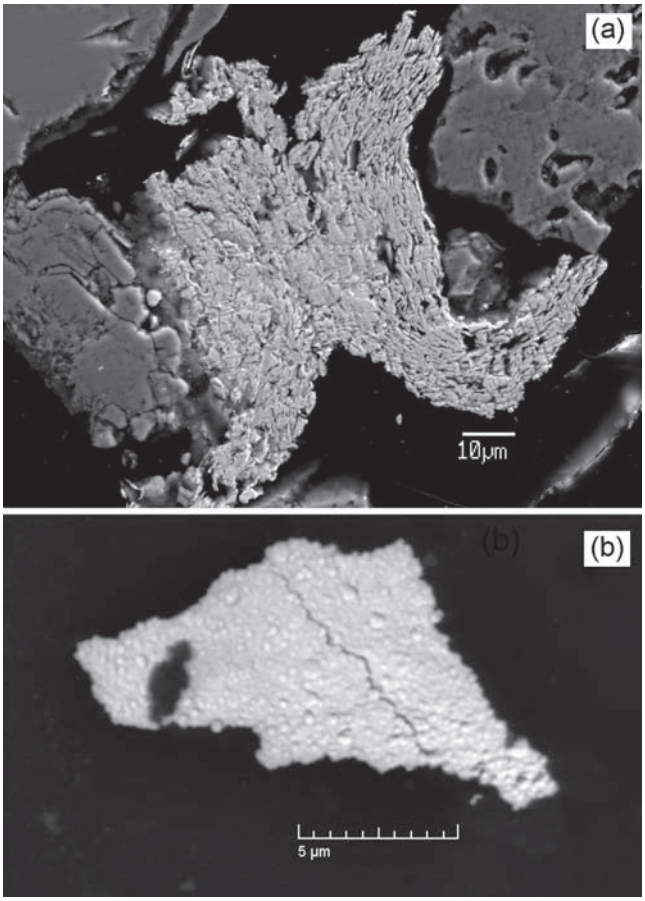

Figure 4.7. a – SEM images of silver grain, b – SEM image of massive silver plate with "bubble-like" surface.

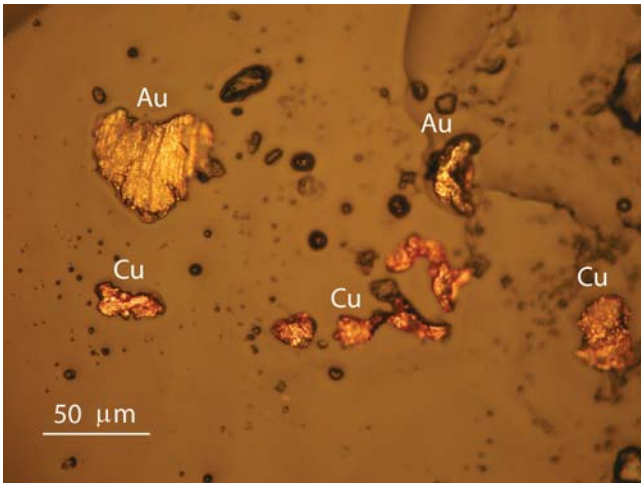

Figure 4.8. Disrupted and skeletal grains native copper and gold in the lower part of transitional layer.

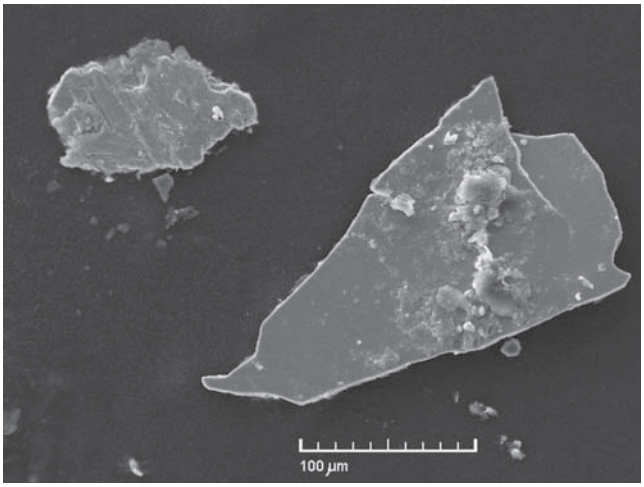

Figure 4.9. SEM image of brass.

Metallic iron was found in the form of separate grains in all studied sections. In the monolith pure iron spherules were noted not only in transitional layer J but also in layers L and M (see details in Chapter 5 and 6).

Gold and copper were determined in all parts of the transitional layer and have the similar morphology, typical for gold and copper in placer deposits (Figure 4.8).

Metallic alloys. In the lower part of the transitional layer we have found the following types of metallic alloys: brass ($Cu_{67}Zn_{33}$ alloy) (Figure 4.9), iridium-osmium alloy (osmiridium – Os 66.82 %, Ir 33.18 %), alloy of nickel, copper, zinc and copper (new mineral

Table 4.3. Representative microprobe analyses (at %) of new ore mineral (gamsite) from the lower part of the transitional layer

Element	1	2	3	4	5	6	7	8	9	10	11	12	13
Ni	70.95	82.44	68.26	69.66	64.74	67.50	73.68	70.62	36.74	61.63	62.27	52.33	52.65
Cu	13.15	10.33	17.43	17.22	18.56	19.20	19.62	16.28	33.23	19.69	20.00	27.27	29.74
Zn	9.06	–	11.26	11.33	12.34	11.65	5.35	10.17	10.43	14.76	15.82	19.77	17.61
Sn	6.85	7.23	1.61	1.79	4.36	1.65	1.64	2.93	30.61	3.92	1.91	–	–

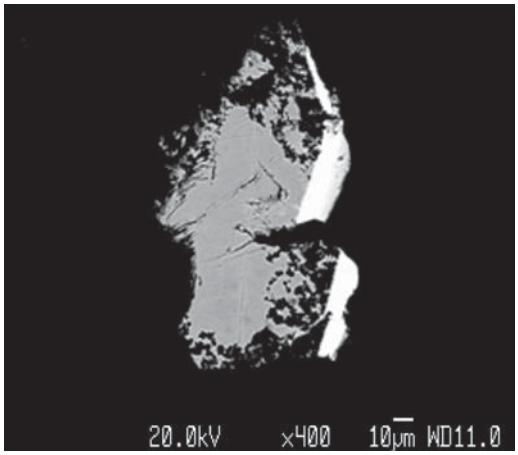

Figure 4.10. BSE image of metallic Fe grain (see Table 4.4).

Table 4.4. Electron microprobe analyses (wt. %) of Fe grain (layer J_0)

Fe	Mn	Ti	Si	Co	Ni	Cr	S	Total
99.56	0.25	0.00	0.03	n.d.	n.d.	0.04	0.04	99.92
99.22	0.31	0.00	n.d.	n.d.	0.03	0.05	0.07	99.68
99.49	0.29	0.00	n.d.	n.d.	n.d.	0.07	0.04	99.89

–gamsite?) (Table 4.3). In the base of the lower part of transitional layer of the Gams 2 section the single grain of metallic iron was found (Table 4.4, Figure 4.10).

Early we have established the presence of awaruite in the upper portion of layer J (Figure 4.11) [*Grachev et al.*, 2005]. Now we have more data allowing to suggest Ni-Fe alloys with different ratios of these elements in Gams [*Grachev et al.*, 2008b] (see details in chapter 5 and 6).

It is necessary to pay attention to the size of the osmiridium grains (the first microns) (Figure 4.12). Despite the detailed thin-sections study, we could find only two grains, therefore Ir enrichment of transitional cannot be connected with osmiridium. It is rather probable, that a source of osmiridium is the ultrabasic Kraubath massif, where such kind of alloy was noted. This massif is located approximately in 100 km to the southeast from Gams [*Malitch et al.*, 2003]. Because osmiridium has a high density (more than 17 g/cm^3), it could not be transferred at such long distances from the source area.

4.3.2 Sulfides

As follows from Table 4.1, the lower part of the transitional layer (the first 6–8 mm Gams 1 and Gams 2 sections) is characterized by essential enrichment by sulfides of iron, arsenic, copper, lead, zinc, molybdenum (Figure 4.13a,b; Figure 4.14a–c, Figure 4.15, Figure 4.16, and Figure 4.17), and also by presence of pentlandite and violarite.

Table 4.5. Electron microprobe analyses (wt. %) of pyrite, arsenopyrite and molybdenite from the rust crust at the base of the transitional layer (J_0)

Fe	Mo	S	Co	Ni	As	Sb	Total
46.18	–	52.65	0.00	0.01	0.02	0.00	98.86
46.39	–	54.01	0.03	0.00	0.00	0.00	100.43
46.39	–	54.11	0.06	0.00	0.00	0.00	100.56
46.50	–	53.46	0.01	0.00	0.00	0.00	99.97
46.21	–	53.47	0.07	0.00	0.21	0.00	99.96
46.42	–	53.51	0.07	0.00	0.17	0.00	100.17
46.14	–	53.95	0.07	0.00	0.15	0.00	100.31
46.36	–	52.85	0.05	0.03	0.18	0.00	99.47
46.58	–	54.12	0.00	0.00	0.14	0.00	100.16
46.67	–	54.12	0.00	0.00	0.19	0.00	100.98
34.99	–	22.47	0.00	0.01	41.96	0.06	99.49
34.96	–	22.22	0.00	0.02	41.68	0.07	98.95
0.05	59.66	39.47	0.00	0.00	0.00	0.00	99.18

The most striking phenomenon is the areal growth of pentlandite crystals, covering a surface of clay unit in the lower part of the transitional layer (Figure 4.17). It is essentially important to note the transformation of pentlandite to violarite ($FeNi_2S_4$) could occurr in supergene conditions (Table 4.6). This is suggested by well expressed shrinkage cracks on the surface of violarite (Figure 4.18).

As it is known, violarite is formed in supergene zones of many massive Ni sulfide deposits (Norilsk, Sud-

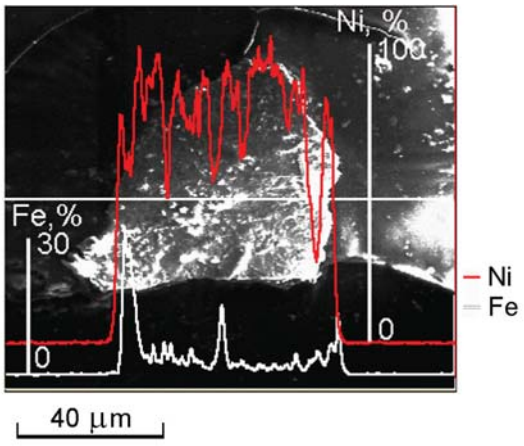

Figure 4.11. Awaruite grain from the upper portion of layer J.

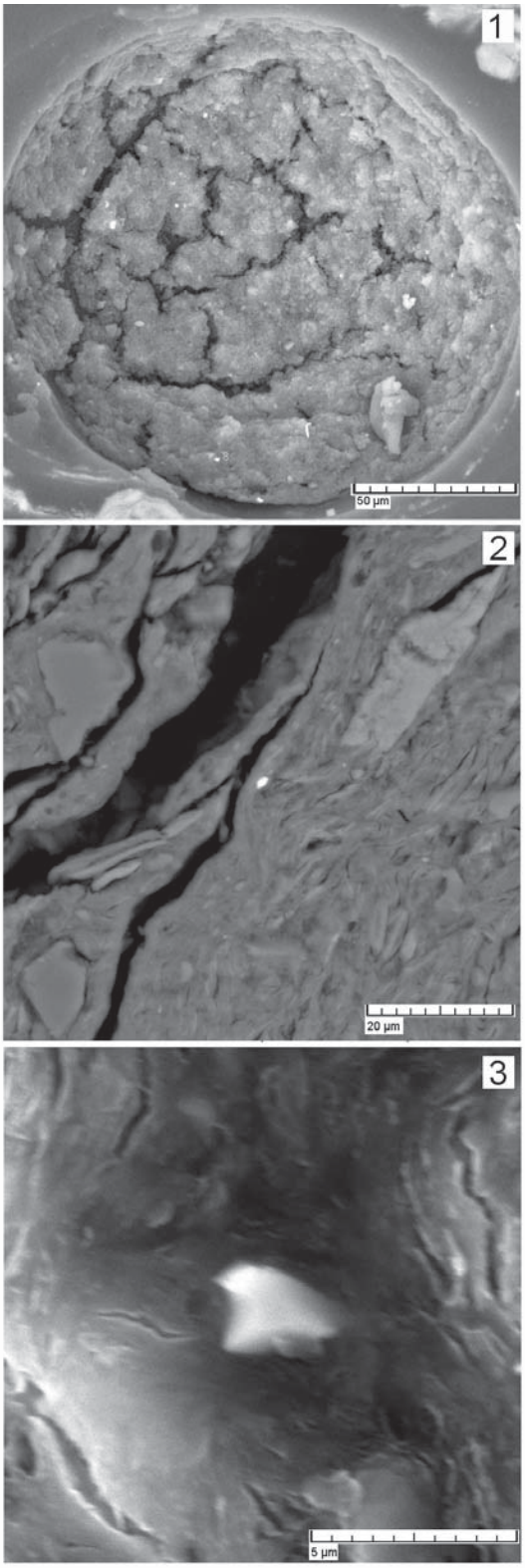

Figure 4.12. 1 – SEM image of inner part of Fe spherule with particle of Os Iridium (number 7), 2 – the same as in 1 (enlarged scale), 3 – SEM image Os Iridium in thin-section (bright grain in centre of microphotograph).

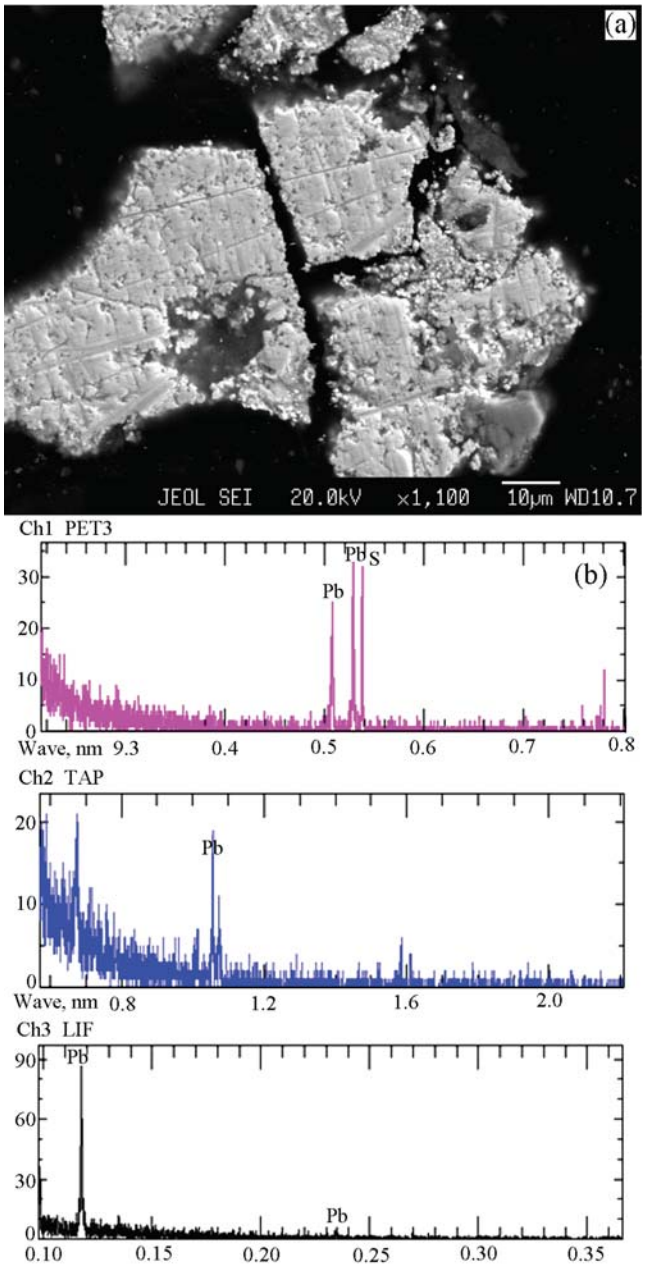

Figure 4.13. (a) SEM image of galena, (b) Bulk WDX spectrum of galena.

bury, Monche-Tundra, etc.). In hydrothermal conditions the rate of transformation pentlandite to violarite is defined by temperature at pH environments from 3 to 5 and this reaction happens under very reducing conditions [*Tenailleau et al.*, 2006].

Pyrite was found in the base of the lower part of layer *J* (units J_0 and J_1) and presented by two modifications: angular pyrite grains with zones of As enrichment (Table 4.5; Figure 4.14b) and framboidal pyrite (Figure 4.14c). It is very likely that framboidal pyrite

Table 4.6. Electron microprobe analyses (wt. %) of violarite

Ni	Fe	S	Co	Cu	Total
19.64	34.24	39.24	1.05	0.01	94.18
34.42	21.47	39.30	1.06	0.06	96.31
21.28	32.91	39.11	0.99	0.16	94.45
25.94	28.78	40.62	1.01	0.06	96.41
22.28	32.40	39.76	0.94	0.02	95.40

can be regarded as fossilized sulfur bacteria formed during the transitional layer deposition as a result of bacteria action. Concentration of pyrite is the highest in the lower part of layer *J* and regularly decreases upward. Pyrite is absent in the Danian sedimens above the transitional layer. Pyrrotine is characterized by firmly fixed chemical composition that is not typical for this mineral chemistry (Table 4.7, Figure 4.15).

Molybdenite, galena and sphalerite were identified only in the lower part of the transitional layer. Such paragenesis of sulfide minerals is an indicator of an anaerobic conditions. The morphology of sphalerite crystals (needle-like nabit) (Figure 4.16) is the best evidence of its syndepositional nature.

4.3.3 Oxides

Spinel Minerals of the spinel group were found in the Gams sequence in the K/T boundary layer of clay and in the overlying Maestrichtian clays. We determined that the rocks contain two spinel populations: Cr-spinel with a low Ni concentration (<0.1%) and spinel rich in Ni (>2%) (Table 4.8 and Table 4.9).

The former was found throughout the whole vertical section of the Gams boundary layer, whereas the latter is contained not only in all portions of transitional layer, but also below in calcareous marlstones. The lower portion of the boundary layer commonly contains spinel in association with single grains of magnesiochromite and chromite.

Table 4.7. Electron microprobe analyses (wt. %) of pyrrotine

Ni	Fe	S	Co	Total
0.26	61.84	37.66	n.d.	99.76
0.28	61.63	38.86	0.02	100.79
0.24	61.80	38.56	0.01	100.61
0.18	62.02	37.03	n.d.	99.23
0.26	62.47	37.74	0.02	100.49
0.19	61.68	37.33	0.02	99.22
0.19	61.73	37.50	0.02	99.44

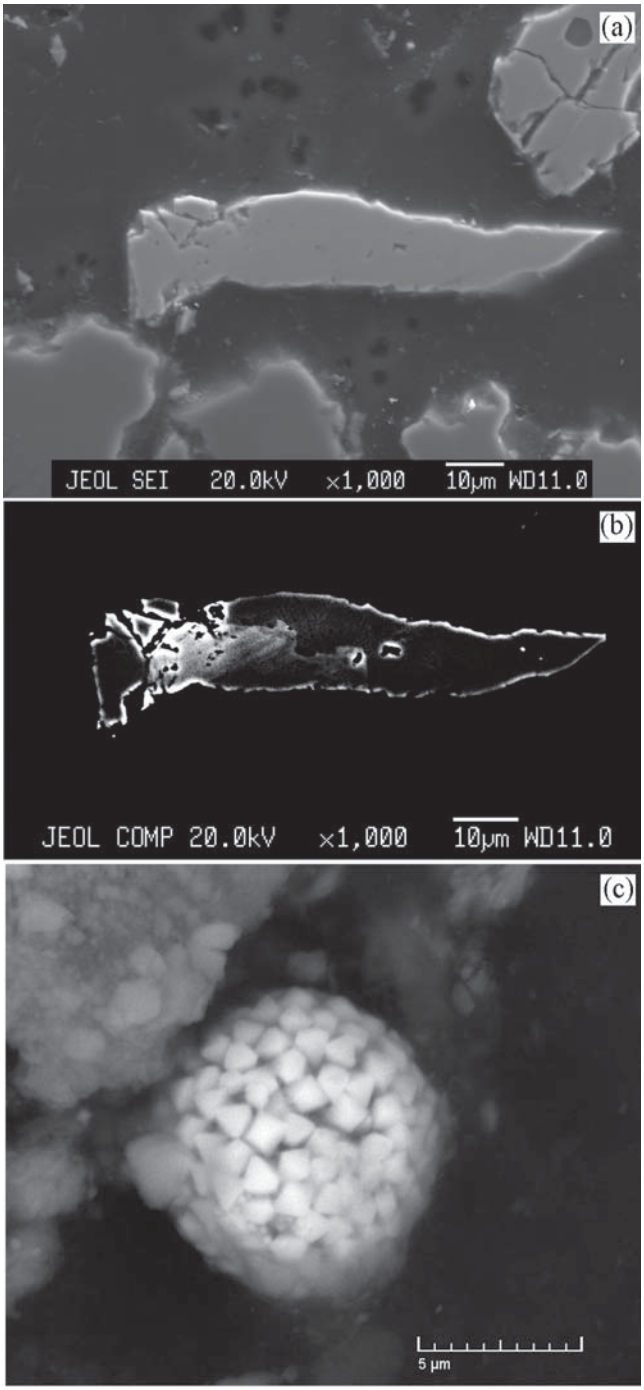

Figure 4.14. (a) SEM image of pyrite, (b) BSE image of pyrite with light zone marks the enrichment of As, (c) BSE image of framboidal pyrite.

The two spinel populations also show different morphologies of their grains. The Cr-spinel typically occurs as angular grains with clearly pronounced serrated edges, a feature suggesting the absence of abrasion (Figure 4.19a). These grains range from 20 to 100–150 μm in size. The Ni-bearing spinel was found in

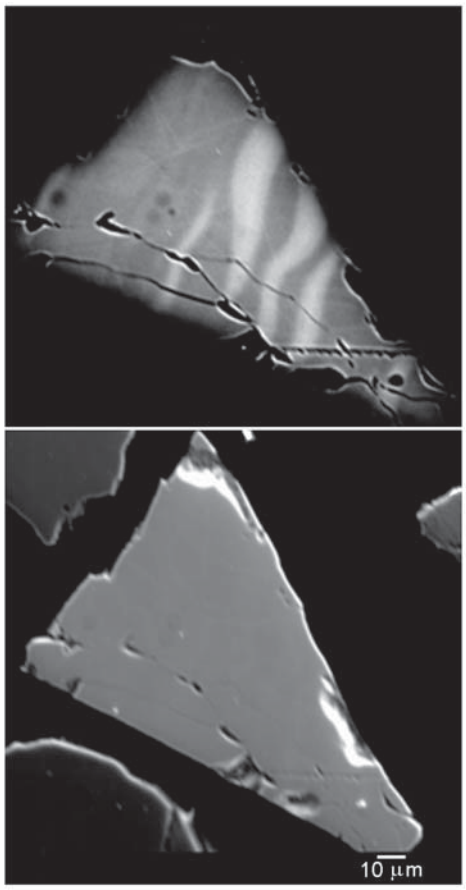

Figure 4.15. BSE image of pyrrotine; light zones – troilite (top). SEM image of pyrrotine (bottom).

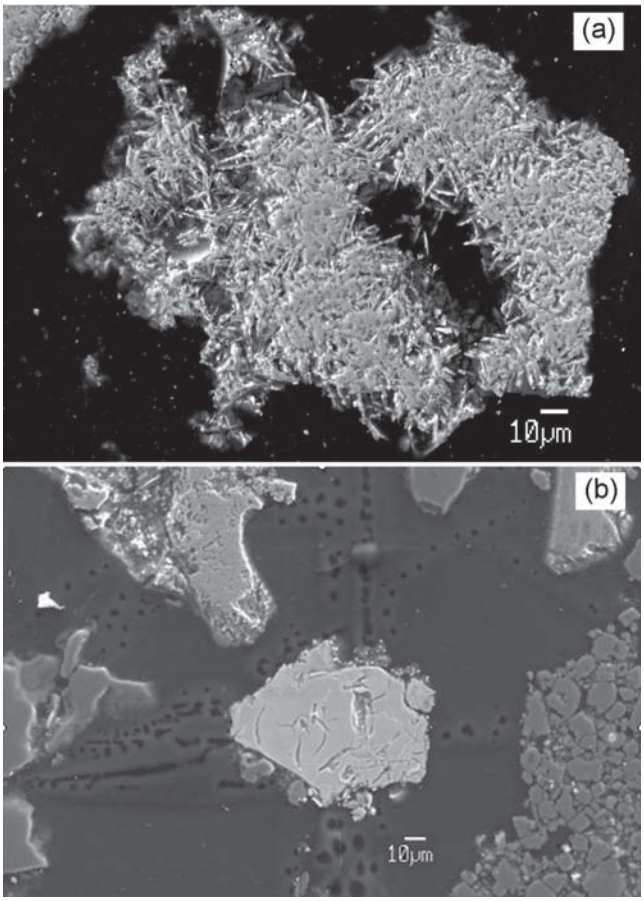

Figure 4.16. SEM images of sphalerite (a) and molybdenite (b).

Table 4.8. Chemical microprobe analyses (wt.%) of Gams chrome spinels

Element	1	2	3	4	5	6	7	8	9	10
SiO_2			1.16	0.45						
Al_2O_3		10.61	11.49	9.69	11.25	8.46	9.25	8.96	7.31	10.05
Cr_2O_3	59.72	59.43	57.90	60.87	55.68	61.31	60.30	61.84	65.07	57.92
FeO	16.24	16.36	13.44	15.25	15.52	16.52	16.50	16.52	15.49	16.32
MgO	17.56	13.60	16.01	13.74	17.24	13.72	13.95	12.67	12.13	15.71
Fe^{2+}/Fe^{3+}	0.26	3.87	4.41	6.54	0.94	3.10	2.89	5.92	18.41	1.48
$Fe^{3+}/Fe^{2+}+ Fe^{3+}$	0.79	0.20	0.18	0.13	0.27	0.24	0.26	0.14	0.06	0.40
Mg/Mg+Al		0.68	0.64	0.65	0.56	0.67	0.55	0.64	0.68	0.66
Cr/Cr+Al		0.78	0.77	0.81	0.77	0.83	0.81	0.82	0.86	0.79
$Mg/Mg+Fe^{2+}$	0.9	0.65	0.72	0.66	0.80	0.66	0.67	0.62	0.60	0.74

Element	11	12	13	14	15	16	17	18	19	20
Al_2O_3	8.71	7.91	9.23	9.72	9.87	9.16	8.43	10.12	6.52	2.71
Cr_2O_3	60.72	62.12	59.48	60.68	60.04	61.44	62.39	59.81	62.85	60.90
FeO	17.42	16.96	16.64	15.64	16.15	15.68	16.31	15.50	23.34	22.48
MgO	13.15	13.01	14.65	13.97	13.94	13.72	12.87	14.57	7.29	13.91
Fe^{2+}/Fe^{3+}	3.34	3.87	2.07	3.68	3.30	4.10	5.43	2.83	16.12	1.03
$Fe^{3+}/Fe^{2+}+ Fe^{3+}$	0.23	0.20	0.32	0.27	0.23	0.20	0.16	0.26	0.06	0.49
Mg/Mg+Al	0.66	0.67	0.67	0.66	0.64	0.65	0.66	0.64	0.58	0.87
Cr/Cr+Al	0.82	0.84	0.82	0.81	0.80	0.81	0.83	0.80	0.87	0.94
$Mg/Mg+Fe^{2+}$	0.64	0.63	0.69	0.67	0.67	0.66	0.63	0.69	0.37	0.68

Note: Analyses: 1–5 – lower part, 5–12 – middle part, 13–20 – upper part of the transitional layer. Fe_2O_3 calculated from stoichimetry.

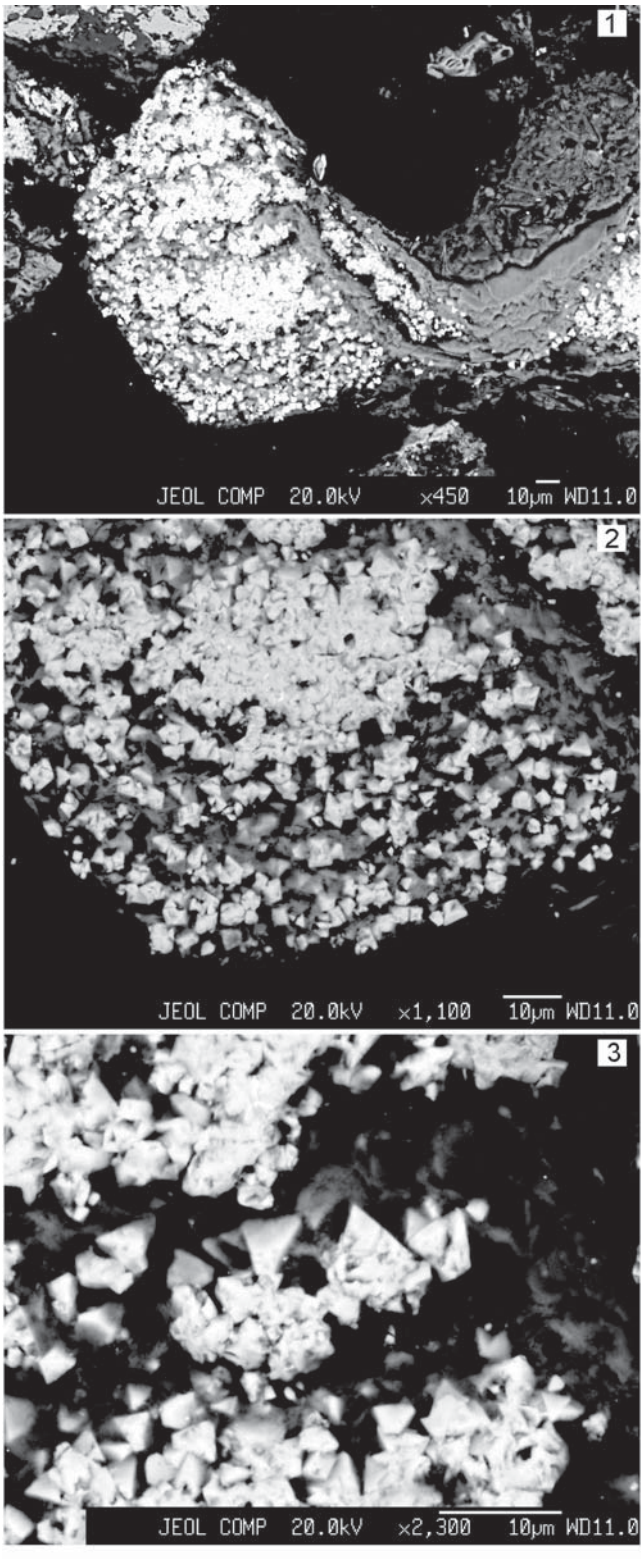

Figure 4.17. 1, 2, 3 – BSE images of pentlandite crystals covering the clay surface; 4 – Bulk WDX spectrum of pentlandite in clay.

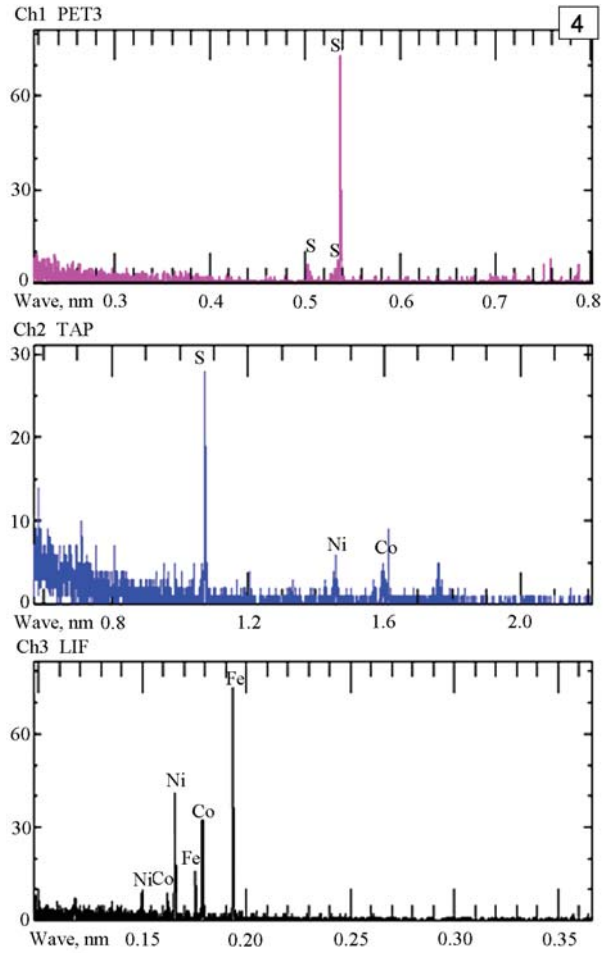

⇐ **Figure 4.17.** Continued.

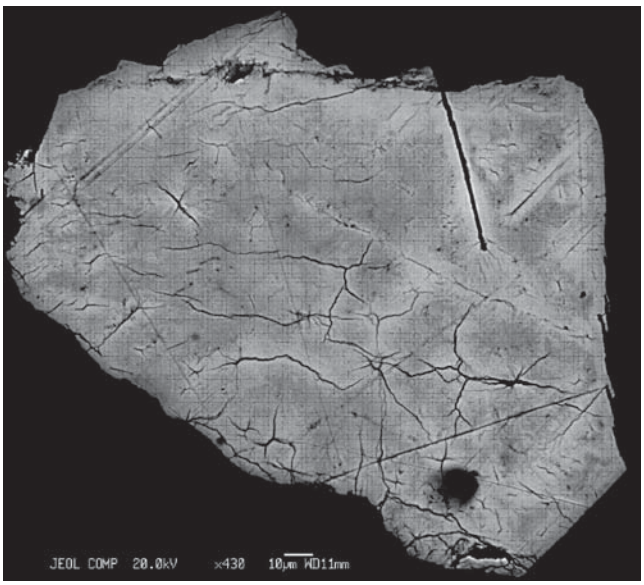

Figure 4.18. BSE image of violarite with shrinkage cracks (Ex. 430).

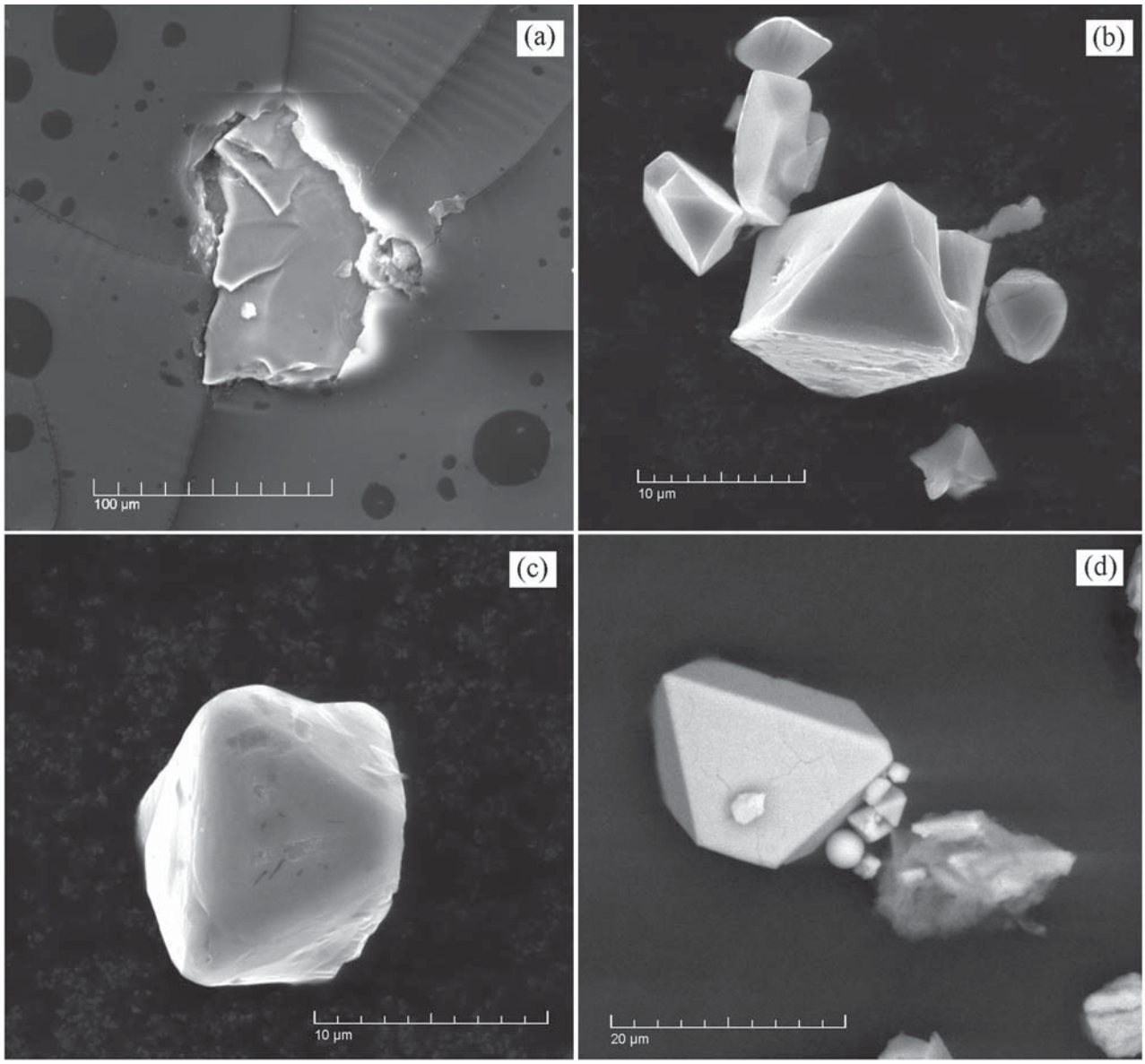

Figure 4.19. SEM images of spinel grains from the Gams stratigraphic sequence: a – Cr-spinel, b, c, d – Ni spinel from the lower, middle and upper parts of the transitional layer correspondingly.

the form of octahedral crystals up to 10–15 μm (Figure 4.19b,c,d).

The Cr-spinel is noted for high and relatively little varying Cr_2O_3 concentrations (from 57% to 65%) and high variations in MgO (7–18%) and FeO (13–23%). Some analyses indicate the presence of TiO_2 (up to 0.6%), MnO (up to 1.6%), ZnO (up to 0.8%), V_2O_5 (up to 0.3%), and NiO (up to 0.1%) (Table 4.8).

Spinel compositions are commonly classified on the basis of their Cr/(Cr + Al) and Mg/(Mg + Fe^{2+}) ratios. As follows from the diagram in Figure 4.20, spinel from the boundary layer of the Gams sequence has very high and little varying Cr# values ($\geq$0.8) and strongly varying Mg#.

As it was demonstrated earlier [*Pober, Faupl*, 1988], spinel from sedimentary rocks of the Upper Gosau Group shows broad variations in its Cr# (from 0.15 to 0.85) at insignificantly varying Mg#, and its compositional points plot within the field of spinel from harzburgites and lherzolites. As can be seen in Figure 4.20, the compositional fields of spinel form the Gams sequence and Gosau Group are clearly separated in the diagram, which testifies that the erosion of Alpine-type peridotites of an ophiolite association

could not provide for detrital spinel for the Gams boundary layer.

The origin of Cr-spinel in the clays could have been related to volcanic processes, because the influence of a mantle plume was proven for the boundary layer in the Gams sequence [*Grachev et al.*, 2005, 2008a], but our samples are characterized by low TiO_2 contents (<1%). The Cretaceous Tainba Formation in southern Tibet, which has a similar age and composition, contains detrital spinel borrowed from basalts related to a mantle plume and contains up to 4% TiO_2 [*Zhu et al.*, 2004], and this mineral from Siberian and Deccan flood basalts contains 18–20% TiO_2 [*Melluso et al.*, 1995; *Zolotukhin et al.*, 1989].

An appealing idea seemed to be searching for possible genetic relations between detrital spinel in the Gams sequence and chromitites in ultrabasic rocks of the Speick Complex at a distance of approximately 100 km southeast of the village of Gams [*Melcher, Meisel*, 2004]. We sampled the chromitites and examined the composition of Cr-spinel from the Kraubath Massif and used the analyses published in [*Melcher, Meisel*, 2004] for comparative analysis.

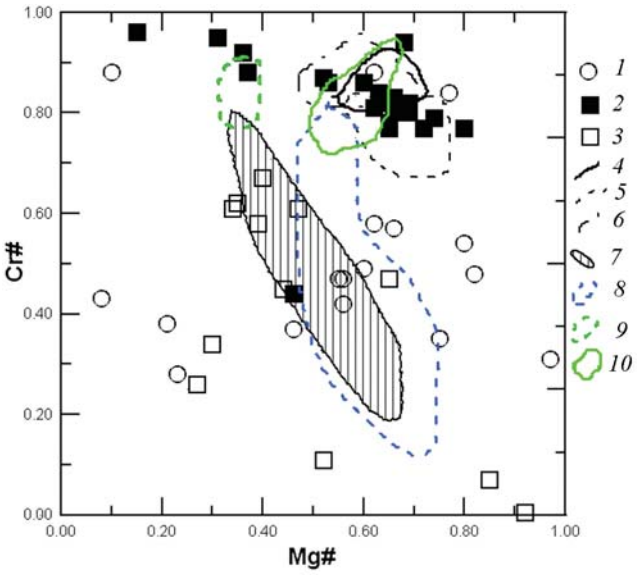

Figure 4.20. Cr# – Cr/(Cr+Al) – Mg# – Mg/(Mg + Fe^{2+}) diagram for spinel from the Gams stratigraphic sequence. 1 – Ni spinel, Gams sequence, 2 – same mineral from elsewhere (see Table 4.9), 3 – Cr-spinel, Gams sequence, 4–6 – Cr-spinel, inclusions in diamonds from South Africa and Yakutia: 4 – South Africa, 5, 6 – Yakutia [*Sobolev et al.*, 2004], 7 – Cr-spinel from the Upper Gosau Group, Eastern Alps [*Pober, Faupl*, 1988], 8 – Cr-spinel from harzburgites and lherzolites [*Stevens*, 1944], 9, 10 – Cr-spinel from chromitites, Hochgrossen and Kraubath massifs, Speick Complex, Eastern Alps [*Melcher, Meisel*, 2004].

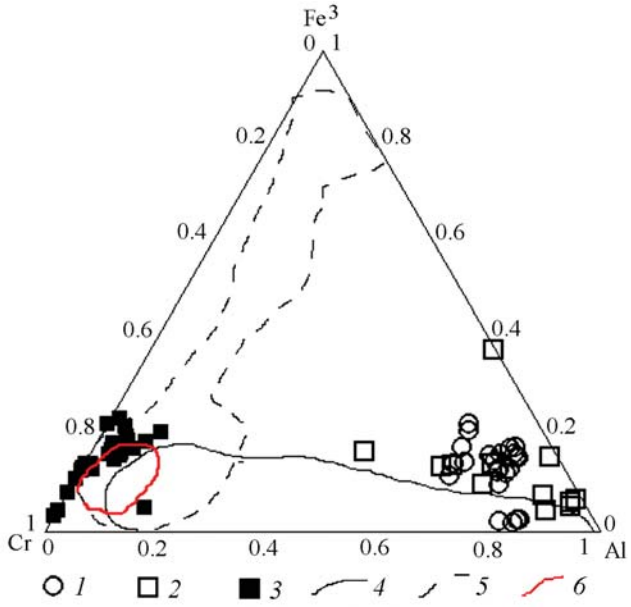

Figure 4.21. Cr-Fe^{3+}-Al diagram for spinel from the Gams sequence. 1 – Ni spinel from the Gams sequence, 2 – same mineral from elsewhere (see Table 4.10), 3 – Cr-spinel from the Gams sequence, 4 – Cr-spinel from Alpine-type ultramafic rocks [*Barnes, Roeder*, 2001], 5 – Cr-spinel from kimberlites [*Barnes, Roeder*, 2001], 6 – Cr-spinel inclusions in diamonds from kimberlites [*Sobolev*, 1974].

The compositional fields of spinel from the Kraubath and Hochgrossen massifs, both of which belong to the Speick Complex, partly overlap the field of spinel from the Gams sequence, but their general Cr# vs. Mg# dependences are exactly opposite. Moreover, spinel from the Speick Complex is higher in TiO_2 (up to 3%) [*Melcher, Meisel*, 2004]. As follows from Figure 4.20 and Figure 4.21, the closest analogue of the Gams Cr-spinel is spinel from kimberlites and inclusions in diamonds [*Barnes, Roeder*, 2001; *Kamensky et al.*, 2002; *Sobolev*, 1974]. In a Cr# vs. Mg# diagram (Figure 4.20), the composition of Cr-spinel from the Gams sequence overlaps the compositions of spinel inclusions in Yakutian and South African diamonds [*Sobolev*, 1974; *Sobolev et al.*, 2004].

The Cr_2O_3 vs. MgO diagram in Figure 4.22 accentuates this similarity revealing a common "peridotite" trend with a strong correlation between Cr and Al typical of Cr-spinel in kimberlites [*Barnes, Roeder*, 2001; *Kamensky et al.*, 2002].

Judging from the data presented above, the detrital Cr-spinel could originate from metamorphic rocks of eclogite composition, which are widespread in Eastern Alps [*Sassi et al.*, 2004, and others]. Single spinel grains were recently found in eclogites from Pohorje [*Janak et al.*, 2006]. Diamonds were found in such

Table 4.9. Chemical microprobe analyses (wt.%) of Gams Ni spinels

Element	1	2	3	4	5	6	7	8	9	10
TiO_2	–	–	–	–	–	–	–	–	–	–
Al_2O_3	1.16	1.27	0.90	10.29	4.96	1.26	11.52	7.88	9.04	5.42
Cr_2O_3	12.35	9.72	10.11	9.59	9.89	10.03	9.38	12.80	12.31	14.59
FeO	67.71	65.93	81.83	72.69	64.76	65.31	55.33	55.50	54.02	67.16
MnO	0.67	0.52	0.73	–	0.66	0.67	–	–	0.65	0.77
MgO	11.65	14.63	1.83	3.98	12.89	14.69	15.15	15.89	16.16	4.15
NiO	2.82	3.02	2.73	2.14	2.98	3.10	6.60	6.14	5.96	7.92
ZnO	3.65	4.91	1.87	1.31	3.86	4.94	1.01	1.32	1.86	
Fe^{2+}/Fe^{3+}	0.23	0.14	0.53	0.60	0.21	0.13	0.19	0.15	0.14	0.56
$Fe^{3+}/Fe^{2+}+Fe^{3+}$	0.81	0.88	0.66	0.62	0.66	0.88	0.84	0.88	0.88	0.65
Mg/Mg+Al	0.93	0.94	0.72	0.33	0.77	0.94	0.62	0.73	0.69	0.49
Cr/Cr+Al	0.88	0.84	0.88	0.38	0.57	0.84	0.35	0.54	0.48	0.28
$Mg/Mg+Fe^{2+}$	0.62	0.77	0.10	0.21	0.66	0.77	0.75	0.80	0.82	0.23

Element	11	12	13	14	15	16	17	18	19
TiO_2	–	–	0.60						
Al_2O_3	6.95	6.48	7.85	8.91	6.87	8.20	6.27	6.58	6.04
Cr_2O_3	14.11	7.03	7.04	5.94	7.87	9.01	8.98	8.62	7.88
FeO	59.17	67.59	68.39	59.96	77.02	62.11	66.09	67.33	67.45
MnO	–	–	–	–	–	1.07	0.84	1.29	1.24
MgO	11.90	11.10	9.05	20.84	1.53	13.66	11.37	10.61	10.26
NiO	7.87	7.25	7.06	7.36	6.72	3.21	3.77	3.70	3.81
ZnO	–	0.55				2.16	2.68	1.88	2.47
Fe^{2+}/Fe^{3+}	0.29	0.28	0.38	0.02	0.62	0.20	0.26	0.28	0.28
$Fe^{3+}/Fe^{2+}+Fe^{3+}$	0.77	0.78	0.73	0.98	0.62	0.83	0.79	0.78	0.78
Mg/Mg+Al	0.68	0.68	0.59	0.75	0.22	0.68	0.70	0.67	0.68
Cr/Cr+Al	0.58	0.42	0.37	0.31	0.43	0.42	0.49	0.47	0.47
$Mg/Mg+Fe^{2+}$	0.62	0.56	0.46	0.97	0.08	0.68	0.60	0.56	0.55

Note: Analyses: 1–5 – lower part, 6–12 – middle part, 13–19 – upper part of the transitional layer. Fe_2O_3 calculated from stoichimetry.

rocks in many complexes throughout the world (in Kazakhstan, China, Norway, Greece, and Germany) [*Mposkos, Kostopoulos,* 2001; *Schulze et al.*, 1996; *Sobolev, Shatsky,* 1990; *Xu et al.*, 1992, and others].

Ni-bearing spinel was fist found in marine deposits at the K/T boundary in Furlo and Petriccio deposits in Italy and in Hole 577 in the Pacific Ocean [*Montanari et al.*, 1983; *Smit, Kyte,* 1984] and then elsewhere, in rocks of various ages, from Archean rocks to modern cosmic dust [*Ben Abdelkader et al.*, 1997; *Bohor et al.*, 1986; *Byerly, Lowe,* 1994; *Kyte, Bohor,* 1995; *Robin et al.*, 1991, 1992, and others]. To distinguish this spinel from

Table 4.10. Chemistry of Ni spinel (wt.%) from the different sections

Oxide	1	2	3	4	5	6	7	8	9	10	11
SiO_2	–	–	–	–	–	0.09	0.01	0.07	0.12	–	0.82
TiO_2	0.6	0.6	1.1	0.8	0.6	0.35	0.51	0.21	0.32	0.10	0.20
Al_2O_3	6.8	6.6	2.5	4.7	8.1	6.62	3.40	8.49	22.07	3.80	2.99
Cr_2O_3	14.2	15.5	1.9	11.5	24.7	11.16	0.65	1.03	0.20	4.70	1.61
FeO	65.9	65.5	83.9	71.4	54.2	64.64	78.28	69.10	53.97	78.90	86.85
MgO	7.6	6.4	5.7	6.7	7.7	12.52	1.15	17.96	21.02	8.60	5.34
MnO	0.7	1.0	1.3	0.8	0.7	0.27	9.94	0.40	0.58	0.10	0.17
CaO	–	–	–	–	–	0.10	0.32	0.50	0.50	–	0.03
NiO	4.2	4.4	3.6	4.1	4.0	3.67	5.50	2.29	1.41	3.80	1.64

Note: K/T boundary: 1–5 – Tunisia [*Robin et al.,* 1991]; 6 – Caravaca, Spain [*Bohor et al.,* 1986]; 7 – Furlo, Italy [*Bohor et al.,* 1986]; 8, 9 – Sites 596 and 577, Pacific [*Kyte and Bohor,* 1995]; 10 – fusion crust of Allende meteorite [*Robin et al.,* 1992]; 11 – cosmic dust [*Robin et al.,* 1991].

Table 4.11. Electron microprobe analyses (wt. %) of rutile

FeO	SiO_2	NiO	CaO	Al_2O_3	Cr_2O_3	TiO_2	Total	Layer
0.71	0.12	0.02	0.01	0.36	0.00	99.42	100.65	3
0.67	0.01	0.05	0.00	0.05	0.03	99.44	100.27	4
0.51	0.13	0.00	0.07	0.11	0.03	100.60	101.46	4
0.74	0.10	0.00	0.02	0.07	0.12	100.45	101.51	4
0.66	0.02	0.00	0.02	0.03	0.03	98.96	99.72	4
0.35	0.00	0.00	0.00	0.00	0.00	100.14	100.54	5
0.69	0.00	0.00	0.00	0.00	0.00	100.17	100.90	5
0.49	0.06	0.00	0.00	0.00	0.00	98.72	99.32	5
3.67	0.00	0.00	0.00	0.00	0.16	88.12	91.99	5
0.92	0.06	0.00	0.03	0.00	0.00	99.13	100.14	5

spinel from magmatic rocks, the former was soon referred to as cosmic spinel [*Robin et al.*, 1992]. The typical composition of this spinel from various deposits is reported in Table 4.10.

Since cosmic spinel was first found in rocks containing impact quartz and high Ir concentrations, the genesis of this mineral was thought to be related to the impact process [*Smit, Kyte,* 1984, and others]. However, findings of Ni spinel in rocks showing no traces of impact events, for example, in cosmic dust and micrometeorites, gave rise to an alternative view, whose proponents believed that the origin of Ni spinel was related to the ablation of a cosmic body when it had entered the atmosphere [*Robin et al.*, 1992; *Toppani, Libourel*, 2003].

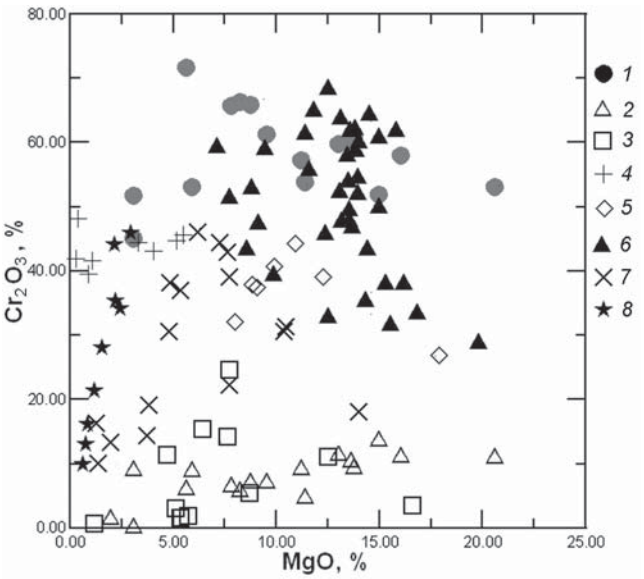

Figure 4.22. Cr_2O_3–MgO (wt. %) diagram for spinel from the Gams sequence in comparison with spinel from elsewhere. 1 – Cr-spinel from the Gams sequence, 2 – Ni spinel from the Gams sequence, 3 – Ni spinel from elsewhere (see Table 4.9), 4 – Ni spinel from the Barberton greenstone belt, 3.6 Ga, [*Byerly, Lowe,* 1994], 5 – Cr-spinel from Cretaceous flysch, Tibet [*Zhu et al.*, 2005], 6 – Cr-spinel from kimberlites [*Mitchel,* 1978; *Simandi et al.*, 2005], 7 – Cr-spinel from flood basalts [*Melluso et al.*, 1995], 8 – Cr-spinel from sulfides [*Zakrzewski*, 1989].

The Gams stratigraphic sequence is principally important in the context of the genesis of Ni spinel, because spinel from these rocks contains more than 2% NiO and was detected not only in the lower part (so called rust layer) but also in the upper and middle vertical portions of the layer.

The chemical composition of Ni spinel from the Gams sequence is close to the composition of this mineral from elsewhere (compare Table 4.9 and Table 4.10). The NiO concentration varies from 2% to 8%, FeO from 54% to 77%, Al_2O_3 from 1% to 10%, and Cr_2O_3 from 5% to 13%. Note that the mineral pervasively contains ZnO (up to 5%).

The Cr# vs. Mg# diagram in Figure 4.20 shows the overlap of the compositional fields of Ni spinel from the Gams sequence and other regions. Cosmic spinel differs from terrestrial spinel in having high concentrations of Ni and Fe^{2+} and displays significant compositional variations.

Another no less important identification feature is the significant difference between the $Fe^{3+}/(Fe^{2+} + Fe^{3+})$ ratios (which were calculated from stoichiometric considerations) of magmatic and cosmic spinel. This ratio is known to be utilized as an indicator of oxygen fugacity and is important for identifying the conditions under which the melt crystallized [*Toppani, Libourel*, 2003]. As follows from Table 4.9 and Table 4.10, these differences are very significant for spinel from the Gams sequence: the Ni spinel has high ratios (0.62–0.98), whereas this parameter of the Cr-spinel ranges from 0.06 and 0.48. These data are consistent with data on the composition of cosmic spinel from the fusion

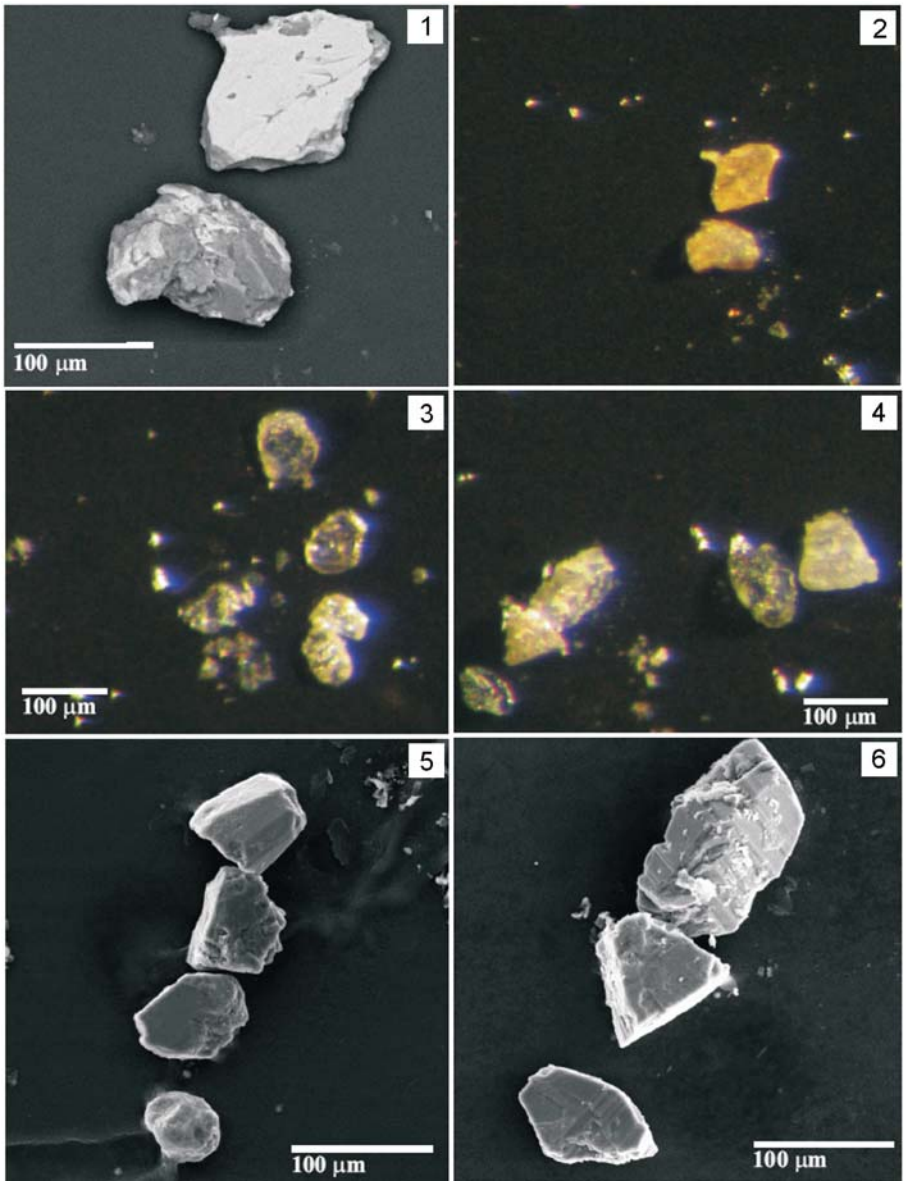

Figure 4.23. SEM images of brookite (1, 2) and anatase (3–6).

crusts of meteorites, in which the $Fe^{3+}/(Fe^{2+} + Fe^{3+})$ ratio varies from 0.75 to 0.90 [*Robin et al.*, 1992].

Rutile Group (brookite, anatase, rutile). These minerals have identical distribution from bottom to top of the transitional layer. We consider their origination as a result of erosion of agjacent metamorphic and igneous rocks during the deposition of layer *J* (Figure 4.23). These minerals have the same chemical composition and rutile analyses are shown in Table 4.11.

Corundum. This mineral has been observed in all parts of the transitional layer. It was absolutely unexpected when we found the strong difference in the chemistry of corundum from lower and upper portions of the transitional layer (Table 4.12).

Another important distinction is the existence of Fe spherule inside the corundum crystal at the bottom of layer *J* (Figure 4.24a,b). Its composition is the next (%): Fe 58.13, Mn 2.80, Ti 13.13, Si 25.48, P 0.36, Al 0.06 (Figure 4.24c). This grain has an orange luminescence under electronic beam.

In the upper portion of layer *J* corundum grains are characterized by angular shape (Figure 4.24d), a blue luminescence under electronic beam and their compo-

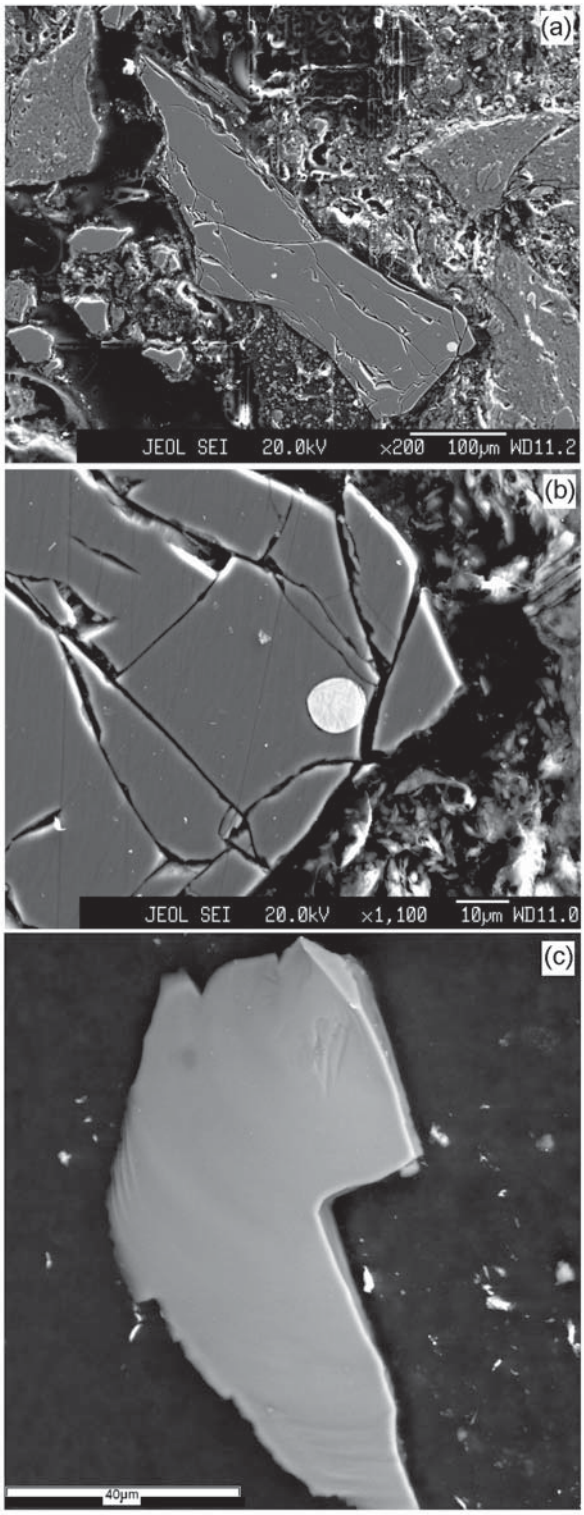

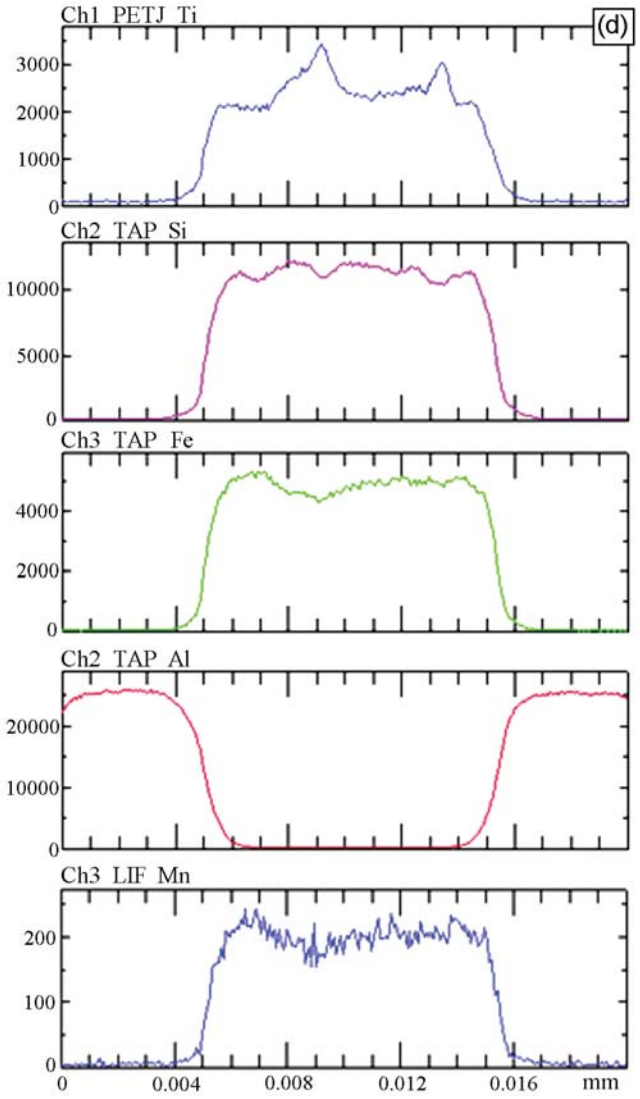

Figure 4.24. a, b – SEM images of corundum with Fe spherules; c – Detrital grain of corundum; d – Variations of elements in Fe spherules cross-section.

sition is similar to corundum from metamorphic rocks which are widespread in Eastern Alps [*Sassi et al.*, 2004, and others] and eclogites from Pohorje [*Janak et al.*, 2006].

Titanomagnetite, according to both MTA and microprobe data, is fixed ubiquitously in thin sections and in heavy and magnetic fractions. Its along-section distribution is irregular but its composition is very similar in the Gams-1 and -2 sections (see details in Chapter 5).

The average concentration TiO_2 = 15% is smaller than the typical averages of rift and spreading basalts (TiO_2 = 20–25%), whose grain composition is uniformly stable [*Pechersky, Didenko*, 1995].

Magnetite. The compositions of many magnetite grains from the Gams-1 boundary layer were measured with a microprobe (see details in Chapter 5). As distinct from titanomagnetites, they often include grains containing noticeable admixtures of Mg, Al, Mn, and

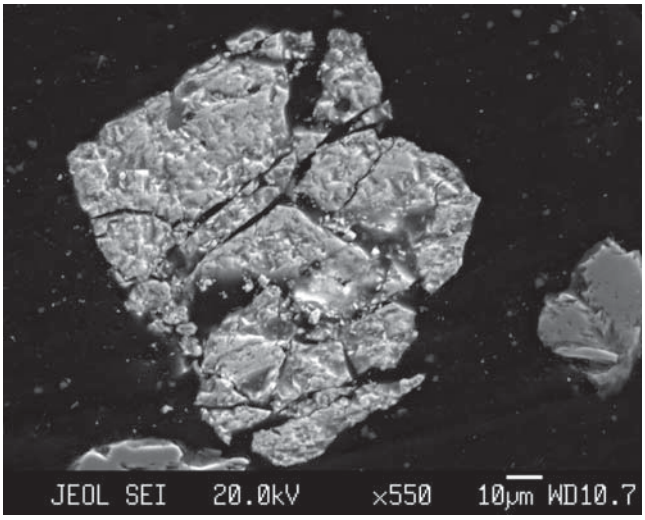

Figure 4.25. SEM image of witherite.

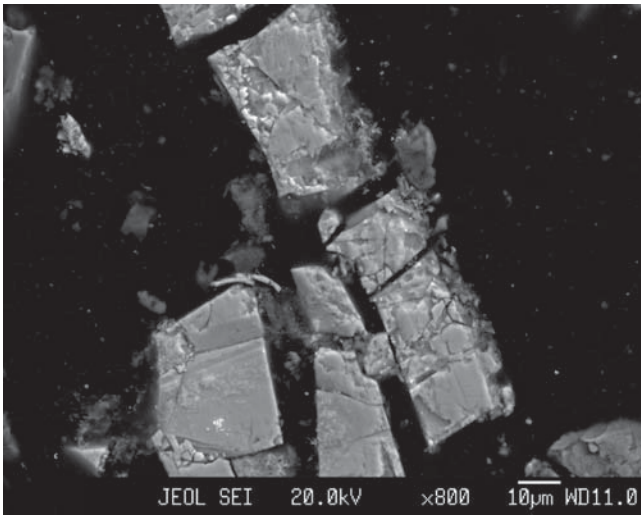

Figure 4.26. SEM image of barite.

Cr. Evidently, these are primary magmatic crystals. Beyond the transitional layer, the well-preserved single crystals of pure magnetite are observed in the Danian sediments. Magnetic fractions contain spherules of magnetite, hematite, and goethite that were likely formed due to oxidation of metallic iron spherules.

The main distinction of titanomagnetites of the Gams-1 and -2 boundary layers from titanomagnetites

Table 4.12. Electron microprobe analyses (wt. %) of corundum

Element	1	2	3	4	5	6	7	8	9	10
SiO_2	0.13	0.04	0.04	0.04	0.00	0.00	0.00	0.00	0.00	0.00
TiO_2	0.64	0.46	0.15	0.15	0.00	0.00	0.00	0.00	0.00	0.00
Al_2O_3	98.87	99.32	99.51	99.20	98.99	99.44	99.87	100.17	99.08	99.39
Cr_2O_3	0.00	0.00	0.00	0.00	0.03	0.00	0.00	0.02	0.00	0.00
Fe_2O_3	0.04	0.04	0.03	0.03	0.00	0.00	0.00	0.00	0.00	0.00
MnO	0.00	0.00	0.00	0.00	0.00	0.00	0.00	0.00	0.00	0.00
MgO	0.00	0.00	0.00	0.00	0.00	0.00	0.00	0.00	0.00	0.00
CaO	0.00	0.00	0.00	0.00	0.00	0.00	0.00	0.00	0.00	0.00
Na_2O	0.00	0.00	0.00	0.00	0.00	0.00	0.00	0.00	0.00	0.00
K_2O	0.00	0.00	0.00	0.00	0.00	0.00	0.00	0.00	0.00	0.00

Element	11	12	13	14	15	16	17	18	19	20
SiO_2	0.52	0.00	0.00	0.02	0.00	0.03	0.00	0.02	0.01	0.00
TiO_2	0.26	Traces	0.01	0.01	0.00	0.00	0.03	0.11	0.06	0.18
Al_2O_3	97.43	98.30	99.70	98.81	98.52	99.16	99.44	98.44	98.16	98.53
Cr_2O_3	0.00	1.79	0.06	1.41	0.00	0.00	1.09	1.34	1.67	0.02
Fe_2O_3	0.34	0.16	0.42	0.34	0.58	0.76	0.30	0.46	0.42	0.45
MnO	0.00	0.00	0.00	0.00	0.00	0.00	0.01	0.03	0.00	0.01
MgO	0.00	0.00	0.01	0.00	0.10	0.01	0.00	0.04	0.04	0.08
CaO	0.01	0.00	0.00	0.00	0.01	0.02	0.01	0.00	0.01	0.00
Na_2O	0.03	0.00	0.01	0.01	0.00	0.00	0.00	0.02	0.02	0.00
K_2O	0.00	0.00	0.00	0.00	0.00	0.01	0.03	0.02	0.02	0.00

Note: 1–4 – the upper part of transitional layer; 5–10 – the lower part of transitional layer (J_0); 11 – volcanic rocks, Tasmania [*Botrill,* 1998]; 12 – marble, Greece [*Liati*, 1988; 13, 14 – eclogite, India [*Shimpo et al.,* 2006]; 15 – corundum bearing xenolith, Australia [*Sutherland et al.,* 2003]; 16 – alluvial ruby, Australia [*Sutherland et al.*, 2003]; 17–19 – garnet peridotite from metamorphic rocks, China [*Zhang et al.*, 2004]; 20 – cordierite-plagioclase xenolith from Skaergaard Marginal Border group [*Markl,* 2005].

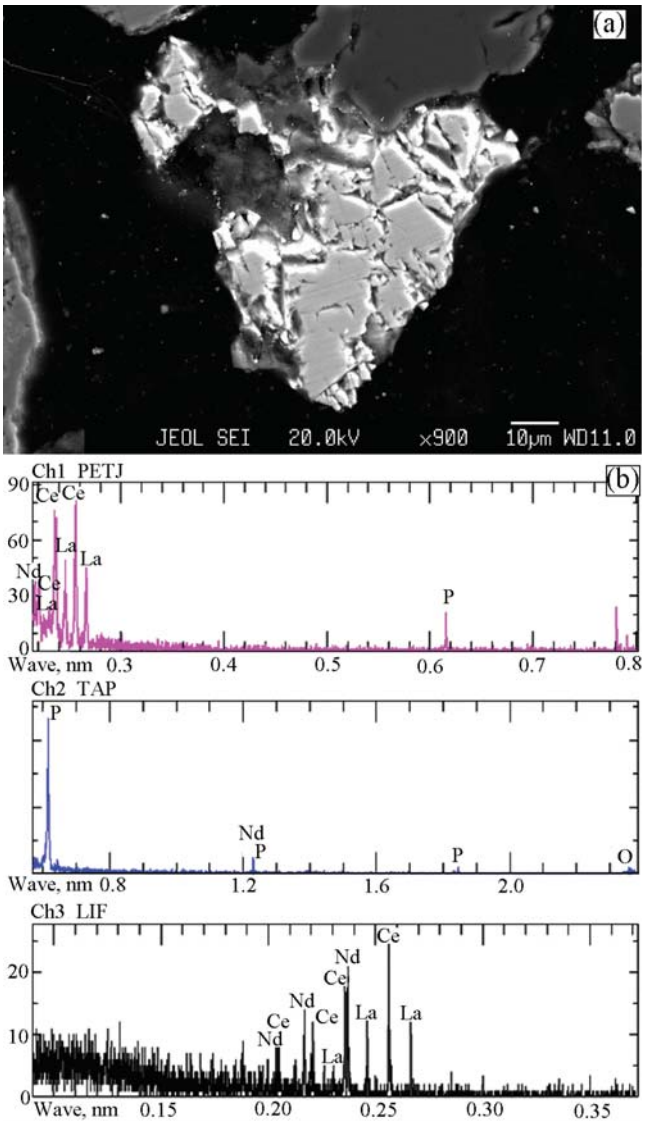

Figure 4.27. a – SEM image of monazite ; b – Bulk WDX spectrum of monazite.

crystallizing in basaltic melts of different types is an unusually small concentration of admixtures (See Table 5.5 and Table 5.6). Apparently, this specific pattern reflects the formation of titanomagnetite crystals from a volcanic aerosol. *Burov* [2005] notes an abrupt rise in the magnetization of sediments caused by their enrichment in ash material beginning from the Permian-Triassic boundary which reflects the global high volcanic activity at that time. It is very likely that a similar volcanic situation took place at the Mesozoic/Cenozoic boundary, producing a volcanic aerosol that contained titanomagnetite without admixtures.

Table 4.14. Electron microprobe analyses (wt. %) of monazite

Oxide	1	2	3	4	5	6
P_2O_5	36.25	44.32	38.13	38.96	39.23	34.50
La_2O_3	17.51	13.74	13.70	14.05	15.52	14.69
Ce_2O_3	33.42	30.88	31.25	32.79	31.78	35.00
Nd_2O_3	12.83	11.06	16.91	14.20	11.96	15.81

4.3.4 Carbonates

From this group we note only witherite (Figure 4.25). Taking into account its paragenesis with galena and sphalerite we suppose the synsedimentary origin of this mineral in an anoxic conditions.

4.3.5 Sulphates

Barite has a typical tabular habit (Figure 4.26). Its composition is characterized by presence of Sr (Table 4.13) and Sr isotope data are necessary for determination of barite origin (diagenetic or hydrothermal).

4.3.6 Phosphates

Monazite, xenotime and apatite were observed in different parts of layer *J* (Table 4.1). This mineral paragenesis is common for diverse crystalline rocks, especially of granites (Figure 4.27a,b, Figure 4.28, Figure 4.29, Table 4.14).

Table 4.13. Microprobe analyses of barite (wt. %) from the lower part of the transitional layer

Oxide	1	2	3	4	5	6	7	8	9
BaO	61.96	63.67	62.39	63.62	63.75	63.08	62.42	61.04	62.76
SrO	2.45	1.92	2.37	2.07	1.93	2.53	2.41	2.83	2.06
CaO	0.33	0.29	0.29	0.28	0.35	0.30	0.34	0.34	0.28
SO_3	36.75	33.89	34.26	32.81	35.06	34.37	34.90	35.58	34.63
MgO	0.00	0.00	0.00	0.00	0.00	0.00	0.07	0.07	0.00
Total	101.49	99.77	99.31	98.78	101.09	100.28	100.17	99.86	99.73

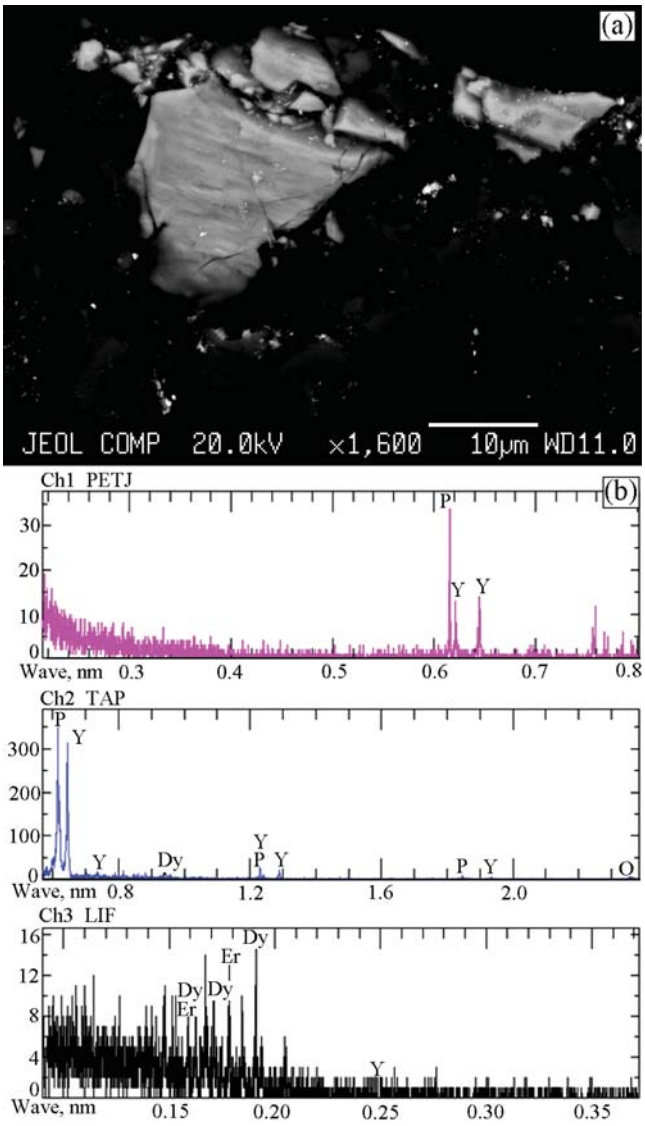

Figure 4.28. a – BSE image of xenotime ; b – Bulk WDX spectrum of xenotime.

4.3.7 Silicates

This class compiles the numerous paragenesis of minerals (Table 4.1). They consist mainly of ultra-stable zircon (Figure 4.30), tourmaline (Figure 4.31), garnet (Figure 4.32), pyroxene (Figure 4.33), olivine, epidote (Figure 4.34), kyanite (Figure 4.35), amphibole (Figure 4.36), muscovite and sphene (Figure 4.37). The chemical composition of the studied silicate minerals is presented in Table 4.15, Table 4.16, Table 4.17, Table 4.18, Table 4.19, and Table 4.20.

These minerals were derived as a result of erosion from igneous and metamorphic rocks, that are widely spread in Eastern Alps.

The presence of strongly rounded zircon grains suggests that they could derive from a source areas located at a great distance from Gams sedimentary basin (Figure 4.30). Garnet grains are partly rounded (Figure 4.32). The rest silicate grains have no visible traces of abrasion and we can propose that their lifetime (time-span of transportation) was very short.

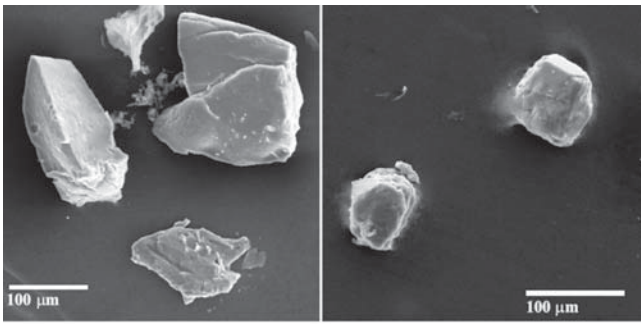

Figure 4.29. SEM image of apatite.

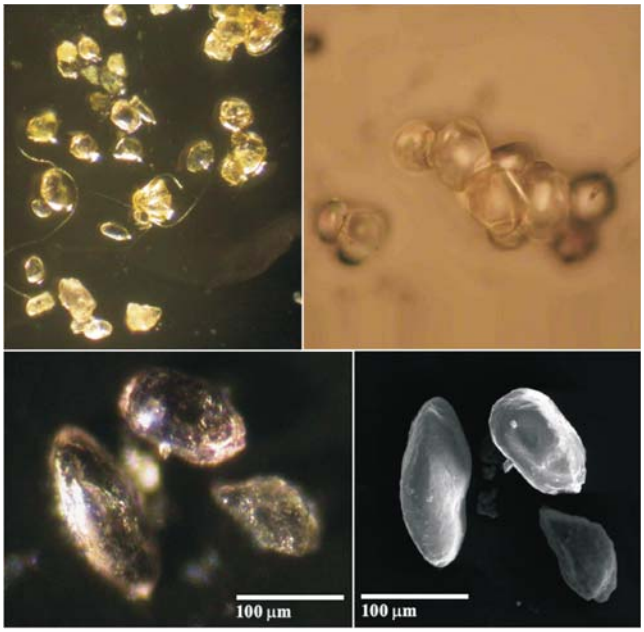

Figure 4.30. Different morphology of zircon grains.

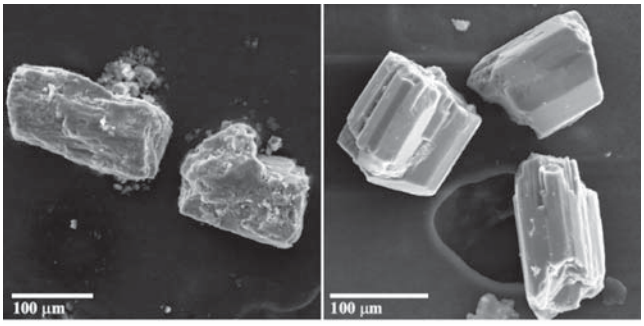

Figure 4.31. SEM image of tourmaline.

Clay minerals. The mineralogical analysis of samples of the fraction <4 μm was conducted by means of X-ray diffraction on a D/MAX-2200m diffractometer. The raw specters were then processed by the Jade-6.0 (MDI, United States) computer program. The quantitative proportions of clay minerals were calculated using the basal reflections in a saturated state, following the method described in [*Biskaye*, 1965]. The sums of clay minerals were normalized to 100%.

The identified clay minerals are smectite (Sm), illite (Il) of the muscovite series, and chlorite (Ch). The proportions of clay minerals are listed in Table 4.21. The absence of kaolinite or its insignificant contents (no more than 5%, which is close to the detection limit of the method) is an important indication of the paleogeographic environment in source area of the sediments.

As follows from Table 4.21, the upper part of the sequence (above layer K) is characterized by the occurrence of a relatively homogeneous assemblage of clay minerals, which is dominated by smectite (37–62%) and illite (29–45%). An analogous assemblage was also found below layer J. The situation with layer K is different: its illite fraction amounts to 70.5%, perhaps due to the intensification of erosion in the source area, because this mineral is usually formed during the erosion of crystalline rocks [*Deconinck et al.*, 2000].

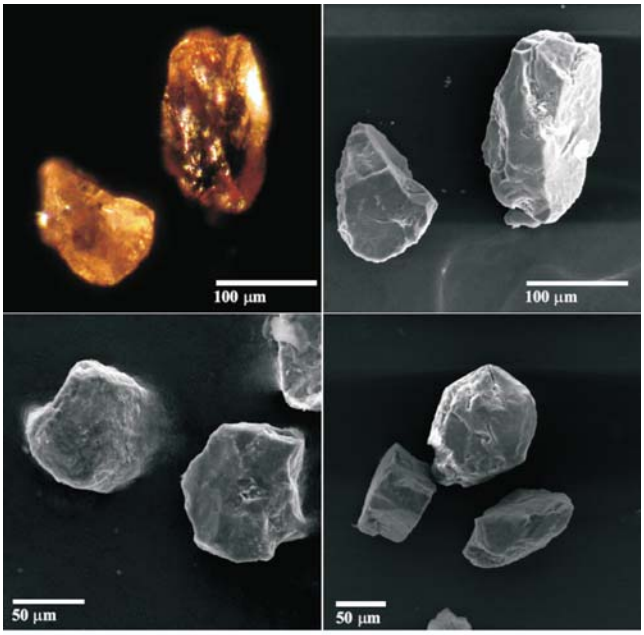

Figure 4.32. SEM images of garnets, slightly rounded.

Of particular interest is layer J, smectite and chlorite contents of which are equal, and clay mineral as-

Table 4.15. Electron microprobe analyses (wt. %) of garnets

Oxide	1	2	3	4	5	6	7	8	9	10	11	12
SiO_2	38.57	38.51	34.94	35.75	39.30	34.02	40.75	38.80	42.16	40.52	42.24	35.57
Al_2O_3	20.48	19.49	16.25	18.19	15.88	14.81	18.80	19.89	20.78	21.02	20.71	16.35
FeO	23.45	26.86	30.63	37.51	35.69	43.80	30.70	26.80	24.09	31.02	21.47	32.86
MnO	8.92	8.67	6.05	4.17	3.61	4.00	3.87	8.65	3.31	4.14	9.78	7.89
MgO	1.33	1.18	2.20	3.22	3.43	2.18	2.24	–	1.12	1.75	0.70	–
CaO	7.25	5.30	9.92	1.16	2.08	1.19	3.64	5.80	8.53	1.56	5.11	7.33
Alm	53.21	60.31	57.37	76.61	74.16	82.23	70.94	62.34	59.68	77.01	54.81	65.40
Sps	20.47	19.72	11.48	8.63	7.60	7.61	9.06	20.38	8.31	10.41	25.29	15.01
Grs	21.04	15.25	23.81	3.04	5.54	2.86	10.78	17.29	27.07	4.96	16.71	18.69
Prp	5.37	4.72	7.35	11.73	12.71	7.30	9.23	–	4.95	7.61	3.19	–

Oxide	13	14	15	16	17	18	19	20	21	22	23
SiO_2	36.82	36.67	36.54	36.52	36.82	36.44	39.44	37.65	37.39	38.04	37.52
TiO_2	0.23	0.19	0.20	0.29	0.34	0.35	0.07	0.20	0.18	0.15	0.18
Al_2O_3	20.71	20.25	20.80	20.40	20.65	20.38	18.80	19.89	20.78	21.14	21.28
Cr_2O_3	–	–	–	–	–	–	0.01	0.03	0.03	–	0.04
FeO	17.80	20.62	25.83	11.45	20.88	19.60	18.39	33.00	32.98	25.41	31.96
MnO	19.57	18.17	8.17	25.33	14.87	16.03	1.03	3.05	2.02	5.14	5.36
MgO	0.38	0.77	0.97	0.20	0.57	0.47	9.11	4.33	4.48	1.01	3.71
CaO	4.59	3.15	7.01	5.61	6.10	6.13	9.51	1.19	1.25	10.09	2.66
Alm	40.29	46.41	57.64	25.64	46.64	44.01	38.43	72.79	73.92	56.04	67.41
Sps	44.87	41.42	18.46	57.46	33.64	36.42	2.18	6.81	4.586	11.48	11.45
Grs	13.31	9.08	20.04	16.10	17.46	17.64	25.46	3.36	3.59	28.51	7.19
Prp	1.53	3.09	3.86	0.80	2.27	1.88	33.94	17.03	17.90	3.97	13.95

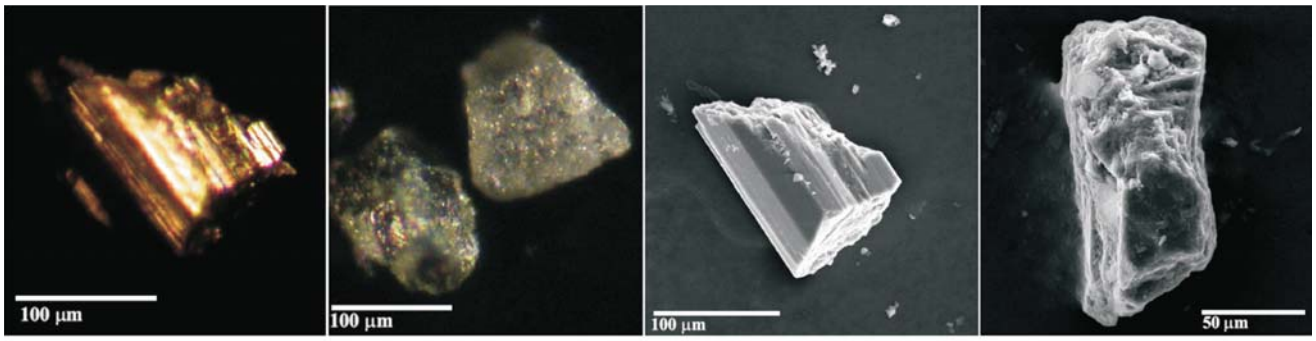

Figure 4.33. SEM images of pyroxenes.

semblage of it is smectite-chlorite-illite (Table 4.21, Figure 4.38). Smectite in sample J-6 has a composition different from those in other samples. The more detailed examination of the compositions within layer J (Table 4.22) has revealed that, having relatively high contents of clay minerals, this layer shows an increase in the ratio of clay to non-clay minerals from Ja to Jc. The illite content also simultaneously increases, whereas that of smectite decreases.

The changes in the spacings of smectites in the air-dry state suggest different occupancies of the crystallographic sheets: Na-Ca smectite (13.0 Å) is contained in unit a, Na-Ca smectite with Ca predominance (13.9 Å) occurs in unit b, and Ca-smectite (14.5 Å) is borne in c. These conclusions are of a preliminary character and require further X-ray diffraction studies.

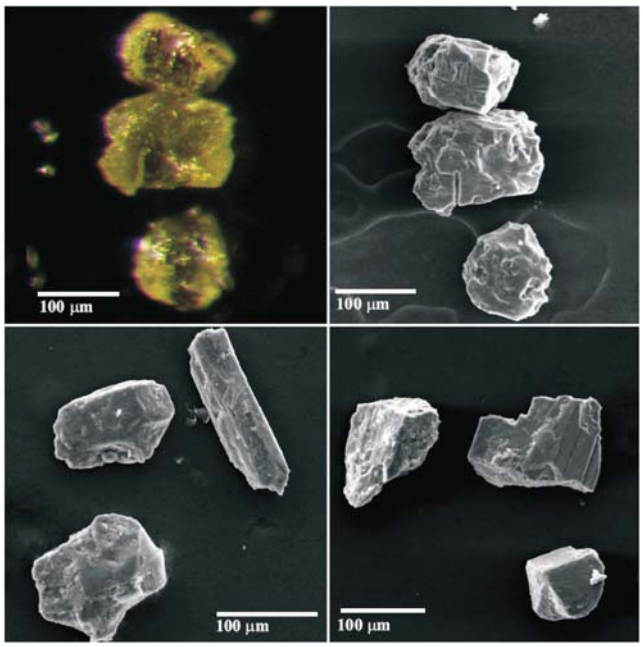

Figure 4.34. Different morphology of epidotes: top left – optical phtograph, the rest photographs are SEM images.

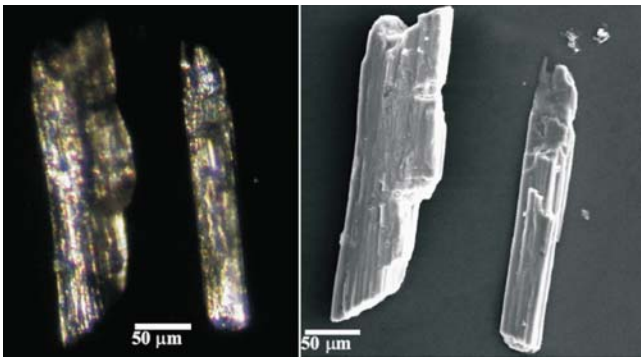

Figure 4.35. Optical (left) and SEM images of kyanites.

Nevertheless, it is important that the lower part of layer J (unit Ja) has a smectite content of >65%, and it systematically decreases upward, whereas the percentage of illite increases to 20% (Table 4.22). Taking into account that this layer appeared to contain titanomagnetite of composition corresponding to the composition of this mineral in basalts, it can be concluded that smectite was formed at the expense of volcanic material.

We have the additional evidence of volcanism influ-

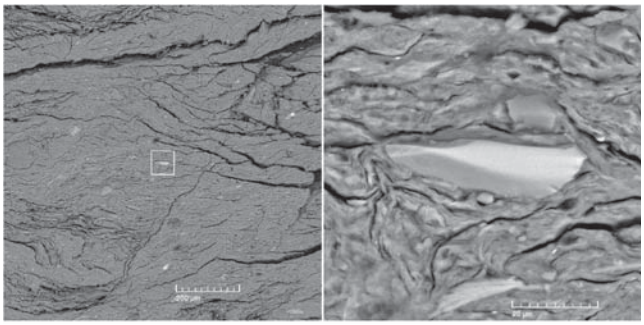

Figure 4.36. SEM image of amphibole grain (thin section).

Table 4.16. Representative microprobe analyses (wt. %) of olivines

Oxide	1	2	3	4	5	6	7	8	9
SiO_2	53.50	52.23	43.37	44.84	45.39	47.75	47.06	45.71	46.08
Al_2O_3	2.38	1.85	–	1.59	–	2.31	–	0.34	–
FeO	3.50	2.21	4.65	3.24	6.01	4.35	2.82	8.02	6.06
MgO	40.62	43.71	51.68	50.33	48.60	45.59	50.12	45.93	47.86
Fo	0.96	0.97	0.95	0.97	0.93	0.95	0.97	0.91	0.93
Fa	0.04	0.03	0.05	0.03	0.07	0.05	0.03	0.09	0.07

Table 4.17. Representative microprobe analyses (wt. %) of pyroxenes

Element	1	2	3	4	5	6	7	8
SiO_2	41.45	43.32	42.22	52.95	52.63	52.53	52.87	52.58
TiO_2	–	–	–	0.10	0.12	0.08	0.07	0.11
Al_2O_3	21.28	20.44	21.15	1.11	1.11	1.08	0.97	0.61
FeO	27.89	23.49	28.16	7.52	7.61	7.39	7.34	7.25
MnO	–	3.23	0.79	0.27	0.27	0.26	0.31	0.59
MgO	2.09	1.45	2.59	13.63	13.43	13.40	13.68	13.47
CaO	7.29	8.06	5.10	23.86	23.86	23.74	23.86	24.24
Na_2O	–	–	–	0.27	0.26	0.25	0.24	0.18
Wo	22.82	23.47	16.30	48.80	49.00	49.11	48.84	49.37
En	9.10	9.36	11.52	38.77	38.37	38.55	38.95	38.16
Fs	68.07	67.13	72.18	12.43	12.62	12.37	12.21	12.46

Table 4.18. Electron microprobe analyses (wt. %) of epidotes

SiO_2	MgO	FeO	CaO	Al_2O_3	Na_2O	MnO	Cr_2O_3	TiO_2	Total
37.40	0.04	11.41	23.18	23.90	0.00	0.19	0.10	0.04	96.26
37.19	0.03	10.88	22.58	23.94	0.00	0.15	0.02	0.03	94.82
37.99	0.01	11.12	23.00	24.15	0.00	0.26	0.02	0.05	96.60
37.50	0.03	9.01	22.91	25.55	0.00	0.17	0.00	0.15	95.32
37.77	0.04	10.82	22.84	24.40	0.00	0.19	0.00	0.09	96.15
38.25	0.02	12.29	23.01	23.04	0.01	0.23	0.13	0.06	97.04
38.29	0.00	11.34	23.90	23.69	0.02	0.07	0.10	0.09	97.50
37.47	0.02	12.73	23.07	22.32	0.01	0.25	0.02	0.03	95.92
37.34	0.00	13.78	23.37	21.77	0.00	0.16	0.06	0.09	96.57
37.49	0.02	11.68	23.03	23.14	0.03	0.29	0.05	0.18	95.91
37.58	0.02	11.79	23.02	23.20	0.01	0.35	0.05	0.15	96.17
37.83	0.04	11.95	23.42	23.11	0.01	0.16	0.03	0.04	96.59
37.73	0.05	12.41	22.94	22.82	0.01	0.29	0.04	0.16	96.45
37.53	0.05	12.16	23.28	22.49	0.00	0.17	0.04	0.09	95.81
37.40	0.00	12.33	23.26	22.51	0.01	0.28	0.03	0.12	95.94
37.19	0.00	12.31	23.07	22.20	0.00	0.24	0.04	0.14	95.19
38.05	0.01	7.61	23.90	26.49	0.00	0.11	0.04	0.20	96.41
37.37	0.04	12.20	23.37	22.73	0.00	0.04	0.05	0.12	95.92
37.21	0.03	12.37	23.51	22.65	0.01	0.07	0.15	0.08	96.09

Table 4.19. Electron microprobe analyses (wt. %) of amphibole

SiO_2	FeO	TiO_2	Al_2O_3	MnO	CaO	MgO	K_2O	Na_2O	Total
45.26	12.92	0.45	11.57	0.23	10.95	11.51	0.62	0.95	94.46
44.23	5.90	0.61	12.37	0.21	11.41	17.06	0.32	2.02	94.13
44.60	5.28	0.59	12.75	0.12	11.80	17.01	0.32	2.01	94.48
44.59	5.51	0.62	12.77	0.11	11.70	16.87	0.32	2.03	94.52
45.06	13.06	0.72	11.01	0.29	11.84	11.57	0.72	1.02	95.29
44.57	5.31	0.67	12.36	0.09	11.67	16.97	0.33	2.03	94.00
44.95	5.45	0.62	12.44	0.12	11.65	17.11	0.31	1.97	94.62
45.12	12.66	0.74	11.70	0.18	11.88	11.55	0.78	1.13	95.74
43.88	16.79	0.45	13.34	0.36	11.50	8.97	0.27	1.44	97.06
43.23	17.02	0.42	14.53	0.37	11.64	8.78	0.32	1.35	97.73

Table 4.20. Electron microprobe analyses (wt. %) of kyanite

SiO_2	FeO	CaO	Al_2O_3	Cr_2O_3	TiO_2	Total
36.73	0.15	0.00	62.15	0.05	0.05	99.14
36.84	0.17	0.00	61.99	0.05	0.01	99.06
36.96	0.09	0.02	62.32	0.01	0.00	99.40
37.20	0.11	0.00	62.57	0.04	0.00	99.92
36.77	0.12	0.00	62.02	0.03	0.02	98.96
37.10	0.77	0.00	62.47	0.00	0.08	100.42
37.00	0.77	0.03	61.97	0.00	0.03	99.80

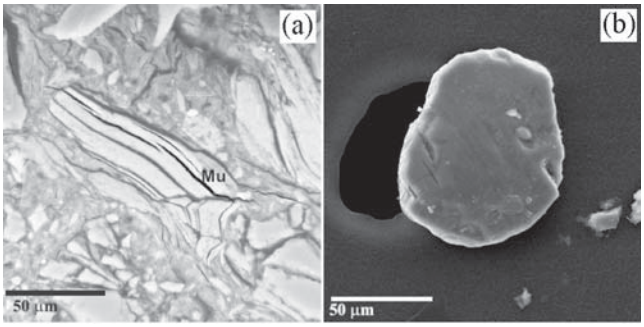

Figure 4.37. SEM images of muscovite grain (a) and sphene grain (b).

ence on sedimentation of the transitional layer. Under microprobe study we found the glauconite (Table 4.23) with inclusions of euhedral bravoite crystals in the lower part of layer *J* (Figure 4.39). Bravoite in the Gams section is characterized by high and changeable concentrations of Ni and Co (Table 4.24). Such chemical composition was determined by unstable circulations of hydrothermal fluids in the Gams basin. It means the synsedimentary origin of bravoite in an anoxic conditions.

In interpreting data on the composition of clay minerals from the Gams sequence, which corresponds to

Table 4.21. Clay minerals composition (%) of the Gams section samples

Distance from the K/T boundary, cm	Sample	Smectite (Sm)	Illite (IL)	Chlorite (Ch)	Mineral associations
20	T-4	53.7	39.3	7.0	illite-smectite
14	Q-3	53.0	37.9	9.1	illite-smectite
14	Q-2	47.7	44.2	8.0	illite-smectite
12	P-5/6	62.2	28.8	9.0	illite-smectite
10	O-4/5	36.8	44.7	18.5	illite-smectite
8	N-7/8	45.1	41.5	13.4	illite-smectite
6	M-4	48.1	40.0	12.0	illite-smectite
4	L-6	51.6	38.1	10.3	illite-smectite
2	K-4	11.9	70.5	17.6	Illite
0	J-6	24.3	49.7	26.0	smectite-chlorite-illite
−8	E-F4	69.8	25.2	13.4	illite-smectite

Table 4.22. Clay minerals composition (%) of the J layer

	Layer	Smectite (Sm)	Illite (IL)	Chlorite (Ch)
1	Ja	65.8	31.6	2.5
2	Jb	53.2	36.0	10.8
3	Jc	44.9	51.1	4.0

a very brief time span (of about of ten thousand years at conservative estimates of the sedimentation rate), it should be noted that these variations could hardly be caused by climatic changes.

As it was emphasized by *Thiry* [2000, p. 211), "...sequential changes in the sedimentary clay mineral assemblages with periods of less than 1 Ma cannot be caused by climatic changes. Records of short-term changes in palaeoclimates appear unrealistic; it is probable that only longer sequences are able to reflect palaeoclimatic changes".

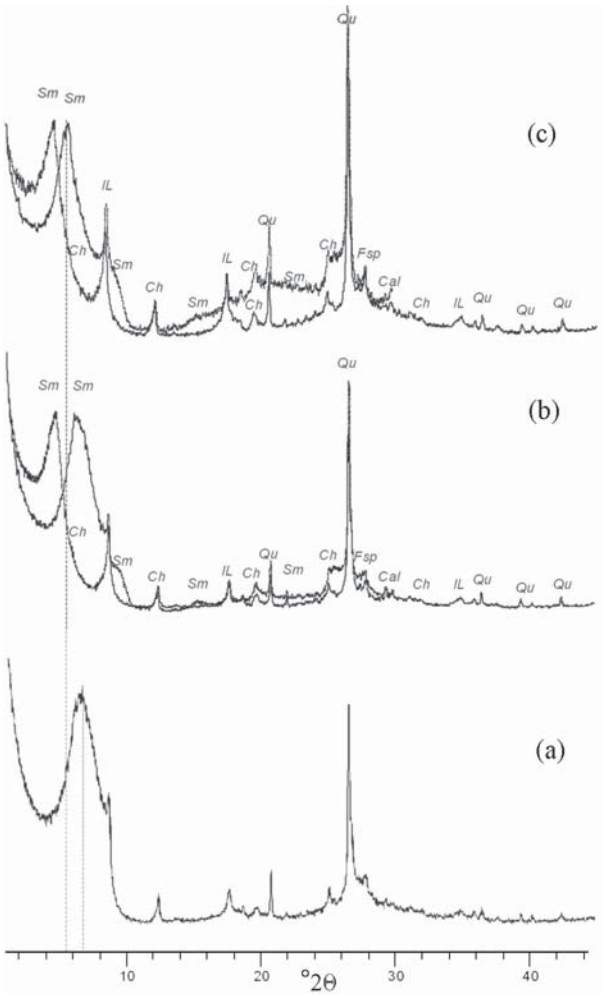

Figure 4.38. XRD patterns of clays from the transitional layer J: a – lower, b – middle, c – upper portions.

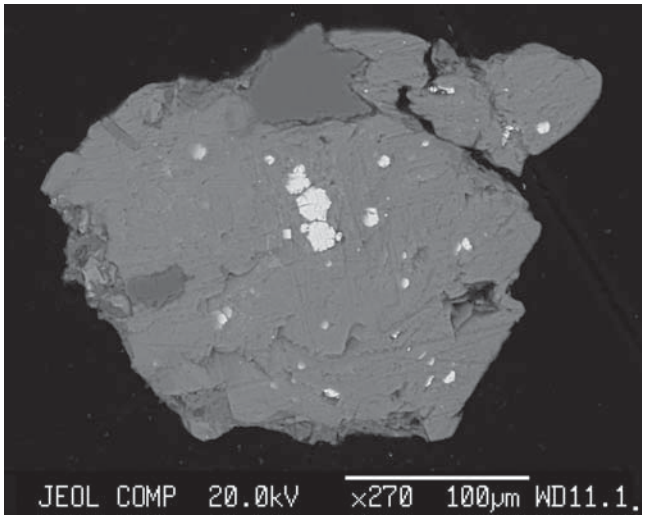

Figure 4.39. BSE image of glauconite with bravoite inclusions.

4.3.8 Vertical mineralogical zonation as an indicator of environments of the transitional layer formation

The study of the chemical composition of minerals from the Gams section revealed the existence of well developed zonation from the bottom to the top of the transitional layer. As follows from the Table 4.1, there are three groups of minerals each of which is only presented in the lower or upper portions of transitional layer. Another group of mineral can be traced through the whole layer *J* from the bottom to the top (Table 4.1). A priori it means the existence of significant difference in conditions of sedimentation.

Lower part of the transitional layer. The first 6–8 mm unit of the transitional layer in the Gams 1 and Gams 2 sections is characterized by significant enrichment of such native metals as copper, gold, silver, platinum and rhenium. The last two were first discovered during the Gams section investigations [*Grachev et al.*, 2008a, 2008b]. Beside it is necessary to mark the existence of metallic alloys: brass, osmiridium and gamsite (alloy of Ni, Cu and Zn).

Another important feature consists of existence of such minerals as arsenopyrite, pyrite, molybdenite, galena, pentlandite, sphalerite, witherite, barite. Such mineral paragenesis gives the direct evidence of anaerobic conditions of deposition. The needle-like shape of sphalerite and pentlandite and areal development of pentlandite crystals on the clay surface indicate the formation of these minerals in situ.

The best sign is the presence of native rhenium in the lower portion of the transitional layer. As we have recently noted [*Grachev et al.*, 2008a], the origin of native rhenium can be only explained in frame of hypothesis

Table 4.23. Representative microprobe analyses of glauconite (wt. %)

SiO_2	NiO	TiO_2	Al_2O_3	FeO	CaO	MgO	MnO	K_2O	Na_2O	BaO	SO_3	F	$-O_2$	Total
35.55	0.24	1.29	16.68	16.55	0.17	13.21	0.25	6.04	0.08	0.22	3.30	0.41	0.17	93.82
36.32	0.15	1.04	16.55	16.17	0.20	14.17	0.24	6.17	0.11	0.23	1.34	0.39	0.17	92.91
36.22	0.02	1.45	16.54	15.16	0.18	13.10	0.22	6.82	0.14	0.63	0.35	0.24	0.09	90.98
35.67	0.31	1.45	16.79	15.70	0.13	12.97	0.25	6.27	0.15	0.28	2.33	0.20	0.07	92.43
30.45	0.11	1.18	13.56	28.77	0.17	10.94	0.22	5.05	0.03	0.21	1.40	0.39	0.18	92.30
23.16	0.11	0.92	10.63	45.30	0.16	8.93	0.17	3.34	0.09	0.00	0.19	0.42	0.17	93.25

of mantle plumes volcanic aerosol.

At the same time in this part of layer *J* we have detected the Ni-spinel of drop-like shape and grains of pure Ni.

The middle part of the transitional layer. In this part of layer *J* we observe the total disappearance of native elements and sulfides (exluding pyrrotine) and metallic alloys. Other minerals (silicates), Cr and Ni, spinels, diamonds and some magnetic minerals are present here (Table 4.1).

The upper part of the transitional layer. Unique mineral paragenesis was found in the upper five millimeters of the layer *J*. It comprises moissanite, paragenesis of diamonds and nickel spherules (first occurrences at the K/T boundary) and pure native nickel as grains of different size and morphology [*Grachev et al.*, 2008c].

Table 4.24. Representative microprobe analyses (wt. %) of bravoite inclusions in glauconite from the base of the transitional layer

Cu	S	Ni	Co	Fe	Total
0.10	51.57	12.08	15.41	19.44	98.60
0.03	52.54	20.25	14.24	13.03	100.09
0.11	52.63	17.32	15.17	14.33	99.56
0.26	53.11	15.21	10.33	20.40	99.31
0.06	52.62	14.57	11.26	21.21	99.72
0.05	52.02	15.40	16.44	15.07	98.98
0.06	52.35	17.14	18.12	12.41	100.08
0.29	51.79	11.59	12.95	21.50	98.12
0.10	53.77	13.43	6.84	26.67	100.81
Formula coefficients					
0.002	1.989	0.255	0.323	0.431	
0.001	1.999	0.421	0.295	0.285	
0.002	2.008	0.361	0.315	0.314	
0.005	2.020	0.316	0.214	0.445	
0.001	2.000	0.303	0.233	0.463	
0.001	1.999	0.323	0.344	0.332	
0.001	1.995	0.357	0.376	0.272	
0.006	2.001	0.245	0.272	0.477	
0.002	2.011	0.274	0.139	0.573	

Pure Ni in the form of spherules with a highly crystalline surface has never been found in magmatic rocks or meteorites, whose Ni always contains significant admixtures of other elements. The characteristic structure of the surface of the Ni spherules could be produced during the fall of a meteorite, which resulted in its ablation. The same mechanism could explain the Ni spinel generation [*Grachev et al.*, 2008b].

4.4 Conclusion

The study of minerals in the transitional layer at the K/T boundary in Gams has revealed and provided for a new approach to understanding the events at the time of this layer deposition. Our data obtained indicate that there are two distinct populations of minerals in the transitional layer and therefore two different stages in deposition history.

The first one includes the sedimentation in anaerobic conditions as the result of volcanic aerosol spreading due to the volcanic activity related to the mantle plume (existence of native platinum, rhenium, sulfides, barite and titanomagnetite). The chemistry of latter mineral is similar to titamagnetites from rift and mantle plumes volcanic rocks.

The environments of sedimentation have been drastically changed during the upper portion of layer *J* deposition. The paragenesis of hexagonal polymorph of diamond (lonsdaleite) with pure nickel spherules first discovered proves an asteroid (meteorite) fall which resulted in the release of energy sufficient not only for the melting of the projectile (asteroid) itself but also for its evaporation.

A principally important problem is the genesis of the Ni spinel, which is not directly related to any impact event (see above and *Grachev et al.* [2007a]). The findings of Ni spinel in hydrothermal systems and in spherules from the Paleocene flood basalts in Western Greenland [*Robin et al.*, 1996; *Rychagov et al.*, 1997] give the evidence the possibility of another mode of formation. The origin of Ni spinels from the transitional layer at the K/T boundary remains open and requires further research.

Chapter 5. Magnetic Properties of Rocks of the Gams Section

5.1 Introduction

According to many data, the Mesozoic-Cenozoic boundary in oceanic and marine deposits is fixed by a higher magnetic susceptibility. Examination of continuous oceanic sedimentary sections including the K/T boundary [*Pechersky, Garbuzenko,* 2005] showed that this boundary often (in ∼30% of cores analyzed) coincides with a peak of the magnetic susceptibility χ. High values of the χ-peak are often confined to surface features of active plumes (traps, flood basalts, etc.). The process of accumulation of magnetic material in sediments is extended in time, ranging from a few tens of thousands to a hundred thousands of years. Researchers usually relate a rise in susceptibility to in influx of terrigenous material into sediments; i.e., it would be oceanic sediments near continents. However, the χ-peak is often absent altogether in oceanic sedimentary cores closest to continents.

Until recently, the behavior of magnetic susceptibility has been studied mainly in sediments at the K/T boundary [*Ellwood et al.,* 2003; *Yampolskaya et al.,* 2004; and others]. The application of rock magnetism as a tool in K/T boundary studies was first performed by *Worm, Banerjee* [1987] in their study of the Petriccio section (Italy) and five DSDP sections in western Pacific and Indian oceans. In Petriccio, these authors measured several magnetic parameters both on bulk sample and on a set of microspherules magnetically extracted from the K/T boundary clay. The magnetic signal of this layer was found to be concentrated in the microspherules, and hysteresis, thermomagnetic, and saturation remanent magnetization results were interpreted as proof of a close-to magnetite composition of the skeletal ferrites contained in the microspherules. *Cisowski* [1988] studied highly magnetic microspherules from the Petriccio K/T boundary section and in bulk samples from marine (Petriccio and Gubbio, Italy) and continental K/T boundary sections (Starkville, Brownie Butte, and Glendive, USA). As a result of investigations the author concluded that the magnetic properties of the spherules were consistent with skeletal magnesioferrites with varying degrees of cation substitution. *Morden* [1993] conducted rock magnetic experiments in the K/T boundary Fish Clay (Denmark), in bulk sample and in a magnetic extraction. The thermomagnetic curves of the magnetic extraction showed the presence of iron particles with low Ni-content. *Griscom et al.* [1999] reported anomalous increases of ferromagnetic resonance intensity (FMR) just at the K/T boundary layer in Caravaca and Sopelana (Spain) and Gubbio (Italy) sections, indicating the presence of spherical fine-grained magnetite particles, also the presence of goethite in Gubbio K/T boundary layer. *Brooks et al.* [1985] used X-ray diffraction and Mössbauer spectroscopy to analyze bulk sample and iron oxide spheroids from the basal K/T boundary layer at Woodside Creek (New Zealand). They identified microcrystalline goethite (10–20 nm) in the matrix and crystalline goethite (>200 nm) and some hematite in the spheroids.

Wdowiak et al. [2001] and *Bhandari et al.* [2002] used Mössbauer spectroscopy and X-ray diffraction in several K/T boundary sections. Magnetic phase was a superparamagnetic goethite and hematite with various particle sizes, depending on the geographic location. These authors supposed a meteoritic origin of these phases condensed from the impact vapor cloud, deposited glomicrospherulesy and subsequently weathered to oxides/oxyhydroxides. *Villasante-Marcos et al.* [2007] investigated rock magnetic properties across several K/T boundary sections, that vary in distance to the Chicxulub impact structure from distal (Agost and Caravaca, Spain), to proximal (El Mimbral and La Lajilla, Mexico). A clear magnetic signature is associated with the firemicrospherules layer in the most distal sections, consisting of a sharp increase in susceptibility and satu-

ration remanent magnetization and a decrease in remanence coercivity. Magnetic properties in these sections point to a ferrimagnetic phase, probably corresponding to the Mg- and Ni-rich, highly oxidized spinels of meteoritic origin. At closer and proximal sections there is an increase in susceptibility and SIRM associated with a rusty layer and with a similar limonitic layer on top of the spherule bed, the magnetic properties indicate a mixture of iron oxyhydroxides dominated by fine-grained goethite. Magnetic, geochemical, and iridium data reject it as a primary meteoritic phase. Based on previous geochemical studies this goethite-rich layer can be interpreted as an effect of diagenetic remobilization and precipitation of Fe.

We can see fragmentary and sometimes contradictory results and their interpretation. We hope, that our detailed study of magnetolithology and magnetomineralogy of epicontinental deposits at the K/T boundary in the sections Koshak (Mangyshlak) [*Pechersky et al.,* 2006b], Gams (Austria) [*Grachev et al.,* 2005; *Pechersky et al.,* 2006a], Teplovka and Klyuchi (the Volga region) [*Molostovsky et al.,* 2006] and Tetritskaro (Georgia) [*Adamia et al.,* 1993; *Pechersky et al.,* 2009] help to clear up the origin of high magnetization of the boundary layer. Results are generalized [*Pechersky,* 2007]. The present section of the monograph is devoted to results of detailed petromagnetic and microprobe studies of the sections Gams-1 and Gams-2.

5.2 Methods of Petromagnetic Studies

Petromagnetic studies included measurements of specific magnetic susceptibility χ, hysteresis characteristics, and A_χ and A_{rs} anisotropies. Results of these measurements are presented in Table 5.1. The susceptibility was measured on the device KLY-2, the remanent magnetization was measured with the magnetometer JR-4, and hysteresis characteristics of samples were analyzed with the help of a coercivity spectrometer [*Burov et al.,* 1986; *Yasonov et al.,* 1998] measuring isothermal magnetization curves in an automated mode. Using the magnetization curves, the following characteristics were determined: specific saturation remanent magnetization M_{rs}, specific saturation magnetization without the paramagnetic+diamagnetic component M_s, remanent coercivity H_{cr}, and coercivity without the paramagnetic+diamagnetic component H_c. The ratios of hysteresis parameters H_{cr}/H_c and M_{rs}/M_s provide constraints on the domain state, i.e., the sizes of magnetic grains [*Day et al.,* 1977]. Measurements on the coercivity spectrometer are used to obtain curves of isothermal magnetization of superparamagnetic particles. After the magnetization field reaches its maximum value, the remanence, measured at the decay stage of the magnetization field, should remain constant in the absence of superparamagnetic and magnetically viscous (fine) particles. In practice, studies of natural samples reveal a decrease in M_r that is caused by the presence of superparamagnetic particles.

The ensemble of magnetic minerals present in samples is analyzed using coercivity spectra of the isothermal remanent magnetization [*Egli,* 2003; *Robertson, France,* 1994; *Sholpo,* 1977].

Thermomagnetic analysis (TMA) of samples was conducted with the help of express Curie balance [*Burov et al.,* 1986] by measuring the temperature dependence of inductive magnetization at a heating rate of 100°C/min. With such a high heating rate attained due to the high sensitivity of the balance, very small samples no more than 10 mm^3 in volume and 0.2 g in mass can be used. The temperature difference across such a small sample does not exceed 10°C. The TMA was conducted in a constant magnetic field of 200 or 500 mT, while the saturation field in some samples is higher; therefore, an inductive magnetization $M_{\rm i}(T)$ was actually measured. The value $M_{\rm i}$ in such magnetic species as magnetite, titanomagnetite, hemoilmenite, and metallic iron is the sum of the saturation magnetization $M_{\rm s}$ and paramagnetic ($M_{\rm p}$) and diamagnetic ($M_{\rm d}$) magnetizations, whereas a high magnetic field of saturation is probably characteristic of some grains of hemoilmenite and ferromagnetic iron hydroxides. Curves of the first and second heating to 800°C were obtained for all samples.

The concentrations of magnetite, titanomagnetite, metallic iron, hemoilmenite, and goethite in samples was estimated by determining, from the curve $M_i(T)$, the contribution to M_i of a given magnetic mineral and dividing this value by the specific saturation magnetization of this mineral. According to [*Nagata,* 1961], we accepted the following values of M_s: ~90 Am^2/kg for magnetite and titanomagnetite, ~200 Am^2/kg for iron, 4 and 10 Am^2/kg for hemoilmenite with $T_C > 300°$ C and 250–260°C, respectively. For goethite, we used data of *Bagin et al.* [1988] implying that the specific saturation magnetization in samples of this mineral varies, depending on their aggregate state, from 0.02 to 0.6 Am^2/kg, which is close to the value of paramagnetic magnetization in iron-bearing paramagnetic minerals. The average value M_s = 0.25 Am^2/kg was accepted for our calculations. Judging from the relationship between saturation magnetization of all magnetic minerals in the sediments studied and their paramagnetic magnetization (Table 5.1), the concentration of magnetic minerals should be five to ten times lower than the total concentration of iron (in the form Fe_2O_3) in rocks estimated according to data of chemical analysis. Inspection of thin sections and magnetic fraction

Table 5.1. Magnetic properties of rocks from the Gams-1 section

Sample no.	d, cm	χ	A_χ	M_{rs}	A_{rs}	E_{rs}	M_s	M_p	M_d	H_{cr}	H_c	H_{cr}/H_c	M_{rs}/M_s	fabric χ	fabric M_{rs}
t27	93	10.9		0.44			1.89	34.3	–1.2	122	22.5	5.41	0.23		
t26	87	9.15		0.9			3.7	34.6	–3.6	109	25.1	4.33	0.24		
t25	82	12		1.33			4.63	31.1	–2.7	114	26.3	4.32	0.29		
t24	77	8.62		0.82			3.24	29.9	–2.1	112	25.9	4.34	0.25		
t23	72	11.7		0.96			3.74	34.3	–3	108	25.6	4.2	0.26		
t22	67	10.8		0.76			3.58	32.2	–2.1	107	23.8	4.48	0.21		
t21	62	11.1		0.86			4.89	28	-0.4	101	20	5.03	0.18		
t20	57	7.25		0.29			1.36	14.8	2.9	93	22.5	4.14	0.21		
t19	52	5.29		0.61			1.74	24.3	–2.5	97	25.3	3.84	0.35		
t18	47	10.8		0.59			1.95	33.3	–2.4	100	22.6	4.41	0.30		
t17	42	10.5		0.62			2.88	34	–2.7	103	22.7	4.53	0.22		
t16	37	12.4													
t16	37	3.22													
t15	32	10.8		0.82			3.28	32.9	–2.4	102	23.3	4.38	0.25		
t14	27	9.71		0.58			3.17	29.4	–2	102	18	5.65	0.18		
$W9_1$	26	13.4	1.14	1.24	1.31	1.24									
$W9_2$	26	16.5		1.23	1.34	1.32	2.05							I	I
$V9_1$	24	12.5	1.08	1.14	1.32	1.31									I
$V9_2$	24	14.4		1.11	1.24	1.16	1.79							I	I
t13	23	11.6		1.01			5.63	32.4	–2.3	101	19	5.33	0.18		I
$U3_1$	22	11	1.21	0.85	1.36	1.23									
$U3_2$	22	11.1	1.12	0.78	1.31	1.17	3.72	35.2	–8.3	102	19.7	5.18	0.21	N	N
$U3_3$	22	9.89		0.75	1.28	1.15								N	N
$T3_1$	20	3.49		0.28	1.13	1.05	0.45								N
$T3_2$	20	3.78		0.41	1.13	1.11								?	N
$T3_3$	20	3.64		0.22	1.1	1.07	0.5	16.2	–6.5	93	35.1	2.66	0.44	?	N
t12	19	3.69												?	N
$S7_1$	18	3.99		0.42	1.31	1.24									
$S7_2$	18	4.15		0.46	1.17	1.17								?	N
t11	17	13.3		0.72			3.69	40.2	–3	101	19.2	5.25	0.19	?	N
$R2_1$	16	11.7		0.4	1.19	1.12	2.06	42.5	–7.4	104	17	6.13	0.19		
$R2_2$	16	11.9	1.08	0.49	1.16	1.11									N
$R2_3$	16	11.5	1.02	0.44	1.22	1.11	1.9								N
t10	15	12		0.69			3.3	38.3	–3	96	15.4	6.23	0.21	I	
t9	14	14.6		0.98			4.65	41.8	–3.4	101	18	5.59	0.21		
$Q1_1$	14	10.9	1.06	0.39	1.2	1.2									
$Q1_2$	14	11.6	1	0.46	1.16	1.16								I	I
t8	13	15.7		1.11			5.4	44.8	-4.4	103	19.2	5.37	0.21		I
$P1_1$	12	12.4	1.02	0.38	1.01	1.01	2.14	43	–8.1	106	15	7.1	0.18		
$P1_2$	12	12.3		0.49	1.06	1.06								N	N
t7	11	4.07		0.35			1.05	12.5	–1.6	82	26.2	3.15	0.34		I
$O1_1$	10	12.7		0.38	1.15	1.13	2.1	43.3	–7.1	113	17.5	6.48	0.18		
$O1_2$	10	12.6		0.54	1.16	1.12									I
$O1_3$	10	12.1	1.03	0.51	1.15	1.09	1.69								I
t6	9	12.1		0.43			3.21	37.2	–2.5	94	13.3	7.04	0.13	N	N
t5	8.5	12.8		0.48			4.18	39	–2.8	84	11.2	7.52	0.11		
$N1_1$	8	12.3		0.72	1.07	1.06									
$N1_2$	8	12.3	1.05	0.63	1.17	1.03								I	I
$N1_3$	8	12.1	1.1	0.59	1.16	1.12	2.25	44.4	–8.6	118	23	5.11	0.26	I	I

Table 5.1. Continued

Sample no.	d, cm	χ	A_χ	M_{rs}	A_{rs}	E_{rs}	M_s	M_p	M_d	H_{cr}	H_c	H_{cr}/H_c	M_{rs}/M_s	fabric χ	fabric M_{rs}
t4	7	11.9		0.52			2.15	39.7	–3.1	108	16.7	6.48	0.24	I	I
$M1_1$	6	12.1	1.03	0.50	1.19	1.19									
$M1_2$	6	11.9		0.74	1.15	0.9	1.62							I	I
M61	6	12.4	1	0.75	1.02	0.99								I	I
t3	5	10.7		0.41			2.55	35.1	–2.6	103	16.9	6.09	0.16		N
$L1_1$	4	10.3		0.72	1.16	1.04	3.09	35.5	–6.5	113	19.2	5.88	0.23		
L21	4	11.2	1.07	0.69	1.17	1.07	2.56	39.3	–7.5	129	27.3	4.71	0.27		N
$L8_1$	4	13.4	1.02	0.7	1.2	1.19								I	I
$L8_2$	4	13.2		0.62	1.21	1.08									N
T2	3	11.9		0.56			2.83	37.9	–3.1	117	19.1	6.15	0.2		N
$K2_1$	2	4.31		0.3	1.08	1.08									
$K2_2$	2	4.02	1.09	0.35	1.01	1.01	0.53							?	N
$K2_3$	2	4.37		0.41	1.05	1.03								?	N
$K2_4$	2	5.3		0.48	1.09	0.93	1.29	18.7	–5.2	91	35.3	2.58	0.37	?	N
t1	1	6.33		0.39			1.54	21.2	–2.2	96	21.5	4.47	0.25	?	N
Jtop	0	11		0.34		1.29	3.29	40	–2	68	9.2	7.38	0.10		
$J7_1$	0	15.4	1.03	0.41	1.02	0.98									
$J7_2$	0	15.7		0.42	1.14	1.09	2.1								N
$J3_1$	0	15.5	1.04	0.68			1.65	51.1	–8.5	67	10.9	6.22	0.23		N
$J3_2$	0	16		0.32	1.31	1.29	1.6								
$J4_1$	0	15.6		0.39	1.31	1.3	1.56	50.9	–6.4	66	13.1	5.06	0.25		N
$J4_2$	0	15.6		0.30	1.31	1.27	2.01	47.2	–5.2	51	9.4	5.37	0.15		N
$J5_1$	0	15.1	1.04	0.41	1.29	1.19									N
$J5_2$	0	15.5		0.42	1.28	1.24									N
$I4_1$	–2	6.65	1.04	0.23	1.16	1.13	0.78								N
$I4_2$	–2	5.68	1.01	0.19	1.12	1.07								I	I
$I4_3$	–2	5.58													I
$H4_1$	–4	5.78		0.22	1.06	1									
$H4_2$	–4	5.05		0.08	1.09		0.36	21.1	–6.5	76	16.4	4.66	0.22		N
$H6_1$	–4	4.98		0.09	1.20	0.96									N
H6-2	–4	5.14	1.02	0.1	1.19	0.99									N
$H6_3$	–4	5.12		0.09	1.07	0.98								N	N
k1	–5	4.85		0.16			1.13	17.2	–1.8	88	13.7	6.4	0.14		N
$G3_1$	–6	5.05		0.09	1.24	0.84									
$G3_2$	–6	4.87		0.09	1.15	1.01									N
$G3_3$	–6	4.9		0.08	1.18	1	0.72								N
$G6_1$	–6	5.19	1.01	0.10	1.20	1.06									N
$G6_2$	–6	5.1		0.09	1.22	1.04									N
$G6_3$	–6	4.97		0.08	1.18	1.08	0.55	20.7	–5.7	98	13.3	7.32	0.14		N
$F6_1$	–8	4.74		0.09	1.22	1.04									N
$F6_2$	–8	4.68		0.09	1.24	1.04	0.66								N
$F6_3$	–8	4.7	1.03	0.09	1.20	1.02									N
$E6_1$	–10	4.64		0.07	1.22	1.03	0.68	19.1	–5.5	93	15.7	5.92	0.11		N
$E6_2$	–10	4.63		0.10	1.19	1.03									N
$E6_3$	–10	4.62	1.02	0.1	1.15	1									N
$D6_1$	–12	4.8		0.11	1.14	1	0.92	19.8	–5.9	78	11.8	6.64	0.12		N
$D6_2$	–12	4.93		0.14	1.13	1.03									N
$D6_3$	–12	4.19	1.03	0.12	1.15	1.03									N
$C6_1$	–14	5.23		0.13	1.17	0.98	0.73	20.7	–6.1	102	18	5.65	0.18		N

Table 5.1. Continued

Sample no.	d, cm	χ	A_χ	M_{rs}	A_{rs}	E_{rs}	M_s	M_p	M_d	H_{cr}	H_c	H_{cr}/H_c	M_{rs}/M_s	fabric χ	fabric M_{rs}
$C6_2$	–14	4.96	1.03	0.20	1.18	0.99									N
$C6_3$	–14	5.02		0.21	1.14	1.05									N
k2	–15	4.91		0.16			1.19	15.3	–1.6	81	12.6	6.41	0.13		N
$B6_1$	–16	4.06	1.02	0.17	1.13	0.98									
$B6_2$	–16	3.93		0.17	1.17	0.95									N
$B6_3$	–16	4.18		0.12	1.17	1.02	0.48	14.9	–3.3	95	28.2	3.35	0.25		N
$A6_1$	–18	4.87		0.17	1.22	1.14	0.65						0.26		N
$A6_2$	–18	4.62		0.16	1.12	1.04									N
$A6_3$	–18	4.84		0.18	1.09	1.05									N
$A6_4$	–18	4.76		0.18	1.17	1.13									N
$A6_5$	–18	4.8		0.16	1.23	1.09									N
k3	–22	4.17		0.10			0.86	15	–1.5	70	12.4	5.65	0.12		N
k5/1	–33	3.67		0.12			0.62	13.6	–1.6	67	15.3	4.35	0.19		
k5/2	–37	3.94													
k6/1	–40	4.42													
k6/2	–45	4.95		0.10			0.9	17.4	–1.9	65	11.8	5.53	0.11		
k7/1	–48	4.55		0.08			0.82	17.1	–2	80	12.8	6.23	0.10		
K8	–52	5.72		0.11			1.02	19.2	–1.6	83	11.3	7.31	0.11		
k9/1	–54	6.68													
k8	–60	6.1													
k10/1	–63	5.48													
k10/2	–70	4.99		0.09			1.05	17.4	–2	77	10.5	7.36	0.08		
k10/3	–78	5.31		0.14			1.53	17.9	–2.7	87	10.9	8	0.09		
				1											
k10/4	–85	5.34		0.14			1.37	17.8	–1.8	85	12	7.08	0.10		
k11	–90	3.14													
k12/1	–95	6.48													
k12/2	–100	8.67													
k13	–102	3.55													
k14/2	–110	8.57													
k14/3	–115	4.93													
k14/4	–120	4.15		0.37			1.16	14.5	–1.8	93	27.4	3.4	0.32		

Note: Samples that were collected in 2000 and 2001 are denoted by capital and lowercase letters respectively. The following notation is used in the table: d, distance from the boundary layer **J**; χ, specific magnetic susceptibility (10^{-8} m^3/kg); M_{rs}, specific saturation remanent magnetization (10^{-3} Am^2/kg); $A_\chi = \chi_{\max}/\chi_{\min}$, anisotropy of magnetic susceptibility; $A_{rs} = Mrs_{\max}/Mrs_{\min}$, anisotropy of saturation remanent magnetization; $E_{rs} = Mrs_{in}^2/Mrs_{\max}Mrs_{\min}$, magnetic fabric ($E_{rs} > 1$ is foliation, $E_{rs} < 1$ is lineation); M_s, specific saturation magnetization (10^{-3} A m^2/kg); M_p, paramagnetic magnetization in a magnetic field of 500 mT at 20°C (10^{-3}A m^2/kg); M_d, diamagnetic magnetization in 500 mT at 20°C (10^{-3} A m^2/kg); H_{cr}, remanent coercivity (mT); H_c, coercivity (mT); $MT\chi$ and $MTrs$, magnetic fabrics as determined by magnetic susceptibility and saturation remanent magnetization, respectively (N and I stand for normal and inverse fabrics, respectively).

showed that the samples contain grains of ilmenite, which is paramagnetic at room temperature; therefore, the resulting estimate of the hemoilmenite concentration is a lower bound of the hemoilmenite and ilmenite concentration in the samples studied. Grains of pyrite and arsenopyrite were found in clay samples from the boundary layer of the Gams-2 section. During heating, such minerals are oxidized and form magnetite; based on the content of newly formed magnetite, we obtained an approximate estimate (the lower bound) for the concentration of Fe-sulfides of the pyrite and arsenopyrite types.

On the whole, the resulting estimates of concentrations of magnetic minerals are rather tentative, but their relative variations reflect the real situation.

Magnetic measurements were used for estimating the concentrations of paramagnetic (paramagnetic iron hydroxides, clays, etc.) and diamagnetic (carbonates

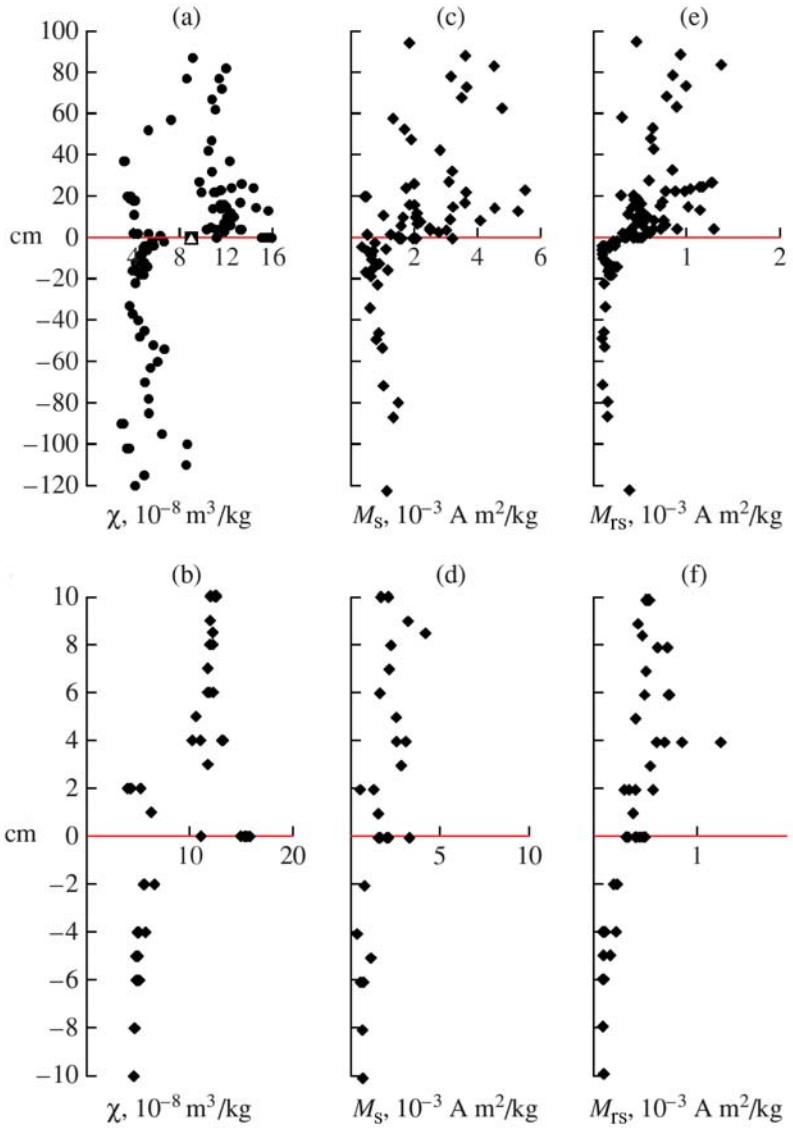

Figure 5.1. Distribution of (a, b) – specific magnetic susceptibility χ (10^{-8} m^3/kg), (c, d) – specific saturation magnetization M_s (10^{-3} Am^2/kg), and (e, f) – specific saturation remanence M_{rs} (10^{-3} Am^2/kg): (a, c, e) – total section; (b, d, f) – $\pm$10 cm interval. The horizontal red line in this and other figures shows the boundary clay layer (K/T boundary).

and quartz) components in the sediments. Paramagnetism of the samples is actually controlled by the iron concentration in paramagnetic minerals, so that paramagnetic magnetization provides general constraints on the iron concentration in the rocks. The "complete", paramagnetic+diamagnetic part of magnetization was determined from the curve of isothermal magnetization at room temperature. If paramagnetic magnetization at room temperature is known, its value at 800°C can be estimated according to the Curie-Weiss law. Diamagnetic magnetization is virtually independent of temperature [*Vonsovskii,* 1971]. Taking into account that all measurements were made in the same magnetic field (in our case 500 mT) or were reduced to the same field (then, a linear dependence of paramagnetic and diamagnetic magnetization on the field was used), simple equations can be used for calculating the paramagnetic and diamagnetic components of magnetization at room temperature:

$$M_p + M_d = M_{20} \ ,$$

$$0.274M_p + M_d = M_{800} \ ,$$

where M_{20} is the paramagnetic+diamagnetic magnetization, which was determined from the curve of room-temperature isothermal magnetization above the sat-

uration field of magnetically ordered (magnetic) minerals present in a sample, and M_{800} is the 800°C magnetization measured in the same field as the value M_{20}. The multiplier $0.274M_p$ is the ratio 295 K/1075 K. These equations yield

$$M_p = 1.378(M_{20} - M_{800}) .$$

Results of these calculations are presented in Table 5.1 and Table 5.2.

To gain additional constraints on the composition of magnetic minerals, we used TMA curves measured during successive heating of samples to various temperatures; this allowed us to detect mineralogical alterations in samples during their heating and distinguish them from Curie points.

The microprobe analysis of the magnetic fraction extracted from several samples was also performed Overall, the microprobe and TMA results are complementary, for example: (a) different compositions of titanomagnetites are determined from microprobe and TMA data, indicating decomposition of titanomagnetite grains (b) according to TMA data, the interlayer $J6_4$ contains nickel, which is not found in the $J6_4$ magnetic fraction and, in contrast, the $J6_5$ magnetic fraction contains nickel-taenite intergrowths that are not observed in the TMA data (this indicates local and extremely irregular occurrence of nickel particles).

5.3 Results of Petromagnetic Studies of the Rocks From Gams-1 Section

Magnetization of rocks (Table 5.1). The values of specific magnetic susceptibility, magnetization, and saturation remanent magnetization in rocks of the Gams-1 section vary within wide limits and generally reflect the main lithologic features of the rocks, namely, the contributions of diamagnetic material (calcite and quartz), paramagnetic material (ferriferous clays and iron hydroxides), and terrigenous magnetic minerals. Accordingly, the least magnetization is observed in the Maastrichtian marls and a series of Danian interbeds enriched in calcite and quartz (in particular, the lens **K** and the layers **S**, **T**, **t16**, and **t19**), while most magnetic are sandy-clayey sediments of Danian in the 4–25-cm interval of the section (Table 5.1 and Figure 5.1). Overall, in accordance with the lithologic control, the along-section distributions of χ, M_s, and M_{rs} are very similar (Figure 5.1). Against this background, the layer **J** is greatly distinguished by a high susceptibility and has no signatures in M_s and M_{rs}; we relate this to a considerable contribution of paramagnetic material to χ. The role of the paramagnetic material is significant in all rocks: its magnetization is 5 to 20 times higher than the total magnetization of magnetic minerals M_s (Table 5.1); the amount of paramagnetic material in sandy-clayey deposits is about twice as large as the amount in marls and limestones (Table 5.1). A positive correlation is observed between M_s and M_{rs} (Figure 5.2a), implying that both magnetizations are controlled by the concentration and composition of magnetic minerals. Noticeable deviations from such a dependence can be accounted for by a significant influence of structural factors on the M_{rs} value. On the one hand, the presence of fine single-domain (SD) grains increases M_{rs} relative to M_s and, on the other hand, the presence of superparamagnetic grains leads to a relative increase in M_s as compared with M_{rs}. The correlation of M_s and M_{rs} with the susceptibility is weaker (Figure 5.2b,c). Apparently, this is due to significant contributions to the susceptibility made by paramagnetic and diamagnetic material (weak correlation in the weakly magnetic range) and superparamagnetic material (weak

Table 5.2. Magnetic properties of samples from the boundary layer and overlying sediments (Gams section)

no.	d, mm	M_s	M_p	M_{rs}	M_{rs}/M_s	H_{cr}	H_c
Gams-2A							
16	57	3.02	49.3	0.66	0.219	129.6	24.04
15	52	3.43	49	0.778	0.227	130.6	23
14	47	3.23	55.1	0.712	0.221	141.4	25
13	43	2.03	50.6	0.703	0.347	138.6	25.78
12	37	2.74	50.6	0.638	0.233	135.6	25.86
9	40	1.93	45.2	0.729	0.378	147.5	31.19
11	26	1.48	55.4	0.548	0.371	99.4	15.24
8	16	3.28	65.3	0.696	0.212	86.5	12.28
7	13	3.4	65	0.75	0.221	78.8	11.56
6	10	4.2	67.4	0.749	0.178	62.8	10.3
5	8	3.59	61.5	0.583	0.163	48.8	8.92
3	7	3.92	54.7	0.437	0.111	19.5	4.8
2	4	2.35	43.9	0.29	0.123	20.3	5.03
1	1	2.2	33.1	0.222	0.1	17.6	4.76
Gams-2B							
5	35	6.53	34.9	0.9	0.138	92.7	18.7
3	13	4.37	49.2	0.81	0.185	80.5	17.4
2	7	5.73	48.9	0.87	0.152	85.4	15.7
1	2	6.54	43.74	1.03	0.157	84.3	16.2
Gams-1							
Jtop	18	3.29	40	0.34	0.103	67.9	9.2
J3	10	7.2	48.3	1.02	0.142	67.4	14.3
J2	5	7.34	55.39	1.28	0.174	30.8	9.5
J1	3	6.48	49	1.09	0.168	42	11.1
J0	1	9.86	47.74	1	0.101	21.2	5.14

Note: The notation is the same as in Table 5.1.

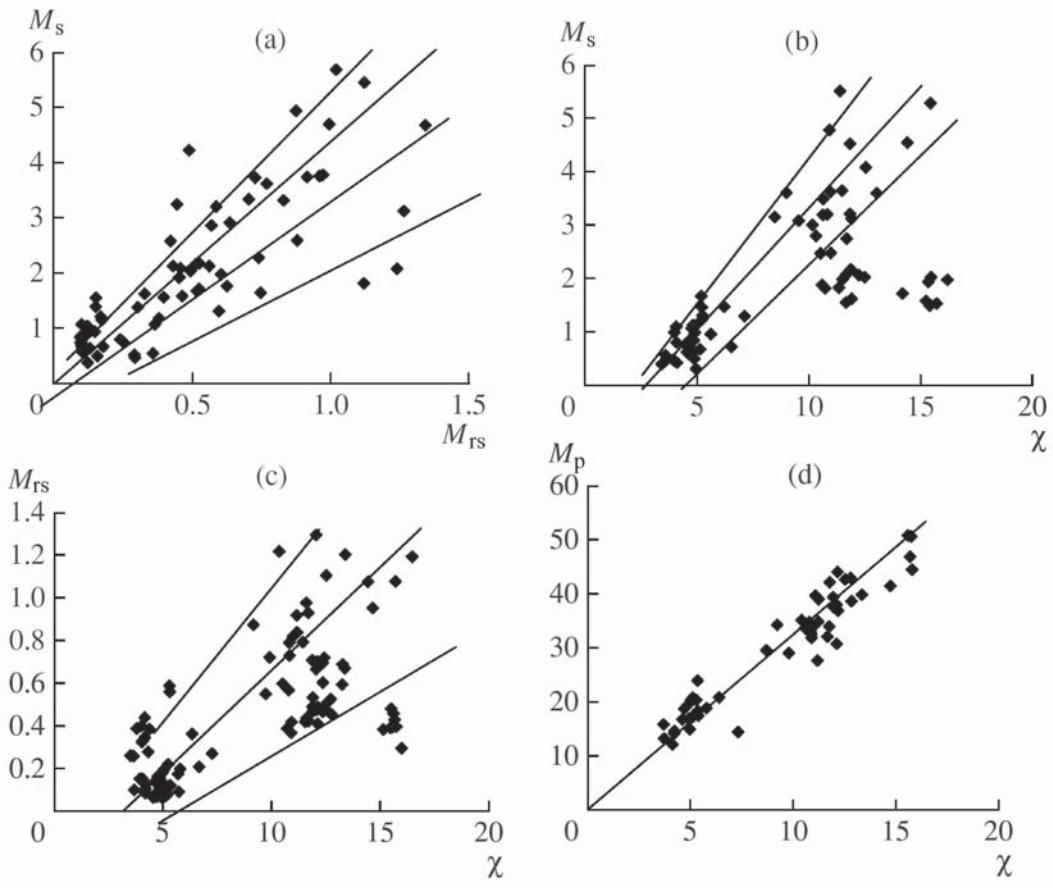

Figure 5.2. Correlation between (a) – M_{rs} and M_s, (b) – M_s and χ, (c) – M_{rs} and χ, and (d) – M_p and χ along the Gams-1 section. The dimensionality is the same as in Figure 5.1.

correlation in the highly magnetic range); these contributions are insignificant in M_s and absent in M_{rs}. The M_s-χ points in Figure 5.2b form two groups; the first group reflects the correlation between these characteristics (the contribution of magnetic minerals to the susceptibility is appreciable), while the second group is characterized by the absence of correlation between M_s and χ: the value M_s being more or less constant, χ varies within wide limits. The latter is due to the contribution of paramagnetic material alone to the susceptibility: all points of the second group were obtained solely from sandy-clayey sediments (Table 5.1). The sensitivity of susceptibility to paramagnetic material is supported by a strong positive correlation between χ and M_p (Figure 5.2d).

The composition of magnetic minerals in Gams-1 sediments was determined from TMA and microprobe analysis data. Analysis of the curves $M_i(T)$ TMA (Figure 5.3) and their derivatives DTMA (Figure 5.4) has revealed the presence of the following nine magnetic phases.

(1) A magnetic phase with T_C = 90–150°C makes a contribution of 10–20% to M_i and is present in all samples studied (Table 5.3). This phase disappears upon heating. It is evident that the phase consists of weakly ferromagnetic iron hydroxides of the goethite type. The along-section variations in the concentration of such goethite are 0.2–0.6% in the Maastrichtian marls, lens **K**, and weakly magnetic interbeds in the Danian deposits and are as high as 1–2.5% in the sandy-clayey sediments of the Danian, reaching a maximum of 2.5% in samples from the boundary layer **J** (Figure 5.5).

(2) A magnetic phase with T_C = 60–140°C in TMA curves of the first heating is masked by magnetic hydroxides (goethite) and by the hyperbolic shape of the TMA curves. The phase is better resolved in the DTMA curves, particularly in those of second heating. Its contribution to M_i does not exceed 10%. It is stable with respect to heating to 800°C and probably arises due to such a heating. This can be Ni-ferrospinel fixed by microprobe in magnetic fraction of Gams-1 samples and in a number of experiments (e.g. see [*Bagin et al.*, 1976,

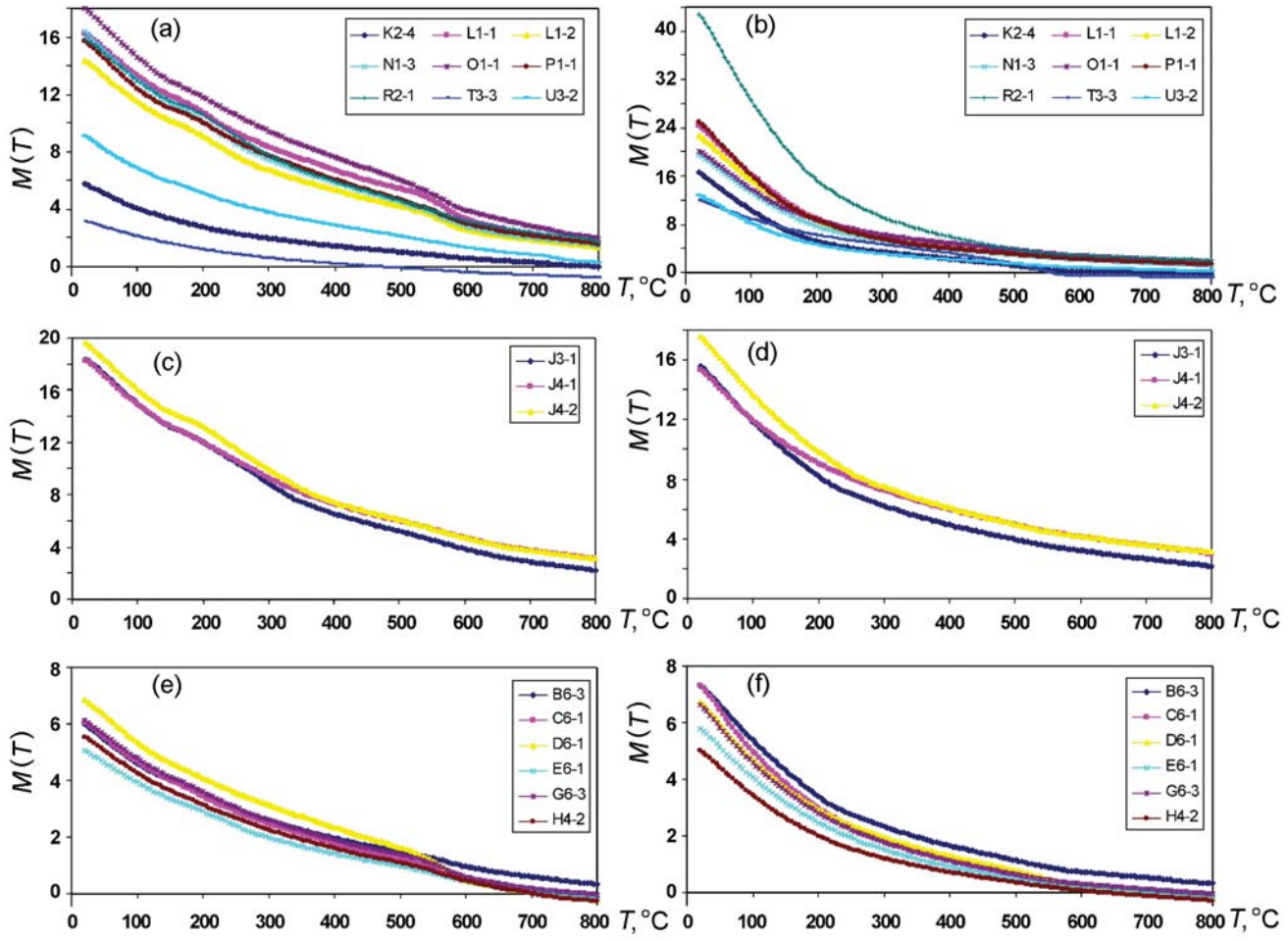

Figure 5.3. Examples of TMA results for the inductive magnetization $M_i(T)$ from the Gams-1 section: (a, c, e) first heating; (b, d, f) second heating.

1977; *Gapeev et al.*, 1988; *Lykov, Pechersky*, 1976, 1977]). No correlation of this mineral with the lithology and mineralogy of rocks is noted (Table 5.3).

(3) A magnetic phase with T_C = 180–300°C is present in samples taken from the 40-cm-long section interval centered at the layer **J**. The contribution of this phase to M_i amounts 0–40% (Table 5.3). Upon heating to 800°C, its concentration in many samples rises by 30–90% and the Curie point often drops (Table 5.3). Successive heatings of sample K2-4 (Figure 5.6) demonstrate that this rise takes place only after heating to 800°C. Heating of many samples to 750°C does not increase the magnetization (it only drops), evidently due to destruction of maghemite, whereas heating to 800°C leads to a noticeable increase in M_i (Table 5.3). Such an increase in M_i accompanied by a drop in T_C is characteristic of hemoilmenite of an intermediate composition. During heating, hemoilmenite is partially homogenized and, as a result, the curve $M_i(T)$ generally assumes a noticeably concave shape. Control heatings of some samples to 1000°C revealed that the concavity of the curve $M_i(T)$ disappears and the value M_i increases by a factor of 2.3 as compared with the result of heating to 800°C (Figure 5.7). This corresponds to the diagram of state of hemoilmenite of an intermediate composition whose range of homogenous states lies above 900°C [*Nagata*, 1961]. The hemoilmenite concentration varies from less than 0.0001% to 0.08% (Figure 5.8). The magnetic fraction of all samples studied with a microprobe contains great amounts of grains (clasts) of ilmenite; the grains are often well-preserved relatively large (more than 50 μm plates (Figure 5.9a,b)). Their concentration in the sediments varies from a few tenths of percent to a few percent, and they are close in composition to pure ilmenite (Table 5.4). They often contain intergrowths and lamellae of rutile. Hemoilmenite grains of a composition corresponding to a Curie point of 200–300°C that are observed in the TMA and DTMA curves are absent. The majority of the hemoilmenite grains are very fine, smaller than the probe size; this is

=

Table 5.3. TMA results for samples from the Gams-1 section

		First heating, T_c (percentage)							Second heating. T_c (percentage)										
no.	d	FS	goethite	GI	maghemite	Ni	MT	TM	haematite	FeNi	Fe	FS	GI	Ni?	MT	TM	haematite	Fe	M_{750}/M_{20}	M_{800}/M_{20}
t27	93		120(5)		210–300					660?	740(10)		200?, 260?						0.82	
t26	87		120(5)		200–300		580(20)		680				200?		580				0.79	
t25	82		130(10)		210–300		580(20)				760?(5)				570				0.81	
t24	77		120(5)		220–300		590(15)		680?		745(10)				590				0.84	4.32
t23	72		120(10)		220–300		580(10)				760?(5)		260?		580				0.82	4.04
t22	67		130(10)		220–300		610(10)		670		725(5)				570		670		0.79	
t21	62		130(10)		230–300			590(20)			760(5)		200?			560			0.77	
t20	57		130(5)		210–300			610(10)								550			0.92	
t19	52		H		210–300?			590(20)			750(10)	110?				530			0.95	
t18	47		130(10)		220–300			590(20)								550			0.78	
t17	42		130(10)		250–300			590(20)	680							560	680		0.79	
t15	32		130(10)		230–300		590(30)		670?						570				0.8	
t14	27		130(5)		200–300		580(30)		680(20)		770(10)	130			580				0.83	1.25
$W9_2$	26	90			300			560?(5)		630?			∼230(40)			500			1	
$V9_2$	24		100(5)	∼310(45)		360?		570(20)					∼210(50)	350?		510			1	
t13	23		130(10)		230		590(10)		680		770?(5)				590				0.82	
$U3_2$	22	70	130(10)	260(25)			590(20)				750(10)		∼210(60)		570			750		1.4
$T3_1$	20		110?(15)	240(15)	360			550(5)			760?(30)					550				
$T3_3$	20	90?					610(25)		690		760(10)	90?	210(35)		580(65)		660?	750?		3.86
t12	19		140	290(20)			600(10)				745(10)									6.5
t11	17		130(10)		240–320		590(20)				730?(5)				590				0.77	
$R2_1$	16		150(15)	250(10)	350		590(20)	590(20)			740(5)		∼200(60)		590	530	680?			2.7
$R2_3$	16		130(5)	250(15)				560(25)					∼220(40)			515			0.95	
t10	15		150(10)		230–300			580								550			0.8	
t9	14.5		120(10)		240–290		570(20)				745(10)				570				0.84	
t8	13		150(5)		230–290		570(20)								570				0.8	
$P1_1$	12		140(10)	250(5)			590(30)						210(70)		580					1.59
t7	11		120(5)	200?(5)				620(10)			765(5)	90, 130	200?			540				1.29
$O1_1$	10		140(10)	210?(5)			590(40)				750(10)		∼210(30)		580					1.12
$O1_3$	10		110(10)	290(10)				550(15)			730?(15)		∼180(35)			535		750?	0.98	
t6	9		130(10)		210–330		580(20)		680?		735(10)				580				0.82	
t5	8.5		140(10)		240–320		600(10)		680?				H		570				0.79	
$N1_3$	8		130(10)	250(15)			590(30)						∼200(40)		590		660			1.19
t4	7		120(10)		230–310			580?(10)								560			0.84	

=

Table 5.3. Continued

		First heating, T_c (percentage)								Second heating. T_c (percentage)									
no.	d	FS	goethite	GI	maghemite	Ni	MT	TM	haematite	FeNi	Fe	FS	GI	Ni?	MT	TM	haematite	Fe	M_{750}/M_{20}	M_{800}/M_{20}
$M1_2$	6		140(10)		315			565(10)			710?(5)									
$M6_1$	6		120L(10)		295		570(30)				770?(15)		∼190(40)		570?				0.95	
t3	5		130(10)		220–310		610(20)		680?						570?				0.85	
$L1_1$	4		120(15)	250(10)			585(25)				760(5)		∼210(70)	450?	580			750		1.5
$L2_1$	4		150(15)	260(10)			590(25)				750(5)		∼240(60)		590		670	750		1.57
t2	3		140(10)		220–330		580(20)				770(10)								0.84	
$K2_4$	2	90		H			590(20)				750(15)	90	∼230(65)		570(30)		660?	750		2.9
t1	1		130(10)	210, 280				630(10)			740?(5)	120	190, 260			520			0.94	
Jtop	0		130(10)		350					660(20)	740(10)		H			540				0.88
$J7_2$	0		120(10)		360						740?(2)		220(30)			515			1	
$J3_1$	0		140(15)		340			590(10)		650(20)	750?(5)		210(30)			550		750?		0.85
$J3_2$	0		130(10)			370		515?(5)			740?(2)		200(25)	365		515		740?		1.03
$J4_1$	0	80	150(10)		230–300			590(10)		650(20)		80	250(30)			530				0.84
$J4_2$	0	80	150(15)	250(5)	350			590(15)		650(20)			250(20)			530	650			0.9
$H4_2$	–4		110(10)					590(40)			740(20)		∼250(50)			560				0.91
k1	–5		150(10)	210(10)	290			580(15)		660(10)	730?(5)	60	210			530			0.85	1.24
$G6_3$	–6		150(10)		200–260		590(30)				780?(5)		∼250(50)		570					1.08
$E6_1$	–1		150(10)		200–450			595(40)			750?(20)	60	∼250(60)			540		740		1.15
$D6_1$	–12		150(10)		210		585(40)				750(20)	70			580			760		0.98
$C6_1$	–14		130(10)		200			585(40)			750?(5)	70				540		730?		1.21
k2	–15		130(5)		300(20)			560(15)		650(5)	760(20)	100				530		760	0.88	1.16
$B6_3$	–16		130(10)	220(15)				590(30)			760(10)		210(40)			550		750		1.22
k3	–22		130(10)		290(20)			610(20)	680?		735?(5)					540			0.88	
k5/1	–33		130(10)	210(10)	290			600(20)	660?				200?			540	660?		0.9	
k/2	–45		130(10)		210–300?			600(30)			730?(5)		150			550			0.82	
k7/1	–48		130(5)		210–30?			590(30)				150?				550			0.82	
k8	–52		140(10)		210–280(20)			590(15)			760?(10)					540			0.81	
k9/1	–54	80	140(10)		380		550(20)		650		765(5)									2.2
k10/2	–70		130(10)		300?		580(20)				760?(10)				570				0.82	
k10/3	–78		140(10)		210–280		580(30)								580					0.86
kO/4	–85		130(10)		210–280			590(20)			750(10)	110			550					0.84
k14/4	–120		140(5)	210(5)	360			620 (20)			735(5)	140	200			530			1.15	

Note: Samples collected in 2000 and 2001 are denoted by capital and lowercase letters, respectively. The following notation is used in the table: d, distance from the boundary layer **J** in cm; T_C, Curie point (percentage in parentheses is the part of the magnetization $M_i(T)$ estimated by extrapolation from the Curie point to room temperature, rough estimates of Curie points are marked by the symbol ∼); FS, ferrospinel; GI, hemoilmenite; maghemite column, temperature of the maghemite-hematite transformation; Ni, metallic nickel; TM, titanomagnetite; MT, magnetite; FeNi, ferro-nickel alloy; Fe, metallic iron; M_{750} and M_{800}, magnetizations after heating to 750°C and 800°C, respectively.

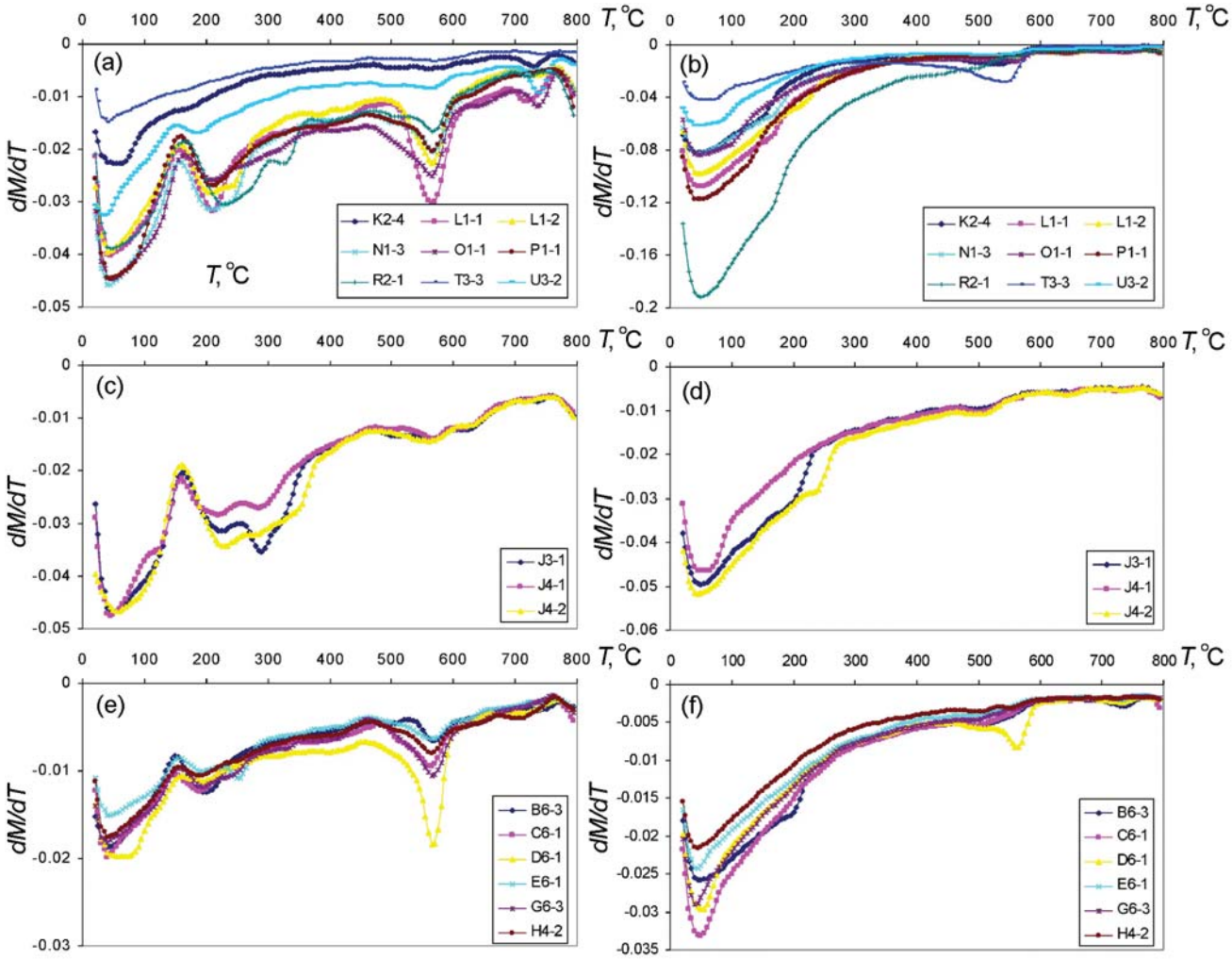

Figure 5.4. Examples of DTMA results dM/dt from the Gams-1 section: (a, c, e) first heating; (b, d, f) second heating.

evident from their high coercivity (see below), and the concentration of hemoilmenite with T_C = 180–300°C is one to two orders smaller than the concentration of ilmenite. Ilmenite grains contain hardly visible very thin lamellae of hemoilmenite close to hematite; their thickness varies from tenths to hundredths of micrometer, and their composition could not be measured with an electron beam of 2–3 μm. Moreover, ilmenite is well drawn away by a magnet, evidently due to hemoilmenite inclusions because pure ilmenite is paramagnetic at room temperature. Therefore, the along-section distribution of hemoilmenite reflects the degree of multiphase oxidation of ilmenite rather than the total concentration of the latter. Such thin lamellae of hemoilmenite and their magnetism were described in [*McEnroe et al.*, 2002].

It is possible that Mg-Al ferrospinels with similar Curie points (200–300°C) form during laboratory heating. The studied sediments (particularly of the sandy-clayey type) contain sufficient amounts of components necessary for such a process [*Grachev et al.*, 2005]. However, no correlation of this magnetic phase with Fe, Mg, and Al concentrations is observed. For example, the magnetic phase with T_C = 200–300°C virtually does not form during successive heatings of samples from the layer **J** that contain the largest amounts of the aforementioned elements (Fe_2O_3 = 7–8%, Al_2O_3 = 17–19%, MgO = 2.6–3%): the curves $M_i(T)$ are similar up to 850°C (Figure 5.6); on the other hand, the content of this magnetic phase increases in a sample from the layer **K** after its heating to above 800°C (Figure 5.6), although the concentrations of these elements in this layer are smaller (Fe_2O_3 = 3.5–4.7%, Al_2O_3 = 5.7–8.9%, MgO = 0.9–1.3%). Another argument favoring this suggestion is gained from thermomagnetic examination of the magnetic fraction extracted from **L** and **W** samples

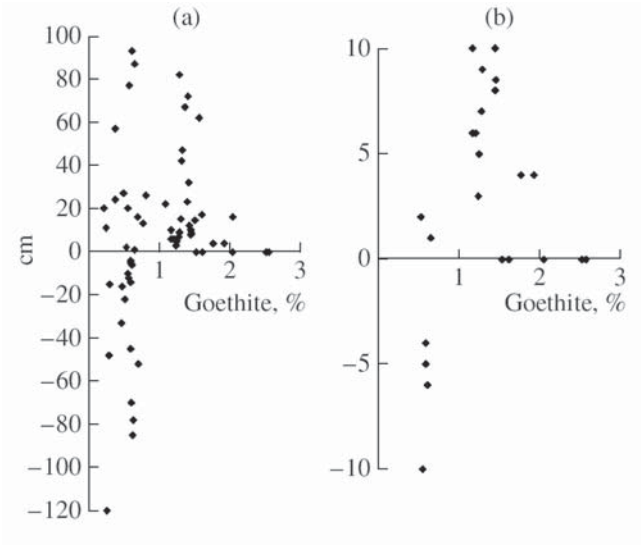

Figure 5.5. Concentration of goethite from TMA data: (a) – the Gams-1 section; (b) – ±10 cm interval.

and their nonmagnetic remainders. As seen from Figure 5.10a, the magnetic fraction that have $T_C \approx 250°C$ phase no less than 20% in concentration is fixed, and the curves $M_i(T)$ of the second and third heatings lie

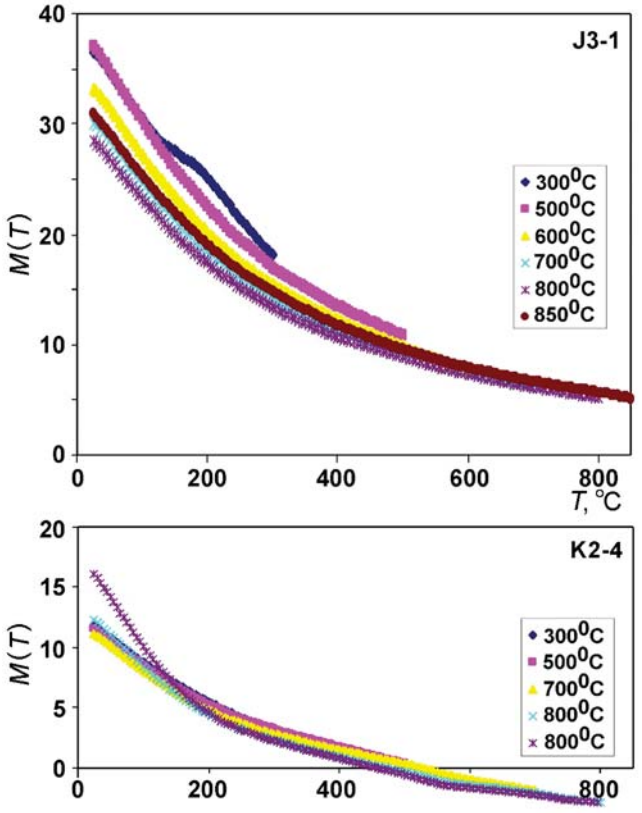

Figure 5.6. Results of successive heatings of samples $J3_1$ and $K2_4$.

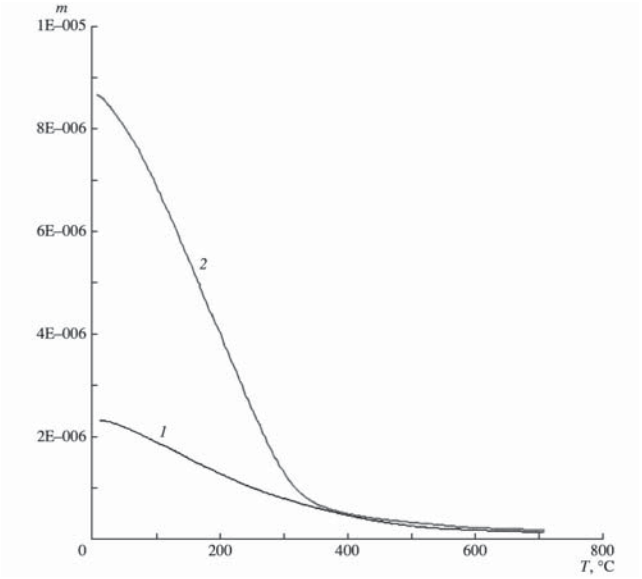

Figure 5.7. TMA results from sample L upon its heating to 800°C (black) and 1000°C (red). m is the magnetic moment (10^{-6} Am^2).

considerably lower than the curve of the first heating because about one-half of magnetite is destroyed, evidently due to its heating-induced oxidation. One might expect that Mg-Al ferrospinels mostly form from the nonmagnetic fraction, but this is not the case: heatings of the latter have led to no changes (Figure 5.10b).

(4) The magnetic phase with T_C = 200–370°C is present in most samples of the section. As seen from data of successive heatings, this phase is commonly de-

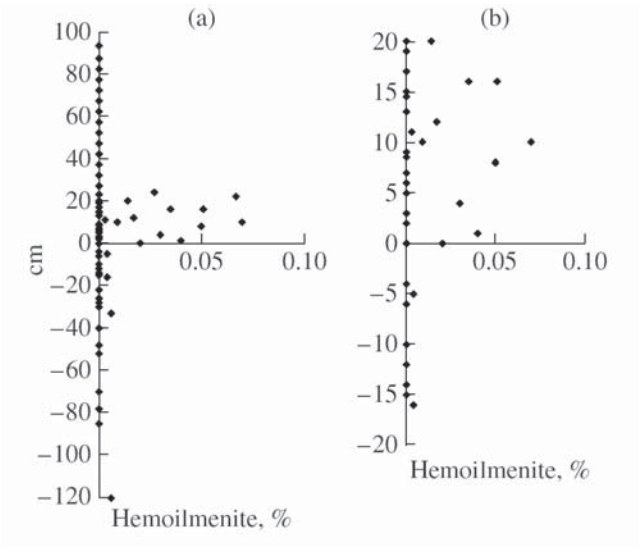

Figure 5.8. Concentration of hemoilmenite from DTA data (a) – along the Gams-1 section and (b) – in the ±10 cm interval.

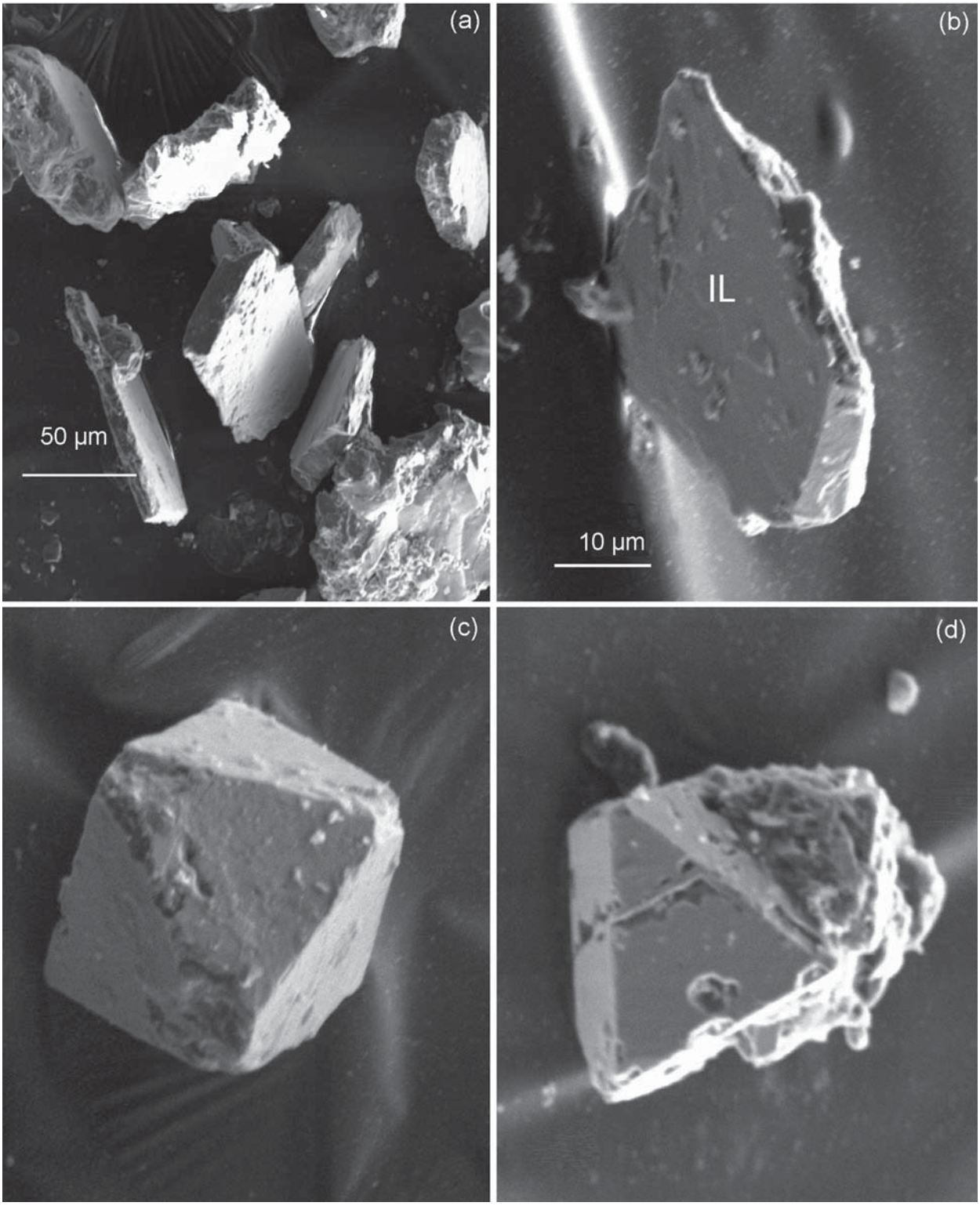

Figure 5.9. Crystals of ilmenite from layers (a) – **K** and (b) – **M** and crystals of magnetite from layers (c) – **M** and (d) – **P**.

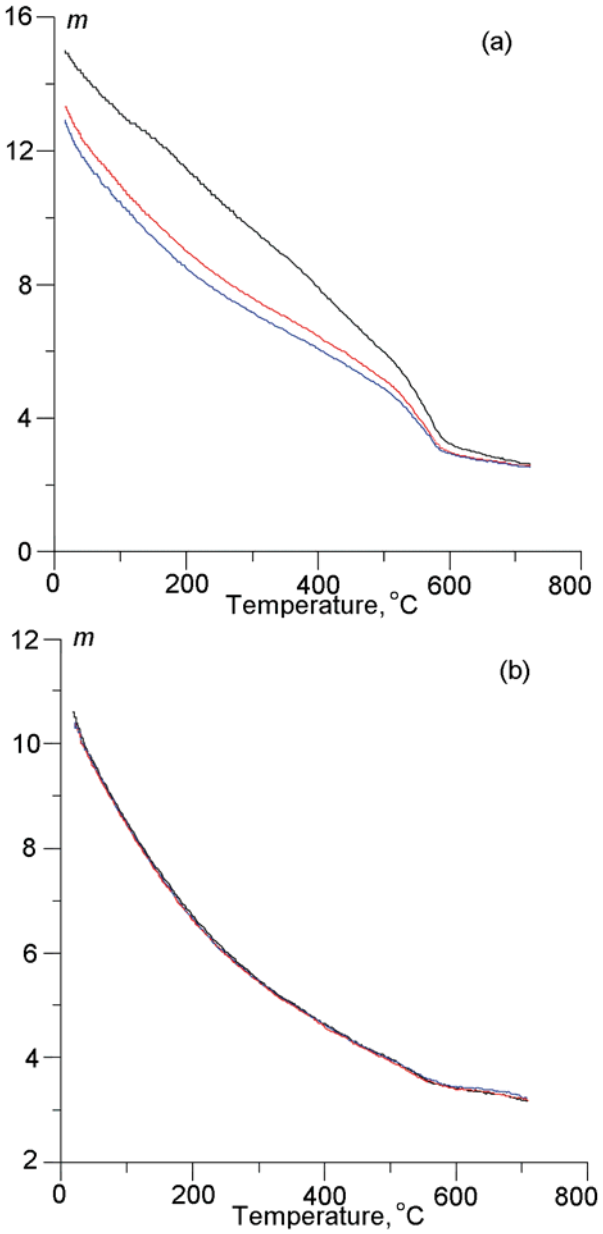

Figure 5.10. TMA data for sample W: (a) – magnetic fraction; (b) – nonmagnetic residual. The black, red, and blue lines are data of first, second, and third heatings, respectively. m is the magnetic moment (10^{-7} Am^2).

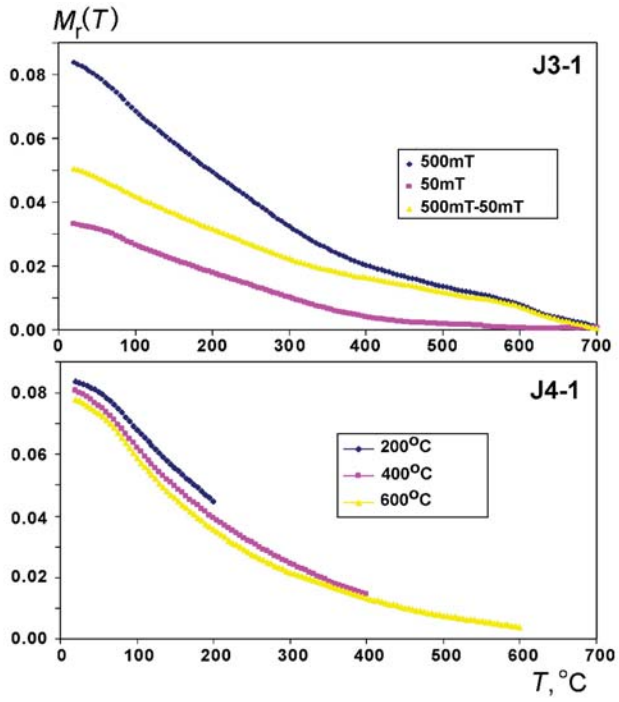

Figure 5.11. TMA data for the remanence $M_r(T)$ formed in fields of 50 and 500 mT from samples $J3_1$ and $J4_1$.

stroyed on heating to 300°C (Table 5.3, Figure 5.6); i.e., in the majority of cases, this is not a Curie point but the temperature of the magnetic mineral destruction (most likely, the usual transformation of maghemite to hematite).

(5) The magnetic phase with T_C = 360°C is found in samples from the layer **J** (samples $J6_4$, $J6_6$, and $J3_2$). Microprobe examination of sample J_6 and its magnetic fraction revealed the presence of metallic nickel in two fragments less than 3 mm in size from the upper parts (samples $J6_6$ and $J6_4$) of the layer **J** (for details, see below and [*Grachev et al.*, 2005]). In the remaining samples of the section, including the layer **J6**, samples $J6_{1,2,3,5,}$ and even a small fragment taken near sample $J6_6$, metallic nickel is not found but its presence in some other samples (e.g. in sample $J3_2$) is indicated by the curves $M_r(T)$, whereas in sample $J4_1$ even the curve $M_r(T)$ yields no evidence for nickel (Figure 5.11). These results imply that, first, nickel is represented by very fine grains whose concentration in the layer **J** apparently averages less than 0.001% (∼0.02, ∼0.01, and 0.1% in small fragments from samples $J3_2$, $J6_4$, and $J6_6$, respectively); this is why the grains cannot be detected in the curve $M_i(T)$ but are recognizable from $M_r(T)$. Second, the discovery of metallic nickel only in some minute specimens points to its local and very irregular occurrence in the layer **J**.

In addition to the layer **J**, the microprobe revealed an intergrowth of pure nickel and copper in sample L6 (Figure 5.12) and single nickel grains in the layers **K** and **M**. TMA results yielded no evidence for the presence of nickel in the layers **K**, **L**, and **M**, thereby confirming its very irregular occurrence.

(6) The magnetic phase with T_C = 510–610°C is present in all studied samples of the section, and its frac-

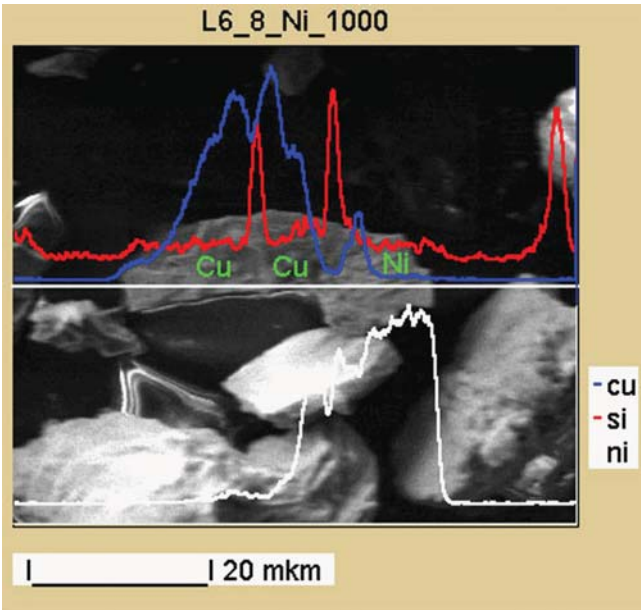

Figure 5.12. Ni-Cu intergrowth in sample L6 (microprobe data).

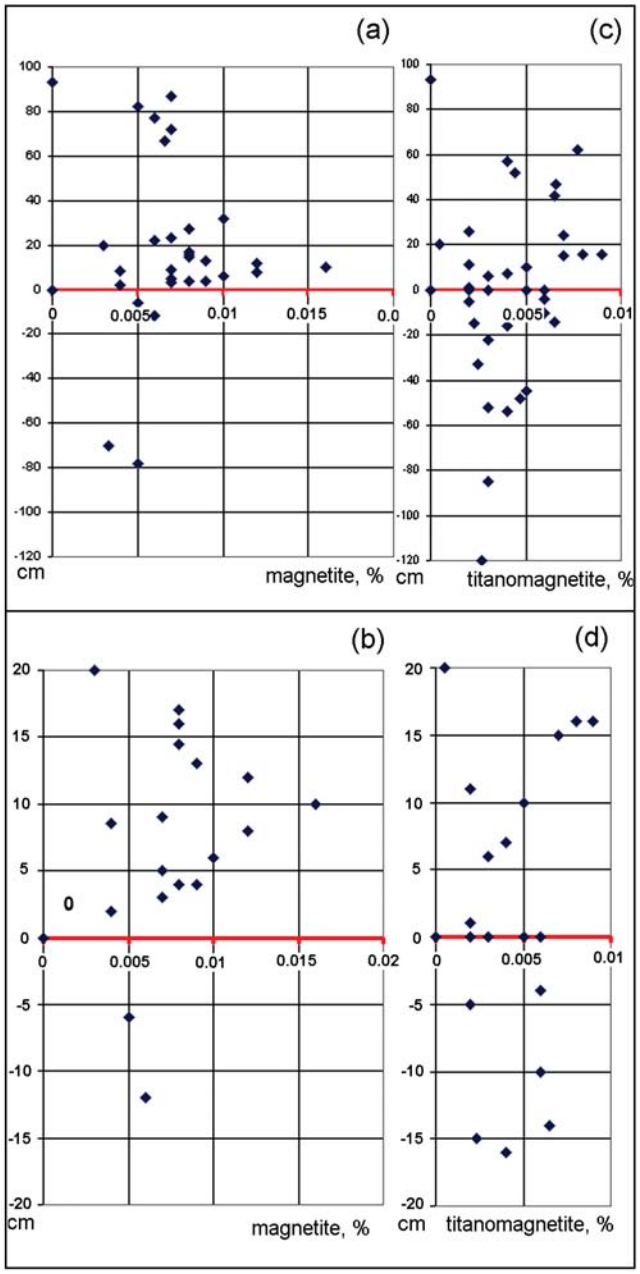

Figure 5.13. Concentration of (a, b) – magnetite and (c, d) – titanomagnetite from TMA data (a, c) – along the Gams-1 section and (b, d) – in the ±20 cm interval.

tion in M_i varies from less than 5 to 40% (Table 5.3). On heating, this phase is commonly preserved, although its amount usually decreases, and T_C is shifted in many samples toward lower temperatures. This is titanomagnetite transformed to magnetite due to multiphase oxidation; in turn, the magnetite has often experienced single-phase oxidation ($T_C > 580$°C). Upon laboratory heating to 800°C, titanomagnetite grains become partially homogenized. This feature suggests the presence of titanomagnetite in many samples of the sections; its concentration varies mainly from 0.001 to 0.01% and its distribution does not depend on the rock composition (Figure 5.13). The presence of titanomagnetite in the layer **J** is confirmed by microprobe data: the grains are close in composition to usual titanomagnetites of basalts ($TiO_2 \sim$ 20–25%) [*Grachev et al.*, 2005]. Unlike the titanomagnetite, magnetite is controlled lithologically, and its concentration rises from zero in the layer **J** to 0.017% in the layer **O** (Figure 5.13). The absence of titanomagnetite in this interval is supported by microprobe data: only magnetite that does not contain titanium is discovered in samples from the layers **K, L, M, O**, and **P** (Table 5.4). The magnetic fraction from the layer **W** includes very fine grains dominated by ilmenite (Table 5.4), while titanomagnetite is fixed only from TMA data. No correlation is observed between the presence of titanomagnetite and the magnetite concentration, implying that their sources are different. Well-preserved single crystals (octahedrons) are very often present among magnetite fragments (Figure 5.9c, d), which is evidence for a nearby provenance or in situ crystallization of magnetite. Such crystals of pure magnetite are evidently of nonmagmatic origin.

The amount of magnetite in **K** and **T** samples increases upon their heating (Table 5.3, Figure 5.3).

(7) Magnetic phase with T_C = 640–660°C is reliably fixed in samples from the layer **J** (Table 5.3) and is possibly present in samples t14 (27 cm), k1 (–5 cm), and k2 (–15 cm). The contribution of this phase to M_i is 5–20%. Heating to 800°C destroys this phase almost com-

pletely, i.e. this is not hematite. Since nickel is present in **J** samples, one might suggest that this is an alloy of iron and nickel: the calculation of iron and nickel using T_C and M_s shows that this can be the alloy Fe_3Ni (possibly taenite). The presence of such alloy is supported by microprobe data [*Grachev et al.*, 2005]. Its concentration is about 0.005%.

(8) The magnetic phase with T_C = 660–680°C arises and is preserved in several samples after their heating to 800°C. Evidently, this is hematite (Table 5.3) that makes a less than 10% contribution to M_i.

(9) The magnetic phase with T_C = 740–770°C is present in many samples, and its contribution to M_i is 0–30% (Table 5.3, Figure 5.3, and Figure 5.4). On heating to 800°C this phase is partially or completely destroyed. Evidently, it is metallic iron with minor admixtures that is oxidized during heating to 800°C. Single microspheruless of pure iron are detected with the microprobe in samples J2 and M4 (Figure 5.14). Its concentration is small (less than 0.002%). Metallic iron is distributed rather homogeneously along the section (Figure 5.15).

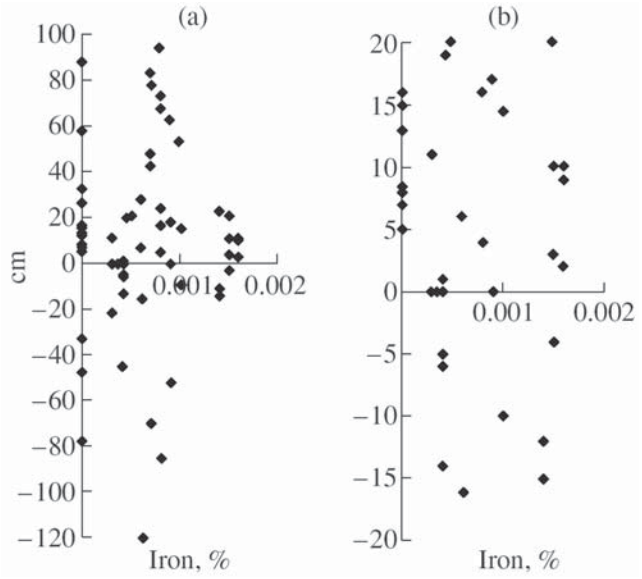

Figure 5.15. Concentration of metallic iron from TMA data (a) – along the Gams-1 section and (b) – in the ±20 cm interval.

Coercivity of magnetic minerals. As seen from coercivity spectra (Figure 5.16a), all samples have similar ensembles of magnetic grains. The spectra of the Maastrichtian marls are most similar to each other and differ insignificantly from the spectra from the **K, S**, and **T** layers of the Danian deposits. The spectra exhibit a smooth increase in the coercivity up to a maximum at 100–140 mT followed by a decrease to a minimum at ∼400 mT with a subsequent rise to 500 mT. Beginning from the layer **L**, the extrema virtually disappear in the coercivity spectra of the sandy-clayey deposits: the coercivity smoothly increases to a limiting field of measurements of 800 mT (Figure 5.16a). Toward upper parts of the section (from **M** to **S** and **T** samples), the spectrum is gradually transformed into spectra of the marl type (Figure 5.16). Against this background, coercivity spectra of the layer **J** are sharply distinguished by a maximum or a flat inflection at 25–40 mT in their low coercivity part. In their remaining parts, the spectra of the layer **J** are similar to those observed in samples of the Danian sandy-clayey sediments, particularly in the layers **N** and **O** (Figure 5.16a).

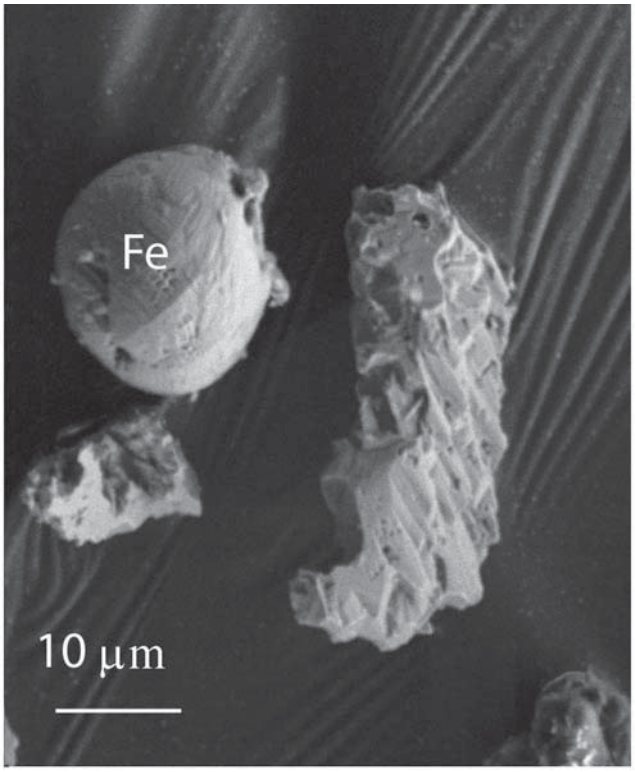

Figure 5.14. Pure iron microspherules and magnetite clasts, sample M4.

Comparison of the coercivity of the rocks with the concentrations and composition of their magnetic minerals (Table 5.1, Figure 5.5, Figure 5.8, Figure 5.13, and Figure 5.15) shows them to be uncorrelated, and only a general tendency of an increase in the coercivity and goethite concentration in the rocks is noticeable. Therefore, the coercivity is primarily controlled by the structural state of magnetic grains rather than their composition and concentration. A gap in the coercivity of samples from layer **J** is well observed from both H_{cr} data (Table 5.1, Figure 5.17) and the spectra.

Judging from the values of H_{cr} and M_{rs}/M_s (Table 5.1, Figure 5.17), single- and pseudo-single-domain

Table 5.4. Composition of minerals of magnetic fractions in samples from the Gams-1 section (microprobe analysis data)

Sample,	mineral	TiO_2	FeO	MgO	MnO	Al_2O_3	Cr_2O_3
L6,	p.1 ilmenite	40.2	51.9	0.9	0.1	0.3	0.0
	p.2 ilmenite	45.4	52.9	0.8	0.0	0.2	0.1
	p.3 ilmenite	46.1	52.2	0.6	0.1	0.2	0.1
	p.4 ilmenite	40.5	56.6	0.4	0.0	0.6	0.1
	p.5 ilmenite	45.5	51.2	0.2	0.0	0.2	0.1
	p.6 ilmenite	44.5	53.2	0.1	0.1	0.2	0.2
	p.7 magnetite	0.0	93.8	0.1	0.2	0.1	0.0
	p.8 magnetite	0.0	93.8	0.2	0.1	0.1	0.1
L7,	p.1 magnetite	0.0	93.9	0.0	0.0	0.5	0.1
	p.2 ilmenite	47.4	50.2	0.5	0.1	0.2	0.0
	p.4 ilmenite and rutile	81.0	15.9	0.0	0.0	0.3	0.0
M4,	p.1 magnetite	0.0	93.1	0.0	0.1	0.1	0.0
	p.2 magnetite	0.0	95.2	0.0	0.2	0.2	0.0
	p.3 ilmenite	47.2	51.2	0.2	0.1	0.2	0.1
	p.4 magnetite	0.0	93.9	0.1	0.1	0.1	0.0
	p.5 magnetite with clay	0.0	82.8	0.9	0.3	2.2	0.1
	p.6 magnetite with clay	0.0	84.6	2.2	0.3	3.0	0.1
O4/5,	p.1 magnetite	0.0	94.1	0.0	0.0	0.2	0.1
	p.2 magnetite	0.0	95.2	0.0	0.2	0.2	0.0
	p.3 ilmenite	46.1	52.2	0.6	0.2	0.2	0.0
	p.4 ilmenite and rutile	80.5	17.9	0.0	0.0	0.3	0.0
	p.5 magnetite	0.0	93.6	0.0	0.1	0.1	0.1
	p.6 magnetite with clay	0.0	88.8	0.7	0.1	0.2	0.1
	p.7 magnetite	0.0	94.6	0.2	0.0	0.2	0.1
	p.8 ilmenite and rutile	82.4	14.2	0.2	0.0	0.1	0.2
	p.8a lamella of rutile	94.5	0.0	0.0	0.0	0.1	0.1
P5, 6,	p.1 ilmenite	46.0	53.9	0.1	0.0	0.2	0.0
	p.2 magnetite	0.0	94.2	0.2	0.1	0.1	0.0
	p.3 magnetite	0.0	93.9	0.0	0.2	0.3	0.1
	p.4 rutile	98.8	0.6	0.1	0.1	0.1	0.0
	p.4a ilmenite	45.4	49.2	0.2	0.1	0.5	0.1
W, upper part							
	p.1 ilmenite	43.0	54.9	0.1	0.0	0.1	0.0
	p.2 ilmenite	45.2	47.2	0.2	0.1	0.6	0.1
	p.3 rutile	98.8	0.6	0.1	0.1	0.1	0.0
W, lower part							
	p.4 ilmenite	45.5	53.9	0.0	0.0	0.3	0.0
	p.5 ilmenite	46.3	49.2	0.1	0.1	0.4	0.1
	p.6 rutile	96.8	1.6	0.0	0.0	0.0	0.0

(PSD) grains prevail in the rocks, but the vast majority of points in the Day diagram (Figure 5.18) lie in the multidomain (MD) region, which is due to the presence of a large number of superparamagnetic grains. In high fields, their M_s effect, as well as paramagnetism (if these grains are very fine), is eliminated. However, in a weak field of the order of H_C, the susceptibility of these grains is high and, therefore, remagnetization takes place in a field significantly smaller than the real value of H_C. Consequently, the ratio M_{rs}/M_s is overestimated. The superparamagnetic magnetization curve is not linear, as in the case of a paramagnetic substance (at room temperature), but has a hyperbolic form typical of ferri- and ferromagnetic species. The removal of the paramagnetic magnetization through a linear approximation does not eliminate the superparamagnetic contribution in M_s, whereas a superparamagnetic component is absent in M_{rs}. This decreases the ratio

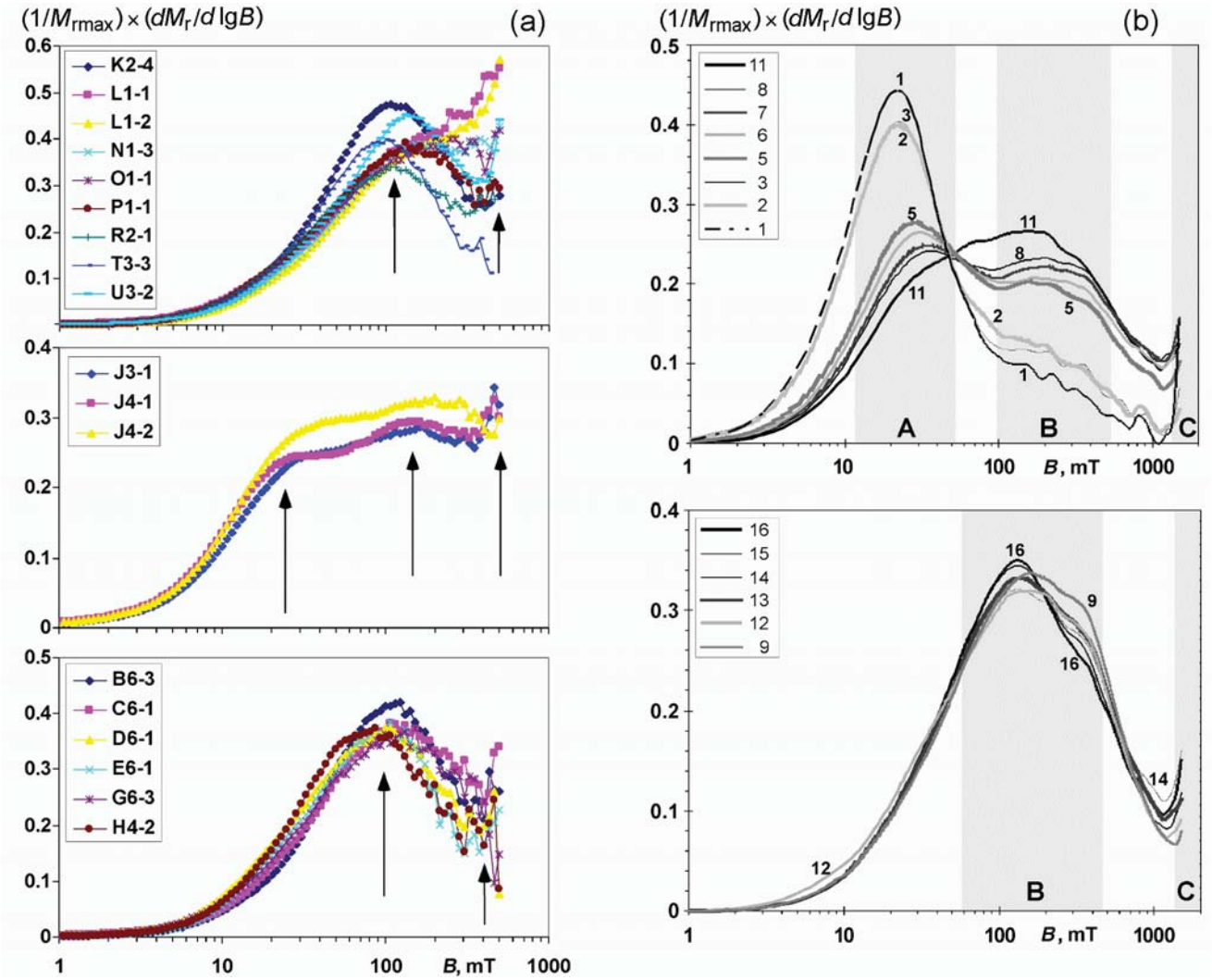

Figure 5.16. Coercivity spectra. (a) – Gams-1 section. The upper, middle, and lower plots are obtained, respectively, from samples of the upper (Danian) part of the section, boundary layer **J**, and lower (Maastrichtian) part of the section. (b) – Gams-2 section, the boundary bed and lower part of the overlying Danian deposits. The upper and lower plots are obtained, respectively, from samples of the boundary bed dominated by low-coercivity material and Danian deposits with absent low-coercivity phase.

M_{rs}/M_s and, as a result, the points in the Day diagram are displaced down- and rightward. Overall, notwithstanding distortions in the values themselves, the general tendency of the H_{cr}/H_c versus M_{rs}/M_s is well seen in the diagram (Figure 5.18). The Day diagram (Figure 5.18) and Figure 5.17 show that the finest SD magnetic grains are present in the lens **K** and layer **T**. On the whole, the Maastrichtian limestones are dominated by larger PSD grains close in size to MD particles, while hard fine magnetic grains of SD or nearly SD sizes prevail in the sandy-clayey sediments of the Danian. The smallest H_{cr} value of magnetic grains in samples from the layer **J** (Figure 5.17, Table 5.1) has no signatures in M_{rs}/M_s and H_{cr}/H_c, thereby emphasizing the coercivity independence of the size of magnetic grains; apparently, H_{cr} is controlled by the presence of magnetically soft nickel and magnetite formed from Fe-sulfides (see Gams-2).

Figure 5.19 presents the curves of magnetization of superparamagnetic particles in the studied samples up to fields of 100 mT. For clarity, the curves are normalized to the superparamagnetic magnetization maximum. They can yield evidence for the predominance of the large or fine superparamagnetic grain size in the spectrum. Very rapid saturation points to the presence of relatively large grains, and vice versa. On the

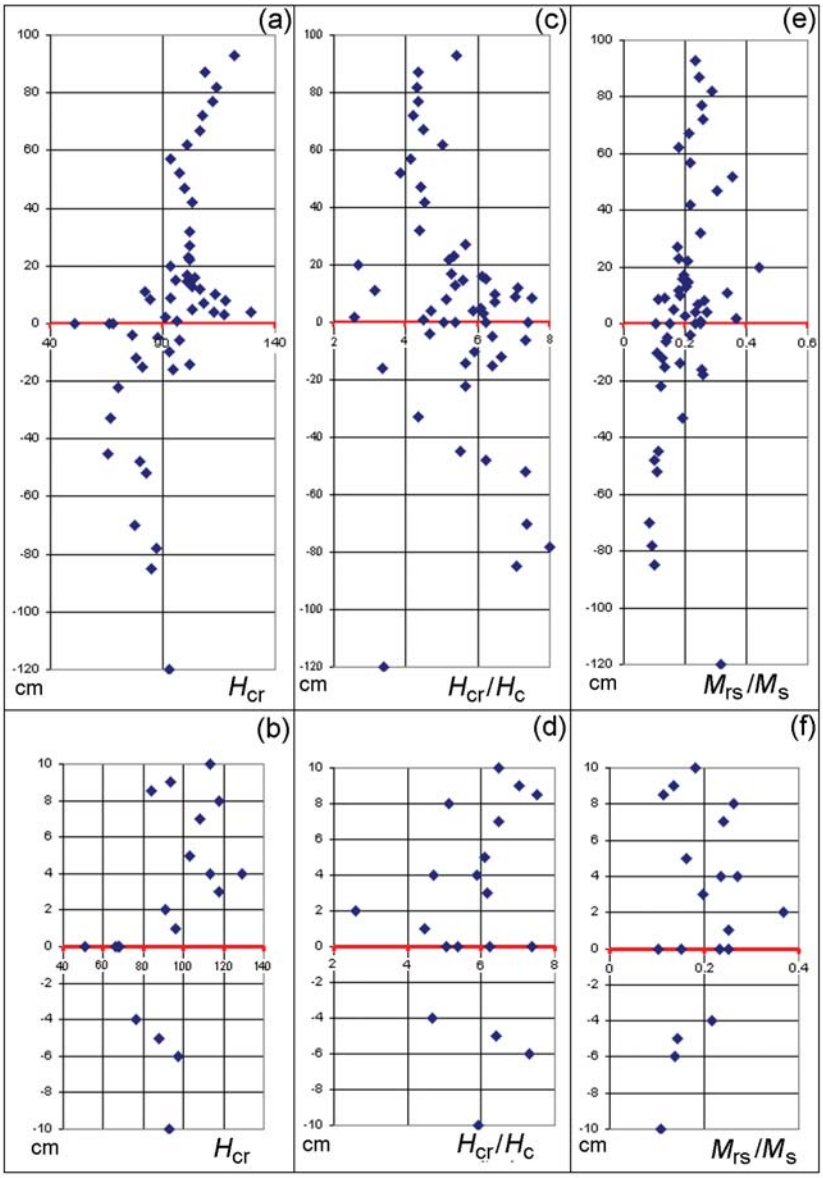

Figure 5.17. Behaviour of (a, b) – remanent coercivity H_{cr} (mT), (c, d) – ratio of remanent coercivity to coercivity H_{rc}/H_c, and (e, f) – ration of saturation remanent magnetization to saturation magnetization M_{rs}/M_s in the Gams-1 section: (a, c, e) – along the section; (b, d, f) – in the $\pm$20 cm interval.

other hand, the presence of grains with large M_s values is favorable for more rapid saturation. Our examples show that the saturation rate in samples from the layer **J** is considerably higher compared to other samples of the section, indicating that larger and probably more magnetic grains are present in J samples. The saturation is slowest in samples of the Danian sandy-clayey rocks; i.e. they contain the finest and probably least magnetic superparamagnetic grains, for example, those of goethite and hemoilmenite, which are significantly more abundant in the Danian sediments as compared with the Maastrichtian marls (Figure 5.5, Figure 5.8, Figure 5.19).

Now we consider how such coercivity spectrum characteristics as the position and amplitude of main extrema correlate with the content of magnetic minerals (Figure 5.20). All minerals (particularly goethite) correlate weakly with the position of spectral maximums; we relate this to the fact that the sediments possibly contain a complex set of iron hydroxides including both high-coercivity grains of acicular goethite and its low-coercivity earthy forms, as well as paramag-

netic hydroxides of iron. A more distinct correlation is observed between the concentrations of goethite, magnetite, titanomagnetite, and hemoilmenite on the one hand and the value of the coercivity spectrum minimum on the other hand, particularly in the sandy-clayey rocks (Figure 5.20). Grains of metallic nickel (its alloy with iron) can also contribute to the low-coercivity part of the spectrum. However, the results of detailed study of the boundary layer (see below) show that this is unlikely. No correlation is found in the case of metallic iron, which can be accounted for by its small concentration.

Anisotropy. The anisotropies of the magnetic susceptibility A_χ and the saturation remanence A_{rs} were measured. All minerals, magnetic, superparamagnetic, paramagnetic, and diamagnetic, contribute to the former, whereas the latter is due solely to magnetic minerals. With rare exceptions, both types of anisotropy behave in a similar way (Table 5.1). The A_χ values of the main group lie within the range 1.0–1.1 and only four samples yielded $A_\chi > 1.1$, while the A_{rs} values of the main group range within 1.12–1.36 and only four samples have $A_{rs} \leq 1.11$. Evidently, this is due to the fact that paramagnetic and diamagnetic parts of the sediments are, on the whole, isotropic and, although calcite and clayey minerals are anisotropic A_χ = 1.13 in calcite and 1.2–1.35 in clays, while quartz is isotropic [*Rochette et al.*, 1992], the distribution of their symmetry axes in the studied sediments is nearly chaotic. Therefore, the magnetic susceptibility anisotropy is controlled in our case by magnetic minerals. Values of A_{rs} show that the studied sediments, with rare exceptions (the horizons **K** and **T**), are anisotropic and their anisotropy is weakly dependent on the rock composition. The A_{rs} anisotropy in the layers **A** to **R** vary within close limits and noticeably increases in the upper horizons **U** to **W**. In each horizon, A_{rs} varies within narrow limits; an exception is the layer **J**, where anisotropy has a large scatter, from 1.02 to 1.32, which can be partly attributed to the presence of authigenic magnetite formed from Fe-sulfides (see the section Gams-2).

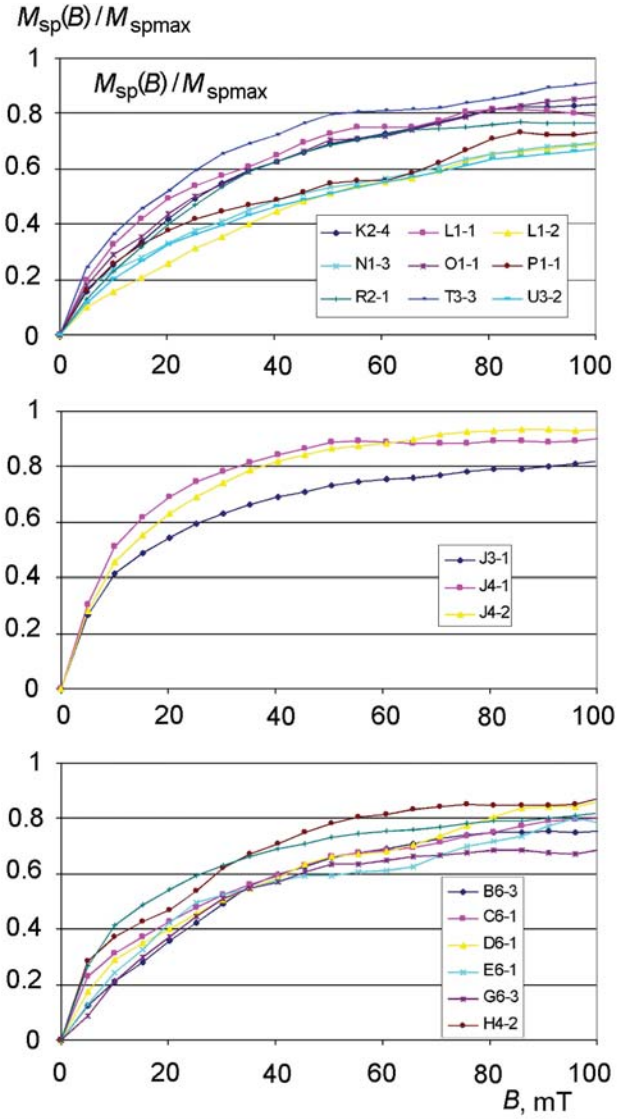

Figure 5.19. Magnetization curves of superparamagnetic grains in the Gams-1 section.

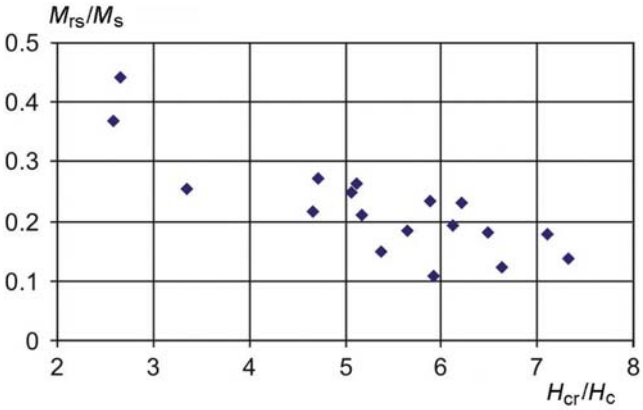

Figure 5.18. H_{cr}/H_c – M_{rs}/M_s variation along the Gams-1 section.

The vast majority of sediments of the section have a magnetic foliation ($E > 1$) and only a few horizons are characterized either by $E \sim 1$ or by very weak linearity (samples of the Maastrichtian layers **B, C, G**, and **H**) (see Table 5.1). All the aforesaid can be explained in terms of the presence of elongated grains of magnetic minerals, compaction of sediments, a certain role of flows, and so on. The presence of magnetic anisotropy and magnetic fabric is evidence for the terrigenous origin of the main mineral carriers of the magnetization in the sediments. Isotropic samples (K, T, and others) can contain authigenic magnetite.

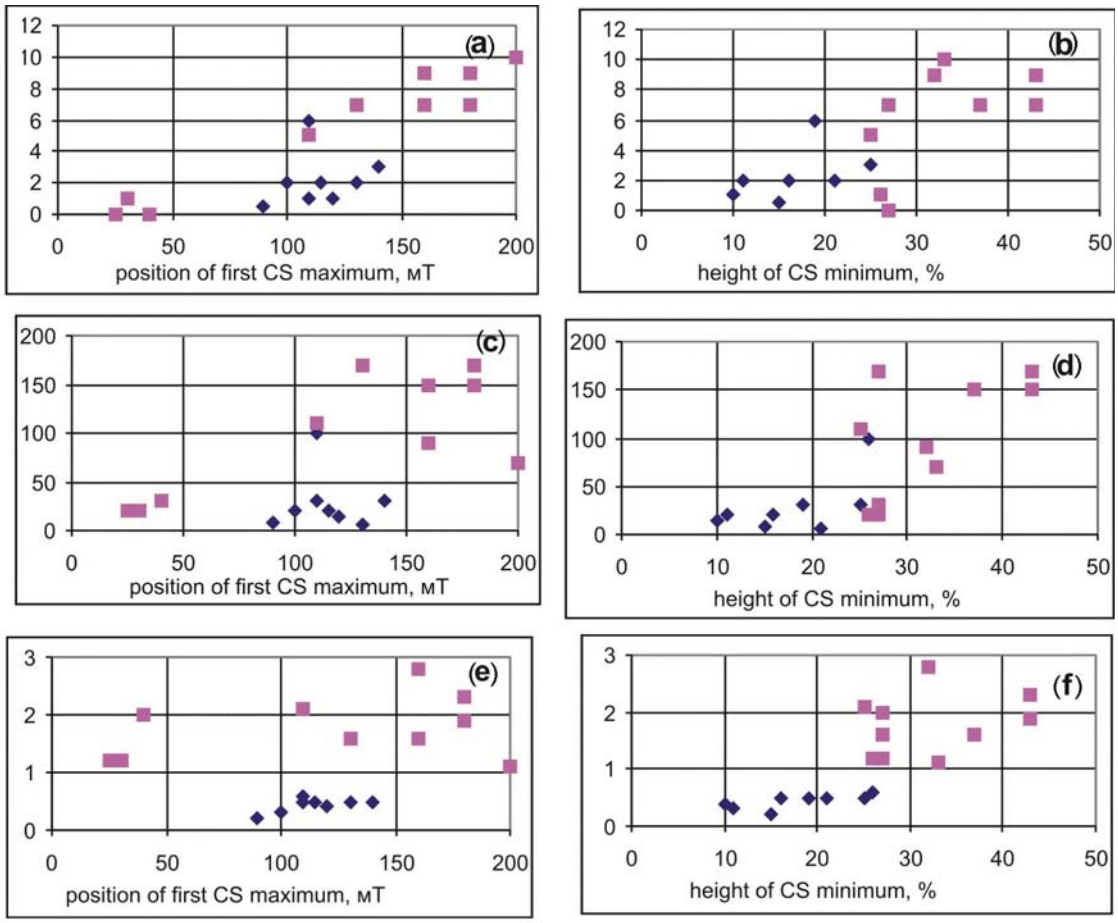

Figure 5.20. Correlation of some characteristics of coercivity spectra with concentrations of magnetic minerals in the Gams-1 section: (a, c, e) – position of the first maximum; (b, d, f) – relative value of the minimum; (a, b) – magnetite; (c, d) – hemoilmenite; (e, f) – goethite. The red squares and blue diamonds are sandy-clayey deposits and limestones, respectively.

Apart from the normal magnetic fabric, with the minimum susceptibility direction being perpendicular to the bedding plane, intervals of an inverse fabric, with the maximum susceptibility direction perpendicular to the bedding plane, are identified. The latter are the horizons **I, L** to **P, Q, V**, and **W**, although samples with the normal fabric are also present in these horizons (Table 5.1). Such an inverse magnetic fabric is inherent in siderite and other Fe-carbonate, and their easy magnetization axis is perpendicular to the "c"-axis of symmetry [*Rochette et al.,* 1992]. However, noticeable amounts of siderite and the like have not been found in the sediments studied; moreover, as noted above, the paramagnetic and diamagnetic parts of A_χ are rather isotropic. Consequently, the connection of the inverse fabric with magnetic minerals is more probable. Normal or inverse fabrics, as determined from the susceptibility and remanent magnetization, coincide and this emphasizes once more a significant role of magnetic minerals in the magnetic susceptibility (Table 5.1). An inverse fabric determined from the magnetic susceptibility is established for acicular goethite and elongated (uniaxial) grains of magnetite. In both cases, the susceptibility is lowest along the longer axis of a grain; i.e. the easy magnetization axis is perpendicular to the grain elongation [*Rochette et al.,* 1992] and the same is noted for the remanent magnetization in acicular goethite [*Bagin et al.,* 1988]. Inverse fabrics in rocks determined from the remanence have been repeatedly noted in literature and are often associated with the tectonic factor [*Rochette et al.,* 1992]. In our case, when sediments of the section are in an undisturbed and undeformed state, the tectonic factor cannot be invoked for the explanation of the inverse magnetic fabric. The value of magnetic anisotropy and specific features of magnetic fabric do not correlate with the composition and concentration of magnetic minerals, but a noticeable general tendency consists in that

solely the normal magnetic fabric is observed in the Maastrichtian marls, in which the goethite concentration is much lower compared to the Danian sandy-clayey sediments (Table 5.1). It is evident that the inverse fabric is primarily related to the presence of acicular goethite among iron hydroxides.

5.3.1 Paramagnetic magnetization

Paramagnetic magnetization is actually controlled by the total amount of iron in rock; in our case, iron concentrates in paramagnetic iron hydroxides, clayey minerals, and weakly ferromagnetic iron hydroxides (primarily minerals of the goethite group). This is evident from the positive correlation of paramagnetic magnetization, first, with the total iron in rocks determined from chemical analysis data and, second, with the goethite concentration (Figure 5.21 and Figure 5.5). The primary relation of paramagnetic magnetization to iron hydroxides is indirectly confirmed by the absence of positive correlation of iron with such clay elements as aluminium and by the strong negative correlation with SiO_2 [*Grachev et al.,* 2005]. Magnetic susceptibility also correlates with paramagnetic magnetization and goethite (Figure 5.1). Thus, the Maastrichtian and Danian deposits differ sharply in paramagnetic magnetization and magnetic susceptibility, i.e. in the iron concentration (the highest values of M_p are fixed in the interval 0–20 cm). The highest concentrations of goethite are also observed in this interval, particularly in the layer **J** (Figure 5.5). Against the large values of M_p in the Danian rocks, the layer **J** is distinguished by maximum values of M_p and χ whereas their minimum values are observed in a sequence of section layers beginning from the **J** top (Figure 5.1, Figure 5.21, Figure 5.22).

The distribution of total iron, expressed in M_p, χ, and goethite concentration, is also reflected in the M_s and M_{rs} values and, accordingly, in concentrations of such magnetic minerals as hemoilmenite, magnetite, and iron. However, this interval also includes samples in which the aforementioned minerals are absent (i.e. the above parameters, particularly the concentrations of metallic iron and titanomagnetite, exhibit large scatters). Moreover, the layer **J** is unrecognisable from both M_s and M_{rs}, while the concentrations of the aforementioned magnetic minerals in this layer are either very low or vanish (Figure 5.1, Figure 5.5, Figure 5.8, Figure 5.13, Figure 5.15).

The value of diamagnetic magnetization is more than two orders of magnitude lower than the paramagnetic magnetization of iron-bearing natural minerals [*Rochette et al.,* 1992], and its estimates appear to lie within determination and calculation uncertainties (Figure 5.21).

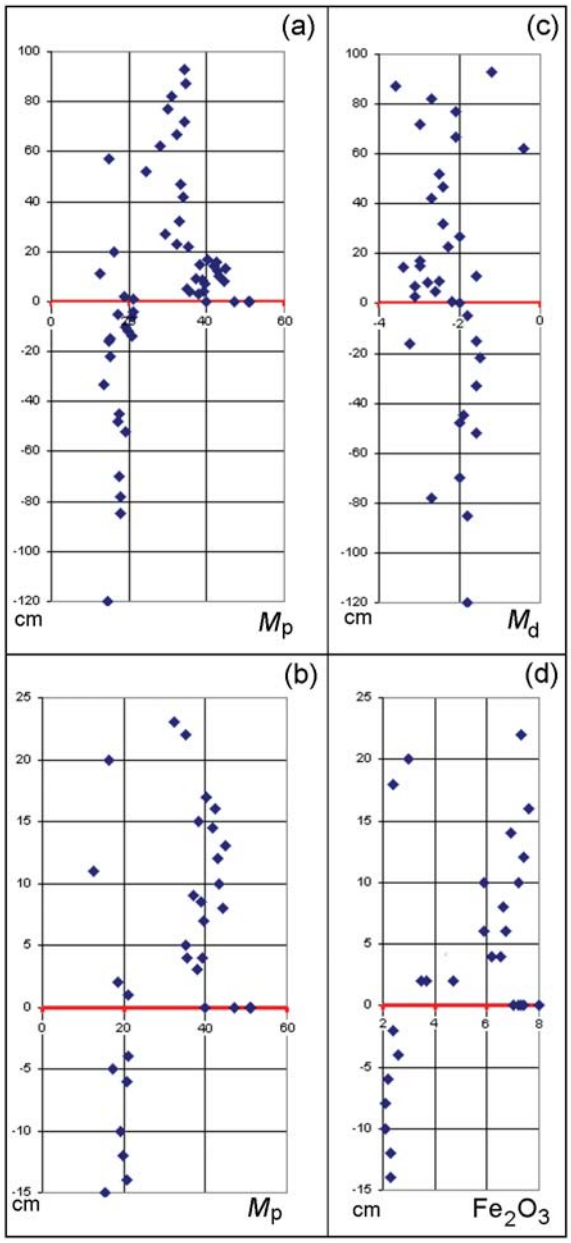

Figure 5.21. Variations in (a, b) – specific paramagnetic magnetization M_p, (c) – diamagnetic magnetization M_d, and (d) – bulk concentration of Fe_2O_3 (wt %). [*Grachev et al.,* 2005].

5.3.2 Discussion of petromagnetic results

The two levels of χ, M_{rs}, and M_s values reliably fixed in the Gams-1 section are (1) weakly magnetic marls of the Maastrichtian occurring below the layer **J**, the lens **K**, and a series of interlayers in the Danian sediments (t7, T3, t16, and t20; Table 5.1), and (2) more magnetic sandy-clayey deposits of the Danian (Table 5.1, Figure 5.1). These two levels are, in gen-

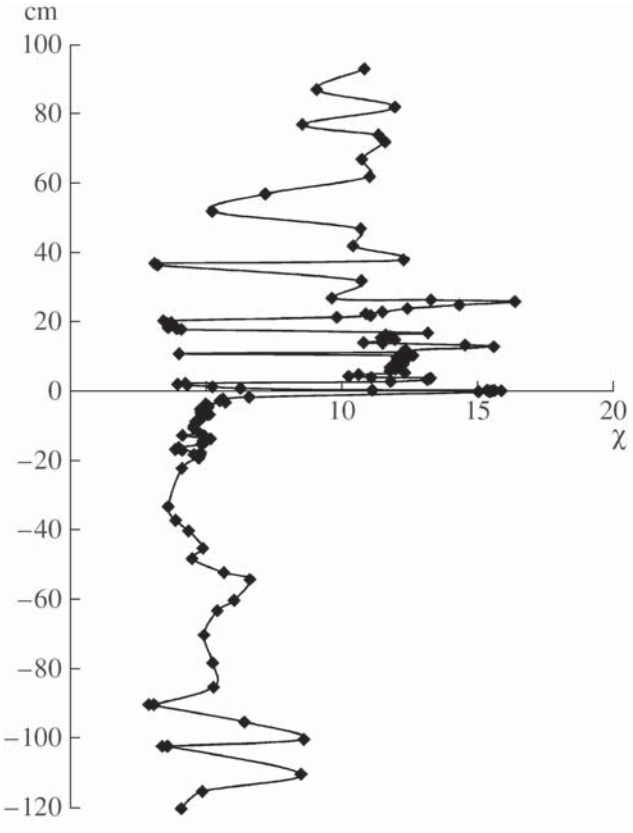

Figure 5.22. Rhythmically recurring drops in the Gams-1 total iron concentration expressed in the magnetic susceptibility χ (10^{-8} m^3/kg). The recurrence interval is 10 and/or 18–20 cm.

eral, consistent with the along-section distributions of magnetite (Figure 5.13), goethite (Figure 5.5), and paramagnetic magnetization (Figure 5.21), i.e. with the total iron concentration in the rocks, and the level are unrecognizable in the distributions of titanomagnetite (Figure 5.13) and metallic iron (Figure 5.15). Within these levels and first of all in the Danian part of the section, drops in the total iron concentration rhythmically recurring at intervals of about 10 and/or 20 cm are expressed in the paramagnetic magnetization and magnetic susceptibility (Figure 5.1, Figure 5.21, Figure 5.22); these intervals could correspond to the shortest periods (15 to 20 kyr – the average precession period of the Earth's rotation axis) of paleoclimatic variations forced by astronomical reasons [*Hinnov, Ogg,* 2007]. This rhythmicity is expressed much more weakly in the Maastrichtian interval of the section, which is apparently due to the weak magnetization of the limestones.

With rare exceptions, the studied sediments have a magnetic foliation pointing to a terrigenous origin of magnetic minerals. Many samples of sandy-clayey rocks have an inverse magnetic fabric. This is primarily related to the presence of acicular goethite, for which the inverse magnetic fabric is typical. Samples with low χ and M_p values (in particular, **K, S**, and **T**) are, unlike other samples, isotropic and distinguished by a significant rise in the amount of secondary magnetite formed due to laboratory heating (Table 5.3). This means that they contain authigenic (isotropic) magnetic and paramagnetic minerals (for example, pyrite) whose heating-induced oxidation results in the formation of magnetite. Such interpretation is supported by data from the Gams-2 section, where grains of pyrite and arsenopyrite are discovered in the lower part of the boundary layer (see below).

Judging from the coercivity spectra, ensembles of magnetic grains are similar in all samples (although they are somewhat different in marls and sandy clayey sediments) and their coercivity are high. An exception is the layer **J**, which contains lower-coercivity magnetic grains (with a coercivity maximum at 25–40 mT) along with a high-coercivity ensemble of magnetic grains similar to those in samples of the Danian sandy-clayey sediments. The high coercivity part of spectrum of the studied rocks is primarily controlled by goethite grains. The low-coercivity part of the **J** spectrum is likely due to grains of secondary magnetite formed from Fe-sulfides, similarly to the lower part of the boundary layer in the Gams-2 section (see below), and can also be related to the possible presence of metallic nickel and iron-nickel alloy.

The along-section distributions of goethite and magnetite are generally similar, mainly reflecting the joint accumulation of these minerals under lithologic control. As noted above, the goethite concentration rises in a jumplike manner beginning from the layer **J**, whereas the magnetite concentration is controlled lithologically with a certain lag: the concentration is very low (or even vanishes) in the Maastrichtian marls up to the layers **J** and t1 and the lens **K**, starts to rise significantly only in the layer **L**, i.e. higher than the K/T boundary by about 4 cm (later by ~4000 yr), and continues to increase up to the layer **O** (Figure 5.13).

The hemoilmenite concentration noticeably increases above the layer **J**, but abruptly drops at higher levels of the section and in the Maastrichtian limestones, marking the zone of stronger oxidation of ilmenite grains in the sediments. This is also the zone of higher accumulation of goethite and magnetite.

The titanomagnetite distribution is chaotic and unrelated to both the lithology of the section and the K/T boundary (Figure 5.13). The concentration of titanomagnetite, wherever it is fixed, varies insignificantly at all levels as distinct from magnetite, hemoilmenite, and goethite. One may state that the presence of titanomagnetite is unrelated to the lithology of the section and,

taking into account its composition typical of basalts, most likely characterizes volcanic eruptive activity and its eolian dispersal.

The along-section distribution of metallic iron is rather chaotic and its scatter in concentration between <0.0001 and 0.0015%. We relate its origin to cosmic dust and meteorites.

An exception against this general background is an anomalous peak of paramagnetic magnetization and magnetic susceptibility in the layer **J**. This is related to the high total concentration of iron that is predominantly present in hydroxides, both paramagnetic and weakly ferromagnetic (goethite); i.e., an abrupt jump in the iron accumulation occurs beginning from the layer **J**. The total concentration of magnetic minerals does not distinguish the layer **J** among other horizons of the section (Figure 5.1), but minimum coercivity values are noted in the **J** samples (Figure 5.16 and Figure 5.17). We relate the latter circumstance to the fact that nickel, iron-nickel alloy, and magnetite formed from pyrite are present in the layer **J** (see below, the section Gams-2). As noted above, metallic nickel and its alloy with iron occur in the layer **J** locally and very irregularly. This phenomenon has not been observed in other sections, while iron hydroxides in the K/T boundary layer occur in anomalous concentrations at a regional and possibly global level.

5.4 Characterization of the Boundary Layer in the Gams Sections

Above we already noted specific features of the boundary clay layer. Based on data of petromagnetic and microprobe studies, we present here a layerwise description of this layer as constrained by data from the sections Gams-1, Gams-2A, Gams-2B, and Gams-1B.

Gams-1 (layer J.) Sample J6 was divided into six interlayers (Gams-1A) and TMA was performed for each of them. Moreover, in order to perform the electron microprobe analysis, magnetic minerals were extracted from each of the interlayers with the help of a powerful constant magnet. The size of the extracted particles varied from a few fractions to a few tens of micrometer. We also studied magnetic properties of boundary layer from other section the Gams-1B at five levels (Table 5.2, Table 5.5). Below we characterize the J6 interlayers (Gams-1A, from bottom to top).

$J6_1$. According to TMA data (Figure 5.23a), the sample contains noticeable amounts of titanomagnetite with T_C = 540°C with a concentration of ∼0.2%. The presence of titanomagnetite is supported by microprobe data: grains of titanomagnetite and ilmenite, occasionally as intergrowths, are discovered. The composition of the titanomagnetite grains (Table 5.6) is at variance with Curie point data, implying that they experienced multiphase alteration (oxidation and decomposition). The grains are fine, oxidize and disappear during heating, as is seen from an abrupt drop in the magnetization value after the first heating to 700°C, and are partially homogenized (a leftward shift of the Curie point to 510°C after the first heating (Figure 5.23a)), which additionally decreases the magnetization. The inflection at ∼150–300°C, absent in the second heating curve, is apparently related to maghemite transformed into hematite at these temperatures. Its concentration amounts to ∼10% of the titanomagnetite concentration. Maghemite is found in nearly all interlayers (Figure 5.23).

$J6_2$. The TMA data (Figure 5.23b) show that the sample contains (a) ∼0.002% magnetite with $T_C \approx 570$°C, (b) ∼0.2% hemoilmenite with $T_C \approx 270$°C (recognizable in the TMA curves of the second and third heatings), and (c) metallic iron (heating of the sample only to 700°C cannot provide reliable TMA constraints on the presence of iron, but the microprobe detected an iron microspherules). The paramagnetic material makes a significant contribution to the magnetization. Fine titanomagnetite grains (fractions of micrometer to a few micrometers) were not identified in this sample. The concentration of magnetic minerals is about 20 times lower as compared with the interlayer $J6_1$.

$J6_3$. The TMA data are similar to those obtained from $J6_1$ and reveal the presence of (a) titanomagnetite with $T_C \approx 500$°C (due to partial homogenisation, the Curie point is shifted to 480°C and the magnetization sharply drops (Figure 5.23c)) and (b) magnetite with $T_C \approx 590$°C. This interlayer is distinguished from $J6_1$ by a significantly lower concentration of magnetic minerals: ∼0.01% titanomagnetite and ∼0.003% magnetite; the flat "tail" most likely points to the absence of metallic iron. The microprobe discovered a particle of magnetite and ilmenite more than 10 μm in size and numerous very fine particles, supposedly of magnetite.

$J6_4$. The TMA data (Figure 5.23d) point to the presence of (a) metallic nickel with $T_C \approx 350$°C (∼0.005%), (b) magnetite with $T_C \approx 590$°C (∼0.002%), and (c) iron (?) with $T_C > 730$°C (determined by extrapolation). A microprobe fixed flaky particles of metallic nickel in the magnetic fraction (see Chapter 6).

$J6_5$. According to the TMA data (Figure 5.23e), the interlayer $J6_5$ contains (a) ∼0.004% magnetite with $T_C \approx 590$°C, (b) 0.05% "hemoilmenite" with $T_C \approx 300$°C, and (c) iron (?) with $T_C \approx$ 700–750°C (extrapolation). The microprobe analysis of the magnetic fraction discovered a nickel grain with segregations of taenite. The

=

Table 5.5. Results of TMA of samples from boundary layer. Gams section

	First heating. T_c (percentage)								Second heating. T_c (percentage)					
no.	FS	goethite	GI	maghemite	MT	M-peak	"pyrite"	haematite	Fe	FS	GI	TM	MT	haematite	M_t/M_0
Gams-2A															
1		130(15)	?	350	?	535(1.2)	595(400)	680 (<5)	760 (<5)		250	480?		675	1.47
2		130(14)		350	?	540(0.9)	590(240)	680 (<5)	750(<5)		200	∼500		675	1.06
3		140(16)	270?	∼350	?	540(1.1)	590(260)	670(<5)			230	∼490		670	1.08
5		130(13)	260?	330	?	540(0.85)	590(240)	670??		∼150	?			670	1.46
6		130(13)	300	350	?	540(0.48)	590(190)	?		∼150	250?	400		?	1.38
7		150(13)	250	320?	?	540(0.41)	590(120)	680 (<5)			240?		570?	680	1.09
8		125(12)	250	300?	?	540(0.45)	590(150)	675(<5)		100	250		570?	675	1.09
9	130	130(4)	210	410	590(20)	no				130		530	575	675	0.99
11		120(11)	250	310	?	545(0.4)	590(130)	680??		150	250	510	580	680	1.14
12		140(6)	220?	300	590(10)	0	no	670??	760?		220	520?	570?	670	1.04
13		140(4)	230	300?	580(30)	0	no	660(<5)	770(<5)		180	520	570	670	0.93
14		140(5)	230	300?	580(30)	0	no	660(<5)	770(<5)		180	520	570	670	0.98
15		140(5)	230	300?	580(30)	0	no	660(<5)	770(<5)		180	520	570	670	0.95
16		120(4)	230?	390	585(30)	0	no	680??	760??		260	520	585	675	0.9
Gams-2B															
5		120(10)	230?	430	585(30)	0	no	680	0			510(<5)	580	670	1.2
3		120(12)	270	330	?	545 (0.4)	585(130)	670	0	100?		510(<10)	580	670	1.13
2		120(10)	260	320	?	540(0.9)	590(260)	680(<5)	0	100	250	510(25)	580(40)	680	1.6
1		130(8)	260	310	?	550(0.45)	590(140)	680?	750(<3)		220	520?	575	670	1.1
Gams-1															
$Jtop$		130(10)		350	0	0	no	660(20)^{ast}	740(10)			540(10)			0.88
$J3$		130(12)	260	350	585(20)	?	?	0	0			510	580		1.08
$J2$		130(10)	260	320	585(15)	0	no	0	750(<1)	H		410(20)	580		0.92
$J1$		120(10)	250	380	580(20)	?	?	0	0	100?	270			660	0.98
$J0$		130(10)		380	580(30)	0	no	680(<3)	770(<1)?	160		460(25)	580		0.87

Note: M-peak – temperature of the maximum of $M_i(T)$ curve (the relative height of maximum is given in parentheses); "pyrite" – Curie point of magnetite, formed from pyrite during TMA (laboratory heating), relative value of magnetization obtained by extrapolation of the $M_i(T)$ curve from peak to room temperature is given in parentheses. * – FeNi-alloy. The rest of notation is the same as in Table 5.2.

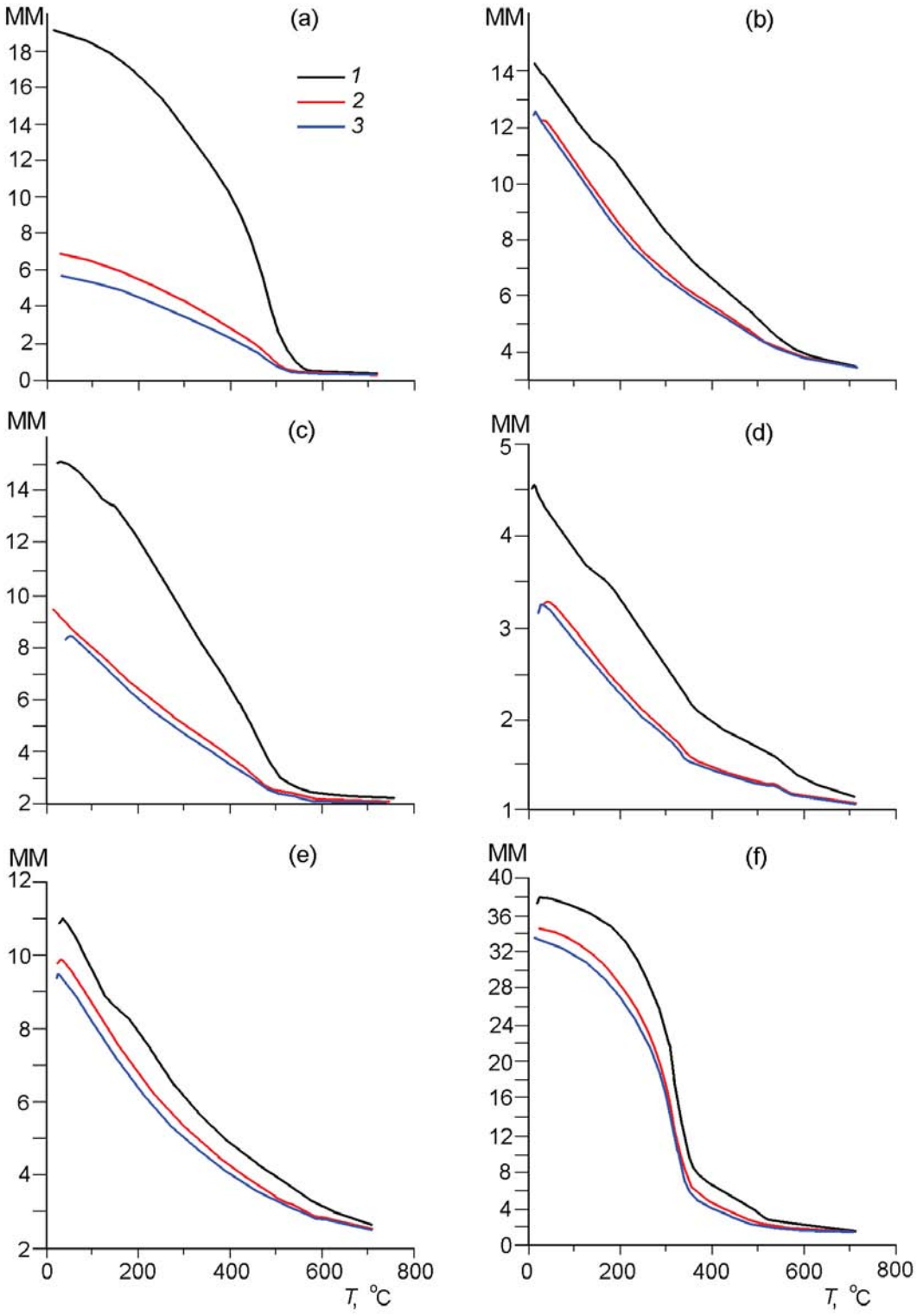

Figure 5.23. Data of the layerwise thermomagnetic analysis of the Gams-1 boundary clay layer J6: interlayers (a) – $J6_1$, (b) – $J6_2$, (c) – $J6_3$, (d) – $J6_4$, (e) – $J6_5$, and (f) – $J6_6$. The black, red, and blue curves are obtained, respectively, during the first, second, and third heatings.

Figure 5.24. Enumerated are interlayers fragments from which were taken for the study of magnetic properties. The hatched line shows the top of the Gams-2A boundary bed. The visible thickness of the bed is 36 mm.

TMA analysis did not detect such grains, i.e. these are single grains.

J6$_6$. The TMA data (Figure 5.23f) fix (a) ~0.4% nickel with $T_C \approx 350$°C and (b) ~0.1% titanomagnetite with $T_C \approx 520$°C. The presence of these components is supported by microprobe data. The enrichment in nickel microspherules is local because such a pattern was not discovered in none of the J6 fragments (see above).

Gams-2 section. Two series of samples from the boundary clay layer ~4 cm thick including overlying sandy-clayey sediments were examined: Gams-2A (Figure 5.26a), and Gams-2B (Table 5.2, Table 5.5, Figure 5.23, Figure 5.24, and Figure 5.26). For comparison, data on the magnetic properties of the Gams-1B boundary layer are also presented. The division into the boundary layer and Danian deposits (Gams-2A) is supported by petromagnetic data: it is seen clearly from the distributions of goethite and "pyrite" and the coercivity spectra H_{cr} and less distinctly from data on magnetite, titanomagnetite, and M_{rs}/M_s (Table 5.2, Table 5.5, Figure 5.16b, Figure 5.25, Figure 5.26, and Figure 5.27).

The total concentration of magnetic minerals is constrained by the values M_s and M_{rs} exhibiting mutually consistent variations (Figure 5.23): the concentration of magnetic minerals rapidly increases from the base of the boundary layer of Gams-2A section to the 10-mm level, above which it decreases rather smoothly. The smallest values of H_{cr}, M_{rs}/M_s, and H_{cr}/H_c are fixed at the very base of the boundary layer; H_{cr} smoothly increases within the boundary layer from 20 to 100 mT. Similar behavior of these characteristics is noted across the Gams-1B layer **J** (Table 5.2, Figure 5.23), whereas small values of M_{rs}, M_s, and H_{cr} and their rise are not observed in the Gams-2B adjoining Gams-2A, i.e. the accumulation regime of magnetic minerals changes significantly. The large values H_{cr}/H_c = 5–6 together with the values M_{rs}/M_s = 0.22–0.38 (Table 5.2) are evidence for strong underestimation of H_c due to the presence of a large number of superparamagnetic particles (see the section Coercivity).

A significantly different pattern is observed in the Gams-2A Danian sandy-clayey deposits (samples 9 and 12–16, Figure 5.24). The concentration, composition, and structural features are quite homogeneous here: M_{rs} and M_s vary within narrow limits (Table 5.2, Figure 5.23), and the coercivity is stably high in the approximately the same interval (Figures 5.16b, 5.23c, and 5.23d); i.e. this is the effect of high-coercivity fine magnetic grains similar in composition. Such a high coercivity is fixed in the Gams-1 Danian sandy-clayey deposits, and its contribution to the coercivity spectra of the layer **J** noticeably drops, which is accompanied by the corresponding drop in the H_{cr} value (Table 5.1, Figure 5.17). Comparison of the coercivity spectra of the boundary layer in Gams-1 and Gams-2A (Figure 5.16) shows that the **J** spectra are most similar to the spectra of the Gams-2A levels 8–11, where the presence of low-coercivity material is less pronounced. The coercivity spectra of Danian deposits are similar in the Gams-1 and Gams-2A sections (Figure 5.16). The high coercivity part of the spectrum similar to that observed in samples of rocks above the boundary layer is present both in samples of the Gams-2A boundary layer and in Gams-1B samples of the layer **J** (Figure 5.16).

The value of paramagnetic magnetization in the boundary layer is similar to or even higher than in Gams-1B and 2B, and its variation pattern is very close to that of M_s and particularly M_{rs} (Figure 5.23); i.e. magnetic and paramagnetic minerals were accumulated concurrently. The largest value of M_p is fixed at the same 10-mm level (interval of samples 6–8, see Table 5.2 and Figure 5.23), near which the coercivity spectra are most close to those of the layer **J**. The value of M_p drops appreciably at the base of the boundary layer. The lowest concentrations of Gams-2A magnetic minerals determined from both M_{rs} and M_s are also fixed here (Figure 5.23). Such a deep drop in M_p is not observed in the Gams-2B and Gams-1B sections.

As seen from TMA and microprobe analysis data (Table 5.5, Figure 5.25), the composition and concentration of magnetic minerals do not differ significantly from those in the layer **J** of Gams-1 except for nickel.

The main magnetic minerals present in boundary layers of the Gams-1B, 2A, and 2B sections are as follows.

As in the layer **J** (Gams-1A and 1B), **Ni-bearing ferrospinel**s (T_C = 60–150°C) are present in several sam-

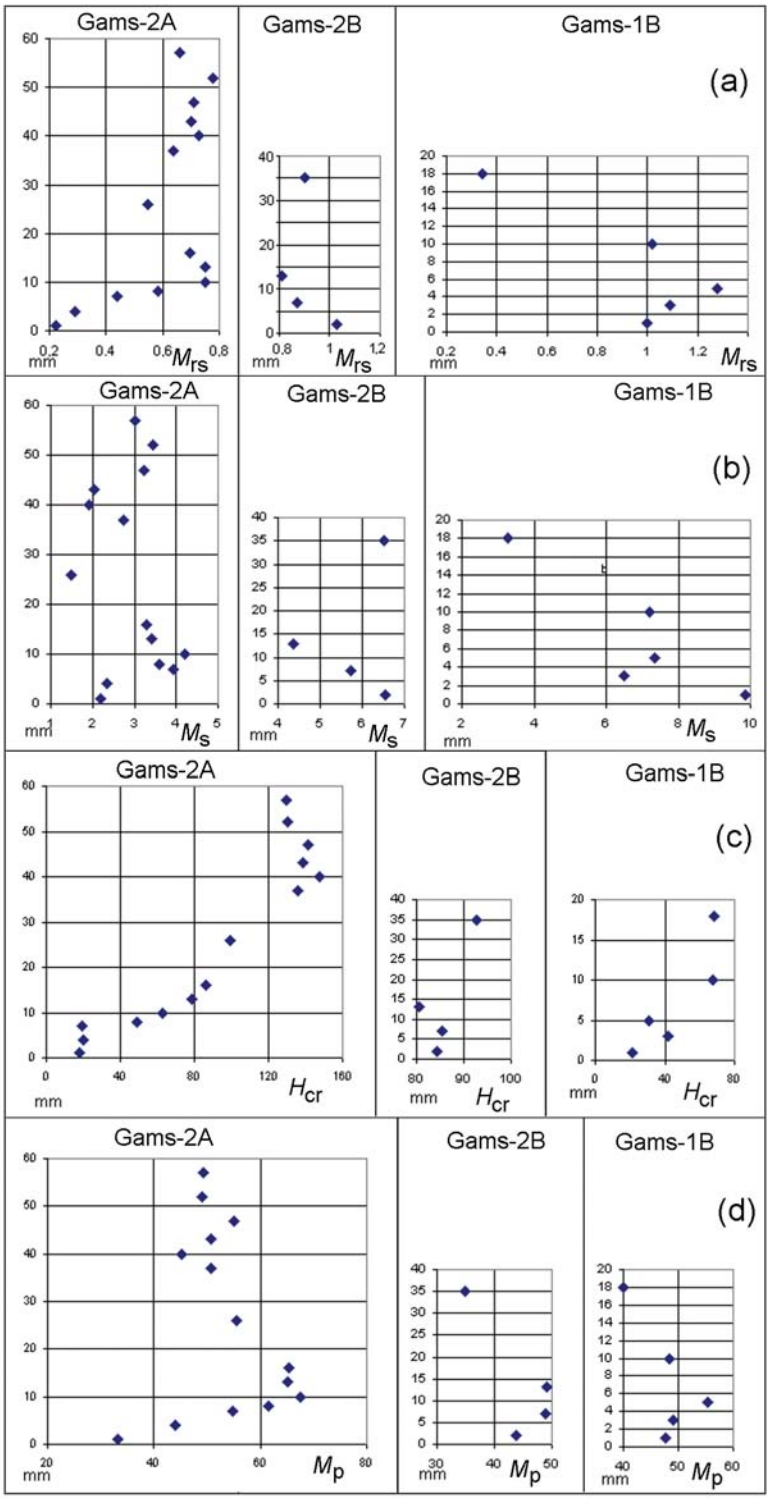

Figure 5.25. Magnetic properties of samples from the boundary layer and overlying sediments of the Gams-2A, Gams-2B, and Gams-1B sections: (a) – M_{rs} (10^{-3} Am^2/kg); (b) – M_s (10^{-3} Am^2/kg); (c) – H_{cr} (mT); (d) – M_p (10^{-3} Am^2/kg).

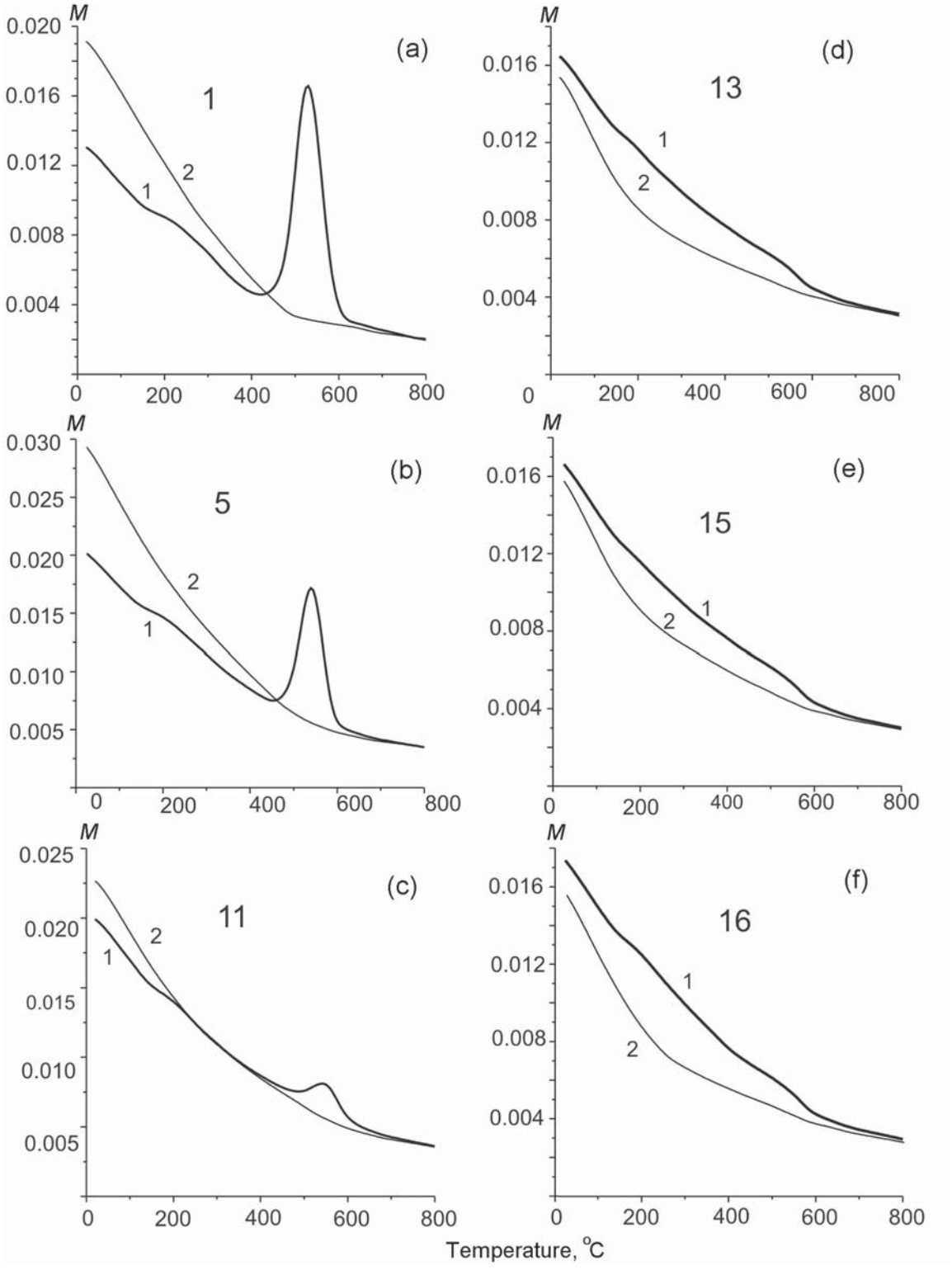

Figure 5.26. Examples of the curves $M(T)$ from Gams-2A boundary clay samples.

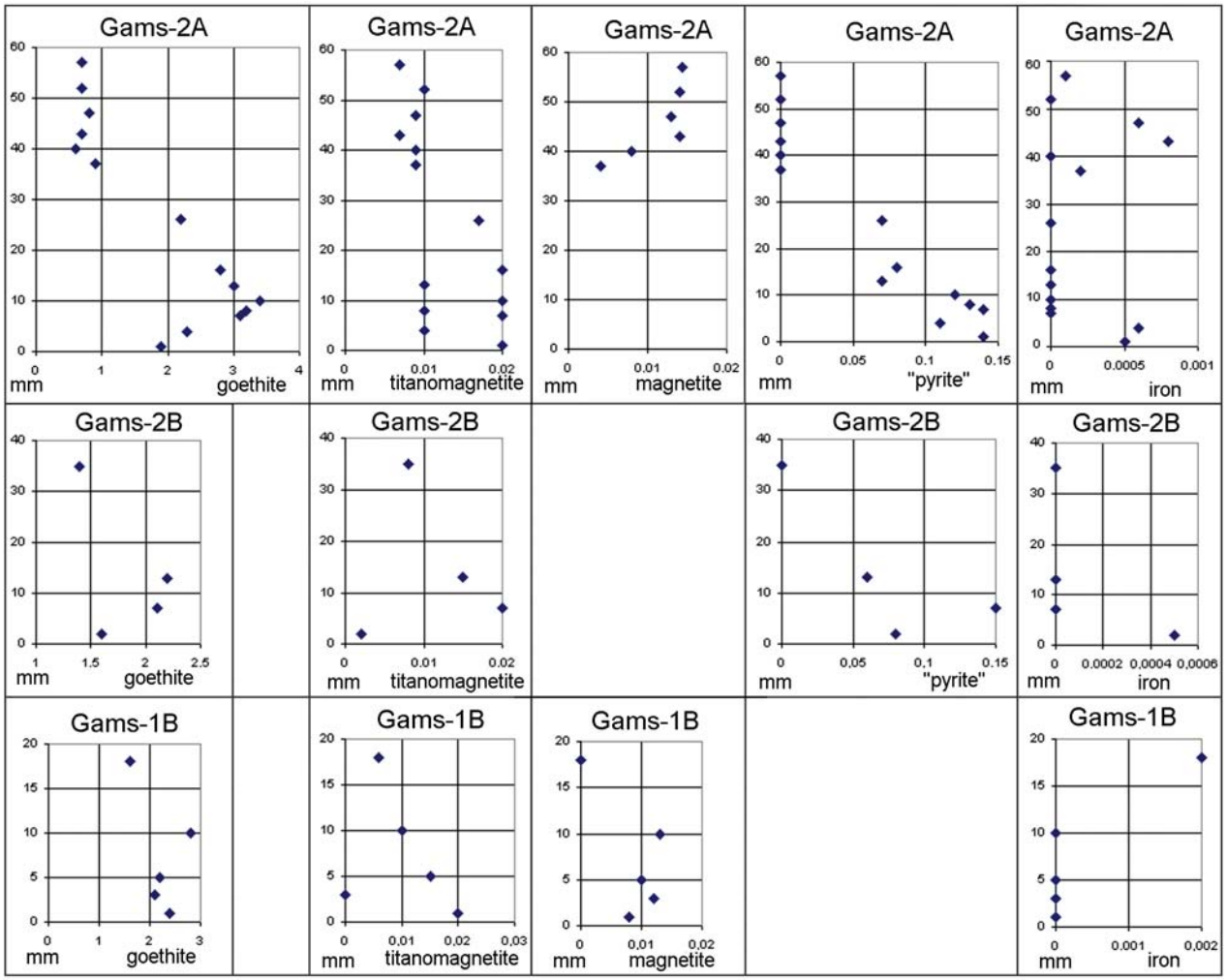

Figure 5.27. Concentrations of magnetic minerals in the Gams-2A, Gams-2B, and Gams-1B sections: titanomagnetite, magnetite, "pyrite" (magnetite formed from "pyrite" during laboratory heating of a sample), and metallic iron. The concentration of magnetite in initial samples of the Gams-2A and 2B sections could not be determined because of the presence of newly formed magnetite. No TMA features indicating the presence of "pyrite" are fixed in the Gams-1B section. A Fe-Ni alloy is fixed only in the uppermost pwqart of the section (Table 5.6).

ples from the Gams-2 boundary layer (Table 5.5). At all the levels of the Gams-1A boundary layer and in the lower and middle parts of the Gams-2B layer, crystals of chrome spinel and Ni-bearing ferrospinel of a complex composition were discovered in the heavy and magnetic fractions (Figure 5.26c, d) [*Grachev et al.*, 2007a]. The chrome spinel is distinguished by a high concentration of Cr_2O_3 (from 57 to 65%) and significant variations in MgO (7–18%) and FeO (13–23%). Spinel of such a composition is not ferromagnetic. The Ni-bearing ferrospinel is most likely magnetic. It is evident that precisely this ferrospinel (at least some of its grains with FeO $\geq$ 60%) is a source of magnetization with T_C = 60–150°C. The amount of these grains can significantly rise if an appreciable part of impurity elements in ferrospinel form "extrinsic" inclusions that do not contain iron or, on the contrary, inclusions are composed of magnetic ferrospinel. Ferrospinels are represented by octahedral crystals up to 10–15 μm in size (Figure 5.26c,d) because its sources are not far off. As seen from Figure 5.26c,d, sharp uncorrelated fluctuations in admixture concentrations are characteristic of the Ni-bearing ferrospinel composition. Such differences in the composition of the Ni-bearing ferrospinel grains, which are very close in the time and place of their deposition, and their very good preservation suggest, on the one hand, that their sources are different and, on the other hand, that the grains are close to the sources or, more specifically, that they have not experienced long-term reworking during their deposition. The combination of these facts implies that cosmic dust is the most probable source of these grains.

Table 5.6. Composition of titanomagnetite grains in the boundary layer of the Gams section

(a) Gams-1

Grain	Layer	TiO_2	FeO*	MgO	CaO	MnO	Cr_2O_3	Al_2O_3
1	$J6_1$	23.0	72.2	0.1	–	0.1	–	0.1
2	$J6_1$	20.8	74.9	0.1	–	0.2	–	0.2
3	$J6_2$	22.2	73.1	0.2	–	0.2	–	0.1
4	Bottom	13.76	75.93	–	–	0.04	–	–
5	"	8.79	80.38	–	–	–	0.04	–
6	"	13.06	76.93	–	–	–	0.07	–
7	Middle	15.97	75.39	0.08	–	0.12	0.07	–
8	"	12.30	78.54	0.08	–	–	0.04	–
9	"	13.73	77.02	–	–	0.16	0.07	–
10	"	15.13	75.54	–	–	0.07	0.09	–
11	Top	14.63	76.92	0.08	–	0.40	0.12	–
12	"	9.41	81.03	–	–	–	0.13	–
13	"	14.56	75.97	0.08	–	0.17	–	0.11
14	"	15.06	77.21	–	–	0.04	0.07	–
15	"	10.32	81.55	–	–	–	0.06	–

(b) Gams-2

Grain	Layer	TiO_2	FeO*	MgO	CaO	MnO	Cr_2O_3	Al_2O_3	SiO_2	NiO
16	2	10.88	79.71	0.03	0.01	0.35	0.11	0.06	0.02	0.02
17	2	12.46	78.06	0.00	0.00	0.37	0.10	0.05	0.00	0.00
18	2	34.54	58.28	0.01	0.01	0.00	0.26	0.06	0.00	0.01
19	2	15.17	75.67	0.04	0.00	0.25	0.06	0.04	0.03	0.00
20	2	13.09	77.13	0.05	0.01	0.38	0.08	0.01	0.00	0.00
21	2	16.43	74.44	0.03	0.01	0.00	0.32	0.01	0.01	0.00
22	3	14.46	75.90	0.02	0.01	0.00	0.15	0.10	0.00	0.00
23	3	11.74	79.72	0.07	0.01	0.29	0.08	0.05	0.00	0.06
24	3	13.41	77.24	0.03	0.00	0.00	0.10	0.10	0.00	0.01
25	3	15.01	74.08	0.02	0.01	0.03	0.13	0.11	0.00	0.00
26	3	20.66	71.58	0.04	0.02	0.28	0.12	0.06	0.02	0.00
27	3	12.58	77.84	0.03	0.00	0.16	0.09	0.06	0.01	0.04
28	3	15.79	74.92	0.03	0.01	0.17	0.17	0.06	0.01	0.01
29	3	13.43	76.40	0.03	0.00	0.00	0.15	0.08	0.05	0.00
30	3	11.37	79.36	0.00	0.01	0.12	0.19	0.12	0.02	0.00
31	3	15.12	75.84	0.05	0.00	0.21	0.10	0.05	0.00	0.03
32	3	14.05	76.51	0.00	0.01	0.14	0.10	0.02	0.01	0.00
33	3	8.73	80.46	0.00	0.02	0.01	0.20	0.10	0.02	0.02
34	3	15.72	74.18	0.00	0.01	0.01	0.21	0.08	0.00	0.02
35	4	13.50	77.93	0.00	0.02	0.03	0.26	0.12	0.01	0.05
36	4	11.06	79.98	0.04	0.01	0.05	0.12	0.06	0.00	0.00
37	4	32.31	60.00	0.00	0.00	1.05	0.03	0.02	0.01	0.00
38	4	13.88	76.77	0.04	0.01	0.04	0.09	0.10	0.00	0.01
39	4	13.81	77.64	0.04	0.02	0.17	0.03	0.00	0.03	0.01
40	4	14.04	76.66	0.03	0.03	0.23	0.07	0.07	0.07	0.01
41	4	29.38	66.71	0.01	0.01	0.42	0.04	0.00	0.00	0.00
42	4	13.73	77.05	0.01	0.00	0.10	0.10	0.10	0.03	0.00

Note: 1–3, heavy fraction from Gams-1A; 4–15, heavy fraction from Gams-1B; 16–42, heavy fraction from Gams-2B. In all tables, the asterisk means that all the iron is reduced to FeO.

The goethite concentration is similar to that in the layer **J** (Figure 5.25a) and varies in nearly the same manner as the paramagnetic magnetization: it smoothly increases from below, reaching a maximum at the same 10-mm level as M_p (Figure 5.25 and Figure 5.23), smoothly decreases in the upper part of the layer and, as in the Gams-1, section abruptly drops to 0.6–0.8% above the boundary with the Danian deposits (Figure 5.5b). The high coercivity implies that crystalline goethite prevails in the Danian sediments, whereas low-coercivity earthy goethite can be present in noticeable concentrations in the Gams-2A section and in negligible amounts in Gams-2B.

The magnetic fraction often contains spherules of goethite and hematite (Figure 5.24c,d) that are evidently oxidation products of metallic iron spherules; they are highly magnetic, which implies that metallic iron has quite probably been preserved at their centers.

Hemoilmenite with $T_C \approx$ 200–300°C is often present in samples from the boundary layer (Table 5.5) and is observed in the form of fine segregations in ilmenite grains that are products of ilmenite oxidation [*Grachev et al.*, 2005; *Pechersky et al.*, 2006a]. According to data of microscopic and microprobe observations, the boundary layer contains a noticeable amount of ilmenite grains.

Titanomagnetite ($T_C \approx$ 400–530°C), according to both MTA and microprobe data, is fixed ubiquitously in thin sections and in heavy and magnetic fractions (Figure 5.24f, Table 5.6); its along-section distribution is irregular and higher concentration compared to the Danian sediments (Figure 5.25), but its composition is very similar in the Gams-1 and -2 sections (Table 5.6a,b). The electron beam fall into either the titanomagnetite matrix (TiO_2 = 8–16%, Table 5.6) or ilmenite lamellae (TiO_2 = 29–34%, Table 5.6) that are, as a rule, noticeably smaller in size than the microprobe ($\sim$2 μm). This is the main cause of the fluctuations in the composition of grains measured by the microprobe. In all cases, the titanomagnetite compositions given in Table 5.6 correspond to calculated Curie points below 400°C, and the average concentration $TiO_2 \approx$ 15% correspond to $T_C \approx$ 300°C, which is below the measured values and points unambiguously to decomposition of titanomagnetite grains measured by the microprobe. The average concentration TiO_2 = 15% is smaller than the typical averages of rift and spreading basalts (TiO_2 = 20–25%), whose grain composition is uniformly stable [*Pechersky, Didenko*, 1995; *Pechersky et al.*, 1975]. On the other hand, titanomagnetite grains present at the base of the Gams-1A boundary layer ($J6_1$, Table 5.6) are typical of rift and similar basalts.

The main distinction of titanomagnetites of the Gams-1 and -2 boundary layers from titanomagnetites crystallizing in basaltic melts of different types is an *unusually small concentration of admixtures* (Table 5.6). Apparently, this specific pattern reflects the formation of titanomagnetite crystals from a volcanic aerosol.

Burov [2005] notes an abrupt rise in the magnetization of sediments caused by their enrichment in ash material beginning from the Permian-Triassic boundary, which reflects the global high volcanic activity at that time. It is very likely that a similar volcanic situation took place at the Mesozoic/Cenozoic boundary, producing a volcanic aerosol that contained titanomagnetite without admixtures.

Magnetite (T_C = 570–590°C) is fixed ubiquitously from TMA data (Figure 5.25). The compositions of many magnetite grains from the Gams-1 boundary layer were measured with a microprobe (Table 5.6). As distinct from titanomagnetites, they often include grains containing noticeable admixtures of Mg, Al, Mn, and Cr. Evidently, these are primary magmatic crystals. The Danian Gams-1 sediments are dominated by well-preserved single crystals of pure magnetite (Table 5.6; Figure 5.24) having evidently the same origin as the pure titanomagnetites (see above).

Magnetic fractions contain spherules of magnetite, hematite, and goethite that have likely formed due to oxidation of metallic iron spherules [*Pechersky et al.*, 2008].

Magnetite content in the 2A and 2B boundary layers not be determined because of magnetite newly forming during laboratory heating.

The boundary layer and Danian deposits sharply differ in thermomagnetic characteristics. The curves $M_i(T)$ are nearly the same as in the layer **J** (Gams-1) and overlying sediments (Figure 5.3c, Figure 5.3d, Figure 5.4c, Figure 5.4d, Figure 5.26a,b,c), whereas a peak above 500°C (a maximum at 540°$\pm$5°C) is present in the curve $M_i(T)$ from the boundary layer (Gams-2A and 2B). The peak height reaches a maximum at the base of the Gams-2A boundary layer, is somewhat larger in the Gams-2B layer, and regularly decreases to zero in the upper part of the layer. Upon reaching the peak, the curve $M_i(T)$ drops to zero at the Curie point (590–595°C), indicating that this is magnetite oxidized during laboratory heating (Figure 5.26a,b); with further heating of the sample to 800°C, the magnetite is oxidized to hematite. As a result, a significant part of the newly formed magnetite is destroyed, and it is almost unrecognisable in the second heating curve $M_i(T)$. As the peak significantly masks the interval 500–600°C, the first heating curve $M_i(T)$ yields no evidence for the initial (natural) magnetite and titanomagnetite, which are often present in Gams-1 section outside the layer **J** (Figure 5.13) and vary within wide limits, from 0 to 0.01–0.02%, in Gams-1A (Figure 5.26)

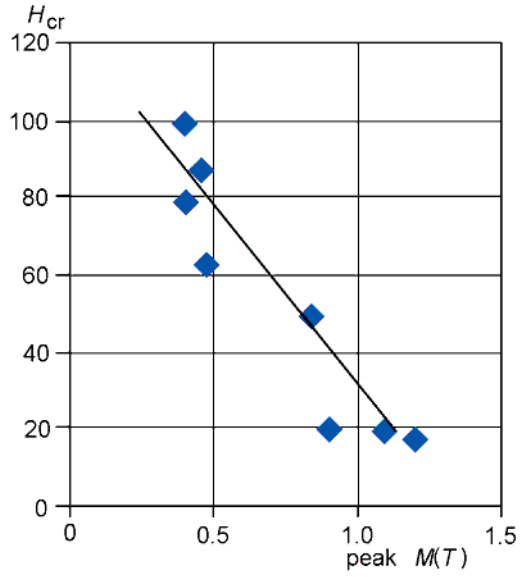

Figure 5.28. Correlation of the relative height of the $M(T)$ peak with H_{cr} in the Gams-2A section.

and Gams-1B (Figure 5.25). According to the second heating curves $M_i(T)$, titanomagnetite (in the Gams-1A and 1B) is present almost all over the boundary layer (Figure 5.25, Table 5.5). Magnetite is reliably fixed only in the Danian deposits, where it is not masked by magnetite newly formed during laboratory heating (Figure 5.25c). Therefore, no constraints are available on the natural magnetite in the boundary layer. Indirect evidence for its presence in Gams-2A is the distinct negative correlation of H_{cr} measured before heating (i.e., before the formation of magnetite) with the $M_i(T)$ peak height (Figure 5.28). The significant predominance of low-coercivity material (according to coercivity spectra and H_{cr}) implies that the amount of magnetite in the Gams-2A boundary layer is significantly larger than in the overlying Danian sediments. It is more natural to relate the formation of magnetite during laboratory heating to the fact that samples from the boundary layer contain iron sulfides such as pyrite and arsenopyrite fixed in the layer according to mineralogical observations. Origination of magnetite during heating of such minerals above 500°C is a common phenomenon considered as a diagnostic indicator of pyrite and arsenopyrite [*Novakova, Gendler,* 1995]. Accordingly, it is reasonably to suppose that some magnetite (about 0.05%) was present in Gams-2A samples before their laboratory heating. The relatively high coercivity of Gams-2B samples ($H_{cr} \approx$ 80–93 mT) indicates that before heating they contained magnetite in small concentrations, and the $M_i(T)$ peak is evidence that Fe-sulfides of the pyrite type are also present in the Gams-2B section. The amount of the newly formed magnetite reflects the amount of the Fe-sulfides ("pyrite"). If the decaying curve $M_i(T)$ is extrapolated above 500°C by a parabola to room temperature, the resulting value can be used for determining the amount of magnetite newly formed from "pyrite". Supposing that all pyrite was oxidized to magnetite, the magnetization of the newly formed magnetite can provide an estimate for the concentration of the original "pyrite" (more precisely, a lower limit for the possible "pyrite" concentration in a sample). Such estimates are presented in Figure 5.25. The "pyrite" grains are evidently very fine, taking into account that, even during the first heating, they are oxidized so easily to magnetite, which in turn are oxidized to hematite.

Metallic nickel (T_C = 360°C) and its alloy with iron. As we wrote, pure nickel was found in samples $J6_4$ and $J6_6$ and taenite was found at various levels of the Gams-1A boundary layer (see above and [*Grachev et al.,* 2008b]). Unlike the Gams-1A section, peculiarly shaped particles of a Ni–Fe–Mo alloy are found in the lower part of the Gams-2B boundary layer and more rarely in its middle part [*Grachev et al.,* 2008b]; they have Ni/Fe ≈ 5–6 and, therefore, are close in composition to awaruite. Such a ratio corresponds to Curie points of 410–430°C, but such a phase was not discovered from TMA data in the Gams-1 and Gams-2 boundary layers, probably due to an irregular distribution of grains of this alloy. Nickel and taenite particles of the Gams-1A type were not found in Gams-2.

Thus, we may state that, first, the Gams-1A nickel particles are homogeneous in composition and evidently formed from the one body (a meteorite); the Gams-2 awaruite particles are homogeneous in composition and, accordingly, also might have formed from the one body (a meteorite); however, both groups of particles significantly differ in composition and, therefore, should be related to different meteorites. Second, Gams-1 and Gams-2 particles differ in time: the former are located in the upper part of the boundary layer (Gams-1), and the latter in the lower part (Gams-2). In other words, these particles belong to meteorites of different ages and are associated with different *local impact events*.

Metallic iron with T_C = 750–770°C is discovered only in the lower part of the boundary layer, whereas in the Gams-1B section it is fixed only in the upper part of the layer (Table 5.5 and Figure 5.25), i.e. at the K/T boundary.

The analysis of data on the boundary layer in the Gams-1 and Gams-2 sections leads to the following conclusions.

(a) The boundary layers in the Gams-1A, 1B, 2A and 2B sections are similar as regards the set of such magnetic minerals as iron hydroxides, hemoilmenite, ti-

tanomagnetite, magnetite, hematite, and metallic iron.

(b) The boundary layers in the Gams-1 and Gams-2 sections differ in the composition and along-section position of metallic nickel and its alloy with iron: compositionally homogeneous pure metallic nickel is present in the upper part of the Gams-1 section, and taenite is found in different parts of the section; in the Gams-2 section, pure nickel is absent and a compositionally homogeneous Ni–Fe–Mo alloy (awaruite) is present at the base of the layer. Therefore, accumulations of nickel and awaruite particles are associated with falls of different small meteorites at different times. The effect of these falls is local and is not felt at a distance of about 0.5 km (the distance between Gams-1 and Gams-2)

c) A significant distinction between boundary layers in the Gams-1 and Gams-2 is that Fe-sulfides of the pyrite type are present in latter section. This is evidence for local occurrence of these minerals.

The distribution of Fe-sulfides across the boundary layer (Gams-2A and 2B) is more regular compared to nickel. First, Fe-sulfides are fixed at the base of the 2A and 2B boundary layers; their concentration is highest there and regularly decreases upward. Fe-sulfides of the pyrite type are absent in the Danian deposits above the boundary layer. A distinct negative correlation exists between the remanent coercivity, characterizing the initial state of magnetic grains in samples (before their laboratory heating), and the sharp rise in the magnetization during laboratory heating of samples from the boundary layer of the Gams-2A and 2B sections (the maximum at $540^\circ \pm 5^\circ$C); this correlation indicates that the material with a low coercivity (determined from both H_{cr} and the coercivity spectrum) is magnetite closely related to Fe-sulfides. By analogy, one may suggest that the low coercivity material in the lower part of the Gams-1B boundary layer is also magnetite. Previously we associated it with the presence of nickel, but the largest enrichment in nickel is fixed in the upper part of the Gams-1 boundary layer, where $H_{cr} > 70$ mT, whereas nickel is absent in its lower part, where H_{cr} = 30–40 mT.

d) Ni-bearing ferrospinel is present all along the boundary layer, and its composition varies within wide limits. The well-preserved shape of its crystals is evidence for nearby sources of ferrospinel grains and/or their rapid delivery into the sediment, for example, from the atmosphere, cosmic dust, and so on. It is natural to suggest that cosmic dust was the source of compositionally so heterogeneous Ni-bearing ferrospinel that arose at the same time and in the same place. Inclusions of Ni-bearing ferrospinel grains are met in particles of metallic iron and awaruite, indicating that they or at least some particles of both types have a common origin.

e) Particles of metallic iron are very rare in the boundary layer. They are noted in the upper and lower parts of the Gams-1 layer and in the lower part of the Gams-2 layer. Considering that, except the boundary layer, metallic iron particles are spread ubiquitously, at least in all of the studied sections including the K/T boundary, and their distribution in time is rather random, it is most likely that the source of the majority of the metallic iron particles is cosmic dust.

(f) The lower part of the layer **J** is noticeably enriched in titanomagnetite and ilmenite whose compositions are typical of rift and plume basalts. In the overlying layers, their concentrations sharply drop to a background level. Such enrichment in titanomagnetite is not fixed in the corresponding part of the Gams-2A section. Here, the titanomagnetite concentration varies throughout the layer thickness within narrow limits (0.01–0.02%) and even decreases at the base of the Gams-2B layer. Hence we may suggest that the interlayer $J6_1$ (Gams-1A and 1B) has recorded the precipitation stage of particles associated with a short-term volcanic eruption and that the precipitation process of titanomagnetite grains was very irregular in both time and space. It is noteworthy that, in both sections except the base of Gams-1A, the Ti concentration in titanomagnetites is appreciably smaller than in rift and plume basalts. All titanomagnetites of Gams-1 and Gams-2 typically have very low concentrations of impurities as compared with usual values in titanomagnetites of igneous rocks, where they generally attain a few percent. This distinction is possibly due to crystallization of the titanomagnetites from a volcanic aerosol. As distinct from titanomagnetites, many grains of magnetite from the boundary layer are characterized by higher concentrations of impurities. Possibly, impurity magnetites are primary magmatic products of acidic magmatism. Apart from this variety, well-preserved crystals of pure magnetite, evidently of nonmagmatic origin, are present in both the boundary layer and Danian deposits. The good preservation of the crystals is evidence for close sources of their accumulation in the sediments.

(g) Only the variations in the concentration of iron hydroxides are similar: it is smallest at the very base of the boundary layer and regularly increases to a maximum in the lower part of the layer ($\sim$10 mm from the bottom), after which it smoothly decreases. This is best expressed in the paramagnetic magnetization.

5.5 Comparative Characterization of Sections Including the K/T Boundary

As noted in Introduction, many researchers fixed the magnetic susceptibility peak at or near the K/T boundary in marine sediments. Thus, a rise in the magnetic

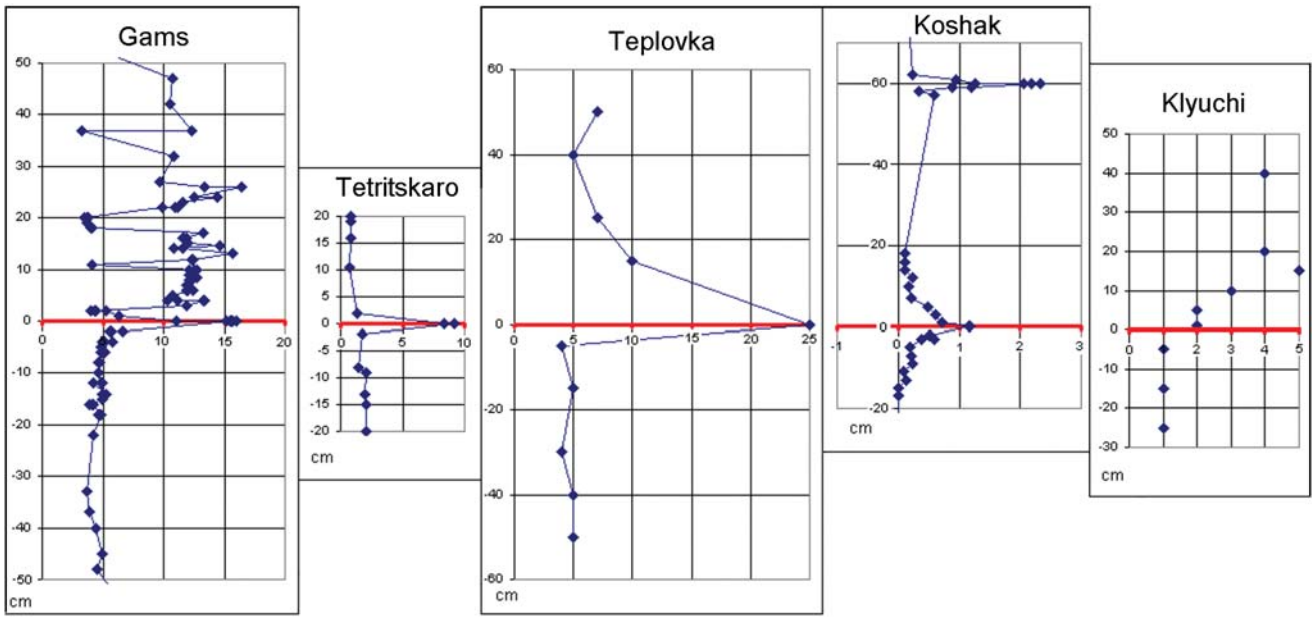

Figure 5.29. Distribution of the magnetic susceptibility χ (10^{-8} m^3/kg) along the Gams-1, Tetritskaro, Teplovka, Koshak and Klyuchi sections.

susceptibility at the K/T boundary has been fixed in one-third of cores sampling the known continuous sections of marine sediments; this rise varies in its time length from a very narrow peak to long time intervals of relative accumulation of iron-bearing minerals in sediments encompassing many hundred thousand years [*Pechersky, Garbuzenko,* 2005]. Anomalous behaviour of the magnetic susceptibility in the boundary layer at the K/T boundary is widespread in continental sediments, where it primarily reflects the accumulation of iron hydroxides. The following two types of anomalous behaviour are observed, depending on the lithology of a section.

1. Maastrichtian carbonate deposits are overlain by Danian sandy-clayey sediments. In this case, a sharp peak of the magnetic susceptibility is fixed in the boundary layer above which, in the Danian sediments, the susceptibility insignificantly drops but is still higher as compared with the Maastrichtian sediments. This pattern is characteristic, for example, of the sections Gams (Austria) [*Pechersky et al.,* 2006a], Teplovka (Volga region) [*Molostovsky et al.,* 2006], and Kubalach (the Crimea) [*Yampolskaya et al.,* 2004].

2. Only a sharp peak of susceptibility confined to a clay layer at the K/T boundary is observed in sections of carbonate deposits near the K/T boundary in-

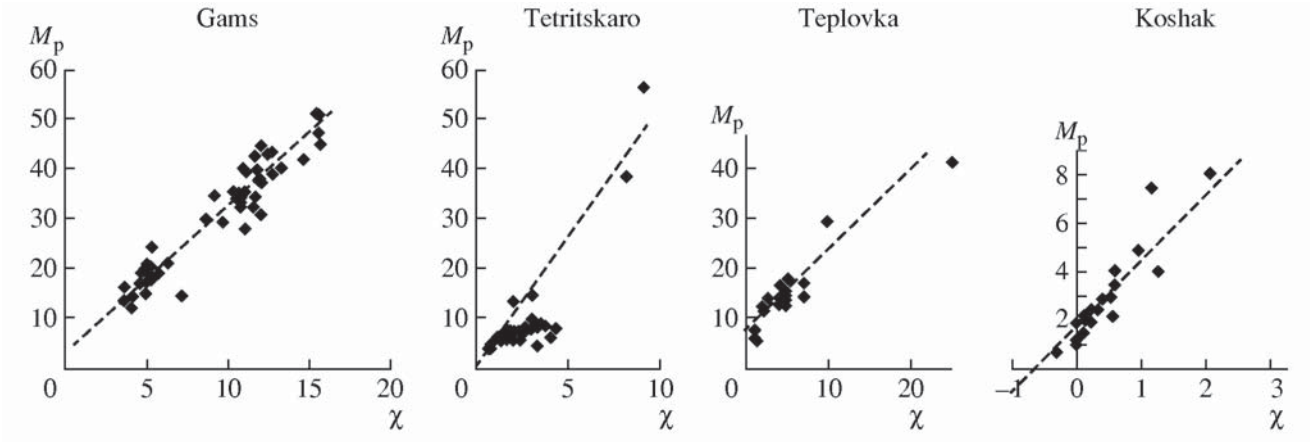

Figure 5.30. Correlation between the magnetic susceptibility χ (10^{-8} m^3/kg) and paramagnetic magnetization M_p (10^{-3} Am^2/kg) in the Gams-1, Tetritskaro, Teplovka, and Koshak sections.

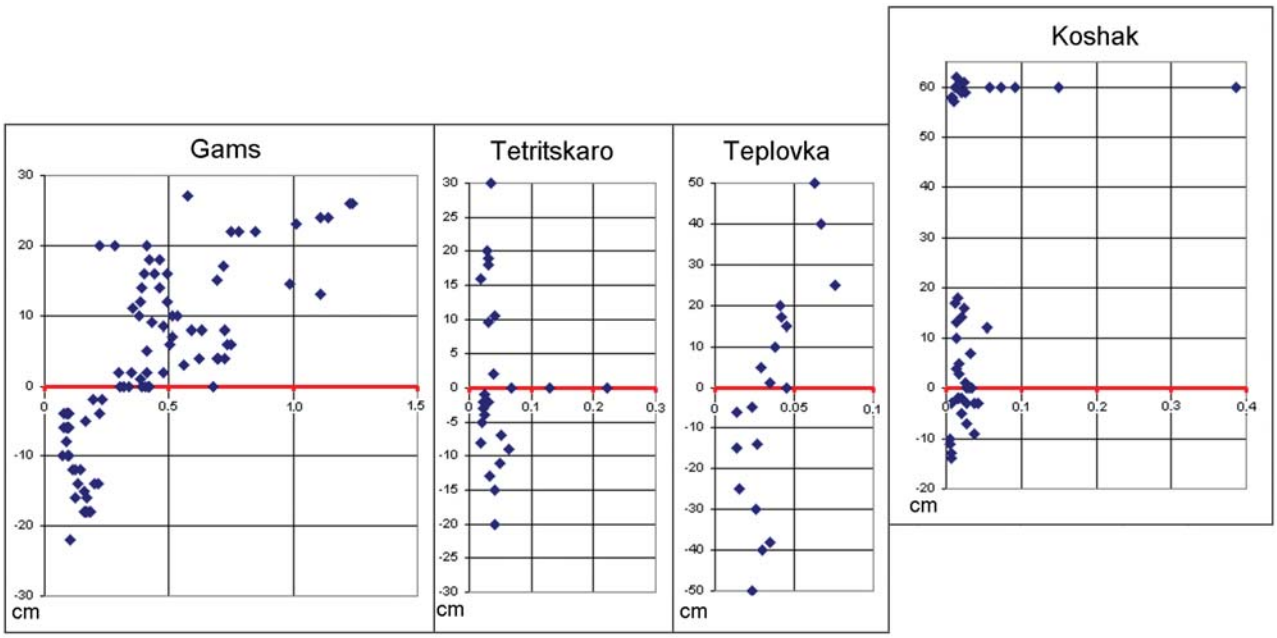

Figure 5.31. Distribution of saturation remanent magnetization M_{rs} (10^{-3} Am^2/kg) along the Gams-1, Tetritskaro, Teplovka, and Koshak sections.

cluding thin clayey interlayers. Such are the sections Koshak (Mangyshlak) [*Pechersky et al.,* 2006b], Tetritskaro (Georgia) [*Adamia et al.,* 1993; *Pechersky et al.,* 2009], Abat (Oman) [*Ellwood et al.,* 2003], Agost and Caravaca (southeast Spain) [*Villasante et al.,* 2007]. Most researchers are inclined to interpret the susceptibility peak as a result of terrigenous runoff and accumulation of magnetic minerals [*Ellwood et al.,* 2003; *Molostovsky,* 2006; *Yampolskaya et al.,* 2004; and others]. Judging from the results of detailed study of the Gams section described above, this is not the case: the main contribution to the susceptibility of the K/T boundary layer is made by paramagnetic iron-bearing minerals. To gain deeper insights into this problem, we consider several sections for which are available measurements of both susceptibility and various petromagnetic characteristics. Actually, in all cases an abrupt jump in the susceptibility is fixed at the K/T boundary (Figure 5.29). However, contributions of magnetic minerals are different, and the contribution of paramagnetic material more often prevails, as is seen from the correlation of magnetic susceptibility with paramagnetic magnetization (Figure 5.30). The distribution of magnetic minerals is clearly demonstrated by the distribution of M_{rs} along the sections, which is primarily controlled by the total concentration of magnetic minerals in sediments; M_s behaves similarly.

As seen from Figure 5.31, M_{rs} reliably localizes the boundary layer only in the Tetritskaro section. It is interesting that the boundary layer is not identified from M_{rs} and M_s data in the Koshak section, while a clayey interlayer lying higher by 60 cm yields evidence for an abrupt rise in both M_{rs} and M_s, i.e. in the concentration of magnetic minerals. Thus, a sharply increased paramagnetic magnetization primarily controlled by the concentration of iron hydroxides is evidently common to K/T boundary layers in all of the above sections (Figure 5.32). The concentration of iron hydroxides is high in the boundary layer, but their distribution is nonuniform: the paramagnetic magnetization is highest in the lower third of the layer (Gams-1 and 2), where it reaches 0.07 Am^2/kg and drops by about two times at the base and in the upper part.

Now we consider the changes of concentrations for various groups of magnetic minerals in the aforementioned sections.

Goethite (Figure 5.33). The variation pattern of goethite in all sections is virtually the same as that of the paramagnetic magnetization. Since the goethite concentration and paramagnetic magnetization are determined independently, such correlation indicates that they are closely associated and that the paramagnetic material consists mostly of iron hydroxides. Therefore, the enrichment in iron hydroxides, in both paramagnetic and weakly ferromagnetic species, is a phenomenon inherent in the K/T boundary.

Hemoilmenite (Figure 5.34). The hemoilmenite concentration varies differently in the sections under consideration, which reflects different degrees of ilmenite oxidation, i.e. different conditions of hemoilmenite formation. Only in the boundary layer of the Tetritskaro

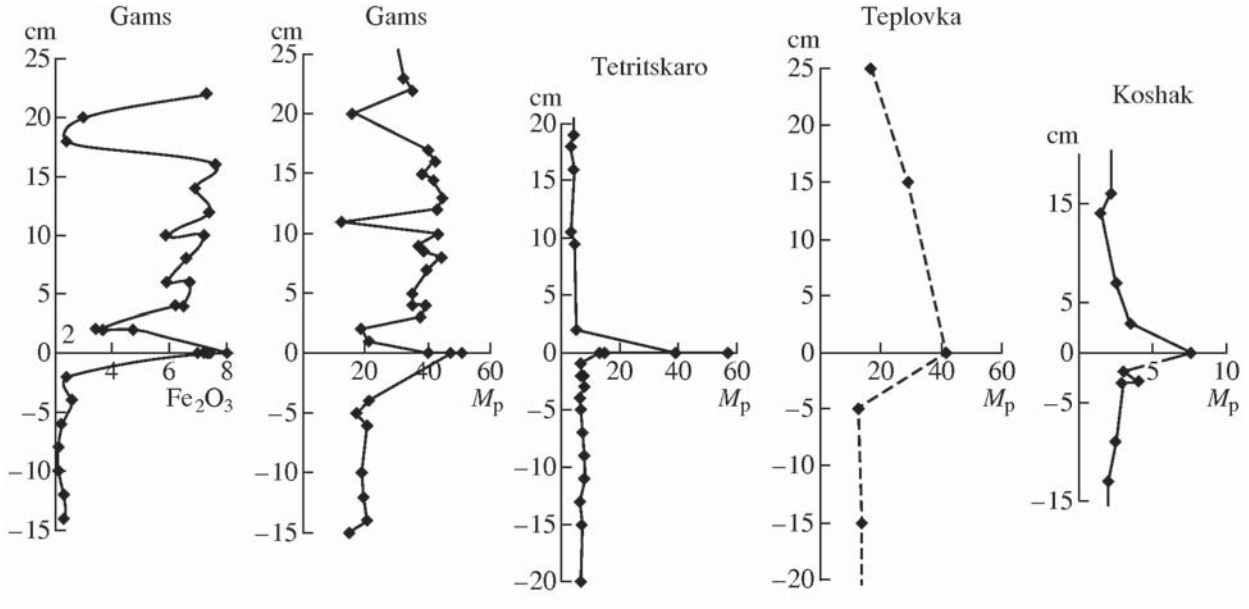

Figure 5.32. Distribution of the paramagnetic magnetization M_p (10^{-3} Am^2/kg) along the Gams-1, Tetritskaro, Teplovka, and Koshak sections and the Gams bulk concentration of iron in the form Fe_2O_3 from chemical analysis data [*Grachev et al.*, 2005].

section its concentration dramatically rises, attaining a value of 0.3%, whereas it is less than 0.05% in the remaining part of this section and in other sections.

Magnetite (Figure 5.35). The magnetite concentration varies within wide limits, from about 0.0005 to 0.02%, and is partly consistent with the lithology of sections: its higher concentrations are fixed in sandy-clayey sediments. As in the case of hemoilmenite, the magnetite concentration is not a reliable indicator of the K/T boundary.

Titanomagnetite (Figure 5.36). The lithologic control of the accumulation of titanomagnetite grains is even weaker. The titanomagnetite concentration varies from one section to another. Thus, titanomagnetite is not found in the Teplovka section; its concentration in the Tetritskaro and Koshak sections is less than 0.001%

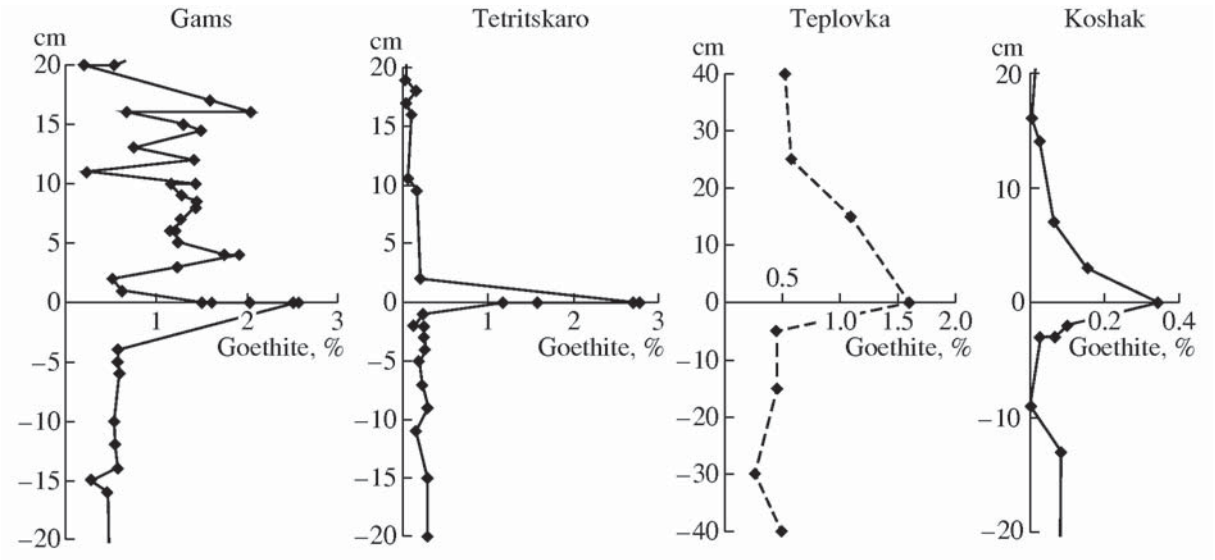

Figure 5.33. Distribution of goethite along the Gams-1, Tetritskaro, Teplovka, and Koshak sections.

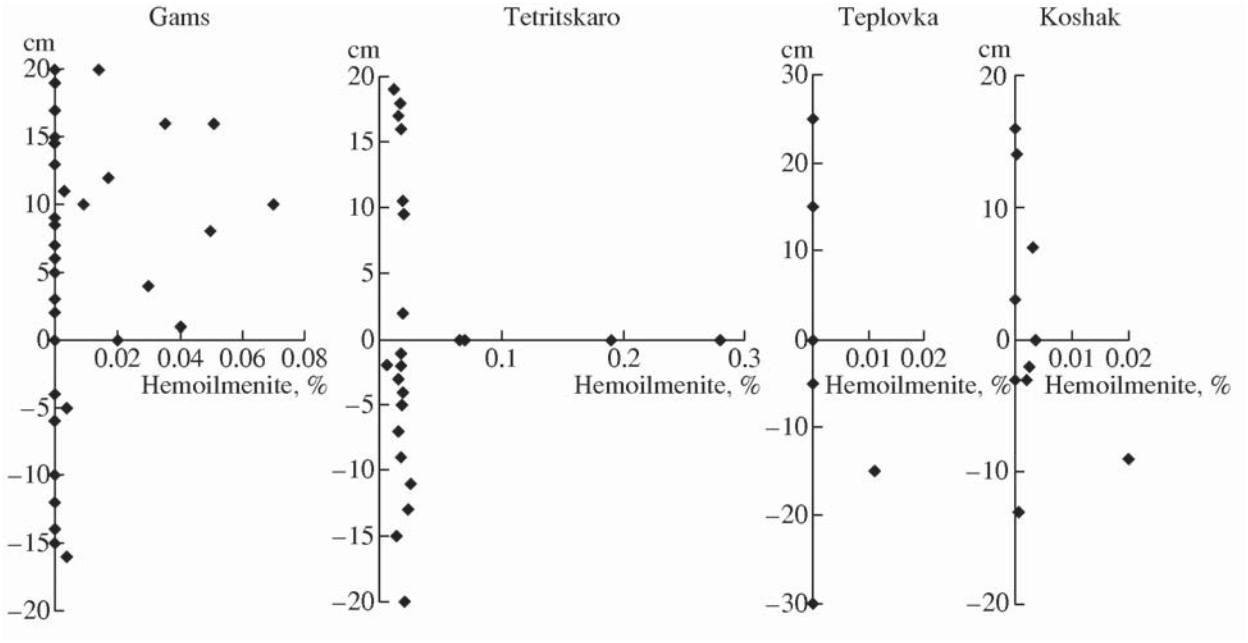

Figure 5.34. Distribution of hemoilmenite along the Gams-1, Tetritskaro, Teplovka, and Koshak sections.

in the Maastrichtian deposits and vanishes in the Danian sediments, and is independent of lithology and varies from less than 0.001 to 0.02% in the Gams section.

Metallic iron (Figure 5.37). The concentration of metallic iron varies widely from section to section. No general pattern (in particular, any correlation with the K/T boundary) is recognizable in the distribution of metallic iron. (For details, see below.)

Fe-sulfides of the pyrite type are discovered in the boundary layer of the Gams-2 section, where their concentration is highest at the base of the layer and smoothly

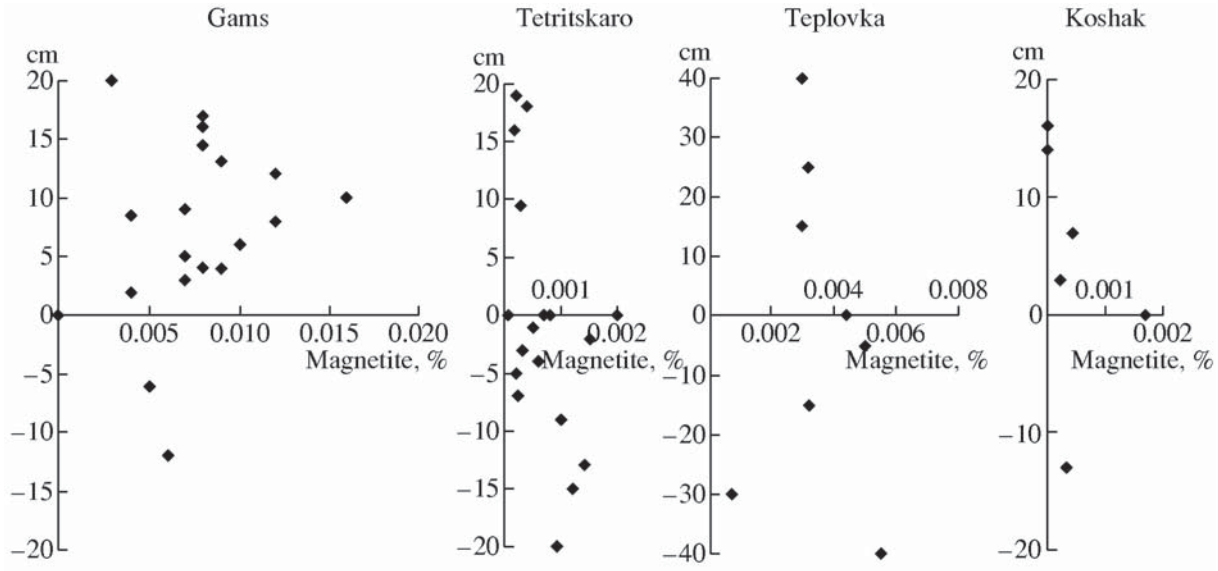

Figure 5.35. Distribution of magnetite along the Gams-1, Tetritskaro, Teplovka, and Koshak sections.

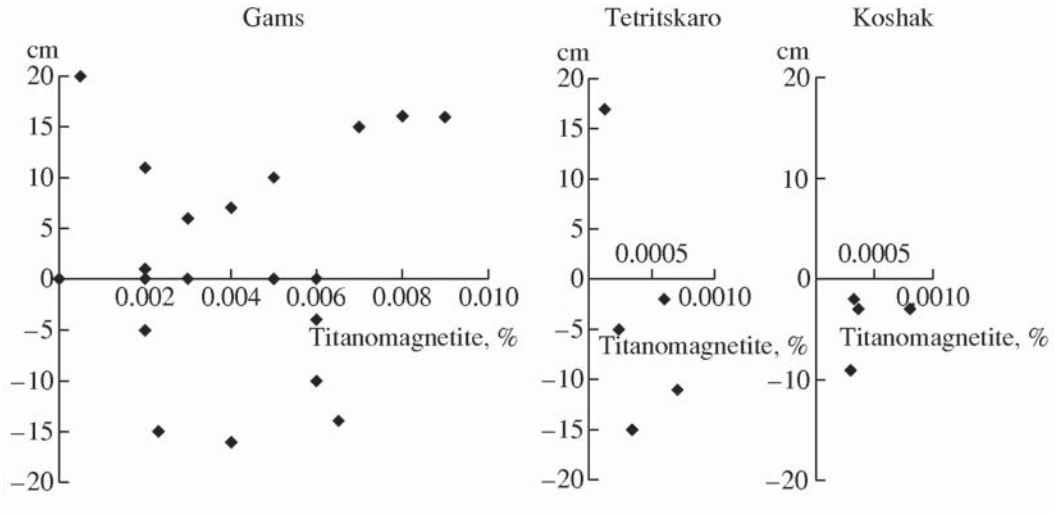

Figure 5.36. Distribution of titanomagnetite along the Gams-1, Tetritskaro, Teplovka, and Koshak sections.

decreases upward across the layer. Fe-sulphides of the pyrite or arsenopyrite type are not discovered in the other sections under consideration.

Metallic nickel and its alloy with iron are found in a few small fragments of samples from the boundary layer of the Gams section. In other sections, nickel and its alloy are not discovered at all; i.e. at present, this is a unique phenomenon.

Thus, only enrichment in iron hydroxides can be regarded as a global feature associated with the K/T boundary. Concentrations of all other magnetic minerals reflect the environments of their formation (for example, particles of cosmic iron and nickel, volcanic grains of titanomagnetite and ilmenite, or magnetite formed from Fe-sulfides of hydrothermal origin) or local conditions of their terrigenous accumulation (for example, magnetite and ilmenite); the magnetic foliation of sediments indicates detrital deposition of iron hydroxides and other magnetic minerals except the sulphide-related magnetite. Furthermore, whereas no correlation exists between the total effects of accumulation of magnetic minerals (M_s and M_{rs}) and paramagnetic minerals (M_p), which reflects their different origins, such correlation is clearly seen, for example, in the boundary layer of the Gams section, and this can

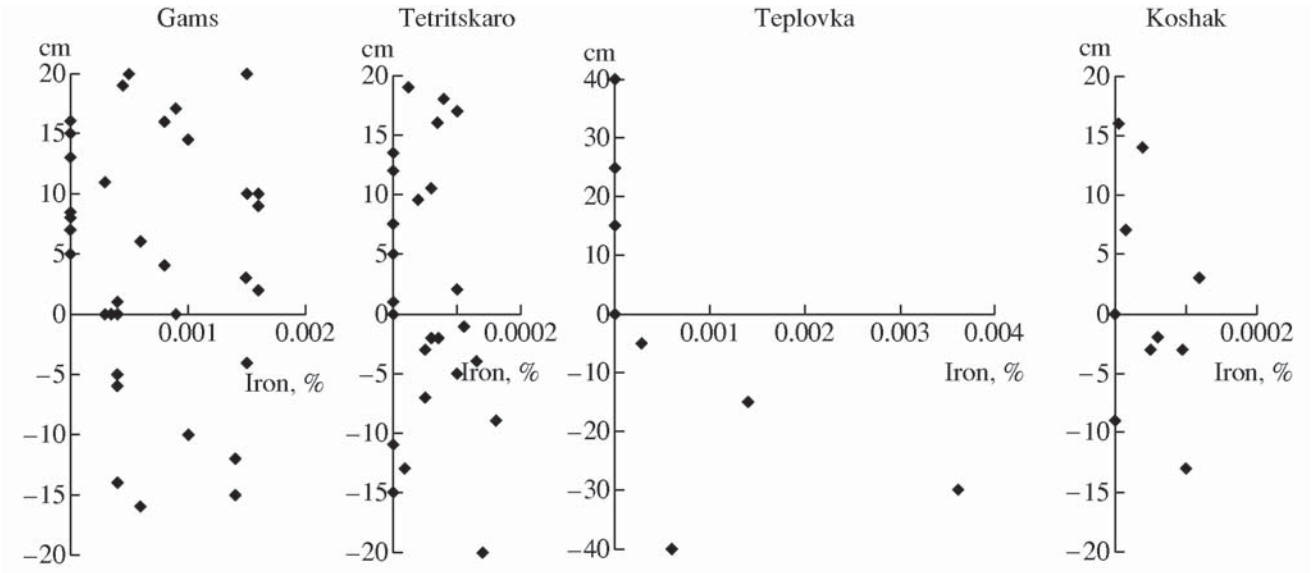

Figure 5.37. Distribution of metallic iron along the Gams-1, Tetritskaro, Teplovka, and Koshak sections.

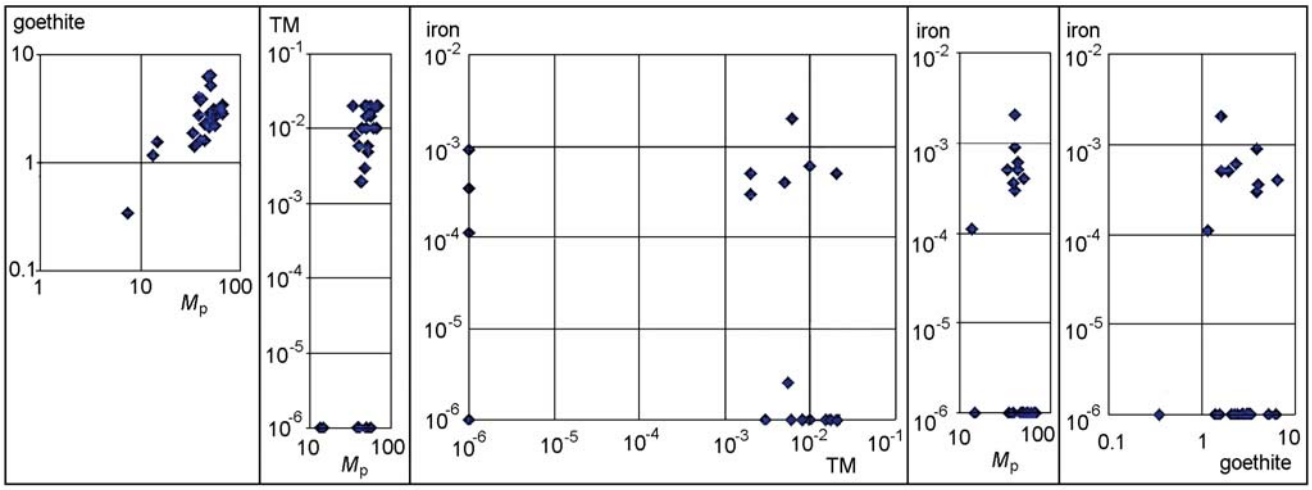

Figure 5.38. Relationships between the concentration of goethite, titanomagnetite, and metallic iron in the boundary bed of the Gams section.

be due to common or similar conditions of accumulation of both magnetic and paramagnetic minerals in the boundary clay.

Metallic iron in sediments at the K/T boundary. Considering the problem of involvement of impact events in the deposition of sediments at the K/T boundary, we dwell in more detail on the distribution of metallic iron in the sediments derived from petromagnetic data. Data on the distribution and amount of particles of metallic iron and nickel both over the Earth's surface and in time are quite limited because direct methods alone were used to detect such particles. TMA data on sediments have not been invoked, although they can provide extensive relevant information about the metallic iron distribution. The TMA has been widely applied in paleomagnetic and petromagnetic studies of various geological objects including sediments and sedimentary rocks of different geological ages, but TMA temperatures were limited by 700°C, which precluded obtaining any information on grains of metallic iron and its composition and concentration. In this monograph and in a series of papers, we tried to partly remove this gap.

We consider available results in two aspects: (1) the distribution of metallic iron over synchronous sediments near the K/T boundary (i.e. over the Earth's surface) and (2) its distribution along section (i.e. over time).

Distribution of metallic iron over the Earth's surface at the K/T boundary. We examine the behaviour of metallic iron in the K/T clay boundary layer, which is the narrowest synchronous interval. The concentration of metallic iron in five widely separated sections varies within wide limits [*Adamia et al.*, 1993; *Grachev et al.*, 2005; *Molostovsky et al.*, 2006; *Pechersky*, 2007; *Pechersky et al.*, 2006a, 2006b, 2008, 2009]: the iron is absent (not discovered from TMA data) in 19 of 28 samples and varies from 0.0001 to 0.004% in the remaining 9 samples. Detailed layerwise analysis of the Gams boundary layer showed that metallic iron is present only in its upper and lower parts. In addition, metallic nickel microspheruless were discovered in the upper part of the layer [*Grachev et al.*, 2005]. Figure 5.38 demonstrates the absence correlation between the main magnetic and paramagnetic components of boundary layer sediments. The points in this figure form two groups, which emphasize the absence of correlation of metallic iron with iron hydroxides, magnetite, and titanomagnetite and reflect different sources and origins of their accumulation; these groups relate to a) samples in which iron, iron hydroxides, magnetite, and titanomagnetite are all present and b) samples in which metallic iron is absent, but iron hydroxides and/or titanomagnetite and magnetite are present. This suggests the following pattern: no iron was accumulated during the few thousand years of the deposition of clay and iron hydroxides of the K/T boundary layer. In the ∼20-kyr interval (20 cm around the K/T boundary, Figure 5.37), the metallic iron varies from ∼0 to 0.002%. In four sections separated by about 1000 to 5000 km, its concentration in the same 20-cm interval varies from section to section by one to two orders or more. The iron is absent at all (not discovered) in the Teplovka and Klyuchi Danian deposits but reaches 0.004% in the upper Maastrichtian part of the Teplovka section. Therefore, the distribution of metallic iron over the Earth's surface near the K/T boundary is extremely irregular.

Table 5.7. Composition of magnetite from the transitional layer of the Gams-1A section

Element	1	2	3	4	5	6	7	8	9	10
TiO_2	1.11	–	–	–	–	0.03	0.27	–	–	–
FeO*	98.89	93.17	97.92	93.1	92.9	98.77	87.76	99.46	99.68	99.28
MgO	–	–	–	0.1	0.4	0.05	1.79	–	–	–
MnO	–	–	–	0.2	0.1	0.08	0.08	0.54	–	0.72
Al_2O_3	–	6.83	2.08	0.1	0.4	0.11	–	–	0.32	–
Cr_2O_3	–	–	–	0.1	–	–	9.13	–	–	–
NiO	–	–	–	–	–	0.08	1.16	–	–	–
Element	11	12	13	14	15	16	17	18	19	20
TiO_2	–	–	–	–	–	–	–	–	–	–
FeO	97.73	96.50	96.91	98.05	98.34	97.73	89.87	91.10	89.87	91.07
MgO	–	–	–	–	–	–	5.83	3.49	5.83	3.52
MnO	0.83	1.02	0.75	0.79	0.71	0.83	0.59	–	0.59	–
Al_2O_3	1.45	2.48	1.56	1.16	0.95	1.45	–	0.72	–	0.72
Cr_2O_3	–	–	–	–	–	–	1.65	2.44	1.65	2.44
NiO	–	–	–	–	–	–	2.06	2.25	2.06	–
CuO	–	–	0.77	–	–	–	–	–	–	–

Note: 1–3, Gams-1A transitional layer (thin section); 4–5, heavy fraction from the middle part of the Gams-1A transitional layer; 6–20, heavy fraction from the middle part of the Gams-1B transitional layer. Unfilled cells correspond to concentrations below the microprobe sensitivity threshold.

Distribution of metallic iron over time. Now we consider the behaviour of iron in intervals of a few hundred thousand years to a few million years encompassing the K/T boundary (Figure 5.37). Along a section (i.e. over time), the iron concentration varies from 0 to 0.002% in the Gams section and to 0.004% in the Teplovka section and does not exceed 0.0002% in the sections Tetritskaro and Koshak (Figure 5.37). The largest concentration values are fixed at different levels in the sections (Figure 5.37), i.e. at different times, and this means that the enrichment in iron was not synchronous. Moreover, a certain lithologic control is noticeable: generally, the iron concentration is higher in the Danian sandy-clayey deposits of the Gams section and lower in the carbonate sediments of the Tetritskaro and Koshak sections. However, samples that do not contain iron are more often met in sandy-clayey deposits and particularly in the boundary layer.

Thus, the distribution of metallic iron is seen to be extremely irregular in both space and time. This can be interpreted in terms of three possible variants: 1) primary extraterrestrial origin implying that metallic iron particles were accumulated in sediments from cosmic dust and falling meteorites, 2) primary terrestrial origin of metallic iron particles, and 3) secondary origin implying that metallic iron particles are oxidized with the formation of iron hydroxides and magnetite. Large fluctuations in the amount of metallic iron in sediments do not conform to a stably constant volume of cosmic dust falling onto the Earth's surface. Possibly this irregularity is accounted for by the fact that the bulk of metallic iron is related to falling meteorites rather than cosmic dust.

Correlation of metallic iron concentration with iron hydroxides, titanomagnetite, and magnetite. As noted above, all studied sections are characterized by close positive correlation between the total iron concentration from chemical analysis data, paramagnetic magnetization M_p, and content of weakly ferromagnetic iron hydroxides (goethite) in sediments near the K/T boundary, which can be explained in terms of the main contribution of iron hydroxides to the paramagnetic magnetization [*Pechersky*, 2007]. The M_p – goethite correlation is demonstrated in Figure 5.39, summarizing data from five sections. Comparing M_p and

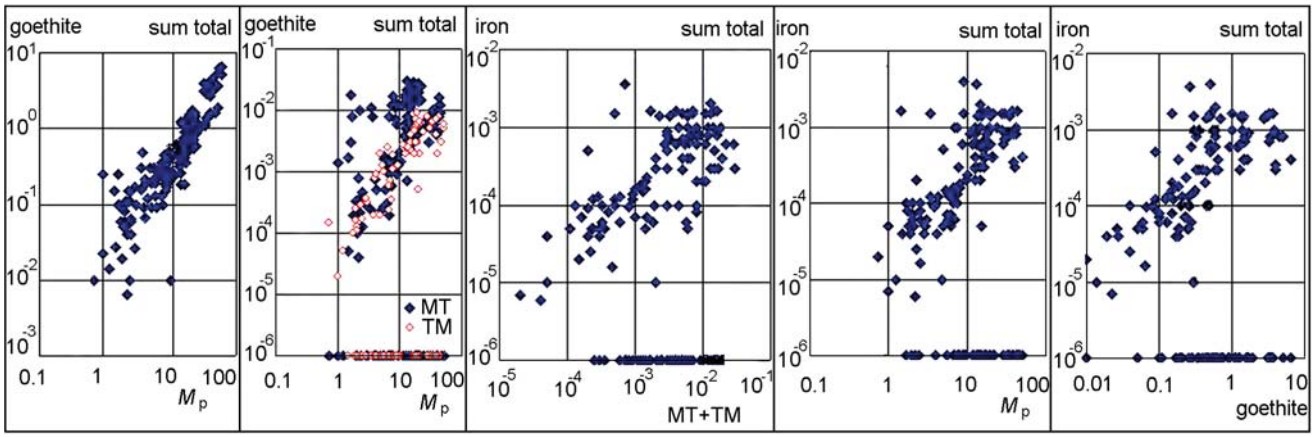

Figure 5.39. Correlation between the paramagnetic magnetization M_p and the concentrations of weakly ferromagnetic iron hydroxides (goethite), magnetite, titanomagnetite, and metallic iron in sediments (summarized data from the Gams, Koshak, Klyuchi, Teplovka, Tetritskaro sections) [*Molostovsky et al.*, 2006; *Pechersky et al.*, 2006a, 2006b, 2007, 2008].

goethite with concentrations of magnetite, titanomagnetite, and metallic iron, two main groups of points are noticeable (Figure 5.39): the first group (a), as distinct of the boundary layer (Figure 5.38), is characterized by a clear correlation between accumulated magnetite, titanomagnetite, and metallic iron, whereas the second group (b) is distinguished by the absence of some magnetic minerals. The coefficients of pairwise correlation were calculated for the above parameters and their logarithms (Table 5.8).

First of all, it is noteworthy that the coefficients of pairwise correlation of logarithms are undoubtedly higher compared to the values themselves, which indicates a decisive role of lognormal distribution of the magnetic characteristics analyzed. If the correlation patterns are considered separately for each section (Figure 5.40–Figure 5.43), the division of points into two groups similar to those observed for the boundary layer (Figure 5.38) is common to all sections: group (a) contains iron, iron hydroxides, and titanomagnetite, and group (b) contains iron hydroxides and/or titanomagnetite but do not contain metallic iron. The interval of values in group (a) is the same as in group (b), but the values in group (b) are often larger than in group (a). The correlation between concentrations of iron hydroxides, titanomagnetite, magnetite, and iron varies from section to section within wide limits: the correlation is stronger for the carbonate sections Koshak (Figure 5.42) and Tetritskaro (Figure 5.43) and appreciably weaker or even absent in sections with significant contribution of sandy-clayey sediments (Figure 5.40 and Figure 5.41). Evidently, the relationship MT+TM – M_p consistently reflects the predominantly terrigenous pattern of the magnetite and titanomagnetite accumulation in sediments, although the actual origin of these minerals (particularly titanomagnetite, judging from its composition) is associated with basaltic volcanism. We should emphasize that a significant contribution to all pairs (except goethite-M_p) is made by group (b), in which one of the components of a pair is absent at all, with concentrations of the second component being appreciable. Such duality of the relationship precludes a "secondary" nature of the iron correlation with titanomagnetite, magnetite, and iron hydroxides. An

Table 5.8. Coefficients of linear correlation for group a

Pairs	Coefficients for values	Coefficients for logarithms
M_p – goethite	0.85	0.91
M_p – titanomagnetite	0.71	0.83
M_p – magnetite	0.29	0.58
M_p – magnetite+titanomagnetite	0.66	0.71
M_p – iron	0.36	0.74
Goethite – iron	0.61	0.79
Magnetite+titanomagnetite – iron	0.21	0.6

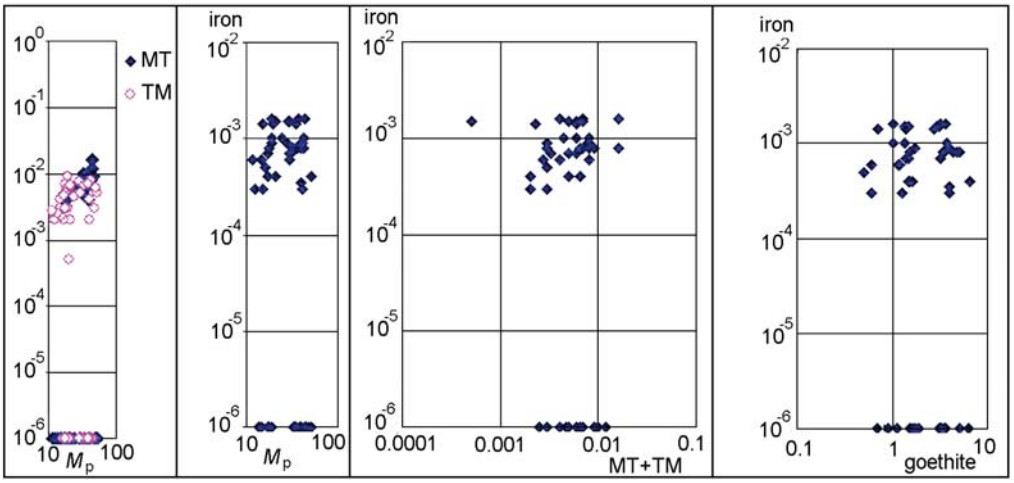

Figure 5.40. Correlation between the paramagnetic magnetization M_p and the concentrations of ferromagnetic iron hydroxides (goethite), magnetite, titanomagnetite, and metallic iron in sediments of the Gams section [*Pechersky et al.*, 2006a, 2007, 2009].

approximately the same extent of oxidation of metallic iron to hydroxides may be suggested and then the correlation between goethite and iron is positive: a rise in the concentration of iron is accompanied by an increase in the amount of its oxidized component. However, the point is that the iron concentration is three orders less than the goethite concentration, implying that metallic iron in the initial state should have been present in concentrations of at least a few percent. However, iron grains close to complete oxidation should also be present, whereas we have a considerable independent group (b), in which metallic iron is absent in a large number of samples and the TM+MT concentration is no less than in group (a). Undoubtedly, titanomagnetite is in no way related to oxidation of metallic iron particles, and other impurities such as titanium are absent in noticeable amounts in particles of metallic iron, nickel, and their alloys. Thus, we have no other choice than to acknowledge the "primary", extraterrestrial and/or terrestrial, nature of the correlations shown in Figure 5.39–Figure 5.43. The duality of the correlations and their different values in samples of group (a) are features normal for different conditions of accumulation of iron hydroxides, magnetite, titanomagnetite, and metallic iron. Once the "secondary" origin of the correlations is precluded, the aforementioned minerals should have been accumulated in sediments in a general way.

In principle, authigenic metallic iron could have formed in sediments and/or igneous rocks, most likely in basalts, but inspection of literature has shown that this is an extremely rare phenomenon, whereas metallic iron is found, albeit in very small concentrations, ubiquitously in sediments. Therefore, extraterrestrial

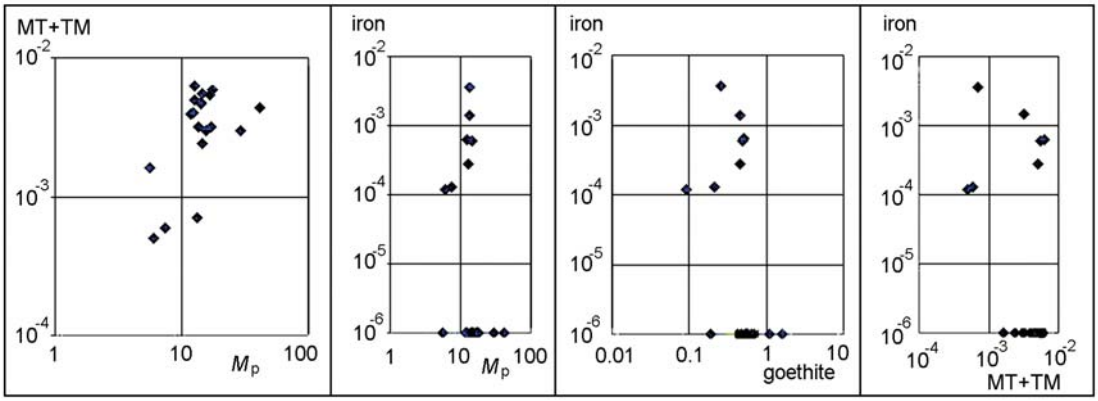

Figure 5.41. Correlation between the paramagnetic magnetization M_p and the concentrations of ferromagnetic iron hydroxides (goethite), magnetite, titanomagnetite, and metallic iron in sediments of the Klyuchi and Teplovka sections [*Molostovsky et al.*, 2006; *Pechersky et al.*, 2007].

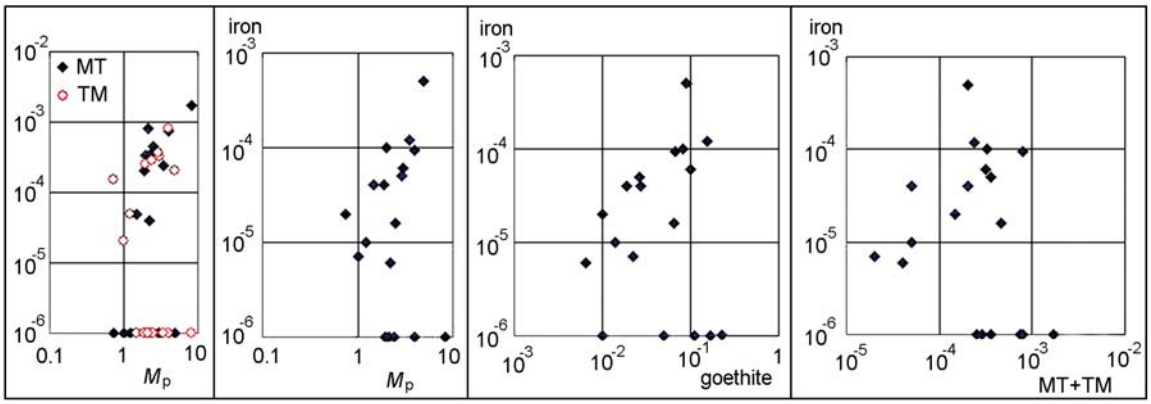

Figure 5.42. Correlation between the paramagnetic magnetization M_p and the concentrations of ferromagnetic iron hydroxides (goethite), magnetite, titanomagnetite, and metallic iron in sediments of the Koshak section [*Pechersky et al.*, 2006b, 2007].

origination of metallic iron particles should also be regarded as a ubiquitous phenomenon. The positive correlation can be considered as evidence for redeposition. Actually, regardless of the actual origin of metallic iron particles, their accumulation can be a result of erosion and redeposition of older rocks containing these particles (a process similar to the formation of placers). Such a process should inevitably give rise to positive correlation between heavy iron minerals washed away from rocks and precipitating in the sediments studied here. Thus, the observed pattern of different positive correlations between iron hydroxides, magnetite, titanomagnetite, and metallic iron reflects different contributions of redeposition to the accumulation of these minerals in the sediments.

5.6 Conclusion

(1) Intense accumulation of iron hydroxides is observed at the K/T boundary, and most likely this a global phenomenon unrelated to local physiographic conditions of accumulation of terrigenous material in sediments. This by no means implies that iron hydroxides were accumulated *everywhere* at the K/T boundary. We only state that the phenomenon is widespread both on continents and in oceans. Apparently, most of iron hydroxides accumulated in the K/T boundary layer and other deposits have different origins: they are products of hydrothermal activity in the first case and terrigenous activity in the second.

(2) As distinct from iron hydroxides, accumulation

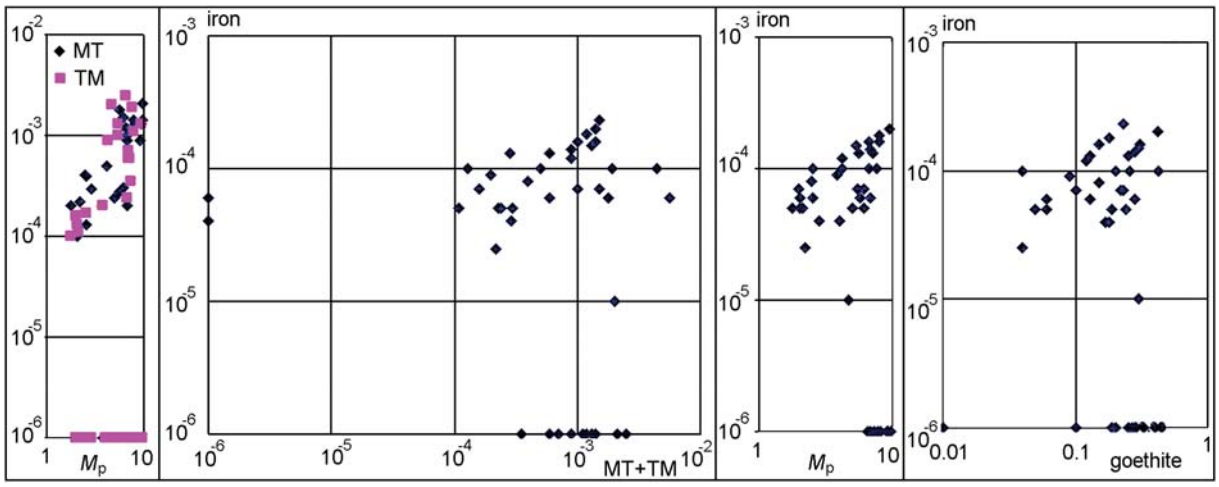

Figure 5.43. Correlation between the paramagnetic magnetization M_p and the concentrations of ferromagnetic iron hydroxides (goethite), magnetite, titanomagnetite, and metallic iron in sediments of the Tetritskaro section [*Pechersky et al.*, 2009].

of other magnetic minerals followed different patterns that evidently reflect the origin of these minerals and local conditions of terrigenous material deposition. Quite possible that iron hydroxides are products of hydrothermal activity similar to the formation of iron-bearing sediments [*Gurvich,* 1998]. Accumulation of iron hydroxides extended in time, attains a maximum in the lower part of the boundary layer and sharply drops upon the transition to over- and underlying deposits of the Danian and Maastrichtian.

(3) The base of the boundary layer **J** (Gams-1) is enriched in titanomagnetite grains of volcanic origin. Titanomagnetite was accumulated through eolian dispersal and precipitation of products of a volcanic eruption. The related process of eruptive activity was short and local.

(4) Iron sulfides in the boundary layer (Gams-2) are evidently of hydrothermal origin. Their amount is largest in the lower part of the Gams-2 boundary layer.

(5) The jump in titanomagnetite accumulation at the base of the boundary layer (Gams-1) is unrelated to impact events; indicators of the latter (the presence of metallic nickel and its alloy with iron) are confined to the upper part of the layer **J**, whereas the interval of a higher concentration of iron hydroxides covers the entire thickness of the boundary layer. Iron sulfides are present in lower part of the boundary clay, and their concentration gradually decreases toward its top, which also cannot be related to impact events. Moreover, an abrupt rise in the iron hydroxide concentration is noted in all of the aforementioned sections, whereas metallic nickel is found only in the Gams section. None of the sections studied yields evidence for enrichment in meteoritic metallic iron particles at the K/T boundary; on the contrary, in the boundary layer they are met mostly in its upper (Gams-1) or lower (Gams-2) part. Therefore, the K/T boundary is not marked by direct indicators of an impact event.

(6) Thus, only the enrichment in iron hydroxides of predominantly hydrothermal origin can be regarded as a global phenomenon consistently associated with the K/T boundary and unrelated to impact events.

(7) The observed pattern of different positive correlations between accumulated iron hydroxides, magnetite, titanomagnetite, and metallic iron point to different implications of redeposition for the accumulation of these minerals, ranging from the initial accumulation stage, when the correlation is absent due to their different primary sources, to formations in which redeposited material plays a significant role. Very likely that single grains of nickel and Ni-Fe alloy in layers **K, L** and **M** (Gams-1) are result of redeposition from boundary layer.

Taking into account the inferences derived from the analysis of the metallic iron and other magnetic minerals distribution in sediments, primarily accumulation of iron and others should be distinguished from its accumulation due to redeposition.

Chapter 6. Cosmic Dust and Micrometeorites: Morphology and Chemical Composition

6.1 Introduction

Investigations of cosmic dust in sedimentary rocks were inspired by the results of the H. M. S. Challenger cruise, during which traces of cosmic matter were discovered for the first time in red deep-sea clays [*Murray, Renard,* 1891]. Samples of ferromanganese nodules and magnetic microspherules up to 100 μm in diameter, which were later called cosmic spherules, were uplifted from a depth of 4300 m during the dredging at two stations in the southern Pacific. However, the iron microspherules gathered by Challenger were studied only in recent years. It was found out that internal parts of the spherules consist of metallic iron (90%) and nickel (10%), whereas their surfaces are covered by thin crusts of iron oxide (J. Jedwab, http://www.ub.ac.be/sciences/cosmicdust.pdf).

In fact, the study of cosmic matter was initiated by the discovery of cosmic spherules in deep-sea clays. However, this problem excited great interest of researchers only after first launches of cosmic vehicles that could sample lunar ground and dust particles in various regions of the solar system. Studies of the Tunguska catastrophe traces and meteoritic dust sampled in the place of the fall of the Sikhote-Alin' meteorite also played an important role [*Florensky,* 1963; *Florensky et al.,* 1968; *Ivanov, Florensky,* 1970; *Krinov,* 1971].

Interest in metallic microspherules displayed by a wide range of researchers has led to the discovery of the microspherules in sedimentary rocks of different ages and origins. For example, metallic microspherules have been found in ices of Antarctic and Greenland [*Maurette et al.,* 1986; *Yada et al.,* 2004], deep-sea oceanic sediments and manganese nodules [*Brownlee,* 1985; *Brownlee et al.,* 1984; *Finkelman,* 1970; *Hunter, Parkin,* 1960; *Parkin et al.,* 1980], and sands of deserts and beaches [*Marvin, Einaudi,* 1967]. Thousands of Fe–Ni alloy spherules from Pleistocene deposits of Alberta (Canada) [*Bi et al.,* 1993] and magnetite microspherules from Holocene fluvioglacial deposits of the Carpathians [*Szoor et al.,* 2001] have been studied. Metallic particles and microspherules are often met in and near meteoritic craters [*El Coresy,* 1966; *Florensky et al.,* 1968; *Raukas,* 2000; *Sobotovich et al.,* 1978; *Stankowski et al.,* 2006].

Metallic microspherules of extraterrestrial origin are known in sedimentary rocks of various ages: Lower and Upper Cambrian [*Korchagin et al.,* 2007; *Raukas,* 2000], Ordovician [*Schmitz et al.,* 1996], and Permian, Triassic, and Jurassic [*Chapman, Lauretta,* 2004; *Miono et al.,* 1993]. Higher concentrations of metallic microspherules of extraterrestrial origin are noted near the Permian–Triassic and Triassic–Jurassic boundaries [*Miono et al.,* 1993] and near the Cretaceous-Paleogene boundary [*Ebihara, Miura,* 1996; *Smit, Romein,* 1985].

Data on microspherules and particles from ancient deposits provide insights into volumes of cosmic matter coming to the Earth, the pattern (uniform or nonuniform) of this influx, variations in the composition of cosmic particles arriving at the Earth, primary sources of this substance, and the influence of these processes on the evolution of life on the Earth. Many of these problems are still far from being solved; however, the accumulation of data and their comprehensive study are undoubtedly favorable for the solution of these problems.

Thus, it is known that the total mass of dust circulating inside the Earth's orbit is about 10^{15} t and, according to various estimates, 4000 to 10,000 t of the cosmic substance falls annually onto the Earth's surface [*Karner et al.,* 2003; *Sobotovich,* 1976; *Yada et al.,* 2004]; particles 50–400 μm in size account for 95% of this substance [*Kurat et al.,* 1994]. As for time variations in the

rate of the influx of cosmic substance to the Earth, this question has remained controversial as yet, notwithstanding a great number of investigations carried out during the past decade.

There is the opinion that the influx rate of cosmic dust with the planetary ratio of helium isotopes $^3He/^4He$ (10^{-4}) varies weakly with time [*Karner et al.,* 2003; *Winckler, Fisher,* 2006]; however, directly opposite data are also available [*Farley,* 1995; *Schmitz et al.,* 1996]. Note that all known estimates are obtained for different time intervals (from hundreds of thousands to tens of millions of years), and the rate is known to depend strongly on the interval of averaging. This is indirectly indicated also by data on variations in the ratio of helium isotopes $^3He/^4He$ at the Cretaceous-Paleogene boundary in the Gams section [*Grachev et al.,* 2007b].

The study of present-day cosmic dust is based on investigations of deep-sea deposits and the glacial cover in Greenland and Antarctic and samples taken from the stratosphere [*Brownlee,* 1985]. According to present based on particle sizes, cosmic dust is subdivided into interplanetary cosmic dust proper (IDPs) with particle sizes smaller than 30 μm and micrometeorites with particle sizes larger than 50 μm [*Genge et al.,* 1997]. *Krinov* [1971] proposed that the finest molten surface fragments of a meteoric body be called micrometeorites. Such a classification is naturally rather arbitrary and, as demonstrated below, in the Gams section we found molten fragments of pure iron a few microns in size; we propose them to be called nanometeorites rather than micrometeorites. Moreover, meteoritic dust, meteoritic iron, and impactites are also distinguished at present [*Raukas,* 2000]. No rigorous criteria for the discrimination between cosmic dust and meteoritic particles have been developed as yet, and even the example of the Gams section we studied shows that metallic particles and microspherules differ in shape and composition more significantly than is provided for by the existing classifications. Thus, the virtually perfect spherical shape, metallic luster, and magnetic properties of particles were regarded as evidence for their cosmic origin. According to *Sobotovich* [1976, p. 107], "the presence of molten spherules, including magnetic ones, is the only morphological criterion for distinguishing the cosmic origin of material studied." A surface texture of microspherules is also regarded as evidence indicating that they belong to the category of meteoritic dust. However, apart from shapes that are very diverse, the substance composition is of fundamental importance as is shown below [*Grachev et al.,* 2008b]. Studies of metallic microspherules (spherules) showed that, along with microspherules of cosmic origin, there is a great amount of spherules of other geneses, such as volcanic activity, vital activity of bacteria, or metamorphism. It is known that Fe microspherules of volcanic origin rarely have a perfect spherical shape and are distinguished by a higher concentration of Ti admixture (more than 10%).

The origin of cosmic dust is still the subject of discussion. According to *Sobotovich* [1976], cosmic dust can represent remains of the primordial protoplanetary cloud. This suggestion was disputed by *Levin, Simonenko* [1973], who believed that the primordial finely dispersed substance has not been preserved.

According to an alternative explanation, the formation of cosmic dust is associated with destruction of asteroids and comets. *Sobotovich* [1976] notes that, if the amount of cosmic dust supplied to the Earth does not change with time (for example, throughout the Phanerozoic), *Levin, Simonenko* [1973] are right.

Notwithstanding a great volume of research, this fundamental question cannot be answered at present because quantitative estimates are few and their accuracy raises doubts. Data of IDP isotope studies using particles gathered in the stratosphere in the framework of the NASA program suggest the existence of particles of presolar origin [*Messenger et al.,* 2003]. Moreover, it was found that the same dust contains such minerals as corundum, moissanite, and diamond, whose origin can be referred to the time before the solar system formation according to data of the carbon and nitrogen isotopy [*Stadermann et al.,* 2006].

We should note that a similar mineral assemblage (diamond, moissanite, and corundum) was discovered in the boundary layer at the K/T boundary in the Gams section [*Grachev et al.,* 2005, 2008a]. The above brief review clearly indicates that the study of cosmic dust in a geological section is very important. This paper presents the first results of the study of the cosmic substance in the transitional clay layer at the Cretaceous-Paleogene boundary in the Gams section, Eastern Alps [*Grachev et al.,* 2005].

6.2 Results of Investigations

A great diversity of metallic particles and microspherules of cosmic origin have been found in the Gams section in the transitional clay layer between the Cretaceous and Paleogene, as well as at two levels in the overlying Paleocene deposits. Particles and microspherules discovered in this section are considerably more diverse in shape, surface texture, and chemical composition than those detected previously in the Cretaceous-Paleogene boundary layers in other regions of the world.

In the Gams section, the cosmic substance is presented by finely dispersed particles of various shapes among which magnetic microspherules 0.7 to 100 μm

Table 6.1. Chemical composition (wt %) of the cosmic substance in the transitional clay layer at the Cretaceous-Paleogene boundary in the Gams section according to the data of microprobe analysis

Element	1	2	3	4	5	6	7	8	9
Fe	18.40	12.24	15.31	15.47	15.17	15.05	19.07	15.94	16.23
Ni	76.31	85.27	78.44	77.37	80.43	84.95	80.24	83.23	82.91
Mn	0.66	–	0.79	0.81	0.89	–	0.89	0.83	0.86
S	4.62	2.49	5.46	6.35	3.51	–	–	–	–
Element	10	11	12	13	14	15	16	17	18
Fe	15.31	15.47	14.70	14.18	14.94	33.74	15.78	15.38	93.83
Ni	78.44	77.37	78.28	79.32	78.77	51.56	83.23	83.60	3.95
Mn	0.79	0.81	0.97	0.70	0.91	0.80	0.99	1.02	2.20
Cr	–	–	–	–	–	2.80	–	–	–
Mg	–	–	–	–	–	7.92	–	–	–
Mo	5.46	6.35	6.05	5.80	5.38	3.18	–	–	–
Element	19	20	21	22	23	24	25	26	27
Fe	16.70	14.09	14.29	13.91	14.21	15.26	14.81	14.65	81.12
Ni	80.90	79.72	79.70	79.92	81.99	79.14	81.39	80.10	10.61
Mn	1.02	0.87	1.12	0.90	0.70	0.73	0.77	–	2.00
Mo	1.38	5.32	4.89	5.27	3.09	4.86	3.03	5.25	–
Element	28	29	30	31	32	33	34	35	36
Fe	16.67	14.96	15.39	97.72	71.79	78.04	15.54	76.87	72.98
Ni	81.16	79.24	80.06	2.28	3.75	17.61	80.36	–	2.19
Mn	0.81	0.98	0.77	–	–	–	0.65	–	–
Mg	1.37	–	–	–	20.42	2.83	–	20.67	–
Cr	–	–	–	–	2.04	–	–	1.42	24.84
Mo	–	4.82	3.77	–	–	–	3.45	–	–

Element	37	38	39	40	41	42	43
Fe	83.60	79.75	82.33	67.88	3.83	99.19	99.25
Ni	2.19	8.15	2.68	17.04	96.17	–	–
Mn	–	–	1.01	–	–	0.81	0.75
Cr	15.26	12.11	12.39	15.09	–	–	–
Pt	–	–	1.58	–	–	–	–

Note: 1–27, 28–35, and 36–43 are, respectively, the lower, middle, and upper parts of the transitional layer.

in size containing 98% of pure iron are most abundant [*Grachev et al.*, 2008a]. Large amounts of such particles in the shape of spheres or microspherules are found in the *J* layer and overlying Paleocene clays (in the *K* and *M* layers).

The following types of metallic microspherules have been discovered: microspherules consisting of pure iron, magnetite, or wustite; microspherules of iron with a chromium admixture; and microspherules of pure nickel. Particles of other shapes consisting of iron-nickel alloy (awaruite) or pure nickel have also been found. Some Fe–Ni particles contain a Mo admixture. Particles of Fe–Ni alloy and pure nickel in the Cretaceous-Paleogene transition clay layer were discovered for the first time.

New results of this study are findings of particles with a high concentration of nickel and a significant amount of molybdenum, microspherules with a Cr admixture, and spiral-shaped iron. The fact that particles differing in shape and composition are confined

Table 6.2. Chemical composition (at %) of Ni spherules in the uppermost part of the transitional layer J_6 according to the microprobe data

Element	Spherule 1	Spherule 2	Spherule 3
O	6.76	8.66	9.31
Na	0.00	–	–
Mg	0.25	–	0.16
Al	0.61	–	1.04
Si	1.23	1.19	0.95
P	0.11	–	–
S	0.00	–	0.02
Cl	0.11	0.55	0.04
K	0.02	–	0.02
Ca	0.13	0.46	0.09
Ti	0.11	0.43	0.07
Cr	0.01	–	0.00
Mn	0.00	–	0.03
Fe	0.23	–	0.35
Co	0.02	–	0.07
Ni	90.41	88.71	87.85

to different parts of the transitional clay layer is also noteworthy. In addition to metallic microspherules and particles, the Gams transitional layer of clay contains Ni-spinel, microdiamonds with microspherules of pure Ni, and ragged plates of Au and Cu that are not detected in the under- and overlying deposits.

Below, we briefly characterize shapes, sizes, surface textures, and chemical compositions of all metallic particles and microspherules discovered in the transitional layer. Information on the chemical compositions of the particles is presented in Table 6.1 and Table 6.2, and the compositions of spherules found in deposits of other ages are given in Table 6.3.

Fe microspherule s (Figure 6.1). Metallic microspherules are found in the Gams section at three stratigraphic levels. One level of findings of Fe microspherules and particles is associated with the transitional clay layer, where Fe particles of various shapes are concentrated. The second level is confined to the overlying finegrained sandstones of the K layer, and the third level, to siltstones of the M layer (*Subbotina fringa* zone) (Figure 6.1, *3*).

According to the surface morphology (texture), we distinguish spheres with a smooth surface (Figure 6.1, *4–6*), a net-hummocky surface texture (Figure 6.1, *1*), and a surface covered by a net of small polygonal joints (Figure 6.1, *11*) or by a system of parallel joints branching from a master joint (Figure 6.1, *2*).

As noted above, microspherules can be hollow (Figure 6.2, *1*), shell-like, or filled with a clayey mineral (Figure 6.1, *8,9*; Figure 6.3, *1*), or they can have an inner concentric structure (Figure 6.1, *10*). Metallic particles and Fe microspherules are met in the entire transitional layer of clay but are concentrated predominantly in its lower and middle parts.

Micrometeorites are represented by molten particles composed of pure Fe or Fe–Ni alloy (awaruite). They are 5–20 μm in size (Figure 6.4). Findings of numerous awaruite particles are confined to the upper part of the transitional J layer, whereas Fe particles are met in both the lower and upper parts of the layer.

Fe plates with a transversely hummocky texture (Figure 6.5, *1,2*). These slightly arched plates consist of iron alone and are 10–20 μm wide and up to 150 μm long. They are met at the base of the transitional J

Figure 6.1. Fe and Ni microspherules from the Cretaceous-Paleogene transition layer in the Gams section (here and below, all photographs are made with a SEM): (1) Fe microspherule with a coarse net-hummocky surface texture from the upper part of the transitional J layer; (2) Fe microspherule with a coarse longitudinal-parallel surface texture from the lower part of the J layer; (3) Fe microspherule with elements of crystallographic cut and a coarse cellular-net surface texture from the M layer; (4) Fe microspherule with a fine net surface texture from the upper part of the transitional J layer; (5) Fe microspherule with a fine cellular-net surface texture from the upper part of the J layer; (6) microspherule with a fine cellular-net surface texture from the K layer; (7) Fe microspherule with a fine cellular-net surface texture from the lower part of the J layer; (8–9) hollow Fe microspherule filled with clayey material (J layer); (10) metallic microspherule with a concentric inner structure from the middle part of the J layer; (11) Fe microspherule with a coarse net-hummocky surface texture from the lower part of the J layer; (12) Fe microspherule with a coarse nethummocky surface texture from the lower–middle part of the J layer; (13) Ni microspherule with surface crystallites from the upper part of the J layer; (14) aggregate of baked Ni microspherules with surface crystallites from the upper part of the transition J layer; (15) aggregate of Ni microspherules with surface microdiamonds (C) from the upper part of the J layer.

⇒

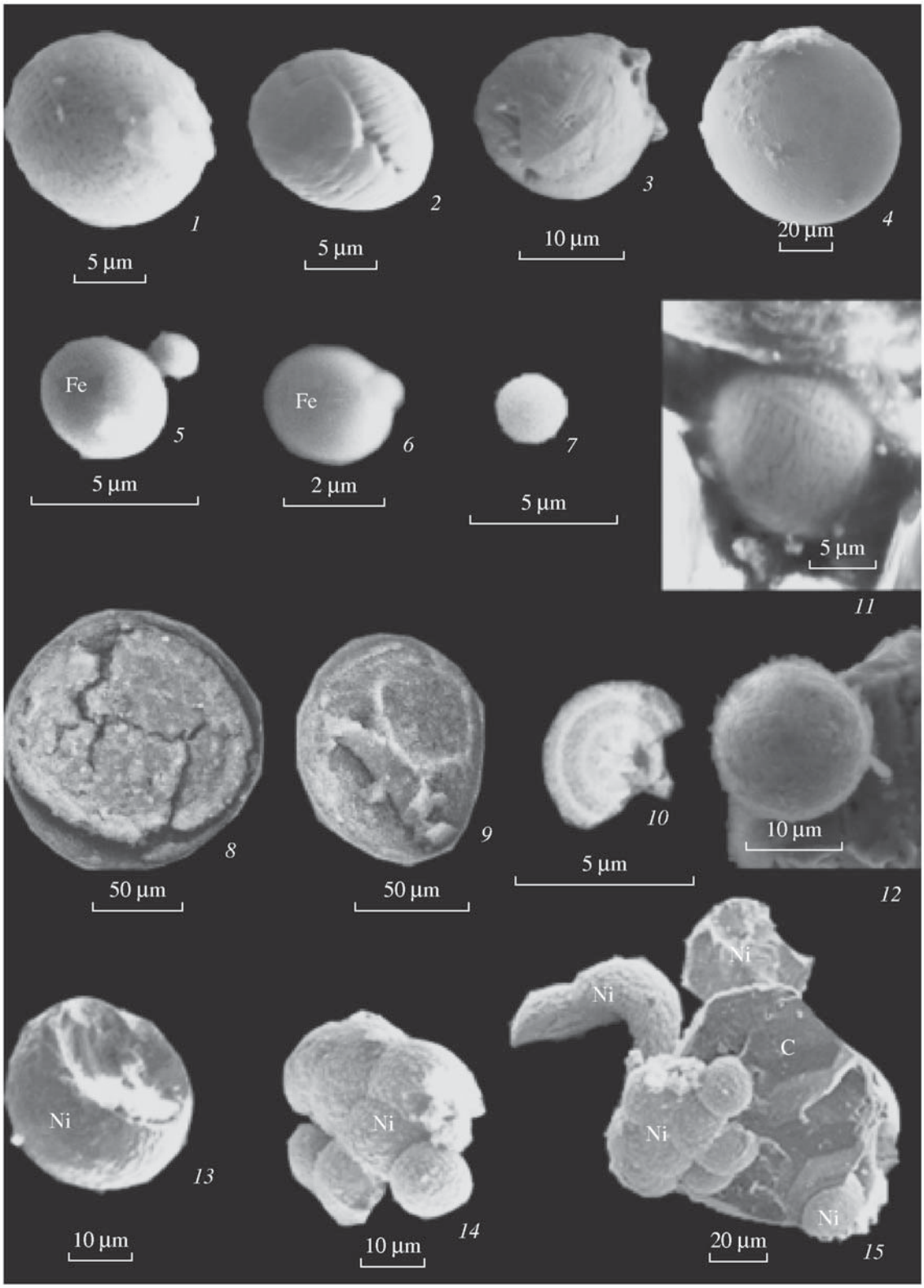
1
5 μm
2
5 μm
3
10 μm
4
20 μm
Fe
5
5 μm
Fe
6
2 μm
7
5 μm
5 μm
11
8
50 μm
9
50 μm
10
5 μm
10 μm
12
Ni
13
10 μm
Ni
14
10 μm
Ni
Ni
C
Ni
Ni
20 μm
15

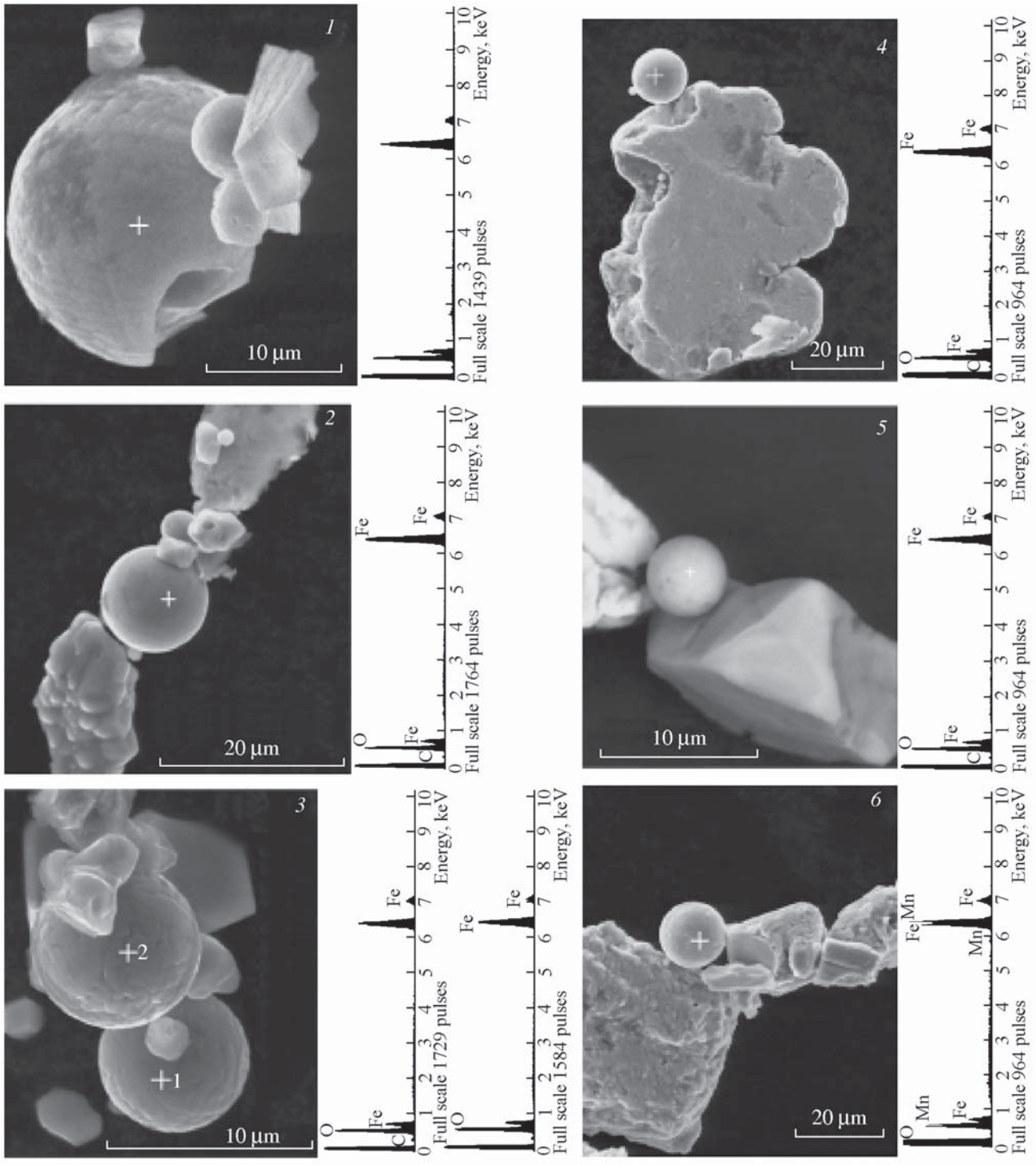

Figure 6.2. Fe microspherules from the Cretaceous-Paleogene boundary layer in the Gams section and their spectra: (1) coarse net-hummocky surface texture, the base of the transitional *J* layer; (2) fine net-cellular surface texture, the base (J_0) of the *J* layer; (3) coarse net-hummocky surface texture, the base (J_0) of the *J* layer; (4) fine netlike surface texture, marl of the *I* layer; (5) fine netlike surface texture, the lower part of the *J* layer; (6) fine netlike surface texture, the base (rust) unit of the *J* layer.

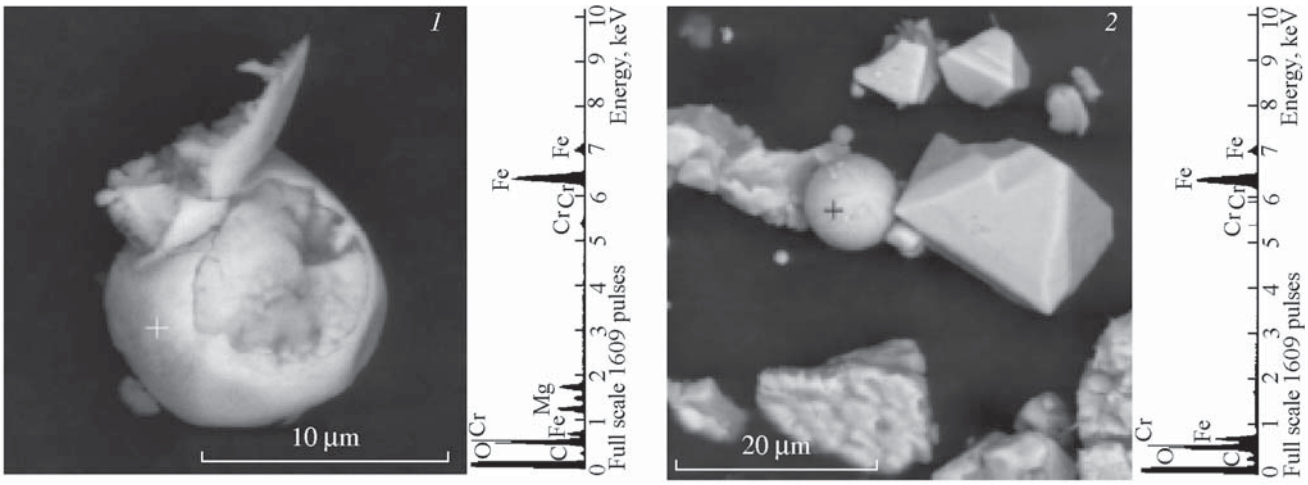

Figure 6.3. Fe microspherules enriched in Cr from the Cretaceous-Paleogene boundary layer in the Gams section and their spectra: (1) Fe–Cr microspherule with a coarse net-hummocky surface texture filled with clayey material, the upper part of the transitional *J* layer; (2) Fe–Cr microspherule with a coarse net-hummocky surface texture, the upper part of the *J* layer.

layer. Fe–Ni plates with a Mo admixture are also found in the lowermost part of the *J* layer (Figure 6.5, *13*; Figure 6.6).

Ni–Fe plates with longitudinal grooves (Figure 6.5, *3,4,7*). Plates of Fe–Ni alloy have an elongated, slightly bent shape and a surface with longitudinal grooves. They are 70–150 μm long and about 20 μm wide. These plates are most widespread in the lower and middle parts of the transitional layer but are also met in its upper part.

Fe plates with longitudinal grooves (Figure 6.5, *5,8,10*). The iron plates with longitudinal grooves coincide in shape and size with plates of Ni–Fe alloy. They are found in the lower and middle parts of the transitional layer.

Metallic iron spirals (Figure 6.5, *10–14*). Hooked pure iron particles in the shape of a regular spiral are of particular interest. They mainly consist of pure Fe and rarely have a Fe–Ni–Mo composition (Figure 6.5, *13*). Spiral-like Fe particles are met in the upper part of

Table 6.3. Chemical composition (wt %) of cosmic dust in various regions of the world

Element	1	2	3	4	5	6	7	8	9	10
Fe	89.48	25	44	80	75	70.94	56.01	4.37	1.11	0.38
Ni	9.97	74	57	20	4	27.63	38.36	95.47	98.78	99.94
Co	0.50	1	2	–	0.5	<0.46	0.10	–	–	–
Mn	–	–	–	–	–	1.24	0.75	0.07	0.03	0.01
Cr	–	–	–	–	–	0.19	0.05	0.11	0.01	0.02
Element	11	12	13	14	15	16	17	18	19	20
Fe	22	72	10	71	68	66	60	44.12	70.08	7.6
Ni	76	2.2	90	2.3	4.4	7.3	3.3	53.96	28.26	92.7
Co	1.4	0.2	1.6	0.4	0.4	0.4	0.3	2.04	1.23	–
Mn	–	–	–	–	–	–	–	–	<0.01	–
Cr	–	–	–	–	–	–	–	0.02	–	–

Note: The columns refer to the following objects: 1, cosmic dust (J. Jedwab, http://www.ub.ac.be/sciences/cosmicdust.pdf); 2–5, magnetite globules from manganese nodules of the Atlantic and Pacific oceans [*Finkelman,* 1970]; 3–10, Ni–Fe spherules from Pleistocene deposits, Canada [*Bi et al.,* 1993]; 11–14, spherules from the Tunguska catastrophe area [*Florensky et al.,* 1968]: core (11, 13) and shell (12, 14); 18, 19, spherules from Eocene limestones, Tuamotu [*Kosakevitch, Disnar,* 1997]; 20, a spherule from deep-sea sediments [*Engrand et al.,* 2005].

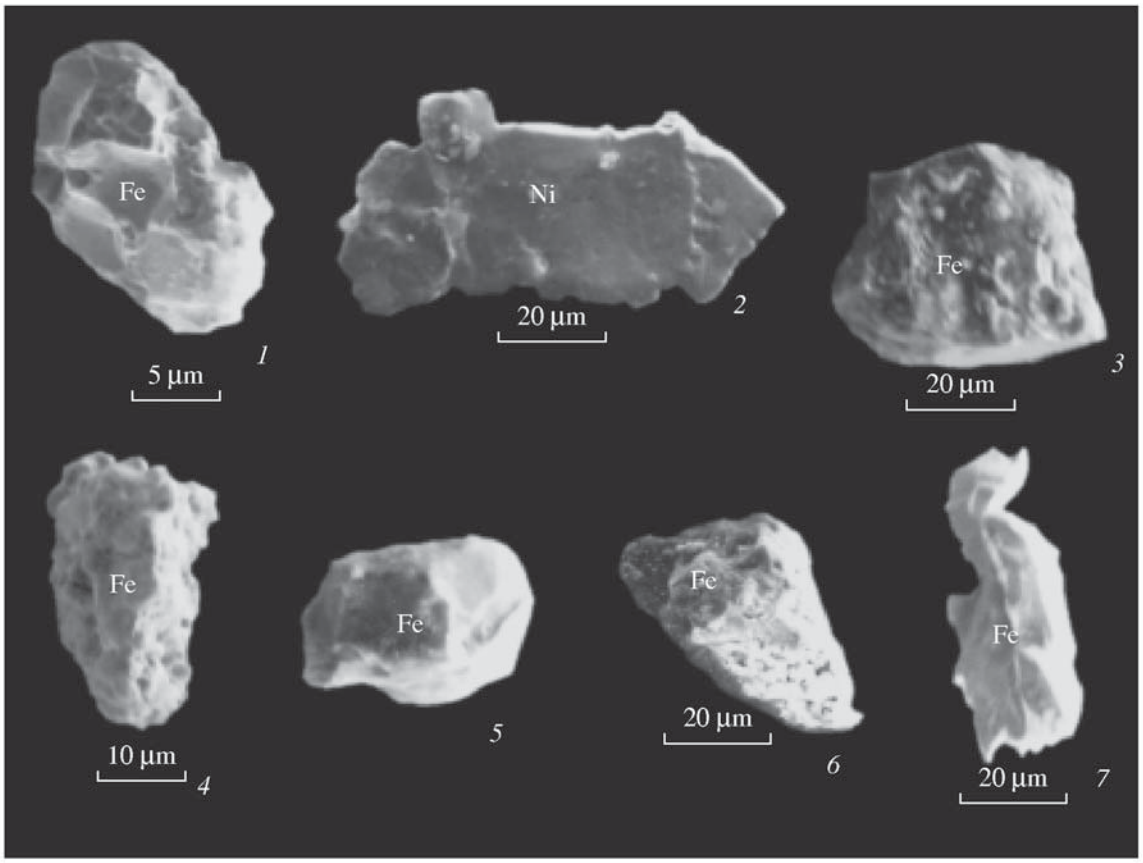

Figure 6.4. Micrometeorites (molten metallic particles) from the Cretaceous-Paleogene boundary layer in the Gams section: (1) Fe particle from the upper part of the transitional *J* layer; (2) Ni particle from the lower–middle part of the *J* layer; (3) Fe particle from the upper part of the *J* layer; (4) Fe particle from the a layer; (5) Fe particle from the upper part of the *J* layer; (6) Fe particle from the lower–middle part of the *J* layer; (7) Fe particle from the middle part of the *J* layer.

the transitional *J* layer and in the overlying sandstone interbed (*K* layer). A spiral-like Fe–Ni–Mo particle is found at the base of the *J* layer.

Microdiamonds and Ni microspherules (Figure 6.1, *13–15*). Several microdiamond grains baked with Ni microspherules are found in the upper part of the transitional *J* layer. The microprobe analysis of nickel spherules carried out with two instruments (equipped with wave and energy-dispersion spectrometers) showed that the Ni spherules consist of virtually pure nickel covered by a thin film of nickel oxide [*Grachev et al.,* 2005]. The surfaces of all nickel spherules are covered with clearly observed crystallites having wellexpressed twins 1–2 μm in size. Such pure nickel in the shape of spherules with a well-crystallized surface is met neither in igneous rocks nor in meteorites, where nickel invariably contains significant amounts of admixtures.

The inspection of the monolith from the section Gams-1 revealed spherules of pure Ni only in the uppermost part of the transitional *J* layer (in the very thin sedimentary layer J_6, whose thickness does not exceed 200 μm), and data of thermomagnetic analysis indicate that metallic nickel is present in the transitional layer beginning from the J_4 sublayer [*Grachev et al.,* 2005; *Pechersky et al.,* 2006a]. In addition to Ni spherules, diamonds are also discovered here. A 1-cm^2 layer removed from a 1-cm cube contains tens of diamond grains and hundreds of nickel spherules (both ranging in size from fractions to tens of microns).

The study of transitional layer samples taken directly from the outcrop revealed diamonds with fine Ni particles on the surfaces of their grains and the presence of moissanite in the upper part of the layer *J*. Previously, microdiamonds were found in the Cretaceous-Paleogene boundary layer in Mexico [*Hough et al.,* 1997].

6.3 Discussion

Iron microspherules with a net-hummocky surface detected in the Gams section are similar to microspherules of baked finely dispersed magnetite found in Pleistocene–Holocene deposits of the Morasko meteorite crater (Poland) [*Stankowski et al.,* 2006] and microspherules with a textured surface described in [*Miono et al.,* 1993] and are identical to microspherules of the Upper Cambrian [*Korchagin et al.,* 2007]. According to the current ideas, a textured surface is inherent only in iron microspherules and particles associated with meteorite falls [*Raukas,* 2000; *Stankowski et al.,* 2006; *Szoor et al.,* 2001]. Thus, the discovered microspherules with a textured surface should be classified as meteoritic dust.

Microspherules with a concentric inner structure found in Gams are analogous to those discovered by the Challenger expedition in deep-sea clays of the Pacific [*Murray, Renard,* 1891]. In Gams, as well as in other regions of the world, hollow microspherules are often filled with clays.

Iron particles of an irregular shape with molten edges or in the shape of spirals and bent hooks and plates are very similar to products of destruction of meteorites falling onto the Earth and can be classified as meteoritic iron [*Raukas,* 2000; *Szoor et al.,* 2001]. Particles of awaruite and pure iron can be assigned to the same category.

However, iron and nickel particles are similar in surface morphology to particles of iron and other metals emitted into the atmosphere during operation of coal power plants [*Giere et al.,* 2003]. Note also that bent Fe particles are similar in shape to various Pele's tears, i.e., lava droplets (lapilli) ejected in the liquid state during volcanic eruptions [*MacDonald,* 1972].

Thus, as seen from the above, the Gams transitional layer of clay has a heterogeneous structure and is clearly subdivided into two parts: iron particles and microspherules prevail in the lower and middle parts of the layer, whereas the upper part is enriched in nickel (awaruite particles and nickel microspherules). This subdivision is confirmed not only by the distributions of iron and nickel particles in clay but also by the data of chemical and thermomagnetic analyses.

Comparison of the data of thermomagnetic and microprobe analyses indicates that the distributions of nickel, iron, and their alloy within the J layer are very irregular; however, according to the results of thermomagnetic analysis, pure nickel is fixed only beginning from the J_4 layer [*Grachev et al.,* 2005; *Pechersky et al.,* 2006a]. We should also note that helical iron is met predominantly in the upper part of the J layer and in the overlying K layer, where the amount of Fe and Fe–Ni particles of isometric or platelike shapes is small.

We should emphasize that such a distinct differentiation in iron, nickel, and iridium, which is characteristic of the transitional clay layer in Gams, is observed in other regions as well. Thus, in New Jersey (the United States), an iridium anomaly is clearly defined at the base of a 6-cm transitional (spherule) layer, whereas impact minerals concentrate only in the upper 1-cm part of the layer [*Olsson et al.,* 2002]. Sharp enrichment in Ni and shock quartz is observed in Haiti at the Cretaceous-Paleogene boundary and in the uppermost part of the spherule layer (unit 1) [*Leroux et al.,* 1995]. It is also noteworthy that siltstones of the a layer (where Fe microspherules are also met in the Gams section), belonging to the middle part of the *Subbotina fringa* zone, are close in age to the layer with an anomalously high Ir concentration in zone 1Pa(1) of the lower Danian in Haiti and to spherule layer 2 (Coxquihui section) in Mexico [*Stinnesbeck et al.,* 2002].

6.4 Conclusion

(1) Many characteristics of the discovered Fe and Fe–Ni spherules are analogous to those of the spherules found in deep-sea clays of the Pacific Ocean by the Challenger expedition [*Murray, Renard,* 1891], in the Tunguska catastrophe area [*Florensky et al.,* 1968], at the fall sites of the Sikhote-Alin' meteorite [*Krinov,* 1971] and Nio meteorite in Japan [*Miura, Uedo,* 2001], in Miocene marls of the Northern Apennines [*Colombetti et al.,* 1998], in present-day deep-sea deposits, and in many other regions of the world (see Table 6.3). In all cases, except for the Tunguska catastrophe area and the fall site of the Sikhote-Alin' meteorite, the formation of both spherules and particles of various morphologies consisting of pure iron (sometimes with a Cr admixture) and Ni–Fe alloy is unrelated to impact events. We derive their formation from cosmic interplanetary dust falling onto the Earth's surface. This process has continued uninterruptedly since the moment of the Earth's formation and is, in a sense, a background phenomenon.

(2) Compositions of many particles studied in the Gams section are similar to the bulk chemical composition of the meteoritic substance found at the fall site of the Sikhote-Alin' meteorite (93.29% iron, 5.94% nickel, and 0.38% cobalt) [*Krinov,* 1971].

The presence of Mo in some particles is not unexpected, because this element is present in many types of meteorites. The Mo concentration in various types of meteorites (iron, stony, and carbonaceous chondrites) ranges from 6 to 7 ppm [*Campbell et al,* 2003; *Murthy,* 1963]. Most important was the discovery of molybden-

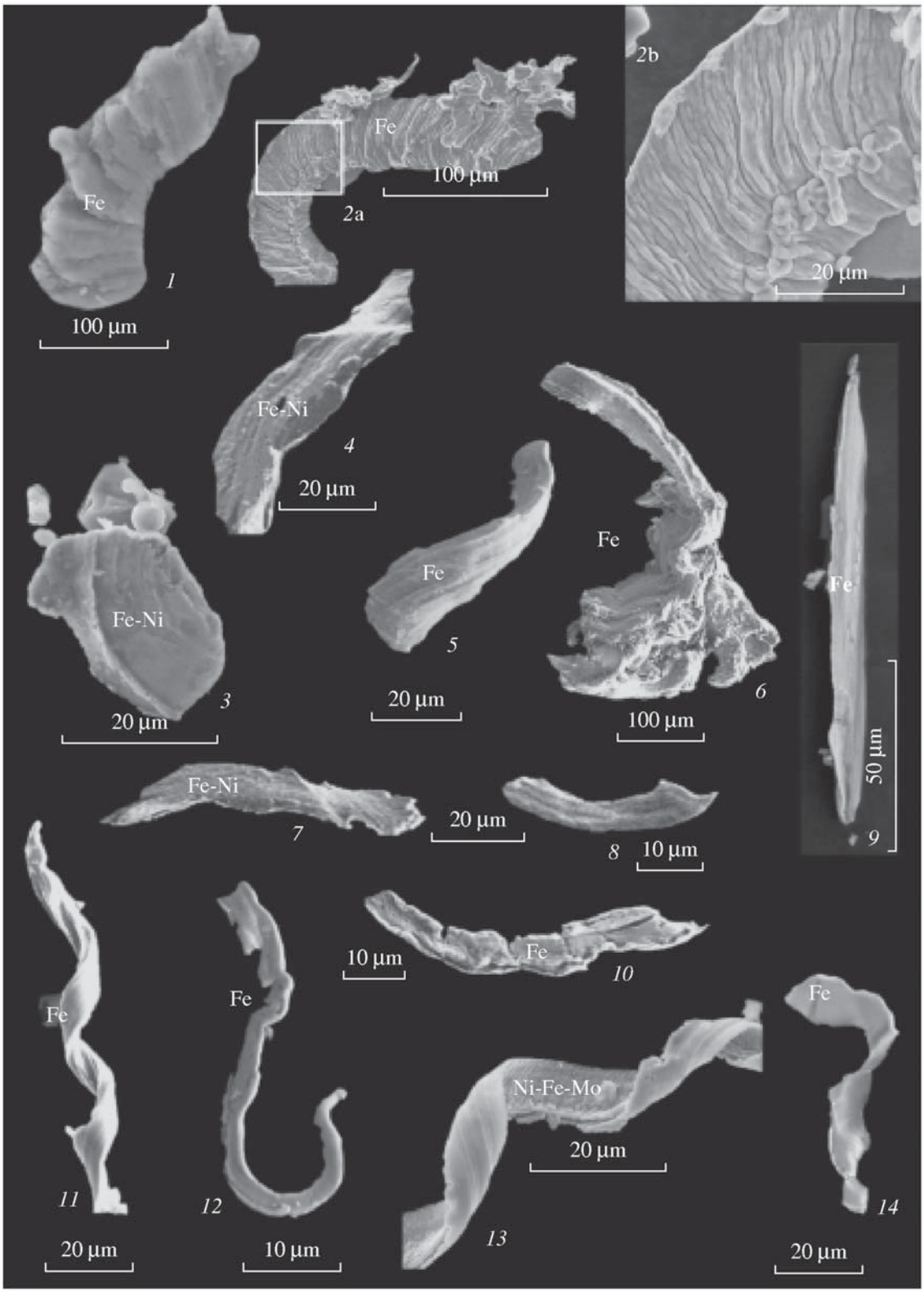

Figure 6.5. Metallic plates of various shapes from the Cretaceous-Paleogene boundary layer in the Gams section: (1) Fe plate with a transverse-hummocky surface texture from the transitional *J* layer; (2a, 2b) Fe plate with a transverse-hummocky surface texture from the base of the *J* layer: (a) general view and (b) a fragment; (3) Ni–Fe (awaruite) particle with a concentric hum-

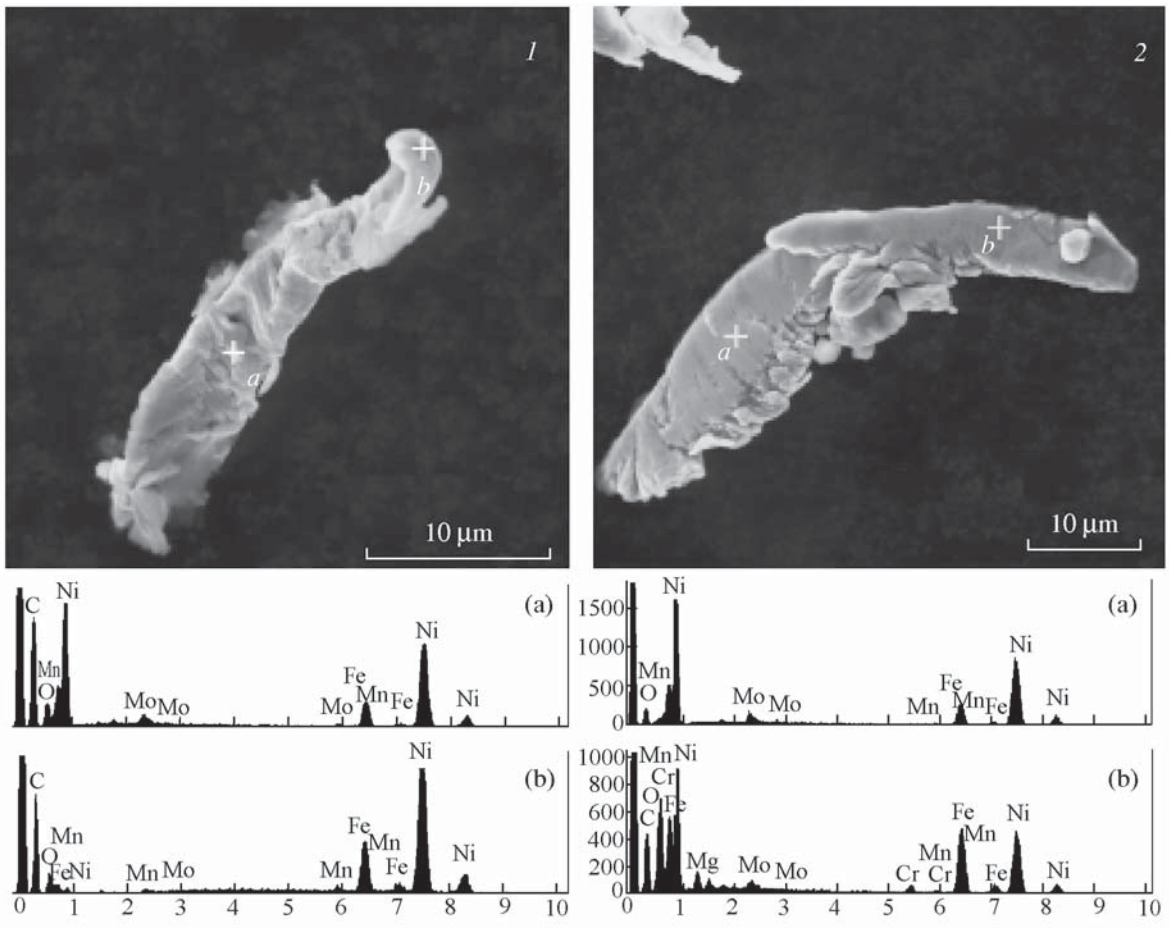

Figure 6.6. Ni–Fe metallic particles (1, 2) enriched in Mo from the base of the transitional J layer.

ite in the Allende meteorite in the form of an inclusion in metallic alloy of the following composition (in wt %): 31.1 Fe, 64.5 Ni, 2.0 Co, 0.3 Cr, 0.5 V, and 0.1 P [*Fuchs, Blander,* 1977]. Native molybdenum and molybdenite were also found in the composition of lunar dust collected by the Luna-16, Luna-20, and Luna-24 automatic probes [*Mokhov et al.*, 2007].

(3) Pure nickel spherules with a well-crystallized surface found for the first time are known neither in magmatic rocks nor in meteorites, where nickel invariably contains a significant amount of admixtures. Such a surface structure of nickel spherules could have formed in the case of an asteroid (meteorite) fall, which would result in release of energy sufficient not only for melting the material of the falling body but also for its evaporation. Metal vapors could have been raised by the explosion to a large height (probably to tens of kilometers), where their crystallization took place.

(4) Awaruite (Ni_3Fe) particles found together with spherules of metallic nickel are a product of the me-

⇐ mocky surface texture from the middle part of the J layer; (4) Ni–Fe (awaruite) plate with surface longitudinal grooves from the lower–middle part of the J layer; (5) Fe plate with surface longitudinal grooves from the lower–middle part of the J layer; (6) baked Fe particles with longitudinal grooves from the lower-middle part of the J layer; (7) Ni–Fe (awaruite) plate with surface longitudinal grooves from the lower–middle part of the J layer; (8) Fe plate with surface longitudinal grooves from the lower–middle part of the J layer; (9) Fe plate from the middle part of the J layer; (10) Fe plate with surface longitudinal grooves from the lower–middle part of the J layer; (11) spiral-like iron from the upper part of the J layer; (12) tubular iron from the K layer; (13) spiral-like Ni–Fe–Mo alloy from the base of the J layer; (14) tubular-twisted Fe plate from the K layer.

teorite ablation and belong to the category of meteoric dust, while molten iron particles (micrometeorites) should be regarded as meteoritic dust (according to Krinov's terminology [*Krinov,* 1971]).

(5) Diamond crystals met together with nickel spherules might have formed during ablation of meteorite from the same vapor cloud in the process of its subsequent cooling. It is known that synthetic diamonds in the shape of single crystals, their intergrowths, twins, polycrystalline aggregates, skeleton crystals, needle-shaped crystals, irregular grains, etc. are obtained by the method of spontaneous crystallization from a solution of carbon in the melt of metals (Ni, Fe) above the line of the graphite-diamond phase equilibrium [*Bokii et al.,* 1986]. Nearly all of the above typomorphic features of diamond crystals were detected in the sample under study.

These results suggest the similarity between the diamond crystallization in the cloud of nickel–carbon vapor during its cooling and the experimental process of diamond spontaneous crystallization from a solution of carbon in a nickel melt. However, a final conclusion on the origin of diamond can be drawn after its detailed isotope investigations, which require a sufficiently large amount of substance.

Thus, the study of the transitional clay layer at the Cretaceous-Paleogene boundary revealed the presence of cosmic substance in all parts of the layer (sublayers J_1 to J_6); however, indicators of an impact event are fixed only beginning from the J_4 sublayer.

Chapter 7. Mantle Plumes and Their Influence on the Lithosphere, Sea-level Fluctuations and Atmosphere

7.1 Introduction

The concept of mantle plumes was clearly formulated in the first work of *Morgan* [1971]. He recognized 20 mantle plumes and considered them to be associated with the convection in the lower mantle, accompanied by heat transfer and by the transport of a comparatively primitive mantle material into the asthenosphere. The ascension of a plume results in the radial horizontal underplating of the material, which gives rise to stresses at the base of lithospheric plates.

An important features that has repeatedly been discussed in the literature is a fixed position of mantle plumes which allows the determination of lithospheric plate motions. Moreover, as was emphasized by Morgan, the initial data on the isotopic (Pb–Pb) ages of basalts from the Gough, Tristan da Cunha, St. Helena, and Ascension Islands may indicate the time during which the lower mantle material can exist without any changes until it is transported by mantle plumes to the surface.

Morgan came to an important conclusion, that mantle plumes are a driving mechanism of lithospheric plates. In this respect, he formulated the following four statements: (1) the majority of mantle plumes are located near the triple junctions of mid-ocean ridge crests, thereby producing the push driving the plates away; (2) mantle plumes arise before the plates start move apart; (3) gravity anomalies and high topographic elevations, observed around each plume, imply that surface volcanic manifestations are not their only effects; and (4) neither mid-ocean ridges nor deep-sea trenches are able to set plates into motion.

Further, Morgan points to intracontinental mantle plumes around the Atlantic: Jurassic Patagonia volcanics related to the Bouvet Island plume; the Parana River complex of ring dikes and flood basalts associated with the Tristan da Cunha Island plume; and the Tertiary Brito-Arctic province of flood basalts and the Skaegaard intrusion (the Iceland or North Atlantic plume). According to Morgan, the development of plumes controlled the formation of both the Atlantic and Indian (Deccan traps and Reunion plume) Oceans.

It is quite evident that the concept of mantle plumes, which originated at the same time as the plate tectonics, is developing into a new paradigm that will incorporate plate tectonics as a constituent element.

7.2 Mantle Plumes and Lithosphere

Influence of mantle plumes on lithosphere is expressed in following major processes:

- intensive volcanic activity leading to outpouring of enormous volumes of lavas in extremely short intervals of time (0.1–0.2 Ma) and formation of volcano-plutonic formations,
- increasing of the lithosphere thickness (underplating) and formation of a high-velocity layer in the base of continental and oceanic lithosphere,
- change of sea-level (eustatic fluctuations).

Mantle plume magmatism. The plume magmatism is characterized by the following major features [*Grachev,* 2003]:

(1) Fissure eruptions result in wide development of flood basalts and shield and lava volcanoes; usual are basalt dike swarms irregularly striking (in contrast to continental rifts). Central-type volcanoes and pyroclastic facies are rare, which distinguishes the mantle plume volcanism from the volcanism of hotspots, island arcs, active margins, and orogenic belts. Acidic

Table 7.1. Characteristics of Phanerozoic mantle plumes volcanism ([*Grachev,* 2003], revised)

Region	Area, km^2	Thickness, m	Age	References
Columbia River	220,000	900	17–6 Ma	[*Hooper,* 1997]
Ethiopia	800,000	to 3500	Pg_1	[*Pik et al.*, 1998]
Yemen	to 100,000	to 1500	31–26.5 Ma	[*Menzies et al.*, 1997]
East Greenland	230,000	to 3000	60–57 Ma	[*Saunders et al.*, 1997]
West Greenland	55,000		60 Ma	[*Saunders et al.*, 1997]
India, Deccan	>1,000,000	2000	67–64 Ma	[*Bhattacharji et al.*, 1996;
			65.6±0.3; 65.4±0.6	*Hofmann et al.*, 2000]
Ninetyeast Ridge			45–80 Ma	[*Weis, Frey,* 1991]
India, Rajmahal	4300	>230	116–113 Ma	[*Kent et al.*, 1995;
Franz Joseph Land			117±2	*Grachev,* 2001]
Madagascar	>10,000	>2000	88 Ma	[*Storey et al.*, 1995]
Ontong Plateau, Pacific	>1,500,000		120–90 Ma	[*Neal et al.*, 1997]
Trinidade			87±2 Ma	
Caribbean-Colombian			93–89 Ma	[*Kerr et al.*, 2002]
Plateau				
Parana River	1,000,000	to 1000	132–137 Ma	[*Stewart et al.,* 1996]
South Africa, Karroo	to 1,000,000	400–1500	182±2 Ma	[*Storey,* 1995]
East Siberia	2,500,000	to 3500	251.2±0.3 Ma	[*Kamo et al.*, 2003]
China, Eimeishan	250,000	to 3700	251.2±0.2 Ma	[*Bowring et al.*, 1998;
			251–253 Ma	*Lo et al.*, 2002]
Kola Peninsula,			370 Ma	[*Tolstikhin et al.*, 1999;
East European platform			356–375 Ma	*Grachev et al.*, 2006c]

differentiates account for a few percent of the total lava volume The total volume of effusive lavas varies from a few hundred thousand to millions of cubic meters, and the duration of magmatic activity is as short as a few million years (Table 7.1). *White, McKenzie* [1995] note that such a high magma production rate cannot be accounted for by melting in the lithosphere, but requires the material supply from greater mantle depths.

(2) According to their petrochemical characteristics, the mantle plume basalts are attributed to basalts of the Fe–Ti type, intermediate between lavas of the alkalic and tholeiitic compositions with the Fenner differentiation trend; in this respect, mantle plume basalts are quite different from basalts of hotspots and rift zones [*Grachev,* 1987, 2000a, 2003]. A distinctive feature of the Fenner trend is the fact that the residual melt is enriched in Ti and Fe and is depleted in Mg, Ca, or Al (or in all of the three elements), as compared with the primary melt composition. Basalts of typical mantle plumes (Hawaii, Iceland, Reunion, and others) have a well-pronounced complete Fenner trend of differentiation, with the weight of its I factor being as large as 75% (for details, see [*Grachev,* 1987]).

(3) Mantle plume basalts are distinguished by a high concentration of MgO (more than 8%) and by usually present picrites. For example, the study of the primary melt composition of the Hawaii and Reunion plumes revealed the presence of basalt komatiites (MgO≥16–18% and $CaO/Al_2O_3 \geq 1$) in addition to usual picrites [*Sobolev, Nikogosyan,* 1994]. The picrite contribution to the total lava volume, as well as magnesia content in the picrites themselves, strongly varies not only from one plume to another, but also within an individual plume. In this respect, basalts of the North Atlantic plume are an excellent example. In West Greenland, picrites account for 30 to 50% of the total lava volume and the MgO concentration reaches 15 to 30% [*Gill et al.,* 1992], whereas in the eastern part of the plume (Hebrides) these values are 5% for picrites and 10 to 18% for MgO [*Kent,* 1995].

According to estimates of various authors [*Albarede,* 1992; *Eggins,* 1992; and others], such melts can form at a mantle melting temperature ranging from 1450 to 1600°C, which agrees with independent estimates made by *Sobolev, Nikogosyan* [1994] for the Reunion and Hawaii plumes and by *Gill et al.* [1992] for West Greenland. Estimates of pressure in primary melts of various recent mantle plumes, made by the same authors, vary from 25–30, 40–50 kbar.

(4) The distribution of rare earth elements (REE) is another important diagnostic indicator of hotspot volcanics [*Le Roex et al.,* 1982; *Schilling et al.,* 1983, 1992]. Significant indicators are the ratios $(La/Sm)_N$ and $(Ce/Yb)_N$; their values in mantle plume basalts

Table 7.2. Iridium concentration (ng/g) in mantle plume volcanics in compare with alkaline intraplate basalts

Region	Ir	References
Greenland Coast, Holes 917, 988, 989, 990	0.10–2.42	[*Philipp et al.*, 2001]
Greenland Coast	0.10–1.58	[*Momme et al.*, 2002]
Rum layered intrusions	5.2–98	[*Power et al.*, 2003]
Rum layered intrusion, Eastern and Western layered series	2.5–3.1	[*Butcher et al.*, 1999]
Deccan traps	0.06	[*Crocket, Paul*, 2004]
Gorgona Island, komatiites	0.6–3.0	[*Brugmann et al.*, 1987]
Cainozoic alkaline basalts, Central Europe	0.01–0.096	[*Agiorgitis*, 1978]

exceed, respectively, 1.8 and 7 [*Le Roex et al.*, 1982; *Schilling et al.*, 1983, 1992].

(5) The most important for the problem under discussion is the high content of platinum group elements (PGE) in mantle plume basalts in comparison with the intraplate alkaline basalts (Table 7.2). The plume volcanics are normally found in association with ultramafic rocks (komatiites and layered intrusions), containing the high concentrations of Ni, Cu, Ir and other PGE (e.g., Noril'sk, Disko Island, and others). Other independent evidence confirming the Ir enrichment in plume volcanic rocks is iridium emissions from active plume volcanoes (see details below).

Thus, several diagnostic features common to various plumes are appropriate for the identification of the mantle plume volcanism. On the other hand, mantle plumes differ depending on region and age. Thus, there is evidence of a certain spatial petrochemical systematics specific to flood basalts of the southern and northern hemispheres [*Gibson et al.*, 1996; *Melluso et al.*, 1995; *Menzies*, 1997; *Storey et al.*, 1995]. Moreover, the variations can be considerable even within an individual volcanic province, as is the case with the Parana or Deccan basalts [*Gibson et al.*, 1996; *Melluso et al.*, 1995].

Periodicity in the mantle plumes evolution. The problem of periodicity in geological processes has frequently been discussed in the geological literature. Recently, attempts were made to interpret the known natural rhythms in terms of the periodicity of deep-seated processes (convective flows in the mantle, dynamo mechanism in the D″ layer, etc.) [*Dobretsov*, 1994; *Loper et al.*, 1988; *Stacey*, 1992; and others].

Vogt [1975] was the first who propose the hypothesis relating the geomagnetic field reversal frequency to rearrangements in the plate kinematics, which occurred approximately at times of 42–45, 70–80, and 110–120 Ma. He developed the idea that the reversal frequency is connected with processes at the core-mantle boundary that give rise to convective flows in the mantle.

Later studies showed that the Cretaceous interval of normal polarity coincides with an increase in the spreading rate and with the wide development of the intraplate volcanism [*Schlanger et al.*, 1981]. Detailed investigations of the islands and submarine volcanoes of the Hawaii–Emperor Ridge revealed that most volcanic eruptions (19 volcanoes of 23) that occurred over the last 10 Myr also coincided with normal polarity periods of the geomagnetic field [*Moberley, Campbell*, 1984]. *Larson* [1991] directly states that no reversals occurred during activity periods of mantle plumes.

These ideas have been further developed in many works (e.g., [*Larson*, 1991; *Larson, Olson*, 1991; *Loper et al.*, 1988; and other]), but the question still remains open.

The Phanerozoic may be subdivided into two distinct periods when no reversals occurred: the Cretaceous period of normal polarity and the Permian–Carboniferous period of reversed polarity. The identification of the possible third period of normal polarity in the Silurian and Late Ordovician needs further studies.

At least two problems are connected with these data. The first is related to the question of why only two plumes are recorded in the history of geomagnetic reversals? The second problem concerns the considerable difference between the time periods of the plume activity (a few million years) and existence of a single polarity geomagnetic field (a few tens million years). Presently, there are no answers to these questions, but it is generally acknowledged that they should be sought for in the origin of processes proceeding in the D″ layer.

Loper et al. [1988] revealed a 26–32-Myr periodicity in the D″ layer instability. Since the temperature gradient in the D″ layer is determined by its thickness [*Stacey*, 1992], variation in the latter controls the dynamo mechanism. The D″ layer consists of thick (75 km) and thin (about 11 km) layers. The stability of the D″ layer is controlled by the thermal structure of the thin layer whose relaxation time t is related to its thickness h and thermal diffusivity k through the formula $t = h^2/k$. Then, assuming k = 1.7 m^2/s [*Loper et al.*, 1988] and h = 11 km, the relaxation time is 22 Myr.

Table 7.3. Major mantle reservoirs ([*Grachev*, 2000a], with complements)

	$^{3}He/^{4}He(10^{-6})$	$^{40}Ar/^{36}Ar$	$^{87}Sr/^{86}Sr$	$^{143}Nd/^{144}Nd$	$^{206}Pb/^{204}Pb$	References
PM	143	0.0001	0.699	0.50660	9.31	[*O'Nions*, 1984]
BSE	>24		0.7047	0.512638		[*O'Nions*, 1984]
PREMA	30		0.7035	0.5130	18.3	[*Zindler, Hart*, 1986]
PHEM	>24		0.704–705	0.5126–0.5128	18.5–19.0	[*Zindler, Hart*, 1986]
FOZO	>11		0.703–0.704	0.5128–0.5130	18.5–19.5	[*Zindler, Hart*, 1986]
LM	40	384.6	0.7033	0.51180		[*Allegre et al.*, 1986]
UM (MORB)	10.1	24800	0.702–0.703	0.5130–0.5133		[*Allegre et al.*, 1986]
DM	6.5	21000	0.701–0.702	0.51320	18.24	[*Chauvel et al.*, 1992]
EM	15		0.7220	0.5121		[*Hart et al.*, 1985]
HIMU	1		0.7029	0.5129	21.5	[*Zindler, Hart*, 1986]
Crust	0.01	>10000	0.7093	0.5101		[*Tolstikhin*, 1975]
Atmosphere	1.399	295.5				[*Ozima et al.*, 1984]

Table 7.4. He, Sr, Nd, and Pb isotope data from basalts of Recent and Phanerozoic mantle plumes ([*Grachev*, 2000a])

	$^{3}He/^{4}He\ (10^{-6})$	$^{87}Sr/^{86}Sr$	$^{143}Nd/^{144}Nd$	$^{206}Pb/^{204}Pb$
Oceanic				
Iceland	30	0.7029–0.7034	0.51296–0.51317	
Galapagos spreading center	1.9–22.9	0.7026–0.7035	0.51290–0.513127	18.4–20.0
Mauna Loa	24.1–27.4	0.70369–0.70375	0.51293	18.11–18.18
Hualali	19.2–24.9	0.7037	0.51293	18.1
Mauna Kea	10–20	0.70350–0.70370	0.51294–0.51301	18.17–18.55
Haleakala	6.6–16.8	0.70314–0.70387	0.51291–0.51310	
Loihi	42.8–44.8	0.70363–0.70376	0.51290–0.51296	18.31
Oahu Island		0.70326–0.70458	0.51267–0.51306	
Samoa Island	10–22	0.7050–0.7070	0.5126–0.51275	19.0–19.1
Easter Island		0.7029–0.7032	0.51294–0.51303	19.4–19.6
Kerguelen Island	7	0.7046	0.51278	18.85
Herd Island	to 18.3	0.7047–0.7050	0.51268–0.51273	
Continental				
Afar	3.4–15.0	0.7027–0.7067	0.51260–0.51315	18.0–19.1
Khamar-Daban Ridge		0.70418–0.7045	0.51268–0.51285	18.0–18.12
Vitim Plateau		0.70405–0.7042	0.51277–0.51284	
Recent Volcanoes of North-Eastern Asia	2.5–18	0.70359–0.7045	0.51283–0.51290	18.55–18.6
North Tien Shan		0.70405	0.51287–0.51330	
Deccan	3.1–13.9	0.7044–0.7093	0.51245–0.51282	18.4–19.3
Rajmahal		0.7041–0.7064	0.51235–0.51287	
Eastern Siberia	1.4–12.7	0.7038–0.7052	0.51239–0.51278	
Parana, $TiO_2 > 2.5\%$		0.7048–0.7078	0.51221–0.51251	
Parana, $TiO_2 < 2.5\%$		0.7046–0.7160	0.51157–0.51215	
Etendeka		0.7044–0.7066	0.51262–0.51283	18.18–19.65
Karroo		0.7049–0.7063	0.51202–0.51236	17.39–17.66
Kola Peninsula	to 30–40	0.7030–0.7050	0.51260–0.51290	

Recently, many authors have paid attention to cycles 30 Myr long [*Dobretsov,* 1994; *Neruchev,* 1999]. Concerning the mantle plumes, an interval of about 60 Myr is preferable, judging from the age of most large provinces of flood basalts such as the Deccan, Parana, North Atlantic and Siberian traps whose relationship with the mantle is rather reliably established (Table 7.1). A more accurate estimate of the periodicity in the volcanism associated with plumes requires a longer observation series covering at least the entire Phanerozoic.

Such a series can be derived from the study of the Nd and Sr isotope variations in Phanerozoic sea-floor sediments [*Faure,* 1989; *Jacobsen, Kaufman,* 1999; *Stille et al.,* 1996; *Veizer et al.,* 1999; and others].

The residence times of Sr and Nd in the sea water are sharply different: about 2×10^6 years for Sr and less than 1×10^3 years for Nd [*Stille et al.,* 1996]. Because the mixing time of the entire water mass in an ocean does not exceed 100 years, the ratio $^{87}Sr/^{86}Sr$ in the water of present oceans slightly varies from one ocean to another, whereas such variations for neodymium are considerable even within an individual ocean [*Faure,* 1989].

Variations in the concentrations of these two elements in marine sediments and fauna are related to two main processes: the transport of continental sediments into oceanic basins (exogenic component) and the interaction within the system basalts–ocean water and fluid regime (endogenic component). Because isotope ratios in the continental crust and in basalts of plumes are sharply different (Table 7.3 and Table 7.4), these two processes have opposite effects. Figure 7.1 shows clear minimums in the isotope ratios $^{87}Sr/^{86}Sr$ encompassing the following time intervals: 150–175, 250–275, 330–360, 360–380, 440–460, and 520–560(?) Ma.

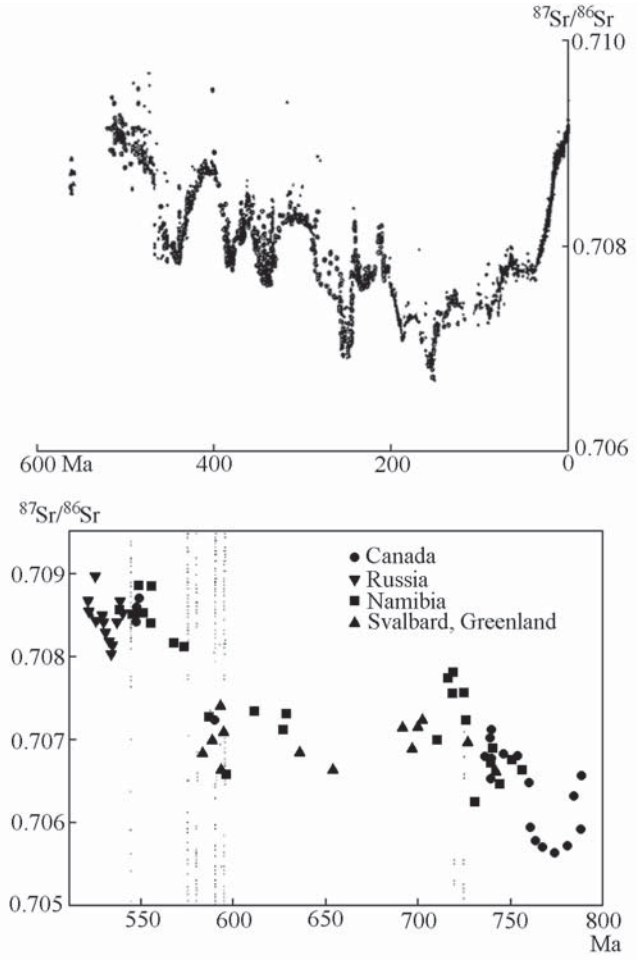

Figure 7.1. The $^{87}Sr/^{86}Sr$ variations in the oceanic water in the Phanerozoic (top) [*Veizer et al.,* 1999] and Late Proterozoic (bottom) [*Jacobsen, Kaufman,* 1999].

The first interval (150–175 Ma) coincides with the initial stage of the Gondwana breakup and with trap eruptions in Africa (Karroo), Antarctic (Ferrara) and Tasmania, related to the initial development stage of the Bouvet plume [*Storey,* 1995]. The second stage manifested itself in eruptions of the Siberian traps, and the third stage resulted in the formation of the vast Kola alkali-ultrabasic province [*Tolstikhin et al.,* 1999] and gave rise to numerous eruptions of flood basalts on the East European platform (Timan and Azov areas, Voronezh anteclise, and Dnieper-Donets aulacogen) [*Grachev et al.,* 1994].

Presently, there is no evidence indicating that the fourth stage was related to mantle plumes, but the following facts are noteworthy [*Qing et al.,* 1998]: (1) one of the largest Phanerozoic transgression occurred during the Caradocian (464–443 Ma), when the land area was reduced and the influx of radiogenic ^{87}Sr was at its minimum; (2) absence of geomagnetic reversals (normal polarity); and (3) wide development of the so-called black shales (bituminous deposits that accumulated in an anaerobic environment). The formation of the latter is considered to be a result of changes in temperature and oxygen concentration in the atmosphere, which occurred at the time of the Cretaceous superplume [*Larson,* 1991]. Within the present continents, there is no evidence that basaltic volcanism took place during this short time interval, but this fact cannot be regarded as an argument against the influx of nonradiogenic strontium from the plume, because such eruptions could occur within the oceanic crust.

The fifth stage, which lasted from 750 to 650 Ma [*Jacobsen, Kaufman,* 1999], coincides with the widely developed trap volcanism of the Late Riphean and Vendian, as has recently been confirmed by data on the Nd and Sr isotope systematic of the China Sinian [*Jedlong et al.,* 1999]. This stage may be associated with the breakup of the supercontinent in the Late Proterozoic.

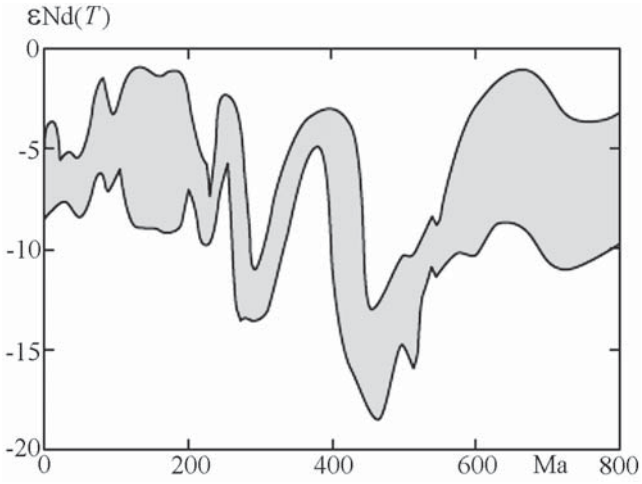

Figure 7.2. The $^{143}Nd/^{144}Nd$ (εNd) variations in the oceanic water in the Phanerozoic and Late Proterozoic [*Keto, Jacobsen,* 1988].

The plot of the $^{87}Sr/^{86}Sr$ variation with time (Figure 7.1) shows no appreciable fluctuations during the last 100 Myr, when at least two peaks in the development of mantle plumes (125–135, 60, and 30 Ma) have been reliably established (see Table 7.1). They are scarcely visible in Figure 7.1, which is likely to be caused by insufficient sampling of the time intervals in question. Actually, a more detailed analysis of the $^{87}Sr/^{86}Sr$ variations over the last 80 Myr gives evidence of a stable minimum in the interval from 90 to 40 Ma [*Ito et al.,* 1998].

The $^{143}Nd/^{144}Nd$ variation plotted in Figure 7.2 (in εNd units measuring the deviation from BSE, see Table 7.3 and Table 7.4) shows maximums at 650, 340–390, 250, 120–170, and 60–80 Ma, as well as a very weak maximum at 30–0 Ma. However, the data on Tethys and the Atlantic Ocean over the last 180 Myr [*Stille et al.,* 1996] rather reliably resolve just the 30-Ma maximum. The comparison of curves plotted in Figure 7.1 and Figure 7.2 shows that, on the whole, maximums of εNd correlate with minimums of $^{87}Sr/^{86}Sr$, which could be expected as noted above. The data on variations in εNd correlate quite well with the known periods of plume development, and the stage of the Vendian trap magmatism is particularly well distinguished [*Jedlong et al.,* 1999].

7.3 Underplating, Topography and Sea-Level Changes

Underplating. *Kaula* [1970] was the first to note the presence of anomalies "that are not quite consistent with the global tectonic pattern of the Earth; these are positive anomalies associated with lava eruptions in both continental and oceanic areas remote from mid-ocean ridges, deep-sea trenches, and island arcs" [*Kaula,* 1970, p. 224]. In this respect, such a typical intraplate mantle plume as the Hawaiian Islands is the most noticeable example: here, a positive free-air gravity anomaly averaging 16 mGal is observed over an area of 6.1×10^6 km^2. Similar, virtually identical values of (free-air and isostatic) gravity anomalies were obtained by Kaula for other, both intracontinental and intraoceanic mantle plumes. Mantle plumes are well recorded by both residual isostatic gravity anomalies and geoid, and cannot be interpreted in terms of standard models of the lithosphere structure, which do not account for deep-seated density inhomogeneities [*Kaban et al.,* 1999].

Formerly, the thick (to 30 km) crust beneath Iceland [*Bott, Gunnarson,* 1980] was somewhat perplexing, because the average thickness of the oceanic crust is 5 to 7 km. The fixism adherents used this fact as an argument for the presence of the crust of continental type here. However, as was established later, there are several oceanic areas of intraplate magmatic activity, characterized by a thick crust; for example, the crustal thickness is 18 to 19 km beneath the Hawaii plume [*Wessel,* 1993] and 14 km beneath the plume of the Marquesas Islands [*Caress et al.,* 1993]. The effect of crustal thickening under mantle plumes was called underplating.

For the first time, the oceanic crust underplating effect was predicted on the basis of the joint analysis of seismological and gravity modeling data from the Hawaiian Islands [*ten Brink, Brocher,* 1987; *Watts, ten Brink,* 1989] thickening beneath the Oahu Island, related to the presence of a hypothetical magma complex at the crustal base (Figure 7.3).

The southwestern Iceland crust, as thick as 24 km, is divided into three layers: the upper layer is 0.7 to 2.5 km thick, and its longitudinal wave velocities (Vp) vary from 2.5 to 5.0 km/s; the intermediate one is 2.5 to 4.0 km thick, with Vp varying from 5.0 to 6.6 km/s; and the thickness of the lower layer averages 17.5 km, and its Vp values range from 6.5 to 7.3 km/s (Figure 7.4) [*Bjarnason et al.,* 1993].

If Iceland is a recent plume, the crustal structure of ancient plumes within the oceanic lithosphere is interesting to consider. Such plumes include the Kerguelen-Herd Plateau formed in the Late Cretaceous (110 Ma) due to very high volcanic activity. The crustal structure under the plateau has recently been determined from a series of refraction profiles [*Charvis et al.,* 1995]. Here, as well as under Iceland, the crust as thick as 25 km is divided into two layers. Layer 2 under the Kerguelen-Herd Plateau is 7 km thick, and its Vp values vary from 4.1 to 6.62 km/s. The crustal structure is dominated by layer 3, about 17 km thick, with its veloc-

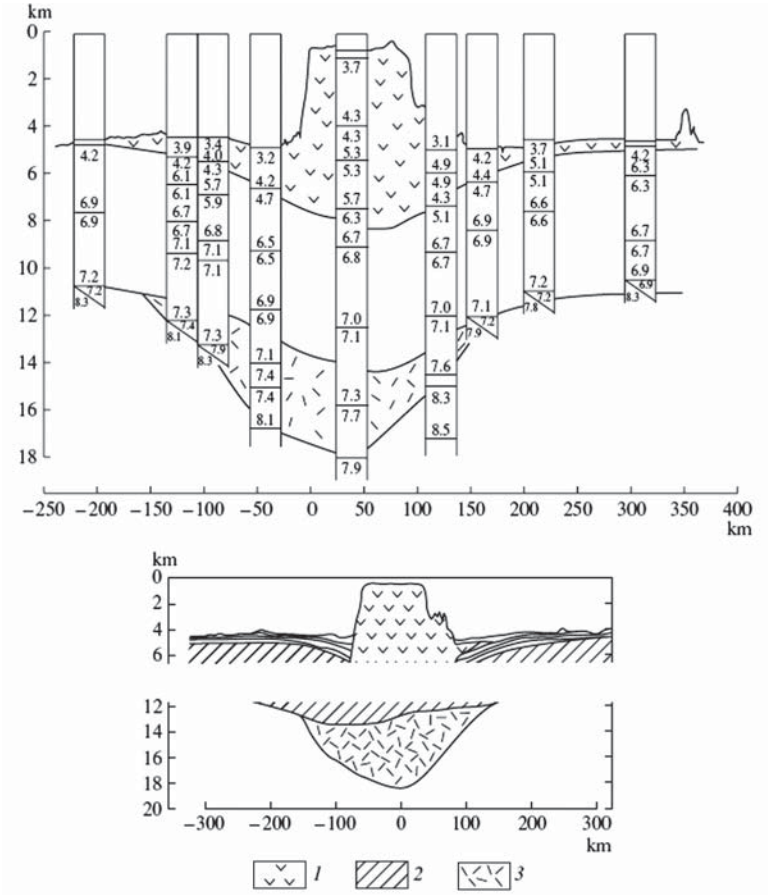

Figure 7.3. Crustal structure under the Hawaii archipelago. Top: seismic sections across the Oahu Island along a profile perpendicular to the Hawaii chain of volcanic islands; the numbers are P wave velocities in km/s [*Watts, Ten Brink,* 1989]. Bottom: interpretation of the section [*Ten Brink, Brocher,* 1987]: (1) volcanic edifice of the Oahu Island; (2) oceanic crust; (3) tentative magma complex at the base of the oceanic crust.

ities Vp varying from 6.54 to 7.42 km/s [*Charvis et al.,* 1995]. The velocity structures beneath the Kerguelen-Herd Plateau, Iceland, and the Hawaiian Islands are similar and, therefore, reflect a general regularity inherent in the mantle plume crust. The crustal thickening and high seismic velocities in the lower crust are due to magmatic activity that results in the solidification of melts and accretion (underplating) of the crust from beneath. However, the underplating effect is recognizable far below the Moho as was established for the ancient mantle plume of the Parana trap province [*VanDecar et al.,* 1995]. Here, a low-velocity mantle anomaly reaching 300 km in diameter extends to depths of at least 500–600 km. This anomaly may be considered as evidence of a density deficit related to the formation of a vast layered intrusion as a result of the solidification of the mantle plume melt. Thus, the crust underplating mechanism gives rise, in the long run, to a structure that I call a plume pillow by analogy with the rift pillow [*Grachev,* 2000a].

Underplating and topography. Another important consequence of underplating is formation of high elevations of areas within large igneous provinces (LIP) (Deccan, South Africa, Eastern Siberia traps) developed in regions of stable tectonic regimes. These areas are distinguished from other platform regions by anomalously high elevations (more than 2000 m) whose origin has been poorly understood until recently.

For instance, the formation of the present Siberian platform (SP) topography was traditionally associated with tectonic movements (neotectonics). Beginning from the 1950s, several maps of neotectonics of this territory have been constructed on various scales (see list of references in [*Grachev,* 2000c]). With minor differences, these maps display fairly large values of neotectonic movement amplitudes (up to 1000 m on the Putorana Plateau). Determining these amplitudes, authors generally assumed that the position of the initial planation surface was close to the sea level but, in the

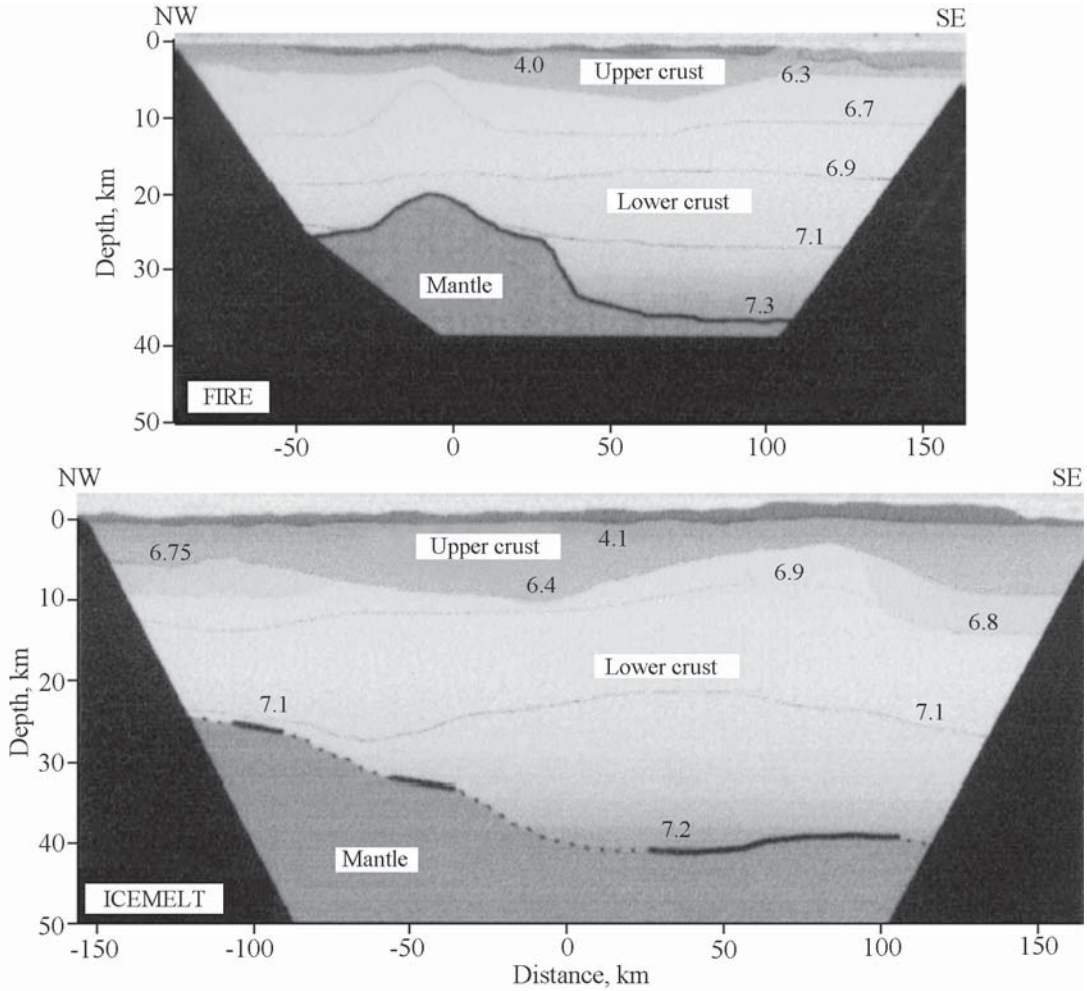

Figure 7.4. Structural model of the crust under Iceland. Top: section across the axial spreading zone FIRE project [*Staples et al.*, 1997]. Bottom: cross section immediately under the central part of the plume (50 to 100 km of the profile), ICEMELT project [*Darbyshire et al.*, 1998].

case of SP, this was not supported by any reliable data. Moreover, it is noteworthy that, in the adjacent West Siberian platform (WSP), which experienced a subsidence in the post-Permian time, a trap formation of the same age and composition as that in the SP occurs at the base of the sedimentary cover. As distinct from the SP, the WSP trap formation has a somewhat smaller thickness but, after the epoch of trap magmatism, the WSP developed as a post-rifting sedimentary basin, while the SP developed as a stable platform region.

As follows from geological evidence, before the onset of trap magmatism in the epoch of deposition of the Tunguska series 100 to 1400 m thick (Middle Carboniferous–Late Permian), the SP territory was represented by a shallow sedimentary basin whose subsidence was compensated for by sedimentation [*Czamanske et al.*, 1998]. This implies that the position of the surface onto which the trap formation lavas flowed was close to the sea level.

Based on the features of geological development, one may state that, in the pre-neotectonic (25 Ma) stage of development, the SP elevations exceeded the present-day values. Actually, the comparison of the elevation distribution with the geological structure shows that the highest elevations are observed in outcrop areas of the trap formation whose age has recently been estimated at 251 Ma [*Reichow et al.*, 2002; *Renne, Basu*, 1991] and, moreover, basalts had mostly formed over a very short time interval (less than 0.2 Myr). After the trap formation, the SP territory was under subaerial conditions, which naturally caused weathering, denudation, and erosion of the relief formed by that

time. Even with minimal estimates of the denudation rate of about 1 m/Myr, about 300 m of basalts should have been scoured and, taking into account the planation, this value should be considerably larger.

Thus, the present SP topography cannot be accounted for in terms of neotectonics. As we mentioned above the other platforms subjected to trap magmatism also have high elevations; for example, these are the Indian platform with Deccan traps (65 Ma) or South African platform with Karroo traps (180 Ma). Moreover, high elevations in such regions are generally characteristic of both areas where lavas have preserved and areas where they are presently scoured.

An arch formation is usually postulated to precede the onset of magmatism in model describing the development of mantle plumes [*Cox,* 1989]. The amplitude and the radius of the uplift depend on many parameters, the most significant of which are distinctions in the viscosity of the plume and surrounding mantle and the thickness and the thermal state of the lithosphere in the region where the plume approaches the lithosphere base. However, in the case of the Siberian platform, no evidence of the existence of an arch before the magmatism onset is present [*Fedorenko, Czamanske,* 1997], as distinct from the coeval Emeishan basalts in China, where the existence of a dome-like uplift with amplitudes of up to 1000 m before the plume magmatism onset has been established reliably enough from geological sections [*He et al.,* 2003].

Although the thickness of the trap formation (3000–3500 m) is observed in the Norilsk and Maimecha–Kotui areas, distinguished by the highest elevations [*Fedorenko, Czamanske,* 1997; *Fedorenko et al.,* 1996], this correlation alone is insufficient to draw any definite conclusions.

First of all, the question arises of why the mantle plume activity in the Siberian platform has led to an uplift of the surface, whereas the same process in Western Siberia caused its subsidence. As is known, the initial stage of the mantle plume development within continents is expressed in the buildup of the pre-rifting regime, when basic lavas (flood basalts, or traps) are erupted against the background of the formation of low-thickness continental sequences of the platform type. The further development of the plume, when it spreads under the lithospheric base, leads to thinning of the crust (the rifting process) and finally to its breakup and the beginning of spreading. A classic example of this evolutionary succession is the Afar triangle region, where all stages described above have been reliably established, being accessible to a direct examination. From a more general standpoint, we may state that mantle plumes are the driving mechanism of the continental-to-oceanic crust transformation.

Based on these ideas, we believe that, beginning from the Triassic, the development of the Siberian and West Siberian platforms was associated with a superplume whose specific evolution was predetermined by the preceding (preplume) geological history, resulting in distinctions in the lithospheric structure [*Grachev, Kaban,* 2006].

Considering the relationship between the topography and specific features of the development of the Siberian platform trap formation, it is basically important to note a distinct correlation between the distribution of elevations and the occurrence of trap fields. Thus, 97% of all SP traps are confined to the Putorana plateau, including its continuation in the Norilsk region [*Sharma et al.,* 1992]. The plateau is located within the most bent part of the Tunguska syneclise and bounded by ancient faults to the north and west. The relief of the plateau is asymmetric: its northern part is characterized by maximum elevations and has distinct boundaries, whereas its southern part is a monocline dipping in the sediment direction at angles of a few tenths of degree and extending for 500–700 km. The results of gravitational modeling using the available complex of geological and geophysical information indicate that the density structure of the Siberia mantle lithosphere is extremely inhomogeneous [*Grachev, Kaban,* 2006]. This conclusion is based on the analysis of mantle gravity anomalies obtained after the effect of crustal density inhomogeneities (including variations in the surface and Moho topographies) was removed from the observed gravity field. The overall amplitude of mantle anomalies within Eastern Siberia exceeds 200 mGal, which is well above the possible determination uncertainties [*Kaban et al.,* 1999]. The values of mantle anomalies are smallest in the central and northwestern Eastern Siberian highland, implying that the density of the mantle lithosphere is minimal here (Figure 7.5).

The density anomalies inferred in the subcrustal layer of Eastern Siberia must be related to variations in the upper mantle composition. In this case, the lower density zone in NW Eastern Siberia can be considered as a direct consequence of mantle plume activity that took place 251 Myr ago. It is noteworthy that the decompaction zone in the upper mantle approximately corresponds to the zone of the maximum thickness of trap formations. Thus, the formation of the present SP topography had been controlled by the thickening of the crust due to underplating caused by the development of a giant mantle plume at 251 Ma.

Underplating and sea-level changes. Fluctuations of sea-level during the Phanerozoic occur in cycles of various duration. Cycles of the first (10^8 year) and second (10^7 years) order are called tectonic-eustatic, the nature of cycles of 10^6 years is unknown and, finally, cycles of 100,000 and 10,000 years are considered

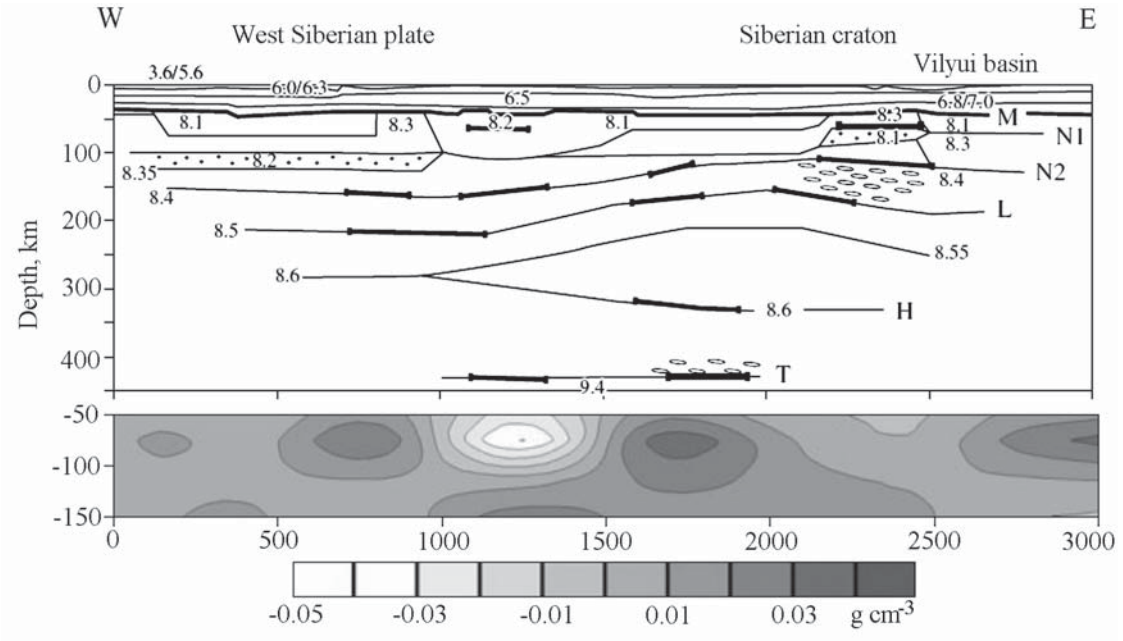

Figure 7.5. Seismic and density structures of the crust and upper mantle of the Siberian Platform West Siberian Basin along the Kimberlit DSS profile [*Grachev, Kaban*, 2006].

glacio-eustatic (Figure 7.6) [*Hallam*, 1981, 1992]. Let us focus our attention on cycles of 10^6 years because their nature remains disputable.

For a long time the mechanism of transgressions and regressions was connected to the geocynclinal process, assuming that closing of geocynclines entailed transgressions on continental platforms. Plate tectonics has shown that either geocynclines or geocynclinal cycles do not exist. It has been suggested that transgressions and regressions are regulated by rate sea-floor spreading [*Pitman*, 1978] as a result by uplifts or changes in the length of Mid-Oceanic Ridges (MOR), which now occupy about 25% of the Earth's area. However in the framework of the current steady-state thermal model of plate tectonics the height of MOR is a constant value, close to a depth of 2700 m [*Bird, Isacks*, 1972]. There are no available data for the Phanerozoic, providing the evidence of the lithosphere thermal regime variations, therefore eustatic fluctuations of sea-level cannot be explained by changing of the global MOR topography a priori. Another suggestion is based of the change of the MOR length in time: the idea was that an increase of volume of ocean basins entails regression and that of the area of mid-oceanic ridges – transgression [*Pitman*, 1978]. But both these two processes are interrelated according to the plate tectonics paradigm, so these effects must neutralize each other.

According to a recently popular hypothesis spreading was believed to change with time. However, the magnetostratigraphic data of the ocean floor have shown that over the past 150 million years the spreading rate altered insighificantly [*Harland et al.*, 1990], and the estimations of formation of the ocean crust during the 180 million years of history of the ocean lie within the interval from 3.0 to 3.4 km^2/year [*Rowley*, 2002]. Hence, the spreading cannot explain eustatic oscillations over the period of 10^6 years.

Another aspect of the problem relates to the fact that eustatic oscillations of the sea level are appearing at more or less regular intervals, and any hypothesis must include justification of such phenomenon. Eustatic oscillations of the sea level cannot be explained only by the processes occurring only within the oceanic crust. Change of the area and height of continental blocks are no less important, although their role has been ignored in some well-known publications [*Hallam*, 1981; *Hardenbol et al.*, 1998; *Pitman*, 1978; *Vail et al.*, 1977; and others]; see reference [*Rowley*, 2002].

Fisher [1984] was the first who provided that a change of area and thickness of continental crust could influence eustatic oscillations of the first order. It was assumed that during the formation of supercontinents thickness of crust increased causing sea regression. For instance, during the Pangea formation in the Late Palaeozoic the sea-level has sharply declined (Figure 7.7). The second minimal value on the curve (Figure 7.7) is related to the Rodinia supercontinent.

Zhang, [2005] has recently explained that during the supercontinent formation the mean height would increase approximately by 0.5 km, the crust thickness – by 3 km and total area would decrease by 7%. This leads to growing of the area of the ocean basins and

sea level drop about 200 m. A mechanism of formation of supercontinents as a result of new model of mantle convection was suggested by V. Trubitsyn (see [*Trubitsyn, Trubitsyn,* 2005], and reference ibid.). Thus eustatic changes of the sea level of the first order find their explanation in frame of plate tectonics paradigma with some modifications.

The cycles of second order lasting from 1 to 10 Ma, as it was mentioned, cannot be connected to changes of the spreading rate or change of the length of mid-oceanic ridges. The most probable driving mechanism, explaining the second order cycles, are mantle plumes, developing within both the continental and oceanic lithospheres and leading to the process of underplating [*Maclennan, Lovell,* 2002].

The concept of mantle plumes allow to explain for the first time the eustatic changes of sea level. Development of mantle plumes within continental lithosphere entails, due to underplating and the formation of high-velocity layer in the base of the crust, uplift of continents and, consequently, regression. Development of mantle plumes within the ocean lithosphere leads to formation of oceanic plateaus, decreasing the volume of ocean basins and causing transgressions. Growth of oceanic plateaus produces moderately rapid sea-level rises (60 m/Ma) but slow falls due to thermal subsidence (10 m/My) [*Miller et al.,* 2005].

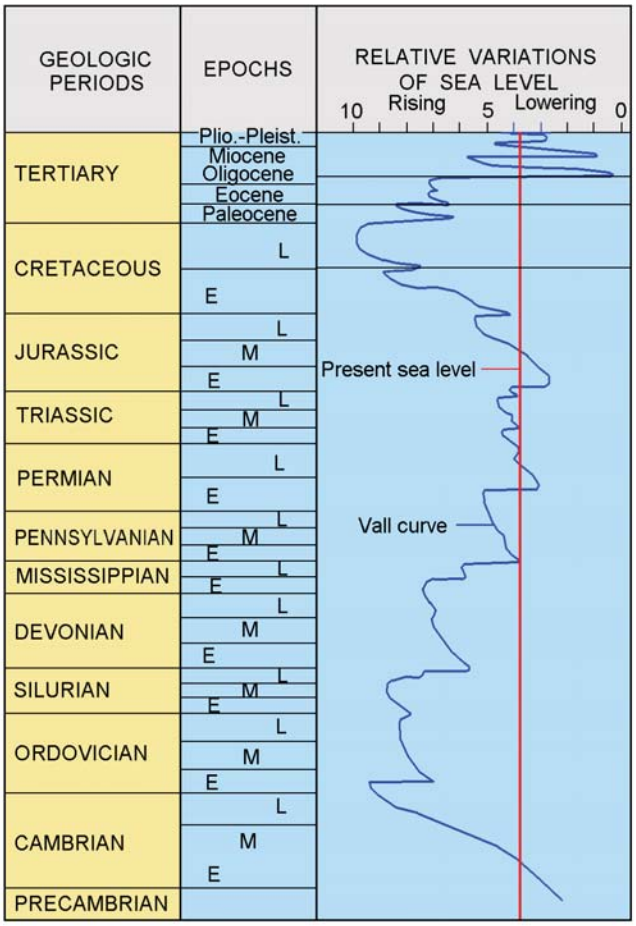

Figure 7.6. Phanerozoic eustatic sea-level plotted relative present sea-level (the Vail curve) [*Vail et al.,* 1977].

7.4 Mantle Plumes and Atmosphere

Volcanism is one of the most important processes, influencing the state of the atmosphere, hydrosphere and environment as a whole. It was estimated that over the last 100 years (1900–2000) there were more than 4200 active volcanoes on the earth's surface [*Halmer, Schminke,* 2003]. At the present time more than 800 active volcanoes are known (active volcanoes exist also at the bottom of the ocean). They act in different geodynamic environments and the chemistry of volcanic gases varies (Table 7.5). Gas emissions from modern volcanoes (surface and submarine) release from 130 to 230 Kt of volatile gases [*Gerlach,* 1992].

The study of volcanic gases has shown that two forms of volcanic gas emissions exist: an active form, occurring during a volcano's eruption and a passive, when a volcano is quiet, and gas emissions occur at its flanks along cracks and ruptures. It has to be mentioned that the volumes of the both types of gas emissions are comparable.

The study of gas composition of several volcanoes has revealed a non-steady character of gas emissions either in time or in space [*Gerlach, Graeber,* 1985; *Sutton,* 1992; *Sutton et al.,* 2001; *Zreda-Gostynska et al.,* 1993; and others]. It complicates data extrapolation in lengthy time intevals. Moreover, the history of research of volcanic activity is aware of the facts of catastrophic eruptions (Toba, 74 thousand years ago; Laki, 1783; Krakatau, 1883; Tambora, 1815, etc.). Their effects were so impressive that they created the expression "volcanic winter" [*De Boer, Sanders,* 2005 (see below)]. These circumstances have to be taken into account while estimating the impact of volatile gas components on the atmosphere and hydrosphere in the geological past.

The chemistry of gases emitted into the atmosphere by volcanic eruptions depends considerably on the nature of the melted substance (mantle), melting temperature and also on the type of eruption (fissure or central type). The main components of volcanic gases are: H_2O, CO_2, CO, CH_4, SO_2, H_2, H_2S, Cl, F, He, Ar, metal chlorides and fluorides [*De Boer, Sanders,* 2005; *Frankel,* 2005; *MacDonald,* 1972; and others].

Composition of mantle fluid. The specific character of chemistry of magmatism of mantle plumes also implies the specificity of fluid regime, related to

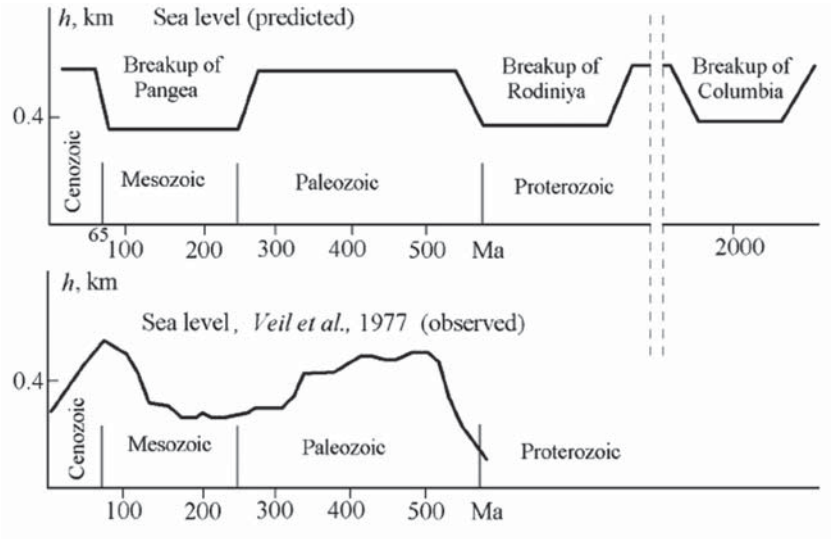

Figure 7.7. Global variations in the sea level: top – predicted as a result of numerical modeling of interacting floating continents [*Trubitsyn, Trubitsyn,* 2005], bottom – the Vail curve [*Vail et al.,*1977].

convective heat and mass transfer of the deep material. Estimaits of the mantle plume fluid composition are based on modelling results and experimental study of fluid inclusions in minerals and xenoliths of spinel lherzolites [*Draibus et al.,* 1997; *Marty, Tolstikhin,* 1998; *Nadeau et al.,* 1999; *Ryabchikov,* 1998; *Trull et al.,* 1993; *Wallace,* 1998; *Wyllie, Ryabchikov,* 2000; and others]. Fluid composition of primitive and depleted mantle differ in their main components (Table 7.6), although a scatter in values is evident, which is related to the transport of volatiles into the mantle during subduction. Most interesting are the estimates of the plume concentrations of H_2O and CO_2, which are the main fluid components controlling such physicochemical processes as metasomatism, partial melting, mantle deformations, etc. The data of Table 7.6 are ambiguous and do not allow one to confidently state that the two mantle reservoirs are basically different. It is appropriate to discuss this problem on the basis of experimental data on fluid compositions in both mantle plume basalts and mantle xenoliths, taking into account their helium signature ($^3He/^4He$) as an indicator of their plume origin [*Marty, Tolstikhin,* 1998]. Although few works have been devoted to the combined study of the He isotope systematics and fluid composition in samples, certain conclusions can be drawn from their results. The data on the fluid composition in basalts and mantle xenoliths in which $^3He/^4He$ exceeds the NMORB show that their H_2O concentration is an order of magnitude higher than in the basalts and xeno-

Table 7.5. Chemical composition of gases of volcanoes (%) from different geodynamic conditions [*Fedotov,* 1984; *Symonds et. al.,* 1994]

Volcano Geodynamics Temperature	Kilauea Plume 1170°C	Erta Ale Divergent boundary 1130°C	Nyiragongo Continental Rift	Momotombo Convergent boundary 820°C	Tolbachik Convergent boundary 920–950°C
H_2O	37.1	77.2	38.9	97.1	70.5
CO_2	48.9	11.3	46.2	1.44	10.9
SO_2	11.8	8.34	4.4	0.50	0.16
H_2	0.49	1.39	0.8	0.70	0.39
CO	1.51	0.44	2.4	0.01	0.57
H_2S	0.04	0.68	–	0.23	0.26
HCl	0.08	0.42	–	2.89	1.08
HF	–	–	–	0.26	0.06

Table 7.6. Fluid composition (ppm) in the primitive and depleted mantles ([*Grachev,* 2000a], revised)

Reservoir	H_2O	CO_2	N_2	Cl	F	References
Primitive Mantle	560–1160	350–430	1.7–3.2	4.8		[*Ryabchikov,* 1998; *Wyllie, Ryabchikov,* 2000]
″	700–1000	100–700	10	20–50	20–30	[*Kogarko, Ryabchikov,* 1988]
″	270±20	440	2			[*Wallace*, 1998]
Depleted Mantle	150–220	270	0.24	1.6		[*McDonough, Sun*, 1995; *Ryabchikov,* 1998]
″	140–200	20–140	2	5–10	5–10	[*Kogarko, Ryabchikov,* 1988]
″	93±31					[*Draibus et al.*, 1997]
NMORB	140±40	30–1014		30–70	100–130	[*Kingsley, Schilling*, 1995; *Rowe, Schilling*, 1979; *Wallace*, 1998]
Hawaii, basalts	450±190 –525±75				319	[*Wallace*, 1998; *Draibus et al.*, 1997]
Iceland, basalts				110–230	200–270*	[*Rowe, Schilling*, 1979]

Note: * According to *Stecher* [1998], F, concentrations have a considerably larger scatter (from 10 to 300 ppm).

liths from degassed reservoirs. In the case of CO_2, such differences are absent, and this conclusion is independently supported by data on variations in the CO_2 concentration and $^3He/^4He$ in mid-ocean ridge basalt glasses and in basalts of mantle plumes [*Marty, Tolstikhin,* 1998] and mantle xenoliths from various regions [*Trull et al.*, 1993], as well as by data on significant variations in the $CO_2/^3He$ ratio in hydrothermal solutions of the Loihi seamount (10^8–10^9) [*Hilton et al.*, 1997]. Also, note that the composition of fluid inclusions in olivines from basalts and dunite xenoliths of the Hawaii and Reunion plumes is dominated by CO_2 (0.3–0.6 wt. %) and H_2O (0.1–1.2 wt. %) [*Sobolev, Nikogosyan*, 1994].

Based on the fluid composition data from Devonian alkali intrusions of the Kola Peninsula, with their fluid CH_4 concentration reaching 97 vol % (Khibiny and Lovozero massifs) [*Kogarko,* 1977], and taking into account the recent hypothesis about the plume origin of these massifs [*Tolstikhin et al.*, 1999], one may suggest high hydrocarbon concentrations in mantle plumes. Similar high concentrations of methane (73–92%) in alkali rocks of the Precambrian Gardar complex and Southern Greenland [*Konnerup-Madsen, Rose-Hansen*, 1982] make the ultrabasic alkali complexes promising for further studies of the mantle plume fluid composition. Recent data [*Nadeau et al.*, 1999] revealed a bimodal distribution of the hydrogen isotope composition in apatite from 15 alkali intrusive complexes ranging in age from 110 Ma to 2.6 Ga (including Devonian alkali intrusions of the Kola Peninsula). A group with δD varying from –52 to –74‰ and with high concentrations of H_2O and CO_2 (up to 1.1 and 0.7%, respectively) crystallized from a nondegassed primitive mantle reservoir.

Gerasimovskii [*Belousov,* 1978] reports that the hydrogen concentration in Iceland basalt fluids varies from 0.22 to 0.99 cm^3/kg (reaching 96 vol %), whereas the CO_2 and CH_4 concentrations are, respectively, 3 and 1 vol %. Along with a high ratio $^3He/^4He$ (more than twice as high as the MORB values of $^3He/^4He$, these data corroborate the hypothesis that the composition of the fluid furnished by mantle plumes is dominated by hydrogen).

Whereas H_2O dominates in the composition of the gas phase of volcanoes, usually comprising more than 60% of the total number (Table 7.5), the most interesting are the variations of the two other main components – CO_2 and SO_2, influencing the atmosphere. The main difference is determined not only by different content of CO_2 and SO_2, which even for separately chosen volcanoes strongly varies in time, but by the nature of a source, namely by melting depleted or nondepleted composition of mantle, content of water and other volatiles in the mantle, and also PT conditions of melting. Depending on a volcano's tectonic position and emanations composition the content of these components varies significantly. From this viewpoint the following geodynamic volcanic situations can be specified: mantle plumes, zones of oceanic and continental rifting, island arcs and active continental margins and areas of interplate oceanic activity (volcanic islands).

The principal difference between volcanic gases of different geodynamic conditions lies in their isotopic helium mark. Ratio R/R_a of the lavas and volcanic gases of modern mantle plumes, like Hawaii, Iceland,

Table 7.7. Basic carbon reservoirs [*Anderson, Arthur,* 1983; *Des Marias,* 2001]

Reservoir	Mass 10^{15} g (Gigatons)	δ^{13}C PDB
Atmosphere	775	–6
Ocean	35,000	0
Land biota	1600	–25
Soils	1000–3000	–25
Nonorganic C (carbonate rocks)	60,000,000	0–1
Organic C	15,000,000	–23
Continental crust	7,000,000	–6
Mantle	342,000,000	–5

Reunion exceeds 12 (where R_a is ratio $^3He/^4He$ = 1.39×10^{-6} in the atmosphere) [*Grachev,* 1998a, 1998b, 2000a, 2003; *Hilton et al.,* 1997]. At the same time gases of the MORB type source (basalts of mid-oceanic ridges) are characterized by ratio $R/R_a = 8\pm1$ [*Tolstikhin,* 1975; and others]. Gases and lavas of island arcs and active continental margins have ratio R/R_a within the limits from 2 to 8, not exceeding the ratio for NMORB [*Poreda, Craig,* 1989]. Such difference in isotopic gas composition is related to the fact that volcanoes of mantle plumes emerge as a result of melting of non-depleted mantle, coming from layer D" on the core and lower mantle boundary [*Grachev,* 2000a]. The content of CO_2 in volcanoes of mantle plumes and continental rifts (for example, Kilauea and Njiragongo volcanoes) prevails over other volcanoes on convergent boundaries (Table 7.5) [*Wardell et al.,* 2004].

Carbon dioxide (CO_2). Several estimations were undertaken of CO_2 influence on the atmospheric, its contribution to the global carbon cycle and analysis of variations δ^{13}C in the geological past [*Crisp,* 1984; *Hards,* 2005; *Marty, Tolstikhin,* 1998; and others]. In estimating the influence of CO_2 on the atmosphere in the geological past the non-steady character of volcanic activity has to be kept in mind, when a "natural" character of events is interrupted by sudden abnormal phases (see below). Thus, for example within the Cameroon volcanic zone (volcanic field Oku) 4400 t of CO_2 flows annually into the crater lake Nios [*Hards,* 2005].

The most contradictory are the evaluations of contribution of CO_2, related to volcanic activity, usually determined by volumes of lava emitted. The principal moment, important for determination of δ^{13}C variations in the past, is related to the volume of emitted magma, which depends on the accuracy of dating of magmatic activity. The available evaluations of CO_2 emission into the modern atmosphere due to activity of all surface volcanoes equal to 300 Mt/year [*Morner, Etiope,* 2002].

Let us look at the data of CO_2 content in lavas and gases of volcanoes of present-day mantle plumes through the example of the most extensively examined volcanoes Kilauea, Hawaii and the fissure eruption of Laki in Iceland (1783–1784), which can serve as criteria for establishing the total CO_2 input of mantle plumes in the geological past into the global carbon cycle (Table 7.7).

Volcano Kilauea (Hawaii). The total emission of CO_2 from Kilauea volcano reaches at least 8800 t/day [*Gerlach et al.,* 2002]. The average CO_2 content in primary (picrite) magmas of Kilauea (MgO = 16.5 wt. %) at temperature 1345°C is estimated as 0.70 ± 0.05 wt. %. According to other estimations, 8500 ± 300 t/day of CO_2 is emitted per 0.18 km^3 of lava, that gives the minimal CO_2 content for initial melt as 0.65 ± 0.02 wt. %. Whereas a stop on the rise, consolidation of melt and its degasation at a depth can change the obtained figures upward [*Gerlach et al.,* 2002]. Close values of CO_2 content in the melt (0.63 wt. %) were obtained at studying of glasses in the basalts of the sea-mountain Loihi (Hawaii) [*Dixon, Clauge,* 2001].

The content of CO_2 in pillow lavas of alkaline basalts of Kilauea varies from 40 to 130 ppm, and in glasses of tholeitic lavas from 90 to 250 ppm [*Coombs et al.,* 2005]. In alkaline basalts from underground flows of volcanic field (North Arch) on Hawaii the concentration of CO_2 is within the limits from 260 to 800 ppm [*Dixon et al.,*

Table 7.8. Estimates on the mass (in megatons) of volatiles, released by the Laki magma at various stages in the eruption [*Thordarsson et al.,* 1996]

	CO_2	SO_2	H_2O	HCl	Hf	Total
Original mass	354.3	139.1	262.6	13.2	29.1	798.3
Total mass released	348.6	122.1	235.4	6.8	15.1	728
Mass released at vents	292.8	98.4	183.1	3.6	8.3	585.0
Mass retained in solidified products	5.7	17.0	27.2	6.4	14.0	70.3
Mass released during lava transport	–	11.6	–	1.7	1.8	–
Mass released after lava emplacement	55.8	12.5	52.3	1.5	5.0	143.4

1997]. Over the summer period of 27 years of observations (1956–1983) Kilauea volcano emitted daily 18×10^{12} g H_2O, 38×10^{12} g CO_2, 7.6×10^{12} g S, 0.5×10^{12} g Cl, 2×10^{12} g F [*Gerlach, Graeber,* 1985].

Lessons of Laki eruption (Iceland). From June 1783 and up to February 1784 along the 27 km long fissure 130 craters were formed. A territory equal to 565 km^2 was buried under the thick basalt cover up to 15 km^3 and the volume of tephra was 0.4 km^3 [*Thordarsson et al.,* 1987, 1996].

Fountains of lava, similar to those of the Hawaii, could be seen at a long distance. During the 8 months of the Laki eruption an immense amount of gases was emitted into the atmosphere, creating turbulent flows, related to the temperature difference between hot flows of lava and the adjacent Vatnajökull glacier. A column of gases has risen to 13 km high, enthralling lower layers of the stratosphere and spreading south-east towards Europe [*De Boer, Sanders,* 2005; *Frankel,* 2005].

As well as water vapor, the gases contained from 5 to 6 vol % CO_2, 3% SO_2, and 1% HCl and Hf. According to different evaluations, during the eruption 122 Mt of SO_2, 235 Mt of H_2O, 349 Mt of CO_2, 15 Mt of Hf and about 7 Mt of HCl were emitted (Table 7.8) [*De Boer, Sanders,* 2005; *Thordarsson et al.,* 1987, 1996]. As a result of SO_2 reaction with water vapors approximately 150 Mt of aerosols of sulfuric acid was formed in the atmosphere. Later examination of ice columns in Greenland has revealed considerable concentrations of H_2SO_4 in the layers, related to 1783–1784 [*Thordarsson et al.,* 1987, 1996].

The Laki eruption of 1783 has led to significant changes in the entire Northern hemisphere. The aerosols spread at a speed of 50 km a day eastward and to the south-east towards Europe. In the Denmark town Groningen at a distance of 1500 km to the south-east of the eruption site, a strong smell of sulfur was so strong that it was hard to breathe. The leaves on trees turned brown and started to fall [*Franklin,* 1784]. According to Franklin's description [*Franklin,* 1784], a sharp rise of mortality rate was noted in Europe. In the summer 1783 over the whole Europe and the bigger part of North America the fog was so thick, that the sun's rays could not penetrate through atmosphere. Therefore, the winter of 1783–1784 in the North America was exceptionally cold – the Mississipi river was frozen! The aerosols lowered the temperature over the whole Northern hemisphere $> 1.3°$ C [*Thordarson, Self,* 1993].

Another well studied object is the Columbia River basalts, one of their elements is the Rosa lava field (Rosa Member), with the area of 40,000 km^2 and the volume of basalts exceeding 1500 km^3, which has formed during a very short period of time – from dozens of days [*Swanson et al.,* 1975] to 10 years [*Thordarsson, Self,* 1996]. The character of degasation and the volume of volatiles (Table 7.9) were determined according to the method, used at examining the fissure eruption of Laki and described in [*Thordarsson et al.,* 1996]. The average magma emission of the Rosa lava field was 7.0×10^6–22.0×10^6 kg/sec. At the same time for the fissure eruption of Laki it was approximately equal to 1×10^7 kg/sec [*Thordarsson, Self,* 1993].

The abovementioned data, being analysed on the basis of actualism, help to evaluate the character of degasation of mantle volcanism in the geological past (trap emissions). Under CO_2 content in lavas about 0.6 wt. % the degasation of Siberian traps with the volume 2.3×10^6 km^3 produces approximately 11,000 Gt (gigatons) [*Reichow et al.,* 2002], leaving unknown the share of active phase of degasation through supplying channels. Given the data of Laki eruption (see Table 7.8), this share equals to about 84%, that gives additional 9240 Gt in relation to Siberian traps. Then the total amount of CO_2, emitted by them, reaches 20,240 Gt. Assuming that the period of volcanic activity of 251 million years ago (the Permian-Triassic boundary) does not exceed 160 thousand years [*Bowring et al.,* 1998], we get the minimal value of 0.13 Gt per year. However, according to [*Rampino et al.,* 2000], this interval can be even shorter $\leq$8000 years, then the increase of CO_2 atmospheric emission will reach about 2.5 Gt a year. This model does not take into account the content of volatiles in pyroclastic phase.

According to another evaluation, the traps of Siberia emitted 4×10^{19} g of CO_2 (40,000 Gt) and 10^{19} g SO_2 into the atmosphere [*Kamo et al.,* 2003], given the data on the activity of Kilauea volcano [*Gerlach, Gratber,* 1985]. In this case we get 5 Gt CO_2 a year, if the period of Siberian traps activity equals 8000 years [*Rampino et al.,* 2000].

Our estimations of Siberian traps, based on the data on degassing of Laki and Kilauea volcanoes (see above), give 0.3 and 0.55 Gt of CO_2 per year accordingly without taking into consideration the content of CO_2 in volcanic ash. If the calculations are based on the data of the Rosa lava field, the figures are going to be bigger. It is obvious that we can only say about the order of values, and the data for Siberian traps (0.3 and 0.55 Gt of CO_2 per year) are rather close and can be used as a basis for discussing the influence of mantle volcanism on the change of the global carbon cycle in the Phanerozoic. Given the atmospheric mass, equal to 775 Gt (Table 7.7) and taking into account the minimal evaluations of yearly CO_2 emission, it is easy to see that less then for 1000 years of the activity of Siberian traps the amount of carbon dioxide will double.

The close values could be obtained for the Deccan traps; some evaluations, based on the reconstruction

Table 7.9. Estimates on the mass (in megatons) of volatiles, dissolved in the Roza magma at various stages in the eruption [*Thordarsson, Self,* 1996]

	SO_2	HCl	Hf	Total
Original mass	13795	1065	4840	19700
Total mass released	12425	704	1774	14903
Mass released at vents	9617	397	1442	11456
Mass retained in solidified products	1369	361	3068	4788
Mass released during lava transport	2808	307	333	3448
Mass released after lava emplacement				

of the initial borders of Deccan traps, give the total volume of 2.6×10^6 km^3 [*Pascoe,* 1964]. In the geological time scale an interval of 1000 years is too short; during this time-span under the conservative estimation of the rate of pelagic sedimentation a layer of 1 cm could be deposited. The layer on 2 cm at the Cretaceous-Paleogene boundary formed during about 2000 years [*Grachev et al.,* 2005]. Both at the Cretaceous-Paleogene boundary and at the Permian-Triassic boundary, shift δ^{13}C towards negative values was established [*Brinkhuis et al.,* 1998; *Erwin,* 2005; *Grachev et al.,* 2005; *Stuben et al.,* 2002; and others]. Such shift of value δ^{13}C can be satisfactorily explained by abnormal input of mantle CO_2 with negative value of δ^{13}C. It follows from the general carbon balance (Table 7.7), for the masses of carbon in endogenous and exogenous reservoirs are equal within the limits of error (approximately 10 Gt) [*Des Marais,* 2001]. On this background the mass of oceanic biota is only 3 Gt and the extinction of biota could not entail a shift of value δ^{13}C.

Modeling of CO_2 content in the atmosphere has shown that the eruption of Siberian traps could lead to an increase of CO_2 concentration by more than 1000 ppm and to significant warming [*Francois et al.,* 2005]. *Berner* [2002] calculated that a change of CO_2 content from steady-state, corresponding to recent pre-industrial content (around 300 ppm) to 1000 ppm would take approximately 3000 years. Given the estimations mentioned above, CO_2 input a result of degasation of trap emissions, similar to the Siberian and Deccan traps, such interval of time could be significantly less than 3000 years.

On estimating the input of CO_2 into the global carbon cycle not only the volcanism of mantle plumes has to be kept in mind, but also the degasation of volcanoes on the active continental margins and mid-oceanic ridges. All those factors make a significant influence on the atmosphere and hydrosphere. For example, the total volume of gases emitted by 3.8×10^9 t of basalts during the fissure Tolbachik eruption in 1975–1976 was comparable with the annual rate of entire active volcanism on Earth [*Fedotov,* 1984].

Another process, responsible for CO_2 emission into the atmosphere, is related to passive degasation at volcanic flanks through cracks and ruptures. It is very difficult to assess this factor quantatively, but the data available produce the grounds to consider this factor's contribution considerable and, possibly, comparable to degasation during the active stage. A good example could be the Mammoth volcano (California) emitting 1200 t/day of CO_2 at a non-active stage and the Yellowstone geothermal area with diffuse degasation comprising 1.6 ± 0.6 Mt/year [*Hards,* 2005].

And, finally, the last factor that has to be taken into consideration and calculating the volume of volatiles in the geological past, is related to the amount of gases in tephra, the volume of which for the present-day intraoceanic plumes reaches from 3.0 to 12.7 km^3/year, and for the island arcs – from 3.4 to 4.1 km^3/year [*Straub, Schmincke,* 1998].

In estimating the influence of CO_2 on the climate it also has to be kept in mind that the average lifetime of CO_2 molecule the atmosphere of the Earth is about 5 years [*Schlesinger,* 1997]. Therefore significant and incessant inflow of CO_2 into the atmosphere is essential for changing the climate. The global warming due to the greenhouse effect begins only together with the increase of CO_2 in the atmosphere for the first dozens of years and local changes can occur during shorter time intervals, as it was happen during the catastrophic Laki eruption in 1783–1784.

Sulfur dioxide (SO_2). During the eruption of Laki 122 Mt of SO_2 were emitted and about 150 Mt of H_2SO_4 in the form of aerosols were formed in the atmosphere [*Thordarsson et al.,* 1987, 1996]. The total amount of SO_2, emitted from Kilauea volcano over the period of 1979–1997, was estimated from 9.45 to 9.93 Mt. It comprises about 3.5% of global SO_2 emission over the same period (230 Mt) [*Sutton et al.,* 2001].

For the plume magmatism of Columbia river (the Rosa lava field) the annual emission of SO_2 was determined as 900 Mt a year, that exceeds the annual SO_2 emission caused by anthropogenic activity [*Park,* 1987] and is almost 4 times higher than the global emission of

SO_2 of all volcanoes on Earth during the same period (230 Mt) [*Sutton et al.*, 2001]. As a result about 18,000 Mt of H_2SO_4 in the form of aerosols emerged over 10 years. The duration of its stay in the troposphere and stratosphere is from 50 to 400 days depending on the size of airborne particles [*Thordarsson, Self*, 1996]. Due a result of this process the sun would be completely covered by clouds, the temperature would drop by 5–15°C and the acid rain would start, entailing the "volcanic or nuclear winter" [*Rampino et al.*, 1988; *Turko et al.*, 1984].

Enrichment of the atmosphere with toxic elements. As well as the gases the volcanism of mantle plumes emits significant amount of microelements into the atmosphere, which are incorporated into aerosols and could be carried at a distance of thousands kilometers from the eruption site [*Stevenson et al.*, 2003; *Stimac et al.*, 1996; and others]. The most detailed study of this process was based on the exhalations of Kilauea volcano.

It was established that the gases emitted by this volcano in January 1983 included significant increase of concentrations of As, Cu, Zn, Cd, Hg, Se, In, Au, Ir compared to the previous cycle of the 4 years of observations [*Zoller et al.*, 1983]. Even in the case of probes taken at a distance of 50 km from the eruption site at the height of 3400 m above the level on wind-induced influence, has revealed Se and In concentrations 400 times exceeding the norm. The content of arsenic in the gases reached 1600 g/m^3.

For S, Cu, Zn, As the enrichment factor is from 10 to 50, and for Ir, Se, Hg, Cd and In is more than 50. The most important result of these observations relates to abnormal contents of Ir during the eruption (up to 0.057 g/m^3), accompanied by higher concentrations of F and Cl [*Gerlach, Graeber*, 1985]. As it was emphasized by W. H. Zoller [*Zoller et al.*, 1983], iridium released as volatile IrF_6.

For non-plume volcanoes the ratio F/Cl changes from 0.01 to 0.05, at the same time for Kilauea volcano it reached 0.5, the same value as for Hekla. As it has shown earlier this high content of F and Cl are characteristic for the mantle plumes basalts [*Schilling et al.*, 1983, 1992].

According to the calculations by W. H. Zoller and I. Olmez [*Olmez et al.*, 1986; *Zoller et al.*, 1983] volcano Kilauea emits Ir into the atmosphere (as IrF_6 and $IrCl_6$) from 26 to 36 g per day, considerably exceeding the value of Ir emission by a basalt melt. The value of Ir emission by a basalt melt into the atmosphere depends on the accepted concentrations of Ir in lava and its volumes per unit time. At the eruption of Kilauea in January 1983 50×10^6 m^3 of basalts were formed, that gives 9 kg of Ir under the content of Ir 0.055 ng/g.

However the content of Ir in basalts of mantle plumes varies: thus in a standard BHVO sample this value was 0.46 ng/g, and in the basalts of Greenland it reaches 3 ng/g. On converting to the lava volume, for example the Deccan traps, the amount of emission could reach 30,000 t, that is comparable to the estimation of Ir outflow at the Cretaceous-Paleogene boundary [*Alvarez et al.*, 1980].

Piton de la Fournaise volcano of the Réunion Island can serve as another example, also related to mantle plumes. The gases of this volcano include high contents of Ir (up to 7.5 ng/g) and As (up to 3700 g/t) [*Toutain*, 1989].

We conclude that volcanism of mantle plumes causes emission of significant amount of arsenic and other heavy elements, which can explain the geochemical peculiarities of profiles at the Cretaceous-Paleogene boundary during the mass extinction of biota (see below).

It is necessary to pay attention to the Large Fissure Tolbachik eruption (LFTE) in 1975–1976, having a lot in common with the fissure eruption of Laki. The overall amount of gases emitted by 3.8×10^9 t basalts over the 15 months of eruption can be compared with the annual value of whole Earth volcanism comprising 8.9×10^6 t [*Fedotov*, 1984]. During the study of LFTE the detailed character of metalliferous exhalations has been revealed (Table 7.10), allowing to draw the following general conclusions:

- the greatest emission of the major (Al, Fe, Na, K, Mg, Ca) and volatile (Cl, F, S, B, Br, Sb, As, P) elements has been established. Significant amounts of Zn, Cu, Mo, Pb, Cs, Rb and other elements were also emitted,
- the LFTE concentrates carried considerable con-

Table 7.10. Elemental concentrations (ppm) in K/T boundary shale from Woodside Creek, New Zealand [*Brooks et al.*, 1984]

Element	K/T boundary layer			
	Bottom	Middle	Top	Mean
As	493	74	27	48
Au*	71	31	24	42
Co	216	216	62	125
Cr	550	175	87	203
Fe (%)	9.6	4.7	3.1	4.05
Ir*	153	49	25	70
Mo	92	31	8	3.9
Ni	1018	515	333	275
Zn	806	381	328	612

Note: * – ng/g.

tents of platinum – the average content was 6.4 mg/l.

Two groups of elements were detected from the eruptive cloud: intensively escaping from the eruptive cloud (Ca, Mg, Co, Sn, Na, K, Ni, also Ag and Au) and remaining in the eruptive cloud (S, Cl, F, B, Cu, Zn, Pb, As, Sb). Volatile and chalcophile elements enrich small fine ash and aerosol particles, while the others remain in the eruptive cloud for a longer period of time and are predominantly emitted into the atmosphere. In the LFTE were found: rhombic sulfur, native copper in the form of tiny dispersed emissions, native gold in the form of particles of thin-platy habitus. High concentrations of chlorine in the LFTE volcanic gases suggests a gold migration as a light volatile chloride [*Fedotov,* 1984]. An important conclusion can be drawn from the significant increasing content of As and Sb in aerosols and atmospheric precipitation (degree of enrichment varies from 10 to 28 for Sb and As).

Chapter 8. Nature of the K/T Boundary and Mass Extinction

8.1 Introduction

There are a lot processes known as presumably responsible for mass extinction. Possible causes of mass extinction were described first in details by *Davitashvili*, [1969] and are slightly revised by the author and listed below:

1. Tectonic factor (topography changes).
2. Chemical composition of atmosphere.
3. Climatic changes.
4. Eustatic sea-level changes.
5. Sea water chemistry changes.
6. Impact events.
7. Cosmic radiation (gamma ray burst).
8. Ozone Depletion from Nearby Supernovae.
9. Earth's magnetic field reversals.
10. Mantle plumes volcanism.

Before embarking on the discussion of the role of the processes just listed, one fundamental question must be answered: How rapidly did particular groups of organisms become extinct and other groups appear in the Earth's history? Until recently, the duration of such turning points was assessed as a few million years. Advances in isotopic dating, in particular, in U-Pb measurements on zircons, afford dating of deposits precise within 0.5–1.0 m.y. and revised geochronology for biospheric crises.

A classic example of the Permian-Triassic boundary is represented by the Meishan section in China, where, owing to new radiometric dating, it was established that the period of a sharp environmental change and a mass biotic extinction spanned between 160,000 and 10,000 years [*Erwin,* 2005]. Similar values were obtained by *Stuben et al.* [2002] for the Elles II K/T boundary section in Tunisia, where Elles II interval from –100 cm to +100 cm encompassed about 100 000 years.

The thickness of the transitional layer at the K/T boundary varies from 1–2 cm [*Fornaciari et al.*, 2007; *Lahodinsky,* 1988b; *Preisinger et al.*, 1986] to 20 cm [*Luciani,* 2002]. Taking into account the conservative evaluations of sediment deposition rates of about 2 cm/1000 yr ([*Stuben et al.,* 2002], and references therein), the transitional layer should have been produced over time spans from 500 to 10,000 yr. Indeed, the existence of hiatuses inside the transitional layer could insignificantly enlarged the duration of its accumulation.

As it was shown in Chapters 3 and 4, the transitional layer in Gams consists of three different parts. The terminal extinction phase coincides with the middle part of transitional layer (barren interval) of 4–5 mm thickness (see Chapter 2). In the Forada section (Italy) a similar interval (dead zone) has the thickness of 21 cm [*Fornaciari et al.,* 2007]. Such difference means the significant variance in time-span of the transitional layer formation from one place to another as a consequence of divergence in rates of sedimentation according to the position on the continental margin. The best example is the K/T sections in Tunisia [*Stuben et al.,* 2002].

The first results of the study the K/T boundary in Gams revealed the existence of two stages in the transitional layer evolution [*Grachev et al.,* 2005]. During the earlier one of these stages (which lasted for approximately 1500 years, as follows from conservative estimates of the sedimentation rate), the transitional layer was formed under the effect of volcanic aerosol. In the course of the later stage, the character of sedimentation was affected by the fall of an asteroid (meteorite), and traces of its material are discernible as spherules of pure metallic Ni, awaruite, and diamond crystals. The conclusions drawn from these results principally provided another look at the reasons for the mass ex-

tinction at 65 Ma ago. These data eliminated the need for opposing volcanism to an impact event: both took place, but the changes in the biota were induced by volcanism, whereas the fall of a cosmic body occurred approximately 500–800 years later.

New data obtained, concerning the geochemistry, the first results of helium isotopes study and in particular mineralogy of the transitional layer, presented in Chapter 3 and 4 allow to define more exactly the conditions of sedimentation. Another first data revealed the presence of cosmic dust particles in all parts of the transitional layer ([*Grachev et al.,* 2007b]; see Chapter 6). All these data give a new insight into the process of the transitional layer formation caused by appearance of its two stage evolution.

8.2 A Two-Stages Evolution of the Transitional Layer

The deposition of the lower part of the transitional layer took place in anoxic conditions. Mineral paragenesis of sulfides and peculiarities of their morphology (Chapter 4) underline the sedimentation in sluggish shallow marine basin. The joint occurrence of needle-like sphalerite, arsenopyrite, pyrite, framboidal pyrite, pentlandite and violarite (Figure 4.14c, Figure 4.16a, Figure 4.18) proves their sinsedimentary origin; all these minerals are authegenic and arose in situ.

Framboidal pyrite, composed by octahedral microcrysts (Figure 4.14c), is a typical mineral-indicator for reducing conditions [*Sassano, Schrijver,* 1989]. Such kind of pyrite was found in sediments at the Permian-Triassic boundary section in Kashmir [*Wignal et al.,* 2005].

The concentration of pyrite is highest at the base of the transitional layer and decreases to the top. Key indicator of processes that characterized the deposition environments is an arsenic incorporation into FeS_2 pyrite (Figure 4.14b). Data in the Table 4.5 confirm the confidence of *Blanchard et al.* [2007] that it is more energetically favourable to substitute arsenic for sulphur rather than for iron in redox conditions. It means that the presence of As in water solution is a result of arsenic emissions due the volcanic activity (see details in Chapter 7).

Titanomagnetite from the base of the transitional layer has a volcanic origin (Chapter 5) and its composition is close to rift and plume basalts. This mineral is characterized by unusually small concentrations of admixtures (Table 5.6) and this specific pattern reflects the formation of titanomagnetite crystals from a volcanic aerosol (Chapter 5). *Burov* [2005] noted an abrupt rise in the magnetization of sediments caused by their enrichment in ash material beginning from the Permian-Triassic boundary, which reflects the global high volcanic activity at that time.

Study of magnetic properties of the Gams sections revealed the high concentration of iron hydroxides in the boundary layer (Chapter 5): accumulation of iron hydroxides extended in time, attains a maximum in the lower part of the boundary layer and sharply drops upon the transition to over- and underlying deposits of the Danian and Maastrichtian.

Accumulation of iron hydroxides at the K/T boundary is most likely a global phenomenon unrelated to local physiographic conditions of accumulation of terrigenous material in sediments ([*Pechersky,* 2007]; see details in Chapter 5).

The first findings of native platinum and rhenium at the base of the transitional layer have the great importance because both these elements are unknown in nature. Their origin could be explained in the frame of a model of volcanic aerosol activity. It follows from the character of the occurrence of Pt in thin films covering the rounded zircon grains and tree-like crystals (Figure 4.6).

The occurrence of native rhenium requires the following comments. There are two possible explanations. The first one is related to its extraterrestrial origin because Re was found the Allende meteorite [*Goresey et al.,* 1977] and in lunar ground [*Bogatikov et al.,* 2004; *Mokhov et al.,* 2007]. However it is most likely that the source of native rhenium is related to volcanic aerosol [*Grachev, Borisovsky,* 2008a]. Emission of such mantle plume volcanoes as Kilauea produces a large amount of Re into the atmosphere [*Norman et al.,* 2004]. The morphology of rhenium grain (absence of traces of reworking) rules out of its terrigenous origin (Figure 4.5).

Mineral paragenesis mentioned above allows to explain the enrichment of the lower part of the transitional layer in Gams with chalcophile (As, Cu, Zn, Pb) and siderophile (Ir, Co, Ni, Mo, Fe) elements. The absence of these elements as the sulfides below and above of the transitional layer could be only explained by a very short impulse of extensive volcanic activity (surficial and submarine) on the Earth.

The first data on helium isotopy in the Gams section showed that the ratio $^3He/^4He$ in the lower part of the layer is 10 to 100 times greater than the values typical of the continental crust [*Grachev et al.,* 2007b]. The ratio $^3He/^4He$ in the Gams section decreases from bottom to top of the transitional layer, and the difference between the lowermost and uppermost units is significant and considerably (by more than ten times) exceeds the measurement uncertainty (5%) (Figure 3.10). It is remarkable that no correlation exists between the ^3He and Ir concentrations, which was observed for the first time

in Pacific pelagic clays for the 70-Ma interval [*Farley,* 1995]. Although the cosmic dust was found in all part of the transitional layer [*Grachev et al.,* 2008b], the He enrichment of the lower part of the Gams section is associated not with cosmic matter but with a change in the source area conditions, most likely, due to volcanic activity.

The deposition of the upper part of the transitional layer in Gams occurred by the influence of impact event. The evidences of such event, as it was shown first by *Grachev et al.* [2005], are the findings of pure nickel spherules with a well-crystallized surface, diamond crystals together with nickel spherules.

The following investigations revealed the occurrence of micrometeorites which are represented by particles composed of pure Fe or Fe-Ni alloy (awaruite) (Figure 6.4). Findings of numerous awaruite particles are confined to the upper part of the transitional *J* layer [*Grachev et al.,* 2008b].

The study of transitional layer samples taken directly from the outcrop in Gams-1 section showed new varieties of diamonds with fine Ni particles on the surfaces of their grains and the presence of moissanite in the upper part of the layer *J*. Previously, microdiamonds were found in the Cretaceous-Paleogene transition layer in Mexico [*Hough et al.,* 1997].

The new data of thermomagnetic analysis together with microprobe study of samples from the Gams 1 and the Gams-2 sections show additional evidence of metallic nickel occurrence (Chapter 5 and 6). The origin of metallic nickel is most likely to be connected with cosmic dust inputting or be a result of ablation of meteorites (see Chapter 5 and 6). New data also confirm such point of view but at the same time prove the presence of cosmic dust from the bottom to the top of the transitional layer [*Grachev et al.,* 2008b].

Because the barren interval (dead zone) coincides with the middle part of the transitional layer (Chapter 2), it means that processes during the lower part of the transitional layer formation were responsible for driving mechanism of the planktonic foraminifera extinction in the Gams section (see below).

Iridium anomaly. An iridium anomaly at the K/T boundary layer has been attributed to an extraterrestrial body (asteroid or meteorite) that struck the Earth some 65 Ma ago. After the appearance of the first paper of *Alvarez et al.* [1980] an extensive literature has evolved which trace the role of this element in resolving the question of the K/T boundary nature and mass extinction.

Our new data show the existence some Ir anomalies in Gams: one at the boundary layer and two other anomalies above and one anomaly below it (Chapter 3). The same kind of appearance was found in other localities [*Ganapathy et al.,* 1981; *Graup, Spettel,* 1989; *Rocchia et al.,* 1990]. Recently *Keller* [2008] demonstrated that the Ir anomaly at the K/T boundary is not related to the Chicxulub impact and crater itself predates the K/T boundary.

Mantle plumes volcanoes emits Ir into atmosphere is large enough to provide the high concentrations in sediments as a result of settling of volcanic aerosol. As it was shown in Chapter 7, if we take the content of Ir in a standard BHVO sample (0.47 ng/g) and convert this value to lava volume of Deccan traps, the amount of emission could reach 30,000 t, that is comparable to the estimation of Ir outflow at the Cretaceous-Paleogene boundary [*Alvarez et al.,* 1980]. Thus, Ir anomaly could not be used as indicator of impact event.

8.3 Mantle Plumes and Mass Extinctions

There is no consensus in the determination of mass extinction. Following D. Jablonski, under mass extinction we mean "... any substantial increase in the amount of extinction (i.e. lineage termination) suffered by more than one geographically widespread taxon during a relatively short interval of geologic time, resulting in an least temporary decline in standing diversity" [*Jablonski,* 1986].

Palaeontologists recognize two types of extinctions: gradual and terminal ones. The gradual extinctions embrace a several or even tens of millions years. For example, the best studied Permo-Triassic extinction included two events: the first one occurred 5–8 Myr earlier than the P/T boundary at the end of the Guadalupian, and the second event occurred at the P/T boundary [*Erwin,* 2005; *Jin et al.,* 2000].

There were five documented large mass extinction events (Big Fives) in the Phanerozoic. These occurred around the Ordovician-Silurian boundary, the Frasnian-Famennian boundary, the Late Permian (P/T), the Triassic-Jurassic boundary and the Cretaceous-Paleogene (K/T) boundary [*Raup, Sepkoski,* 1986]. These Big Fives imply the terminal character of extinction (Table 8.1).

Our investigations of the K/T boundary in Gams have shown that in the studied sections the so-called mass extinction of foraminifera in the terminal Cretaceous resulted in the disappearance of only several genera ([*Grachev et al.,* 2005]; see Chapter 2). The rest genera gradually extincted below the transitional layer and above it. This deterioration of planctonic foramonifera coincides with maximum concentrations of As, Pb, Zn, Cu, Cr, Ir, Pb in the lower part of the transitional layer in Gams.

Table 8.1. Phanerozoic mantle plumes volcanism and the epochs of biotic mass extinction

Mantle plumes*, Ma ago		Mass extinction**, Ma ago	
Columbia River, Khamar-Daban	17±1 16±1	Middle Miocene	14±3
Ethiopia, Afar, Yemen	35±2	Late Eocene	36±2
Deccan, Greenland, Ninetyeast Ridge, Reunion	65.6±0.3; 5.4±0.6 65–60 80–60 69.5±4.5	Maastrichtian/Paleocene	65±1
Madagascar, Ontong Plateau, Trinidade	88–90 92±2 87±2	Cenomanian	91
Rajmahal, Kerguelen Franz Joseph Land	113–116 117±2	Aptian	110±3
Parana River	132±3–137±5	Tithonian	137±7
Karroo, Ferrara	182±2	Bajocian	173±3
Central Atlantic	200±4	Rhaetian/Norian	211±8
East Siberia, Emeishan	251.2±0.2	Tatarian/Pliensbachian	248–254
Kola Peninsula, East European platform	370 356–375	Frasnian/Famennian	367–374

Note: *[*Grachev,* 1998a], revised; ** [*Raup, Sepkoski,* 1986]. See also Table 7.1.

The long discussion concerning the causes of mass extinction elucidated the two main processes: impact and mantle plume volcanism.

A satisfactory hypothesis for such kind of mass extinction should explain the synchronous occurrence of a variety of processes during a very short (<1 m.y.) time interval in various shells of the Earth-lithosphere, hydrosphere, and atmosphere. Of all natural processes yet known that might be responsible for catastrophic biospheric changes in the Phanerozoic geologic record-i.e., over the past 540 million years and that occurred simultaneously in aqueous environment and on land,

Table 8.2. The main possible causes of Big Five extinctions

Event	Number of extincted families, %*	Rate of extinction, number of extincted families in Myr**	Causes of extinction
End of Ordovician	26	19	Glaciation?
End of Devonian	21	10	Volcanism, impact, cooling, anoxia
End of Permian	51	16	Volcanism, impact, regression
End of Triassic	22	12	Volcanism, impact, anoxia
End of Cretaceous	16	17	Volcanism, impact

Note: * [*Hallam*, 2005]; ** [*Raup, Sepkoski,* 1982].

we favor the set of processes related to mantle plumes (Table 8.2, Figure 8.1).

Carbon has two stable isotopes – light isotope ^{12}C and heavy isotope ^{13}C. The content of these isotopes in natural carbon is equal accordingly 98.93% and 1.07%. The isotopy of carbon allows to determine the nature of the source of gases, namely the ratio of isotopes ^{12}C to ^{13}C, usually expressed as $\delta^{13}C$ (‰). For volcanic gases of mantle plumes and divergent plates boundaries purely mantle values of $\delta^{13}C$ (–4.0±2.5‰) are typical, at the same time for volcanic gases on convergent plates boundaries a considerable shift in values $\delta^{13}C$ is observed – from –12 to +2.5%, indicating the input of the ocean crust during subduction. The main reservoirs of carbon are shown in Table 7.7.

During Phanerozoic the stationary regime of the carbon cycle was repeatedly violated, entailing a shift of value $\delta^{13}C$ towards negative values. It was incessantly emphasized in many publications that that such shifts were related to the epochs of mass extinction of biota, which coincided in time with manifestations of plume magmatism [*Erwin,* 2005; *Jin et al.,* 2000]. As an example let us show the three most extensively studied boundaries of such changes: Permian-Triasssic (251 Ma), Cretaceous-Paleogene (65 Ma) and Paleogene-Eocene (55 Ma).

A significant shift of value $\delta^{13}C$ at the K/T boundary occurred in the most well studied sections (Agost , Caravaca, Gams and others) 2–3 cm lower the boundary, that under the conservative estimations of sedimentation rate (about 1–2 cm/1000 years) took only 2–3 thousand years. At the same time the late Devonian (Fransnian-Famennian boundary is characterized by global positive shift $\delta^{13}C$ [*Godderis, Joachimski,* 2004], providing direct evidence in favor of the "non-plume" reasons of this shift in comparison with other critical boundaries.

The principal question can be asked: were the violations in the global carbon cycle the reason of mass extinction, or were they the consequence of extinction?

Had the shift $\delta^{13}C$ been related to mass extinction, then on all the critical borders of Phanerozoe it would have had a similar trend towards the area of negative values $\delta^{13}C$, but this condition was not observed.

Another aspect of the problem is related to determining the time interval when the shift of value $\delta^{13}C$ occurred. As it was revealed by the extensively researched sections on the K/T boundary in Europe, the violation of the global carbon cycle happened very quickly (1000–2000 years), that considerably limits the choice of acceptable justification of such short-time changes.

Table 8.3. Elemental concentrations (ppm) in the K/T boundary section at York Canyon section, New Mexico [*Gilmore et al.,* 1984]

Element	Layer at the K/T boundary		Layer above/below the K/T boundary	
	Variations	Average	Variations	Average
As	1–95	36	0.2–46	4.1
Co	1.2–53	9.8	0.7–4.0	2.7
Cr	46–102	67.3	0.9–5.0	3.3
V	110–187	137	10–67	27
TiO_2	1.38–2.67	2.00	0.40–0.95	0.76

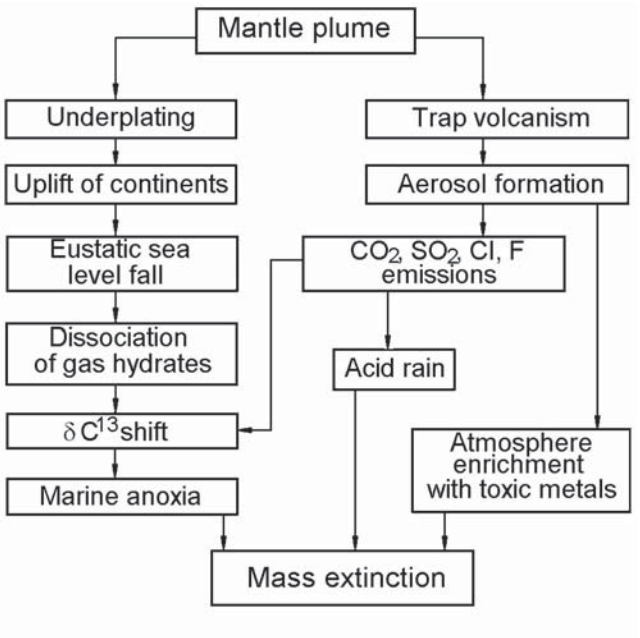

Figure 8.1. The principal scheme illustrating the links between mantle plumes and mass extinctions.

8.3.1 Arsenic at the Cretaceous-Paleogene boundary.

Smit, Hertogen [1980], paying attention to a very high content of As, Co, Ni, Cr, Se and Sb at the transitional layer of clay the K/T boundary in Caravaca section (Spain), assumed that the inflow of these elements was related to the erosion of adjacent areas of drift differently from Ir and Os, having the impact origin. Other multiple publications devoted to other sections at the K/T boundary confirmed the fact of high contents of As.

An As anomaly was established in Oman (up to 15 ppm at the background concentration of 2–3 ppm along the section) both on the boundary between the Cretaceous and Paleogene and lower – at a distance over 1 m, in both cases a very well expressed corre-

Table 8.4. Elemental concentrations (ppm) at the K/T boundary section in Caravaca, Spain [*Smit, Hertogen,* 1980]

Element	Layer below the K/T boundary	Layer at the K/T boundary	Layer above the K/T boundary
As	2.07	225.9	1.66
Co	9.06	270	5.59
Cr	56.9	499	69.6
Ni	24.2	1066	40.6
Os*	0.08	16.1	0.41
Ir*	0.13	25.5	0.34

Note: * – ng/g.

Table 8.5. Elemental concentrations (ppm) at the K/T boundary in Agost section, Spain [*Martínez-Ruiz et al.,* 1992]

Element	Layer below the K/T boundary	Layer at the K/T boundary	Layer above the K/T boundary
As	4	380	16
Co	8	160	34
Cr	52	540	243
Ni	49	556	140
Cu	13	218	50
Zn	53	568	130
Ir*	1.1	24.4	16.5

Note: * – ng/g.

lation of contents of As with Ir, Ni, Cr, Zn was noted [*Ellwood et al.,* 2003]. In Tunisia for the K/T boundary layer according to the factor analysis data the mutually correlated behavior of As with Ni, Zn, Fe, Cu was mentioned [*Stuben et al.,* 2002].

Two sections of the K/T boundary layer in the south of Turkmenia characterized by higher concentrations of As – up to 16 ppm [*Alekseev et al.,* 1988], in Kyzylsay profile (the Mangyshlak Peninsula) – 32 ppm. In Stevns Klint section (Denmark) the concentration of As in the transitional layer reaches 96 ppm [*Alvarez et al.,* 1980], and according to other data from 70 to 140 ppm [*Nazarov et al.,* 1983]. It is worth mentioning that in both cases abnormal concentrations of As are accompanied by anomalies of concentration of Ir, Ni, Co, Cu, Fe. In Bottacione and Contecca (Gubbio, Italy) the content of As in K/T transitional layers varies from 6 to 19 ppm [*Ebihara, Miura,* 1996].

Very important are the data, obtained for profile Woodside Creek in New Zealand [*Brooks et al.,* 1984], where the K/T transitional layer (0.8 cm thick) was analyzed not as a whole, as it was usually done, but was divided into three parts (lower, middle and upper) (Table 7.10).

As it could be seen from Table 8.3–Table 8.5, the systematic changes of concentration of As from the lower to the upper part of profile was observed at the K/T boundary in the most of localities. It is impossible to explain such behavior of As remaining in the framework of the impact hypothesis, given its content in meteorites does not exceed 2 ppm [*Hamaguchi et al.,* 1969]. R. R. Brooks et al. [*Brooks et al.,* 1984] tried to assume that the high concentration of As was related to regeneration processes in the ocean at that time, but approximately 20-fold decrease of arsenic content at the top of the boundary layer contradicts it (Table 7.10). For such short time (first hundreds of years) the character of environments could not significantly change.

In conclusion we have to mention that the study of smaller particles in volcanic dust samples on the ice surface in the Antarctic revealed Ir concentrations reaching 7.6 ng/g as well as high values of As, Au, Se and Sb. Enrichment of glassy dust particles of these elements was connected to iridium condensation from recent volcanic aerosols [*Koeberl,* 1989].

Thus, the As and other toxic elements enrichment at the K/T transitional layers is a global phenomenon, embracing both high and low latitudes and this phenomenon is a consequence of mantle plume volcanism (see details in Chapter 7).

8.3.2 Poisoning by toxic elements at the K/T boundary: The killing mechanism sensu stricto.

Toxic elements include As, Pb, Cu, Mo, Ni, Co and they are acquired by organisms through air, water and plants. Very small quantities of these atoms can cause serious biological damage. Arsenic concentrationis are higher than 5 ppm causes the lethal outcome but most poisoning appears to come from ingest (food and drink).

The causal relationship between extinction of dinosaurs and high concentations of toxic elements was established *Zhao et al.* [2002]. The study of dinosaur eggshells in the Nanxiong Basin (South China) revealed the significant enrichment of As, Cr, Pb, Zn and other trace elements at the K/T boundary layer containing the eggshells (Figure 8.2). It may have been caused by the assimilations of these elements by dinosaurs through air, water and food and laid by them

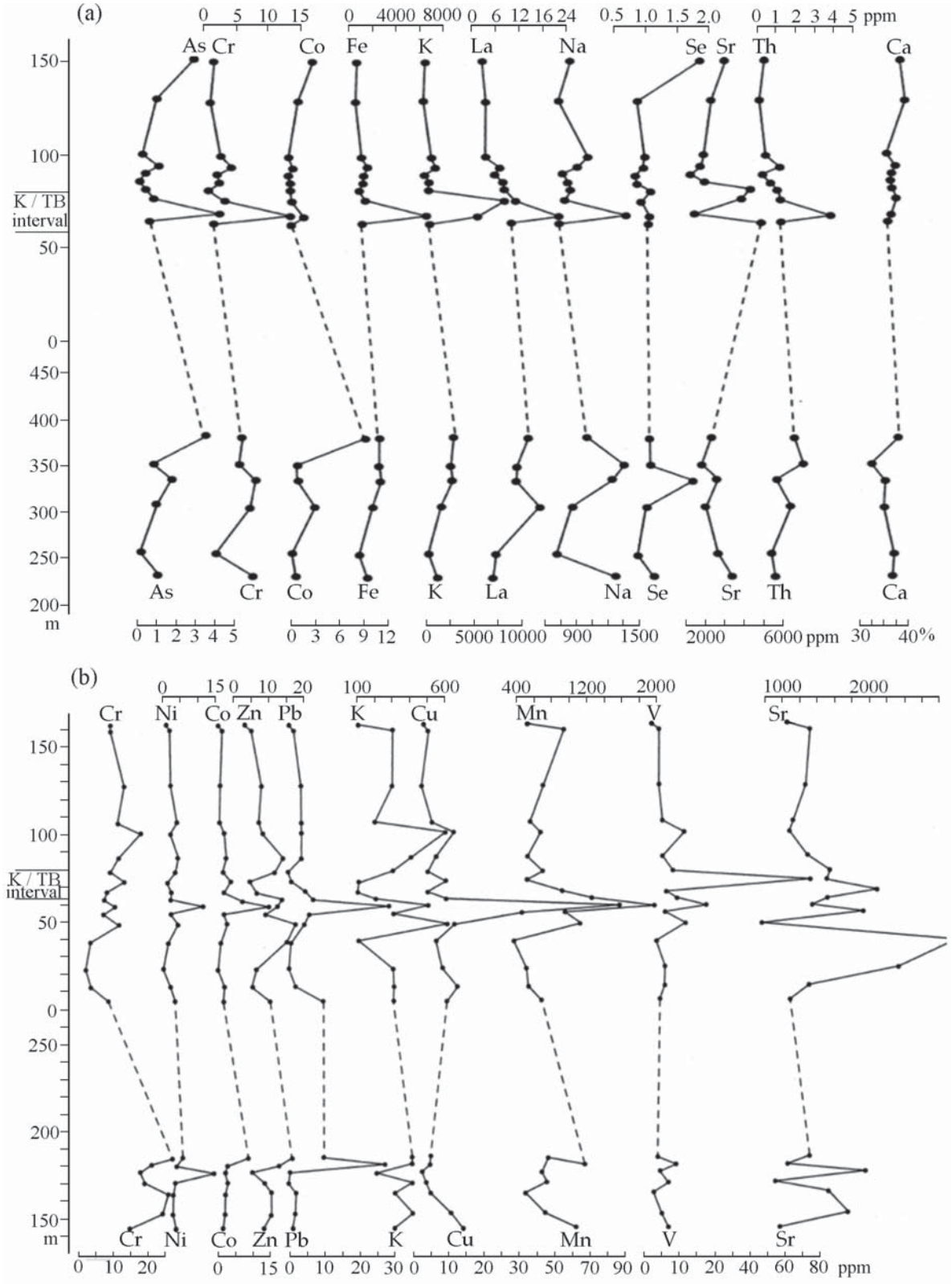

Figure 8.2. Variations of As and other trace elements in the eggshell samples at the K/T boundary layer in the Nanxiong basin (South China) [*Zhao et al.,* 2002].

then into the eggs. An excess of mentioned trace elements transmitted to eggs from dinosaur's food caused abnormal embryonic development and considerably reduced the ability of reproduction. Extinction dinosaurs corresponds to a time span of about 250 ka while the terminal phase of extinction occurred at the K/T boundary [*Zhao et al.,* 2002].

If we compare our data of trace elements concentrations in the Gams section (Figure 3.4) with the same elements from the K/T boundary section in China (Figure 8.2) we can observe their identical distribution. Thus, we propose that similar conditions existed both in the sea and on the land at the K/T boundary all over the world.

Conclusion

1. The Gams stratigraphic sequence is characterized by a clearly pronounced transitional layer at the K/T boundary and many peculiarities of this layer were first studied. The lower part of the sequence notably differs from the upper part by high concentration of As, Zn, Cu, Pb, Cr, Ir, Co, V, Ni. In the upper portion of the transitional layer the content of all these elements significantly decrease. The high As concentration in the lower part of the transitional layer in the Gams section together with an enrichment of Zn, Co, Cu, Pb was recorded at the K/T boundary in nearly all similar sections of the world. This fact cannot be explained in terms of the impact paradigm, because the As concentration does not exceed 2 ppm in meteorites [*Hamaguchi et al.,* 1969].

2. In comparison with the first results [*Grachev et al.,* 2005] we found four Ir anomalies: the large well expressed anomaly at the K/T boundary, two other anomalies below and above the boundary. These results are in contradiction with the K/T boundary stratotype at El Kef (Tunisia) where Ir anomaly coincides with a rust-coloured goethite clay layer, which is 1 mm to 3 mm thick [*Robin et al.,* 1991]. In our opinion the Ir enrichment in clays at the K/T boundary layer is not necessarily of cosmic origin, but may originated from mantle plume volcanism [*Koeberl,* 1989]. As Keller has recently shown [*Keller,* 2008], iridium anomalies are not unique and therefore not infallible K/T markers.

3. The ratio $^3He/^4He$ in the Gams section changes from the bottom to the top of the transitional layer, and the difference between the lowermost and uppermost units is significant and considerably (by more than ten times) exceeds the measurement uncertainty (5%). It is shown that no correlation exists between the ^3He and Ir concentrations. The ^3He enrichment of the lower part of the Gams section is associated not with cosmic matter but with a change in the source area conditions, most likely, due to volcanic activity whose influence, independent of He isotope studies, has been established from anomalous concentrations of As, Zn, Cu, Pb, Cr, Ir, Co, V, Ni and mineral composition.

4. The lower part of the transitional layer has a smectite content of >65%, and it systematically decreases upward, whereas the percentage of illite increases to 20%. Because this layer appeared to contain titanomagnetite corresponding to composition of this mineral chemistry in basalts, it can be concluded that smectite was formed at the expense of volcanic material.

5. Variations in the concentrations of rare earth elements in the Gams sequence are insignificant. This flat configuration of the NASC-normalized REE patterns is typical of the rocks of Mesozoic and Cenozoic continental margins (including those in the modern Atlantic) [*Murray,* 1994] and testify to a significant contribution of terrigenous material to the character of REE fractionation.

6. The study of minerals in the transitional layer at the K/T boundary in Gams allow to explain the behavior of trace elements. Our data obtained indicate that there are two distinct populations of minerals in the transitional layer and therefore two different stages in deposition history. The first one includes the sedimentation in anaerobic conditions as the result of volcanic aerosol spreading due to the volcanic activity related to the mantle plume (existence of native platinum, rhenium, sulfides, barite and titanomagnetite).

The environments of sedimentation have been drastically changed during the upper portion of layer deposition. The paragenesis of hexagonal polymorph of diamond (lonsdaleite) with pure nickel spherules first discovered proves an asteroid (meteorite) fall which resulted in the release of energy sufficient not only for the melting of the projectile (asteroid) itself but also for its evaporation.

7. A principally important problem is the genesis of the Ni spinel, which was found, along with sediments at the Cretaceous-Paleogene boundary, also in cosmic dust, micrometeorites, cosmic spherules, and the fusion crusts of meteorites, i.e., is not directly related to any impact event. The findings of Ni spinel in hydrothermal systems and in spherules from the Paleocene flood basalts in Western Greenland [*Robin et al.,* 1996; *Rychagov et al.,* 1997] give the evidence the possibility of another mode of formation. The origin of Ni spinels from the transitional layer at the K/T boundary remains open and requires further research.

8. Intense development of iron hydroxides, observed at the K/T boundary is most likely a global phenomenon unrelated to local physiographic conditions of accumulation of terrigenous material in sediments. Most of iron hydroxides accumulated at the K/T boundary layer have different origins. Quite possible that iron hydroxides are products of hydrothermal activity similar to the formation of iron-bearing sediments. Accumulation of iron hydroxides extended in time, attains a maximum in the lower part of the boundary layer and sharply drops upon the transition to over- and underlying deposits of the Danian and Maastrichtian.

9. Many characteristics of the discovered Fe and Fe-Ni spherules are analogous to those of the spherules found in deep-sea clays of the Pacific Ocean by the Challenger expedition [*Murray, Renard,* 1891], in the Tunguska catastrophe area [*Florensky et al.,* 1968], at the fall sites of the Sikhote-Alin' meteorite [*Krinov,* 1971] and many other places. In all cases, except for the Tunguska catastrophe area and the fall site of the Sikhote-Alin' meteorite, the formation of both spherules and particles of various morphologies consisting of pure iron (sometimes with a Cr admixture) and Ni-Fe alloy is unrelated to impact events. We derive their formation from cosmic interplanetary dust falling onto the Earth's surface. This process has continued uninterruptedly since the moment of the Earth's formation and is, in a sense, a background phenomenon.

10. Compositions of many particles studied in the Gams section are similar to the bulk chemical composition of the meteoritic substance found at the fall site of the Sikhote-Alin' meteorite (93.29% iron, 5.94% nickel, and 0.38% cobalt) [*Krinov,* 1971]. The presence of Mo in some particles is not unexpected, because this element is present in many types of meteorites. The Mo concentration in various types of meteorites (iron, stony, and carbonaceous chondrites) ranges from 6 to 7 ppm [*Campbell et al,* 2003; *Murthy,* 1963]. Native molybdenum and molybdenite were also found in the composition of lunar dust collected by the Luna-16, Luna-20, and Luna-24 automatic probes [*Mokhov et al.,* 2007].

11. Pure nickel spherules with a well-crystallized surface found for the first time are known neither in magmatic rocks nor in meteorites, where nickel invariably contains a significant amount of admixtures. Such a surface structure of nickel spherules could have formed in the case of an asteroid (meteorite) fall, which would result in release of energy sufficient not only for melting the material of the falling body but also for its evaporation. Metal vapors could have been raised by the explosion to a large height (probably to tens of kilometers), where their crystallization took place. Awaruite particles found together with spherules of metallic nickel are a product of the meteorite ablation.

12. Diamond crystals met together with nickel spherules might have formed during ablation of meteorite from the same vapor cloud in the process of its subsequent cooling. It is known that synthetic diamonds in the shape of single crystals, their intergrowths, twins, polycrystalline aggregates, skeleton crystals, needle-shaped crystals, irregular grains, etc. are obtained by the method of spontaneous crystallization from a solution of carbon in the melt of metals (Ni, Fe) above the line of the graphite-diamond phase equilibrium [*Bokii et al.,* 1986]. Nearly all of the above typomorphic features of diamond crystals were detected in the Gams samples under study.

These results suggest the similarity between the diamond crystallization in the cloud of nickel-carbon vapor during its cooling and the experimental process of diamond spontaneous crystallization from a solution of carbon in a nickel melt. However, a final conclusion on the origin of diamond can be drawn after its detailed isotope investigations, which require a sufficiently large amount of substance. Thus, the study of the transitional clay layer at the K/T boundary revealed the presence of cosmic substance in all parts of the transitional layer; however, indicators of an impact event are fixed only beginning from the $J4$ unit.

13. The variations in δ^{18}O and δ^{13}C in the vertical section show a pronounced shift toward negative values at the K/T boundary, from 5‰ to 23‰ PDB for δ^{18}O. It is important to emphasize that the minimum δ^{18}O and δ^{13}C values are characteristic of the units of layer J occurring below the unit corresponding to the impact event (samples $J_{6/3}$ and $J_{6/4}$). The most remarkable fact is that no microfauna was found in these units. These anomalies in the variations of the carbon and oxygen isotopic ratios in the Gams sequence are close to the analogous variations documented elsewhere. The temperature variations still are to be evaluated by the isotopic composition of the organogenic carbon in the skeletons of the foraminifers.

14. The distribution of foraminifers in the K/T boundary in the Gams section shows that the extinction of foraminifer genera began well before the accumulation of the layer J. The deterioration could result from an input of arsenic and other siderophile elements as volcanic aerosol activity, which resulted in poisoning from arsenic in an anoxic environments. Barren interval (dead zone) was detected in the middle part of the transitional layer before the appearance of impact event.

Conclusions made above differ from all preexisting interpretations of the transitional layer at the boundary between the Cretaceous and Paleogene and make it possible to resolve the problem of the reasons for the mass extinction of living organisms at 65 Ma ago. Our research eliminates the need in opposing volcanism to an impact event, because both of them took place, but the changes in the biota were related to volcanism, as also was the appearance of the Ir anomaly itself. The cosmic body fell only some 500–800 years later!

References

Abramovich S., Keller G., Stuben D., Berner Z. (2003), Characterizaton of late Campanian and Maastrichtian planktonic forminiferal depth habitats and vital activities based on stable isotopes, *Palaeogeogr. Palaeoclimatol. Palaeoecol., 202*, 1, doi:10.1016/S0031-0182(03)00572-8.

Adamia Sh., Salukadze N., Nazarov M. A., Gongadze G., Gavtadze T., Kilasonia E., Asanidze B. Z. (1993), Geological events at the Cretaceous-Paleogene boundary in Georgia (Caucasus), *Geol. Carpathica, 23* (3), 35–43.

Adatte Th., Keller G., Burns S. (2002), Paleoenvironment across the Cretaceous-Tertiarytransition in eastern Bulgaria, *Geol. Soc. Am. Special Paper, 356,* 231–251.

Agiorgitis G. (1978), Distribution of iridium in some basalts of southeastern Central Europe, *Tschermarks Mineral. Petrogr. Mitt., 25,* 89–94.

Albarede F. (1992), How deep do common basaltic magmas form and differentiate, *J. Geophys. Res., 97*, 10,997–11,099, doi:10.1029/91JB02927.

Allegre C. J., Staudacher Th., Sarda Ph. (1986), Rare gas systematics: Formation of the atmosphere, evolution and structure of the EarthOs mantle, *Earth Planet. Sci. Lett., E81*, 27–150.

Alegret L., Thomas E. (2004), Benthic foraminifera and environmental turnover across the Cretaceous-Paleogene boundary at Blake Nose (ODP Hole 1049C, Northwestern Atlantic), *Palaeogeogr. Palaeoclimatol. Palaeoecol., 208,* 59–93, doi:10.1016/j.palaeo.2004.02.028.

Alekseev A. S., Nazarov M. A., Barsukova L. D., et al. (1988), Cretaceous/Tertiary boundary in South Turkmenia and its geochemistry, *Bull. Moscow Nat. Soc. Geology, 63*(2), 55–69.

Alvarez L. W., Alvarez W., Asaro F., Michel H. V. (1980), Extraterrestrial causes for the Cretaceous-Tertiary extinction, *Science, 208*, 1095, doi:10.1126/science.208.4448.1095.

Alvarez W. (2002), Compiling the evidence for impact at seven mass extinctions, in Impacts and the origin, evolution and extinction of life, *A Rubey Colloquim,* 66 p., Univ. California, Los Angeles.

Alvarez W., Alvarez L. W., Asaro F., Michel H. V. (1984), The end of the Cretaceous: Sharp boundary or gradual transition?, *Science, 223*, 1183, doi:10.1126/science.223.4641.1183.

Alvarez W., Smit J., Lowrie W., Asaro A. (1992), Proximal impacts deposits at the Cretaceous-Tertiary boundary in the Gulf of Mexico: A restudy of DSDP Leg 77, Sites 536 and 540, *Geology, 20*, 697, doi: 10.1130/0091-7613(1992)020<0697:PIDATC>2.3.CO;2.

Anderson T. F., Arthur M. A. (1983), Stable isotopes of oxygen and carbon and their application to sedimentologic and paleoenvironmental problems, in: *Stable isotopes in sedimentary geology,* edited by M. A. Arthur, T. F. Anderson, I. R. Kaplan, J. Veizer and L. S. Land, vol. 10, pp. 1–151, SEPM Short Course, Columbia.

Anufriev G. S. (1999), Growth Rate of Deep-Water Fe-Mn Nodules and Isotope Flows to the Ocean Floor, *Dokl. Akad. Nauk 364*, 683–686.

Anufriev G. S., Boltenkov B. S. (1996), Isotopic Composition and Growth Rates of Pacific Fe–Mn Nodules, *Litol. Polezn. Iskop.,* (5), 552–560.

Arenillas I., Arz J. A., Molina E., Dupuis C. (2000), An independent test of planktic foraminiferal turnover across the Cretaceous-Paleogene (K/T) boundary at El Kef, Tunisia: Catastrophic mass extinction and possible survivorship, *Micropaleontology, 46*(1), 31–49.

Bagin V. I., Gendler T. S., Avilova T. A. (1988), *Magnetism of Iron α-Oxides and Hydroxides,* 180 p., IFZ AN SSSR, Moscow.

Bagin V. I., Gendler T. S., Dainyak L. G., Sukhorada A. V. (1976), Thermal transformations of biotite, *Fiz. Zemli,* (9), 66–76.

Bagin V. I., Gendler T. S., Dainyak L. G., Sukhorada A. V. (1977), Stability of magnetic products of biotite decomposition, *Fiz. Zemli,* (1), 71–78.

Barnes S. J., Roeder P. L. (2001), The range of spinel compositions in terrestrial mafic and ultramafic rocks, *J. Petrol., 42,* 2279, doi:10.1093/petrology/42.12.2279.

Bauer J., Fiala J., Hrichova R. (1963), Natural a-silicon carbide, *Am. Min., 48,* 620–634.

Beloussov V. V., Ed. (1978), *Iceland and the Mid-Ocean Ridge: Geochemistry,* Nauka, Moscow, 55–147.

Ben Abdelkader O., Ben Salem H., Donze P. (1997), The K/T Stratotype section of El Kef (Tunisia): Events and biotic turnovers, *Geobios., 21,* 235, doi:10.1016/S0016-6995(97)80098-8.

Berggren W. A., Norris R. D. (1997), Biostratigraphy, phylogeny and systematics of Paleocene trochospiral planktic foraminifera, *Micropaleontology, 43,* Suppl. 1, I–II, 1–116, doi:10.2307/1485988.

Berner R. A. (2002), Examination of hypotheses for the Permo –Triassic boundary extinction by carbon cycle modeling, *Proc. Natl. Acad. Sci. USA, 99,* 4172–4177, doi:10.1073/pnas.032095199.

Bhandari N., Verma H. C., Upadhyay C., Tripathi A., Tripathi R. P. (2002), Global occurrence of magnetic and superparamagnetic iron phases in Cretaceous-Tertiary boundary clays, in: *Catastrophic events and mass extinctions: Impacts and beyond,* edited by C. Koeberl and K. G. MacLeod, GSA Special Paper no. 356, pp. 201–211, Geological Society of America, Boulder, Colorado.

Bhattacharji P. K., Mukherjee R. (1984), Petrochemistry of metamorphosed pillows, and the geochemical status of

the amphibolites (Proterozoic) from the Sirohi district, Rajasthan, India, *Geol. Mag., 121,* 465–473.
Bi D., Morton R. D., Wang K. (1993), Cosmic Nickel–Iron Alloy Spherules from Pleistocene Sediments, Alberta, Canada, *Geochim. Cosmochim. Acta, 57*, 4129–4136, doi:10.1016/0016-7037(93)90359-5.
Bird J. M., Isacks B., Eds. (1972), *Plate tectonics,* 563 p., AGU, Washington.
Biskaye P. E. (1965), Mineralogy and sedimentation of recent deep-sea clay in the Atlantic Ocean and adjacent seas and oceans, *Geol. Soc. Am. Bull., 73,* 803, doi:10.1130/0016-7606(1965)76[803:MASORD]2.0.CO;2.
Bjarnason I. Yh., Menke W., Flovenz O. G., Caress D.W. (1993), Tomographic Image of the Mid-Atlantic Plate Boundary in South Western Iceland, *J. Geophys. Res., 98,* 6607–6622, doi:10.1029/92JB02412.
Blanchard M., Alfredsson M., Brodholt J., Wright K., Richard C., Catlow A. (2007), Arsenic incorporation into FeS_2 pyrite and its influence on dissolution: A DFT study, *Geochimica Cosmochimica Acta, 71*, 3, 624–630, doi:10.1016/j.gca.2006.09.021.
Bobrievich A. P., Kalyuzhuyi V. A., Smirnov G. I. (1957), Moissanite in kimberlites of the East Siberian Platform, *Dokl. Akad. Nauk SSSR, 115*(6), 1189–1192.
Bogatikov O. A., Mokhov A. V., Kartashov P. M., et al. (2004), Ores Microparticles in a Lunar Regolith from Mare Fecunditatis, *Dokl. Earth Sci., 395*, 448.
Bohor B. F., Foord E. E., Ganapathy R. (1986), Magnesioferrite from the Cretaceous-Tertiary boundary, Caravaca, Spain, *Earth Planet. Sci. Lett., 81,* 57, doi:10.1016/0012-821X(86)90100-7.
Bohor B. F., Foord E. E., Modreski P. J., Triplehorn D. M. (1984), Mineralogic evidence for an impact event at the Cretaceous-Tertiary boundary, *Science, 224,* 867, doi:10.1126/science.224.4651.867.
Bokii G. B., Bezrukov G. N., Klyuev Yu. A., Neletov A. M., Nepsha V. I. (1986), *Natural and Synthetic Diamonds,* 221 pp., Nauka, Moscow.
Botrill R. S. (1998), A corundum-quartz assemblage in altered volcanic rocks, Bond Range, Tasmania, *Min. Magazine, 62,* 325–332, doi:10.1180/002646198547710.
Bott M. H. P., Gunnarson K. (1980), Crustal Structure of the Iceland-Faeroe Ridge, *J. Geophys. Res., 47*, 221–227.
Bowring S. A., Erwin D. H., Jin Y. G., Martin M., Davidek K., Wang W. (1998), U/Pb zircon geochronology and tempo of the end-Permian mass extinction, *Science, 280,* 1039–1045.
Brinkhuis H., Bujak J. P., Smit J., Versteegh G. J. M., Visscher H. (1998), Dinoflagelatte-based sea surface temperature reconstructions across the Cretaceous-Tertiary boundary, *Palaeogeogr. Palaeoclimatol. Palaeoecol., 141,* 67, doi:10.1016/S0031-0182(98)00004-2.
Brooks R. R., Hoek P. L., Reeves R. D., Johnston R. C., Wallace J. H., Ryan D. E., Holzbecher J., Collen J. D. (1985), Weathered spheroids in a Cretaceous/Tertiary boundary shale at Woodside Creek, New Zealand, *Geology, 13,* 738–740, doi:10.1130/0091-7613(1985)13<738:WSIACB>2.0.CO;2.
Brooks R. R., Reeves R. D., Yang X.-H., et al. (1984), Elemental Anomalies at the Cretaceous-Tertiary Boundary, Woodside Creek, New Zealand, *Science, 226,* 539–542.
Brownlee D. E. (1985), Cosmic Dust: Collection and Research, *Ann. Rev. Earth Planet. Sci., 13,* 147–173, doi:10.1146/annurev.ea.13.050185.001051.
Brownlee D. E., Bates B. A., Wheelock M. M. (1984), Extraterrestrial Platinum Group Nuggets in Deep-Sea Sediments, *Nature, 309,* 603–605, doi:10.1038/309693a0.
Brugmann G. E., Arndt N. T., Hofmann A. W., Tobschall H. J. (1987), Noble metal abundances in komatiite suites from Alexo, Ontario, and Gorgona island, Colombia, *Geochim. Cosmochim. Acta, 51,* 2159–2169, doi:10.1016/0016-7037(87)90265-1.
Burov B. V. (2005), Boundary between the Permian and Triassic Rocks in the Moscow Syneclise Reconstructed from the Rock Sequences Exposed in the Kichenenga River Basin, *Russian J. Earth Sci., 7*(2), 107–114, doi:10.2205/2005ES000176.
Burov B. V., Nourgaliev D. K., Yasonov P. G. (1986), *Palaeomagnetic Analysis,* 167 p., KGU, Kazan.
Butcher A. R., Pirrie D., Prichard H. M., Fisher P. (1999), Platinum-group mineralization in the Rum layered intrusion, Scotish Hebrides, UK, *J. Geol. Soc. London, 156,* 213–216, doi:10.1144/gsjgs.156.2.0213.
Byerly G. R., Lowe D. R. (1994), Spinel from archean impact spherules, *Geochim. Cosmochim. Acta, 58,* 3469, doi:10.1016/0016-7037(94)90099-X.
Campbell A. J., Simon S. B., Humayun M., Grossman L. (2003), Chemical Evolution of Metal in Refractory Inclusions in CV3 Chondrites, *Geochim. Cosmochim. Acta, 67*(17), 3119–3134, doi:10.1016/S0016-7037(02)00837-2.
Caress D. W., Mutter J. C., McNutt M. K., Detrick R. S. (1993), Seismic Refraction Evidence for Crustal Underplating beneath the Marquesas Island Hotspot Trace, *Trans. Am. Geophys. Un., 74,* 563.
Carlisle D. B., Braman D. R. (1991), Nanometre-size diamonds in the Cretaceous-Tertiary boundary clay of Alberta, *Nature, 352,* 708, doi:10.1038/352708a0.
Chapman M. G., Lauretta D. (2004), Iron Spherules from the Triassic-Jurassic Boundary Zone of the Lower Moennave, Nevada: A Preliminary Report on Possible Extraterrestrial Dust Deposits, in: *32nd IGC Florence 2004, Scientific Sessions*, Abstracts (Part 2), p. 1141.
Charvis Ph., Recq M., Operato St., Brefort D. (1995) Deep Structure of the Northern Kerguelen Plateau and Hotspot-Related Activity, *Geophys. J. Int., 122*, 899–924, doi:10.1111/j.1365-246X.1995.tb06845.x.
Chauvel C., Hofmann A. W., Vidal Ph. (1992), HIMU.EM: The French Polynesian connection, *Earth Planet. Sci. Lett., 110,* 99–119.
Cisowski S. M. (1988), Magnetic properties of K/T and E/O microspherules: Origin by combustion?, *Earth Planet. Sci. Lett., 88*, 193–208, doi:10.1016/0012-821X(88)90057-X.
Colombetti A., Ferrari G., Nicolodi F., Panini F. (1998), Some Metallic Spherules in Calcareous–Marly Sediments of the Romahoro Flysch, Sestola-Vidiciatico Tectonic Unit (Modena District, Northern Apennines, Italy), *Planet. Space Sci., 46*, 329–340, doi:10.1016/S0032-0633(97)00165-7.
Coombs M. L., Thomas W., Sisson Th. W., Lipman P. W. (2005), Growth history of Kilauea inferred from volatile concentrations in submarine-collected basalts, *J. Volcanol. Geother. Res.,* 151, 19–49, doi:10.1016/j.jvolgeores.2005.07.037.
Cowie J. W., Ziegler W., Remane J. (1989), Stratigraphic Commission accelerates progress, 1984–1989, *Episodes, 112*, 79–83.
Cox K. G. (1989), The Role of Mantle Plumes in the Development of Continental Drainage Patterns, *Nature, 342*, 873–877, doi:10.1038/342873a0.
Crisp J. A. (1984), Rates of magma emplacement and volcanic output, *J. Volcanol. Geotherm. Res., 20,* 177–211, doi:10.1016/0377-0273(84)90039-8.
Crocket J. H., Paul D. K. (2004), Platinum-group elements in

Deccan mafic rocks: A comparison of suites differentiated be Ir content, *Chem. Geol., 208,* 273–291, doi:10.1016/j.chemgeo.2004.04.017.

Czamanske G. K., Gurevich A. B., Fedorenko V. A., Simonov O. (1998), Demise of the Siberian Plume: Paleogeographic and Paleotectonic Reconstruction from the Prevolcanic and Volcanic Records, North-Central Siberia, *Int. Geol. Rev., 40,* 95–115.

Darbyshire F. A., Bjarnoson I. Th., White R., Flovenz O. G. (1998) Crustal Structure above the Iceland Mantle Plume Imaged by ICEMELT Refraction Profile, *Geophys. J. Int., 135,* pp. 1131–149.

Davitashvili L. Sh. (1969), *The causes of mass extinction*, 440 p., Nauka, Moscow.

Day R., Fuller M., Schmidt V. A. (1977), Hysteresis properties of titanomagnetites: Grain-size and compositional dependence, *Phys. Earth Planet. Int., 13*, 260–266, doi:10.1016/0031-9201(77)90108-X.

Deconinck J., Blanc-Valleronb M., Rouchyb J., Camoinc G., Badaut-Trauthb D. (2000), Palaeoenvironmental and diagenetic control of the mineralogy of Upper Cretaceous–Lower Tertiary deposits of the Central Palaeo–Andean basin of Bolivia (Potosi area), *Sediment. Geol., 132*, 263, doi:10.1016/S0037-0738(00)00035-X.

Des Marais D.J. (2001), Isotopic evolution of the biogeochemical carbon cycle during the Precambrian, in: *Stable Isotope Geochemistry,* vol. 43, edited by J. W. Valley and D. R. Cole, pp. 555–578, Reviews in Mineralogy and Geochemistry.

De Boer J. Z., Sanders D. Th. (2005), *Volcanoes in human history,* Princeton Univ. Press, 295 p.

Dittert N., Henrich R. (2000), Carbonate dissolution in the South Atlantic Ocean: Evidence from ultrastructure breakdown in Globigerina bulloides, *Deep Sea Res., Pt. I*(47), 603–620.

Dixon J. E., Clauge D. A. (2001), Volatiles in basaltic glasses from the Loichi seamount, Hawaii: Evidence for a relatively dry plume component, *J. Petrol., 42,* 627–654, doi:10.1093/petrology/42.3.627.

Dixon J. E., Clauge D. A., Wallace P. J., Poreda R. (1997), Volatiles in alkalic basalts from the North Arch volcanic field, Hawaii: Extensive degassing of deep submarine-erupted alkalic series lavas, *J. Petrol., 38,* 911–939, doi:10.1093/petrology/38.7.911.

Di Pierro S., Gnos E., Crobety B., et al. (2003), Rock-forming moissanite (natural α-silicon carbide), *Am. Mineral, 88,* 1817–1821.

Dobretsov N. L. (1994), Periodicity in Geological Processes and Deep Geodynamics, *Geol. Geofiz.,* (5), 5–19.

Dolenec T., Pavsic J., Lojen S. (2000), Ir anomalies and other elemental markers near the Palaeocene-Eocene boundary in a flysch sequence from the Western Tethys (Slovenia), *Terra Nova, 12,* 199, doi:10.1046/j.1365-3121.2000.00292.x.

Draibus G., Yagouts E., Wenke H. (1997), Water in the Earth's Mantle, *Geol. Geofiz.,* (1), 269–275.

Dubinin A. V. (1993), Inductively coupled plasma mass spectrometry: Determinations of REE in standard references samples of oceanic deposits, *Geokhimia, 24,*(11), 1605.

Ebihara M., Miura T. (1996), Chemical characteristics of the Cretaceous-Tertiary boundary at Gubbio, Italy, *Geochim. Cosmochim. Acta, 60,* 5133–5144, doi:10.1016/S0016-7037(96)00282-7.

Egger H., Rögl F., Wagreich M. (2004), Biostratigraphy and facies of Paleogene deep-water deposits at Gams (Gosau Group, Austria), *Ann. Naturhistor. Mus. Wien, 106A,* 291–307.

Egger H., Wagreich M. (2001), Upper Paleocene – Lower Eocene nannofossils from the Gosau Group of Gams/Styria (Austria), Österreichische Akademie der Wissenschaften, *Schriftenreihe der Erdwissenschaftlichen Kommissionen, 14,* 465–472.

Eggins S. M. (1992), Petrogenesis of Hawaiian Tholeiites, *Contrib. Mineral. Petrol., 110,* 387–410, doi:10.1007/BF00310752.

Egli R. (2003), Analysis of the field dependence of remanent magnetization curves, *J. Geophys. Res., 108,* doi:101029/2002JB002023.

Ellwood B., MacDonald W., Wheeler C., Benoist S. (2003), The K/T boundary in Oman: Identified using magnetic susceptibility field measurements with geochemical information, *Earth Planet. Sci. Lett., 206,* 529–540, doi:10.1016/S0012-821X(02)01124-X.

El Coresy A. (1966), Metallic Spherules in Bosumtwi Crater Glasses, *Earth Planet. Sci. Lett., 1,* 23–24, doi:10.1016/0012-821X(66)90099-9.

Engrand C., McKeegan K. D., Laurie A., et al. (2005), Isotopic Compositions of Oxygen, Iron, Chromium, and Nickel in Cosmic Spherules: Toward a Better Comprehension of Atmospheric Entry Heating Effects, *Geochim. Cosmochim. Acta, 69,* 5365–5385, doi:10.1016/j.gca.2005.07.002.

Erwin D. H. (2005), *Extinction: How Life on Earth Nearly Ended 250 Million Years Ago,* Princeton Univ. Press, 296 p.

Eugster O., Geiss J., Krahenbuhl U. (1985), Noble gas abundances and noble metal concentrations in sediments from the Cretaceous-Tertiary boundary, *Earth Planet. Sci. Lett., 74,* 27–34, doi:10.1016/0012-821X(85)90163-3.

Farley K. A. (1995), Cenozoic Variations in the Flux of Interplanetary Dust Recorded by ^{3}He in a Deep-Sea Sediment, *Nature, 376,* 153–156, doi:10.1038/376153a0.

Faupl P., Pober E., Wagreich M. (1987), Facies development of the Gosau Group of the eastern parts of the Northern Calcareous Alps during the Cretaceous and Paleogene, in: *Geodynamics of the Eastern Alps,* edited by H. W. Flügel and P. Faupl, pp. 142–155.

Faure G. (1989), *Osnovy izotopnoi geologii (Fundamentals of Isotope Geology),* Mir, Moscow, 590 pp..

Fedorenko A., Czamanske G. K. (1997), Results of New Field and Geochemical Studies of the Volcanic and Intrusive Rocks of the Maymecha–Kotuy Area, Siberian Flood-Basalt Province, Russia, *Int. Geol. Rev., 392,* 479–531.

Fedorenko A., Lightfoot P. C., Naldrett A. J., et al. (1996), Petrogenesis of the Siberian Flood-Basalt Sequence at Noril'sk, *Int. Geol. Rev., 38,* 99–135.

Fedotov S. A., Ed. (1984), *Large Tolbachik fissure eruption, Kamchatka 1975–1976,* 637 p., Science, Moscow.

Finkelman R. B. (1970), Magnetic Particles Extracted from Manganese Nodules: Suggested Origin from Stony and Iron Meteorites, *Science, 167,* 982–984.

Fisher A. G. (1984), Two Phanerozoic supercycles, in: *Catastropes and Earth history,* edited by W. A. Berggren and J. A. Van Couvering, Princeton Univ. Press, Princeton.

Florensky K. P. (1963), Problem of Cosmic Dust and the Current State of the Study of the Tunguska Meteorite, *Geokhimiya,* (3), 284–296.

Florensky K. P., Ivanov A. V., Kirova O. A., Zaslavskaya N. I. (1968), Phase Composition of Finely Dispersed Extraterrestrial Matter of the Tunguska Meteorite, *Geokhimiya,* (10), 1174–1182.

Fornaciari E., Giusberti L., Luciani V., Tateo F., Agnini C., Backman J., Oddone M., Rio D. (2007), An expanded Cretaceous-Tertiary transition in a pelagic setting of the Southern Alps (central-western Tethys), *Palaeogeography, Palaeo-*

climatology, Palaeoecology, 255, 98–131, doi:10.1016/j.palaeo.2007.02.044.

Francois L., Grarad A., Godderis Y. (2005), Modelling atmospheric CO_2 changes at geological time scale, in: *Garnets de Geologie/Notebooks on Geology,* pp. 11-14, Brest. Memoir 2005/02.

Frankel Ch. (2005), *Worlds on Fire, Volcanoes on the Earth, the Moon, Mars, Venus and Io,* Cambridge Univ. Press, 358 p.

Franklin B. (1784), Meteorological imagination's and conjectures, *Manchester Lit. Philos. Soc., Mem. Proc. 2,* 122.

Fuchs L. H., Blander M. (1977), Molybdenite in Calcium–Aluminium-Rich Inclusions in the Allende Meteorite, *Geochim. Cosmochim. Acta, 41,* 1170–1175.

Ganapathy R., Gartner S., Jiang M.-J. (1981), Iridium anomaly at the Cretaceous-Tertiary boundary in Texas, *Earth Planet. Sci. Lett., 54,* 393, doi:10.1016/0012-821X(81)90055-8.

Ganns O., Knipscheer H. C. G. (1954), Das Alter der Nierentaler und Zwieselalmschichten des Beckens von Gosau, *Neues Jahrbuch für Geologie und Paläontologie, 99*, 361–378.

Gapeev A.K., Tsel'movich V. A. (1988), Microstructure and composition of multiphase-oxidized natural and synthetic titanomagnetites, *Fiz. Zemli,* (10), 42–49.

Gardin S. (2002), Late Maastrichtian to early Danian calcareous nannofossils at Elles (Northwest Tunisia), A tale of one million years across the K/T boundary, *Palaeogeogr. Palaeoclimatol. Palaeoecol., 178,* 211, doi:10.1016/S0031-0182(01)00397-2.

Genge M. J., Crady M. M., Hutchinson R. (1997), The Texture and Compositions of Fine-Grained Antarctic Micrometeorites: Implications for Comparisons with Meteorites, *Geochim. Cosmochim. Acta. 61,* 5149–5162, doi:10.1016/S0016-7037(97)00308-6.

Gerlach T. M. (1992), Present-day CO_2 emissions from volcanoes, *Trans. Am. Geoph. Un., 72,* 254–255.

Gerlach T. M., Graeber E. J. (1985), Volatile budget of Kilauea Volcano, *Nature, 313,* 273–277, doi:10.1038/313273a0.

Gerlach T. M., McGee K. A., Elias T., Sutton J., Doukas M. (2002), Carbon dioxide emission rate of Kilauea Volcano: Implications for primary magma and the summit reservoir, *J. Geophys. Res. 107,* 3–1 – 3–15.

Gibson S. A., Thompson R. N., Dickin A. P., Leonardos O. H. (1996), Erratum to High-Ti and Low-Ti Mafic Potassic Magmas: Key to Plume-Lithosphere Interactions and Continental Flood-Basalt Genesis, *Earth Planet. Sci. Lett., 141,* 325–341, doi:10.1016/0012-821X(96)00041-6.

Giere R., Carleton L. E., Lumpkin G. R. (2003), Micro and Nanochemistry of Fly Ash from a Coal-Fired Plant, *Am. Mineral, 88,* 1853–1863.

Gill R. C., Pedersen A. K., Larsen J. G. (1992), Tertiary Picrites in West Greenland: Melting at the Periphery of a Plume, Magmatism and the Cases of the Continental Break-up, *Geol. Soc. Special Publ.,* (68), 335–348.

Gilmore J. S., Knight J. D., Orth C. J., et al. (1984), Trace elements patterns at a non-marine Cretaceous-Paleogene Boundary, *Nature, 307,* 224–228, doi:10.1038/3078/307224a0.

Godderis Y., Joachimski M. M. (2004), Global change in the Late Devonian: modelling the Frasnian-Famennian short-term carbon isotope excursions, *Palaeogeogr. Palaeoclimatol. Palaeoecol., 202,* 309–329, doi:10.1016/S0031-0182(03)00641-2.

Goresey A. E., Nagel K., Dominik B., Ramdohr P. (1977), Potential Presolar Material in Ca, Al rich inclusions of Allende, *Meteoritics, 12,* 215–216.

Grachev A. F. (1987), *Rift Zones of the Earth,* 2nd ed., Nedra, Moscow, 285 pp.

Grachev A. F. (1998a), The Khamar-Daban Range as a Hotspot of the Baikal Rift: Chemical Geodynamics Evidence, *Phys. Solid Earth,* (3), 3–28.

Grachev A. F. (1998b), The Saga on the Solar Helium in the Earth's Mantle, *Zemlya i Vselennaya,*(5) 3–10.

Grachev A. F. (2000a), Mantle Plumes and Geodynamics, *Phys. Solid Earth, 36,*(4), 263–294.

Grachev A. F. (2000b), Geodynamic reasons for global catastrophes, *Zemlya i Vselennaya ,* (5), 13.

Grachev A. F., Ed. (2000c), *Neotectonics, Geodynamics, and Seismicity of Northern Eurasia,* 487 pp., Probel, Moscow.

Grachev A. F. (2001), A new view on the origin of magmatism of the Franz Josef Land, *Phys. Solid Earth, 37,*(9), 744–756.

Grachev A. F. (2003), Identification of mantle plumes based on the study of isotopic and geochemical characteristics of volcanic rocks, *Petrology, 11,*(6), 618–654.

Grachev A. F., Borisovsky S. E., Grigor'eva A. V. (2008a), The First Find of Native Rhenium in the Transitional Clay Layer at the Cretaceous-Paleogene Boundary in the Gams Section (Eastern Alps, Austria), *Doklady Earth Sciences, 422,* (7), 1065–1067, doi:10.1134/S1028334X08070131.

Grachev A. F., Kaban M. K. (2006), Factors Responsible for the High Position of the Siberian Platform, *Phys. Solid Earth, 42,*(12), 987–998, doi:10.1134/S1069351306120032.

Grachev A. F., Korchagin O. A., Kollmann H., Pechersky D. M., Tsel'movich V. A. (2005), A new look at the nature of the transitional layer at the K/T boundary near Gams, Eastern Alps, Austria, and the problem of the mass extinction of the biota, *Russian J. Earth Sci., 7,* 1–45, doi:10.2205/2005ES000189.

Grachev A. F., Korchagin O. A., Tsel'movich V. A. (2006a), Cosmic Matter in Clay at the Cretaceous-Paleogene Boundary (Gams, Eastern Alps), in: *Physicochemical and Petrophysical Research in Earth Sciences*, IFZ RAN, Moscow, p. 21.

Grachev A. F., Korchagin O. A., Tsel'movich V. A., Kollmann H. (2008b), Cosmic Dust and Micrometeorites in the Transitional Clay Layer at the Cretaceous-Paleogene Boundary in the Gams Section (Eastern Alps): Morphology and Chemical Composition, *Phys. Solid Earth, 44,*(7), 555–569.

Grachev A. F., Nikolaev V. A., Nikolaev V. G. (2006c), East European platform development in the Late Precambrian and Paleozoic: Structure and sedimentation, *Russian J. Earth Sci., 8,*(4), 1–22, doi:10.2205/2006ES000203.

Grachev A. F., Nikolaev V. G., Seslavinsky K. B. (1994), *Evolution of the Structure, Sedimentation, and Magmatism in the East European Platform in the Late Precambrian and Paleozoic (Tectonics and Magmatism of the East European Platform),* pp. 5–36, Geo-inveks, Moscow.

Grachev A. F., Pechersky D. M., Borisovsky S. E., Tsel'movich V. A. (2008c), Magnetic Minerals in Sediments at the Cretaceous-Paleogene Boundary (the Gams Section, Eastern Alps), *Phys. Solid Earth, 44* (10), 789–803.

Grachev A. F., Tsel'movich V. A., Korchagin O. A., Kollmann H. (2007a), Two Spinel Populations from Cretaceous-Paleogene Boundary Clay Layer in the Gams Stratigraphic Sequence, Eastern Alps, *Russian J. Earth Sci., 9,* ES2002, doi:10.2205/2007ES000297.

Grachev A. F., Kamensky I. L., Korchagin O. A., Kollmann H. (2007b), First data on He isotopic signatures in the Cretaceous-Paleogene clay boundary layer at Gams, Eastern Alps, *Phys. Solid Earth, 43,*(9) 7.

Graup G., Spettel B. (1989), Mineralogy and phase chemistry

of an *Ir*-enriched pre-K/T layer from the Lattengebirge, Bavarian Alps, and significance for the KTB problem, *Earth Planet. Sci. Lett., 95,* 271, doi:10.1016/0012-821X(89)90102-7.

Griscom D. L., Beltran-Lopez V., Merzbacher C. I., Bolden E. (1999), Electron spin resonance of 65-million-year-old glasses and rocks from the Cretaceous-Tertiary boundary, *J. Non Cryst. Solids, 253,* 1–22, doi:10.1016/S0022-3093(99)00340-3.

Gurvich E. G. (1998), *Oceanic Metalliferous Sediments,* Nauchnyi Mir, Moscow, 340 p.

Hallam A. (1981), *Facies interpretation and the stratigraphic record,* Mir, Moscow, 327 pp.

Hallam A. (1992), *Phanerozoic sea-level changes,* 266 pp., New York, Columbia University Press.

Hallam T. (2005), *Catastrophes and lesser calamities, The causes of mass extinctions*, 226 p., Oxford University Press, Oxford.

Halmer M. M., Schmincke H.-U. (2003), The impact of moderate-scale explosive eruptions on stratospheric gas injections, *Bull. Volcanol., 65,* 433–440, doi:10.1007/s00445-002-0270-x.

Hamaguchi H., Onuma N., Hirao Y., et al. (1969), The abundances of arsenic, tin and antimony in chondritic meteorites, *Geochim. Cosmochim. Acta, 33,* 507–518, doi:10.1016/0016-7037(69)90130-6.

Hardenbol J., Thierry J., Farrey M. B., et al. (1998), Cretaceous sequence chronostratigraphy, (chart 4), Cenozoic biostratigraphy (chart 3), *SEPM, Spec. Publ., 60,* 3–13.

Hards V. (2005), Volcanic contributions to the global carbon cycle, *British Geol. Survey Publ.,* (10), 26 p.

Harland W. B., Armstrong R. L., Cox A. V., Craig L. E., Smith A. G., Smith D. E. (Eds) (1990), *The Geologic Time Scale,* 263 pp., Cambridge Universiry Press, Cambridge, UK.

Hart R., Hogan L., Dymond J. (1985), The closed-system approximation for evolution of argon and helium in the mantle, crust and atmosphere, *Chem. Geol., 52.* 45–73.

He Bin Yi-Gang Xu, Chung S.-L., et al. (2003), Sedimentary Evidence for a Rapid, Kilometer-Scale Crustal Doming Prior to the Eruption of the Emeishan Flood Basalts, *Earth Planet. Sci. Lett., 213,* 391–405, doi:10.1016/S0012-821X(03)00323-6.

Herm D. (1962), Stratigraphische und mikropaläontologische Untersuchungen der Oberkreide im Lattengebirge und Nierental (Gosaubecken von Reichenhall und Salzburg, Bayerische Akademie der Wissenschaften, mathematisch-naturwissenschaftliche Klasse, *Abhandlungen, Neue Folge 104,* 7–119.

Herm D., Hillebrandt A. R., Höfling R., Martini E., Perch-Nielsen K., Exkurtion E. (1981), Lattengebirge und Untersberg-Vorland, *Geol. Bavarica, 82,* 181–232.

Hillebrandt A. R. (1962), Das Alttertiär im Becken von Reichenhall und Salzburg, Bayerische Akademie der Wissenschaften, mathematisch-naturwissenschaftliche Klasse, *Abhandlungen, Neue Folge 108*, 9–182.

Hildebrand A. R., Penfield G. T., Kring D. A. (1991), Chicxulub crater: A possible Cretaceous-Tertiary boundary impact crater on the Yucatan peninsula, Mexico, *Geology, 19,* 867, doi: 10.1130/0091-7613(1991)019<0867:CCAPCT>2.3.CO;2.

Hilton D. R., McMurtry G. M., Kreulen R. (1997), Evidence for extencive degassing of the Hawaiian mantle plume from helium-carbon relationships at Kilauea volcano, *Geophys. Res. Lett., 24,* 3065–3068, doi:10.1029/97GL03046.

Hinnov L. A., Ogg J. G. (2007), Cyclostratigraphy and the astronomical time scale, *Stratigraphy, 4*, 239–251.

Hofmann C., Feraud G., Courtillot V. (2000), $^{40}Ar/^{39}Ar$ dating of mineral separates and whole rocks from the Western Ghats lava pile: Further constraints on duration and age of the Deccan traps, *Earth Planet. Sci. Lett., 180,* 13–27, doi:10.1016/S0012-821X(00)00159-X.

Hooper P. (1997), The Columbia river flood basalt province: Current status, in: *Large igneous provinces: Continental, oceanic and planetary flood basalts Geophysical Monograph Series 100,* edited by J. J. Mahoney and M. F. Coffin, pp. 1–27, AGU, Washington.

Hough R. M., Gilmour I., Pillinger C. T., et al. (1995), Diamond and silicon carbide in impact melt rock from the Ries impact crater, *Nature, 378,* 41–44, doi:10.1038/378041a0.

Hough R. M., Gilmour I., Pillinger C. T., et al. (1997), Diamonds from the Iridium-Rich K/T Boundary Layer at Arroyo El Mimbral, Namaulipas, Mexico, *Geology, 25,* 1019–1022, doi: 10.1130/0091-7613(1997)025<1019:DFTIRK>2.3.CO;2.

Hsu K. J., He Q., McKenzie A. (1982), Mass mortality and its environmental and evolutionary consequences, *Science, 216,* 249, doi:10.1126/science.216.4543.249.

Huber B. T., Quillevere F. (2005), Revised Paleogene planktonic foraminiferal biozonation for the Austral realm, *J. Foraminiferal Res., 4,*(35), 299–314, doi:10.2113/35.4.299.

Hunter W., Parkin D. W. (1960), Cosmic Dust in Recent Deep-Sea Sediments, *Proc. R. Soc. London, Ser. A, Math. Phys. Sci., 255,*(1282), 382–397.

Ito T., Usui A., Kajiwara Y., Nakano T. (1998), Strontium Isotopic Compositions and Paleoceanographic Implication of Fossil Manganese Nodules in DSDP/ODP Cores, Leg 1-126, *Geochim. Cosmochim. Acta, 62,* 1545–1554, doi:10.1016/S0016-7037(98)00051-9.

Ivanov A. V., Florensky K. P. (1970), Intensity of Fallout of Finely Dispersed Cosmic Matter onto the Earth, *Geokhimiya,* (11), 1365–1372.

Jablonski D. (1986), Causes and consequences of mass extinctions: a comparative approach, in: Elliot D. K., ed. *Dynamics of extinction*, John Wiley and Sons, N.Y., 183–229.

Jacobsen S. B., Kaufman A. J. (1999), The Sr, C and O Isotopic Composition of Neoproterozoic Seawater, *Chem. Geol., 161,* 37–57, doi:10.1016/S0009-2541(99)00080-7.

Janak M., Froitzheim N., Vravec M. (2006), Ultrahigh-Pressure metamorphism and exhumation of garnet peridotite in Pohorje, Eastern Alps, *J. Metamorph. Geol., 24,* 19, doi:10.1111/j.1525-1314.2005.00619.x.

Jedlong Y., Weiguo S., Zongzhe Zongzh, et al. (1999), Variations in Sr and C Isotopes and Ce Anomalies in Successions from China: Evidence for the Oxygenation of Neoproterozoic Seawater?, *Precambrian Res., 93,* 215–233, doi:10.1016/S0301-9268(98)00092-8.

Jin Y. G., Wang Y., Wang W., Shang Q. H., Cao C. Q., Erwin D. H. (2000), Pattern of Marine Mass Extinction Near the Permian-Triassic Boundary in South China, *Science, 289*, 432–436.

Jones A. P., Price D. G., DeCarli P. S., Proce N., Clegg R. (2003), Impact decompression melting: A possible trigger for impact induced volcanism and mantle hotspots?, in: *Impact Markers in the Stratigraphic Record,* edited by C. Koeberl and F. Martínez-Ruiz, p. 91, Springer, Berlin.

Kaban M. K., Schwintzer P., Tikhotsky S. A. (1999), Global Isostatic Residual Geoid and Isostatic Gravity Anomalies, *Geophys. J. Int., 136,* 519–536, doi:10.1046/j.1365-246x.1999.00731.x.

Kamensky F. V., Sablukov S. M., Sablukova L. I. (2002), Kimberlites from the Wawa Area, Ontario, *Can. J. Earth Sci., 39,* 1819, doi:10.1139/e02-089.

Kamensky I. L., Tolstikhin I. N., Vetrin V. R. (1990), Juvenile Helium in Ancient Rocks: I, ^{3}He Excess in Amphiboles from 2.8 Ga Charnokite Series–Crust-Mantle Fluid in Intracrustal Magmetic Processes, *Geochim. Cosmochim. Acta, 54,* 3115, doi:10.1016/0016-7037(90)90127-7.

Kamo S. L., Gerald K., Czamanske G. K., Amelin Y., Fedorenko V. A., Davis D. W., Trofimov V. R. (2003), Rapid eruption of Siberian flood-volcanic rocks and evidence for coincidence with the Permian-Triassic boundary and mass extinction at 251 Ma, *Earth Planet. Sci. Lett., 214,* 75–91, doi:10.1016/S0012-821X(03)00347-9.

Karner D. B., Levine J., Muller R., et al. (2003), Extraterrestrial Accretion from the GISP2 Ice Core, *Geochim. Cosmochim. Acta, 67,* 751–763, doi:10.1016/S0016-7037(02)01145-6.

Karoui-Yaakoub N., Zaghbib-Turki D., Keller G. (2002), The Cretaceous-Tertiary (K/T) mass extinction in planktic foraminifera at Elles I and El Melah, Tunisia, *Palaeogeogr. Palaeoclimatol. Palaeoecol., 178,* 233–255, doi:10.1016/S0031-0182(01)00398-4.

Kaula U. M. (1970), Tectonics and the Earth's Gravity Field, in: *The Nature of Solid Earth,* edited by E. Robertson, Cambridge (USA), McGraw-Hill, 210–225.

Keller G. (1988), Extinction, survioship and evolution of planktonic foraminifera across the Cretaceous/Tertiary boundary at El Kef, Tunisia, *Mar. Micropaleontol., 13,* 239, doi:10.1016/0377-8398(88)90005-9.

Keller G. (2002), Guembelitria-dominated late Maastrichtian planktic foraminiferal assemblages mimic early Danian in central Egypt, *Mar. Micropaleontol., 47,* 71, doi:10.1016/S0377-8398(02)00116-0.

Keller G. (2008), Impact stratigraphy: Old principle, new reality, in: Evans, K. R., Horton, J. W., Jr., King, D. T., Jr., and Morrow, J. R., eds., *The Sedimentary Record of Meteorite Impacts*, The Geological Society of America, Special Paper 437, 147–178.

Keller G., Adatte Th., Stinnesbeck W., Luciani V., Karoui-Yaakoub N., Zaghbib-Turki D. (2002a), Paleoecology of the Cretaceous-Tertiary mass extinction in planktonic foraminifera, *Palaeogeogr. Palaeoclimatol. Palaeoecol., 178,* 257–292, doi:10.1016/S0031-0182(01)00399-6.

Keller G., Adatte Th., Gardin S., Bartolini A., Bajpai S. (2008), Main Deccan volcanism phase ends near the K/T boundary: Evidence from the Krishna-Godavari Basin, SE India, *Earth and Planetary Science Letters, 268*, 293–311, doi:10.1016/j.epsl.2008.01.015.

Keller G., Li L., MacLeod N. (1996), The Cretaceous/Tertiary boundary stratotype section at El Kef, Tunisia: How catastrophic was rhe mass extinction?, *Palaeogeogr. Palaeoclimatol. Palaeoecol., 119,* 221, doi:10.1016/0031-0182(95)00009-7.

Keller G., Stinnesbeck W. (2000), Iridium and the K/T boundary at El caribe, Guatemala, *Int. J. Earth Sci., 88,* 840, doi:10.1007/s005310050310.

Keller G., Stinnesbeck W., Adatte Th., Stuben D. (2002b), Multiple impacts across the Cretaceous-Tertiary boundary, *Earth Sci. Rev., 203,* 327–363.

Kent R. W. (1995), Magnesian Basalts From the Hebrides, Scotland: Chemical Composition and Relationship to the Iceland Plume, *J. Geol. Soc. London, 152,* 979–983.

Kerr A. C., Tarney J., Kempton P. D., Spadea P., et al. (2002), Pervasive mantle plume head heterogeneity: Evidence from the late Cretaceous Caribbean-Colombian oceanic plateau, *J. Geophys. Res., 107,*(B7), 2140, doi:10.1029/2001JB000790.

Keto L. S., Jacobsen S. B. (1988), Nd isotopic variatiobs of Phanerozoic paleoceans, *Earth Planet. Sci. Lett., 90,* 395–410.

Kingsley R. H., Schilling J. G. (1995), Carbon in Mid-Atlantic ridge basalt glasses from 28°N to 63°N: Evidence for a carbon-enriched Azores mantle plume, *Earth Planet. Sci. Lett., 129,* 31–53, doi:10.1016/0012-821X(94)00241-P.

Koeberl C. (1989), Iridium enrichment in volcanic dust from blue ice fields, Antarctica, and possible relevance to the K/T boundary event, *Earth Planet. Sci. Lett., 92,* 317–322, doi:10.1016/0012-821X(89)90056-3.

Koeberl C. (1997), Impact cratering: the mineralogical and geochemical evidence, in: *The Ames Structure and Similar Features,* edited by K. Johnson and J. Campbell, p. 30, Geol. Survey Circular, Oklahoma.

Kogarko L. N. (1977), *Genesis of Agpaitic Magmas,* 225 pp., Nauka, Moscow

Kogarko L. N., Ryabchikov I. D. (1988), Differentiation of the Earth's Mantle, *Geokhimiya,* (2), 223–235.

Kollmann H. (1963), Zur stratigraphischen Gliederung der Gosauschichten von Gams, *Mitt. Ges. Geol. Bergbau Stud., 13,* 189–212.

Kollmann H. (1964), Stratigraphie und Tektonik des Gosaubeckens von Gams (Steiermark, Österreich), *Jahrbuch der Geologischen Bundesanstalt, 107,* 189–212.

Kollmann H., Sachsenhofer R. (1998), Zur Genese des Gagats von Gams bei Hieflau (Oberkreide, Steiermark), *Mitteilungen des Referats für Geologie und Paläontologie,* Landesmuseum Joanneum, Sonderheft, 2, 223–238.

Kollmann H., Summesberger H. (1982), *WGCM – 4th Meeting,* Guide Book: Gosau Basins in Austria, 105 p.

Konnerup-Madsen J., Rose-Hansen J. (1982), Volatiles associated with alkaline igneous rift activity in the Ilimaussaq intrusions and the Gardar granitic complexes (South Greenland), *Chem. Geol., 37,* 79–93.

Korchagin O. A., Dubinina S. V., Tsel'movich V. A., Pospelov I. I. (2007), Possible Impact Event in the Late Cambrian, *Global Geol., 10,* 78–82.

Kosakevitch A., Disnar J. R. (1997), Nature and Origin of Chemical Zoning in the Metal Nucleus and Oxide Cortex of Cosmic Spherules from the Tuamotu Archipelago, French Polynesia, *Geochim. Cosmochim. Acta, 61,* 1073–1082, doi:10.1016/S0016-7037(96)00380-8.

Krinov E. L. (1971), New Studies of the Fallout and Findings of the Sikhote-Alin' Meteorite Shower, in: *Problems in Cosmochemistry and Meteoritics*, pp. 117–128, Naukova Dumka, Kiev.

Krylov A. Ya., Mamyrin B. A., Silin Yu. I., Khabarin L. V. (1973), Helium Isotopes in Oceanic Sediments, *Geokhimiya,* (2), 284–288.

Kühn O. (1930), Das Danien der Äußeren Klippenzone bei Wien, Geologische und Paläontologische Abhandlungen, *Neue Folge, 17,* 495–576.

Küpper K. (1956), Stratigraphische Verbreitung der Foraminiferen in einem Profil aus dem Becken von Gosau (Grenzbereich Salzburg-Oberösterreich), *Jahrbuch der Geologischen Bundesanstalt, 99,* 273–320.

Kurat C., Koeberl C., Presper T., et al. (1994), Petrology and Geochemistry of Antarctic icrometeorites, *Geochim. Cosmochim. Acta, 58,* 3879–3904, doi:10.1016/0016-7037(94)90369-7.

Kyte F. T., Bohor B. F. (1995), Nickel-Rich magnesiwustite in Cretaceous-Tertiary boundary spherules crystallized from

ultramafic, refractory silicate liquids, *Geochim. Cosmochim. Acta, 59,* 4967.

Kyte F. T., Bostwick J. A. (1995), Magnesioferrite spinel in Cretaceous/Tertiary boundary sediments of the Pacific basin: remnants of hot, early ejecta from the Chicxulub impact?, *Earth Planet. Sci. Lett., 132,* 113–127.

Lahodynsky R. (1988a), Geology of the K/T boundary site at Knappengraben creek (Gams, Styria), IGCP Project 199 Rare events in geology; Abstracts, *Berichte der Geologischen Bundesanstalt, 15,* 33–36.

Lahodynsky R. (1988b), Lithostratigraphy and sedimentology across the Cretaceous/Tertiary Boundary in the Flyschgosau (Eastern Alps, Austria), *Revista Espanola Paleont.,* spec. vol. 1988 73–82.

Larson R. L., Olson P. (1991), Mantle Plumes Control Magnetic Reversal Frequency, *Earth Planet. Sci. Lett., 107,* 437–447, doi:10.1016/0012-821X(91)90091-U.

Lee C. A., Wasserburg G. J., Kyte F. T. (2003), Platinum-group elements (PGE) and rhenium in marine sediments across the Cretaceous–Tertiary boundary: Constraints on Re-PGE transport in the marine environment, *Geochim. Cosmochim. Acta, 67,* 655–670, doi:10.1016/S0016-7037(02)01135-3.

Leroux H., Rocchia R., Froget L., et al. (1995), The K/T Boundary at Beloc (Haiti): Compared Stratigraphic Distributions of the Boundary Markers, *Earth Planet. Sci. Lett., 132,* 255–268, doi:10.1016/0012-821X(95)00032-8. (1995).

Levin B. Yu., Simonenko A. N. (1973), The Earth among Dust and Stones, *Priroda,* (4), 7–14.

Le Carde V., Debenay J.-P., Lesourd M. (2003), Low pH effects on Ammonia beccarii test deformation: Implications for using test deformations as a pollution indicator, *J. Foraminiferal Res., 1,*(33), 1–9.

Le Roex A. P., Dick H. J., Reid A. M., Erlank A. J. (1982), Ferrobasalts from the Spiess Ridge Segment of the Southwest Indian Ridge, *Earth Planet. Sci. Lett., 60,* 437–451, doi:10.1016/0012-821X(82)90079-6.

Liati A. (1988), Corundum- and Zoisite-bearing Marbles in the Rhodope Zone, Xanthi Area (N. Greece): Estimation of the Fluid Phase Composition, *Mineral. Petrol., 38,* 53–60, doi:10.1007/BF01162481.

Lisitsyn A. P. (1978), *Processes of Oceanic Sedimentation,* 392 pp., Nauka, Moscow.

Lo C.-Y., Chung S.-L., Lee T.-Y., Wu G. (2002), Age of the Emeishan flood magmatism and relations to Permian-Triassic boundary events, *Earth Planet. Sci. Lett., 198,* 449–458.

Loper D. E., McCartney K., Buzyna G. (1988), A Model of Correlated Episodicity in Magnetic-Field Reversals, Climate and Mass Extinctions, *J. Geol., 96,* 1–15.

Luciani V. (2002), High-resolution planktonic foraminiferal analysis from the Cretaceous-Tertiary boundary at Ain Settara (Tunisia): Evidence of an extended mass extinction, *Palaeogeogr. Palaeoclimatol. Palaeoecol., 178,* 299, doi:10.1016/S0031-0182(01)00400-X.

Lykov A. V., Pechersky D. M. (1976), Stability range of magnetic minerals in basalts from magnetic data, *Izv. Akad. Nauk SSSR, Fiz. Zemli,* (12), 58–63.

Lykov A. V., Pechersky D. M. (1977), Experimental study of magnetic properties of basalts in relation to their formation conditions, *Izv. Akad. Nauk SSSR, Fiz. Zemli,* (4), 65–74.

MacDonald G. A. (1972), *Volcanoes (Prentice-Hall),* (Englewood Cliffs, N.J. 1972, Mir, Moscow, 1975).

McDonough W. F., Sun S.-S. (1995), The composition of the Earth, *Chem. Geol., 120,* 223–253.

Maclennan J., Lovell B. (2002), Control of regional sea level by surface uplift and subsidence caused by magmatic underplating of Earth's crust, *Geology, 30,*(8), 675–678, doi: 10.1130/0091-7613(2002)030<0675:CORSLB>2.0.CO;2.

Magaritz M. (1989), 13C minima follow extinction event: A clue to faunal radiation, *Geology, 17,* 337, doi: 10.1130/0091-7613(1989)017<0337:CMFEEA>2.3.CO;2.

Malitch K. N., Thalhammer O. A. R., Melcher F., Knauf V. V., Melcher F. (2003), Diversity of platinum-group mineral assdemblages in banded and podiform chromitite from the Kraubath ultramafic massif, Austria: Ecidence for an ophiolite transition zone?, *Mineralium Deposita, 38,* 282–297.

Mamyrin B. A., Tolstikhin I. N. (1981), *Helium Isotopes in Nature,* Energoizdat, Moscow, 185 pp.

Mamyrin B. A., Tolstikhin I. N., Anufriev G. S., Kamensky I. L. (1969), Anomalous Isotopic Composition of Helium in Volcanic Gases, *Dokl. Akad. Nauk SSSR, 184,*(5), 1197–1199.

Mandl G. W. (2000), The Alpine sector of the Tethyan shelf – Examples of Triassic to Jurassic sedimentation and deformation from the Northern Calcareous Alps, *Mitt. Österr. Geol. Ges., 92,* 61–78.

Marcantonio F., Higgins S., Andersen R. F., et al. (1998), Terrigenous helium in deep-sea sediments, *Geochim. Cosmochim. Acta, 62,* 1535–1543, doi:10.1016/S0016-7037(98)00091-X.

Marcantonio F., Kumar N., Stute M., et al. (1995), A Comparative Study of Accumulation Rates Derived by He and Th Isotope Analysis of Marine Sediments, *Earth Planet. Sci. Lett., 133,* 549–555, doi:10.1016/0012-821X(95)00079-R.

Markl G. (2005), Mullite-corundum-spinel-cordierite-plagioclase xenoliths in the Skaergaard Marginal Border group: multi-stage interaction between metasediments and basaltic magma, *Contrib. Mineral. Petrol., 149*, 196–215, doi:10.1007/s00410-004-0644-5.

Martínez-Ruiz F., Ortega-Huertas M., Palomo I., Barbieri M. (1992), The geochemistry and mineralogy of the Cretaceous-Tertiary boundary at Agost (southeast Spain), *Chem. Geol., 95,* 265–281, doi:10.1016/0009-2541(92)90016-X.

Marty B., Tolstikhin I. N. (1998), CO_2 fluxes from mid-ocean ridges, arcs and plumes, *Chem. Geol., 145,* 233–248, doi:10.1016/S0009-2541(97)00145-9.

Marvin U. B., Einaudi M. T. (1967), Black Magnetic Spherules from Pleistocene Beach Sands, *Geochim. Cosmochim. Acta, 3,* 1871–1884, doi:10.1016/0016-7037(67)90128-7.

Mathez E. A., Fogel R. A., Hutchson I. D., Marshnitsev V. K. (1995), Carbon isotopic composition and origin of SiC from kimberlites of Yakutia, Russia, *Geochim. Cosmochim. Acta, 59,* 781–791, doi:10.1016/0016-7037(95)00002-H.

Maurette M., Jehanno C., Robin E., Hammer C. (1986), Characteristics and Mass Distribution of Extraterrestrial Dust from the Greenland Ice Cap, *Nature, 328,* 699–702, doi:10.1038/328699a0.

McEnroe S. A., Harrison R. Y., Robinson P., Langenhorst F. (2002), Nanoscale hematite-ilmenite lamellae in massive ilmenite rock: An example of lamellae magnetism with implication for planetary magnetic anomalies, *Geophys. J. Int., 151,* 890–912, doi:10.1046/j.1365-246X.2002.01813.x.

Melcher F., Meisel Th. (2004), A metamorphosed Early Cambrian Crust-Mantle transition in the Eastern Alps, *Aust. J. Petrol., 45,* 1689, doi:10.1093/petrology/egh030.

Melluso L., Beccaluva L., Brotzu P., Gregnanin A., Gupta A., Morbidelli L., Traversa G. (1995), Constraints on the nature of the mantle sources beneath the Deccan Traps from the petrology and geochemistry of the basalts from Gujarat (Western India), *J. Petrol., 36,* 1393.

Menzies M., Baker J., Chazot G., Al'Kadasi M. (1997), Evo-

lution of the Red Sea Volcanic Margin, Western Yemen, Large Igneous Provinces, in: *Continental, Oceanic and Planetary Flood Basalts, Geophys. Monogr. Ser.,* vol. 100, edited by J. J. Mahoney and M. F. Coffin, pp. 29–43, AGU, Washington.

Merrihue C. (1964), Rare gas evidence for cosmic dust in modern Pacific red clay, *Ann. N. Y. Acad. Sci., 119,* 351–367, doi:10.1111/j.1749-6632.1965.tb47445.x.

Messenger S., Stadermann F. J., Floss Ch., et al. (2003), Isotopic Signatures of Presolar Materials in Interplanetary Dust, *Space Sci. Rev., 106,* 155–172, doi:10.1023/A:1024637704533.

Miller K. G., Kominz M. A., Browning J. V., et al. (2005), The Phanerozoic record of global sea-level Change, *Science, 310,* 1293–1298.

Miono S., Nakayama Y., Shoji M., et al. (1993), Origin of Microspherules in Paleozoic–Mesozoic Bedded Chert Estimated by PIXE Analysis, *Nucl. Instrum. Methods Phys. Res., B75,* 435–439, doi:10.1016/0168-583X(93)95691-W.

Mitchel R. H. (1978), Mineralogy of the Elwin Bay Kimberlites, Somerset Island, N.W.T. Canada, *Am. Mineral., 63,* 47.

Miura Y., Uedo Y. (2001), Iron Spherules and Melted Fragments Found at Rice-Field of Nio Meteorite Shower Site in Yamaguachi, Japan, *Lunar Planet. Sci. XXXII,* CD-ROM.

Moberly R., Campbell J. F. (1984), Hawaiian Hotspot Volcanism Mainly during Geomagnetic Normal Intervals, *Geology, 12,* 459–463, doi: 10.1130/0091-7613(1984)12<459:HHVMDG>2.0.CO;2.

Mokhov A. V., Kartashov P. M., Bogatikov O. A. (2007), *Moon under a Microscope,* 122 pp., Nauka, Moscow.

Molina E., Alegret L., Arenillas I., Arz J. A., Gallala N., Hardenbol J., Salis S., Sterbaut E., Vandenberghe N., Zaghbib-Turki D. (2006), The Global Boundary Stratotype Section and Point for the base of the Danian Stage (Paleocene, Paleogene, Tertiary, Cenozoic) at El Kef, Tunisia – Origin definition and revision, *Episodes, 29,*(4), 263–273.

Molodenskii S. M. (2005), On Stress in the Earth's Mantle during the Fall of a Large Cosmic Body, *Rus. J. Earth. Sci., 7,* 1, doi:10.2205/2005ES000193.

Molostovsky E. A., Fomin V. A., Pechersky D. M. (2006), Sedimentogenesis in Maastrichtian-Danian basins of the Russian plate and adjacent areas in the context of plume geodynamics, *Russian J. Earth Sci., 8,* ES6001, doi:10.2205/2006ES000206.

Momme P., Tegner Ch., Brooks C. K., Keays R. R. (2002), The behaviour of platinum-group elements in basalts from the East Greenland rifted margin, *Contrib. Mineral. Petrol., 143,* 133–153, doi:10.1007/s00410-001-0338-1.

Montanari A., Hay R. L., Alvarez W. (1983), Spheroids at the Cretaceous-Tertiary boundary are altered impact droplets of basaltic composition, *Geology, 11,* 668, doi: 10.1130/0091-7613(1983)11<668:SATCBA>2.0.CO;2.

Morden S. J. (1993), Magnetic analysis of K/T boundary layer clay from Stevns Klint, Denmark, *Meteoritics, 28,* 595–599.

Morgan W. J. (1971), Convection Plumes in the Lower Mantle, *Nature (London), 230,* 42–45, doi:10.1038/230042a0.

Morner N. A., Etiope G. (2002), Carbon degassing from the lithosphere, *Global Planet. Change, 33,* 185–203, doi:10.1016/S0921-8181(02)00070-X.

Mposkos E. D., Kostopoulos D. K. (2001), Diamond, former coesite and supersilicic garnet in metasedimentary rocks from the Greek Rhodope: A new ultrahigh-pressure metamorphic Province Established, *Earth Planet. Sci. Lett., 192,* 497, doi:10.1016/S0012-821X(01)00478-2.

Mukhopadhyay S., Farley K. A., Montanari A. (2001), 35 Myr record of helium in pelagic limestones in Italy: Implications for interplanetary dust accretion from the early Maastrichtian to the middle Eocene, *Geochim. Cosmochim. Acta, 65,* 653–669, doi:10.1016/S0016-7037(00)00555-X.

Murray R. W. (1994), Chemical criteria to identify the depositional environment of cherts: General principales and applications, *Sediment. Geol., 90,* 213, doi:10.1016/0037-0738(94)90039-6.

Murray S., Renard A. F. (1891), *Report on Deep-Sea Deposits Based on the Specimens Collected during the Voyage of H. M. S. Challenger in the Years 1872 to 1876,* vol. 3, Neil, Edinburgh.

Murthy V. R. (1963), Elemental and Isotopic Abundances of Molybdenum in Some Meteorites, *Geochim. Cosmochim. Acta, 27,* 1171–1178, doi:10.1016/0016-7037(63)90098-X.

Nadeau S. L., Epstein S., Stolper E. (1999), Hydrogen and Carbon Abundances and Isotopic Ratios in Apatite from Alkaline Intrusive Complexes with a Focus on Carbonatites, *Geochim. Cosmochim. Acta, 63,* 1837–1851, doi:10.1016/S0016-7037(99)00057-5.

Nagata T. (1961), *Rock–Magnetism,* 350. p., Maruzen, Tokyo.

Nazarov M. A., Barsukova L. D., Kolesov G. M., et al. (1983), Origin of Ir anomaly at the Maastrichtian-Danian boundary, *Geochemistry,* (8), 1160–1178.

Neal C. R., Mahoney J. J., Kroenke L. W., et al. (1997), Ontong Java Plateau, in: *Large igneous provinces: Continental, oceanic and planetary flood basalts Geophysical Monograph Series 100,* edited by J. J. Mahoney and M. F. Coffin, pp. 183–216, AGU, Washington.

Neruchev S. G. (1999), Periodicity of Major Geological and Biological Events in the Phanerozoic, *Geol. Geofiz.,* (4), 493–511.

Nier A. O., Schlutter D. J., Brownlee D. E. (1990), Helium and neon isotopes in deep Pacific Ocean sediments, *Geochim. Cosmochim. Acta, 54,* 173–182, doi:10.1016/0016-7037(90)90205-Y.

Norman M. D., Garcia M. O., Bennet V. C. (2004), Rhenium and chalcophile elements in basaltic glasses from Ko'olau and Moloka'I volcanoes: Magmatic outgassing and composition of the Hawaiian plume, *Geochim. Cosmochim. Acta, 68,* 3761–3777, doi:10.1016/j.gca.2004.02.025.

Novakova A., Gendler T. S. (1995), Metastable structural-magnetic transformations in sulfides in course of oxidation, *J. Radioanal. Nucl. Chem. 190*(2), 363–368, doi:10.1007/BF02040013.

Officer Ch. B., Hallam A., Drake Ch. L., Devine J. D. (1987), Late Cretaceous and paroxysmal Cretaceous/Tertiary extinctions, *Nature, 326,* 143–148, doi:10.1038/326143a0.

Officer Ch. B., Drake Ch. L. (1985), Terminal Cretaceous environmental events, *Science, 227,* 1161, doi:10.1126/science.227.4691.1161.

Olmez I., Finnegan D. L., Zoller W. H. (1986), Iridium emission from Kilauea volcano, *J. Geoph. Res., 91,* 653–663, doi:10.1029/JB091iB01p00653.

Olsson R. K., Hemleben C., Berggren W. A., Huber B. T. (1999), Atlas of Paleocene planktonic foraminifera, *Smithson. Contrib. Paleobiol., 85*(I–VI), 1–252.

Olsson R. K., Miller K. G., Browning J. V., et al. (2002), Sequence Stratigraphy and Sea-Level Change across the Cretaceous–Tertiary Boundary on the New Jersey Passive Margin, *Geol. Soc. Am. Spec. Pap., 356,* 97–108.

O'Nions R. K. (1984), *Isotopic evolution of the crust and mantle/Patterns of change in Earth evolution,* pp. 291–302, Springer-Verlag, Berlin.

Ozima M., Takayanagi M., Zashu S., Amari S. (1984), High $^{3}He/^{4}He$ ratio in ocean sediments, *Nature, 311,* 448–450.

Pardo A., Adatte Th., Keller G., Oberhansli H. (1999), Paleoenvironmental changes across the Cretaceous-Tertiary boundary at Koshak, Kazakhstan, based on planktic foraminifera and clay mineralogy, *Palaeogeogr. Palaeoclimatol. Palaeoecol., 154,* 247–273, doi:10.1016/S0031-0182(99)00114-5.

Park C. C. (1987), *Acid rain: Rhetoric and reality,* 272 p., Methuen, N.Y.

Parkin D. W., Sullivan R. A. L., Andrews J. N. (1980), Further Studies on Cosmic Spherules from Deep-Sea Sediments, *Phil. Trans. R. Soc. London. Ser. A. Math. Phys. Sci., 297,* 495–518.

Pascoe E. H. (1964), *A Manual of the Geology of India and Burma,* Government of India, Calcutta.

Patterson D. B., Farley K. A., Norman M. D. (1999), ^{4}He as a tracer of continental dust: A 1.9 million year record of aeolian flux to the west equatorial Pacific Ocean, *Geochim. Cosmochim. Acta, 63,* 615–625, doi:10.1016/S0016-7037(99)00077-0.

Patterson T. R., Fowler A. D., Huber B. T. (2004), Evidence of hierarchical organization in the planktonic foraminiferal evolutionary record, *J. Foraminiferal Res., 34,* 85–95, doi:10.2113/0340085.

Pechersky D. M. (2007), The Geomagnetic Field at the Paleozoic/Mesozoic and Mesozoic/Cenozoic Boundaries and Lower Mantle Plumes, *Izv. Phys. Solid Earth, 42,* 844–854, doi:10.1134/S1069351307100072.

Pechersky D. M. (2008), Enrichment of Sediments in Iron Hydroxides at the Mesozoic-Cenozoic Boundary: A Synthesis of Petromagnetic Data, *Phys. Solid Earth, 44,* 232–238.

Pechersky D. M., Asanidze B. Z., Nourgaliev D. K., Sharonova Z. V. (2009), Petromagnetic and magnetostratigraphic characteristics of sediments at the Mesozoic-Cenozoic boundary: Tetritskaro (Georgia) section, *Izv. Phys. Solid Earth, 45,* (in press).

Pechersky D. M., Bagin V. I., Brodsky S. Yu., Sharonova Z. V. (1975), *Magnetism and magmatic rocks formation,* 288 p., Nauka, Leningrad.

Pechersky D. M., Didenko A. N. (1995), *Paleo-Asian Ocean,* 297 p., OIFZ RAN, Moscow.

Pechersky D. M., Garbuzenko A. V. (2005), The Mesozoic-Cenozoic Boundary: Paleomagnetic Characteristic, *Russian J. Earth Sci., 7*(2), doi:10.2205/2005ES000174.

Pechersky D. M., Grachev A. F., Nourgaliev D. K., Sharonova Z. V. (2008), Petromagnetic properties of sediments at the K/T boundary (Gams section, Austria), *Izv. Phys. Solid Earth, 44*(5), 55–74.

Pechersky D. M., Grachev A. F., Nourgaliev D. K., Tsel'movich V. A., Sharonova Z. V. (2006a), Magnetolithologic and magnetomineralogical characteristics of deposits at the Mesozoic/Cenozoic boundary: Gams section (Austria), *Russian J. Earth Sci., 8*(3) ES3001, doi:10.2205/2006ES000204.

Pechersky D. M., Nourgaliev D. K., Sharonova Z. V. (2006b), Magnetolithologic and Magnetomineralogical Characteristics of Sediments at the Mesozoic/Cenozoic Boundary: The Koshak Section (Mangyshlak Peninsula), *Izv. Phys. Solid Earth 42,* 957–970, doi:10.1134/S1069351306110097.

Peryt D., Lahodynsky R., Rocchia R., Boclet D. (1993), The Cretaceous-Paleogene boundary and planktonic foraminifera in the Flyschgosau (Eastern Alps, Austria), *Palaeogeogr. Palaeoclimatol. Palaeoecol., 104,* 239–252, doi:10.1016/0031-0182(93)90135-6.

Peybernes B., Fondecave-Wallez M.-J., Youssef M. B. (1996), Planktonic foraminifera and depositional sequences dated by the grade-dating method within the Cretaceous-Tertiary boundary type section of El Kef (NW Tunisia), *Revue de Micropaleontol, 39*(2), 125–136, doi:10.1016/S0035-1598(96)90032-X.

Philipp H., Eckhardt J.-D., Puchelt H. (2001), Platinum-group element (PGE) in basalts of the seaward-dipping reflector sequence, SE Greenland coast, *J. Petrol., 42,* 407–432, doi:10.1093/petrology/42.2.407.

Pik R., Deniel C., Coulon Ch., et al. (1998), The northwestern Ethiopian Plateau flood basalts: Classification and spatial distribution of magma types, *J. Volcanol. Geotherm. Res., 81,* 91–111.

Piller W. E., Egger H., Erhart C. W., et al. (2004), Die stratigraphische Tabelle von Österreich 2004 (sedimentäre Schichtfolgen).

Pitman W. C. (1978), III. Relationship between eustasy and stratigraphic sequences of passive margins, *Geol. Soc. Am. Bull., 89,* 1389–1403, doi: 10.1130/0016-7606(1978)89<1389:RBEASS>2.0.CO;2.

Pober E., Faupl P. (1988), The chemistry of detrital chromian spinel and its implications for the geodynamic evolution of the Eastern Alps, *Geol. Rundsch., 77,* 641, doi:10.1007/BF01830175.

Poreda R., Craig H. (1989), Helium isotope ratios in circum-Pacific volcanic arcs, *Nature, 338,* 473–479.

Power M. R., Pirrie D., Andersen C. O. (2003), Diversity of platinum-group element mineralization styles in the North Atlantic Igneous province: new evidence from Rum, UK, *Geol. Mag., 140,* 499–512, doi:10.1017/S0016756803008045.

Preisinger A., Aslanian S., Brandstatter F., Grass F., Stradner H., Summesberger H. (2002), Cretaceous–Tertiary profile, rhythmic deposition and geomagnetic polarity of marine sediments near Bjala, Bulgaria, *Geol. Soc. Am., Special Paper, 356,* 213.

Preisinger A., Zobetz E., Gratz A. J., Lahodynsky R., Becke M., Mauritsch H. J., Eder G., Grass F., Rögl F., Stradner H., Surenian R. (1986), The Cretaceous/Tertiary boundary in the Gosau Basin, Austria, *Nature, 322,* 797–799, doi:10.1038/322794a0.

Premoli Silva I., Sliter W. V. (1999), Cretaceous paleoceanography: Evidence from planktonic foraminiferal evolution, in: *Evolution of the Cretaceous ocean-climate system, Special Paper 332,* edited by E. Barrera and C. C. Johnson, pp. 301–328, Geological Society of America.

Qing H., Barnes Ch. R., Buhl D., Veizer J. (1998), The Strontium Isotopic Composition of Ordovician and Silurian Brachiopods and Conodonts: Relationships to Geological Events and Implications for Coeval Seawater, *Geochim. Cosmochim. Acta, 62,* 1721–1733, doi:10.1016/S0016-7037(98)00104-5.

Rampino M. R., Prokoph A., Adler A. C. (2000), Tempo of the end-Permian event: High-resolution cyclostratigraphy at the Permian-Triassic boundary, *Geology, 28,* 643–646, doi:10.1130/0091-7613(2000)28<643:TOTEEH>2.0.CO;2.

Rampino M. R., Self S., Strothers R. B. (1988), Volcanic Winters, *Ann. Rev. Earth Planet. Sci., 16,* 73–99, doi:10.1146/annurev.ea.16.050188.000445.

Raukas A. (2000), Investigation of Impact Spherules–A New Promising Method for the Correlation of Quaternary Deposits, *Quaternary Int., 68–71,* 214–252.

Raup D., Sepkoski J. (1982), Mass extinctions in the marine fossil record, *Science, 215,* 1501–1503, doi:10.1126/science.215.4539.1501.

Raup D., Sepkoski J. (1986), Periodic extinction of families

and genera, *Science, 231*(4740), 833–836, doi:10.1126/science.11542060.

Reichow M., Saunders A. D., White R. V., Pringle M. A., Al'Mukhamedov A., Medvedev A., Kirda N. P. (2002), $^{40}Ar/^{39}Ar$ dates from the West Siberian Basin: Siberian Flood Basalt Province doubled, *Science, 296,* 1846–1849.

Renne P. R., Basu A. R. (1991), Rapid eruption of the Siberian Traps flood basalts at the Permo-Triassic boundary, *Science, 253,* 176–179, doi:10.1126/science.253.5016.176.

Robertson D. J., France D. E. (1994), Discrimination of remanence-carrying minerals in mixtures, using isothermal remanent magnetization acquisition curves, *Phys. Earth Planet. Inter., 82,* 223–234, doi:10.1016/0031-9201(94)90074-4.

Robin E., Bonté Ph., Froget L. (1992), Formation of spinels in cosmic objects during atmospheric entry: A clue to the Cretaceous-Tertiary boundary event, *Earth Planet. Sci. Lett., 108,* 181, doi:10.1016/0012-821X(92)90021-M.

Robin E., Rocchia R., Lefevre I. (1991), The compositional variation of K/T spinel in Tunisia: Evidence for a global deluge of projectile debris, *Earth Planet. Sci. Lett., 107,* 715, doi:10.1016/0012-821X(91)90113-V.

Robin E., Swinburne N. H. M., Froget L., Rocchia R., Gayraud J. (1996), Characteristics and origin of the glass spherules from the Paleocene flood basalt province of western Greenland, *Geochim. Cosmochim. Acta., 60,* 815, doi:10.1016/0016-7037(95)00433-5.

Rocchia R., Boclet D., Bonté Ph., Jehanno C., Chen Y., Courtillot V., Mary C., Wezel F. (1990), The Cretaceous-Tertiary boundary at Gubbio revisited: vertical extent of the Ir anomaly, *Earth Planet. Sci. Lett., 99,* 206–219, doi:10.1016/0012-821X(90)90111-A.

Rochette P., Jackson M., Aubourg C. (1992), Rock magnetism and interpretation of anisotropy of magnetic susceptibility, *Rev. Geophys. 30,* 209–226.

Rodrigues-Tovar F. J., Martínez-Ruiz F., Bernasconi S. M. (2004), Carbon isotope evidence for the timing of the Cretaceous-Paleogene macrobenthic colonosation at the Agost section (southeast Spain), *Palaeogeogr. Palaeoclimatol. Palaeoecol., 203,* 65, doi:10.1016/S0031-0182(03)00660-6.

Rosen O. M., Ali A., Abbyasov A. A., Tipper J. C. (2004), MINLITH–an experience-based algorithm for estimating the likely mineralogical compositions of sedimentary rocks from bulk chemical analyses, *Comput. Geosci., 30,* 647, doi:10.1016/j.cageo.2004.03.011.

Rowe E. C., Schilling J. G. (1979), Fluorine in Iceland and Reykjanes ridge basalts, *Nature, 279,* 33–37.

Rowley D. B. (2002), Rate of plate creation and destruction: 189 Ma to present, *GSA Bull., 114,* 927–933.

Ryabchikov I. D. (1998), Fluid Regime of the Earth's Mantle, *Vestn. OGGGGN, Ross. Akad. Nauk, 3*(5).

Rychagov S. N., Glavatskich S. F., Sandimirova E. I. (1997), Ore ans silicate magnetic globules as an indicators of structure and fluid regime of modern hydrothermal system of Baransky volcano, Iturup Island, *Dokl. Russian Aca. Sci., 356,* 677.

Sanders D. Th. (1998), Tectonically controlled Late Cretaceous terrestrial to neritic deposition (Northern Calcareous Alps, Tyrol, Austria), *Facies, 39,* 139–178, doi:10.1007/BF02537015.

Sassano G. P., Schrijver K. (1989), Framboidal pyrite: Early-diagenetic, late-diagenetic and hydrothermal occurrences from the Acton Vale quarry, Cambro-Ordovician, Quebec, *Am. J. Sci., 289,* 167–179.

Sassi R., Mazzoli C., Miller Ch., Konzett J. (2004), Geochemistry and metamorphic evolution of the Pohorie mountain eclogites from the Austroalpine basement of the Eastern Alps (Northern Slovenia), *Lithos, 78,* 235, doi:10.1016/j.lithos.2004.05.002.

Saunders A. D., Fitton J. G., Kerr A. C., et al. (1997), The North Atlantic igneous province, in: it Large igneous provinces: continental, oceanic and planetary flood basalts Geophysical Monograph Series 100, edited by J. J. Mahoney and M. F. Coffin, pp. 45–93, AGU, Washington.

Schilling J.-K., Kingsley R. H., Hanan B. B., McCully B. L. (1992), Nd-Sr-Pb isotopic variations along the Gulf of Aden: Evidence for Afar mantle plume-continental lithosphere interaction, *J. Geophys. Res., 97,* 10,927–10,966, doi:10.1029/92JB00415.

Schilling J.-K., Zajac M., Evans R., Jonston T., White W., Devine J. D., Kingsley R. H. (1983), Petrologic variations along the Mid-Atlantic Ridge from 29°N to 73°N, *Am. J. Sci., 283,* 510–586.

Schlanger S. O., Jenkyns H. C., Premoli Silva I. (1981), Volcanism and Vertical Tectonics in the Pacific Basin Related to Global Cretaceous Transgressions, *Earth Planet. Sci. Lett., 52,* 435–449, doi:10.1016/0012-821X(81)90196-5.

Schlesinger W. H. (1997), *Biogeochemistry: An analysis of global change,* 2nd ed., CA: Academic Press, San Diego, 558 pp.

Schmitz B., Keller G., Stenvall O. (1992), Stable isotope and fo raminiferal changes across the Cretaceous-Tertiary boundary at Stevns Klint, Denmark: Arguments for long-term oceanic instability before and after bolide-impact event, *Palaeogeogr., Palaeoclimatol., Palaeoecol., 96,* 233–260.

Schmitz B., Lindstrom M., Asaro F., Tassinari M. (1996), Geochemistry of meteorite-rich limestone strata and fossil meteorites from the lower Ordovician at Kinnekulle, Sweden, *Earth Planet. Sci. Lett., 145,* 31–48, doi:10.1016/S0012-821X(96)00205-1.

Schulze D. I., Wiese D., Steude J. (1996), Abundance and distribution of diamonds in eclogites revealed by volume visualization of CT X-ray scans, *J. Geol., 104,* 109.

Sharma M., Basu A. R., Nesterenko G. V. (1992), Temporal Sr-, Nd-, and Pb-Isotopic Variations in the Siberian Flood Basalts: Implications for the Plume-Source Characteristics, *Earth Planet. Sci. Lett., 113,* 365–381, doi:10.1016/0012-821X(92)90139-M.

Shimpo M., Tsunogae T., Santosh M. (2006), First report of garnet-corundum rocks from southern India: implications for prograde high-pressure (eclogite-facies?) metamorphism, *Earth Planet. Sci. Lett., 242,* 111–129, doi:10.1016/j.epsl.2005.11.042.

Sholpo L. E. (1977), *Rock Magnetism Applications to Geological Problems,* 183 p., Nedra, Leningrad.

Siegl-Farkas A., Wagreich M. (1996), Correlation of palyno-(spores, pollen, dinoflagellates) and calcareous nannofossil zones in the Late Cetaceous of the Northern Calcareous Alps (Austria) and the Transdanubian Central Range (Hungary), *Advances Austro-Hungarian Joint Geological Research, 127,* 135.

Simandi G. J., Ferbey T., Levson V. M. (2005), Kimberlite and diamond indicator minerals in Northeast British Columbia, Canada – A reconnaissance survey, British Columbia Ministry of Energy, *Mines Petroleum Resources Geofile,* (25) 25 pp.

Smit J. (2005), The section of the Barranco del Gredero (Caravaca, SE Spain): A crucial section for the Cretaceous/Tertiary boundary impact extinction hypothesis, *Journal Iberian Geology, 31* (1), 179–191.

Smit J., Romein J. T. (1985), A Sequence of Events across the Cretaceous-Tertiary Boundary, *Earth Planet. Sci. Lett., 74,* 155–170, doi:10.1016/0012-821X(85)90019-6.

Smit J., Hertogen J. (1980), An extraterrestrial event at the Cretaceous-Tertiary boundary, *Nature, 285,* 198–200.

Smit J., Kyte F. T. (1984), Siderophile-Rich magnetic spheroids from the Cretaceous-Tertiary boundary in Umbria, *Nature, 310,* 403, doi:10.1038/310403a0.

Smit J., Roep T. B., Alvarez W., Montanari A. (1992), Coarse grained, clastic sandstone complex at the K/T boundary around the Gulf of Mexico: Deposition by tsunami waves induced by the Chicxulub impact?, *Geol. Soc. Am., Spec. Pap., 307,* 151.

Sobolev A. V., Nikogosyan I. K. (1994), Igneous Petrology of Long-Living Mantle Flows: The Hawaii (Pacific Ocean) and the Reunion Island (Indian Ocean), *Petrologiya, 2,* 131–168.

Sobolev N. V. (1974), *Deep Nodules in Kimberlites and the Problem of the Upper Mantle Composition,* 264 pp., Nauka, Novosibirsk.

Sobolev N. V., Logvinova A. M., Zedgenezov D. A., Seryotkina Y. V., Yefimova E. S., Floss Ch., Taylor L. A. (2004), Mineral inclusions in microdiamonds from kimberlites of Yakutia: A comparative study, *Lithos, 77*(1–4), 225–242. doi:10.1016/j.lithos.2004.04.001.

Sobolev N. V., Shatsky V. S. (1990), Diamond inclusions in garnets from metamorphic rocks: A new environment for diamond formation, *Nature, 343,* 742, doi:10.1038/343742a0.

Sobotovich E. V. (1976), *Cosmic Matter in the Earth's Crust,* Atomizdat, Moscow, 159 pp.

Sobotovich E. V., Bondarenko G. N., Koromyslechenko T. I. (1978), *Cosmic Matter in Oceanic Sediments and Glacial Covers,* Naukova Dumka, Kiev, 118 pp.

Spaun G. (1968), Die geologischen Vorarbeiten und der Sondierstollen des Ennskraftwerkes Landl (with a contribution by H. Kollmann), *Mitt. Ges. Geol. Bergbaustud., 18,* 341–366.

Stacey F. D. (1992), *Physics of the Earth,* 3rd ed., Brisbane, Brookfield, 513 pp.

Stadermann F. J., Floss Ch., Wopenka B. (2006), Circumstellar Aluminum Oxide and Silicon Carbide in Interplanetary Dust Particles, *Geochim. Cosmochim. Acta, 70,* 6168–6179, doi:10.1016/j.gca.2006.08.025.

Stankowski W. T. J., Katrusiak A., Budzianowski A. (2006), Crystallographic Variety of Magnetic Spherules from Pleistocene and Holocene Sediments in the Northern Foreland of Morasko-Meteorite Reserve, *Planet. Space Sci., 54,* 60–70, doi:10.1016/j.pss.2005.08.005.

Staples R. K., et al. (1997), Faroe-Iceland Ridge Experiment. 1. Crustal Structure of Northeastern Iceland, *J. Geophys. Res., 102,* pp. 7849–7866.

Stecher O. (1998), Fluorine Geochemistry in Volcanic Rock Series: Examples from Iceland and Ian Mayen, *Geochim. Cosmochim. Acta, 62,* 3117–3130, doi:10.1016/S0016-7037(98)00210-5.

Stevens R. E. (1944), Compositions of some chromites of the Western Hemisphere, *Am. Mineral., 29,* 1.

Stevenson D. S., Johnson C. E., Highwood E. J., Gauci V., Collins W. J., Derwent R. G. (2003), Atmospheric impact of the 1783–1784 Laki eruption: Part I Chemistry modeling, *Atmos. Chem. Phys., 3,* 487–507.

Stewart K., Turner S., Kelley S., et al. (1996), 3-D, ^{40}Ar–^{39}Ar geochronology in the Parana flood basalt from province, *Earth Planet. Sci. Lett., 143,* 95–109.

Stille P., Steinmann M., Riggs S. R. (1996), Nd Isotopic Evidence for the Evolution of the Paleocurrents in the Atlantic and Tethys Oceans during the Past 180 Ma, *Earth Planet. Sci. Lett., 144,* 9–19.

Stimac J., Hickmott D., Abell R., et al. (1996), Redistribution of PB and other volatile trace metals during eruption, devitrification and vapor-phase crystallization of the Bandekier Tuff, New Mexico, *J. Volcanol. Geoterm. Res., 73,* 254–256.

Stinnesbeck W., Keller G., Schulte P., et al. (2002), The Cretaceous–Tertiary (K/T) Boundary Transition at Coxquinhui, State Veracruz, Mexico: Evidence for an Early Danian Impact Event?, *J. South Am. Earth Sci., 15,* 497–509, doi:10.1016/S0895-9811(02)00079-2.

Storey B. C. (1995), The Role of Mantle Plumes in Continental Break-Up: Case Histories from Gondwanaland, *Nature (London), 377,* 301–308, doi:10.1038/377301a0.

Stradner H., Rögl F. (1988), Microfauna and nannoflora of the Knappengraben section (Austria) across the Cretaceous /Tertiary boundary, IGCP Project 199 Rare events in geology; Abstracts, *Berichte der Geologischen Bundesanstalt, 15,* 25–26.

Strakhov N. M. (1962), *Fundamentals of the Theory of Lithogenesis,* vol. 2, 574 pp., Nauka, Moscow.

Straub S. M., Schmincke H.-U. (1998), Evaluating the tephra input into Pacicfic ocean sediments: Distribution in space and time, *Geol. Rundsch., 87,* 461–476, doi:10.1007/s00531050222.

Stuben D., Kramar U., Berner Z., Stinnesbeck W., Keller G., Adatte Th. (2002), Trace elements and stable isotopes in foraminifera of the Elles II K/T profile: Indications for sea-level fluctuations and primary productivity, *Palaeogeogr. Palaeoclimatol. Palaeoecol., 178,* 321–345, doi:10.1016/S0031-0182(01)00401-1.

Stuben D., Kramar U., Harting M., Stinnesbeck W., Keller G. (2005), High-resolution geochemical record of Cretaceous-Tertiary boundary sections in Mexico: New constraints on the K/T and Chicxulub events, *Geochim. Cosmochim. Acta, 69*(10), 2559–2579, doi:10.1016/j.gca.2004.11.003.

Summesberger H. (1985), Ammonite zonation of the Gosau Group (Upper Cretaceous, Austria), *Ann. Naturhistor. Mus. Wien, 87,* 145–166.

Summesberger H., Kennedy W. J. (1966), Turonian ammonites from the Gosau Group (Upper Cretaceous, Northern Calcareous Alps, Austria) with a revision of Barroisiceras haberfellneri (Hauer), *Beitrage zur Palaonologie, 21,* 105–177.

Summesberger H., Wagreich M., Tröger K.-A., Jagt J. W. M. (1999), Integrated biostratigraphy of the Santonian/Campanian Gosau Group of the Gams area (Late Cretaceous; Styria, Austria), *Beitrage zur Palaontologie, 24,* 155–205.

Sutherland F. L., Coenraads R. R., Schwarz D., et al. (2003), Al-rich diopside in alluvial ruby and corundum-bearing xenoliths, Australian and SE Asian basalt fields, *Min. Magazine, 67,* 717–732.

Sutton A. J. (1992), A prototype system for continuous on-site chemical monitoring of volcanic gas and condensate with field testing at Kilauea, Hawaii, *Open File Rep. 92-678,* 169 pp., U.S. Geol. Surv.

Sutton A. J., Elias T., Gerlach T. M., Stokes J. B. (2001), Implications for eruptive processes as indicated by sulfur dioxide emissions from Kilauea volcano, Hawaii, 1979–1997, *J. Volcanol. Geotherm. Res., 108,* 283–302, doi:10.1016/S0377-0273(00)00291-2.

Sutton A. J., McGee K. A., Casadevall T. J., Stokes J. B. (1992), Fundamental volcanic-gas-study techniques: An integrated approach to monitoring, in: *Monitoring volcanoes: Techniques and strategies used by the staff of the Cascades Volcano Observatory, 1980-90,* edited by J. W. Ewert and D. A. Swan-

son, pp. 181–188, U.S. Geological Survey Bulletin 1966.
Swanson D. A., Wright T. L., Helz R. T. (1975), Linear vent systems and estimated rates of magma production and eruption for the Yakima basalt of the Columbia Plateau, *Am. J. Sci., 275,* 877–905.
Symonds R. B., Rose W. I., Bluth G. J. S., Gerlach T. M. (1994), Volcanic-gas studies: Methods, results, and applications, in: *Volatiles in Magmas, Reviews in Mineralogy,* vol. 30, edited by M. R. Carroll and J. R. Holloway, pp. 1–66.
Szoor Gy., Elekes Z., Rozsa P., et al. (2001), Magnetic Spherules: Cosmic Dust Or Markers of a Meteoritic Impact?, *Nucl. Instrum. Methods Phys. Res. Sect. B, 181,* 557–562.
Tandon S. K. (2002), Records of the influence of Deccan volcanism on contemporary sedimentary environments in Central India, *Sediment. Geol., 147,* 177.
Taylor S. R., McLennan S. M. (1985), *The Continental Crust: Its Composition and Evolution,* 151 pp., Blackwell, Oxford.
Ten Brink U. S., Brocher T. M. (1987), Multichannel seismic evidence for a subcrustal intrusive complex under Oahu and a model for Hawaiian Volcanism, *J. Geophys. Res., 92,* 13687–13707.
Tenailleau Ch., Pring A., Etschmann B., et al. (2006), Transformation of pentlandite to violarite under mild hydrothermal conditions, *Am. Mineral., 91,* 706–709, doi:10.2138/am.2006.2131.
Thiry M. (2000), Palaeoclimatic interpretation of clay minerals in marine deposits: An outlook from the continental origin, *Earth Sci. Rev., 49,* 201, doi:10.1016/S0012-8252(99)00054-9.
Thordarsson Th., Self S. (1993), The Laki (Skatfar Fires) and Grimsvotn eruptions in 1783–1785, *Bull. Volcanol., 55,* 233–263, doi:10.1007/BF00624353.
Thordarsson Th., Self S. (1996), Sulfur, chlorine, and fluorine degassing and atmospheric loading by the Roza eruption, Columbia River Basalt Group, Washington, USA, *J. Volcanol. Geotherm. Res., 74,* 49–73, doi:10.1016/S0377-0273(96)00054-6.
Thordarsson Th., Self S., Larson G., Steinthorsson S. (1987), Eruption sequence of the Skaftar Fires 1783–1785, Iceland, *Eos, 68,* 1550.
Thordarsson Th., Self S., Oskarson N., Hulsebosch T. (1996), Sulfur, chlorine, fluorine degassing and atmospheric loading by the 1783–1784 Laki (Skaftar Fires) eruption in Iceland, *Bull. Volcanol., 58,* 205–225, doi:10.1007/s004450050136.
Tolstikhin I. N. (1975), Helium isotopes in the Earth's interior and in the atmosphere: a degassing model of the Earth, *Earth Planet. Sci. Lett., 26,* 88–96, doi:10.1016/0012-821X(75)90180-6.
Tolstikhin I. N., Kamensky I. L., Marty B., et al. (1999), Low Mantle Component in 370 Ma Old Kola Ultrabasic-Alkaline-Carbonatite Complexes: Evidences from Rare Gas Isotopes and Related Trace Elements, *Russian J. Earth Sci.,* (2), 1.
Tolstikhin I. N., Lehmann B. E., Loosli H. H., Gautshi A. (1996), Helium and argon isotopes in rocks, minerals and related groundwaters: a case study in northern Switzerland, *Geochim. Cosmochim. Acta, 60,* 1497–1514, doi:10.1016/0016-7037(96)00036-1.
Toppani A., Libourel G. (2003), Factors controlling compositions of cosmic spinels: Application to atmospheric entry conditions of meteoritic materials, *Geochim. Cosmochim. Acta, 67,* 4621, doi:10.1016/S0016-7037(03)00383-1.
Toutain J.-P. (1989), Iridium-desring sublimates at a hot-spot volcano (Piton de la Fournaise, Indian ocean), *Geophys. Res. Lett., 16,* 1391–1394, doi:10.1029/GL016i012p01391.
Tripati A., Elderfield H. (2005), Deep-sea temperature and circulation changes at the Paleocene-Eocene thermal maximum, *Science, 308,* 1894–1898, doi:10.1126/science.1109202.
Trubitsyn V. P., Trubitsyn A. P. (2005), Evolution of mantle plumes and uplift of continents during the Pangea breakup, *Russian J. Earth Sci., 7,* 1–16, doi:10.2205/2005ES000179.
Trull T., Nadeau S. L., Pineau F., Polve M., Javoy M. (1993), C–He Systematics in Hotspot Xenoliths: Implications for Mantle Carbon Contents and Carbon Recycling, *Earth Planet. Sci. Lett., 118,* 43–64, doi:10.1016/0012-821X(93)90158-6.
Turko R. P., Tun O. B., Akkerman T. P., Pollack J. B., Sagan L. (1984), Climatic Consequences of a Nuclear War, *V Mire Nauki,* (10), 4.
Vail P. R., et al. (1977), Seismic strtigraphy and global changes of sea level, *Am. Assoc. Pet. Geol. Memoir,* (26), 49–212.
VanDecar J. C., James D. E., Assumpcao M. (1995), Seismic Evidence for a Fossil Mantle Plume beneath South America and Implications for Plate Driving Forces, *Nature, 378,* 25–31, doi:10.1038/378025a0.
Veizer J., Ala D., Azmy K., et al. (1999), $^{87}Sr/^{86}Sr$, $\delta^{12}C$, $\delta^{18}O$, Evolution of Phanerozoic Seawater, *Chem. Geol., 161,* 59–88, doi:10.1016/S0009-2541(99)00081-9.
Villasante-Marcos V., Martínez-Ruiz F., Osete M. L., Urrutiafucugauchi J. (2007), Magnetic characterization of Cretaceous-Tertiary boundary sediments, *Meteorit. Planet. Sci., 42*(9), 1505–1527.
Vogt P. R. (1975), Changes in Geomagnetic Reversals Frequency at Times of Tectonic Change: Evidence for Coupling between Core and Upper Mantle, *Earth Planet. Sci. Lett., 25,* 313–321, doi:10.1016/0012-821X(75)90247-2.
Vonsovskii S. V. (1971), *Magnetism,* Nauka, Moscow, 1031 pp.
Wagreich M. (1993), Subcrustal tectonic erosion belts – A model for the Late Cretaceosu subsidence of the Northern Calcareous Alps (Austria), *Geology, 21,* 941–944.
Wagreich M. (1994), Bericht über geologische Aufnahmen in Oberkreide- und Tertiärsedimenten der Nördlichen Kalkalpen auf den Blättern 100 Hieflau und 101 Eisenerz, *Jahrbuch der Geologischen Bundesanstalt, 137,* 477–478.
Wagreich M. (1995), Subduction tectonic erosion and Late Cretaceous subsidence along the northern Austroalpine margin (Eastern Alps, Austria), *Tectonophysics, 242,* 63–78.
Wagreich M. (2001), Paleocene – Eocene paleogeography of the Northern Calcareous Alps (Gosau Group, Austria), in: *Paleogene of the Eastern Alps,* edited by E. Piller and M. W. Rasser, pp. 57–75, Österreichische Akademie der Wissenschaften, Schriftenreihe der Erdwissenschaftlichen Kommissionen, 14.
Wagreich M. (2004), Biostratigraphy and lithostratigraphy of the Krimpenbach Formation Upper Santonian – Campanian), Gosau Group of Gams (Austria), *Ann. Naturhistor. Mus. Wien, 106A,* 123–138.
Wagreich M., Faupl P. (1994), Palaeogeography and geodynamic evolution of the Gosau Group of the Northern Calcareous Alps (Late Cretaceous, Eastern Alps, Austria), *Palaeogeogr. Palaeoclimatol. Palaeoecol., 110,* 235–254, doi:10.1016/0031-0182(94)90086-8.
Wagreich M., Krenmayr H.-G. (1993), Nannofossil biostratigraphy of the Late Cretaceous Nierental Formtion, Northern Calcareous Alps (Bavaria, Austria), *Zitteliana, 20,* 67–77.
Wallace P. J. (1998), Water and Partial Melting in Mantle Plumes: Inferences from the Dissolved H_2O Concentrations of Hawaiian Magmas, *Geophys. Res. Lett., 25,* 3639–3642, doi:10.1029/98GL02805.
Wardell L. J., Kyle P. R., Chaffin C. (2004), Carbon dioxide and

carbon monoxide emission rates from an alkaline intraplate volcano: Mt. Erebus, Antarctica, *J. Volcanol. Geotherm. Res., 131,* 109–121, doi:10.1016/S0377-0273(03)00320-2.

Watts A. B., Ten Brink U. S. (1989), Crustal structure, flexure and subsidence history of the Hawaiian islands, *J. Geophys. Res., 94,* 10,473–10,500.

Wdowiak T. J., Armendarez L. P., Agresti D. G., Wade M. L., Wdowiak S. Y., Claeys Ph., Izett G. (2001), Presence of an iron-rich nanophase material in the upper layer of the Cretaceous-Tertiary boundary clay, *Meteorit. Planet. Sci., 36,* 123–133.

Weigel O. (1937), Stratigraphie und Tektonik des Beckens von Gosau, *Jahrbuch der Geologischen Bundesanstalt, 87,* 11–40.

Weis D., Frey F. A. (1991), Isotope geochemistry of Ninetyeast Ridge basalts: Sr, Nd, and Pb evidence for the involvement of the Kerguelen hot spot, in: *Proceedings of the Ocean Drilling Program,* edited by J. Weissel, J. Peirce, E. Taylor, J. Alt, et al., pp. 591–610, Scientific Results, 121. College Station, TX: Ocean Drilling Program.

Wessel P. (1993), A Reexamination of the Flexural Deformation beneath the Hawaiian Islands, *J. Geophys. Res., 98,* 12,177–12,190, doi:10.1029/93JB00523.

White R. V., Saunders A. D. (2005), Volcanism, impact and mass extinctions: incredible or credible coincidences?, *Lithos, 79,* 299–316, doi:10.1016/j.lithos.2004.09.016.

White R., McKenzie D. (1995), Mantle Plumes and Flood Basalts, *J. Geophys. Res., 100,* 17,543–17,585, doi:10.1029/95JB01585.

Wicher C. A. (1956), Die Gosau-Schichten im Becken von Gams(Österreich) und die Foraminiferengliederung der höheren Oberkreide der Tethys, *Paläontologische Zeitschrift, 30,* 87–136.

Winckler G., Fisher H. (2006), 30,000 Years of Cosmic Dust in Antarctic Ice, *Science, 313,* 491, doi:10.1126/science.1127469.

Wignall P. B., Newton R., Brookfield M. E. (2005), Pyrite framboid evidence for oxygen-poor deposition during the Permian-Triassic crisis in Kashmir, *Palaeogeogr., Palaeoclimatol., Palaeoecol., 216,* 183–188.

Wille-Janoschek U. (1996), Stratigraphie und Tektonik der Schichten der Oberkreide und des Alttertiärs im Raume von Gosau und Abtenau (Salzburg), *Jahrbuch der Geologischen Bundesanstalt, 109,* 91–172.

Worm H. U., Banerjee S. K. (1987), Rock magnetic signature of the Cretaceous-Tertiary boundary, *Geophys. Res. Lett., 14,* 1083–1086, doi:10.1029/GL014i011p01083.

Wyllie P. J., Ryabchikov I. D. (2000), Volatile components, magmas and critical fluids in upwelling mantle, *J. Petrol., 41*(7), 1195–1206, doi:10.1093/petrology/41.7.1195.

Xu S., Okay A. I., Sengor A. (1992), Diamond from the dabie shan metamorphic rocks and its implications for tectonic setting, *Science, 256,* 80, doi:10.1126/science.256.5053.80.

Yada T., Nakamura T., Takaoka N., et al. (2004), The Global Accretion Rate of Extraterrestrial Materials in the Last Glacial Period Estimated from the Abundance of Micrometeorites in Antarctic Glacier Ice, *Earth Planets Space 56,* 67–79.

Yampolskaya O. B., Pimenov M. V., Fomin V., Guzhikov A., Yakovishina E. V., Bronnikova Yu. A. (2004), Magnetic properties of Cretaceous-Paleogene boundary deposits in the Mountainous Crimea: Preliminary results, in: *Paleomagnetism and Magnetism of Rocks,* Theory, Practice, and Experiment, pp. 276–279, KGU, Kazan.

Yasonov P. G., Nourgaliev D. K., Bourov N. V., Heller F. (1998), A modernized coercivity spectrometer, *Geol. Carpathica, 49*(3), 224–226.

Zachos J. C., Rohl U., Schellenberg S. A., et al. (2006), Rapid acidification of the ocean during the Paleocene-Eocene thermal maximum, *Science, 308,* 1611–1615, doi:10.1126/science.1109004.

Zakrzewski M. (1989), Chromian spinel from Kusa, Bergslagen, Sweden, *Am. Mineral., 74,* 448.

Zhang Y. (2005), Global tectonic and climatic control of mean elevation of continents and Phanerozoic sea-level change, *Earth Planet. Sci. Lett., 237,* 524–531, doi:10.1016/j.epsl.2005.07.015.

Zhang R. Y., Liou J. G., Zheng J. P. (2004), Ultra-high-pressure corundum-rich garnetite in garnet peridotite, Sulu terraine, China, *Contrib. Mineral. Petrol., 147*, 21–31, doi:10.1007/s00410-003-0545-z

Zhao Z. K., Mao X. Y., Chai Z. F., Yang G. Ch., Kong P., Ebihara M., Zhao Z. H. (2002), A possible causal relationship between extinction of dinosaurs and K/T iridium enrichment in the Nanxiong Basin, South China: evidence from dinosaur eggshells, *Palaeogeogr. Palaeoclimat. Palaeoecol., 178,* 1, doi:10.1016/S0031-0182(01)00361-3.

Zhou L., Kyte F. T. (1988), The Permian-Triassic boundary event: A geochemical study of three Chinede sections, *Earth Planet. Sci. Lett., 90,* 411, doi:10.1016/0012-821X(88)90139-2.

Zhu B., Delano J. W., Kidd W. S. F. (2005), Magmatic compositions and source terranes estimated from melt inclusions in detrital Cr-rich spinels: An example from mid-cretaceous sandstones in the Eastern Tethys Humalaya, *Earth Planet. Sci. Lett., 233,* 295, doi:10.1016/j.epsl.2005.02.001.

Zhu B., Kidd W. S. F., Rowley D. B., Currie B. S. (2004), Chemical compositions and tectonic significance of chrome-rich spinels in the Tianba Flysch, Southern Tibet, *J. Geol., 112,* 417, doi:10.1086/421072.

Zindler A., Hart S. (1986), Chemical geodynamics, *Ann. Rev. Earth Planet. Sci., 14,* 493–571.

Znamenskii V. S., Korzhinskii M. A., Shteinberg G. S., et al. (2005), Rheniite (ReS_2)—A Natural Rhenium Disulfide from Fumaroles of Kudryavyi Volcano (Iturup Island, the Kurile Archipelago), *Zapiski Ross. Mineral. O-va,* (5), 32–39.

Zoller W. H., Parrington J. R., Kotra J. M. P. (1983), Iridium enrichment in airborne particles from Kilauea volcano, January 1983, *Science, 222,* 1118–1120.

Zolotukhin V. V., Vasiliev Yu. R., Dyuzhikov O. A. (1989), *Diversity of flood basalts and their parental magmas: An example of the Siberian Platform,* 245 pp., Nauka, Novosibirsk.

Zreda-Gostynska G., Kyle P. R., Finnegan D. L. (1993), Chlorine, fluorine, and sulfur emissions from Mount Erebus, Antarctica and estimated contributions to the Antarctic atmosphere, *Geophys. Res. Lett., 20,* 1959–1962, doi:10.1029/93GL01879.

Electronic Supplement

This section is titled as *Electronic Supplement* following the tradition. In fact electronic version of this book is the basic one, the so-called "version of record," while POP (printed-on-paper) version has the status of "print companion." The electronic version is freely accessible on web sites of The Geological Survey of Austria (`http://www.geologie.ac.at/`) and Geophysical Center, Russian Academy of Sciences (`http://eos.wdcb.ru`).

The electronic version of this book includes thousands of internal links to and from floats (figures and tables) and to items in the References section. Items registered in CrossRef have active links to the corresponding response pages. The Author Index section is enhanced with back referencing option. Note, that page numbers in bold provide links to corresponding reference items in the References section, while page numbers in italic provide links to particular spots on pages where in-text reference to the work of corresponding author is placed. That is why some page numbers in italic can occur twice and more.

To explore all the capabilities of the electronic version we recommend to use Adobe Acrobat Reader, versions 8 and later.

Author Index

Subject Index